UNIVERSITY OF NAPLES FEDERICO II
Department of Structural Engineering

PH.D. PROGRAMME IN SEISMIC RISK
COORDINATOR PROF. ALDO ZOLLO
XXIII CYCLE

FULVIO PARISI

PH.D. THESIS

Non-Linear Seismic Analysis of Masonry Buildings

TUTOR PROF. NICOLA AUGENTI

2010

ACKNOWLEDGMENTS

I would express my sincere gratitude to Prof. Nicola Augenti for initiating and supporting me in analytical and experimental research on masonry constructions. His guidance has given me the chance to develop an 'unshakeable' scientific methodology and deep love for research. I am also grateful to him and Prof. Gaetano Manfredi for giving me the opportunity to work in an outstanding academic department and to exploit my passion for earthquake engineering. Without their support, this significant achievement would not have been possible.

I wish to acknowledge the contribution of the Italian Network of University Laboratories for Earthquake Engineering (ReLUIS), whose support has been essential especially to carry out experimental research in the framework of ReLUIS-DPC 2005-2008 project funded by the Italian Department of Civil Protection.

A great acknowledgment is due to Dr. Andrea Prota and Dr. Gian Piero Lignola for their precious collaboration and suggestions in some experimental and numerical investigations. Their devotion to research is a model for me.

I would like to thank also my colleagues and friends in the Department of Structural Engineering, for sharing this 'adventure' with me and exchanging knowledge about several topics. Special thanks to Carmine, Simona and Fabio for making me feel like home in a work environment.

Finally, I am particularly grateful to all my family for their love, patience and support every day during my Ph.D. studies.

TABLE OF CONTENTS

LIST OF FIGURES ..... **IX**

LIST OF TABLES ..... **XV**

LIST OF ABBREVIATIONS ..... **XVII**

ABSTRACT ..... **XIX**

CHAPTER 1 - INTRODUCTION **1**

1.1. FOREWORD 1
1.2. RESEARCH OBJECTIVES 2
1.3. THESIS OUTLINE 4

CHAPTER 2 - STRUCTURAL ANALYSIS **6**

2.1. LINEAR VERSUS NON-LINEAR ANALYSIS 6
2.2. STATIC VERSUS DYNAMIC ANALYSIS 8
2.2.1. Time-Domain Analysis 10
2.2.2. Frequency-Domain Analysis 12

CHAPTER 3 - SEISMIC RISK **14**

3.1. SEISMIC HAZARD 15
3.2. EXPOSURE 19
3.3. SEISMIC VULNERABILITY 19
3.4. MITIGATION OF SEISMIC RISK 20

CHAPTER 4 - SEISMIC DESIGN OF STRUCTURES **22**

4.1. PERFORMANCE-BASED DESIGN 22
4.1.1. Brief History of Performance-Based Standards 23
4.1.2. Fundamentals of Performance-Based Design 25
4.1.3. Intensity, Demand, and Damage Measures 28
4.1.4. Decision-making in Performance-Based Design 29
4.2. STRUCTURAL MODELLING 31
4.2.1. General Remarks 31
4.2.2. Lumped Plasticity Modelling 32
4.2.3. Spread Plasticity Modelling 34
4.3. SEISMIC DESIGN CRITERIA AND DETAILING RULES 36
4.3.1. Key Design Parameters 40
4.3.2. Structural Regularity 42
4.4. FORCE-BASED VERSUS DISPLACEMENT-BASED DESIGN 46

CHAPTER 5 - NON-LINEAR STATIC PROCEDURES **49**

5.1. ESTIMATION OF SEISMIC CAPACITY 49
5.1.1. General Remarks 49
5.1.2. Force-Based versus Displacement-Based Procedures 52

5.1.3. Control Strategies 54
5.1.4. Single-Mode versus Multi-Mode Procedures 55
5.1.5. Constant versus Adaptive Load Profiles 57
5.1.6. Three-Dimensional Effects 63
5.1.7. Non-Linear Static Analysis according to EC8, FEMA356 and Italian Building Code 66
5.2. ESTIMATION OF SEISMIC DEMAND AND PERFORMANCE 67
5.2.1. The Capacity Spectrum Method 67
5.2.2. The Displacement Coefficient Method 71
5.2.3. The N2 Method 73

CHAPTER 6 - SEISMIC ANALYSIS OF MASONRY BUILDINGS 80

6.1. IN-PLANE FAILURE MODES OF URM WALLS 81
6.2. THE RAN METHOD 82
6.2.1. Foreword 82
6.2.2. Fundamental Assumptions 82
6.2.3. Open issues 84
6.2.4. Analysis Steps 85
6.2.5. Geometrical Modelling and Boundary Conditions 85
6.2.6. Flexural Strength Domains of Pier Panels 86
6.2.7. Flexural Strength Domains of Spandrel Panels 89
6.2.8. Shear Strength Domains 90
6.2.9. Force-Displacement Diagrams 92
6.2.10. Global Analysis and Estimation of Strength Demands 96
6.2.11. Assessment of Lateral Load-Bearing Capacity 98
6.3. THE SAM METHOD 99
6.3.1. Foreword 99
6.3.2. The Pier Element 99
6.3.3. The Spandrel Element 101
6.3.4. Modelling and Analysis of the Building 102
6.4. THE TREMURI COMPUTER PROGRAM 104
6.4.1. Foreword 104
6.4.2. The Masonry Macro-element 105
6.4.3. Modelling and Analysis of the Building 111

CHAPTER 7 - THE EVOLUTIONARY SPREAD PLASTICITY MACRO-ELEMENT 113

7.1. NON-LINEAR BEHAVIOUR OF THE MACRO-ELEMENT 113
7.2. STRENGTH DOMAINS 117
7.2.1. Pier Panels 118
7.2.2. Spandrel Panels 137
7.3. THREE-DIMENSIONAL STRENGTH DOMAINS 154
7.3.1. Strength Domains for EPP Constitutive Model 156
7.3.2. Strength Domains for Turnšek-Čačovič Constitutive Model 163
7.3.3. Strength Domains for EC6 Constitutive Model 169
7.3.4. Strength Domains for Augenti-Parisi Constitutive Model Related to Compression Orthogonal to Mortar Bed Joints 175
7.3.5. Strength Domains for Augenti-Parisi Constitutive Model Related to Compression Parallel to Mortar Bed Joints 181
7.4. MOMENT-CURVATURE DIAGRAMS 188
7.4.1. Moment-Curvature Diagrams for EPP Constitutive Model 191
7.4.2. Moment-Curvature Diagrams for Turnšek-Čačovič Constitutive Model 192

7.4.3. Moment-Curvature Diagrams for EC6 Constitutive Model 194
7.4.4. Moment-Curvature Diagrams for Augenti-Parisi Constitutive Model Related to Compression Orthogonal to Mortar Bed Joints 196
7.4.5. Moment-Curvature Diagrams for Augenti-Parisi Constitutive Model Related to Compression Parallel to Mortar Bed Joints 197
7.4.6. Remarks 199
7.5. FORCE-DISPLACEMENT DIAGRAMS 201
7.5.1. Force-Displacement Diagrams of Macro-Elements 201
7.5.2. Force-Displacement Diagrams of Wall Storeys 211

CHAPTER 8 - NEW STATIC PUSHOVER PROCEDURES 214

8.1. PUSHOVER ANALYSIS OF MASONRY WALLS WITH OPENINGS 215
8.2. PUSHOVER ANALYSIS OF MASONRY BUILDINGS 218
8.2.1. Non-Adaptive Pushover Analysis 220
8.2.2. Adaptive Pushover Analysis 224

CHAPTER 9 - APPLICATION ON A MASONRY BUILDING 227

9.1. DESCRIPTION OF THE STRUCTURE 227
9.2. SEISMIC HAZARD ASSESSMENT 229
9.2.1. Framework and Methodology 229
9.2.2. Seismic Hazard at the Site of the Building 230
9.3. NON-LINEAR ANALYSES 231
9.3.1. Methodology 231
9.3.2. Discussion of Results 232
9.4. DAMAGE MAPS 238
9.5. CONCLUDING REMARKS 240

CHAPTER 10 - CONCLUSIONS AND POTENTIAL FUTURE DEVELOPMENTS 242

10.1. RESEARCH OUTCOMES 242
10.1.1. Flexural Strength Domains and their Evolution 242
10.1.2. Moment-Curvature Diagrams, Flexural Strength and Ductility of URM Cross-Sections 244
10.1.3. Force-Displacement Diagrams 244
10.1.4. Pushover Procedures for Masonry Walls and Buildings 245
10.1.5. Experimental Outcomes Supporting Non-Linear Analysis 246
10.2. POTENTIAL FUTURE DEVELOPMENTS 247

REFERENCES 249

APPENDIX A - EXPERIMENTAL TESTING FOR CONSTITUTIVE MODELLING IN COMPRESSION 263

A.1. RESEARCH OBJECTIVES 264
A.2. NON-LINEAR BEHAVIOUR OF MASONRY IN COMPRESSION 264
A.3. MATERIALS USED FOR EXPERIMENTAL TESTING 265
A.4. EXPERIMENTAL PROGRAM AND MAIN RESULTS 266
A.4.1. Experimental Setup and Test Protocol 266
A.4.2. Compression Tests in the Direction Orthogonal to Bed Joints 266
A.4.3. Compression Tests in the Direction Parallel to Bed Joints 269
A.5. PROBABILISTIC DATA SETS AND CONSTITUTIVE EQUATIONS 271
A.5.1. Masonry Subjected to Compression in the Direction Orthogonal to Bed Joints 271
A.5.2. Masonry Subjected to Compression in the Direction Parallel to Bed Joints 274

APPENDIX B - EXPERIMENTAL TESTING FOR CONSTITUTIVE MODELLING IN SHEAR 276

B.1. RESEARCH OBJECTIVES 277
B.2. EXPERIMENTAL PROGRAM 277
B.2.1. Materials and Tested Specimens 278
B.2.2. Experimental Setup and Test Protocol 279
B.3. PROCESSING OF EXPERIMENTAL DATA 281
B.3.1. Experimental Constitutive Curves 281
B.3.2. Strength and Deformation Parameters 283
B.3.3. Shear Modulus, Fracture Energy and Dilatancy 283
B.4. CHARACTERISATION OF MOHR-COULOMB STRENGTH MODEL 287
B.5. DEVELOPMENT OF A SHEAR RESPONSE SURFACE 289

APPENDIX C - EXPERIMENTAL TESTING FOR NON-LINEAR SEISMIC ANALYSIS 293

C.1. RESEARCH OBJECTIVES 294
C.2. EXPERIMENTAL PROGRAM 294
C.2.1. Design of the Tested Wall 294
C.2.2. Geometry of the As-Built Wall and Material Properties 295
C.2.3. Geometry of the Repaired Wall and Material Properties 296
C.2.4. Experimental Setup and Instrumentation 298
C.2.5. Loading Protocols 301
C.3. DAMAGE PATTERNS 302
C.4. ANALYSIS OF EXPERIMENTAL FORCE-DISPLACEMENT CURVES 305
C.5. IDEALISATION OF EXPERIMENTAL FORCE-DISPLACEMENT CURVES 309

LIST OF FIGURES

Figure 3.1 Seismic hazard at a site (adapted from Lanzo and Silvestri, 1999) 17
Figure 4.1 Damage levels under increasing seismic intensity (adapted from Hamburger) 27
Figure 4.2 Performance matrix in Vision 2000 27
Figure 4.3 Definition of spread plasticity macro-elements within masonry walls 34
Figure 4.4 Fibre modelling of a reinforced concrete beam (Manfredi et al., 2007) 35
Figure 4.5 Displacement ductility demand versus lateral strength capacity 38
Figure 4.6 Ductility versus strength reduction factor (adapted from Park and Paulay, 1975) ... 39
Figure 4.7 Flexural and shear damage of a pier panel 41
Figure 5.1 Non-linear incremental static (pushover) analysis 50
Figure 5.2 Pushover curves for different force patterns (Mwafy and Elnashai, 2001) 53
Figure 5.3 Modification of spectral amplification for first and second modes (Antoniou, 2002) 56
Figure 5.4 Effects of spectral amplification on pushover curve (Antoniou and Pinho, 2004a) . 58
Figure 5.5 Total updating of force pattern (Antoniou, 2002) 59
Figure 5.6 Pushover curve from adaptive analysis and force pattern variation (Antoniou, 2002) 59
Figure 5.7 Incremental updating of force pattern (Antoniou, 2002) 60
Figure 5.8 Comparison between conventional force-based analysis, non-adaptive displacement-based analysis, and IDA (Antoniou and Pinho, 2004b) 62
Figure 5.9 Total versus incremental updating in DAP (Antoniou and Pinho, 2004b) 62
Figure 5.10 BST surface (De la Llera and Chopra, 1995) 65
Figure 5.11 Graphic representation of CSM (Mwafy, 2001) 70
Figure 5.12 Graphic representation of DCM 71
Figure 5.13 Definition of ductility-related strength reduction factor (Fajfar, 1999) 76
Figure 5.14 Displacement demand estimation for (a) low- and (b) high-period structures 76
Figure 6.1 In-plane failure modes of URM panels 82
Figure 6.2 Macro-element modelling of a masonry wall with openings 82
Figure 6.3 Labelling of panels within the *k*-th wall of a masonry building 86
Figure 6.4 Limit states for eccentric compression 87
Figure 6.5 Flexural strength domains of a pier panel 88

Figure 6.6 Flexural strength domain of a spandrel panel 89
Figure 6.7 Strength domains for (a) squat panel and (b) slender panel 91
Figure 6.8 Types of force-displacement diagrams for pier panels 93
Figure 6.9 Frame-equivalent idealisation of a masonry wall with openings 99
Figure 6.10 Pier element and effective height 100
Figure 6.11 Types of lateral behaviour of the spandrel element (Magenes et al., 2001) 102
Figure 6.12 Kinematic and static parameters of the macro-element 105
Figure 6.13 Elasto-plastic lateral behaviour of a masonry panel 110
Figure 7.1 Comparison between constitutive laws of masonry under uniaxial compression 114
Figure 7.2 Evolution of the macro-element under varying deformation demand 115
Figure 7.3 Limit states for eccentric compression 118
Figure 7.4 Turnšek-Čačovič constitutive law 119
Figure 7.5 Strength domains at CLS and ELS for Turnšek-Čačovič constitutive law 123
Figure 7.6 Comparison between strength domains at ULS 125
Figure 7.7 EC6 constitutive law 126
Figure 7.8 Polynomial approximation of EC6 constitutive law 127
Figure 7.9 Strength domains at CLS and ELS for EC6 constitutive law 130
Figure 7.10 Comparison between strength domains at ULS 131
Figure 7.11 Augenti-Parisi constitutive laws (typical form for both directions) 133
Figure 7.12 Strength domains at CLS and ELS for Augenti-Parisi model (orthog. dir.) 134
Figure 7.13 Comparison between strength domains at ULS 135
Figure 7.14 Comparison between strength domains at CLS and ELS 136
Figure 7.15 Comparison between strength domains at ULS for strain ductility $\mu_\varepsilon = 1.75$ 137
Figure 7.16 Strength domains at ELS and ULS for EPP constitutive law 140
Figure 7.17 Strength domains at ELS and ULS for Turnšek-Čačovič law 142
Figure 7.18 Strength domains at ELS and ULS for EC6 constitutive law 143
Figure 7.19 Strength domains at ELS and ULS for Augenti-Parisi constitutive law (paral. dir.) 146
Figure 7.20 Comparison between strength domains at ELS 146
Figure 7.21 Comparison between strength domains at ULS 147
Figure 7.22 Comparison between strength domains at ULS for strain ductility $\mu_\varepsilon = 1.75$ 147
Figure 7.23 Strength domain evolution under increasing strain ductility (Turnšek-Čačovič law) 148
Figure 7.24 Ultimate bending moment versus strain ductility (Turnšek-Čačovič model) 149

Figure 7.25 N/N_m–$M/(N_m \cdot H)$–μ_ε strength domain for Turnšek-Čačovič model 150
Figure 7.26 N/N_m–μ_ε surface for Turnšek-Čačovič model 150
Figure 7.27 $M/(N_m \cdot H)$–μ_ε surface for Turnšek-Čačovič model 151
Figure 7.28 Strength domain evolution under varying strain ductility (Augenti-Parisi model) 151
Figure 7.29 Ultimate bending moment versus strain ductility (Augenti-Parisi model) 152
Figure 7.30 N/N_m–$M/(N_m \cdot H)$–μ_ε strength domain for Augenti-Parisi model 152
Figure 7.31 N/N_m–μ_ε surface for Augenti-Parisi model 153
Figure 7.32 $M/(N_m \cdot H)$–μ_ε surface for Augenti-Parisi model 153
Figure 7.33 Internal and external forces acting on the masonry panel 154
Figure 7.34 Three-dimensional strength domain at ELS for EPP model 159
Figure 7.35 Three-dimensional strength domain at ULS for EPP model 159
Figure 7.36 V/N_m–N/N_m strength domains for EPP model: (a) ELS; (b) ULS 160
Figure 7.37 V/N_m–e/H strength domains for EPP model: (a) ELS; (b) ULS 162
Figure 7.38 Three-dimensional strength domain at ELS for Turnšek-Čačovič model 166
Figure 7.39 Three-dimensional strength domain at ULS for Turnšek-Čačovič model 166
Figure 7.40 V/N_m–N/N_m strength domains for Turnšek-Čačovič model: (a) ELS; (b) ULS 167
Figure 7.41 V/N_m–e/H strength domains for Turnšek-Čačovič model: (a) ELS; (b) ULS 169
Figure 7.42 Three-dimensional strength domain at ELS for EC6 model 172
Figure 7.43 Three-dimensional strength domain at ULS for EC6 constitutive model 173
Figure 7.44 V/N_m–N/N_m strength domains for EC6 model: (a) ELS; (b) ULS 174
Figure 7.45 V/N_m–e/H strength domains for EC6 model: (a) ELS; (b) ULS 175
Figure 7.46 Three-dimensional strength domain at ELS for Augenti-Parisi model (orthog. dir.) 178
Figure 7.47 Three-dimensional strength domain at ULS for Augenti-Parisi model (orthog. dir.) 178
Figure 7.48 V/N_m–N/N_m domains for Augenti-Parisi model (orthog. dir.): (a) ELS; (b) ULS . 179
Figure 7.49 V/N_m–e/H domains for Augenti-Parisi model (orthog. dir.): (a) ELS; (b) ULS 181
Figure 7.50 Three-dimensional strength domain at ELS for Augenti-Parisi model (paral. dir.) 184
Figure 7.51 Three-dimensional strength domain at ULS for Augenti-Parisi model (paral. dir.) 185
Figure 7.52 V/N_m–N/N_m domains for Augenti-Parisi model (paral. dir.): (a) ELS; (b) ULS ... 186

Figure 7.53 V/N_m–e/H domains for Augenti-Parisi model (paral. dir.): (a) ELS; (b) ULS 188
Figure 7.54 Behaviour of URM cross-section under (a) low compression and large curvature and (b) high compression and small curvature 189
Figure 7.55 Characteristic points of normalised moment-curvature diagram 190
Figure 7.56 Moment-curvature diagrams for EPP model 191
Figure 7.57 Variation in curvatures and curvature ratios for EPP model 191
Figure 7.58 Moment-curvature diagrams for Turnšek-Čačovič model 193
Figure 7.59 Variation in curvatures and curvature ratios for Turnšek-Čačovič model 193
Figure 7.60 Moment-curvature diagrams for EC6 model 194
Figure 7.61 Variation in curvatures and curvature ratios for EC6 model 195
Figure 7.62 Moment-curvature diagrams for Augenti-Parisi model (orthog. dir.) 196
Figure 7.63 Variation in curvatures and curvature ratios for Augenti-Parisi model (orthog. dir.) 196
Figure 7.64 Moment-curvature diagrams for Augenti-Parisi model (paral. dir.) 198
Figure 7.65 Variation in curvatures and curvature ratios for Augenti-Parisi model (paral. dir.) 198
Figure 7.66 Yielding curvature versus axial force 199
Figure 7.67 Ultimate curvature versus axial force 199
Figure 7.68 Comparison between moment-curvature diagrams for $N/N_m = 0.1$ 200
Figure 7.69 Curvature ductility versus strain ductility 200
Figure 7.70 Axial strain field throughout the inner resistant domain of the macro-element 203
Figure 7.71 Building up V–δ_M curve in strain control 208
Figure 7.72 Incremental iterative procedure for the force-displacement curve of a panel 209
Figure 7.73 Force-displacement curve of a URM panel failing in flexure 210
Figure 7.74 Force- versus deformation-controlled force-displacement curves 211
Figure 7.75 Force- versus deformation-controlled force-displacement curves for a wall storey 213
Figure 8.1 Flow-chart of pushover procedure for the masonry wall with openings 216
Figure 8.2 Flow-chart of pushover procedure for the masonry building 221
Figure 9.1 Ground floor plan of the building 228
Figure 9.2 Macro-element model of the building 228
Figure 9.3 (a) Seismic source model ZS9 and (b) a_g map for probability of exceedance of 10% in 50 years (URL: http://zonesismiche.mi.ingv.it/) 229
Figure 9.4 Incidence angle of seismic input 232

Figure 9.5 Pushover curves for different incidence angles: (a) modal force pattern; (b) uniform force pattern 233
Figure 9.6 (a) d_{dem}/d_{alw} and (b) I_{DD} versus incidence angle 234
Figure 9.7 Capacity and demand parameters versus incidence angle for modal force pattern 235
Figure 9.8 Capacity and demand parameters versus incidence angle for uniform force pattern 236
Figure 9.9 Lateral stiffnesses versus incidence angle: (a) modal and (b) uniform patterns 236
Figure 9.10 Supply displacement ductility versus incidence angle 237
Figure 9.11 (a) R_μ and (b) α_u/α_1 versus incidence angle 237
Figure 9.12 Comparison between strength reduction (or behaviour) factors 238
Figure 9.13 Expected and collapse damage maps related to ground floor plan: (a,c) $\alpha = 30°$; (b,d) $\alpha = 150°$ 239
Figure 9.14 Damage indices at (a) displacement demand and (b) collapse; (c) index ratios ... 240
Figure A.1 Typical constitutive law of masonry under uniaxial compression 264
Figure A.2 Specimen (a) before and (b) after compression test in the direction orthogonal to mortar bed joints 267
Figure A.3 Experimental stress-strain curves (orthog. dir.) 267
Figure A.4 Specimen (a) before and (b) after compression test in the direction parallel to mortar bed joints 269
Figure A.5 Transverse splitting of a specimen 270
Figure A.6 Experimental stress-strain curves (paral. dir.) 270
Figure A.7 Probabilistic stress-strain curves (orthog. dir.) 272
Figure A.8 Comparison between empirical and mean experimental curves (orthog. dir.) 273
Figure A.9 Comparison between proposed and existing constitutive models 273
Figure A.10 Probabilistic stress-strain curves (paral. dir.) 274
Figure A.11 Comparison between empirical and mean experimental curves (paral. dir.) 275
Figure B.1 Specimen geometry (dimensions in mm) and arrangement of LVDTs 278
Figure B.2 Experimental setup for direct shear tests 279
Figure B.3 Front view of a specimen 279
Figure B.4 Cross-section of the experimental setup 280
Figure B.5 Experimental and mean stress-strain curves for (a) $\sigma = 0.25$ MPa 282
Figure B.6 Experimental and mean stress-strain curves for $\sigma = 0.50$ MPa 282
Figure B.7 Experimental and mean stress-strain curves for $\sigma = 0.75$ MPa 283

Figure B.8 Secant shear modulus versus shear strain for different pre-compression levels 284
Figure B.9 Fracture energy increment versus horizontal relative displacement 284
Figure B.10 Fracture energy versus confining stress 285
Figure B.11 Dilatancy curves for (a) σ = 0.25 MPa, (b) σ = 0.50 MPa, and (c) σ = 0.75 MPa 286
Figure B.12 Dilatancy coefficient versus confining stress.....287
Figure B.13 (a) Characterisation of Mohr-Coulomb strength model and (b) friction angle versus confining stress 288
Figure B.14 (a) Empirical and mean experimental stress-strain curves; (b) regularised curves 290
Figure B.15 Partition of $(\overline{\sigma},\overline{\gamma})$ plane and construction of shear response surface 291
Figure B.16 Shear response surface.....292
Figure C.1 Geometry of as-built specimen (dimensions in cm) 295
Figure C.2 Geometry of IMG-repaired specimen (dimensions in cm) 297
Figure C.3 (a,b) Filling of cracks with mortar injections; (c,d) application of IMG system....297
Figure C.4 Experimental setup: (a) front view and (b) lateral view 298
Figure C.5 Arrangement of displacement transducers on the wall: (a) front; (b) back.....300
Figure C.6 Input versus response time-histories.....301
Figure C.7 Damage patterns: (a) as-built wall; (b) pre-damaged wall; (c) repaired wall.....302
Figure C.8 Damage to the spandrel panel: (a) as-built wall; (b) pre-damaged wall; (c,d) repaired wall 303
Figure C.9 Damage to the pier panels: (a) as-built wall; (b) pre-damaged wall; (c,d) repaired wall 304
Figure C.10 (a) Near-collapse state of the repaired wall; (b) damage to the spandrel panel ...305
Figure C.11 Monitoring of lateral stiffness under increasing resisting force.....305
Figure C.12 Experimental force-displacement curve for monotonic test on as-built wall.....306
Figure C.13 Experimental force-displacement curve for cyclic test on pre-damaged wall 307
Figure C.14 Experimental force-displacement curve for cyclic test on repaired wall 307
Figure C.15 Envelopes of experimental force-displacement curves.....308
Figure C.16 Bilinear idealisation of experimental curves for monotonic test on as-built wall 310
Figure C.17 Bilinear idealisation of experimental curves for cyclic test on pre-damaged wall 311
Figure C.18 Bilinear idealisation of experimental curves for cyclic test on repaired wall 311

LIST OF TABLES

Table 7.1 Resisting moments and other parameters for EPP model 192
Table 7.2 Curvatures and other parameters for EPP model 192
Table 7.3 Resisting moments and other parameters for Turnšek-Čačovič model 194
Table 7.4 Curvatures and other parameters for Turnšek-Čačovič model 194
Table 7.5 Resisting moments and other parameters for EC6 model 195
Table 7.6 Curvatures and other parameters for EC6 model 195
Table 7.7 Resisting moments and other parameters for Augenti-Parisi model (orthog. dir.) 197
Table 7.8 Curvatures and other parameters for Augenti-Parisi model (orthog. dir.) 197
Table 7.9 Resisting moments and other parameters for Augenti-Parisi model (paral. dir.) 198
Table 7.10 Curvatures and other parameters for Augenti-Parisi model (paral. dir.) 199
Table 9.1 Seismic hazard parameters for Gesualdo (Italy) 231
Table 9.2 S_S and C_C factors, spectrum characteristic periods and *PGA* demand 231
Table A.1 Strength, limit strains and strain ductility (orthog. dir.) 268
Table A.2 Secant elastic moduli and Poisson's ratios (orthog. dir.) 268
Table A.3 Strength, limit strains and strain ductility (paral. dir.) 270
Table A.4 Secant elastic moduli and Poisson's ratios (paral. dir.) 271
Table B.1 Mean strength and strain parameters 283
Table B.2 Peak cohesion and friction angle for different masonry types 289
Table C.1 Mechanical properties of constituent materials 296
Table C.2 Experimental response parameters of the specimens 306
Table C.3 Parameters of idealised SDOF system, overstrength and strength reduction factor 309

LIST OF ABBREVIATIONS

AD	acceleration-displacement
CLS	cracking limit state
CQC	complete quadratic combination
CSM	capacity spectrum method
CULS	cracked ultimate limit state
DAP	displacement-based adaptive pushover
DBD	displacement-based design
DCM	displacement coefficient method
DDBD	direct displacement-based design
DE	discrete-element
DI	damage index
DM	damage measures
DOF	degree of freedom
DV	decision variable
EBD	energy-based design
EC6	Eurocode 6
EC8	Eurocode 8
EDP	engineering demand parameter
ELS	elastic limit state
EPP	elastic-perfectly plastic
FAP	force-based adaptive pushover
FBD	force-based design
FE	finite-element
FEMA	Federal Emergency Management Agency
FO	fully operational
IBC	Italian building code
IDA	incremental dynamic analysis
IDR	interstorey drift ratio
IM	intensity measure
IMG	inorganic matrix-grid
INGV	Italian National Institute of Geophysics and Volcanology
LD	limited damage
LELS	linear elastic limit state
LS	life safety

LSD	limit state design
LVDT	linear variable differential transformer
MCE	maximum credible earthquake
MDOF	multi-degree-of-freedom
MMPA	modified modal pushover analysis
MPA	modal pushover analysis
NC	near collapse
NELS	non-linear elastic limit state
NSP	non-linear static procedure
NTR	no-tensile-resistant
PBD	performance-based design
PBEE	performance-based earthquake engineering
PDF	probability density function
PGA	peak ground acceleration
PGD	peak ground displacement
PGV	peak ground velocity
PP	performance point
PSHA	probabilistic seismic hazard analysis
RC	reinforced concrete
RM	reinforced masonry
SDOF	single-degree-of-freedom
SDR	strength degradation factor
SLS	serviceability limit state
SPO	static pushover
SRSS	squared root of sum of squares
ULS	ultimate limit state
URM	unreinforced masonry
UULS	uncracked ultimate limit state

ABSTRACT

Non-linear analysis is the most viable tool to get accurate predictions of the actual response of *masonry structures* under earthquake loading. Analytical methods based on the idealisation of masonry walls with openings as systems of macro-elements allow not only to capture the main failure modes observed after past earthquakes, but also to ensure a limited computational demand in engineering practice.

The present thesis deals with *non-linear incremental static (pushover) analysis* on masonry buildings modelled through *evolutionary spread plasticity macro-elements*.

In the first part of the work, fundamentals of structural analysis, seismic risk, and performance-based seismic design are reviewed along with non-linear static procedures and macro-element methods for seismic analysis of masonry buildings.

The second part of the work deals with theoretical advances in non-linear seismic analysis of masonry buildings. In particular, an evolutionary spread plasticity macro-element has been developed and static pushover procedures for individual masonry walls, as well as entire buildings, are presented and discussed in detail.

The proposed macro-element has been defined as 'evolutionary' because its inner reacting domain changes as the lateral drift demand increases. Such an evolution is caused by the spreading of cracking and yielding within the masonry. Namely, tensile cracking of masonry induces significant reductions in the effective width of cross-sections, which then depends on the magnitude of the given lateral drift (*geometrical non-linearity*). Yielding of masonry develops near the extreme parts of the macro-element, which are subjected to maximum bending moment. *Mechanical non-linearity* of masonry in compression is also taken into account through a deformation-based approach. In fact, the mechanical behaviour of the macro-element is characterised for different constitutive laws of masonry, by means of (1) two- and three-dimensional flexural strength domains (to be coupled with classical strength domains), (2) moment-curvature relationships, and (3) force-displacement diagrams.

Two-dimensional strength domains derived from strength degrading constitutive models allow to account for more real characteristics of masonry. The comparison between flexural strength domains corresponding to different constitutive models have shown that current simplified formulas lead to higher values of ultimate shear force and bending moment, if the given axial force is not significantly higher than one-half of the allowable axial force. The implementation of full non-linear stress-strain relationships (which have been obtained by recent uniaxial compression tests in the direction orthogonal to mortar bed joints of masonry) has been found to provide more

conservative estimations of ultimate shear force corresponding to flexural failure of macro-elements (i.e., toe crushing). Flexural strength domains have been defined at cracking, elastic, and ultimate limit states of masonry cross-sections and panels, in both cracked and uncracked conditions. The explicit consideration of strain ductility of masonry has allowed to assess the evolution in strength domains. In this regard, less significant variations in both ultimate shear force and bending moment have been detected for a given axial force lower than one-fourth of the allowable axial force. Finally, flexural strength of macro-elements has been also investigated for any boundary condition through the development of *three-dimensional strength domains* corresponding to elastic and ultimate limit states, in both cracked and uncracked conditions.

Moment-curvature relationships have been defined for rectangular unreinforced masonry cross-sections by means of an incremental iterative procedure. Their development has allowed to assess key parameters of sectional behaviour, such as flexural overstrength, strength degradation due to strain softening of masonry, yielding and ultimate curvatures, and curvature ductility. Such parameters have been estimated for a number of constitutive laws and the relationship between curvature and strain ductilities has been also investigated. The implementation of empirical stress-strain relationships presented in the first appendix of this thesis has let to derive moment-curvature relationships where both yielding and ultimate strains of masonry, as well as strain softening, are explicitly considered. It has been found that, if the applied axial force does not exceed one-half of the allowable axial force, the ratio between curvature ductility and strain ductility is greater than unity and does not depend on the magnitude of the applied axial force.

In order to define *force-displacement diagrams* of macro-elements, a specific incremental iterative procedure has been developed; it is based on the monitoring of the maximum axial strain over the cross-section(s) subjected to the maximum bending moment. It has been shown that force-controlled procedures can lead to significant underestimations of displacement capacity of masonry panels and to underestimations of both lateral stiffness and maximum resisting shear force.

Force-based pushover procedures in response control have been developed for individual walls with openings and entire masonry buildings, separately, in order to predict also their non-linear softened response. Such procedures have been implemented in a novel computer program named RAN CODE, which is specifically devoted to structural analysis of masonry buildings. Amongst several numerical applications aimed at validating the developed procedures, the outcomes of a series of global pushover analyses on a masonry building designed in compliance with Eurocode 8 and Italian building code are discussed.

The pushover procedure developed for single masonry walls with openings could be employed in the case of existing buildings (either single buildings or building units within aggregates), which have often flexible floor diaphragms and lacking, or poor, connections between diaphragms and walls, as well as between orthogonal walls.
The procedure developed for global pushover analysis of masonry buildings accounts for torsional effects due to both inherent (i.e., structural) and accidental eccentricities between centres of mass and centres of stiffness. The use of spread plasticity macro-elements which change with the given deformation state allows to relate the 'local' response of masonry panels to the 'global' response of the structure.
Finally, three appendices include results and empirical models obtained through *experimental programs* aimed at supporting non-linear modelling and analysis of masonry buildings.
Appendix A deals with *mechanical characterisation of masonry* under uniaxial compression along directions parallel and orthogonal to mortar bed joints. Such a characterisation is consisted in the definition of mechanical parameters and constitutive models able to simulate non-linear behaviour of masonry up to large inelastic strains.
Appendix B deals with mechanical characterisation of masonry in sliding shear along mortar bed joints. Also in this case, both classical and advanced mechanical parameters have been defined and empirical models have been derived. Such models include shear stress versus shear strain relationships and a shear response surface, which allows to simulate non-linear shear behaviour of unit-mortar interfaces over the whole range of allowable strains (that is, from elastic to inelastic range).
Appendix C summarises the main results of three *quasi-static lateral loading tests* on a full-scale masonry wall with a opening and no tensile-resistant elements (e.g., reinforced concrete bond beams, steel ties), which is the typical case of existing masonry buildings. Namely, the first monotonic test allowed to investigate non-linear behaviour of the wall up to the first significant damage to the spandrel panel above the opening. The second test was carried out on the pre-damaged wall under cyclic displacements, in order to assess residual properties and to reach some hints on seismic performance of masonry walls subjected to earthquake sequences. The last test was performed under cyclic displacements on the wall after repairing and upgrading of the spandrel panel with an inorganic matrix-grid composite system. The aim of that test was to assess the effectiveness of the strengthening system for seismic retrofit of masonry structures and rapid remedial works during seismic emergency scenarios. Data processing for all lateral loading tests has shown that the damage to the spandrel panel affected both load-carrying capacity and strength degradation of the wall, whereas rocking behaviour of piers produced large displacement capacity and low residual drifts (that is, high re-centring capacity).

KEYWORDS: *Masonry Buildings, Non-Linear Seismic Response, Spread Plasticity Macro-Elements, Static Pushover Analysis.*

Chapter 1 - INTRODUCTION

1.1. Foreword

In recent years the focus of research in the field of masonry constructions has grown significantly. The widespread presence of these constructions in the built heritage, particularly in high-seismicity countries such as Italy, has highlighted the need to extend the state of knowledge in theoretical, numerical, and experimental research, in order to assess and reduce the vulnerability of existing masonry buildings. Therefore, some issues of structural modelling and analysis, which have been addressed just for concrete and steel structures until a few years ago, are currently being analysed also for masonry structures.

Non-linear seismic analysis and *macro-element modelling* of masonry buildings are, amongst others, key research topics of structural earthquake engineering. In this context, the challenge is (1) to better estimate the non-linear seismic response through incremental static analysis, and (2) to build up simplified structural models able to simulate the main failure modes observed after past seismic events with limited computational work.

Non-linear static procedures applied within macro-element methods allow to combine two different needs, even though equally important: simplified assessment of performance and damage under increasing seismic intensity, according to the philosophy of performance-based earthquake engineering (PBEE); and validation and further processing of analytical predictions.

Non-linear static procedures have been recognised as a viable alternative to complex, although more rigorous, nonlinear dynamic analyses. Second, macro-element methods capture the main features of non-linear seismic response of the so-called ‘standard’ masonry buildings (namely, buildings with regular layout of openings), even if they are based on a simplified idealisation of walls as systems of panels. If local out-of-plane collapse mechanisms are prevented through proper measures (i.e., effective wall-to-wall and wall-to-diaphragm connections by means of reinforced concrete ring beams, or steel ties), the masonry building shows a ‘box-type’ response under earthquake loading. In such conditions, a *global seismic analysis* can be carried out to get realistic performance predictions. The floor diaphragms distribute horizontal actions among the walls which in turn provide earthquake resistance to the whole structure depending on the lateral strength and deformation capacities of their constituent macro-elements.

Macro-element methods allow to easily overcome high difficulties of finite-element (FE) and discrete-element (DE) methods, regarding both masonry modelling (in terms of geometry and mechanical properties) and the interpretation of results. Nevertheless, these numerical methods are still presently the unique available tools for structural assessment of highly-irregular and historical/monumental constructions.
From a modelling standpoint, masonry can be analysed either in its real configuration within numerical methods (e.g., as an assemblage of stone units with or without mortar joints), or alternatively as equivalent homogeneous material within macro-element methods or FE macro-models. In the case of regular masonry assemblages, mechanical behaviour should be distinguished at least along the directions parallel and orthogonal to mortar bed joints. In this way, material orthotropy can be taken into account by assigning different values of mechanical properties along the aforementioned directions. Conversely, in the case of chaotic masonry assemblages, masonry can be modelled as isotropic material. Since tensile strength of masonry is significantly lower than compressive strength, the equivalent continuum material cannot be assumed to be isoresistant. To perform simplified calculations, masonry is typically modelled as no-tensile-resistant (NTR) material to define flexural strength of macro-elements.
Geometrical modelling of masonry walls within macro-element methods is quite simple and in compliance with analysis criteria of current building codes, because structural performance is assessed by comparing capacity to demand at both global and single-component levels. On the contrary, numerical methods are not directly consistent with that methodology because internal forces and displacements are to be derived through repeated averaging and integration operations over stress and strain fields. To assess the attainment of a specific limit state, the required computational work is thus too high for engineering practice. Due to all above considerations, research efforts in the field of masonry structures have been addressed toward the development of macro-element models and non-linear computational procedures.

1.2. Research Objectives

The recognition of a direct relationship between earthquake-induced deformations and attained damage, as well as the need for response-controlled procedures able to get reliable seismic behaviour predictions up to high levels of strength degradation, have emphasised that proper modelling and non-linear strategies are needed for masonry buildings. To this end, theoretical and experimental research presented in the present thesis was aimed at developing an evolutionary spread plasticity macro-element and incremental non-linear static (pushover) procedures for single masonry walls and entire masonry buildings.
According to current criteria for multi-level seismic performance assessment, structural

modelling and analysis are here discussed for individual masonry components (i.e., panels) and buildings as a whole, starting from RAN macro-element method (Augenti, 2004).

A deformation-based mechanical approach is applied to build up a spread plasticity macro-element whose characteristics change with the given deformation state due to mechanical and geometrical non-linearities. Strength and displacement capacities are respectively defined through strain ductility-dependent strength domains and force-displacement curves which depend on the dominant failure mode (toe crushing, bed-joint or stair-stepped sliding, or diagonal tension cracking). Non-linear response of the macro-element is affected by shearing and flexural deformations.

The flexural behaviour of the macro-element is defined from strain fields by using different stress-strain relationships and performing closed-form integrations over deformation-dependent domains. Amongst the stress-strain relationships used in this study, those obtained by compressive tests on tuff masonry panels along the directions orthogonal and parallel to mortar bed joints are also considered. A strain field monitoring over the macro-element and the choice of a suitable constitutive model allow to include the following features: effective cross-section evolution due to masonry cracking (geometrical non-linearity); masonry micro-cracking at small strains (mechanical non-linearity in the elastic range); and strength degradation at medium and large strains (mechanical non-linearity in the plastic range). To investigate interaction between axial (compressive) force, shear force and bending moment (or alternatively axial force eccentricity), three-dimensional strength domains are defined. For a given stress-strain relationship, these domains do not depend on boundary conditions at end sections of the masonry panel. Flexural deformations experienced by the panel are analysed also at sectional level by means of moment-curvature diagrams derived for different constitutive laws of masonry. Such a modus operandi gives some hints on the influence of strain ductility and axial force on curvature ductility of unreinforced masonry (URM) cross-sections.

Non-linear shear behaviour is investigated through results and empirical models derived from direct shear tests on tuff masonry specimens. In particular, sliding shear along mortar bed joints of masonry is also analysed for future implementation in macro-element models.

To assess seismic performance of a single masonry wall or a whole masonry building, two different pushover procedures are formulated looking to relate global response to local response of each panel. In the case of a building, non-linear torsional behaviour is considered in the analysis procedure via step-by-step updating of shear centre location based on actual distribution of secant lateral stiffnesses. The proposed pushover procedures are response-controlled in order to capture strength degradation. Both

constant and adaptive load profiles can be defined in pushover analysis. In the latter case, the lateral force pattern is assumed to be dependent on the actual acceleration demand (i.e., the so-called 'spectral amplification') and the fundamental mode (single-mode load profiles). Hence, multi-mode dynamic analysis at each analysis step is not needed and the lateral force pattern can be associated with normalised displacements resulting from the previous step. Adaptive pushover procedure is then a single-run analysis.

Quasi-static lateral testing of a perforated masonry wall without tensile-resistant elements, such as tie-beams, has provided useful information for modelling and analysis of existing masonry buildings. Main results of this experimental program are presented and discussed in this thesis, in order to deepen the contribution of spandrels (i.e., the horizontal coupling elements) to non-linear seismic capacity.

Some of the theoretical formulations and seismic analysis procedures presented herein have been implemented into a computer program named RAN CODE, which is devoted to structural analysis and safety verifications of masonry buildings under gravity loads and seismic actions.

1.3. Thesis Outline

The present thesis is aimed at presenting and discussing the main research developments on non-linear seismic analysis of masonry buildings attained during the Ph.D. programme. The first part of the work deals with general topics related to structural analysis (Chap. 2), seismic risk (Chap. 3), and seismic design of structures (Chap. 4). Non-linear static procedures and macro-element methods for seismic analysis of masonry buildings are then reviewed in Chapters 5 and 6, respectively.

The second part of the work is completely devoted to the development of an evolutionary spread plasticity macro-element (Chap. 7), and pushover procedures for masonry walls with openings and buildings (Chap. 8). The macro-element behaviour is defined by means of two- and three-dimensional strength domains, moment-curvature curves, and force-displacement diagrams. The proposed pushover procedures are force-based and response-controlled.

A numerical application of the developed pushover procedures is presented in Chapter 9 to assess seismic performance of a masonry building designed in compliance with Eurocode 8 (EC8) (CEN, 2004) and Italian building code (IBC) (IMIT, 2008). Non-linear analyses were carried out by means of RAN CODE for different directions of seismic input. Structural performance is then discussed through pushover curves, polar plots of seismic demand and capacity, expected damage maps, and collapse maps. Chapter 10 summarises the main advances in the field of non-linear analysis in terms of macro-element modelling and global seismic assessment procedures.

This thesis concludes with three appendices on experimental testing carried out to support the development of modelling and non-linear analysis procedures. Appendix A deals with non-linear modelling of masonry under uniaxial compression along the directions orthogonal and parallel to mortar bed joints. Appendix B regards constitutive modelling in sliding shear with special emphasis not only to classical mechanical parameters of masonry structures, but also to those used within refined FE modelling. Finally, Appendix C summarises the outcomes of quasi-static lateral loading tests on a full-scale masonry wall with a opening, in order to get a preliminary evaluation of the role of spandrels within existing masonry buildings.

Chapter 2 - STRUCTURAL ANALYSIS

Structural analysis requires necessarily a modelling of the real construction. This stage consists in assumptions about mechanical behaviour of materials, geometry of structural components, boundary conditions, and applied actions (in terms of type, magnitude, direction, orientation, and their combination). In other words, the analyst has to carry out: (1) *mechanical modelling*, where constituent materials are characterised through strength and deformation parameters, stress-strain relationships, and strength models; (2) *geometrical and contraints modelling*, where dimensions of structural elements and their mutual and external constraints are defined; and (3) *load modelling*, where one has to distinguish environmental and man-made actions due to construction location and its use, respectively.

Depending on the assumptions about material behaviour and loading conditions, structural analysis can be performed in linear or non-linear range, statically or dynamically. In this chapter, the main analysis types are critically and briefly discussed without any specific reference to earthquake engineering methods.

2.1. Linear versus Non-Linear Analysis

The methods of structural analysis can be classified on the basis of the relationship between static and kinematic parameters, namely stress-strain relations at material level and force-displacement relations at component/global structural level. These relationships can be linear or non-linear. The former describe a straight line or a planar surface, the latter describe a curved line or surface.

The structural analysis type to be carried out, and hence the relevant modelling, depends on the target performance level chosen by the designer, that is the target value of a reference parameter or set of parameters to be controlled.

If the analyst want to assess serviceability of the construction defined by the designer or stakeholder, then mechanical, geometrical and constraint non-linearities can be neglected. In fact, the structure is regarded in a condition where non-linearity sources are not typically significant. Conversely, if the structure is analysed under severe loading conditions to assess life safety or even collapse prevention limit states, different non-linearity sources should be included in the analysis to simulate the actual behaviour. Therefore, linear and non-linear analyses are complementary themselves, because the former allows to define the safety against pre-defined operational levels in

serviceability conditions, while the latter is aimed at identifying ultimate capacity of the structure.

As well known, the main non-linearities (each of them removes some hypotheses of linear analysis) can be grouped in the following types:

(1) *Mechanical non-linearity*. A non-linear constitutive law expressed in the form of σ–ε or τ–γ relationship is assumed for the structural material, so stresses are not proportional to the relevant strains. Young's or shear modulus of the material can increase or decrease under increasing strain. Material non-linearity may be also due to strain-rate sensitivity or time-dependent deformation increase due, for instance, to creep or shrinkage.

(2) *Geometrical non-linearity*. Such a non-linearity can be induced by large strains or large displacements. In the former case the Taylor series expansion of strains cannot be truncated at the linear term, while in the large displacement theory the equilibrium equations are to be written considering the actual deformed shape of the structure through a second-order, linearised, or upper-order theory. First-order theory includes the deformed shape just to evaluate displacements, while upper-order theories assume that stiffness changes with deformations according to non-linear relationships.

Geometrical non-linearity can affect the behaviour of structures composed by materials with tensile strength much lower than compressive strength. This is the case of masonry and concrete structures where NTR material models are used. In the case of masonry, tensile strength is neglected just for flexural resistance predictions, while it provides significant contribution to shear resistance. The assumption of zero tensile strength induces partially-resistant cross-sections, whose effective width depends on the magnitude of internal forces. As a result, a non-linear relationship between applied loads and displacements exists because load variations induce significant modifications in the effective cross-sections of the structural element. Its elastic behaviour can be regarded as the sum of a linear contribution related to uncracked cross-sections and a non-linear contribution related to cracked cross-sections. If the assumption of small strains does not apply for the material being considered, structural analysis should be necessarily carried out through non-linear methods since effects could not be superposed.

(3) *Constraint non-linearity*. In the context of linear analysis one assumes two-way constrains, namely constrains able to react in both orientations of applied loads. Nevertheless, if single-way constraints are to be considered, the boundary conditions of the structure change depending on the loading pattern defined by the analyst. It is also underlined that mutual constraints between different structural elements can change as a result of cracking or yielding of constituent materials.

Such an interaction may be difficult to be taken into account.

Although the presence of the aforementioned non-linearities is known, linear analysis is often preferred over its non-linear counterparts and non-linearity effects are considered after the analysis through different procedures or modification factors. For instance, mechanical non-linearity can be taken into account through the adoption of secant moduli, rather than those tangent.

In linear analysis, only one solution of structural equilibrium exists according to the Kirchhoff's principle of uniqueness, and the principle of effects superposition applies since the current structural configuration does not depend on previous configurations. On the contrary, in full non-linear analysis the equilibrium solution may not exist or not be unique and the effects' superposition is not allowed because the current state of the structure has a memory of previous states.

The inclusion of plastic hinges in structures made of quasi-brittle or ductile materials allows to avoid a full non-linear analysis because a linear behaviour can be assumed between the formation of two consecutive plastic hinges. Then, a sequence of linear analyses can be performed on the structure subjected to individual load increments, if constraints are updated at the locations of plastic hinges. Each linear analysis provides the structural response under the applied load increments and the actual response is determined as the sum of the single contributions. Plastic hinges lead to build up *lumped plasticity models* which do not consider special effects due, for instance, to pinching or bond slip of reinforcing bars in reinforced concrete (RC) structures.

As discussed in Chapter 8, the RAN method proposed by Augenti (2004) for masonry buildings has been extended to perform full non-linear analysis by *spread plasticity modelling* associated with the idealisation of masonry walls with openings as systems of macro-elements. Therefore, the actual structural configuration under a given loading condition has memory of the previous states.

2.2. Static versus Dynamic Analysis

Structural analysis can be carried out not only in the linear or non-linear range, but also in static or dynamic conditions depending on the magnitude of accelerations and velocities induced by external loads to inertia masses. Static equilibrium equations are a special case of the equations of motion and apply when accelerations and velocities can be neglected in the structural analysis. As well known, when considering equations of motion one must define not only elastic and inelastic properties of the structure, but also inertia and dissipative properties[1].

[1] In general, additional forces should be also considered when applying active control devices to the structure for seismic protection purposes.

Dead and occupancy-related live loads can be considered to be statically or quasi-statically applied to the structure. This means that their maximum magnitude is assumed to be reached through an incremental process so slow as to be seen as infinite sequence of elementary processes related to consecutive time instants[2]. A dynamic analysis could then be even wrong since the structural behaviour is not significantly time-dependent. Static analysis of the structure consists in solving the following equilibrium equation:

$$\mathbf{K}\mathbf{x} = \mathbf{F} \tag{2.1}$$

where **K** stands for the stiffness matrix of the system, **x** is the displacement vector, and **F** is the load vector.

If a non-linear static analysis of the structure has to be performed, the stiffness is not known as it depends on the equilibrium solution, namely the structural response under the given loading condition. Eq. (2.1) specialises as follows:

$$\mathbf{K}(\mathbf{x})\mathbf{x} = \mathbf{F} \tag{2.2}$$

and can be solved by means of classical or refined algorithms, such as Newton-Raphson, constant stiffness method (or modified Newton-Raphson), secant stiffness method, and mixed stiffness method.

During the nominal life of the structure one can expect the presence of variable loads (e.g., wind, earthquake, cyclic loads, etc.) inducing dynamic excitation in inertia masses. In these conditions, static analysis could provide unrealistic predictions of the actual behaviour of the structure owing to dynamic amplification effects generated by velocities and accelerations, which are not considered into Eqs. (2.1) and (2.2). The structural response should be then analysed in the time domain through the methods of structural dynamics: static equivalent analysis and dynamic analysis (Clough and Penzien, 1994). The former is based on the solving of the equilibrium equation accouting for dynamic amplification effects via proper factors. In this way, even though structural response is not analysed in the time domain, one can estimate effects due to the actual dynamic loads by solving the following equilibrium equation:

$$\mathbf{K}\mathbf{x} = a\mathbf{F} \qquad \text{with } a > 1 \tag{2.3}$$

where the scalar $a > 1$ is said to be *dynamic amplification factor* and is provided by codes and standards on the basis of past dynamic analyses.

Dynamic analysis of the structure consists in solving the *equation of motion*:

$$\mathbf{M}\ddot{\mathbf{x}}(t) + \mathbf{C}\dot{\mathbf{x}}(t) + \mathbf{K}\mathbf{x}(t) = \mathbf{F}(t) \tag{2.4}$$

which describes the equilibrium between applied loads and inertia, damping, and elastic forces during time. Eq. (2.4) is an ordinary, second-order, inhomogeneous

[2] The average of load increments applied to the structure is equal to their temporal average in a given reference period. In such a case, the incremental process is said to be *ergodic*.

differential equation including not only static parameters (namely, **K**, **x** and **F**), but also: the time variable *t*; the mass matrix **M**; the damping matrix **C**; the relative acceleration vector $\ddot{\mathbf{x}}$; and the velocity vector $\dot{\mathbf{x}}$. Opposed to static analysis, both first and second derivative of displacement vector are not zero and the load vector is strictly dependent on time.

The coefficients in Eq. (2.4) are typically constant with time (*time-invariant systems*), but they can change or not with the structural configuration resulting in non-linear or linear response of the dynamic system. A physical interpretation of the equation of motion is that the applied loads **F** are equilibrated by inertia forces $\mathbf{M}d^2\mathbf{x}(t)/dt^2$, damping forces $\mathbf{C}d\mathbf{x}(t)/dt$, and elastic forces $\mathbf{K}\mathbf{x}(t)$ at each time instant.

Associating input energy with external loads, the equation of motion can be rewritten in terms of energy. The structure is then assumed as a system that oscillates around the initial position exchanging several energy types with the environment (namely, the surrounding soil-fluid system) during time. Potential energy turns into kinetic energy, elastically stored energy, damping energy, and hysteretic energy in the case of non-linear behaviour. Hysteretic energy is associated with plastic deformations which increase with time under cyclic loading. When the external actions vanish, structural motion decreases with time up to the attainment of the resting condition. The energy stored in the structure is equal to that dissipated by hysteresis and corresponds to a permanent damage.

As stated above, dynamic analysis can be carried out in linear or non-linear range. The main solving strategies are the direct integration of the equation of motion and the spectral analysis. The former is performed in the time domain and applies to any structural type, the latter is performed in the frequency domain and applies to linear systems without particular complexity.

2.2.1. Time-Domain Analysis

Linear dynamic analysis in the time domain consists in a step-by-step integration of the equation of motion and is based on the assumption that matrices **C** and **K** are constant with time under varying structural response. In such conditions, the system is said to be *linear* and *time-invariant*, so the solution of the equation of motion is relatively simple to be determined.

A closed-form integration of Eq. (2.4) can be carried out only if external actions are described by mathematical functions. In this case, the integral solution of differential equations corresponding to degrees of freedom (DOFs) of the structure[3] can be

[3] Free lagrangian coordinates, namely linearly independent and non-zero displacements associated with inertia masses of the structure.

represented as the sum of the *complimentary* (*integral*) *function* related to the initial system conditions[4] and the *particular integral* related to the actions which modify the natural motion. The complimentary function describes the transient response of the system, which vanishes with time due to damping, while the particular integral describes the steady-state response whose frequency is equal to that of external actions. The steady-state response is characterised by a displacement vector which can be set equal to the product of the static term by a dynamic amplification factor.

Generally, external actions are represented by a random time-variant distribution so Eq. (2.4) can be solved only through numerical methods (e.g., using the Newmark method) based on the integration of an acceleration, velocity, or displacement record of a past event. Considering a set of significant records for the site where the structure is located, a statistical significance can be assigned to the structural analyses aiming at a response prediction under potential future events.

In some particular cases like as, for instance, those of structures sensitive to interaction with environmental actions, the system is to be considered as *time-variant*. Solving of the equation of motion is then very complex and advanced numerical strategies are needed.

The evolutionary behaviour of highly non-linear structures can be assessed in two different modes. The former consists in solving the equation of motion by considering a linear elastic system with constant coefficients, but characterised by: a secant stiffness matrix $\mathbf{K}_{eq}$ corresponding to the ultimate displacement of an idealised bilinear force-displacement diagram; and an equivalent viscous damping matrix $\mathbf{C}_{eq}$ whose coefficients are evaluated on the basis of both viscous and hysteretic dampings. Eq. (2.4) is then modified as follows:

$$\mathbf{M}\ddot{\mathbf{x}}(t)+\mathbf{C}_{eq}\dot{\mathbf{x}}(t)+\mathbf{K}_{eq}\mathbf{x}(t)=\mathbf{F}(t) \tag{2.5}$$

The second alternative procedure is to solve directly the equation of motion in the non-linear range:

$$\mathbf{M}\ddot{\mathbf{x}}(t)+\mathbf{C}\dot{\mathbf{x}}(t)+\mathbf{K}\left[\mathbf{x}(t)\right]\mathbf{x}(t)=\mathbf{F}(t) \tag{2.6}$$

where the coefficients are constant with time and depend on the actual deformed configuration of the structure. In such a case, dynamic analysis reaches the maximum level of complexity and requires special care in both mechanical and input modelling.

It is emphasised that a correct choice of numerical solving method along with its parameters are needed to ensure stability and accuracy of mathematical solution.

Once the configuration of the structural system is known at each time instant, internal forces on each structural component can be estimated and the safety level assessed.

[4] The Cauchy problem is solved, for instance, by assuming: $\mathbf{x}(t=0)=0;\ \dot{\mathbf{x}}(t=0)=0$.

2.2.2. Frequency-Domain Analysis

The analysis of a dynamic system in the frequency domain allows to drastically reduce the computational work of the time-domain analysis, even though it is rather simple just in the linear range. The first stage of this analysis method is the transformation of the time response $\mathbf{x}(t)$ in the spectral response $\mathbf{X}(f)$ defined in the frequency domain. The frequency domain representation of the original (actual) function is derived via *Fourier transform*, which is the integral form of the Fourier series expansion (related to discrete problems) and is defined also for non-periodic functions[5].

The original response function of the structural system is then regarded as superposition of an infinite number of harmonic functions which in turn, in discrete problems, are ordered according to the relation $f_n = n\, f_1$ (where f_1 is the fundamental frequency and f_n is the natural frequency associated with the n-th mode).

The bijection between the functions $\mathbf{x}(t)$ and $\mathbf{X}(f)$ is symbolically indicated as follows:

$$\mathbf{x}(t) \Leftrightarrow \mathbf{X}(f) \tag{2.7}$$

The amplitude of the complex function is said to be *Fourier spectrum* and is defined as:

$$\left|\mathbf{X}(f)\right| = \sqrt{R(f)^2 + I(f)^2} \tag{2.8}$$

being $R(f)$ the real part and $I(f)$ the imaginary part of the function. The parameter:

$$\theta(f) = \arctan\left[\frac{I(f)}{R(f)}\right] \tag{2.9}$$

is called *phase* (or *initial angle*) since in the complex plane it represents the angle between the amplitude vector $|\mathbf{X}(f)|$ and the axis of real numbers.

Once the amplitudes of the *transfer function* $\mathbf{H}(f)$ and the load vector $\mathbf{F}(f)$ in the frequency domain have been defined, the amplitude of the time response $\mathbf{X}(f)$ can be derived through the following equation:

$$\left|\mathbf{X}(f)\right| = \left|\mathbf{H}(f)\right| \cdot \left|\mathbf{F}(f)\right| \tag{2.10}$$

This relation describes the system response as output signal of a filter with gain $\mathbf{H}(f)$ subjected to the input signal $\mathbf{F}(f)$.

For each harmonic function, one can derive the amplitude and the phase, and hence the amplitude and phase spectra which represent the frequency content of the time response function.

Finally, the frequency domain response $\mathbf{X}(f)$ is retransformed in the time domain response $\mathbf{x}(t)$ by means of the *inverse Fourier transform*. Generally, dynamic analysis of structures under seismic input focuses on the amplitude of response parameters (i.e.,

[5] The non-periodic function $\mathbf{x}(t)$ can be considered as a periodic function with period $T \to \infty$.

displacements, velocities, and accelerations), rather than the phase, so only amplitude spectra are typically defined.

If the system is linear and time-invariant, the matrix equation of motion can be converted in a system of uncoupled linear differential equations, through modal decomposition. From a physical viewpoint, if one assume a finite number of vibration modes for the structure being analysed, zero damping and the possibility of defining a set of generalised coordinates, modal decomposition consists in the transformation of the actual linear dynamic system with n DOFs in n different linear single-degree-of-freedom (SDOF) systems, each having a specific frequency. Therefore, the evolutionary response of the actual multi-degree-of-freedom (MDOF) system is analysed as a proper combination of a number of SDOF systems. In other terms, the displacement vector $\mathbf{x}(t)$ is represented as linear combination of n vectors, each related to a single mode of vibration of the structure. *Fourier analysis* allows to solve dynamic equilibrium of linear systems by means of the superposition of elementary responses of n load vectors.

Once the structural configuration is known at each time instant, the maximum values of internal forces and displacements can be determined for each structural component, so safety verifications can be performed for the limit states of interest.

The dynamic analysis of a structural system in the frequency domain can highlight the key role of damping. The amplitude spectrum allows the identification of the natural frequencies of a MDOF system. When the input has a dominant frequency equal to a natural frequency of the system, the structural response increases indefinitely denoting the *resonance* phenomenon. This is the reason why the natural frequencies are also called *resonance frequencies*. Nevertheless, in real structures with limited resistance, a magnification of motion occurs instead of resonance, vanishing at the attainment of structural collapse. Although structural damping is quite low especially in the elastic range, it allows to avoid magnification of motion and thus the collapse.

The problem of the motion's magnification exists, for instance, in the case of lattice towers and long-span bridges. The latter may suffer aeroelastic instability phenomena due to high-intensity wind actions. Due to this potential problem, the wind-structure interaction is analysed in detail and simulated through scaled models in wind galleries.

If the coefficients of the equation of motion change with time, the spectral analysis becomes more complex and a higher computational work is needed to perform advanced analyses. A typical problem is the seismic soil-structure interaction for which the damping matrix $\mathbf{C}$ cannot be expressed as a linear combination of the matrices $\mathbf{M}$ and $\mathbf{K}$. In this case, the Rayleigh hypothesis does not apply and the structural system is called *non-classically damped*, as opposed to typical *classically damped systems*.

Chapter 3 - SEISMIC RISK

One of the main objectives of earthquake engineering is the mitigation of seismic risk, that is the minimisation of human, social, and economic *losses* and the maintainance of full operational level for infrastructures and strategic facilities (e.g., hospitals and civil protection offices) under seismic events. Direct losses are, for instance, damage and collapse of structural and non-structural elements; indirect losses are service interruptions.

The great importance of earthquake engineering research is confirmed by the high perception of both *seismic hazard* and *vulnerability* by the population (Faccioli and Paolucci, 2005). This remark has been properly demonstrated by a recent investigation aimed at updating the seismic risk maps for the Italian territory with new data on the real estate by the 2001 census of the Italian Institute of Statistics (Bramerini and Di Pasquale, 2008). By dividing the real estate in different vulnerability classes[6], it has been found that:

- 18.1% of buildings located in Italy are highly vulnerable;
- the real estate consists essentially of masonry buildings (61.5%) and RC buildings (24.7%);
- most of buildings has a number of storeys lower than 4 (two-storey masonry and RC buildings are 45.7% of the real estate);
- 72% of residential buildings has not been designed with a-seismic rules; and
- 45% of buildings is over 40 years old.

Given the high seismic risk in Italy, a satisfactory understanding of key concepts underlying research advances until now is needed.

Seismic risk (denoted as R) is the total amount of losses at a site or region during an earthquake with a given probability of exceedance in a given reference period[7]. In the probabilistic sense, seismic risk is the probability that a pre-defined level of losses due to earthquakes (denoted as L) is exceeded within a given reference period in a specific territorial area of interest. Based on this definition, risk is cumulative because it includes fatalities and injuries, as well as social-economic losses, which are caused by

[6] The Italian Department of Civil Protection divided the real estate in three vulnerability classes: high (A); medium (B); low (C).

[7] This period is the time interval in which earthquakes are observed. From a design standpoint, it is related to the nominal life of the construction, its expected occupancy level, and its importance for civil protection purposes.

different seismic events and are evaluated, for instance, in a one year period.
The risk level can be estimated at different territorial scales, from regional to specific site, so its evaluation involves different scientific fields: seismology; geophysics; geology; geotechnics; structural engineering; regional and urban planning; insurance engineering; and estimo. Formally, seismic risk is defined by the following functional product:

$$R = H \cdot V \cdot E \tag{3.1}$$

where H is seismic hazard, V is seismic vulnerability, and E is *exposure*.

3.1. Seismic Hazard

Seismic hazard is the totality of physical effects, both direct and indirect, induced by the earthquake and able to produce losses in human activities.
The intensity of the seismic ground motion in a specific territorial area depends mainly on the following parameters: the *input energy* released by the seismic source[8] (which is a function of the source dimensions and fracture mechanism); *directivity effects* (which depend, inter alia, by the location of the site with respect to the source); and *source-to-site distance*. These factors affect the characteristics of seismic motion at the bedrock, namely the so-called *shakebility* or *regional seismic hazard* (denoted as H_B), which is evaluated in ideal conditions of horizontal topographic surface and free field (i.e., the absence of soil-structure interaction effects).
From a mathematical point of view, the seismic ground motion recorded by seismometers, velocimeters, and accelerometers, is respectively described by the displacement field $\mathbf{u}(\mathbf{x},t)$, velocity field $d\mathbf{u}(\mathbf{x},t)/dt$, and acceleration field $d^2\mathbf{u}(\mathbf{x},t)/dt^2$, associated with the location vector $\mathbf{x}$ of the measurement device. Therefore, the empirical description of the seismic motion depends not only on the characteristics of the source and propagation medium, but also on the response of the measurement device. This means that, for instance, seismic motion recorded by a seismometer is the *convolution*[9] of three functions: $\mathbf{S}(\xi,t)$ which describes the seismic motion over the fracture surface, namely the slip $\Delta\mathbf{u}$ produced by the fracture process; the Green

[8] *Seismic source* is a slip process over a fracture surface (which is typically called *fault*) representing the discontinuity surface (geometrically assumed to be planar in seismology) induced in the Earth's crust by high tectonic forces. During the fracture process, several types of seismic waves are radiated by the source. The waves undergo geometrical attenuation due to crustal discontinuities and inelastic attenuation due to mechanical non-linearities of rocks and soils, along their path from the source to the surface. Thus, Earth behaves as a filter for seismic waves produced by the source. For severe earthquakes producing strong motion records, the fracture can propagate up to the surface.

[9] Convolution between functions is implicitly carried out also when the effects superposition is applied to linear systems.

function $\mathbf{G}(\mathbf{x},\xi,t)$ which describes the propagation of seismic waves from the source to the location of the receiver, namely the ground displacement field at the points $\mathbf{x}$ produced by the slip in the points $\boldsymbol{\xi}$ over the fracture surface; and the function $\mathbf{I}(\mathbf{x},t)$ which describes the modification of the actual ground motion due to the response of the measurement device (that is, the seismometer in this case).

The displacement recorded at the surface in the time domain is expressed as follows:

$$\mathbf{u}(\mathbf{x},t) = \mathbf{S}(\xi,t) * \mathbf{G}(\mathbf{x},\xi,t) * \mathbf{I}(\mathbf{x},t) \tag{3.2}$$

where the symbol $*$ represents the convolution integral. Such an equation can be rewritten in the frequency domain in the following form:

$$\mathbf{u}(\mathbf{x},\omega) = \mathbf{S}(\xi,\omega) \cdot \mathbf{G}(\mathbf{x},\xi,\omega) \cdot \mathbf{I}(\mathbf{x},\omega) \tag{3.3}$$

through the convolution theorem. Once the instrument response is known, one can get the actual seismogram in the time domain:

$$\mathbf{U}(\mathbf{x},t) = \mathbf{S}(\xi,t) * \mathbf{G}(\mathbf{x},\xi,t) \tag{3.4}$$

and its frequency domain form:

$$\mathbf{U}(\mathbf{x},\omega) = \mathbf{S}(\xi,\omega) \cdot \mathbf{G}(\mathbf{x},\xi,\omega) \tag{3.5}$$

so the seismic motion at the source can be evaluated through the following equation:

$$\mathbf{S}(\xi,\omega) = \frac{\mathbf{U}(\mathbf{x},\omega)}{\mathbf{G}(\mathbf{x},\xi,\omega)} \tag{3.6}$$

It follows that seismic hazard assessment at the bedrock requires a *deconvolution* of the instrument response. If the focus of the study is the seismic motion at the source, the Green function has to be deconvolved removing, thus, geometrical and inelastic attenuations throughout the rocks along the source-to-site path of seismic waves. These operations need for the use of inversion methods that allow to estimate the seismic motion at the source based on that measured at the ground surface. Non-linear regression analyses are then carried out on data measured at different surface locations.

Effects on community, built heritage, and physical environment are significantly affected also by local seismic response of soil deposits at the site. It is then needed the assessment of *local seismic hazard* (H_L) which accounts for the change in the seismic motion from the bedrock to the surface, due to the dynamic response and topography of soil deposits (Lanzo and Silvestri, 1999; Vinale, 2008). In fact, site conditions can influence the amplitude, frequency content, and duration of seismic ground motion.

The functional dependence of seismic hazard on the characteristics of the source and propagation medium (rocks), source-to-site distance, and properties of local soil deposits, can be briefly expressed as follows:

$$H = H_B \cdot H_L \tag{3.7}$$

Figure 3.1 shows the main physical phenomena affecting seismic hazard at a site. It is emphasised that the effects on the environment observed in the *near source* are different from those observed in the *far field*[10]. Near source effects include, inter alia, *forward directivity* which can be identified as velocity pulses in recorded ground motion time-histories. The observation of the source *radiation pattern* allows the identification of major radiation along a specific direction, rather than others. In fact, the faulting mechanism cannot be considered as a spherical source, nor a point surface. The investigation of directivity effects on both physical and built environments is thus one of the most attractive topics in engineering seismology and structural earthquake engineering.

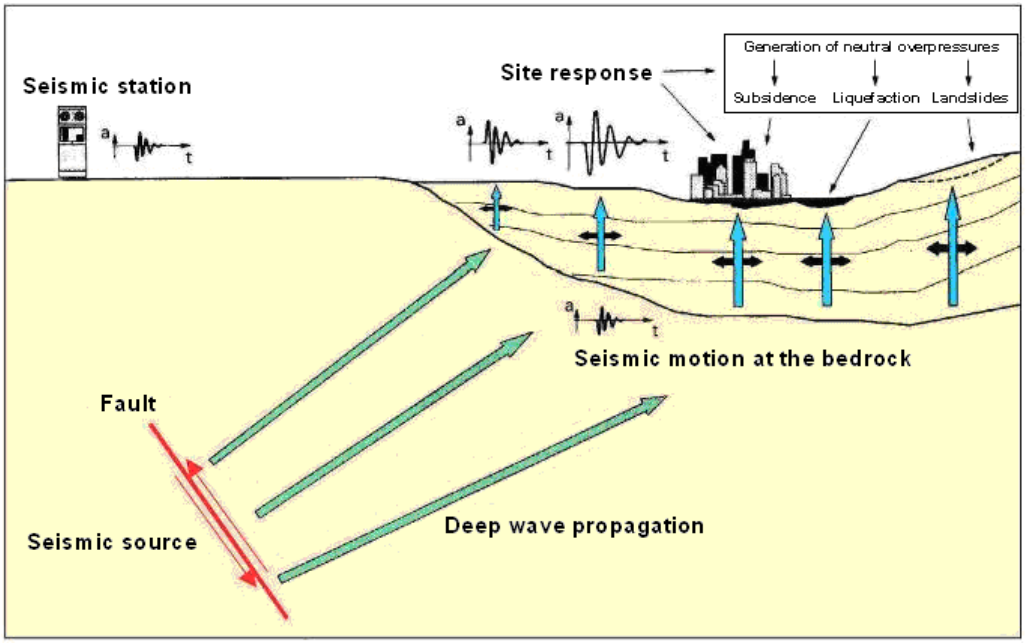

Figure 3.1 Seismic hazard at a site (adapted from Lanzo and Silvestri, 1999)

[10] Typically, we talk about *near fault* (or *near source*) for the area surrounding an active source. The contour of this area is typically defined as the closed line at a distance from the source's surface projection equal to the linear dimensions of the source. In the near source, both the shape and type of seismic waves are considerably affected by the source characteristics, and hence by the faulting mechanism. Sites located at greater distances from the seismic source belong to the *far field* and seismic ground motion measured at their locations is mainly influenced by inelastic attenuation. Such a deamplification of seismic motion along the source-to-site path is take into account in seismic hazard assessment by means of specific *attenuation laws*. The latter establish a non-linear dependence of an intensity measure with magnitude, distance, and other parameters.

Hazard can be assessed through deterministic methods based on seismic scenarios, probabilistic methods (considering esplicitly both dimensions and location of the source or the source zone model, as well as the annual rate of occurrence), or stochastic methods (Kramer, 1996).

In the probabilistic sense, seismic hazard is the probability that a pre-defined value of an *intensity measure* (*IM*) is exceeded at a site or region within a given reference period. The probabilistic method proposed by Cornell (1968), which is based on the definition of seismic source models with a homogeneous occurrence rate, allows to estimate the probability of exceeding a pre-defined level of seismic intensity in a given time interval or, alternatively, the seismic intensity level corresponding to a given probability of exceedance in the reference period. A return period of the design earthquake can also be defined as a function of the probability of exceedance in the reference period. Assuming the occurrence of seismic events as a homogeneous stochastic process, the Poisson's relationship can be used to estimate the return period. For instance, one can estimate the *IM*-value corresponding to a probability of exceedance equal to 10% in 50 years or, alternatively, to a return period of 475 years. The ouput of seismic hazard analysis is the hazard curve at a specific site, namely the graphic representation of the probability of exceedance in a given reference period versus an *IM*, or else the hazard map of a region, namely the *IM* spatial distribution corresponding to a unique probability of exceedance in a reference period.

Therefore, seismic hazard analysis consists in the following steps: seismic source modelling; application of an attenuation law; and site response analysis. The first two steps lead to the *seismic macro-zonation* of a region, while the last step allows to obtain a *seismic micro-zonation*.

Probabilistic seismic hazard analyses (PSHAs) by research groups of national programs S1-S6, funded by the Italian National Institute of Geophysics and Volcanology (INGV), and Seismic Risk Office of the Italian Department of Civil Protection, allowed to build up both static and interactive maps of seismic hazard. These maps are related to different *IM*s, probabilities of exceedance in 50 years, and percentiles, and are overlapped on a reference grid with 5 km node spacing and 10751 nodes (Meletti and Montaldo, 2007). To that end, IBC (IMIT, 2008) establishes a probability of exceedance for each limit state. Once the return period of the design earthquake has been chosen, seismic hazard parameters at a site can be derived from those related to the reference nodes which, in turn, are listed in tables reported in Annex B of IBC. In this way, seismic design of structures is carried out for a uniform hazard, thanks to a site-dependent approach, rather than that zone-dependent.

The *IM* considered by IBC is the horizontal *peak ground acceleration* (*PGA*) which is defined as reference peak horizontal acceleration on soil type A (i.e., rock, or the

bedrock for other soil types) a_g multiplied by a soil factor S due to site amplification effects:

$$PGA = a_g S = a_g S_S S_T \tag{3.8}$$

being S_S the stratigraphic amplification factor and S_T the topographic amplification factor.

3.2. Exposure

Exposure is said to be the totality of elements (e.g., people, structures and their content, transportation systems, utility networks) regarding potential losses during seismic events.

Depending on the scope of the risk assessment, exposure may include a single building with its occupants and content or, alternatively, a portfolio of buildings, infrastructures and inhabitants of a whole region. Clearly, a reliable estimation of seismic risk requires databases regarding population, structures, infrastructures and other facilities, which are to be adequately classified in terms of type, function and occupancy level.

The optimization of exposure is a task for urban and territorial planners. Sites subjected to higher seismic hazard should not be characterised by high occupancy level in order to ensure effectiveness of emergency plans provided by civil protection.

At global scale, a significant exposure growth has been observed especially within emerging and developing countries. Conversely, seismic vulnerability of the built environment does not reduce, apart from industrialised countries where advanced building codes have been already passed. Seismic vulnerability of the physical environment is even increasing due to continuous speculative acts.

3.3. Seismic Vulnerability

Seismic vulnerability of an individual soil-foundation-structure system, or the built and physical heritages, represents conceptually the exposure sensitivity to a certain seismic intensity level, namely the totality of the expected losses expressed as a fraction of those exposed at risk.

At regional level and for a high number of elements such as buildings, vulnerability can be defined in terms of potential damage of a class of structures with similar characteristics and subjected to a given seismic hazard level. In such a case, vulnerability can be regarded as the product of three components: built environment vulnerability; physical environment vulnerability; and territorial vulnerability. The former is the proneness of facilities to suffer damage under the expected design earthquake; the second vulnerability factor is associated with physical phenomena (e.g., liquefaction, subsidence, slope instability, tsunami, surface fracture processes)

which can be generated by an earthquake; and the last second vulnerability factor (which is assessed at provincial or municipal scales) is the proneness to damage to infrastructures and utility networks.

With reference to the built heritage, the output of vulnerability analysis is represented by several damage levels of one or more structures under varying *IM* aimed at the characterisation of seismic motion. As shown in Section 4.1, the structures should comply with different performance levels, each corresponding to a specific damage state. In the case of non-linear static analysis, the vulnerability analysis of a building can be deterministically interpreted assuming the expected displacement as *engineering demand parameter* (*EDP*) and the *PGA* or spectral acceleration related to the resisting base shear as *IM*.

In the case of probabilistic analysis, *fragility curves* are developed to assess the relationship between the probability of a given damage level and an *EDP* conditional on the seismic intensity. Such curves allow to account for uncertainty associated with seismic demand and capacity.

3.4. Mitigation of Seismic Risk

As mentioned above, 'mitigation' of seismic risk means 'minimisation' of human, economic, social, and cultural losses. The main objective is clearly the minimisation of fatalities and injuries, even though it is worth noting that earthquakes are not the major cause of death at global scale. Indeed, in the United States of America, even eight seismic events with magnitude not lower than 6 have occurred between 1970 and 1995, causing 85 deaths. In the same time period, deaths due to human or accidental errors in the medical field have been equal to 9000.

The mitigation of seismic risk requires:

- the development of an effective civil protection system in the pre-event time through knowledge dissemination and the realisation of specific earthquake early warning systems (Gasparini et al., 2007), as well as in the post-event time by means of emergency management according to pre-defined procedures reported within emergency plans;
- the design and realisation of facilities in compliance with a-seismic criteria;
- the reduction of vulnerability of both existing structures and infrastructures;
- the control of the exposure level;
- the continuous updating of seismic codes according to research advances; and
- the definition of insurance policies, as occurred in Turkey after the 17 August 1999 Kocaeli (or Izmit) earthquake.

In the framework of scientific research, the attainment of the aforementioned objectives needs for:

- the accurate definition of seismic hazard because its overestimation would lead to build up overconservative and highly expensive structures, while its underestimation would induce heavy damage and a lot of fatalities;
- a quantitative damage analysis by means of a reliable mechanical modelling and indices specifically defined for each structural type (this topic has not yet been fully analysed in the case of masonry constructions); and
- the development of systems able to assess seismic alert conditions through a decision-making process and reliable technologies.

In the last years, a satisfactory collaboration between Italian seismologists and engineers has led to a considerable improvement in the code-based seismic hazard assessment in Italy, allowing seismic design of structures through elastic response spectra very close to *uniform hazard response spectra* derived from PSHAs. Preliminary studies have shown that these new tools could lead to 30% mean savings on both newly-constructed and retrofitted structures. In fact, according to the multi-level performance-based approach of IBC, the peak horizontal acceleration at a site (a_g) is no longer approximated to the upper limit of the interval reported in the previous seismic zonation, but it is estimated as a function of the specific site location with respect to the closest reference nodes. For instance, a peak horizontal acceleration equal to 0.17g would be approximated as 0.25g. IBC is also based on the modification of both the characteristic periods and the maximum spectral acceleration of elastic response spectra, depending on two further seismic hazard parameters. From such a standpoint, EC8 (CEN, 2004) is much more approximate than IBC, being it based just on two spectral shapes. A shape is related to earthquake with magnitude lower than 5.5, and the other is related to earthquakes with magnitude greater than 5.5.

Chapter 4 - SEISMIC DESIGN OF STRUCTURES

Since the 90s of the last century, first in USA and New Zealand and then in Europe and Japan, seismic design of structures has considerably changed owing to significant advances in non-linear structural behaviour prediction. The need for minimisation of catastrophic effects due to earthquakes has given strong pulse to the development of design criteria and innovative methods of analysis. New-generation seismic codes have been also passed in earthquake-prone regions, allowing safety verifications based on PBEE concepts. In this chapter, some fundamentals of seismic design are deal with special emphasis to masonry constructions.

4.1. Performance-Based Design

Seismic motion at the base of a structure induces random patterns of cyclic actions along the height. Strength and displacement demands are generated throught the structure by acceleration, velocity, and displacement time-histories at both local and global levels. The magnitude of such demands depends obviously on seismic intensity and hence increases with the return period of the earthquake.

Until a few years ago, the seismic design of a structure was carried out in a way to provide sufficient lateral resistance against the base shear induced by the design earthquake. The estimation of the base shear was based on the use of inelastic horizontal acceleration spectra. The only scope of the designer was then to prevent collapse under severe seismic events. Actually, even at this key performance level, it has been recongnised that the ability of dissipative structures with medium/high fundamental period to suffer earthquakes depends on satisfactory displacement capacity and supply ductility at both local and global levels, rather than high resistance. If one provide not only strength but also ductility and displacement capacity to the structure, the design process and verification methods allow to control damage and collapse mechanisms. Namely, except for low-period structures for wich lateral resistance is often the key capacity parameter, several performance parameters should be checked to get a satisfactory seismic response. These parameters are related not so much to the linear elastic range, as to that non-linear (see Sects. 4.3.1 and 4.5).

In earthquake-prone countries the occurance rate of seismic events is high so it is extremely important to meet not only the no-collapse requirement (as done until a few years ago), but also the operational performance under low-intensity earthquakes. The

effects of these earthquakes can be indeed significant in terms of economic losses due to use interruption and non-structural damage. Like structural damage and collapse, also these effects should be avoided within acceptable risk intervals to get an effective seismic design.

A novel design philosophy has been proposed to ensure different performance levels, each associated with specific design requirements to be satisfied by means of iterative optimisation procedures. This multi-level performance approach is then the basis of *performance-based design* (PBD)[11] and is the natural extension of limit state design to the new-generation earthquake engineering. In fact, it is underlined that a 'limit state' is a condition after which the structure no longer meets performance levels for which it has been designed. Whilst structural safety verifications in the classical limit state design (LSD) consisted in comparing a *design force* S_d to a *design strength* R_d, PBD makes a comparison between *demand D* and *capacity C*. In other words, we check not only that:

$$S_d \leq R_d \tag{4.1}$$

according to LSD, but also that demand is lower than capacity as follows:

$$D \leq C \tag{4.2}$$

Demand is the effect of the design earthquake, while capacity is a measure of resources available in the structure to resist against the design earthquake. The logic step from LSD to PBD is then a generalisation.

The implementation of PBD requires a reliable estimation of seismic demand through proper tools of engineering seismology, as well as a realistic estimation of seismic capacity through analysis methods of earthquake structural engineering (In the case of inelastic systems, demand and capacity are related each other.). Such operations should be carried out accounting for uncertainty in seismic hazard, site response, structural materials, and capacity models. PBD is intended to make an 'estimation' (not a 'determinination') based on quantitative concepts and reliable standards.

4.1.1. Brief History of Performance-Based Standards

In 1992, Federal Emergency Management Agency (FEMA) funded the ATC-33 project to develop guidelines on seismic retrofit of buildings. This initiative was the first step toward the codification of PBD and, particularly, the quantitative assessment of seismic response of structures. This task is presently carried out by defininig multiple

[11] PBD falls within the so-called *performance-based engineering* (PBE) which is aimed at matching 'quantitative' requirements (e.g., structural, plant, and economic) corresponding to 'qualitative' performance levels assigned by the construction customer. The undertaken technical assessment should allow the implementation of a decision-making process in uncertain conditions.

performance levels, each expressed through specific parameters within pre-defined uncertainty limits. Being predictions, seismic assessment is performed (either directly or indirectly) within a framework no longer deterministic, but probabilistic.

The main features of PBD for seismic design of new buildings were organically dealt with in SEAOC Vision 2000 (OES, 1995) for the first time. Two years later, FEMA 273 (ATC, 1997a) and its commentary in FEMA 274 (ATC, 1997b) falling within the American *National Earthquake Hazard Reduction Program* (NEHRP), extended this new approach for seismic rehabilitation of existing buildings. Such three documents were the first-generation PBD codes.

The current multi-level seismic design falls in the second-generation design codes and was originated by FEMA 343 (BSSC, 1999), which includes some application examples, and FEMA 356 (ASCE, 2000), which provided a significant improvement in both seismic analysis procedures and verification criteria reported in FEMA 273. These further updatings of American regulations have allowed to deepen the key PBD concepts and have been included in the most advanced seismic codes, at both national and international levels, such as EC8 and IBC. Nevertheless, both research and professional community have highlighted the following limitations in the last performance-based codes:

- the accuracy level of the seismic assessment procedures is still unable to predict the actual seismic response of buildings with low uncertainty;
- the verification criteria are sometimes too conservative or absolutely not conservative;
- design solutions provided by PBD methods are not yet reliable and advantageous from an economic point of view; and
- specific parameters and procedures should be defined to communicate pros and cons of different design solutions to customers, stakeholders, and decision-makers.

In order to reduce seismic risk through PBD, the next-generation codes should include:

- performance levels defined with continuity by means of proper measures like repair costs, deaths, and downtime, which are able to provide useful information to decision-makers being it possible to convert any individual design solution into monetary losses;
- estimation procedures of potential repair costs, deaths, and downtime, for both new and existing buildings;
- seismic verification criteria for non-structural components, whose damage induces significant economic losses;
- comprehensive methodologies able to communicate the accuracy level associated with the seismic response prediction, as well as the uncertainty level of the seismic hazard assessment;

- refined analytical methods for seismic response prediction; and
- reliable verification criteria for both local and global performance through different parameters.

The above-mentioned innovative features are considered into FEMA 445 (ATC, 2006), which deals with basic principles of PBD and the development of new seismic analysis methods and design procedures.

4.1.2. Fundamentals of Performance-Based Design

Performance-based design is an iterative process which begins with selection of performance objectives by customer[12], followed by the development of a complete project which is updated until safety verifications are satisfied in compliance with the pre-defined objectives. An acceptable risk level with specific allowable damage states is then identified for the structure under a given seismic intensity level, leading to direct and indirect losses (see Chap. 3).

To define design objectives, performance levels are first established. To that end, Vision 2000 introduced the following damage states for constructions:

- *Fully Operational* (FO): no damage and full usability.
- *Operational* (O): moderate damage only to non-structural components, as well as slight damage to structural components and repairability; usability during a seismic event not ensured, but quick restoration allowed.
- *Life Safety* (LS): significant damage to both structural and non-structural components.
- *Near Collapse* (NC): safety of occupants not ensured, while allowing residual load-bearing capacity against gravity loads.

Both limit and damage states of the structure correspond to each performance level and are to be checked accordingly. In analogy to what American regulations establish and according to Eurocodes, IBC defines the following *serviceability limit states* (SLSs):

- *Fully operational*, which is to be assessed under frequent (i.e., low-intensity) seismic events in the case of both strategic and critical structures;
- *Limited damage* (LD), which is to be assessed under occasional (i.e., medium-intensity) seismic events in the case of ordinary structures;

[12] It is emphasised that such a modus operandi should not be in compliance with ‘prescriptive’ codes which do not provide different solutions to both designers and customers, nor proper safety levels, opposed to their performance-based counterparts. The uncertainty level about seismic demand and capacity estimation cannot be assessed as well. In fact, absolute safety can never be obtained since a non-zero failure probability can be estimated in any case. Neglecting this aspect can produce hazardous design solutions because one think about unlimited safety, although it cannot be actually reached.

and the following *ultimate limit states* (ULSs):

- *Life safety*, which is to be assessed under rare (i.e., high-intensity) seismic events in the case of ordinary structures;
- *Near collapse*, which is to be assessed under highly-rare seismic events (i.e., the maximum credible earthquake, MCE) in the case of both strategic and critical structures.

The following damage states correspond to the aforementioned limit states:

- slight damage (losses up to 5% of the replacement cost);
- moderate damage to non-structural components and repairable damage to structural components (losses up to 15% of the replacement cost);
- moderate damage to structural components (losses up to 30% of the replacement cost) and potential injuries; structure able to suffer a high number of plastic cycles (and hence to dissipate a high amount of input energy) with no considerable strength degradation, allowing residual resistance against gravity loads; and
- severe damage to structural components (losses higher then 30% of the replacement cost) and inability to ensure safety for successive seismic events, and hence potential need for construction demolition.

Given the importance of non-structural damage for economic losses, researchears have recognised the need for the seismic demand and capacity estimation of such components, in order to assess them under earthquake loading. Presently, we assess seismic demand in terms of acceleration and drift for non-structural elements, but their capacity is under investigation through fragility curves.

With reference to global capacity assessment of a structure, pushover analyses are currently used and non-linear response under a given load pattern is represented through a base shear versus lateral displacement diagram named '*pushover curve*'. Figure 4.1 shows clearly different damage states attained by a building structure subjected to earthquake excitation. The coupling of a specific seismic intensity level with a performance level of the structure is the *design performance objective*, according to the performance matrix reported in Vision 2000 (Fig. 4.2). Such a matrix relates four earthquake performance levels with design earthquake levels expressed in terms of return period or, equivalently, in terms of probability of exceedance in a 50-years reference period).

From a quantitative standpoint, the design performance objective is identified at the end of the seismic analysis in a point expressed in terms of *IM* and *EDP*. As discussed below, the use of capacity curves and demand spectra in non-linear static procedures allows to identify a performance point PP which represents the equilibrium condition of the structure at a given displacement demand, assumed to be an *EDP* (see Chap. 5).

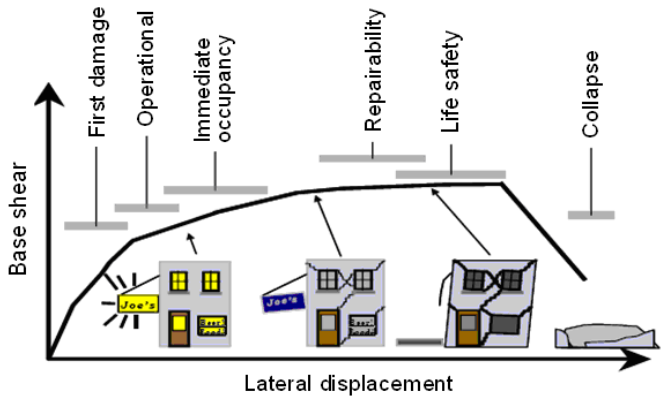

Figure 4.1 Damage levels under increasing seismic intensity (adapted from Hamburger)

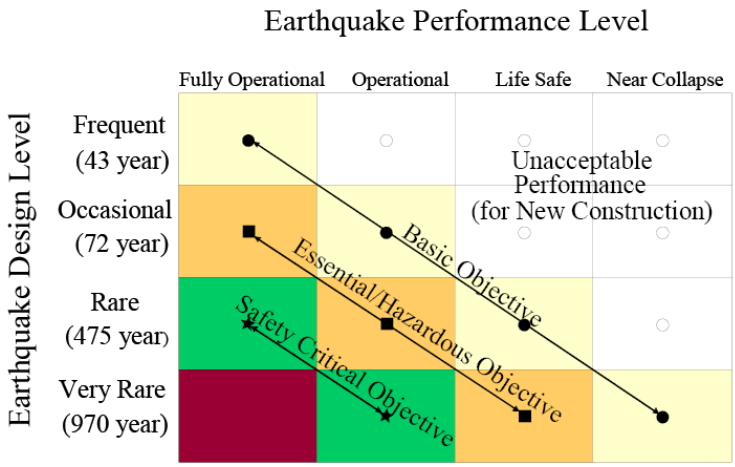

Figure 4.2 Performance matrix in Vision 2000

In the framework of the *capacity spectrum method* (ATC, 1996; Fajfar, 1999; ATC, 2005), which was also included in the *N2 method* (Fajfar e Gašpersič, 1996; Fajfar, 2001; Freeman, 1998) reported in EC8 and IBC, the performance point is obtained as the intersection between the '*capacity spectrum*' and the '*demand spectrum*' corresponding to the limit state under consideration (i.e., a pre-defined seismic hazard level). These spectra are respectively defined as the transformations of pushover curve and design spectrum in a spectral displacement versus spectral acceleration format[13].

[13] The design spectrum is obtained by reducing the ordinates of the elastic response through a ductility- or damping-related strength reduction (or behaviour) factor. In this way, the design spectrum is respectively obtained on the basis of a ductility factor or an equivalent viscous damping factor. In the latter case, both elastic and hysteretic damping are taken into account according to ATC 40 (ATC, 1996). Therefore, *overdamped spectra* can be defined instead of *constant ductility inelastic spectra*.

4.1.3. Intensity, Demand, and Damage Measures

From an engineering viewpoint, seismic demand can be expressed by means of parameters derived from seismic ground motion records or can be derived by assessing linear or non-linear response of the structure. To estimate the most probable damage level suffered by the structure under a seismic event, one has to employ demand indices representing the destructive potential of the earthquake. Regarding this topic, *PGA* is the most used *IM* even though not appropriate in some cases, so one can consider alternatively:

- the *peak ground velocity* (*PGV*), which gives interesting information on the earthquake destructiveness being related to hysteretic energy demand[14];
- the *peak ground displacement* (*PGD*);
- the ratio *PGA*/*PGV*, which provides important information on the earthquake frequency content, damage potential (which increases as this ratio reduces), and hysteretic energy demand;
- the *Arias intensity* I_A (Arias, 1970), which is a significant demand index having multiple advantages with respect to other parameters, such as *Housner spectral intensity* I_H;
- the *Cosenza & Manfredi index* I_d (Cosenza and Manfredi, 1997), which is directly related to the energy content of the earthquake.

The first three indices are *peak IMs*, while the others are *integral IMs*. They are seismic ground motion parameters which allow to predict the earthquake destructiveness just on the basis of seismic records. Both structural and non-structural damages can also be assessed through the following *EDPs* based on a linear response of a SDOF system:

- the *pseudo-acceleration* $S_a(T,\xi)$, which is directly associated with the strength demand (expressed in terms of base shear) and is rather correct to be used in the case of low-period structures;
- the *pseudo-velocity* $S_v(T,\xi)$, which is a measure of both the earthquake kinetic energy and hysteretic energy demand, especially in the case of medium-period structures;
- the *spectral displacement* $S_d(T,\xi)$, which is a direct measure of both structural and non-structural damages due to the attainment of limit values of *interstorey drift ratio* (*IDR* or θ); the latter is defined as the ratio between the lateral interstorey drift and the interstorey height and is considered to be a key design parameter in displacement-based design/assessment procedures, so seismic safety is checked by comparing the displacement demand on the structure to displacement capacity;

[14] Hysteretic energy, along with elastic strain energy, is a fraction of the energy absorbed by a structural system to resist against the input energy of the earthquake.

- the *Housner spectral intensity* I_H (Housner, 1952), which is a measure of hysteretic energy demand derived from direct integration over a specific period interval.

Some *EDPs* related to non-linear SDOF response are:

- the *inelastic pseudo-acceleration* $S_{ai}(T,\xi)$;
- the *inelastic spectral displacement* $S_{di}(T,\xi)$;
- the *kinematic* (or *monotonic*) *displacement ductility* μ_{mon};
- the *cyclic displacement ductility* μ_{cyc};
- the *hysteretic displacement ductility* μ_{hyst}; and
- the *hysteretic energy demand* E_H;

where T and ξ represent the fundamental period and the equivalent viscous damping factor, respectively. The importance of residual *IDRs* has been also recently investigated as a measure of seismic performance, and hence as further *EDP*, by Pampanin et al. (2002) and Pettinga et al. (2007).

The above-mentioned three types of ductility are presently some of the most used inelastic parameters (Cosenza et al., 1989): μ_{mon} can also be estimated through pushover analysis, while the others can be derived from non-linear dynamic analysis, as in the case of hysteretic energy demand. Actually, the parameters μ_{cyc}, μ_{hyst} and E_H are yet too complex to be determined in the case of masonry structures, given that non-linear dynamic analysis has not yet been fully validated for these structural types.

Once the seismic demand on a structure is known, the damage can be quantitatively defined via *damage measures* (*DMs*), namely structural parameters which allow controlling the evolutionary state of the structure up to collapse.

At global structural level, damage is typically expressed in terms of roof drift, or *IDR*, in the case of dissipative structures, and in terms of base shear, spectral acceleration, or *PGA* in the case of non-dissipative structures. Conversely, at single-component level, damage can be effectively quantified in terms of chord rotations. For non-structural components like those belonging to plants or strategic structures, whose repair or replacement costs can be much greater than those of structural components (for instance in the case of hospitals and industrial buildings), *peak floor accelerations* should be also assessed.

4.1.4. Decision-making in Performance-Based Design

The implementation of a specific *EDP*, or set of *EDPs*, able to provide a quantitative description of seismic performance allows thinking in both economic and time terms, which are key measures in seismic risk assessment at both single-structure and regional levels.

According to FEMA 445, the seismic design of a structure is to be necessarily followed

by a *cost-benefit analysis* because total losses can be estimated for each expected damage level. This modus operandi allows to identify the most effective economical-technical design solution. Given a set of design solutions, the designer should be able at demonstrating to the decision-maker the economic viability of a specific solution with respect to others by means of one or more *decision variables* (*DVs*).

One can use, for instance, the *life cycle cost*, which is defined as the sum of initial, maintenance, and repair costs during the whole nominal life of the structure. In this way, given that economic losses due to an earthquake can be significant, the attainment of the design performance objectives is not sufficient in the absence of an accurate estimation of both construction and repair costs associated with damages expected for each design solution. While the construction cost is certain, repair costs are affected by a high uncertainty level almost equal to the earthquake occurrence probability. As a result, the expected global cost for a given design solution can be estimated as the sum of the construction cost and the repair cost multiplied by the aforementioned probability. The most advantageous solution for the decision-maker can then be assumed to be that associated with the lowest globale cost.

Among the losses expected for a design earthquake with a given return period, one should consider also downtime, which is the expected time for retrofit interventions on the damaged structure, as well as potential deaths and injuries. Given the presence of several variables, *multi-criteria decision-making procedures* can provide valuable support to the selection of the design solutions for both new and existing buildings. Clearly, measures associated with different variables should be properly normalised and weighed.

In the probabilistic framework, Aslani and Miranda (2005) proposed a seismic loss assessment procedure which is a generalisation of traditional seismic analysis methods and consists of the following steps:

(1) seismic hazard assessment aimed at estimating a given *IM*;
(2) seismic response prediction of the structure, which is devoted to associate an *EDP* to the chosen *IM*;
(3) quantitative damage analysis of the structure aimed at assessing a *DM*, or else a *damage index* (*DI*), which should be properly defined for the specific structural type at which the structure belongs;
(4) seismic loss assessment, which consists in the transformation of damage to loss, the latter expressed through a *DV* such as the cost, downtime, injuries, or deaths.

Such a methodology is much more exhaustive of the classical discrete PBD approach, since it addresses the seismic performance assessment for continuous design variables.

In closing, it is emphasised the need for loss assessment to select retrofit solutions in the case of historical and monumental constructions including also non-structural

losses under frequent low-intensity earthquakes. Monetary losses related to architectural and artistic elements (e.g., paintings, sculptures, and other artworks) can be much greater than those induced by structural damage.

4.2. Structural Modelling

4.2.1. General Remarks

The elasto-plastic behaviour of materials and structures is highly complex to be analysed due to a high number of parameters which should be used in its characterisation. Therefore, a simplified theoretical modelling is often performed to get a realistic simulation of the actual behaviour and the need for limited computational work.

In the classical continuum mechanics where monotonic loading is considered, material non-linearity can be included in a simplified mode by assuming, for instance, some of the constitutive relationships:

- *rigid-plastic*, which is acceptable in the case of elastic strains negligible with respect to those inelastic;
- *elastic-perfectly plastic* (EPP) with limited or unlimited strain ductility;
- *elasto-plastic with hardening/softening*.

These are non-evolutionary models and the following hypotheses are considered for them:

- homogeneous and isotropic material;
- monotonic loading;
- small strains and displacements;
- no creep, shrinkage, and relaxation; and
- presence of non-zero *supply* (*monotonic*) *strain ductility* $\mu_{\varepsilon,alw}$, either limited or unlimited, expressed as the ratio between the ultimate strain ductility and the yielding strain ductility.

The latter parameter is opposed to *demand strain ductility* $\mu_{\varepsilon,dem}$ induced by applied loads and defined as the demand inelastic strain divided by the yielding strain.

In structural earthquake engineering, non-linear material behaviour is rather difficult to be modelled due to cyclic and random nature of seismic loading. Specific material models should be implemented not only to simulate the evolutionary cyclic response and the ability to resist against further loading, but also to define specific failure criteria based on parameters which can be characterised through proper experimental tests. To that end, a number of *evolutionary models*, either degrading or not, can be defined, depending on the material type (Cosenza and Manfredi, 2000). Tomaževič and Lutman (1996) proposed a hysteretic model for reinforced masonry (RM) walls. Over

fourty hysteretic models are available, for instance, in RUAUMOKO code. The implementation of the above-mentioned models and criteria is needed to perform non-linear time-history analysis.
In the context of multi-level PBD, different intermediate damage levels should be also defined; their quantitative definition is even more complex than that of the collapse state. In the case of masonry structures, since dynamic analysis methods has not yet been validated, static seismic actions are considered in both linear and non-linear ranges. Mechanical modelling is then carried out in the framework of classical mechanics where monotonic constitutive laws, as well as strength/deformation parameters, can be considered. As specified in Section 4.3.1, monotonic ductility rather than cyclic or hysteretic ductility should be defined for masonry constructions. Namely, damage accumulation under cyclic loading is not included even though it should be taken into account especially for seismic response prediction under earthquake sequences, like as the 1997-1998 Umbria & Marche and the 2009 L'Aquila sequences which have both occurred in Italy. In fact, cyclic damage accumulation can significantly affect the seismic response of masonry structures as well.
Material non-linearity can be considered by means of two different approaches: *lumped plasticity modelling* and *spread* (or *distributed*) *plasticity modelling*. The former can deal with macroscopic damage of structures only, the latter is able to simulate inelastic response of structures in detail by means of refined analytical methods.
Non-linear modelling of structures begins at material level, going through sectional and single-component levels, and ending at global structural level. A ductility factor can be defined at each structural level and, typically, it decreases from material to global level (see Sect. 4.3.1).

4.2.2. Lumped Plasticity Modelling

In *lumped plasticity models*, inelastic behaviour of materials is concentrated in limited parts of structural elements. This approach is currently employed in the analysis of both framed and frame-equivalent structural models. Framed structures are typically systems made of RC, steel, or wooden one-dimensional elements. Conversely, frame-equivalent models are derived from an idealisation of structural systems composed by two-dimensional elements, such as masonry walls with openings. In the latter, *pier panels* (i.e., the vertical structural components) and *spandrel panels* (i.e., the horizontal structural components) are assumed to be like columns and beams, respectively, while *joint* (or *cross*) *panels* (i.e., the structural components that link spandrel and pier panels together) represent the beam-column joints of the frame-equivalent model. Both frame models are typically intended to be composed by elements with an elastic central beam-column element and the end ductile parts named *plastic hinges*.

The computational work associated with lumped plasticity modelling is considerably lower than that required by spread plasticity modelling, which is discussed below. Nevertheless, a number of advanced computer programs (e.g., SEISMOSTRUCT, OPENSEES) are based on the latter modelling strategy and produce reliable predictions in the case of both steel and RC structures. Distributed plasticity modelling does not need for particular care, opposed to that required when defining locations of plastic hinges throughout the structure. It is just needed the knowledge of the element dimensions and stress-strain relationships.

The concept of plastic hinge has been traditionally applied to structures where demand-to-capacity ratios in flexure are much higher than those related to shear behaviour. Nonetheless, interaction between internal forces is to be considered by means of proper limit domains.

Incremental non-linear static analysis of structural systems composed by one-dimensional elements can be performed once the analyst has defined the location and moment-rotation diagram of plastic hinges. Since the location of plastic hinges depends not only on the geometry of the structure, but also on the loading condition, the application of *limit analysis* theorems should be iterative. As well known, this analysis method is able to provide only ultimate response predictions.

In the framework of multi-level PBD where different performance states are assessed under varying seismic intensity levels, a *step-by-step analysis* is needed. In this way, plastic hinge locations are an analysis output rather than an input. Non-linear analysis is then regarded as a sequence of linear analyses, each performed on a structural model updated at the previous load step (force-controlled analysis) or displacement step (displacement- or response-controlled analysis). Presently, incremental seismic analysis can be carried out under both static and dynamic loads and is one of the most advanced and investigated topics in earthquake engineering. With reference to incremental static analysis, it is emphasised that *force-controlled analysis* consists in the application of a lateral force pattern and the estimation of the corresponding lateral displacements. Conversely, *displacement-controlled analysis* consists in the application of lateral displacements and the estimation of the resulting lateral forces. Alternatively, *response-controlled analysis* means that displacements are iteratively derived under increasing lateral displacement at a control point and invariant lateral force pattern. Response- and displacement-controlled analyses allow to simulate structural strength degradation due to gradual collapse of individual components. Classical methods of pushover analysis are based on the assumption of an invariant lateral force pattern, so seismic analysis is carried out controlling the lateral forces and, if any, the lateral displacement at the control point. Response-controlled analysis is more computationally demanding since at each displacement step the lateral

displacements are believed to be correct if the resulting lateral force pattern matches that assumed before the analysis is run. As shown in Chapter 8, response-controlled force-based pushover procedures have been developed for masonry buildings modelled in compliance with the macro-element approach of the RAN method (Augenti, 2004).

4.2.3. Spread Plasticity Modelling

Distributed plasticity models include mechanical non-linearity over the whole length of structural elements; different mesh techhiques can be used. For instance, in the case of masonry buildings each wall with openings can be idealised as a system of macro-elements. The evolutionary behaviour of macro-elements is affected by cracking and yielding. In the RAN method proposed by Augenti (2004), the lateral response of pier panels is represented through V–δ diagrams, being V the lateral force on the masonry panel and δ the relevant displacement. Those diagrams are the graph of functions describing the lateral behaviour from linear to non-linear range. The functions $\delta(V)$ were obtained through closed-form integration of bending curvatures ϕ and shear strains γ over the inner domain in which masonry is loaded in compression. That domain is assumed to be non-prismatic to include the effect of masonry cracking under increasing lateral force and constant axial (compressive) force (Fig. 4.3).

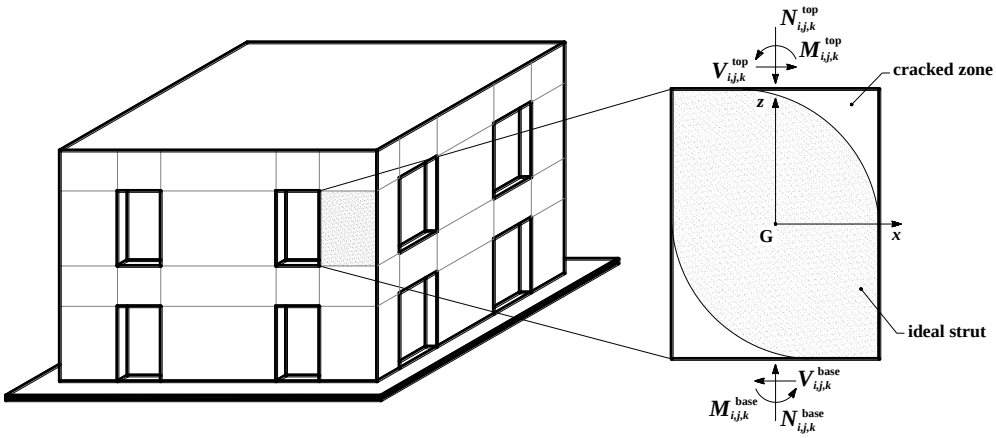

Figure 4.3 Definition of spread plasticity macro-elements within masonry walls

Such a phenomenon induces geometrical non-linearity because the effective width of cross-sections depends on the magnitude of the applied lateral load. Macro-element modelling is then particularly suitable in the case of wall structures.

Spread plasticity can also be considered through *refined elasto-plastic FE models* (see Chap. 6), e.g., micro- or macro-modelling based on the formulations proposed by Lourenço (1996). FE analysis can be performed by means of DIANA code. In complete

micro-modelling, masonry units, mortar joints, and their interfaces are separately modelled assuming different failure models and constitutive laws. Simplified micro-modelling consists in the separate modelling of masonry units without mortar jonts which are replaced by unit-mortar interfaces. Finally, FE macro-modelling is based on the masonry homogeneisation through computational techniques.

Refined FE modelling allows to simulate structural behaviour composed by two- or three-dimensional components, but it is affected by high difficulties in the definition of mechanical parameters for finite elements and manipulation of analytical results. In addition, numerical analyses have shown that analysis duration depends significantly on the model dimensions and analytical results can be highly mesh-sensitive.

Fibre modelling also accounts for distributed plasticity throughout steel and RC structures. In such a case, inelasticity is considered within the whole structural element (e.g., beam, wall) by meshing through a number of one-dimensional finite elements. Figure 4.4 shows, for instance, fibre modelling of a RC beam.

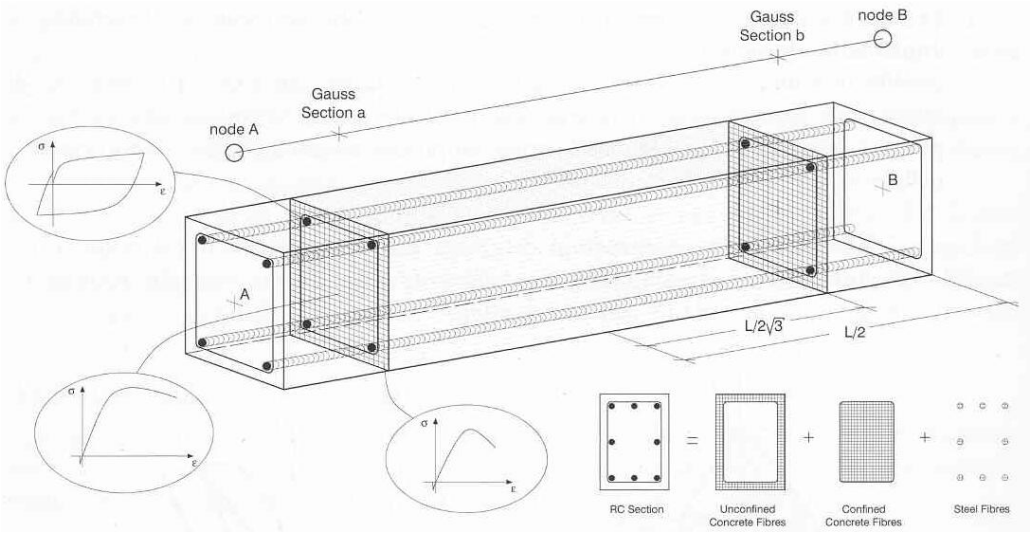

Figure 4.4 Fibre modelling of a reinforced concrete beam (Manfredi et al., 2007)

The structural element is divided in three types of fibres: some fibres are used for modelling of longitudinal steel reinforcing bars; other fibres are defined for confined concrete within the cross-section core; and further fibres are considered for unconfined concrete included in the concrete cover. In this regard, many experimental data have shown that both ultimate strain and compressive strength of confined concrete increase within the core due to triaxial stress state.

For each fibre, the stress/strain field is assessed in the non-linear range by using $\sigma-\varepsilon$ constitutive laws defined for constituent materials (as shown in Fig. 4.4). Both

internal forces and displacements are derived at each cross-section through integration over fibres. Thus, the greater is the number of fibres under consideration, the higher is the accuracy level in the estimation of yielding within the structural component, and hence in the prediction of its non-linear behaviour. For each cross-section, the stress/strain field is derived from numerical integration of non-linear uniaxial response of each fibre. Longitudinal stresses and strains of the whole element are obtained through a further integration in proper control cross-section called 'Gauss sections', as in FE analysis. In other words, the behaviour of the structural element is assessed via double integration over both Gauss sections and the element length. Such a modelling strategy is then more suitable in the case of structural systems composed by one-dimensional elements.

4.3. Seismic Design Criteria and Detailing Rules

Seismic design is considerably different from that performed under gravity loads. Stiffness and strength are provided to structures subjected to dead and live loads, in order to minimise damage under frequent variable loads and ensure safety against ULS. Additional properties are to be provided to structures subjected also to earthquake loading, aiming at obtaining the best global response.

The issue of damage has different features depending on the particular design strategy being adopted (e.g., inelastic response control, base isolation, passive energy dissipation) and the design earthquake expected for the limit state being assessed. In any case and for any design strategy, an earthquake-resistant structure should meet the following general requirements:

- *structural simplicity*, in order to provide evident and direct paths for seismic force transmission, reaching much reliable seismic response predictions;
- *uniformity* and *symmetry*, in order to get sufficiently balanced distributions of inertia masses, stiffnesses, and strengths, both in plan and along the height of the structure, allowing (1) a uniform global response on the basis of no significant eccentricities between stiffness and mass centres, (2) concentrations of internal forces, and (3) high ductility demands;
- *redundancy*, in order to ensure progressive redistribution of internal forces as yielding develop throughout the structure;
- structural systems able to ensure *rather equal stiffness and resistance against both horizontal components of design earthquake actions*, and hence the ability to resist against horizontal actions acting in any direction of the building plan;
- *adequate torsional stiffness and resistance*, in order to avoid non-uniform distributions of strength, ductility, and displacement demands due to torsional effects;

- *rigid and sufficiently-resistant horizontal diaphragms*, in order to ensure horizontal actions transfer between different lateral load-resisting elements (i.e., frames, walls, cores) proportionally to their stiffness in the case of elastic response of all components, and to their strength in the case of inelastic response of all components; and
- *foundation systems with high flexural and axial stiffness*, in order to avoid unfavourable effects due to spatial variation of seismic ground motion (e.g., relative horizontal displacements between different masonry piers or columns).

In general, earthquake-resistant structures can be designed in a way to show *dissipative* or *non-dissipative response* under high-intensity earthquakes. In the case of ordinary structures, seismic design should address the attainment of dissipative response in order to control damage. In such a case, a fraction of the input energy is stored within *dissipative elements* or *critical zones* due to repeated plastic cycles. To obtain a global collapse mechanism of the structure, and thus the maximum energy dissipation capacity, *Capacity Design* is currently suggested by the most advanced seismic codes. This design method assigns major strength to non-dissipative elements in order to ensure elastic response under internal forces transmitted by dissipative elements and zones. To this aim, the following procedure is suggested:

- *overstrength* is assigned to 'brittle' elements/mechanisms, opposed to 'ductile' elements/mechanisms; and
- diaphragms are designed under increased horizontal forces in order to ensure force transfer between lateral load-resisting elements up to collapse.

To ensure a satisfactory global seismic response of the structure, construction details in critical zones and connections should be carefully designed and specified within project documents. To this aim, the most advanced seismic codes establish *detailing rules* for each structural type.

Hierarchy of strengths and capacity design, which are respectively included in IBC and EC8, have different meanings even though complimentary themselves. The scope of seismic design is to produce a hierarchy in the failure and collapse modes, where ductile mechanisms should be followed brittle failure modes. Therefore, brittle elements/mechanisms are designed against internal forces greater than capacity of ductile elements/mechanisms. In this way, seismic design is controlled by capacity of dissipative elements/mechanisms, rather than seismic strength demands. The ability to suffer large displacements under a given strength demand is then ensured to structures with no base isolation systems or supplemental energy dissipation devices.

As discussed in Chapter 6, the RAN method assumes that spandrel panels are brittle elements with respect to pier panels, so safety verifications are performed in terms of

strength for spandrel panels without considering any dependence on deformations. Nevertheless, it is underlined that the energy dissipation capacity of spandrel panels is still under investigation in the case of URM buildings, so capacity design does not apply to control ductility and hierarchy of collapse modes under severe earthquakes.

If structural response is non-dissipative, seismic design is aimed at providing elastic resistance also for high-intensity earthquakes. Both national and international seismic codes still allow to perform linear static and dynamic analyses, but non-linear structural response is to be indirectly considered. To that end, EC8 (CEN, 2004) and IBC (IMIT, 2008) provide a *behaviour factor* for each structural type, based on the expected supply ductility, overstrength, and regularity. This factor allows to design structures under strength demand lower than that associated with elastic response. As well known, displacement ductility demand reduces as the lateral strength capacity increases and, vice versa, strength demand reduces under increasing supply ductility (Fig. 4.5). Thus, strength and ductility change as sand in the vials of an hourglass.

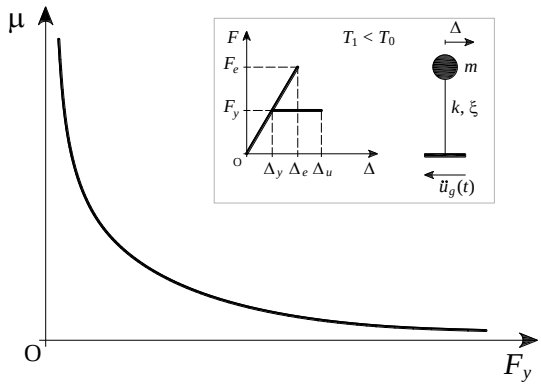

Figure 4.5 Displacement ductility demand versus lateral strength capacity

In the case of dissipative systems, behaviour factor is higher than unity and is employed to reduce elastic spectral accelerations, namely the strength demand on the structure. Inelastic acceleration response spectra reported in EC8 and IBC are defined in ductility control, as they are numerically obtained by solving the equation of motion at a pre-defined supply ductility level. It is then believed that energy dissipation capacity depends mainly on supply ductility. The most critical point of linear seismic analyses is thus the assumption of a strength reduction factor before analysis is run. In the last decades, many relationships have been proposed to define the strength reduction factor as a function of supply ductility, fundamental period of vibration, site conditions, forward directivity effects, and so on. Nevertheless, it is emphasised that the theoretical relationship between behaviour factor and ductility is presently assessed just for SDOF systems, while it is still an open issue in the case of MDOF systems.

Since behaviour factor depends mainly on supply ductility and fundamental period of the structure, it is clear that a simplified assessment can be carried out by identifying first the period interval in which the fundamental period T_1 falls. In 1982 Newmark and Hall assumed the presence of a period of separation T_C between constant-acceleration and constant-velocity branches demonstrating, through a series of numerical analyses, that an 'equal displacement rule' can be applied to medium- and high-period structures with $T_1 > T_C$, while an 'equal energy rule' can be applied to low-period structures with $T_1 < T_C$. The latter structures are, for instance, masonry buildings. The equal displacement rule assumes that the inelastic displacement is equal to that elastic, while the equal energy rule assumes that the stored energy of the actual inelastic system is equal to the elastic strain energy of the ideal elastic system. Figure 4.6 shows displacement ductility μ versus the inverse of strength reduction factor R diagrams derived by non-linear regression analyses on different elasto-plastic SDOF systems in both cases of equal displacement rule and equal energy rule (Park and Paulay, 1975).

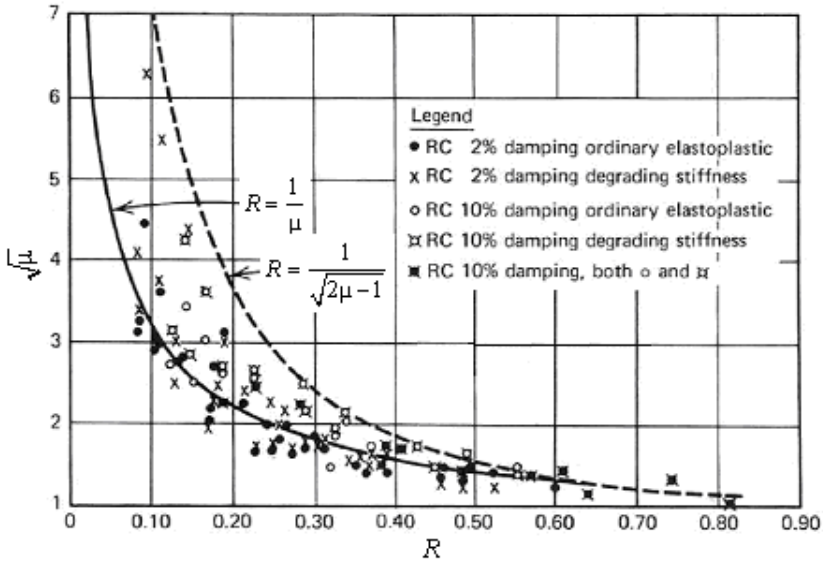

Figure 4.6 Ductility versus strength reduction factor (adapted from Park and Paulay, 1975)

It can be shown that equal displacement rule leads to a strength reduction factor equal to ductility, while equal energy rule provides a strength reduction factor lower than ductility. In the case of non-dissipative systems, the strength reduction factor is assumed equal to unity, so seismic design is based on the use of elastic response spectra. This is the case of SLS verifications, systems with limited ductility at both local and global levels, and structural systems with passive control of vibrations (i.e., base isolation and energy dissipation).

4.3.1. Key Design Parameters

In the PBD framework, an earthquake-resistant structure should have:

- sufficient *lateral stiffness* to ensure serviceability and limited damage to non-structural elements under frequent and occasional seismic events;
- sufficient *lateral resistance* to minimise both structural and non-structural damage under occasional and rare seismic events; and
- sufficient *displacement capacity* and *supply ductility*, so that structural components are able to suffer large deformations without significant strength degradation under rare and MCE.

The first requirement ensures small displacements under a given magnitude of lateral actions. The second requirement allows to mitigate damage associated with inelastic structural response. The last requirement ensures the maximum exploitation of inelastic structural capacity under severe earthquakes. In particular, ductility can be defined at different structural levels:

- *Material level*. The ratio between inelastic strain ε_i (or γ_i) and yielding strain ε_e (or γ_e) is said to be *strain ductility* (μ_ε) and can be identified on stress-strain diagrams (e.g., σ–ε in tension/compression and τ–γ in shear/torsion).
- *Sectional level*. The ratio between inelastic bending curvature ϕ_i and yielding bending curvature ϕ_e is said to be *curvature ductility* (μ_ϕ) and can be identified on moment-curvature diagrams (i.e., M–ϕ).
- *Single-component level*. The ratio between inelastic displacement δ_i and yielding displacement δ_e is said to be *displacement ductility* (μ_δ) and can be identified on force-displacement diagrams (V–δ). Alternatively, *rotational ductility* (μ_φ) can be defined, for instance, in the case of plastic hinges.
- *Global level*. The ratio between inelastic roof displacement Δ_i and yielding roof displacement Δ_e of the structure is said to be *global displacement ductility* (μ_Δ) and can be identified on pushover curves, namely base shear versus lateral displacement (V_b–Δ_c) diagrams. Alternatively, the roof displacement can be replaced by the lateral displacement at any other control point of the structure.

This means that global ductility of a whole structural system depends on those of individual components which, in turn, are functions of sectional and material ductilities. In the case of masonry buildings, the evolutionary spread plasticity macro-element presented in Chapter 7, as well as the pushover procedures presented in Chapter 8, allow to get a direct relationship between global displacement ductility and local ductility of both individual macro-elements and their constituent materials. This is a key feature in design/assessment of masonry buildings subjected to earthquake loading. Equilibrium and compatibility equations allow passing from local material

level to global structural level. Therefore, seismic design of dissipative earthquake-resistant structures under severe seismic events should be carried out by assessing that ductility demands do not exceed ductility capacities. A similar comparison should be also performed in terms of displacements.

In the case of masonry structures, another damage type can also be identified even in the elastic range, that is, the flexural cracking due to tensile stresses higher than tensile strength of masonry. While hysteretic damage affects especially structural systems made of ductile materials (like as steel and RC), cracking damage affects typically masonry structures. Since their response depends considerably on spread cracking, it follows that:

- mechanical non-linearity due to micro-cracking of masonry in compression should be considered even in the elastic range of seismic response;
- displacement ductility does not fully quantify energy absorption/dissipation capacity of masonry structures; and
- a suitable damage index for masonry constructions should be defined not only in terms of kinematic ductility (and, if any, a form of low-cycle plastic fatigue), but also in terms of cracking amplitude and reversibility in the elastic range. Reversibility is the ability of the masonry structure to close flexural and/or shear cracks under load reversals. For instance, flexural cracks due to tension in rocking walls are a typical example of reversible cracking which induces limited permanent damage allowing large displacement capacity as well as re-centring response. Conversely, toe crushing in bending does not provide reversibility in the lateral response resulting, inter alia, in effective height reduction of masonry piers.

  Figure 4.7 shows toe crushing in a masonry pier of a building damaged by the M_w 7.2 Haiti earthquake which occurred on 12 January 2010 at 21:53:10 UTC. The pier failed first in flexure and after in tension shear.

Figure 4.7 Flexural and shear damage of a pier panel

Supply ductility and displacement capacity are key parameters in seismic design of structures since they allow:

- life safety and collapse prevention, because further strength demand is balanced with higher ability to suffer plastic cycles, avoiding brittle mechanisms and hence sudden and catastrophic collapses;
- limitation of seismic accelerations and displacements throughout the structure, and thus minimisation of damage to non-structural components, thanks to higher energy dissipation capacity;
- optimization of element dimensions and hence of construction costs, given that the structure should not remain in the elastic range under severe earthquakes, suffering significant damage; and
- elongation of the fundamental period of the structure, which is put away from the earthquake dominant period to avoid magnification of vibrations.

Therefore, seismic design of the structure based on the control of inelastic response consists in:

(1) the attainment of displacement capacity not lower than demand, in order to provide earthquake resistance for a pre-defined acceptable damage level; and
(2) the verification of supply ductility of individual structural elements not lower than ductility demand corresponding to displacement demand on the structure.

It is underlined that thinking in supply ductility does not means thinking in terms of displacement capacity. In fact, the definition of displacement ductility for a given structural element leds to assume that the allowable inelastic displacement is proportional to the yielding displacement. As a result, the accuracy in displacement capacity estimation is affected by approximations in the elastic response prediction. On the contrary, when defining displacement capacity, the inelastic response prediction does not depend on that related to elastic response.

4.3.2. Structural Regularity

Past earthquakes have shown a key role of structural regularity in seismic design of buildings, because it ensures a rather uniform distribution of both strength and ductility demands on individual structural elements. Regularity is just apparently qualitative since any unfavourable concentration of internal forces and deformations within a few elements is effectively avoided, resulting in quite uniform damage distribution throughout the structure. It is indeed underlined that global ductility demand increases as the lateral strength of the structure reduces, while local ductility demands increases with irregularity in seismic response. The lack of structural regularity leads to a dramatic reduction in the energy dissipation capacity of the whole structure owing to: (1) torsionally-induced displacements in the presence of rigid floor diaphragms;

(2) soft storeys; and (3) incomplete load paths due, for instance, to misaligned walls, columns, or floor diaphragms (the latter at the same floor level).
Structural regularity includes general requirements discussed at the beginning of Section 4.3 and should be checked both in plan and elevation, paying care to the following issues: *shape*; *stiffness and strength distribution*; and *mass distribution*.

- **Structural regularity in plan**

From a morphologic viewpoint, the requirement of regularity in plan is first believed to be met if the area of floor diaphragms is not too high. Conversely, in the case of larger floor areas, non-linear seismic response can be affected by: (1) the generation of higher inertia forces; (2) significant damage due to torsionally-induced displacements of lateral load-resisting elements, which are high even at small torsional rotations of floor diaphragms; (3) non-negligible spatial variation of seismic ground motion (so coherency between seismic inputs at the base of lateral load-resisting elements should be checked); and (4) flexible floor diaphragms with respect to lateral load-resisting elements.
To get a satisfactory plan regularity, the shape of the building plan should be symmetric and simple. Regarding the concept of symmetry, earthquake-resistant structures are typically classified on the basis of the presence of two or more symmetry axes, one symmetry axis, or no symmetry axis. Regarding simplicity, convex plans are distinguished from concave plans, the lower is the maximum ratio between setbacks and transverse dimensions of the building plan, the simpler is the building plan itself. Lack of symmetry induces major problems mainly due to the following reasons:

- structural eccentricity between the centre of stiffness and the centre of mass at each floor level in the elastic range, and between the centre of strength and the centre of mass in the plastic range (assuming all yielded elements)[15], induces storey torques and hence non-uniform distributions of strength and displacement demands especially on peripherical elements; and
- the absence of pre-defined principal stiffness/strength directions leads to the need for their analytical assessment or, alternatively, for investigation on the maximum demands under varying incidence angle of seismic input.

It is emphasised that eccentric cores at the locations of staircases and elevators induce high torques, resulting in damage concentrations and dramatic reduction in the energy dissipation capacity of the whole structure. In addition, the presence of setbacks leads to higher sensitivity of the construction to potential ruptures of floor slabs due to

[15] The centre of strength should be taken into account in order to assess the distribution of shear forces at ULS, given that the consideration of the centre of initial stiffness leads to a lack of conceptual consistency with safety verifications at ULS.

localization of deformations. Therefore, if a complex plan shape cannot be avoided, at least one of the following measures should be made: the separation of the whole structure in a number of sub-systems through proper joints; the stiffening of building corners; the modification of right angles in obtuse angles; and a suitable distribution of lateral load-resisting elements aimed at reaching a uniform distribution of both strength and ductility demands.

With reference to the mass distribution in plan, the presence of heavy equipments, large water tanks or pools, archives, or libraries, leads to significant variations in the distribution of inertia forces over the floor diaphragm.

- **Structural regularity in elevation**

The above-mentioned concepts can be almost fully extended to the requirement of structural regularity in elevation. Also in this case, structural shape, symmetry, and uniformity in the distribution of stiffness, strength, and inertia mass, should be considered. As the height and slenderness of the building increase, both base shear and overturning moment increase as well, because the increase in both the global inertia mass and the location of the centre of mass along the height is more rapid than the reduction in spectral acceleration due to period elongation. This variation occurs as a result of the increase in the number of storeys and the effective height of the equivalent SDOF system.

The building floor area may be constant, decreasing, or increasing along the height. The best shape is obviously that associated with a floor area which decreases from the base to the top of the building. In fact, in such conditions the centre of mass is located at lower floor levels resulting in a lower overturning moment. At the same time, sufficient lateral stiffness is ensured at each floor level. It is underlined that regularity in elevation is met if the building façades are symmetric and the floor areas are rather equal. Indeed, large setbacks induce dangerous concentrations of both strength and deformation demands, resulting in unfavourable local collapse modes and lower energy dissipation capacity of the structure. If façades with large setbacks cannot be avoided, proper vertical seismic joints running along the whole height of the building are needed. The joint dimensions are to be accurately designed in a way to avoid pounding of adjacent buildings.

Significant stiffeness/strength variations along the height of the building should be avoided to allow uniform distribution of internal forces under earthquake loading. Weaker elements or soft storeys induce damage concentrations resulting in a higher failure probability of the structure. It is also emphasised that such a problem is much more important close to the base of the building, as the storey shear tends to the base shear.

The presence of soft storeys is typically due to the following circumstances: (1) masonry pier panels or columns significantly taller than those located at the other floor levels; (2) the lack of continuity of lateral load-resisting elements along the whole building height; and (3) the presence of masonry infills only at some floor levels. The first two circumstances may occur, for instance, in the presence of storeys with special use, like those containing garages, department stores, cinemas, theatres, conference halls, and gyms. Weaker elements are generally less vulnerable than soft storeys, as shown by past seismic events such as the 1994 Northridge earthquake. In the case of masonry buildings, large irregularities due to non-prismatic piers can produce heavy damage, since the failure of some piers can induce premature collapse of the building.
In most cases, masonry buildings are characterised by irregular mass distributions due to the presence of live loads with different magnitude at the different floor levels. The presence of libraries, archives, heavy concentrated masses (e.g., equipments), and high occupancy, induces less uniformity in the distribution of the expected inertia forces, resulting in significant variations of storey shear and overturning moment along the height. Also these circumstances produce heavy damage to structural components.

- **Structural regularity according to Italian building code and EC8**

The new Italian building code (IBC) passed by the Italian Ministry of Infrastructures and Transportation (IMIT, 2008) provides simplified rules to assess structural regularity before seismic analysis is run. Such rules are in compliance with EC8. To that end, IBC suggests first the maximisation of structural redundancy and, if needed, seismic joints able to transform the whole structure in uncoupled sub-systems.
Regarding buildings, a construction can be assumed to be *regular in plan* if the following requirements are met:

(a) the plan shape is compact and rather symmetric with respect to, at least, two orthogonal directions in terms of inertia masses and stiffnesses;
(b) the building plan can be included in a rectangle having a lengthening ratio lower than 4;
(c) any setback does not exceed 25% of the total dimension of the building plan in the same direction; and
(d) the floor diaphragms can be considered as sufficiently resistant and rigid in their own plane with respect to lateral load-resisting elements.

A structure can be assumed to be *regular in elevation* if it meets the following requirements:

(e) all lateral load-resisting elements (e.g., frames and shear walls) run along the whole height of the building;
(f) inertia mass and lateral stiffness are constant or change gradually without

significant variations, from the base to the top of the building (mass variations from a floor level to another do not exceed 25%; the lateral stiffness does not have a reduction higher than 30% and an increase higher than 10% from a floor level to the overlaying floor level); buildings are considered to be regular in elevation in terms of stiffness, in the presence of shear walls, RC cores, prismatic masonry walls and cores, or braced steel frames, providing at least 50% of the earthquake resistance; and

(h) gradual setbacks do not exceed 30% of the dimension of the former floor diaphragm, nor 20% the dimension of the underlying floor diaphragm; no limitations are given for the top floor level in the case of constructions with more than four storeys.

The requirement (g) is not mentioned here being it related only to frame building structures.

4.4. Force-Based versus Displacement-Based Design

Traditionally, the design spectral acceleration at the fundamental period has been always assumed as a good seismic demand parameter in the engineering practice. Seismic design of structures is then based on the estimation of the base shear as the product of the global inertia mass by the pseudo-acceleration at the fundamental period. In fact, in the presence of low equivalent viscous damping and period of vibration lower than 4, the inertia force can be assumed to be equal to the equivalent static force (i.e., the lateral stiffnes multiplied by the maximum expected displacement). Then, the base shear is regarded as a lateral strength demand on the structure. The distribution of strength demands along the height of the building depends on the assumed response displacement profile, while the horizontal distribution at each floor level depends on the in-plane flexibility of diaphragms. Therefore, linear equivalent static analysis falls within a *force-based design* (FBD) approach (namely, a design by verification), which is affected by weak assumptions on both elastic and inelastic response of the structure (e.g., stiffness distribution and strength reduction factor). Lateral displacements are not explicitly taken into account in the safety verifications and their estimation is based on the assumption of displacement ductility and equal energy/displacement rule.

Opposed to this approach, seismic design of structures can also be carried out in terms of displacements or energies, namely it can be a *displacement-based design* (DBD) or an *energy-based design* (EBD). DBD was proposed and carefully assessed by several researchers like as Priestley, Calvi, and Kowalsky (2007). It is particularly interesting because global collapse of the structure is assumed to occur when displacement demand reaches capacity at the performance state of interest. The earthquake capacity

of structures is then expressed in terms of displacements, rather than forces, since they are directly correlated with both structural and non-structural damage.

A classical example is based on the response assessement of EPP structural systems. Under high-intensity earthquakes, the yielding point is significantly exceeded so the demand-to-capacity ratio in terms of lateral strength is almost equal to unity. The collapse is thus reached as the lateral displacement attains a limit value.

This evidence leads to the need for the interpretation of seismic actions on structures as displacement demands, rather than (only) strength demands. FBD leads to high underestimations of earthquake resistance. Similarly, if the seismic assessment is based on linear equivalent static analysis, it tends to 'hide' the seismic *overstrength* due to redistribution of internal forces occurring after the failure of the weakest structural element, in the case of masonry structures. Based on the above considerations, the most advanced seismic codes allow to apply DBD in seismic design of structures or, at least, to perform a displacement-based assessment of existing structures (e.g., by means of static pushover analysis). It is clear that seismic demand on structures is then to be estimated through design displacement response spectra which, in turn, are to be derived by scaling the elastic response spectra through a *displacement amplification factor* A_D. Such a factor is used also in seismic assessment at ULS based on linear equivalent static analysis and is denoted as μ_d by IBC. This factor is defined as a function of the adopted strength reduction factor and the fundamental period of vibration.

Since an accurate estimation of seismic demand is needed, DBD procedures highlighted some open issues in engineering seismology related to the definition of seismic input in terms of displacements by means of specific design displacement spectra. Based on a high number of digital records of past earthquakes occurred in Japan and Europe, Faccioli et al. (2004) derived interesting results on the characteristics of these spectra, allowing to employ *direct displacement-based design* (DDBD) procedures (Priestley et al., 2007) as a viable alternative to FBD. DDBD procedures seem to be rather simple for engineering practice, and able to ensure design performance objectives in compliance with PBD framework. This is the reason why DDBD was included in some seismic codes of earthquake-prone contries, like as New Zealand (NZSEE, 1996).

Also DDBD is based on the definition of an equivalent elasto-plastic SDOF system, but the latter is characterised by means of effective stiffness at the maximum displacement demand and equivalent viscous damping factor. Such a factor is expressed as the sum of the elastic viscous damping, which is quite low (even if always present in the structure), and the hysteretic viscous damping, which is rather high (but present just in the plastic range). Displacement demand is related to the performance

level under consideration, while effective damping depends on the hysteretic energy of the equivalent SDOF system. Design displacement spectra are defined by amplifying the equivalent viscous damping (ξ_{eq}) to be used in the equations of the elastic response spectra. Thus, *overdamped spectra* are used instead of constant-ductility inelastic spectra. The base shear is then estimated as the product of the effective stiffness by the displacement demand, and its distribution along the height is defined by considering the actual profile of inelastic displacements.

Hysteretic energy demand is a another key parameter which is well correlated with damage in the presence of repeated plastic cycles induced by seismic ground motion. In such a case, the supply ductility reduces due to low-cycle plastic fatigue and damage accumulation, resulting in potential premature collapse with respect to its monotonic counterpart. Damage accumulation can play a key role also in the case of masonry structures subjected to earthquake sequences. Given that only a few experimental data on hysteretic energy are available at present for masonry walls, EBD methods do not still apply to masonry buildings. Estimating hysteretic energy could allow to perform damage analysis through non-linear static procedures by using the Park & Ang damage index ($I_{P\&A}$), which is a linear combination of demand-to-capacity ratios expressed in terms of displacements and hysteretic energy (Fajfar and Gašpersič, 1996). Therefore, seismic safety could be assessed by checking that $I_{P\&A} \leq 1$.

Chapter 5 - NON-LINEAR STATIC PROCEDURES

In the last decade, research community has recognised *non-linear static procedures* (NSPs) as effective tools for seismic performance predictions at different earthquake intensity levels. Static structural analyses allow to avoid complex, even if rigorous, non-linear time-history analyses. Such an advantage is much more evident by high difficulties related to (1) selection and scaling of seismic input, (2) definition of evolutionary hysteretic models, and (3) interpretation of analysis results, which are open issues in earthquake engineering especially in the case of masonry constructions.
Seismic performance assessment requires the estimation of *capacity* and *demand*. In the case of inelastic systems, there is a relationship between capacity and demand because seismic response changes as cracking and yielding develop.
In the present chapter, the main methods currently available in the literature for the estimation of seismic capacity and demand are reviewed and discussed. For the sake of clarity, such methods are grouped in separate sections.

5.1. Estimation of Seismic Capacity

5.1.1. General Remarks

Non-linear incremental static (pushover) analysis is the application of the classical incremental iterative method of plastic structural analysis. *Static pushover* (SPO) *analysis* was employed for the first time in earthquake engineering by Gulkan and Sozen (1977), and Saiidi and Sozen (1981), as displacement-based seismic assessment method. Krawinkler (1995) proposed its use also in seismic design. The scope of pushover analysis is to get the best estimation of the evolutionary dynamic response of structures subjected to acceleration/displacement time-histories compatible with both site-specific seismic hazard and design spectra provided by codes. In other terms, such an analysis is aimed at obtaining a simplified estimation of response predictions which could be derived by *incremental dynamic analysis* (IDA) (Vamvatsikos and Cornell, 2002), also called *dynamic pushover analysis*. The latter consists of multiple non-linear dynamic analyses under spectrum-compatible accelerograms which are suitably selected and scaled on the basis of a proper *IM* supposed to be well-correlated with structural and/or non-structural damage. The accuracy of SPO predictions can be assessed by comparing the pushover curve to the median IDA curve.
Static pushover analysis (simply called ‘pushover analysis’ in this thesis) consists in

the application of a pattern (adaptive or not) of monotonically-increasing lateral loads (forces or displacements) on a non-linear structural model subjected to gravity loads. The structure is then laterally pushed up to collapse in a way to estimate its evolutionary seismic response. An analysis step corresponds to each lateral load increment/variation and the structural equilibrium in the non-linear range is numerically assessed through a series of iterations ending at the attainment of numerical convergence. The structural analysis is stopped in one of the following cases:

(1) attainment of a pre-defined limit state;
(2) attainment of global collapse; or
(3) loss of numerical stability.

Structural response at each analysis step is represented on a Cartesian plane having *horizontal displacement at the control point* Δ_c[16] on the abscisse axis and *base shear* V_b on the ordinates axis. A *pushover curve*, namely the output of the analysis, is the graphic representation of the relationship between the earthquake resistance and the gloal displacement of the structure. Pushover analysis is based on the assumption that the seismic response of a MDOF system is directly related to that of an equivalent SDOF system with appropriate mass, stiffness, strength, and ductility. The actual structure is then transformed in a SDOF system through the *substitute-structure approach* proposed by Shibata and Sozen (1976). To this aim, the dynamic response of the MDOF system is assumed to be time-invariant, namely conditional only on a single mode of vibration characterised by a shape vector $\mathbf{\Phi}$ constant with time at any deformation level.

Figure 5.1 shows the main stages of pushover analysis, highlighting the transformation of the actual structure in an equivalent SDOF system.

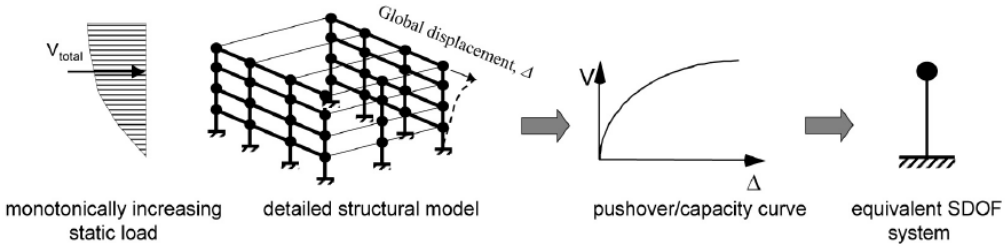

Figure 5.1 Non-linear incremental static (pushover) analysis

[16] The control point is typically assumed as the centre of mass at the roof level. This assumption is not based on a specific theoretical rule and is likely derived from former applications of pushover analysis to bridge piers where the top lateral displacement was monitored. Such a displacement is not always a reliable parameter for building response predictions.

Using the label * to identify the characteristics of the equivalent elasto-plastic SDOF system, the lateral displacement is associated with the actual displacement at the control point of the structure as follows:

$$d^* = c\,\Delta_c \tag{5.1}$$

being c a response modification factor defined as:

$$c = \frac{\boldsymbol{\Phi}^{\mathrm{T}}\mathbf{M}\boldsymbol{\Phi}}{\boldsymbol{\Phi}^{\mathrm{T}}\mathbf{M}\mathbf{1}} = \frac{\boldsymbol{\Phi}^{\mathrm{T}}\mathbf{M}\boldsymbol{\Phi}}{m_e^*} \tag{5.2}$$

where **1** is the unit vector and m_e^* the inertia mass of the equivalent SDOF system. It is clear that c can be computed only once the vector $\boldsymbol{\Phi}$ has been defined. If the latter vector is related to a specific mode of vibration, then the factor c is equal to the inverse of the modal participation factor Γ. The bilinear idealisation of the pushover curve of the actual structure allows to define the equivalent SDOF system characteristics as follows:

$$d_e^* = c\,\Delta_{c,e} \qquad V_u^* = \boldsymbol{\Phi}^{\mathrm{T}}\,\mathbf{V}_u \qquad k^* = V_u^* \big/ d_e^* \tag{5.3}$$

being $\Delta_{c,e}$ the yielding displacement and $\mathbf{V}_u$ the lateral force vector at the maximum base shear $V_{b,max}$. It has been shown that accurate response predictions can be obtained also if the response modification factor is assumed to be constant, in the case of small-to-medium variations in the modal shape vector. This is true particularly if dynamic response is mainly governed by the fundamental mode (Krawinkler and Seneviratna, 1998; Lawson et al., 1994; Fajfar and Gašpersič, 1996).

In the last years, different strategies of incremental static analysis have been proposed, aiming at their wide application to structures affected by high strength/stiffness degradation, irregularities, sensitivity to higher modes of vibration, and P-Delta effects. Pushover analysis procedures can be classified in terms of:

- *applied lateral loads* (i.e., force- versus displacement-based procedures);
- *control strategy* (i.e., load- versus response-controlled procedures);
- *number of vibration modes* under consideration (i.e., single- versus multi-mode procedures); and
- *load pattern* (non-adaptive versus adaptive procedures).

In general, pushover analysis allows to simply estimate (Krawinkler and Seneviratna, 1998):

- flexural and shear strength demands on potential brittle structural elements and their connections;
- deformation demands in potential ductile elements, able to dissipate input energy;
- effects of both strength degradation and failure of individual elements on the global seismic response of the structure;

- effects of stiffness and/or strength irregularities in plan and elevation, which can be identified through the graphic representation of seismic damage (potential concentrations are simple to be identified);
- the sequence of failure modes and their influence on the pushover curve;
- critical elements subjected to high inelastic ductility and deformation demands;
- the accuracy of the assumed load profile; and
- global overstrength and supply strength reduction factor related to displacement ductility.

The last capacity parameters allow to assess the strength reduction factor employed in FBD through linear equivalent seismic analysis.

Classical pushover procedures are affected by some limitations due to the impossibility of capturing directly dynamic response effects associated with higher modes and damage accumulation under cyclic loading (Kim and D'Amore, 1999; Naeim and Lobo, 1999). Potential effects of seismic ground motion duration and kinetic energy cannot be also simulated through static pushover analysis.

5.1.2. Force-Based versus Displacement-Based Procedures

The classical pushover analysis is based on the application of two different patterns of lateral forces: a 'modal' load pattern proportional to inertia masses multiplied by first-mode displacements; and a 'uniform' load pattern proportional to inertia masses. For each lateral load pattern, the structure is subjected to successive force increments through a load multiplier (namely, keeping constant the ratios between consecutive applied forces) up to the attainment of one of the conditions mentioned in Section 5.1.1. Displacements at different load steps represent the response of the structure and are consistent with equilibrium and compatibility under a given pattern of lateral forces.

Once the lateral force profile $\mathbf{F}_0 = (1 \ldots \beta_i \ldots \beta_n)^T$ has been defined ($\beta_i = m_i\phi_i/m_1$ and $\phi_i = z_i/H$ for modal pattern, and $\beta_i = m_i/m_1$ for uniform pattern), the lateral force vector $\mathbf{F}^{(k)} = (F_1 \ldots F_i \ldots F_n)^T$ at a given load step k is defined as follows:

$$\mathbf{F}^{(k)} = \lambda^{(k)} \mathbf{F}_0 \tag{5.4}$$

where $\lambda^{(k)}$ is the load multiplier defined through a load/response control strategy (see Sect. 5.1.3).

Given that response of inelastic systems depends on demand, the pushover curve related to a given force pattern is different from that related to the other pattern. In the case of regular structures, pushover curves corresponding to modal and uniform lateral force patterns form a *region* including IDA predictions. In fact, the modal force pattern allows capturing the elastic dynamic response of the structure, while the uniform force

pattern (corresponding to a constant distribution of horizontal accelerations along the height of the structure) allows capturing the inelastic dynamic response after heavy damage throughout the structure. Frequently, an inverse triangular force pattern is used instead of the modal pattern, assuming a linearised first-mode shape. The uniform pattern induces typically a higher earthquake resistance with respect to both modal and inverse triangular patterns, as a result of higher overturning moment[17]. This statement was demonstrated by Mwafy and Elnashai (2001) by comparing pushover curves corresponding to the above-mentioned lateral force patterns (Fig. 5.2).

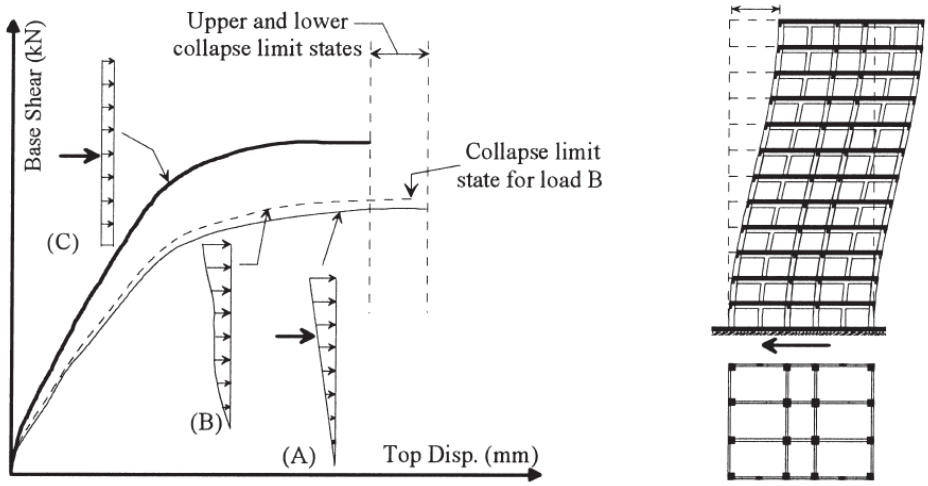

Figure 5.2 Pushover curves for different force patterns (Mwafy and Elnashai, 2001)

The lateral forces simulate inertia forces induced at several floor levels by earthquake loading, and hence its direct application seems to be more appropriate to statically simulate the dynamic response of the structure. Nevertheless, since the attainment of limit deformations has been recognised to be the main cause of damage, especially in ductile structural systems, pushover procedures based on the application of lateral displacements, rather than forces, have been developed. In such a case, lateral forces applied along the height of the structure are derived from the given lateral displacements through structural analysis. It follows that in displacement-based procedures the relative importance of lateral forces remains the same with reference to both structural equilibrium and simulation of inertia forces estimated through IDA.

In the case of displacement-based pushover analysis, the structure is subjected to a displacement vector $\boldsymbol{\Delta}^{(k)} = (\Delta_1 \ldots \Delta_i \ldots \Delta_n)^T$ which is derived by incrementing the shape

[17] The centroid of the uniform force pattern is lower than those of both modal and inverse triangular patterns, so the overturning moment reaches its minimum value.

vector $\boldsymbol{\Delta}_0 = (1 \ldots \omega_i \ldots \omega_n)^T$ at each step *k*, as follows:

$$\boldsymbol{\Delta}^{(k)} = \alpha^{(k)} \boldsymbol{\Delta}_0 \tag{5.5}$$

where $\alpha^{(k)}$ is the load multiplier resulting from total or incremental updating. By solving the equilibrium equation $\mathbf{F}^{(k)} = \mathbf{K}^{(k)}\boldsymbol{\Delta}^{(k)}$ in compliance with kinematic compatibility, one can simulate the evolution in the resisting base shear $V_b = \mathbf{1}^T\mathbf{F}$ under varying displacement Δ_c.

5.1.3. Control Strategies

The computational strategy employed in classical pushover procedures is based on the *load control*, namely the control of the lateral forces acting on the structure.

If the analysis procedure is based on the application of lateral force, then the load control means to monotonically increase the multiplier $\lambda^{(k)}$ in Eq. (5.4) and to estimate the corresponding displacement vector $\boldsymbol{\Delta}^{(k)}$. The control strategy allows to predict only non-linear response of non-degrading structural systems. For them, the pushover curve has a rising branch and the collapse is associated with the attainment of the peak resisting base shear.

Actually, structures may resist against displacement demands larger than those corresponding to the maximum earthquake resistance, even though a strength degradation takes place and is graphically represented by a post-peak falling branch on the pushover curve. This statement has highlighted the inadequacy of load-controlled pushover analyses (Antoniou and Pinho, 2004a). Therefore, a series of procedure able to change the force multiplier have been proposed, in order to simulate also the post-peak softened response. Such procedures are mainly based on the *response control*. At each given step and up to the global collapse, or numerical instability, they consist of the following stages: (1) definition of a displacement increment at the control point; (2) estimation of the relevant resisting lateral forces, keeping constant the load profile; and (3) the estimation of lateral displacements (both translations and torsional rotations) at each floor level. This procedure is then aimed at estimating the structural response that meets a pre-defined load profile under varying lateral displacement at the control point. Namely, one has to check that the lateral displacement at the control point increases and a pre-defined load profile is met. To this end, the multiplier $\lambda^{(k)}$ is changed along with the vector $\boldsymbol{\Delta}^{(k)}$ at each analysis step. It is underlined that:

- structural degrading response could be assessed also through a *mixed control* strategy consisting in the load control in the pre-peak range and in the response control in the post-peak range; and
- response control in force-based approaches does not consists in monitoring the whole displacement profile, so response-controlled pushover procedures should not

be confused with displacement-based procedures; in the latter, the load control is rather equal to the response control, because the load profile is the lateral displacement pattern.

5.1.4. Single-Mode versus Multi-Mode Procedures

The lateral forces or displacements imposed to the structure are typically defined considering the fundamental mode of vibration. In the case of tall buildings, highly-irregular structures, or constructions with high response sensitivity to damage evolution (i.e., non-uniform distribution of cracking and yielding), higher modes of vibration should be also considered if they affect considerably the global seismic response.

Paret et al. (1996), Sasaki et al. (1998), and Kunnath and Gupta (2000) were, amongst others, the first researchers which proposed non-linear static analysis methods able to include higher mode effects. In the case of tall buildings, in order to consider higher mode effects, FEMA 356 (ASCE, 2000) suggests to assume a lateral force vector $\mathbf{F} = \mathbf{M}\,\mathbf{H}^k$, being $\mathbf{H}$ the vector containing the normalised heights of the floor levels and k a factor which is a function of the fundamental period T_e, as follows:

$$k = \begin{cases} 1.0 & \text{for } T_e \le 0.5\text{s} \\ 1.0 + 0.5\left(T_e - 0.5\right) & \text{for } 0.5\text{s} < T_e < 2.5\text{s} \\ 2.0 & \text{for } T_e \ge 2.5\text{s} \end{cases} \tag{5.6}$$

Therefore, one get the inverse triangular force pattern if $T_e \le 0.5$ s, while k increases linearly in the interval]1,2[if 0.5 s < T_e < 2.5 s.

In multi-mode procedures, the load profile is derived from modal shapes through quadratic combination rules. In the Freeman formulation, the higher mode effects are included in the definition of lateral forces by means of the squared root of sum of squares (SRSS) modal combination rule. The number of vibration modes considered in the analysis is that corresponding to a participating mass not lower than 90% of the total inertia mass. The lateral forces depend also on *spectral amplification*, namely the acceleration demand associated to each mode of vibration. That modus operandi allows to consider the change in relative importance between different modes of vibration due to period elongations, as damage develops throughout the structure. The fundamental period increases generally more than the others, reaching also final values even equal to five times the initial value. The period elongation related to higher modes of vibration may induce a spectral amplification of the fundamental mode much lower than that associated, for instance, to the second mode of vibration, as shown in Figure 5.3.

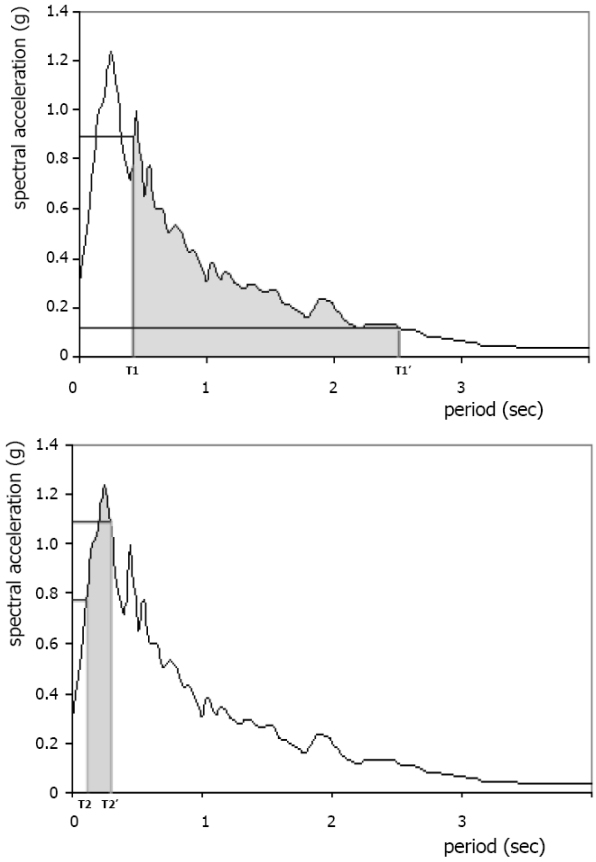

Figure 5.3 Modification of spectral amplification for first and second modes (Antoniou, 2002)

Valles et al. (1996) proposed to include the contribution of higher modes through the definition of an *equivalent fundamental mode* based on the SRSS modal combination rule. The force vector is then obtained through the equation:

$$\mathbf{F} = \mathbf{M}\,\boldsymbol{\phi}_{eq} \tag{5.7}$$

being:

$$\boldsymbol{\phi}_{eq} = (\phi_{eq,1} \ldots \phi_{eq,i} \ldots \phi_{eq,n})^{T} \quad \text{con} \quad \phi_{eq,i} = \sqrt{\sum_{j=1}^{n} \left(\Gamma_j \phi_{ij}\right)^2} \tag{5.8}$$

Chopra and Goel (2002) developed the *modal pushover analysis* (MPA) which includes the contribution of all significant modes of vibration for seismic demand estimation. In such a procedure, pushover analysis is carried out for each individual mode. Pushover curves related to different modes of vibration of the structure are reduced and idealised with bilinear relationships in a way to define a series of equivalent SDOF systems. Displacement demand (i.e., the target displacement) is thus estimated through the design spectrum, and response parameters of the actual structure

are finally assessed. Maximum demand values associated with the modes of vibration under consideration are combined to estimate the total demand. Since the lateral forces corresponding to the first two or three modes are typically sufficient to characterise the dynamic response of the structure, MPA is not computationally too demanding if compared to other procedures. Nevertheless, MPA makes quite complex the estimation of displacement demand through the *capacity spectrum method* (see Sect. 5.2.1) due to potential displacement reversals induced by gradual yielding in pushover curves associated with higher modes of vibration (Hernández-Montes et al., 2004; ATC, 2005; Goel and Chopra, 2005).

Chopra et al. (2004) proposed also a *modified modal pushover analysis* (MMPA) in which seismic demand associated with higher modes is estimated by assuming an elastic response of the structural system. The total demand related to more modes of vibration is obtained through a pushover analysis performed for the fundamental mode and a multi-mode dynamic analysis performed for the higher modes.

5.1.5. Constant versus Adaptive Load Profiles

Traditionally, non-linear static analysis has been carried out keeping constant the lateral load pattern (forces or displacements) through a single multiplier. Alternatively, an *adaptive* (or *evolutionary*) *pushover analysis* can be performed by updating the load profile at each analysis step, in order to follow the evolution in the structural response as the damage develops. The modification in the structural properties may involve not only the global lateral stiffness, but also the modes of vibration and spectral amplification. This information can be included in the adaptive analysis via multi-mode dynamic analysis carried out at each step by assuming the actual secant stiffness.

Bracci et al. (1997) proposed for the first time a pushover procedure based on fully adaptive load profiles. The analysis begins with the assumption of the initial load pattern, which is generally triangular, while successive load increments are determined from the base shear and storey shears related at the previous step.

A different procedure was proposed by Gupta and Kunnath (2000): the applied load is constantly updated on the basis of current dynamic characteristics of the structure, taking into account a site-specific spectrum. To that end, at each step an eigenvalue analysis is carried out by assuming the tangent or secant stiffness associated with deformations of the previous load increment. The lateral forces related to the *j*-th mode of vibration and acting at the *i*-th floor level are obtained as follows:

$$F_{ij} = \Gamma_j \, \phi_{ij} \, M_i \, S_{a,j} \tag{5.9}$$

being: Γ_j the modal participation factor; ϕ_{ij} the normalised modal displacement; M_i the inertia mass at the *i*-the floor level; and $S_{a,j}$ the spectral amplification associated with

the period T_j. Mwafy and Elnashai (2001) found that the inclusion of spectral amplification of each mode into Eq. (5.9) allows to get a better consistency with IDA response predictions.

Figure 5.4 shows the comparison carried out by Antoniou and Pinho (2004a) where spectral amplification was estimated through elastic response spectra. These researchers emphasised also the need for the estimation of effects due to different damping levels related to several modes on global response prediction.

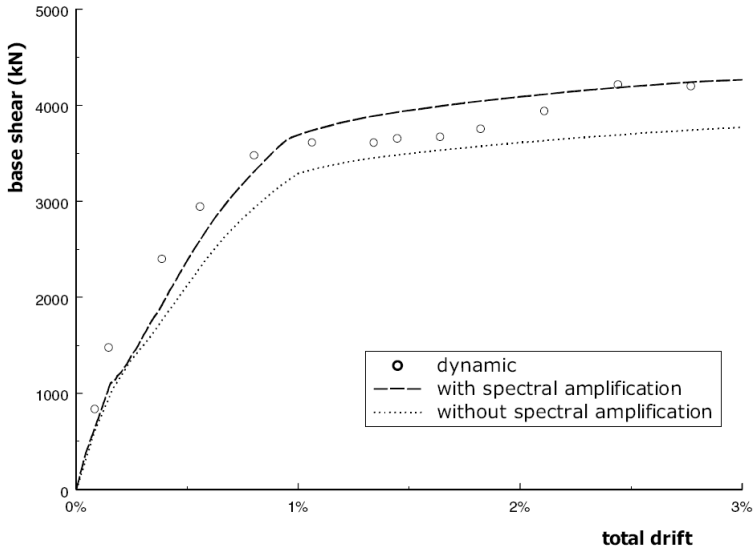

Figure 5.4 Effects of spectral amplification on pushover curve (Antoniou and Pinho, 2004a)

Pushover analysis is performed for each mode and then the resulting lateral forces are combined through the SRSS rule as follows:

$$F_i = \sqrt{\sum_{j=1}^{n} F_{ij}^2} \tag{5.10}$$

The lateral forces derived from modal combination are finally summed up to those obtained at the previous step. At the end of an analysis step, the lateral stiffness is computed to be employed in the eigenvalue analysis related to the subsequent step. Although the estimation of interstorey drifts and sequence of collapse modes is typically satisfactory, the use of the SRSS rule to combine response predictions provided by different pushover analyses (each performed on an individual mode) does not ensure equilibrium at the end of each analysis step.

Elnashai (2001) proposed an adaptive pushover procedure able to include, in a single analysis run rather than combining results from more analyses, all features mentioned above. The force vector is updated by introducing a normalised force vector $\bar{\mathbf{F}}^{(k-1)}$ into

Eq. (5.4), which thus specialises in the following equation of *total updating*:

$$\mathbf{F}^{(k)} = \lambda^{(k)} \bar{\mathbf{F}}^{(k-1)} \mathbf{F}_0 \tag{5.11}$$

It is underlined that, in the case of adaptive pushover, the shape vector $\mathbf{F}_0$ should be defined as uniform, in order to avoid any modification in the load vector corresponding to the modal characteristics which, in turn, are related to the stiffness computed at the previous step.

Figure 5.5 shows the definition of the force vector at a given analysis step, while Figure 5.6 illustrates the variation in the lateral force pattern under increasing roof drift of a regular five-storey frame structure.

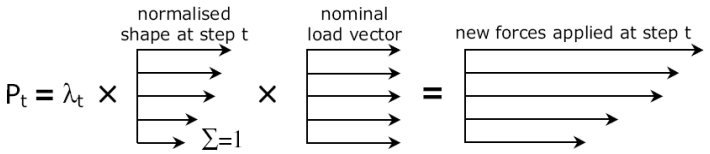

Figure 5.5 Total updating of force pattern (Antoniou, 2002)

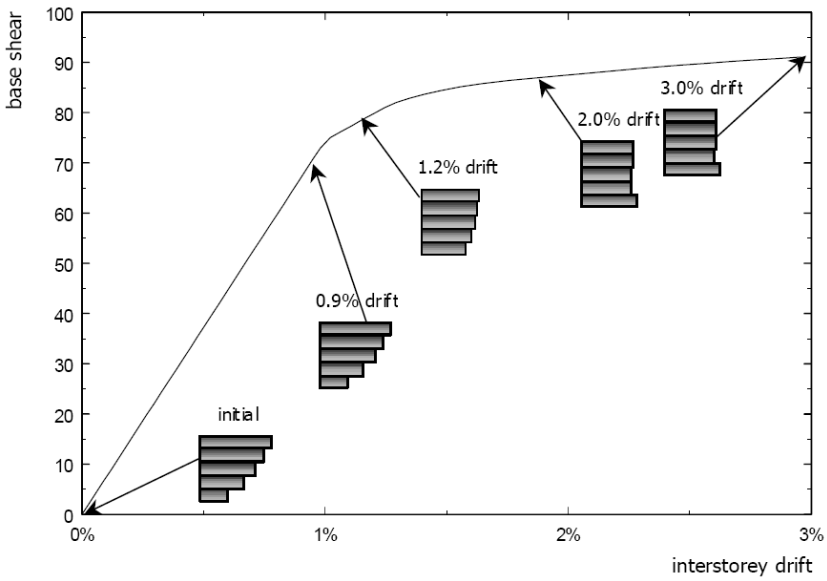

Figure 5.6 Pushover curve from adaptive analysis and force pattern variation (Antoniou, 2002)

Alternatively, the load can be modified through an *incremental updating* strategy (Fig. 5.7) where the load increment $\delta\mathbf{F}^{(k)}$ is changed on the basis of the modal characteristics corresponding to the response prediction at the previous step.

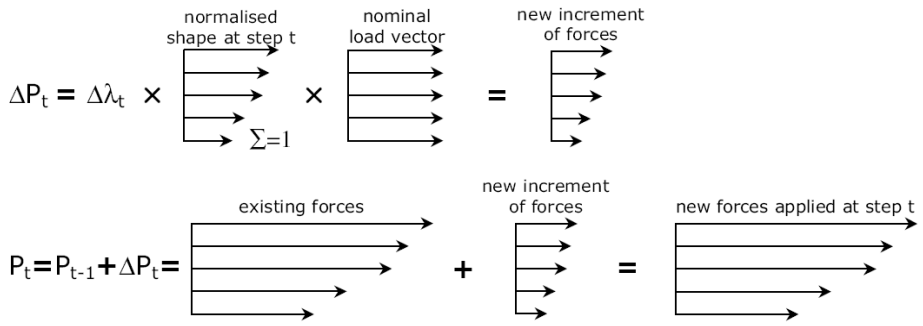

Figure 5.7 Incremental updating of force pattern (Antoniou, 2002)

The total force vector is then defined via the following equation:

$$\mathbf{F}^{(k)} = \mathbf{F}^{(k-1)} + \boldsymbol{\delta}\mathbf{F}^{(k)} = \mathbf{F}^{(k-1)} + \lambda^{(k)}\bar{\mathbf{F}}^{(k-1)}\,\mathbf{F}_0 \tag{5.12}$$

The vector $\bar{\mathbf{F}}^{(k-1)}$ changes the shape (not the magnitude) of the applied forces; each vector component is obtained through a normalisation to the base shear, namely as follows:

$$\bar{F}_i^{(k-1)} = \frac{F_i^{(k-1)}}{\sum_{i=1}^{n} F_i^{(k-1)}} \tag{5.13}$$

If the modes of vibration cannot be assumed to be fully uncoupled, the complete quadratic combination (CQC) rule is to be used. Accordingly, the lateral force at the *i*-th level can be defined as follows:

$$F_i = \sqrt{\sum_{j=1}^{n}\sum_{k=1}^{n}\left(F_{ij}\,\rho_{jk}\,F_{ik}\right)} \tag{5.14}$$

being ρ_{jk} the cross-correlation factor defined through the following equation:

$$\rho_{jk} = \frac{8\xi^2(1+r)r^{1.5}}{\left(1-r^2\right)^2 + 4\xi^2 r(1+r)^2} \quad \text{with} \quad r = \frac{\omega_k}{\omega_j} \tag{5.15}$$

The latter equation includes the equivalent viscous damping ξ (which, for the sake of simplicity, is assumed to be the same for all modes of vibration) and the natural angular frequencies ω_j and ω_k corresponding to the modes under consideration.

In the case of RC frame structures, Antoniou and Pinho (2004a) demonstrated that pushover analysis based on adaptive force patterns do not generally provide significant improvements in seismic capacity estimation, even though they are better from a conceptual standpoint. As shown by Priestley (2003), quadratic combination rules of modal contributions for the definition of load increments at each analysis step lead inevitably to positive increments, and hence a monotonic increase in the load vector. It

is thus not possible any applied load reversal. Potential reversals should be necessarily considered if one intend to simulate irregular distributions of inertia forces in the plastic range. Therefore, the vector $\overline{\mathbf{F}}^{(k-1)}$ should be defined as the weighed vectorial sum of several modal contributions. It was also observed that *force-based adaptive pushover* (FAP) analysis may provide wrong predictions at large inelastic deformations, since it tends to overestimate inelastic deformations in damaged zones (that is, an apparent damage localization) and to underestimate them elsewhere. Lateral stiffness of damaged structural elements reduces and modal shapes provided by eigenvalue analysis change, resulting in a concentration of force increments at the successive step. It follows a kind of vicious circle that leads to overestimate deformations of the first damaged elements.

In the case of regular structures, adaptive pushover analysis provides a pushover curve which lies between those corresponding to constant load profiles. Conversely, in the case of highly-irregular structures, adaptive analysis follows IDA predictions providing a pushover curve which does not lie between those provided by non-adaptive pushover.

In order to overcome the limitations of force-based non-adaptive pushover analysis (e.g., the inability to capture potential force reversals), Antoniou and Pinho (2004b) proposed a *displacement-based adaptive pushover* (DAP) analysis. In fact, displacement-based pushover with constant load profiles provide wrong predictions since the collapse mechanism is not the output of the analysis, but it is chosen before the analysis is run. As a result, displacement-based pushover analysis should be necessarily adaptive, in order to avoid any 'constraint' in seismic response predictions due to a pre-defined collapse mode. Figure 5.8 shows that displacement-based non-adaptive pushover analysis leads to wrong estimations of IDA results, opposed to force-based analysis.

In the adaptive procedure proposed by Antoniou and Pinho (2004b), Eqs. (5.11) and (5.12) related to total and incremental updating of lateral forces, respectively, are rewritten in terms of displacements as follows:

$$\boldsymbol{\Delta}^{(k)} = \alpha^{(k)} \overline{\boldsymbol{\Delta}}^{(k-1)} \boldsymbol{\Delta}_0 \tag{5.16}$$

$$\boldsymbol{\Delta}^{(k)} = \boldsymbol{\Delta}^{(k-1)} + \delta\boldsymbol{\Delta}^{(k)} = \boldsymbol{\Delta}^{(k-1)} + \alpha^{(k)} \overline{\boldsymbol{\Delta}}^{(k-1)} \boldsymbol{\Delta}_0 \tag{5.17}$$

Opposed to force-based pushover analysis, displacement-based pushover analyses on a series of RC structures demonstrated that total updating is not suitable. In fact, it tends to overestimate deformations in the first damaged elements (which is also a limitation of FAP) and to numerical instability problems. The latter are avoided by incremental updating of the displacement vector because its modification is carried out in a gradual mode. Figure 5.9 illustrates a comparison between pushover curves obtained with both types of displacement vector updating.

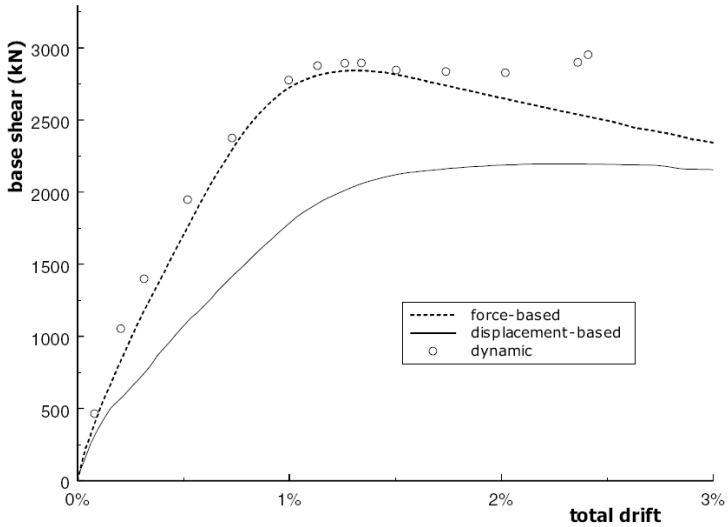

Figure 5.8 Comparison between conventional force-based analysis, non-adaptive displacement-based analysis, and IDA (Antoniou and Pinho, 2004b)

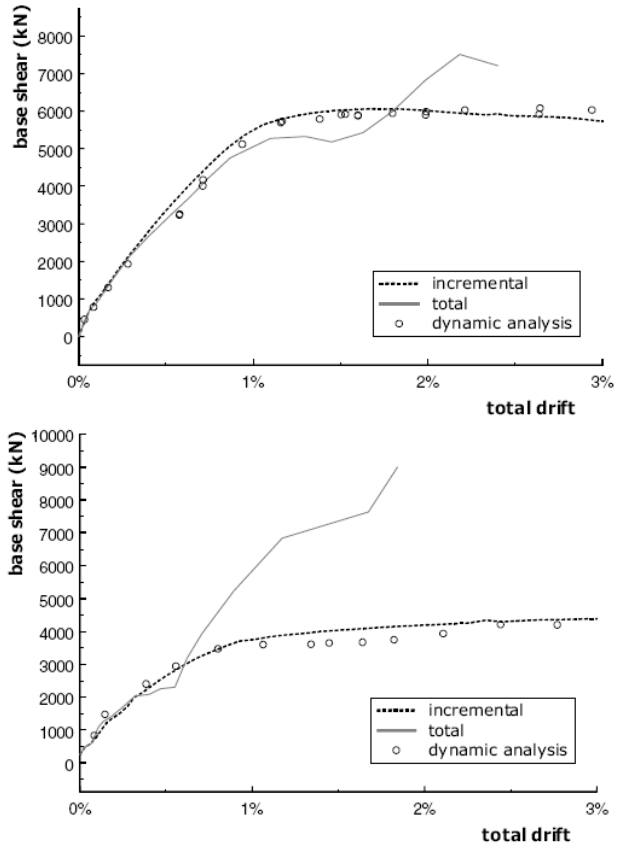

Figure 5.9 Total versus incremental updating in DAP (Antoniou and Pinho, 2004b)

The vector $\bar{\boldsymbol{\Delta}}^{(k-1)}$ changes the shape (not the magnitude) of the given lateral displacements and each component is defined through the following equation:

$$\bar{\Delta}_i^{(k-1)} = \frac{\Delta_i^{(k-1)}}{\max\left\{\Delta_i^{(k-1)}\right\}_{i=1\ldots n}} \tag{5.18}$$

so the maximum displacement is proportional to the load multiplier $\alpha^{(k)}$, according to the load control strategy.

The displacements Δ_i can be estimated in two different modes: (1) directly from eigenvalues through the SRSS or CQC combination rule (*displacement-based scaling*); or (2) from interstorey drifts θ_i defined as the difference between eigenvalues related to two consecutive floor levels (*interstorey drift-based scaling*). In the former case, lateral displacements are computed as follows:

$$\Delta_i = \sqrt{\sum_{j=1}^{n} \Delta_{ij}^2} = \sqrt{\sum_{j=1}^{n} \left(\Gamma_j \phi_{ij}\right)^2} \tag{5.19}$$

while in the latter case, they are computed via the following equation:

$$\Delta_i = \sum_{k=1}^{i} \theta_k \quad \text{with} \quad \theta_i = \sqrt{\sum_{j=1}^{n} \theta_{ij}^2} = \sqrt{\sum_{j=1}^{n} \left[\Gamma_j \left(\phi_{i,j} - \phi_{i-1,j}\right)\right]^2} \tag{5.20}$$

The inclusion of interstorey drifts makes more clear the relationship between inelastic structural response and deformation demand. The spectral displacement amplification $S_{d,j}$ can also be considered to weigh drifts. Thus, Eq. (5.20) specialises as follows:

$$\Delta_i = \sum_{k=1}^{i} \theta_k \quad \text{with} \quad \theta_i = \sqrt{\sum_{j=1}^{n} \theta_{ij}^2} = \sqrt{\sum_{j=1}^{n} \left[\Gamma_j \left(\phi_{i,j} - \phi_{i-1,j}\right) S_{d,j}\right]^2} \tag{5.21}$$

Lateral forces are then derived through structural analysis and are not 'constrained' at any pre-defined profile. This allows to simulate also potential force reversals, according to IDA predictions.

5.1.6. Three-Dimensional Effects

The inclusion of three-dimensional effects in pushover analysis is a key issue. In general, SPO is separately performed along orthogonal directions of the building plan. Nevertheless, several researchers proposed analysis methods (either simplified or more accurate) to include the influence of torsional response on seismic capacity of buildings or, alternatively, on seismic demand. The main issues deal with: (1) the application of lateral forces in one or both directions of the building plan; (2) the combination rule to be employed if both forces are applied on the building; (3) the points of application of lateral forces; (4) the implementation of strength, stiffness, and mass eccentricities; and (5) the ability to apply adaptive profiles on three-dimensional

models, as well as the strategy to be used for their step-by-step updating.

Kilar and Fajfar (1996, 1997) proposed a pushover procedure for asymmetric buildings based on the definition of two-dimensional macro-elements (namely, lateral load-resisting sub-systems like as frames, and single/coupled shear walls) aimed at a simplified non-linear modelling of three-dimensional structures. The behaviour of each macro-element is defined through a bilinear, or multi-linear, relationship between the base shear and the roof displacement. The global pushover curve is then obtained through a step-by-step analysis which allows monitoring the formation of plastic hinges within the structure. The procedure is able to assess torsional effects and their influence on the seismic capacity of the building.

Moghadam and Tso (1996, 2000a) proposed a more accurate non-adaptive single-mode method by extending two-dimensional pushover analysis to three-dimensional structures. The seismic response of the MDOF system is related to that of a SDOF system assuming that the dynamic response of the building is governed by the fundamental mode of vibration. The main difference with two-dimensional pushover methods is that both translations along the *x*- and *y*-axes of the building plan, as well as torsional rotations of floor diaphragms, are considered within the modal shapes. The displacement vector is then defined as follows:

$$\mathbf{\Delta} = \begin{bmatrix} \mathbf{\Phi}_x \\ \mathbf{\Phi}_y \\ \mathbf{\Phi}_\theta \end{bmatrix} \Delta_c(t) = \mathbf{\Phi}\,\Delta_c(t) \tag{5.22}$$

where $\Delta_c(t)$ is a generalised coordinate representing the displacement at the control point; and $\mathbf{\Phi}$ is the displacement shape vector assumed for the building. Nevertheless, such a methodology provides good response predictions at the flexible end of the building, while it leads to highly underestimate the seismic response at the rigid end (Rutenberg and De Stefano, 1997).

A variant of the method proposed by Moghadam and Tso was developed by Penelis and Kappos (2002). The load vector (including lateral forces and storey torques) is derived from translations and rotations resulting from multi-mode dynamic analysis with response spectrum. The transformation of the structure in a SDOF system is carried out once a 'hybrid' SDOF system has been characterised. Such an oscillator has both translational and torsional modes. This approach is an extension of classical methods based on the SDOF system idealisation, but it does not consider higher mode effects, nor force redistribution due to gradual yielding of structural components.

Faella and Kilar (1998) investigated the accuracy of three-dimensional pushover analysis by comparing its predictions to those obtained by dynamic analyses. The force vectors are applied along a single plan direction at the locations of the centres of mass. A parametric investigation was performed to assess the optimal location of the points

where lateral loads should be applied. It was concluded that acceptable response predictions in terms of displacements can be obtained on both rigid and flexible ends of the building, by changing the locations of the points of application of lateral forces. For a given structure, it is clearly that different optimal locations correspond to increasing damage levels. As a consequence, adaptive load profiles are needed because they change with the evolutionary distribution of lateral stiffnesses throughout the structure.

Based on a similar investigation, Kilar and Fajfar (2001) suggested to carry out SPO separately along two directions and to combine their results through the SRSS rule. These researchers found that the accuracy of the method could be improved if the point of application of lateral forces is displaced within the limit eccentricities reported in EC8. The authors represented the torsional response of the buildings under investigation by means of the *Base Shear – Torque* (BST) *surface* proposed by De la Llera and Chopra (1995) to describe all possible terns (V_{bx}, V_{by}, T) corresponding to global collapse (Fig. 5.10). It was found that BST surfaces of multi-storey buildings can be derived by a series of incremental static analyses. Such surfaces allow to understand the seismic response of plan-irregular buildings, and hence to design and assess these structures in seismic zones.

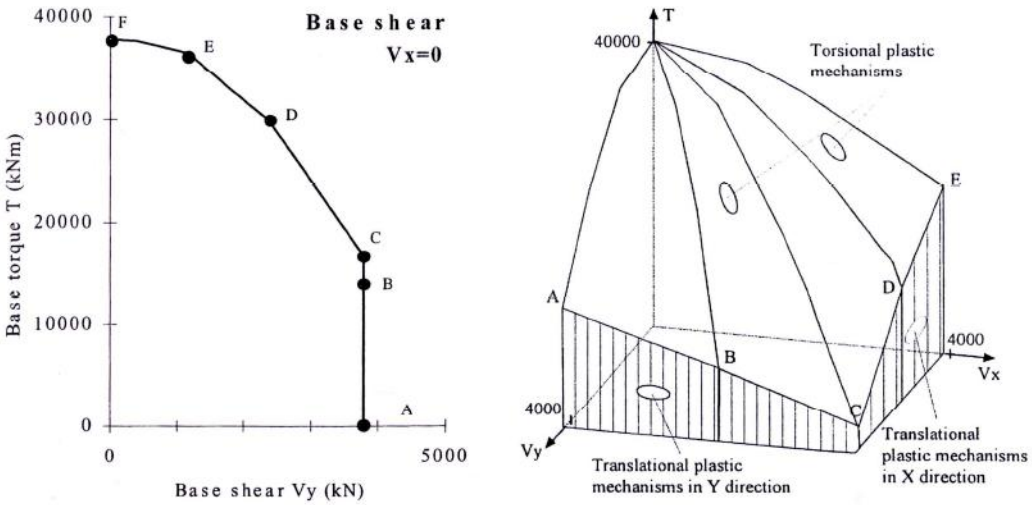

Figure 5.10 BST surface (De la Llera and Chopra, 1995)

A preliminary investigation by Antoniou (2002) showed the good accuracy of FAP for seismic response prediction of three-dimensional structures, highlighting some problems related to the choice of the lateral displacement pattern.

Meireles et al. (2006) assessed DAP by comparing its results with IDA predictions in

the case of the SPEAR asymmetric building. IDAs were carried out considering a bidirectional seismic input which was represented by seven different spectrum-compatible acceleration time-histories. Interstorey drifts due to torsional response were found to be slightly underestimated. The comparison between pushover curves provided by DAP and by conventional non-adaptive pushover procedures (based on inverse triangular force pattern) showed that the latter lead to accurate predictions in the case of low-rise buildings which are regular in elevation. DAP consisted in the simultaneous application of lateral displacements along two orthogonal directions of the building plan. Response predictions were also modified concluding that a single analysis is sufficient if modal contributions are combined within each analysis step. The computational work of this procedure is thus much lower than that associated with MPA (Chopra and Goel, 2002). The latter consists indeed in the combination of more SPOs, each performed for a single mode of vibration.

5.1.7. Non-Linear Static Analysis according to EC8, FEMA356 and Italian Building Code

The identification of the advantages and limitations of the methods discussed above led to the definition of two groups of load profiles for pushover analysis within the most advanced seismic codes. Such an approach is aimed at providing conservative seismic response estimations as the envelope of results corresponding to two procedures selected from those belonging to two groups of load patterns (Kunnath, 2004).

In particular, EC8 (CEN, 2004) considers two force patterns: 'uniform' and 'modal'. FEMA 356 (ASCE, 2000) suggests to carry out SPO at least for load profiles selected from both groups of load patterns listed below. The first group includes force patterns proportional to:

- lateral forces defined as $\mathbf{F} = \mathbf{M}\,\mathbf{H}^{k}$, being k the factor expressed by Eq. (5.6);
- the first-mode elastic shape;
- storey shears derived from linear analysis with response spectrum.

The second group of lateral forces includes the following patterns:

- mass-proportional;
- adaptive.

IBC (IMIT, 2008) suggests the same lateral force patterns with the exception of the first pattern belonging to the first group, which is assumed to be inverse triangular (k = 1), namely proportional to the product of masses by the heights of floor diaphragms. It is worth noting that EC8 recognises that SPO leads to underestimate displacements at the rigid end of the plan (namely, the end where lateral displacements are lower), in the case of both torsionally-flexible structures (i.e., those having a

torsional first mode of vibration) and buildings with a torsional second mode of vibration. This understimation occurs also if accidental eccentricities at the centres of mass are considered in pushover analysis. Therefore, lateral displacements at the rigid end can be amplified according to the output of multi-mode dynamic analysis performed on the three-dimensional elastic model.

5.2. Estimation of Seismic Demand and Performance

According to PBD, seismic demand should be estimated for each limit state of interest. This estimation should include non-linear response of the structure to get accurate predictions of the actual seismic performance. To this aim, given the high difficulties related to IDA and interpretation of its results, one of the following procedures can be employed: the *capacity spectrum method*, which was suggested by ATC 40 (ATC, 1996) for the first time; the *displacement coefficient method*, which is reported in FEMA 356 (ASCE, 2000) and FEMA 440 (ATC, 2005); and the *N2 method*, which is reported in EC8 (CEN, 2004) and IBC (IMIT, 2008).

In the following sub-sections, the key features of such methods are discussed. They are called *non-linear static procedures* (NSPs) in the literature. The main scope is to assess seismic demand through a spectral representation of non-linear response, which is made possible by: (1) the idealisation of the actual MDOF structure as an equivalent elasto-plastic SDOF system; and (2) the transformation of the elastic demand in the inelastic demand by increasing structural damping or, alternatively, defining a global displacement ductility.

5.2.1. The Capacity Spectrum Method

The capacity spectrum method (CSM) was first proposed by Freeman et al. (1975) for rapid assessment of the seismic risk of building classes. Its outstanding ability to give a graphic representation of the seismic performance of a given structure has been widely recognised for seismic design/assessment of buildings (Freeman, 1998). In fact, any damage level can be directly correlated with an earthquake intensity level. Seismic capacity is then compared to demand over the same Cartesian plane having the spectral displacement on the abscisse axis and the spectral acceleration on the ordinates axis (*acceleration-displacement*, AD, *format*). The periods of vibration correspond to rays outgoing from the coordinate system origin. The procedure consists in the following stages:

(1) Definition of the pushover curve V_b–Δ_c by means of pushover analysis or less sophisticated methods;

(2) Assessment of the dynamic properties of the structure (i.e., period of vibration, modal shapes, modal participation factors, and participating mass);

(3) Transformation of the pushover curve in the *capacity spectrum*, namely in the spectral acceleration (S_a) versus spectral displacement (S_d) curve, as follows:

$$S_a = \frac{V_b}{M_1^*} \qquad S_d = \frac{\Delta_c}{\Gamma_1 \phi_{c,1}} \tag{5.23}$$

where Γ_1 is the participation factor of the fundamental mode:

$$\Gamma_1 = \frac{\boldsymbol{\Phi}^{\mathrm{T}}\mathbf{M}\mathbf{1}}{\boldsymbol{\Phi}^{\mathrm{T}}\mathbf{M}\boldsymbol{\Phi}} = \frac{m_e^*}{\boldsymbol{\Phi}^{\mathrm{T}}\mathbf{M}\boldsymbol{\Phi}} \tag{5.24}$$

and M_1^* is the relevant participating mass:

$$M_1^* = \frac{\left(\boldsymbol{\Phi}^{\mathrm{T}}\mathbf{M}\mathbf{1}\right)^2}{\boldsymbol{\Phi}^{\mathrm{T}}\mathbf{M}\boldsymbol{\Phi}} = \frac{\left(m_e^*\right)^2}{\boldsymbol{\Phi}^{\mathrm{T}}\mathbf{M}\boldsymbol{\Phi}} \tag{5.25}$$

The relationship between spectral acceleration and spectral displacement is:

$$S_a = \left(\frac{2\pi}{T}\right)^2 S_d = \omega^2 S_d \tag{5.26}$$

so the slope of the ray outgoing from the axes origin reduces as the period of vibration increases.

(4) Bilinear or multi-linear idealisation of the capacity spectrum by defining, for instance: the elastic stiffness as the secant stiffness at a base shear equal to 0.6-0.7 times the maximum resisting force; the ultimate displacement as the lateral displacement corresponding to a base shear reduction not higher than 15-20%; and finally the ultimate force through the equal energy rule.

(5) Conversion of the 5%-damping elastic response spectrum in a *demand spectrum* which is defined in the AD format via the following equation:

$$S_d = \left(\frac{T}{2\pi}\right)^2 S_a \tag{5.27}$$

The elastic demand is then to be reduced in order to account for damping increase associated with the hysteretic response of the structure. Considering a given number of increasing damping ratios, one can get a set of inelastic demand spectra. In the classical version of CSM, seismic demand was defined through overdamped spectra, rather than constant-ductility inelastic spectra.

(6) Quantification of the seismic performance of the structure in terms of maximum acceleration and displacement for the SDOF system. A *performance point* (PP) can be identified as the intersection of the capacity and demand spectra, the latter corresponding to a suitable damping level. If the capacity spectrum has no

intersection with the demand spectrum, then the structure does not resist against the design earthquake.

From an analytical standpoint, an iterative procedure is needed to identify PP; it goes on until the effective damping of the equivalent SDOF system is computed. Such an iterative procedure is required because, in the case of inelastic systems, seismic capacity depends on seismic demand. In fact, when the structure suffers damage due to large drifts induced by seismic ground motion, its lateral stiffness reduces and the fundamental period of vibration elongates. Therefore, given that the spectral acceleration depends on the period, also the seismic demand changes with the dynamic properties of the structure. It is also underlined that yielding induces energy dissipation by hysteresis (whose magnitude depends on the amplitude and stability of plastic cycles). Given that hysteretic energy is not released by the structure, damping produces a drop in the displacement.

Figure 5.11 illustrates the main stages of CSM. As the displacement demand increases the lateral stiffness of the system (which is estimated on the capacity spectrum) reduces, the period of vibration increases, and the pseudo-acceleration reduces as well. If the fundamental period of the system is higher than the lower bound period of the constant-velocity branch of the demand spectrum, the elasto-plastic SDOF system is subjected to a displacement demand equal to that associated with a linear elastic response (*equal displacement rule*). Conversely, in the case of masonry structures, the fundamental period falls within the interval associated with the constant-acceleration branch of the response spectrum, so the displacement demand is higher than that associated with a linear elastic response (*equal energy rule*).

CSM has two main limitations. First, no physical evidence gives a justification of a stable relationship between hysteretic energy and equivalent viscous damping, especially in the case of highly-inelastic systems. Second, the period associated with the intersection of the capacity curve with the overdamped spectrum cannot be related to the actual dynamic response of the inelastic system. In the United States of America, such considerations have led to assume another method for the estimation of seismic demand, which is based on amplification factors for the elastic displacement demand (see Sect. 5.2.2). In fact, while ATC 40 (ATC, 1996) referred explicitly to the procedure by Freeman, both FEMA 273 (ATC, 1997a) and the successive American standards have focused on the *displacement coefficient method* (DCM).

The classical version of CSM was modified by Fajfar (1999), which proposed the use of constant-ductility inelastic spectra, rather than overdamped spectra. In such a way, the influence of global ductility demand is also taken into account. This variant includes the N2 method (see Sect. 5.2.3). Two procedures based on constant-ductility spectra were also developed by Chopra and Goel (1999), as alternative tools to those

reported in ATC 40. In their investigation, three different R_μ–μ–T relationships were employed, namely those developed by Newmark and Hall (1982), Krawinkler and Nassar (1992), and Vidic et al. (1994). Finally, Albanesi et al. (2000) proposed a simplified variant of CSM which allows eliminating the need for iterations in the seismic demand estimation. That procedure is based on the use of *variable damping response spectra*, which are similar to conventional response spectra.

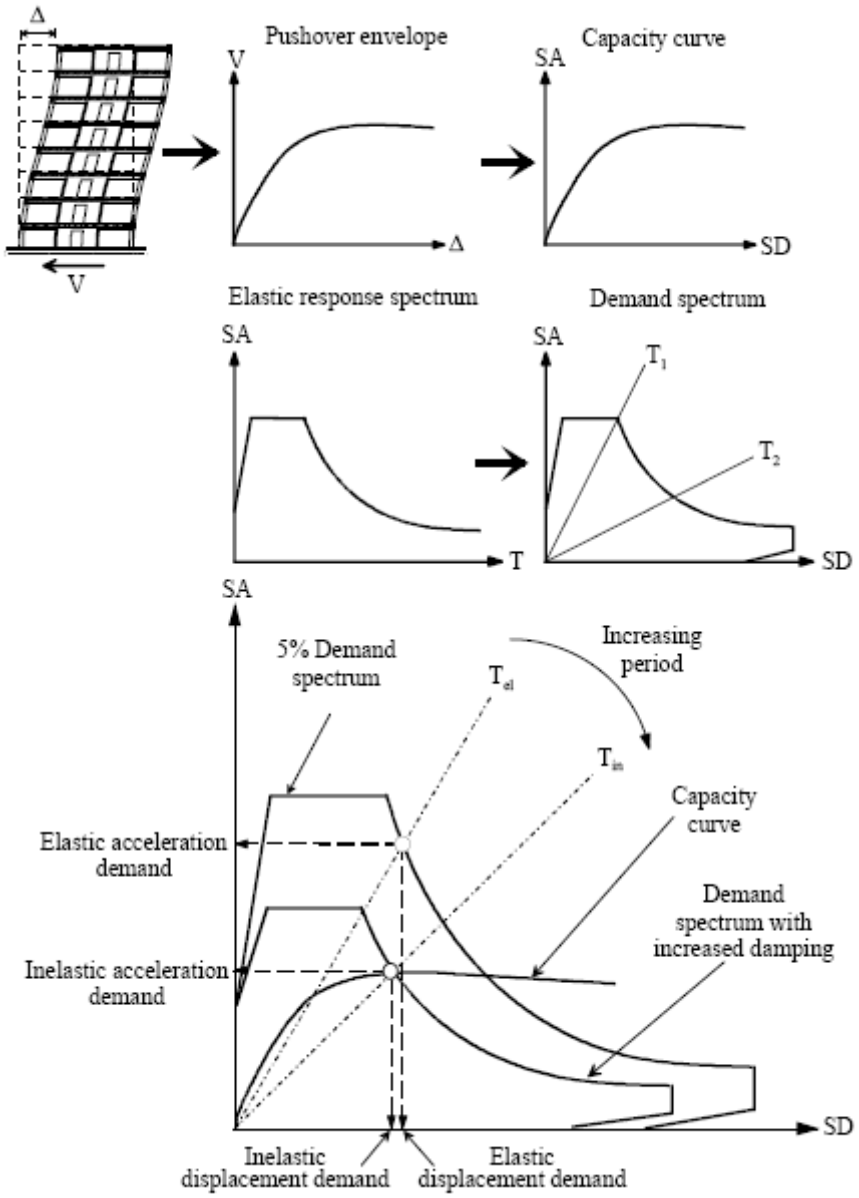

Figure 5.11 Graphic representation of CSM (Mwafy, 2001)

5.2.2. The Displacement Coefficient Method

Such a method was first reported into FEMA 273 and allows to estimate displacement demand (namely, the target displacement) through a numerical procedure which does not include the transformation of the pushover curve in the AD format. The original version applies only in the case of regular buildings and negligible torsional effects due to higher modes of vibration.

The pushover curve is idealised as a bilinear force-displacement diagram. The effective period T_e is estimated as a function of the initial period T_i associated with the elastic stiffness. Then, the target displacement is defined as the product of the elastic demand by a number of coefficients (Fig. 5.12).

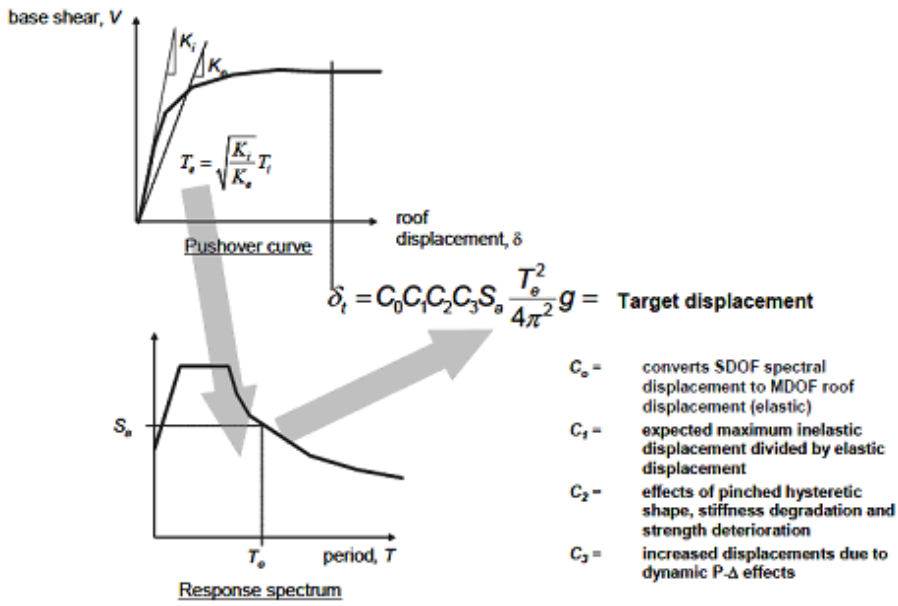

Figure 5.12 Graphic representation of DCM

In particular, the effective period of the structure in the direction considered over the building plan can be estimated as follows:

$$T_e = T_i \sqrt{\frac{K_i}{K_e}} \tag{5.28}$$

where: T_i and K_i are respectively the period and the lateral stiffness obtained through multi-mode dynamic analysis on the elastic structural model; and K_e is the effective stiffness at 0.6 times the maximum base shear.

In the case of buildings with rigid floor diaphragms, the target displacement can be computed through the following equation:

$$\Delta_t = C_0 C_1 C_2 C_3 S_a\left(T_e\right)\frac{T_e^2}{4\pi^2} g \tag{5.29}$$

where:

- $S_a(T_e)$ is the spectral acceleration at the effective period;
- C_0 is a modification factor which allows to estimate the elastic roof displacement of the MDOF system as a function of the elastic displacement demand on the SDOF system; such a factor can be approximated as the participation factor of the fundamental mode;
- C_1 is a modification factor which allows to estimate the maximum displacement on an elastic-perfectly plastic SDOF system as a function of that experienced by the same SDOF system with elastic linear behaviour; this factor is defined as follows:

$$C_1 = \begin{cases} 1.0 & \text{for } T_e \geq T_c \\ \dfrac{1.0 + \left(R-1\right)\dfrac{T_c}{T_e}}{R} \geq 1.0 & \text{for } T_e < T_c \end{cases} \tag{5.30}$$

  where T_c is the lower bound period of the constant-velocity branch of the response spectrum, while R is the strength reduction factor;
- C_2 is a modification factor accounting for the influence of pinched hysteretic shape, stiffness degradation, and strength deterioration, on the displacement demand; and
- C_3 is an amplification factor accounting for dynamic P-Delta effects, which depends on the post-peak response of the SDOF model.

The procedure for the estimation of the target displacement is summarised also into FEMA 356 (ASCE, 2000), while FEMA 440 (ATC, 2005) provides interesting formulations for more accurate estimations of the elastic displacement modification factors, including also characteristics of the seismic ground motion (be it near source or far field). FEMA 440 estiblishes that torsional effects should be considered only if floor diaphragms can be assumed to be rigid in their own plane. In such a case, an additional amplification factor, defined as the ratio between the maximum displacement at any point of the diaphragm and the average displacement, is take into account. On the contrary, in the case of flexible diaphragms, the target displacement should be amplified through a coefficient equal to the ratio between the maximum displacement at any point of the roof diaphragm and the displacement at centre of mass located at the same level.

Akkar and Metin (2007) investigated the accuracy of procedures reported in FEMA 440 for the application of CSM and DCM. A great number of non-linear dynamic analyses were performed on SDOF and MDOF systems under both near source (ordinary and pulse-like) and far field ground motion records. It was found that

both NSPs can provide rather accurate predictions of deformation demand in terms of median values, also in the case of near source records. Statistical errors conditional on strength reduction factor *R* showed that DCM tends to provide conservative estimation under increasing *R*-values.

Erduran and Kunnath (2010) carried out an interesting investigation aimed at improving DCM for degrading MDOF systems. Those researchers found that it is very difficult to get high *R*-values (i.e., not lower than 6) in the case of low-period structures (e.g., masonry constructions), so demand coefficients should be defined by considering the specific value of strength reduction factor. The simplified formulae which define the coefficient C_2 lead to underestimate the displacement demand in the case of low-period structures with stiffness degradation. A set of non-linear analyses were also performed to assess the influence of both strength degradation and P-Delta effects on the displacement demand in the case of systems subjected to both near source and far field seismic ground motions. Therefore, simplified formulas for the definition of a displacement amplification factor able to include not only the stiffness and strength degradations, but also P-Delta effects.

5.2.3. The N2 Method

Such a procedure was proposed by Fajfar and Fischinger (1989), and can be applied also to damage analysis (Fajfar and Gašpersič, 1996). It is a very effective NSP and is the reference method in both EC8 and IBC, being in compliance with multi-level PBD (Fajfar, 2000) and suitable for plan-irregular structures in the presence of accidental eccentricities (Fajfar, 2006; De Stefano and Pintucchi, 2008; Magliulo et al., 2008). The basic idea comes back from the *Q*-model by Saiidi and Sozen (1981), but its last variant was reformulated also in the AD format (Fajfar, 1999) to joint advantages of CSM, in terms of graphic representation, with the sound physical meaning of constant-ductility inelastic demand spectra.

In the N2 method, 'N' stands for non-linear seismic analysis and '2' for two-dimensional structural model. The original version of the method was indeed based on:

- the development of two separate mathematical models of the structure;
- the assessment of seismic capacity through SPO; and
- the use of an inelastic response spectrum for the demand estimation and the global performance assessment.

The capacity model should include the main non-linearities affecting the structure to be assessed. SPO allows then to characterise non-linear response and to identify displacement limits on the pushover curve. The idealisation of the MDOF system as an equivalent elasto-plastic SDOF system is carried out through a homothetic reduction of pushover curves. Such a reduction is performed by means of the modal participation

factor and the modal displacement at the control point. The elasto-plastic SDOF system is defined by bilinear idealisation of the reduced pushover curve, so the inelastic displacement demand is derived (without any iteration) as a function of both the elastic period of the SDOF system and the 'demand' strength reduction factor, by means of R_μ–μ–T relations like that proposed by Vidic et al. (1994).

The use of an elasto-plastic model with hardening, rather than the EPP model, to idealise the reduced pushover curve leads to a reduction in the target displacement, namely the maximum displacement demand defined as the product of the elastic displacement demand by the kinematic ductility μ.

The bilinear idealisation of the scaled pushover curve leads to estimate the yielding force $V_e^* = V_y^*$. Once the effective mass m_e^* and the elastic stiffness k_e^* of the equivalent SDOF system have been computed (see Sect. 5.1.1), the elastic period can be defined as follows:

$$T_e^* = 2\pi\sqrt{\frac{m_e^*}{k_e^*}} = 2\pi\sqrt{\frac{m_e^* d_y^*}{V_y^*}} \tag{5.31}$$

The ratio between the demand elastic resisting force and the yielding force of the SDOF system provides the 'demand' strength reduction factor associated with displacement ductility:

$$R_\mu = \frac{m_e^* S_{a,e}}{V_y^*} = \frac{S_{a,e}}{S_{a,y}} \tag{5.32}$$

The ductility demand μ can be estimated through a R_μ–μ–T relation, so that the inelastic displacement demand can be obtained from that related to the elastic system, namely $S_{d,e}$.

In particular, the maximum inelastic displacement can be estimated through the following equations:

$$\begin{aligned} d_{\max}^* &= \frac{d_{\max,e}^*}{R_\mu}\left[\left(R_\mu - 1\right)\frac{T_c}{T_e^*} + 1\right] = \frac{\mu}{R_\mu} d_{\max,e}^* \geq d_{\max,e}^* \qquad \text{for } T_e^* \leq T_c \\ d_{\max}^* &= d_{\max,e}^* = S_{d,e} \qquad \text{for } T_e^* \geq T_c \end{aligned} \tag{5.33}$$

If Eq. (5.32) gives a strength reduction factor not higher than unity, the structure behaves elastically so the maximum displacement is equal to the elastic demand.

Seismic performance assessment of the structure is thus carried out by checking that the displacement demand derived from one of Eqs. (5.33) does not exceed the displacement capacity d_u. The latter is defined before the bilinear idealisation of the scaled pushover curve is performed. For instance, one can identify the ultimate displacement capacity of the structure at a given base shear drop. If the displacement

demand at the limit state of interest is not higher than the relevant displacement capacity, the distribution of inelastic demand throughout the actual structure can be assessed by amplifying the inelastic displacement demand on the equivalent SDOF system through the first-mode participation factor, as follows:

$$\Delta_{\max} = \Gamma_1 \, d^*_{\max} \tag{5.34}$$

At this displacement, internal forces and deformations of the structure can be computed to assess local demands on individual structural components. The maximum displacement Δ_{max} is clearly the target displacement Δ_t considered in DCM.

In the N2 method, hysteretic damage is not taken into account by increasing the equivalent viscous damping of the elastic SDOF system, but considering an equivalent elasto-plastic system. Thus, Eq. (5.27) cannot be applied and the demand spectrum in the AD format is to be defined through the following equations:

$$S_a = \frac{S_{a,e}}{R_\mu} \qquad S_d = \frac{\mu}{R_\mu} S_{d,e} = \frac{\mu}{R_\mu} \frac{T_e^*}{4\pi^2} S_{a,e} = \mu \frac{T_e^*}{4\pi^2} S_a \tag{5.35}$$

being:

$$\begin{aligned} R_\mu &= 1 + (\mu - 1)\frac{T_e^*}{T_c} && \text{for } T_e^* \le T_c \\ R_\mu &= \mu && \text{for } T_e^* \ge T_c \end{aligned} \tag{5.36}$$

Such equations[18] allow assessing the maximum strength reduction in compliance with supply displacement ductility. The latter is defined on the idealised force-displacement diagram as the ratio between the ultimate displacement (not the demand displacement) and the yielding displacement. In that case, the strength reduction factor is not associated with demand, but is a measure of seismic capacity.

It is underlined that Eqs. (5.36) are an approximation of the following equations derived by Vidic et al. (1994):

$$\begin{aligned} R_\mu &= 1 + (\mu - 1)\frac{T_e^*}{T_0} && \text{for } T_e^* \le T_0 \\ R_\mu &= \mu && \text{for } T_e^* \ge T_0 \end{aligned} \tag{5.37}$$

where: $T_0 = 0.65\ \mu^{0.3}\ T_c \le T_c$.

Figure 5.13 shows a comparison between the R_μ–μ–T relationships defined by Eqs. (5.37) and those obtained by assuming the period T_0 equal to the characteristic period T_c of the seismic ground motion. The latter is typically defined to be the lower bound period of the constant-velocity branch of the response spectrum.

[18] The former is related to the equal energy rule, the latter to the equal displacement rule.

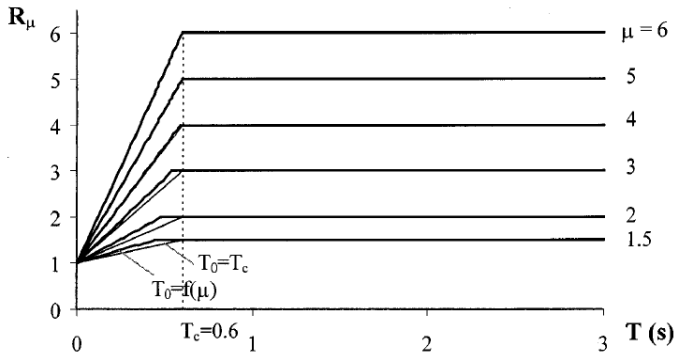

Figure 5.13 Definition of ductility-related strength reduction factor (Fajfar, 1999)

The assumption $T_0 = T_c$ is conservative as it leads to a slight underestimation of the R_μ-factor in the interval $[0,T_c]$, and hence to an acceleration demand (i.e., a required strength) higher than that actual. Figures 5.14a and 5.14b show the graphic identification of PP for low-period structures (that is, with $T^* < T_c$) and high-period structures (that is, with $T^* > T_c$), respectively. PP is defined as as the intersection between the constant-ductility demand spectrum and the bilinear capacity spectrum. The latter is derived from the bilinear force-displacement diagram through Eqs. (5.23). One can see that the inelastic displacement demand on low-period structures is larger than the elastic demand (Fig. 5.14a), while they are the same in the case of high-period structures (Fig. 5.14b).

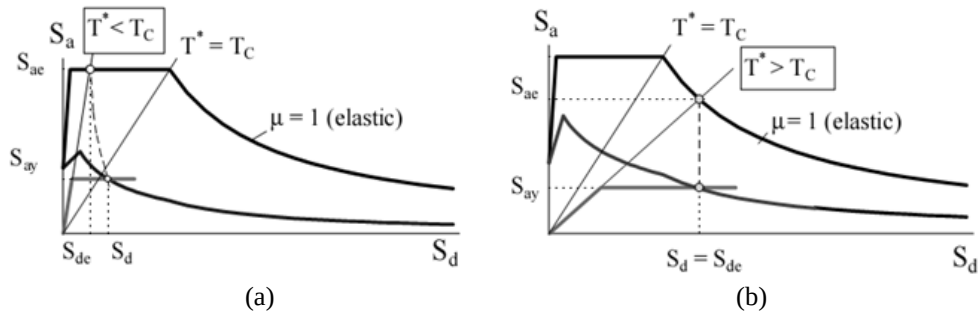

Figure 5.14 Displacement demand estimation for (a) low- and (b) high-period structures

Typically, design acceleration is lower than yielding acceleration of the structure. In fact, overstrength makes possible a further strength reduction through an overstrength factor denoted as R_s. IBC defines the overstrength factor α_u/α_1 as the ratio between 0.9 times the maximum resisting base shear and that corresponding to the failure of the weakest structural element. Therefore, the overall strength reduction factor (namely, the behaviour factor) is defined as $R = R_\mu R_s$.

- **Some remarks on strength reduction factors**

A comprehensive review on strength reduction factors was presented by Miranda and Bertero (1994). Eight different R_μ–μ–T relations were discussed and R_μ was found to be, on average, rather constant and equal to μ in the case of records on rock soil and medium-to-high periods of vibration. The same conclusion was found by Vidic et al. (1994) by investigating the influence of the hysteresis model, earthquake magnitude, and damping model, on the strength reduction factor. Assuming a bilinear force-displacement SDOF model with 10% hardening ratio, R_μ was found to be 20% higher than that obtained for a stiffness-degrading model with the same hardening ratio. R_μ was also found to be higher in the case of 2% damping (rather than 5%) and mass-proportional damping (rather than current stiffness-proportional damping).

More recently, Gupta and Krawinkler (2000) and Miranda (2000) investigated the relationship between the inelastic and elastic displacements concluding that the mean ratio $S_{d,i}/S_{d,e}$ at medium-high periods was equal to 1.0 and 0.85, respectively. A unitary ratio confirms then the validity of the equal displacement rule for flexible structures. Miranda found that the ratio $S_{d,i}/S_{d,e}$ does not depend on the earthquake magnitude, nor on the peak ground acceleration and epicentral distance (near source records are an exception). The scatter in results was found to increase with the level of inelastic deformation and was characterised by typical coefficients of variation for earthquake engineering applications (that is, lower than 0.4 for $\mu = 6$ and lower than 0.3 for $\mu = 3$). Nevertheless, the equal displacement rule leads to large underestimations of inelastic displacement in the following cases: (1) near source records; (2) hysteresis cycles with significant pinching or, alternatively, stiffness and/or strength degradation (Rahnama and Krawinkler, 1993); and (3) systems with low resistance (e.g., ratio between yielding force and elastic strength demand lower than 0.2; Whittaker et al., 1998). The equal displacement rule was found to produce unsatisfactory predictions in the case of flexible soils (Miranda, 1993; Riddell, 1995) for which modified inelastic spectra, or correction factors for displacement demand, should be used.

In the case of low-period structures, the inelastic displacement is larger than the elastic displacement; consequently, the strength reduction factor is lower than ductility. The period of vibration T_0 (below which the inelastic displacement begins to be larger than the elastic displacement) depends on the frequency content of the record. If μ is about 0.4, T_0 is rather equal to T_c. As μ increases or reduces, T_0 increases and reduces as well, as shown by the equation by Vidic et al. (1994). If $T < T_0$, the inelastic displacement is more sensitive to structural properties than in the case of medium-high periods, so less accurate estimates of displacement demand are obtained. Nonetheless, rigid structures are less vulnerable to displacements so that, in general, the latter do not govern the seismic design.

It is emphasised that R_μ–μ–T relations can be applied only to design spectra, while both elastic and inelastic response spectra can be obtained by non-linear time-history analysis for a set of accelerograms. Such response spectra can then be transformed in demand spectra. Conversely, any R_μ–μ–T relationship is not compatible with elastic spectra derived from specific records.

Damage accumulation effects, which cannot be neglected in the case of existing buildings, can be taken into account by means of *equivalent ductility*, according to Fajfar (1992). Such ductility is lower than monotonic (or kinematic) ductility because it includes the damage accumulation due to hysteretic energy dissipation. Alternatively, Cosenza and Manfredi (1992) proposed to amplify the displacement demand. Cosenza et al. (2010) proposed several equations which allow to define both demand and capacity of elastic-perfectly plastic SDOF systems, including explicitly the effect of damage accumulation through several indices (i.e., Park & Ang index, hysteretic energy index, and low-cycle plastic fatigue index). Inelastic acceleration, displacement, or capacity spectra can be defined through a damage factor p_{dam} which accounts for the earthquake damage potential.

- **Extension of N2 method to plan-irregular buildings**

As stated above, the N2 method was extended to plan-irregular structures by Fajfar (2006). The transformation of the MDOF system in an equivalent SDOF system can be carried out as in the case of a two-dimensional structural model, providing that torsional effects are considered as follows:

- displacement amplification due to torsional rotations can be conservatively estimated through multi-mode dynamic analysis (important assumption in the inelastic range); and
- potential unfavourable effects on the rigid end predicted by elastic analysis (e.g., displacements lower than those corresponding to the case of plan-symmetric building) can be neglected, since in general they reduce up to about zero in the inelastic range.

In particular, the N2 method for plan-asymmetric buildings consists of the following stages:

(1) *Pushover analysis on a three-dimensional model*. The lateral loads are applied at the centres of mass, separately along two directions of the building plan, and in both positive and negative orientations. For each direction, the displacement demand at the centre of mass of the roof level is computed and the maximum value between those related to both load orientations is considered.

(2) *Multi-mode dynamic analysis of the three-dimensional model*. The analysis is separately performed along the two above-mentioned directions and the relevant results are combined through the SRSS rule.

(3) *Correction of pushover analysis predictions*. The effects of plan irregularities are taken into account through a correction factor derived from multi-mode dynamic analysis. This factor is defined as the ratio between the normalised displacement at a point of the roof diaphragm derived from elastic modal analysis and that predicted by pushover analysis. The former normalised displacement is that suffered by a given point of the roof diaphragms, divided by the displacement of the centre of mass at the same floor level. If the normalised displacement derived from elastic modal analysis is lower than unity, no modification factors apply (which means that potential torsionally-induced displacement deamplifications are not considered). The correction factor is separately defined for each plan direction and depends on the floor level under consideration.

(4) *Seismic demand estimation*. The displacement demand at the centres of mass (both amplitude and distribution along the height of the building) is estimated through the classical version of the N2 method, which is based just on pushover analysis. Pushover predictions are then multiplied by correction factors.

Chapter 6 - SEISMIC ANALYSIS OF MASONRY BUILDINGS

A number of structural analysis methods based on models with increasing accuracy have been developed for masonry constructions. The method employed for structural analysis depends on the modelling strategy being adopted (see Chap. 2). In general, structural models can be classified as *continuous* and *discontinuous*. The former can be solved through direct methods, namely closed-form integration or series expansion of functions, or numerical methods based on *a posteriori* discretisation of solution, namely finite difference method or numerical integration[19]. Discountinuous models are instead structural systems composed by one- or two-dimensional elements, finite elements (FEs), boundary elements (DEs), or discrete elements.

Macro-elements models are typically used for seismic analysis of masonry constructions (Augenti, 2004): each bearing wall with openings is regarded as an equivalent frame composed by one-dimensional elements with axial, flexural and shear flexibilities. Alternatively, numerical models based on FEs (Lourenço, 1996; Gambarotta and Lagomarsino, 1997a,b; Calderini and Lagomarsino, 2008; Luciano and Sacco, 1998) or DEs (Cundall, 1988; Hart et al., 1988; Lemos, 2006) can be employed, especially in the case of historical structures.

In order to simulate seismic response of masonry constructions, the main failure modes observed after past earthquakes should be captured. Although numerical modelling allows to assess in accurate mode the structural behaviour of masonry constructions, its high computational work is not generally sustainable in engineering practice. Key issues in numerical methods are: (1) geometrical modelling of rubble and multi-leaf masonry assemblages; (2) the assumption of reliable values of refined mechanical properties of both masonry and its constituent materials (i.e., masonry units and mortar), which require complex and expensive experimental investigations; and (3) the correlation between stress/strain fields in the continuum model and conventional limit states defined in terms of internal forces and drifts for individual structural components. The identification of FEs to be monitored for capturing the attainment of limit drifts is often ambiguous and needs for repeated operations of averaging, extrapolation, and integration. It is also underlined that sensitivity analyses

[19] *A posteriori* discretisation of solution leads to discontinuous solutions of a continuum model, because both stresses and strains are computed only in the nodes of a regular mesh overlapped to the model.

are needed for mesh calibration, since it can affect the analytical predictions. Due to such a problem, numerical methods are even more difficult to be applied to medium-large structures. Nevertheless, FE and DE methods remain the unique available tools for structural assessment of highly-irregular and historical/monumental masonry structures. The latter are often characterised by vaults and domes. In such cases, FE micro-modelling (either simplified or detailed) or macro-modelling of masonry can be used, for instance, by applying numerical formulations developed by Lourenço (1996).
Given that numerical methods are affected by several difficulties related to both masonry modelling and manipulation of results, in the last decades the macro-element methods have been recognised to be effective for capturing the main features of non-linear seismic response of 'standard' masonry buildings. The term 'standard' means that the building is composed by 'regular' masonry walls with openings (namely, walls with openings aligned in both horizontal and vertical directions) which are well connected at their intersections. The use of macro-element methods is perfectly consistent with, inter alia, the need for seismic assessment at different performance levels, according to the most advanced seismic codes (CEN, 2004; ATC, 2005; IMIT, 2008). In fact, the evolutionary structural response can be simulated by direct monitoring of lateral drifts on several macro-elements; the attainment of limit states of interest for design/assessment can then be captured with a limited computational work.
In the following sections, the main in-plane failure modes of URM walls, as well as the main features of some macro-element methods are briefly reviewed and discussed. Seismic demand and capacity on individual masonry walls/panels for safety verifications against out-of-plane failure modes are out of the scope of this thesis.

6.1. In-Plane Failure Modes of URM Walls

Global seismic analysis of masonry buildings captures typically failure mechanisms occurring in the longitudinal plane of individual walls. In general, in-plane failure modes can be classified as follows:

- *flexural toe crushing* (Fig. 6.1a), which includes crushing cracks aligned with the axial force at the wall toes, as well as tensile cracks orthogonal to the axial force;
- *sliding shear cracking*, which is characterised by relative sliding along a mortar bed joint (Fig. 6.1b), or stair-stepped diagonal cracking involving both mortar joints and masonry units (Fig. 6.1c); and
- *tension shear cracking* (Fig. 6.1d), which consists of diagonal cracking; the fracture process begins at wall centroid and propagates along the diagonal toward the toes.

For each failure mode, the allowable lateral force depends on the given axial force, boundary conditions, length-to-width ratio, and mechanical properties of masonry.

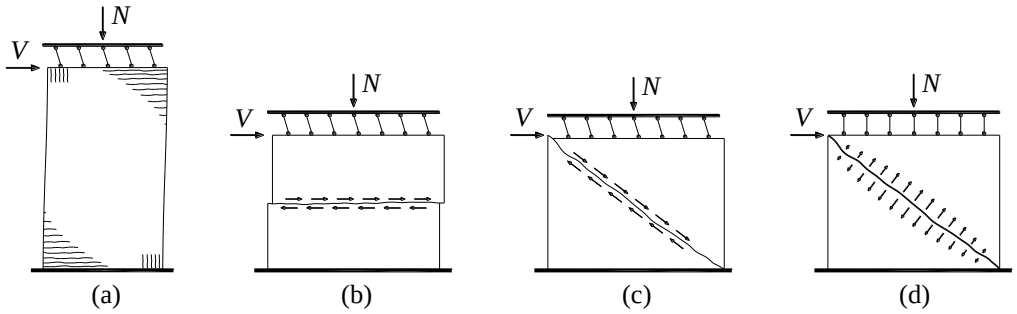

Figure 6.1 In-plane failure modes of URM panels

6.2. The RAN Method

6.2.1. Foreword

The RAN method (which is the acronim of *Raithel Aldo and Augenti Nicola*) was developed by Raithel, Augenti and other researchers since 1981 and was presented for the first time at the 2nd Italian National Conference ASS.I.R.C.CO. (Augenti et al., 1984a-g). The same authors investigated also the force-displacement relationship and ultra-elastic deformations of masonry panels (Augenti et al., 1987a,b). A detailed discussion on the RAN method was made by Augenti (2004). A preliminary investigation on the seismic response of 'irregular' walls with openings (Augenti, 2006) and mixed masonry-RC buildings (Augenti e Parisi, 2008a-c, 2009a) has been also performed in recent years.

6.2.2. Fundamental Assumptions

The RAN method allows to perform linear static analysis of masonry buildings composed by walls with openings and horizontal floor diaphragms, and to estimate the lateral load-bearing capacity of individual walls. Extending the contour lines of the openings, one can identify *spandrels* and *piers*, namely the horizontal and vertical masonry strips between openings, respectively (Fig. 6.2).

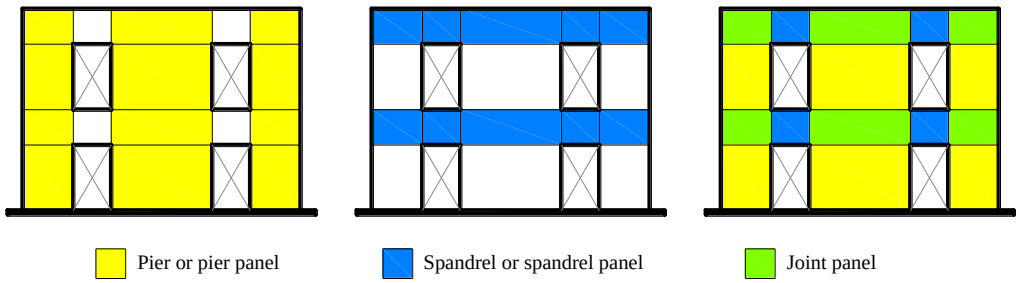

Figure 6.2 Macro-element modelling of a masonry wall with openings

The spandrels transfer both horizontal and vertical loads to the piers, providing their coupling under lateral actions. The piers ensure load transfer to the foundation system. The intersection between spandrels and piers allows to identify also the following types of macro-elements: *pier panels*, which are the vertical structural components between two consecutive spandrels; *spandrel panels*, which are the horizontal structural components between two consecutive piers; and *joint panels*, which link spandrels and piers together.

Spandrels affect seismic response of walls, but their non-linear strength/deformation capacity is quite complex to be defined (Augenti, 2007). On the contrary, the lateral behaviour of pier panels can be simply simulated on the basis of the large amount of available experimental data (see, for instance, *Database Murature UNINA-DIST* at the website of the Italian National Network of University Laboratories for Earthquake Engineering, ReLUIS; URL: http://www.reluis.it/dbuninadist). Assuming pier panels to be rigid and infinitely resistant in their own plane, the modelling of masonry walls consists in the modelling of spandrel and pier panels.

The global seismic analysis is then performed under the following hypotheses:

- masonry is a homogeneous NTR-EPP material in uniaxial compression;
- masonry walls with openings have rigid spandrels and are orthogonal themselves and well connected to rigid diaphragms at each floor level;
- doubly-fixed pier panels have axial, flexural, and shear flexibilities[20], as well as zero Saint Venant torsional stiffness and zero out-of-plane lateral stiffness;
- spandrel panels are rigid and brittle;
- joint panels are rigid and infinitely resistant;
- the lateral resistance of both pier and spandrel panels depends on the dominant failure mode (namely, toe crushing, tension cracking, or sliding shear);
- limit states of individual panels defined through strength domains corresponding to different sectional stress distributions, based on the strength criteria adopted for the failure modes;
- horizontal seismic actions are applied to the centres of mass at the floor levels;
- the lateral response of pier panels is simulated by means of force-displacement curves; the latter are summed until the minimum inelastic displacement of a pier panel is reached, in order to define the force-displacement curve of a given storey;
- the axial load on the pier panels is due to both gravity loads and horizontal actions; and
- the collapse of the building occurs when the lateral resistance of the weakest pier panel is reached.

[20] The boundary conditions of masonry panels are assumed to be constant during the analysis.

The masonry panels are assumed to be prismatic with rectangular cross-section. Actually, wall connections would induce the need for modelling masonry panels with L-, T-, or X-shaped cross-section. Nevertheless, the assumption of rectangular cross-sections is generally conservative because it leads to overestimate strength demands.
The RAN method allows to simulate the evolution in lateral stiffness of individual masonry panels, and hence its distribution throughout the structure, due to masonry cracking and yielding of masonry even at small elastic deformations. Therefore, the adopted procedure does not consider an equivalent 'cracked' stiffness for individual walls, avoiding approximations due to some code suggestions. In fact, both EC8 (CEN, 2004) and IBC (IMIT, 2008) allow to assume the effective lateral stiffness equal to one-half of the initial stiffness.
It is underlined that both EC8 and IBC allow to include spandrel panels within the capacity model of the structure, provided that their safety level is checked and the following requirements are met:

- in the case of new buildings, orthogonal walls are connected by RC ring beams and the lintels above the openings are well-anchored to adjoining piers;
- in the case of existing buildings, spandrel panels are supported by a lintel, arch, or effective lintel (able to give support also after damage in the spandrel), and are effectively anchored to adjoining piers or, alternatively, are able to provide lateral resistance through a diagonal strut resisting mechanism.

6.2.3. Open issues

The current main limitation of the RAN method was its inability to be applied in pushover analysis; this thesis is then aimed at extending some features of the RAN method to the non-linear range. Nevertheless, apart from this main limitation, some issues can be identified in the classical RAN method. In fact, response predictions for building with highly-irregular walls (i.e., high misalignments of openings in the horizontal and/or vertical directions) are under validation. RM walls and flexible diaphragms (e.g., wooden or mixed steel-tile floor slabs, masonry vaults) are not considered in the structural analysis.
The assumption of rigid spandrels is acceptable in the presence of both RC ring beams and lintels above the openings. Such tensile resistant elements provide high stiffness to the spandrel, allowing the assumption of doubly-fixed pier panels. In the case of existing masonry buildings with flexible floor diaphragms and without RC ring beams, the model adopted in the RAN method could lead to overestimate the global stiffness and load-bearing capacity and to underestimate displacement capacity of the structure. Nevertheless, as mentioned above, the role of spandrels on boundary conditions and coupling of pier panels, especially in the non-linear range, is still under investigation.

6.2.4. Analysis Steps

The RAN method consists mainly of the following stages:

(1) computation of axial forces on pier panels due to gravity loads;
(2) estimation of base shear as a function of the approximated fundamental period and distribution along the height of the building (CEN, 2004; IMIT, 2008);
(3) horizontal stiffness-proportional distribution of lateral actions at each floor level;
(4) computation of lateral forces acting on individual walls with openings and evaluation of axial forces induced by them on pier panels;
(5) computation of axial forces on pier panels as the sum of those related to gravity loads and seismic actions;
(6) estimation of lateral resistance of pier panels at different limit states through shear force – axial force domains;
(7) definition of force-displacement curves of both pier panels and their storeys under the axial forces estimated at the step (5);
(8) assessment of each masonry wall by comparing, at each storey, the storey shear to the allowable storey shear at elastic limit state (ELS) or ULS;
(9) computation of shear forces acting on individual pier panels and their relevant secant stiffnesses[21], if safety verifications are met;
(10) redistribution of storey forces in proportion to secant lateral stiffnesses and iteration of steps (4)–(9) until current shear forces are equal to those computed at the previous step;
(11) computation of internal forces on both joint and spandrel panels, at each storey; and
(12) safety verification of spandrel panels against shear and flexural failure modes; three-dimensional limit strength domains are used to define flexural capacity at the ELS (Augenti, 2007).

In the presence of irregular walls, axial force variations in pier panels due to seismic actions is estimated numerically because they depend on shear forces (Augenti, 2006).

6.2.5. Geometrical Modelling and Boundary Conditions

As stated in Section 6.2.2, the discretisation of each masonry wall with openings is carried out by identifying *n* horizontal strips[22] and *m* vertical strips. Such strips are defined by extending the contour lines of openings (i.e, door and window openings).
The position of masonry panels is defined by the indices *i*, *j*, *k* which refer to horizontal

[21] Lateral stiffness of masonry panels reduces significantly with cracking and yielding, resulting in variations in the horizontal distribution of storey forces.
[22] The numebr of horizontal strips is two times the number of storeys; in fact, the latter are composed by a spandrel and a set of pier panels and openings.

strip, vertical strip, and wall, respectively. The indices *i* and *j* are assumed to increase from the top to the base of the wall, and from the left to the right in the positive orientation of the coordinate axis of the building plan, respectively. In this way, pier panels are identified by even *i* and odd *j*, joint panels are identified by odd *i*, *j*, and spandrel panels are identified by odd *i* and even *j* (Fig. 6.3).

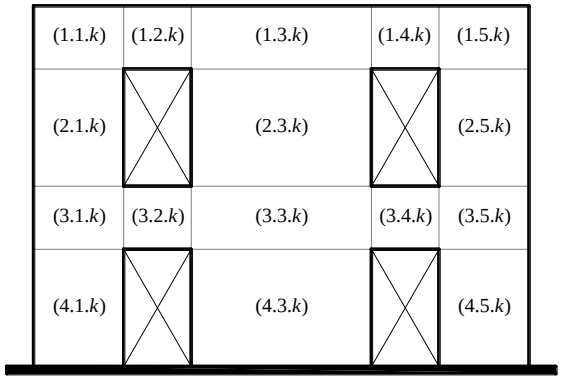

Figure 6.3 Labelling of panels within the *k*-th wall of a masonry building

Each masonry panel has length *B*, height *H*, and thickness *s*. The height of pier panels can be assumed to be not lower than that of the adjacent openings, in the case of regular walls. Conversely, the effective height of pier panels in the case of irregular walls can be assumed to be equal to that of the opening which follows it in the orientation of the seismic action. It is underlined that parapets do not necessarily induce structural irregularity of masonry walls, because they can have small thickness and lack of continuity with adjacent piers.

6.2.6. Flexural Strength Domains of Pier Panels

Denoting by *N* the axial force, *V* the shear force, and *M* the bending moment, the flexural strength of a pier panel can be defined through *N*–*V* interaction domains. Once the axial force due to both gravity and seismic loads is known, the lateral strength at ELS or ULS can be computed. In the case of doubly-fixed pier panel, the lateral behaviour under a given force or displacement is emisymmetric. It follows that strength domains of end sections are the same and each symmetric with respect to the axial force axis. Given that the lateral strength depends on the resisting bending moment at the end sections, the *N*–*V* interaction domain can be derived by scaling the bending moment *M*(*N*) values through a factor related to boundary conditions. Under eccentric compression, three different strength domains can be defined at: (1) *linear elastic limit state* (LELS); (2) *non-linear elastic limit state* (NELS); (3) *cracked*

ultimate limit state (CULS); and (4) *uncracked ultimate limit state* (UULS). The limit lines of the strength domains are described by equations derived from a *stress-based approach*, namely through the definition of sectional normal stress diagrams for the limit states of interest. To this aim, it is assumed that:

- LELS corresponds to a linear sectional diagram of normal stresses with minimum value equal to zero at an extreme fibre (*cracking limit state*, CLS) and maximum value equal to uniaxial compressive strength of masonry (denoted as σ_k) at the extreme compressed fibre (Fig. 6.4a);
- NELS corresponds to a linear sectional diagram of normal stresses with minimum value equal to zero at an inner fibre (cracked cross-section with effective width b lower than the gross width B) and maximum value equal to σ_k (Fig. 6.4b);
- CULS corresponds to a uniform sectional diagram of normal stresses equal to σ_k, with $b < B$ (Fig. 6.4c); and
- UULS corresponds to a uniform sectional diagram of normal stresses equal to σ_k, with $b = B$.

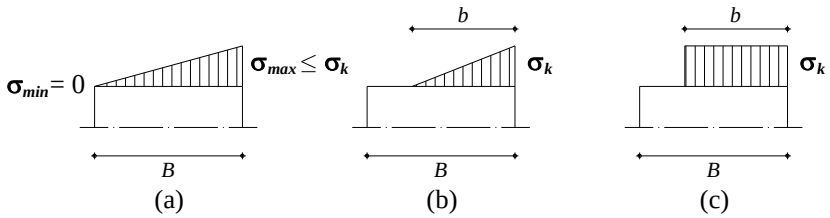

Figure 6.4 Limit states for eccentric compression

Assuming an EPP σ–ε constitutive law for masonry under uniaxial compression, the assumption of the aforementioned limit states does not allow to include mechanical non-linearity in the elastic range, but only geometrical non-linearity due to cracking of cross-section. Axial strains cannot be controlled over cross-section resulting in the partial exploitation of the inelastic capacity of masonry, as well as the inability to simulate the strength evolution under increasing damage. Finally, elasto-plastic sectional states are represented by bilinear stress diagrams.

In order to include the effect of strength degradation within masonry under increasing plastic strains (namely, *strain softening*), IBC suggest to consider a compressive strength reduction equal to 15%. This is equivalent to the application of a stress-block criterion, as typically made for design of RC cross-sections. The boundary of the flexural strength domain is then described by the following equation:

$$\bar{V}_p = \frac{B}{2\varsigma H}\left(\bar{N} - \bar{N}^2\right) \tag{6.1}$$

where: $\bar{V}_p = V_p/N_u$ is the ultimate flexural strength normalised to the ultimate axial force $N_u = \sigma_k\ B\ s$; ς is a factor related to boundary conditions and is between 0.5 (doubly-fixed panel) and 1 (cantilever panel); and $\bar{N} = N/N_u$ is the given axial force normalised to N_u. For a normalised axial force falling in the interval [0,0.5], LELS is equivalent to CLS and the flexural strength is estimated as follows:

$$\bar{V}_l = \frac{B}{6\varsigma H}\bar{N} \tag{6.2}$$

As the lateral force increases under constant axial force, the cross-section reaches NELS at which corresponds a flexural strength equal to:

$$\bar{V}_e = \frac{B}{2\varsigma H}\left(\bar{N} - \frac{4}{3}\bar{N}^2\right) \tag{6.3}$$

For a normalised axial force falling in the interval [0.5,1], the cross-section reaches UELS (namely, ELS without cracking) and the relevant flexural strength is defined as follows:

$$\bar{V}_e = \frac{B}{6\varsigma H}\left(1 - \bar{N}\right) \tag{6.4}$$

Figure 6.5 shows the flexural strength domains for the limit states being considered. It is underlined that the flexural strength does not drastically increase from ELS to ULS, for low axial forces. Conversely, a significant strength increase is predicted from CLS to ELS.

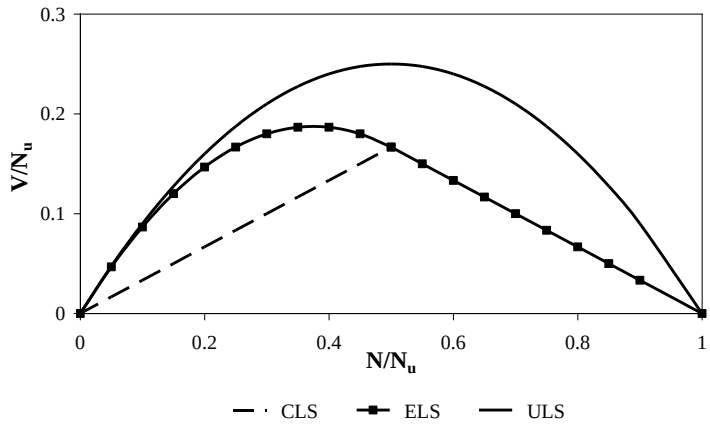

Figure 6.5 Flexural strength domains of a pier panel

6.2.7. Flexural Strength Domains of Spandrel Panels

Whilst doubly-fixed and cantilever pier panels define the limit boundary conditions of the actual pier panels, the knowledge about spandrel panels is still lacking. In the last two years, specific experimental tests have been carried out, for instance, by Gattesco et al. (2009) and Augenti et al. (2010b), in order to investigate the inelastic capacity of spandrel panels and the influence of spandrels on non-linear response of masonry walls with openings. Theoretical analyses have been also performed to define flexural strength domains including, inter alia, tensile strength of masonry (Cattari and Lagomarsino, 2008) and actual strain ductility (see Sect. 7.1.2).

Augenti (2007) proposed some equations to define three-dimensional flexural strength domains which do not depend on boundary conditions at the end sections since they include both translational and rotational equilibrium of the panel. The allowable shear force is different for the end sections, resulting in different flexural strength domains. The presence of flexural reinforcement induces a change in the strength domain shape providing flexural strength also for tensile axial forces. It is emphasised that, in the RAN method, spandrel panels are assumed to fail in flexure when ELS is reached. This assumption is consistent with that of rigid spandrels, and thus doubly-fixed pier panels.

Figure 6.6 illustrates the N/N_u–V/N_u–e/H interaction domain for a given end section of a spandrel panel with dimensions 90×140×60 cm and subjected to zero external loads (It is noted that e is the eccentricity of the axial force with respect to the centroid of the panel.). The latter do not induce modifications on the lateral behaviour of the macro-element, but only small translations of the strength domain along the coordinate axes of shear force and axial force.

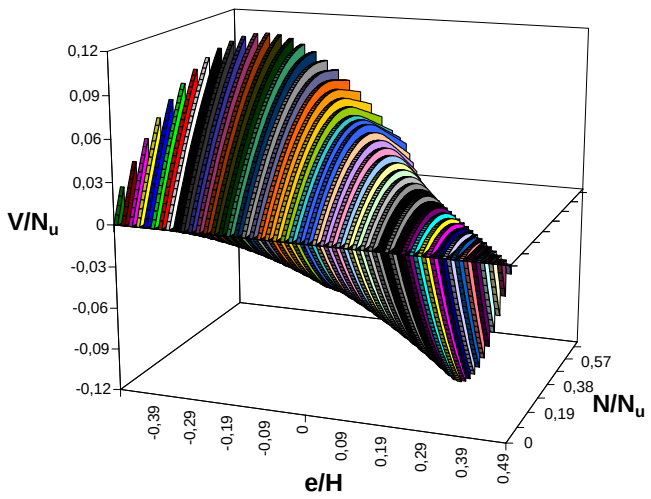

Figure 6.6 Flexural strength domain of a spandrel panel

Interested readers can refer to Augenti (2004) and Section 7.3.1 of the present thesis for a detailed discussion of this subject. It is underlined that two-dimensional interaction domains in the planes *V*–*N*, *e*–*V*, and *N*–*e*, can be derived from the three-dimensional domain at constant values of *e*, *N*, and *V*, respectively (Augenti, 2007). Such domains allow to check safety against flexural failure and to define three safety factors by keeping constant two parameters and increasing only the last parameter.

6.2.8. Shear Strength Domains

Shear strength of both pier and spandrel panels is defined by means of local strength criteria which do not include equilibrium. Namely, diagonal tension cracking is assumed to occur when the principal tensile stress at the centroid of the panel reaches tensile strength of masonry, according to Turnšek and Čačovič (1971). Sliding shear strength is predicted through the Mohr-Coulomb failure model, namely assuming that relative sliding occurs when the maximum shear stress at the mid cross-section of the panel reaches the sliding shear strength. Also in this case, shearing deformations are not controlled.

The lateral strength corresponding to diagonal tension cracking is defined as follows:

$$\bar{V}_t = \beta \sqrt{1 + \frac{\bar{N}}{p\,\beta}} \tag{6.5}$$

where: β is the ratio between diagonal tensile strength at zero confining stress (τ_k) and uniaxial compressive strength of masonry (σ_k); and p is a shear stress distribution factor defined as the ratio between the maximum and the average shear stresses (τ_{max} and $\tau_n = V/Bs$, respectively). The factor p is typically set to: 1 in the case of panels with aspect length-to-width ratio H/B not greater than 1 (i.e., squat panels); 1.5 in the case of panels with H/B not lower than 1.5 (i.e., slender panels); and H/B itself in the case of panels with H/B falling in the interval]1,1.5[.

The lateral strength corresponding to sliding shear is defined as follows:

$$\bar{V}_a = \frac{1}{p}\left(\gamma + \mu_a \bar{N}\right) \tag{6.6}$$

where: γ is the ratio between sliding shear strength at zero confining stress (τ_c) and uniaxial compressive strength of masonry (σ_k); and μ_a is the friction coefficient.

In the case of bed-joint sliding, both cohesive and frictional strengths have 'local' meaning, being they related to shear response of mortar bed joints. The friction coefficient reduces as the average normal (confining) stress increases, as follows:

$$\mu_a = \frac{0.17}{\sqrt[3]{\left(\sigma_n / \sigma_k\right)^2}} \tag{6.7}$$

In the case of stair-stepped diagonal sliding, both masonry units and mortar joints are involved so the friction coefficient is regarded as a property of the whole masonry. For this failure mode, past experimental tests have shown that friction coefficient falls in the range [0.3,0.8]. Both EC6 (CEN, 2005a) and IBC (IMIT, 2008) provide $\mu_a = 0.4$.
Since shear failure criteria do not ensure the equilibrium of the masonry panel, their limit strength domains are to be overlapped to those corresponding to flexural limit states. It follows that the final limit strength domain of a masonry panel is the minimum envelope of those corresponding to different failure modes. Figures 6.7a and 6.7b show respectively the limit strength domains related to a squat panel with $H/B = 1$ and to a slender panel with $H/B = 1.5$, in the case of $\beta = \gamma = 0.03$.

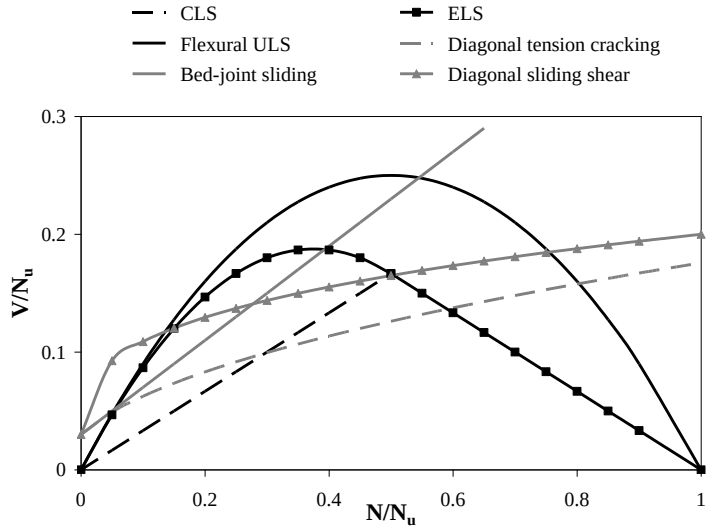

(a)

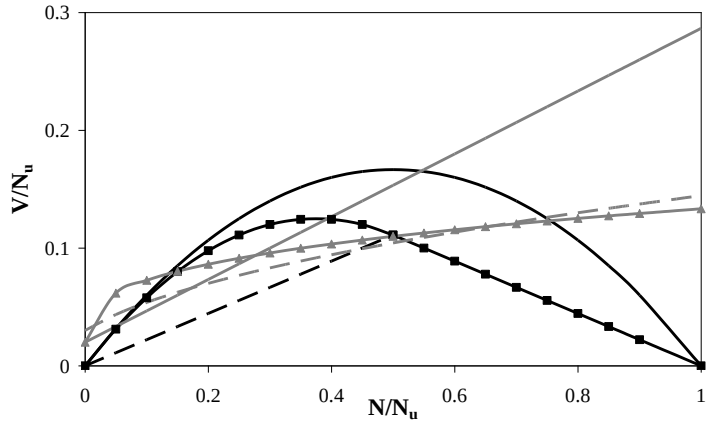

(b)

Figure 6.7 Strength domains for (a) squat panel and (b) slender panel

6.2.9. Force-Displacement Diagrams

Spandrels affect significantly the earthquake resistance of masonry walls with openings since they provide lateral coupling among piers. Therefore, the structural model should be solved including both equilibrium and displacement compability. Lateral strength should be related to displacement capacity in order to include compatibility between lateral displacements of pier panels within structural analysis.

It is underlined that displacement compatibility should be considered also in the case of cracked or highly-flexible spandrels, if rigid floor diaphragms well connected to load-bearing walls (e.g., through RC ring beams) are present. In such a case, pier panels cannot be considered to be doubly-fixed so their lateral stiffness reduces toward that associated with cantilever panels. In the absence of effective connections among piers, no lateral displacement compatibility should be taken into account and the limit strength domains presented in Sections 6.2.6–6.28 are sufficient to assess the lateral resistance of the wall. The vulnerability of the latter depends directly on the lateral strength of piers which are expected to fail in flexure, because of their cantilever-type boundary conditions and high slenderness.

In the RAN method, force-displacement (V–δ) diagrams are first defined for single pier panels and then for each storey of single walls with openings. Both the lateral strength and stiffness are estimated under varying lateral displacement between end sections of pier panels at the same storey of a given wall. Since the lateral strength depends also on the given axial forces on pier panels, the force-displacement curve of each macro-element is built up for a given axial force. The shape of the curve depends on the failure mode which, in turn, is associated with the minimum ultimate lateral strength among those corresponding to flexural and shear mechanisms. As the relative lateral displacement increases, the resisting force increases while the lateral stiffness reduces.

The force-displacement diagram of a single pier panel is defined in *force control*, namely the lateral displacement is computed under monotonically-increasing shear force. On the contrary, given that displacement compatibility has to be met, the force-displacement curve of an entire wall storey is defined in *displacement control*, namely through numerical evaluation of resisting shear forces corresponding to each given displacement and their summation aimed at computing the resisting storey shear.

- **Force-displacement diagrams of pier panels**

Given an axial force $N_{i,j,k} = R_{i,j,k} + S_{i,j,k}$ on the pier panel (i, j, k) (being $R_{i,j,k}$ and $S_{i,j,k}$ its fractions due to gravity loads and horizontal seismic actions, respectively), the resiting shear forces corresponding to shear failure modes (V_t,V_a) and flexural limit states (V_l,V_e,V_p) can be estimated through the relevant N–V interaction domains. The force-displacement curve in force control is the plot of a monotonically-increasing function

$\delta = \delta(V)$; such a function is defined in the displacement interval $[0,\delta_u]$, being δ_u the lateral displacement corresponding to the ultimate lateral strength of the panel.

The displacement function has different mathematical expressions depending on whether the pier panel has linear elastic, non-linear elastic, or plastic lateral response. In the linear elastic range, the panel is fully resistant; in the non-linear elastic range, the panel is partially resistant due to gradual cracking of masonry, and hence reduced effective width of some cross-sections along the height; in the plastic range, the lateral response of the panel is also affected by gradual yielding of masonry. Cracking of cross-sections induces geometrical non-linearity because the effective cross-sections depend on the magnitude of the applied load.

The relative lateral displacement between the end sections of the panel is regarded as the sum of the lateral displacements due to shearing deformation (δ_V) and flexural deformation (δ_M). The general equation used for the definition of the lateral displacement as a function of the applied shear force is:

$$\delta = \delta_V + \delta_M = \chi \frac{V H}{G A} \zeta_V + \frac{V H^3}{\rho E I} \zeta_M \tag{6.8}$$

where: χ, A, and I are respectively the shear factor (equal to 1.2 in the case of rectangular cross-sections), the gross area, and the moment of inertia of the cross-section; E and G are the Young's and shear moduli of masonry, respectively; ρ is a factor related to the boundary conditions and varies between 3 (case of cantilever panels) and 12 (case of doubly-fixed panels); and, finally, ζ_V and ζ_M are corrective functions equal to unity in the linear elastic range, and greater than unity in both the non-linear elastic and plastic ranges. The analytical expressions of these corrective functions are reported in (Augenti, 2004).

Defining $V_s = \min(V_t,V_a)$, if $V_p \leq V_s$ the pier panel fails in flexure and the force-displacement curve is composed by: a linear elastic branch for a shear force falling in the interval $[0,V_l]$; a non-linear elastic branch for a shear force falling in the interval $[V_l,V_e]$; and a plastic branch with hardening for a shear force falling in the interval $[V_e,V_p]$ (Fig. 6.8a).

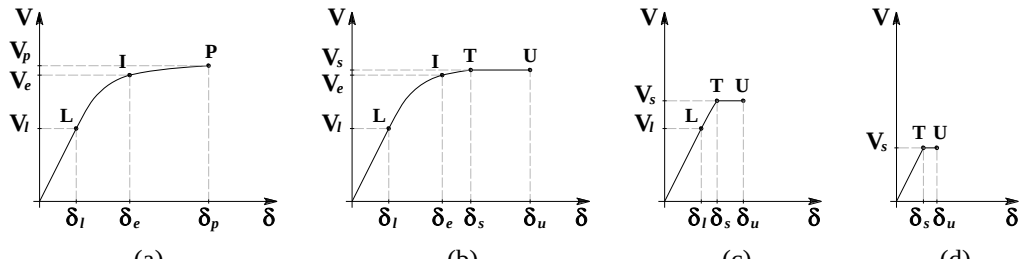

Figure 6.8 Types of force-displacement diagrams for pier panels

If $V_s \leq V_p$ or $V_s \leq V_e$ or $V_s \leq V_l$, the panel fails in shear and the force-displacement is assumed to be characterised by a plastic plateau by distinguishing the following cases:

(1) $V_s \leq V_p$: the force-displacement curve is composed by a linear elastic branch for a shear force falling in the interval $[0,V_l]$, a non-linear elastic branch for a shear force falling in the interval $[V_l,V_s]$, a plastic branch with hardening for a shear force falling in the interval $[V_e,V_s]$, and a plateau (Fig. 6.8b). In such a case, the displacement ductility of the panel is the product of the flexural displacement ductility $\mu_{d,M}$ associated with the interval $[V_e,V_s]$ by a pre-defined shear displacement ductility $\mu_{d,V}$ set to 1.5–2.

(2) $V_s \leq V_e$: the force-displacement curve is composed by a linear elastic branch for a shear force falling in the interval $[0,V_l]$, a non-linear elastic branch for a shear force falling in the interval $[V_l,V_s]$, and a plateau with displacement ductility $\mu_d = \mu_{d,V}$ (Fig. 6.8c).

(3) $V_s \leq V_l$: the force-displacement curve is composed by a linear elastic branch followed by a plateau with displacement ductility $\mu_d = \mu_{d,V}$ (Fig. 6.8d).

Eq. (6.8) allows to estimate the lateral displacements corresponding to the shear forces V_l, V_e, and $V_u = \min(V_p,V_t,V_a)$.

If the panel fails in shear (that is, $V_u = V_s \leq V_p$), Eq. (6.8) allows to plot the rising branches of the force-displacement curve, while the plateau is defined by amplifying the lateral displacement $\delta_s = \delta(V_s)$ by displacement ductility μ_d.

In general, it can be stated that, as the given axial force increases, the lateral strength increases too, while both displacement capacity and supply displacement ductility reduce.

- **Force-displacement diagrams of wall storeys**

Once the force-displacement curves of pier panels belonging to the same storey of a wall with openings have been defined, the force-displacement diagram of the entire wall storey can be characterised. The lateral load-bearing capacity of the storey, namely the maximum resisting storey shear, is the sum of the individual lateral strengths of pier panels, even though it is assumed to be limited to the minimum displacement capacity of the most rigid pier panel at ULS. In order to characterise the force-displacement curve, the following limit displacements are defined for the wall storey:

- the displacement capacity at LELS, $\delta_{l,(i,k)} = \min\{\delta_{l,(i,j,k)}\}_{j=1\ldots n}$;
- the displacement capacity at NELS, $\delta_{e,(i,k)} = \min\{\delta_{e,(i,j,k)}\}_{j=1\ldots n}$; and
- the displacement capacity at ULS, $\delta_{u,(i,k)} = \min\{\delta_{u,(i,j,k)}\}_{j=1\ldots n}$.

Such limit displacements identify the extreme points of the branches of the force-displacement curve. The graphic construction is carried out by numerical computation

of the shear force V that produces a lateral displacement δ equal to the target displacement δ^*; the latter is monotonically increased within the interval $[0,\delta_{u,(i,k)}]$. In other terms, the following equation is numerically solved:

$$\delta\left(V_{i,j,k}\right)-\delta^{*}=0 \tag{6.9}$$

by meeting the following convergence criterion:

$$\left|\frac{\delta\left(V_{i,j,k}^{(k)}\right)-\delta^{*}}{\delta^{*}}\right|\leq \mathrm{tol}_{\delta} \tag{6.10}$$

and assuming, for instance, a numerical tollerance $\mathrm{tol}_{\delta} = 10^{-5}$. Eq. (6.9) can be solved through numerical procedures, such as Newton-Raphson and secant stiffness methods. The Newton-Rahpson method can be applied by defining the residual function:

$$R\left(V_{i,j,k}^{(k)}\right)=\delta\left(V_{i,j,k}^{(k)}\right)-\delta^{*} \tag{6.11}$$

and neglecting the terms of higher order in its Taylor series expansion, the convergence is reached when the following equation is satisfied:

$$R\left(V_{i,j,k}^{(k)}\right)+R'\left(V_{i,j,k}^{(k)}\right)\left(V_{i,j,k}^{(k+1)}-V_{i,j,k}^{(k)}\right)=0 \tag{6.12}$$

with:

$$R'\left(V_{i,j,k}^{(k)}\right)=\left.\frac{dR}{dV}\right|_{V_{i,j,k}^{(k)}}$$

The recursive formula of the Newton-Raphson method can then be expressed as:

$$V_{i,j,k}^{(k+1)}=V_{i,j,k}^{(k)}-\frac{R\left(V_{i,j,k}^{(k)}\right)}{R'\left(V_{i,j,k}^{(k)}\right)} \tag{6.13}$$

If the secant stiffness method is used, the derivative of the residual function is approximated as its incremental ratio; from a geometrical standpoint, this means that the tangent line is approximated as the secant line through two points of the plane V–δ. Therefore, assuming:

$$R'\left(V_{i,j,k}^{(k)}\right)=\frac{\delta\left(V_{i,j,k}^{(k)}\right)-\delta\left(V_{i,j,k}^{(k-1)}\right)}{V_{i,j,k}^{(k)}-V_{i,j,k}^{(k-1)}} \tag{6.14}$$

one can get the following recursive equation:

$$V_{i,j,k}^{(k+1)}=V_{i,j,k}^{(k)}-R\left(V_{i,j,k}^{(k)}\right)\frac{V_{i,j,k}^{(k)}-V_{i,j,k}^{(k-1)}}{\delta\left(V_{i,j,k}^{(k)}\right)-\delta\left(V_{i,j,k}^{(k-1)}\right)} \tag{6.15}$$

where $V^{(0)} = 0$ and $V^{(1)} = V_u$ can be assumed as initial values of shear force.

Once Eq. (6.9) has been solved for each pier panel, the shear forces corresponding to a lateral displacement $\delta_{i,j,k} = \delta^*$ ($\forall j = 1\ldots m$) are known. The maximum storey shear

resisted by the *i*-th storey of the *k*-th wall is then obtained by summing up shear forces computed for the individual pier panels, namely as follows:

$$V_{i,k} = \sum_{j=1}^{m} V_{i,j,k}(\delta^*) \tag{6.16}$$

The force-displacement curve of the wall storey is a tool that can be particularly useful to assess structural regularity in elevation in terms of lateral stiffness. For each wall *k*, the distribution of secant lateral stiffnesses of each storey *i* can be assessed. Therefore, defining the secant lateral stiffness of the wall storey as:

$$k_{i,k} = \frac{V_{i,k}}{\delta_{i,k}}$$

the requirement of structural regularity in elevation in terms of lateral stiffness is met if the following condition is satisfied:

$$0.7 \leq \frac{k_{i,k}}{k_{i+2,k}} \leq 1.1$$

according to EC8 and IBC.

6.2.10. Global Analysis and Estimation of Strength Demands

By defining both strength and displacement capacities of pier panels (and hence those of load-bearing walls) through interaction domains and force-displacement curves, the seismic response of the building can be assessed through linear static analysis under a given design base shear.

In FBD, once the initial fundamental period has been defined, the base shear can be estimated and distributed along the height of the building in proportion to both inertia masses and height of floor diaphragms. The horizontal seismic action F_i at the *i*-th floor level is assumed to be applied at the location of the centre of mass, separately along mutually orthogonal directions *x, y* of the building plan. Assuming first that pier panels are doubly-fixed and fully resistant[23], the horizontal force can be distributed in proportion to lateral stiffnesses of pier panels considering also both structural and accidental eccentricities between the centre of mass and the centre of stiffness. The horizontal distribution of lateral forces at each floor level is then carried out by assuming warping torsion (Benjamin, 1959): This modus operandi is acceptable only if the floor diaphragm is rigid in its own plane and well connected to load-bearing walls. Conversely, in the case of highly-flexible floor diaphragms, each wall tends to be subjected to seismic actions which are proportional to their relevant inertia masses. In the absence of floor connections (e.g., ring beams, steel ties), the walls are also

[23] Only in such conditions the lateral stiffness is known before the analysis is run.

subjected to out-of-plane seismic actions that increase significantly the probability of local failure modes.

In the case of rigid floor diaphragm, the seismic force acting on a given pier panel can be estimated by assuming zero out-of-plane lateral stiffness and considering the combination of effects due to seismic actions applied along two plan directions. Therefore, if one assume the seismic forces in the *x*- and *y*-directions as 'primary' and 'secondary' actions, respectively (that is, the combination $E_x + \alpha E_y$)[24], the pier panel *u* parallel to the *x*-direction is loaded by:

$$F_{ux} = \pm F_x \, k_{ux} \left[\frac{1}{k_x} + \frac{\left(y_G \pm e_{a,y} - y_C\right)\left(y_u - y_C\right)}{I_C} \right] \pm \alpha F_y \, k_{ux} \frac{\left(x_G \pm e_{a,x} - x_C\right)\left(y_u - y_C\right)}{I_C} \tag{6.17}$$

while the panel *v* parallel to the *y*-direction is subjected to:

$$F_{vy} = \pm F_x \, k_{vy} \frac{\left(y_G \pm e_{a,y} - y_C\right)\left(x_v - y_C\right)}{I_C} \pm \alpha F_y \, k_{vy} \left[\frac{1}{k_y} + \frac{\left(x_G \pm e_{a,x} - x_C\right)\left(x_v - x_C\right)}{I_C} \right] \tag{6.18}$$

Such equations include: the storey forces F_x and F_y (which have the same magnitude if fundamental periods are assumed to be equal along both directions of the plan); the lateral stiffness of the pier panel parallel to the plan direction under consideration (k_{ux} and k_{vy}); the coordinate of the centroid of the pier panel in the direction orthogonal to that of the seismic force (y_u and x_v); the coordinates (x_G, y_G) of the centre of mass *G*; the coordinates (x_C, y_C) of the centre of stiffness *C*; the components ($e_{a,x}$, $e_{a,y}$) of the accidental eccentricity *e*, according to EC8 and IBC; and the polar moment of inertia of lateral stiffnesses I_C, namely the torsional rigidity of the storey. The latter is defined as follows:

$$I_C = \sum_{u=1}^{m} k_{ux} \left(y_u - y_C\right)^2 + \sum_{v=1}^{n} k_{vy} \left(x_v - x_C\right)^2 \tag{6.19}$$

Once the seismic forces on the pier panels have been estimated, one can compute the horizontal force acting at the *i*-th floor level of the *k*-the wall:

$$F_{i,k} = \sum_{j=1}^{m} F_{i,j,k} \tag{6.20}$$

as well as the storey shear:

$$V_{i,k} = \sum_{r=1}^{i} F_{r,k} \tag{6.21}$$

[24] EC8 and IBC provide $\alpha = 0.3$, even if some researchers have suggested to assume $\alpha = 1$, especially in the near field.

which is clearly the sum of the horizontal forces acting at the floor level under consideration and at the underlying floor levels.

The horizontal forces acting on a given masonry wall induce an overturning moment at each floor level, and hence variations $S_{i,j,k}$ in axial forces on the pier panels (Augenti, 2004). In fact, as anticipated in Section 6.2.9, the total axial force acting on a given pier panel is assumed to be $N_{i,j,k} = R_{i,j,k} + S_{i,j,k}$. Depending on its magnitude, one can estimate lateral strengths of individual pier panels and storeys, as well as their relationship with lateral displacement, through limit strength domains and force-displacement curves. The sign of the axial force variation depends on the orientation of lateral forces and the location of the panel with respect to the centre of axial stiffness of the storey. Therefore, seismic forces induce some pier panels to be undercompressed and others to be overcompressed. Given that overturning moment increases along the height, from the top to the base, and that axial forces due to gravity loads are lower at the upper storeys, the most vulnerable pier panels to seismically-induced axial force variations are those located at the upper and lower storeys. The axial force variation $S_{i,j,k}$ can drastically influence the failure mode and, sometimes, can be equal and opposite to the resulting force $R_{i,j,k}$, inducing tensile failure.

If the safety verification is satisfied (i.e., the storey shear is not higher than the lateral strength at each wall storey), one can compute both the actual shear forces on the pier panels and the relevant secant lateral stiffnesses. The horizontal distribution of storey forces can then be repeated for the updated distribution of lateral stiffnesses and the procedure can be iterated until the actual the distribution of shear forces on individual pier panels is estimated with minor numerical error.

The bending moment at the end sections of a given pier panel can be defined as $M_{i,j,k} = V_{i,j,k} H_{i,j,k}/2$, so internal forces in both joint and spandrel panels can be computed through equilibrium conditions. The safety verification of the building includes also that of spandrel panels at ELS.

6.2.11. Assessment of Lateral Load-Bearing Capacity

Especially if seismic safety requirements are not met, the assessment of lateral load-bearing capacity can be very useful as intermediate analysis between linear and pushover analyses, in order to design strengthening/upgrading interventions aimed at reducing seismic vulnerability. In the RAN method this objective is reached through a force-controlled incremental static procedure performed on each individual wall. The lateral forces are monotonically increased through a load multiplier α by assuming the lateral force pattern of linear static analysis. Since the lateral resistance of each wall with openings depends also on the magnitudes of axial force variations, and hence on the magnitude of lateral forces, an iterative procedure is run to compute the load

multiplier corresponding to the attainment of the allowable storey shear at a given storey of the wall under consideration or, alternatively, the tensile strength within a pier panel. Therefore, this procedure allows to estimate the load multiplier of an ideal SPO analysis, since it is stopped at the failure of the weakest pier panel. A conservative estimation of seismic vulnearability of the masonry building is then carried out, by determining the allowable PGA at ULS.

6.3. The SAM method

6.3.1. Foreword

The SAM method (where SAM is the acronym of *Seismic Analysis of Masonry walls*) is based on a frame-equivalent idealisation of masonry walls with openings and was proposed by Magenes and Calvi (1996) accounting for interesting experimental results on a masonry wall and a whole building (Calvi and Magenes, 1994; Magenes et al., 1995). More recently, Magenes and Della Fontana (1998) proposed the SAM II variant of the method, which was implemented into a computer program named ANDILWALL by using, inter alia, the computer solver ANSR-I (Mondkar and Powell, 1975). The SAM II method allows to perform multi-mode dynamic analysis and SPO analysis of masonry buildings with rigid floor diaphragms. Over an actual masonry wall with openings one can identify: *pier elements* and *spandrel elements*, which are modelled as one-dimensional elements with both flexural and shear flexibilities; and *joint elements*, which are modelled as rigid end offsets (Fig. 6.9).

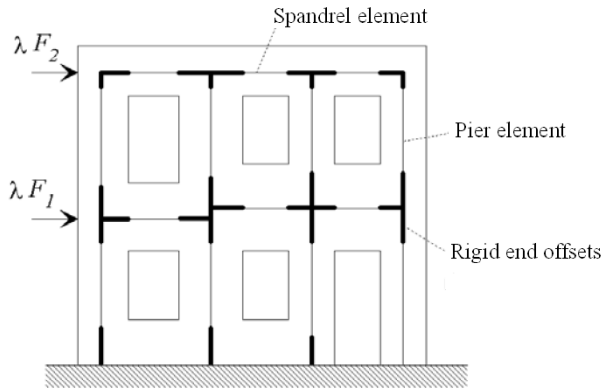

Figure 6.9 Frame-equivalent idealisation of a masonry wall with openings

6.3.2. The Pier Element

Such a masonry element is assumed to be made of a flexible part with effective height H_{eff} according to Dolce (1991), and two rigid end offsets (Fig. 6.7). The lateral

behaviour of the element is supposed to be linear elastic up to the attainment of flexural or shear strength, and then perfectly plastic until the ultimate chord rotation is reached. The inelasticity is lumped within plastic hinges.

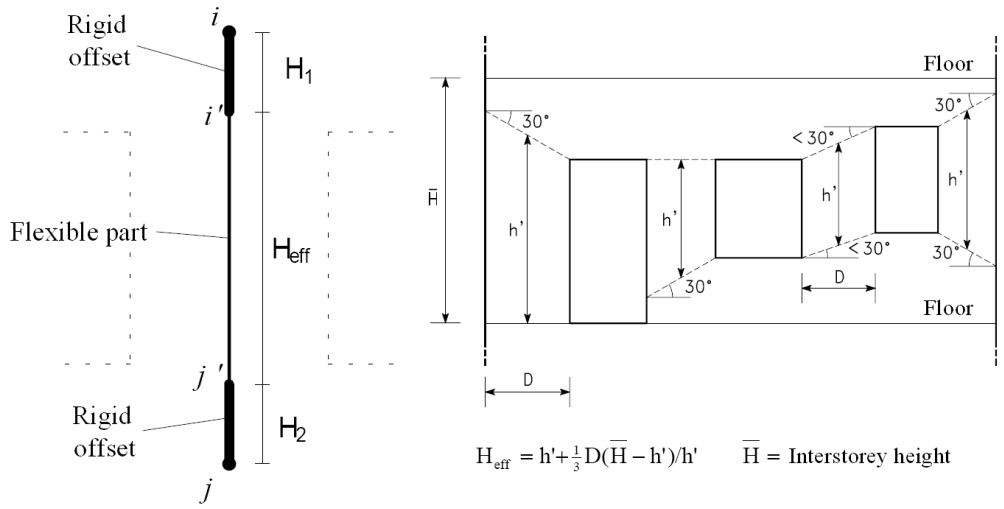

Figure 6.10 Pier element and effective height

The ultimate bending moment of the plastic hinge is defined as follows:

$$M_u = \frac{N B}{2}\left(1 - \frac{\sigma_n}{0.85 f_d}\right) \tag{6.22}$$

which can be rewritten as:

$$\bar{V}_u = \frac{B}{2H_0}\left(\bar{N} - \frac{\bar{N}^2}{0.85}\right) \tag{6.23}$$

where H_0 is the distance of the cross-section corresponding to zero bending moment from the base of the panel. Eq. (6.22) includes the average normale stress and the uniaxial compressive strength of masonry.

The lateral strength corresponding to diagonal tension cracking is computed as follows:

$$V_u = 0.9 V_{\max} = 0.9 \tau_u B s \tag{6.24}$$

where shear strength of masonry is defined as:

$$\tau_u = \min\left(\tau_{ws}, \tau_b\right) \tag{6.25}$$

being:

$$\tau_{ws} = \frac{c + \mu \sigma_n}{1 + \alpha_V} \tag{6.26}$$

the shear strength corresponding to stair-stepped sliding along mortar bed joints, and:

$$\tau_b = \frac{f_{bt}}{2.3(1+\alpha_V)}\sqrt{1+\frac{\sigma_n}{f_{bt}}} \tag{6.27}$$

the shear strength corresponding to stair-stepped sliding involving both mortar joints and masonry units. The term *c* into Eq. (6.26) represents the sliding shear strength at zero confining stress, namely cohesion, while α_V is a shear factor defined as $\alpha_V = M/(N\,B)$. Eq. (6.27) includes tensile strength of masonry units, denoted as f_{bt}.

Lateral deformation is measured in terms of *chord rotation* θ, which is regarded as the sum of a flexural contribution φ and a shearing contribution γ. Magenes and Calvi (1997) found that masonry panels with different aspect ratios failed in shear at rather similar drift levels, under combined compression and shear. Conversely, a higher scatter was found for allowable displacement ductility. Based on this outcome, displacement capacity of masonry panels was directly defined in terms of ultimate drift, rather than yielding displacement times displacement ductility. In the case of doubly-fixed panels, chord rotation can be defined as $\theta_i = \theta_s = \theta = \delta/H$.

Bed-joint sliding is assumed to occur at the end sections of the flexible part of the panel and the relevant lateral strength can be estimated through the following equation:

$$V_d = \beta B s\left(c+\mu\frac{\sigma_n}{\beta}\right) = B s\frac{1.5c+\mu\sigma_n}{1+3\frac{c\,\alpha_V}{\sigma_n}} \tag{6.28}$$

where β is the ratio between the effective width *b* and the gross width *B*, as follows:

$$b = \beta B = 3\left(\frac{1}{2}-\frac{V}{N}\alpha_V\right)B = 3\left(\frac{1}{2}-\frac{V H_0}{N B}\right)B \tag{6.29}$$

Such an equation corresponds to a linear sectional diagram of normal stresses. An EPP response is assumed also for this failure mode. Assuming the tensile strength of masonry to be zero in bending, pier elements are considered as fully resistant under compressive axial force, accounting for axial force variations induced by seismic forces.

6.3.3. The Spandrel Element

Non-linear modelling of this element does not differ from that related to the pier element. Indeed, an effective length is defined and both flexural and shear failure modes are considered. In particular, a plastic hinge is introduced at the attainment of the ultimate bending moment for flexural failure, while the ultimate lateral strength for shear mechanisms is only due by cohesion, as follows:

$$V_u = c B s \tag{6.30}$$

provided that mortar bed joints are parallel to the longitudinal axis of the element and

compression orthogonal to them can be assumed equal to zero.

Two limit values are defined for the average chord rotation: γ_1, which corresponds to the beginning of the residual strength branch; and γ_2, which identifies the collapse of the panel. The residual strength is defined as αV_u (Fig. 6.11). The parameters α, γ_1 and γ_2 should be characterised through proper experimental tests and allow to reproduce both brittle and ductile responses, for instance assuming γ_1 at yielding and $\alpha = 1$, respectively.

In the SAM method, steel ties and RC ring beams can also be modelled. Ties are modelled as EPP tensile-resistant rods at which pre-tensioning forces can be assigned. RC bond beams are modelled as one-dimensional elements with potential for plastic hinges in the inelastic range.

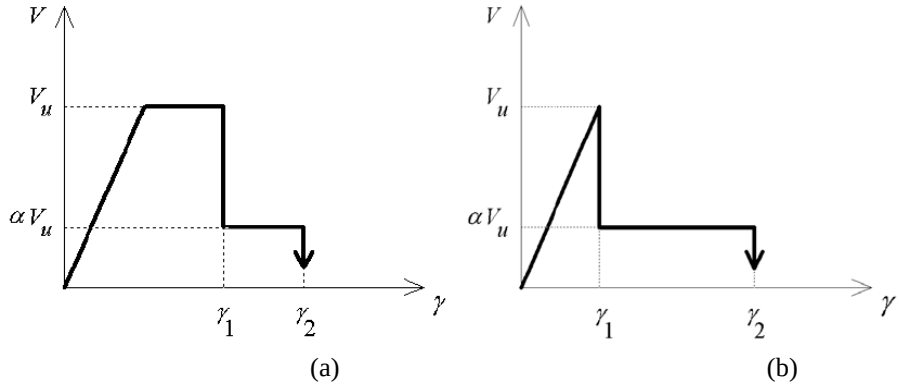

Figure 6.11 Types of lateral behaviour of the spandrel element (Magenes et al., 2001)

6.3.4. Modelling and Analysis of the Building

Three-dimensional frame-equivalent modelling allows to consider also out-of-plane stiffness/strength of pier panels, as in the case of the RAN method. To this aim, force-displacement diagrams similar to those related to in-plane lateral behaviour can be defined, and different effective heights can be assumed to account for different boundary conditions. The effective height of pier panels for out-of-plane response is typically assumed to be the interstorey height.

At wall intersections, rectangular corss-sections are considered and compatibility between vertical displacements is imposed through rigid end offsets which, in turn, are mutually connected by means of a spherical hinge. Such a modelling allows to simulate transverse connections among masonry walls.

The former version of the SAM method was aimed at performing incremental static analysis ‘by hand’, similarly to the RAN method. Given an initial magnitude of lateral

forces, the horizontal distribution between pier elements at each floor level was first assumed to be proportional to initial lateral stiffnesses. Assuming the notation of the RAN method, bending moment at the end sections of a given panel (*i*, *j*) were computed as:

$$M^{s}_{i,j} = V_{i,j}\, H^{0s}$$
$$M^{i}_{i,j} = V_{i,j}\, H^{0i} \qquad (6.31)$$

with $H^{0s} = H^{0i} = H/2$.

For each increment of lateral forces, the bending moments at the end sections of spandrel elements were computed through the following equations:

$$M^{s}_{i,j} = \rho^{s}_{i,j}\left[V_{i-1,j-1}\left(0.5\,H_{i,j-1} + H^{0i}_{i-1,j-1}\right) + V_{i+1,j-1}\left(0.5\,H_{i,j-1} + H^{0s}_{i-1,j-1}\right)\right]$$
$$M^{d}_{i,j} = \rho^{d}_{i,j}\left[V_{i-1,j+1}\left(0.5\,H_{i,j+1} + H^{0i}_{i-1,j+1}\right) + V_{i+1,j+1}\left(0.5\,H_{i,j+1} + H^{0s}_{i+1,j+1}\right)\right] \qquad (6.32)$$

which include the following distribution coefficients defined in the VEM method by Fusier and Vignoli (1993a):

$$\rho^{s}_{i,j} = \rho^{d}_{i,j} = 1 \qquad \text{for end pier elements;}$$

$$\rho^{s}_{i,j} = \frac{s_{i,j}\, H^{3}_{i,j} / B_{i,j}}{s_{i,j}\, H^{3}_{i,j} / B_{i,j} + s_{i,j-1}\, H^{3}_{i,j-1} / B_{i,j-1}}$$
$$\rho^{d}_{i,j} = \frac{s_{i,j}\, H^{3}_{i,j} / B_{i,j}}{s_{i,j}\, H^{3}_{i,j} / B_{i,j} + s_{i,j+1}\, H^{3}_{i,j+1} / B_{i,j+1}} \qquad \text{for inner pier elements.}$$

Therefore, the shear forces were evaluated as follows:

$$V^{s}_{i,j} = V^{d}_{i,j} = \frac{M^{s}_{i,j} + M^{d}_{i,j}}{B_{i,j-1} + 2\,B_{i,j} + B_{i,j+1}} \qquad (6.33)$$

and were compared to the lateral strengths for shear and flexural mechanisms. If the safety verification was not satisfied, the exceeding shear force was first multiplied for the distance between cross-sections corresponding to zero and maximum bending moments (initially assumed to be one-half of the panel length), and then was distributed among elements converging in the node. Such a redistribution induced a variation in the point of zero bending moment within pier elements. Once the axial force due to both gravity and seismic loads was known, pier elements were assessed. If also this verification was not satisfied, the exceeding shear force were distributed among elements which were still resistant at the same storey, proportionally to their relevant initial elastic stiffness. This procedure were repeated for successive increments of lateral forces up to the attainment of ultimate displacement at least in the weakest pier element of a given wall. Such a displacement was defined as yielding displacement times displacement ductility.

As discussed above, the SAM II method is based on the direct definition of displacement capacity for both pier and spandrel elements through the assumption of a limit drift ratios.
Internal forces are redistributed until lateral strength of spandrel elements is reached; at this state, plastic hinges are introduced at the end sections and boundary conditions of pier elements are modified. The updating of boundary conditions for pier elements during incremental analysis produces force-displacement curves which changes as the lateral stiffness reduces. Since the lateral stiffness of pier elements is assumed to be constant and equal to the cracked stiffness in the elastic range, non-linear response is mainly due to varying constraints.
For each boundary condition, the force-displacement curve is idealised as bilinear. The pushover curve is then plotted up to global building collapse or loss of numerical stability (see Sect. 5.1).

6.4. The Tremuri computer program

6.4.1. Foreword

The method implemented in the computer program TREMURI is based on the definition of a masonry macro-element with axial, flexural, and shear flexibilities (Brencich and Lagomarsino, 1998), and modelling of masonry buildings consisting in the assemblage of frame-equivalent wall models with rigid offsets at the end sections of macro-elements (Brencich et al., 1998).
The analysis method was assessed through experimental tests carried out on a brick masonry building by Magenes et al. (1995) at the University of Pavia, Italy. Both the macro-element and analysis procedure were improved by Penna (2002) and Cattari et al. (2004). More recently, Cattari and Lagomarsino (2007) extended the analysis procedure to mixed masonry-RC buildings, while Galasco et al. (2006) proposed an adaptive variant of the method.
Opposed to SAM II, the matrix analysis procedure implemented within TREMURI allows to include also in-plane flexibility of floor diaphragms in the capacity model, and hence to analyse existing buildings with wooden, metallic, or vaulted diaphragms. In the case of mixed masonry-RC structures, one can separately define: macro-elements for both RC shear walls and masonry panels; membrane elements for floor diaphragms; and rod elements for ties, RC ring beams, columns, and beams. Internal variables[25] are included in the macro-element to simulate not only flexural mechanisms including toe crushing effects, but also shear mechanisms and their evolution in terms of both strength and stiffness degradation.

[25] These parameters simulate plastic evolution in the strength domain.

6.4.2. The Masonry Macro-element

The former version of the method was based on a macro-element composed by a central rigid part and two extreme parts with bending flexibility. Six kinematic DOFs were associated with the macro-element, three for each flexible part. Each tern of DOFs included two translations and a rotation. The inelasticity was assumed to be lumped in the flexible parts resulting in a lumped plasticity model.

In recent years, two further DOFs were attributed to the centroid of the panel, in order to account for shear mechanisms and rocking; as a result, eight DOFs are now associated with the macro-element. Shear failure modes are captured by controlling average response parameters able to simulate stress/strain fields within the overall masonry panel. Therefore, shear failure modes are not associated with local conditions over individual discontinuity surfaces.

Figure 6.12 shows the above kinematic parameters of the macro-element and their relevant static parameters. In particular, the following kinematic variables are defined: two terns (u,φ,w) simulating axial and flexural response of the panel; and a couple (ϕ,δ) related to axial and shear response. Bending flexibility is considered at the ends (1) and (3) of the macro-element (having dimensions b×a×s); shear flexibility is assigned only to the central part (2) (having dimensions b×h×s); and axial flexibility is assigned to all parts of the macro-element. Both kinematic and static models have been also reformulated by Penna (2002).

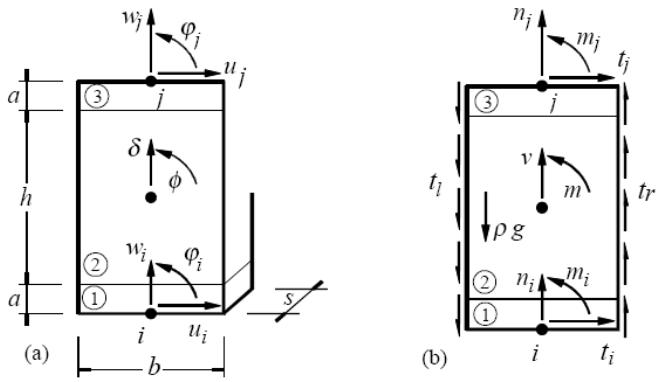

Figure 6.12 Kinematic and static parameters of the macro-element

The macro-element is defined as one-dimensional element with two nodes (i, j) and its kinematics is described by the following displacement vector:

$$\mathbf{a}^t = \left\{ u_i \;\; w_i \;\; \varphi_i \;\; u_j \;\; w_j \;\; \varphi_j \;\; \delta \;\; \phi \right\} \tag{6.34}$$

assuming that length of the estreme flexible parts tends to zero ($a \rightarrow 0$). Static parameters are used to define the following vector of internal forces associated with the

nodes (*i*, *j*) and to the centroid of the central part:

$$\mathbf{q}^t = \left\{ n_i \;\; t_i \;\; m_i \;\; n_j \;\; t_j \;\; m_j \;\; v \;\; m \right\} \tag{6.35}$$

The following external actions are also considered: weight for unit area, denoted as $\rho g s$ (Fig. 6.12); and tangential forces t_r and t_l acting along the lateral surfaces and potentially due to adjacent panels. Based on translational and rotational equilibrium of the central part of the macro-element, one can derive the following equations:

$$\begin{aligned} v &= -n_i - n_j - \left(t_r - t_l\right) h + G \\ m &= -m_i - m_j + t_j \, h - \left(t_r - t_l\right) b \, h / 2 \end{aligned} \tag{6.36}$$

where $G = \rho g s b h$ is the weight of the panel.

Non-linear constitutive equations of the macro-element are based on the following hypotheses: zero tensile strength in the extreme parts; and sliding shear with damage in the central part. In this way, axial and flexural responses was uncoupled from shear response, as well as their relevant inelastic and damage mechanisms.

For the extreme parts of the macro-element, the constitutive equations establish a relationship between the kinematic parameters w_i,φ_i [w_j,φ_j] and their corresponding static parameters n_i,m_i [n_j,m_j]. Such equations are uncoupled if it results $|m/n| \le b/6$, namely until the cross-section of the panel is fully compressed. In this case, the cross-section is fully resistant because the axial force is applied to a point falling in the central core of inertia. Therefore, denoting by $k = 2E/h$ the axial stiffness for unit area, one can get:

$$\begin{aligned} N &= k \, b \, s \, w \\ M &= \frac{k}{12} s b^3 \varphi \end{aligned} \tag{6.37}$$

and hence:

$$|e| = \left| \frac{M}{N} \right| = \frac{\left| \frac{k}{12} s b^3 \varphi \right|}{\left| k \, b \, s \, w \right|} = \frac{\frac{k}{12} s b^3 |\varphi|}{k \, b \, s |w|} = \frac{b^2 |\varphi|}{12 |w|} \le \frac{b}{6} \tag{6.38}$$

From a kinematic point of view, being $w < 0$ according to the assumption of NTR masonry in bending, the latter equation can be expressed as:

$$|\varphi| \le -\frac{2w}{b} \tag{6.39}$$

This means that, under a given axial force (and hence the translation w) the rotation φ increases linearly with the bending moment until the above-mentioned static and kinematic conditions are satisfied. Otherwise, the cross-section becomes cracked; the assumption of small displacements allows to estimate inelastic contributions of internal forces due to eccentric compression, as well as the following equations:

$$N = k\,b\,s\,w - \frac{k\,s}{8|\varphi|}\left(|\varphi|b + 2w\right)^2$$
$$M = \frac{k}{12}s\,b^3|\varphi| + \frac{k\,s}{24}\frac{\left(-|\varphi|b + w\right)}{\varphi|\varphi|}\left(|\varphi|b + 2w\right)^2 \tag{6.40}$$

In the case of cracked cross-section, the axial force and the bending moment are coupled and the relationship between w and φ can be written as:

$$w = \frac{|\varphi|b}{2} - \sqrt{\frac{-2|\varphi|N}{k\,s}} \tag{6.41}$$

In addition to geometrical non-linearity induced by sectional cracking, the macro-element behaviour is also affected by compressive damage which is described by means of two parameters.

At a given non-linear state of the panel, the translation w exceeds the limit value $w_R = \sigma_R/k$ in a part of the cross-section identified by the ratio $\zeta = p/b$, which is one of the aforementioned damage parameters. The ratio $\mu = w_{max}/w_R$ is the second damage parameter which measures the ductility demand on the extreme fibre, and hence the resulting stiffness degradation. Figure 6.18 illustrates the elasto-plastic stress and displacement states of an uncracked cross-section under eccentric compression.

If $w_{max} < w_R$ when the macro-element is unloaded, the stress state depends on the load history through the parameters μ and ζ: yielded fibres are then characterised by a degraded stiffness k^* which is a function of ductility according to the following equation:

$$k^*(x,\mu,\zeta) = \frac{k}{\frac{\mu-1}{\zeta b}x + 1} \qquad \text{with } x \in \left(\left(\frac{1}{2} - \zeta\right)b, \frac{b}{2}\right] \tag{6.42}$$

The diagram of normal stresses is then linear in the elastic part of the cross-section, and non-linear in the remaining yielded part, as described by the following equations:

$$\sigma(x) = \begin{cases} k\left(-w_0 - \varphi\,x\right) & \text{for } x \in \left[-\frac{b}{2}, \left(\frac{1}{2} - \zeta\right)b\right] \\ k\left(-w_0 - \varphi\,x\right)\dfrac{\zeta b}{(\mu-1)x + \zeta b} & \text{for } x \in \left]\left(\frac{1}{2} - \zeta\right)b, \frac{b}{2}\right] \end{cases} \tag{6.43}$$

Nevertheless, the degraded branch of the diagram of normal stresses can be approximated as linear without significant error, so a simple non-linear corrective procedure for internal forces can be defined by assuming an EPP constitutive law in compression and zero tensile strength in bending.

Due to the different distribution of normal stresses in the elastic and plastic ranges, the

axial force can be estimated by assuming:

$$N = N^{el} - N^{*} \tag{6.44}$$

where N^{el} is the axial force in the elastic range and $N^{*}$is expressed as:

$$N^{*}(\mu, \zeta, w_{\max}) = k\frac{\mu - 1}{\mu}\zeta b s w_{\max} \tag{6.45}$$

Similarly, the non-linear correction of the bending moment can be obtained as follows:

$$M = M^{el} - M^{*} \tag{6.46}$$

where M^{el} is the bending moment in the elastic range and $M^{*}$is expressed as:

$$M^{*}(\mu, \zeta, w_{\max}) = \left(\frac{\zeta}{3} - \frac{1}{2}\right) b N^{*} \tag{6.47}$$

Such corrections can be made either if normal stresses reduce owing to stiffness degradation, or if masonry strength is exceeded once again.

Regarding the macro-element part (1), the constitutive equations which describe the cyclic behaviour under eccentric compression can be expressed also as:

$$\begin{aligned} n_i^{*} &= -\frac{k s}{8\left|\varphi_i - \phi\right|}\left[\left|\varphi_i - \phi\right| b + 2\left(\delta - w_i\right)\right]^2 H\left(\left|e_i\right| - \frac{1}{6} b\right) \\ m_i^{*} &= -\frac{k s}{24\left(\varphi_i - \phi\right)\left|\varphi_i - \phi\right|}\left[\left(\varphi_i - \phi\right) b - \left(\delta - w_i\right)\right]\left[\left|\varphi_i - \phi\right| b + 2\left(\delta - w_i\right)\right]^2 H\left(\left|e_i\right| - \frac{1}{6} b\right) \end{aligned} \tag{6.48}$$

being $H(\bullet)$ the Heaviside function[26].

The shear response of the masonry panels is analysed by assuming a uniform diagram of shear stress γ within the central part (2), namely:

$$\gamma = \frac{u_i - u_j}{h} + \phi \tag{6.49}$$

so the constitutive equations are expressed as the sum of a linear elastic contribution and an inelastic contribution t_i^{*}, which are defined as:

$$\begin{aligned} t_i &= \frac{G A}{h}\left(u_i - u_j + \phi h\right) + t_i^{*} \\ t_i^{*} &= -\frac{G A}{h}\frac{G c \alpha}{1 + G c \alpha}\left(u_i - u_j + \phi h + \frac{h}{G A} f\right) \end{aligned} \tag{6.50}$$

The inelastic contribution depends on: a frictional action *f*, which is opposed to shear stress; a damage variable α, which increases with the shear strain γ; and a parameter *c*,

[26] As well known, it is the unit step function and is a discontinuous function whose value is zero for negative argument and one for positive argument. The Heaviside function is the integral of the Dirac delta function and is assumed to be 1/2 at zero argument in current numerical applications, according to the 'half maximum rule'.

which controls the magnitude of plastic strain up to the attainment of strength. The laws of variation of f and α were defined in an incremental form on the basis of two different yielding conditions and the relevant plastic flow criteria. The sliding shear yielding condition and the shear strain criterion are respectively written as follows:

$$\Phi_s = |f| - \mu n \leq 0 \tag{6.51}$$

$$\dot{\gamma}^* = \frac{f}{|f|}\dot{\lambda} \tag{6.52}$$

where: μ is the friction coefficient; $\dot{\gamma}^*$ is the inelastic strain rate; and $\dot{\lambda}$ is the plastic multiplier. The damage of the macro-element due to cracking within the central part is quantified through the damage variable $\alpha \in [1, +\infty[$, whose evolution is limited by the following condition:

$$\Phi_d = Y(\mathbf{s}) - R(\alpha) \leq 0 \tag{6.53}$$

being:

- $Y(\mathbf{s}) = \frac{1}{2}\frac{\gamma^*}{c\alpha^2}$ the energy dissipated by damage;
- $R(\alpha)$ the *toughness*, which describes strength degradation with damage; and
- $\mathbf{s} = \{ t \;\; n \;\; m \}^t$ the vector of internal forces.

Assuming that toughness increases until the damage variable reaches the value $\alpha_c = 1$ and decreases at higher damage levels, the formulation reviewed above allows to simulate stiffness degradation, peak load, and strength degradation, in a simplified mode.

The global constitutive model of the macro-element can be written in the following form:

$$\mathbf{q} = \mathbf{k}\,\mathbf{a} + \mathbf{q}^* + \mathbf{q}^0 \tag{6.54}$$

where:

- $\mathbf{q}^* = \{ n_i^* \;\; t_i^* \;\; m_i^* \;\; n_j^* \;\; t_j^* \;\; m_j^* \;\; v^* \;\; m^* \}^t$ includes non-linear components of internal forces which are computed through evolutionary equations as functions of the damage variable α and the frictional action f;
- $\mathbf{q}^0 = \{ 0 \;\; 0 \;\; 0 \;\; 0 \;\; 0 \;\; 0 \;\; v^0 \;\; m^0 \}^t$ includes the external actions $v^0 = G + (t_l - t_r)h$ and $m^0 = -(t_l - t_r)bh/2$;
- $\mathbf{k}$ is the elastic stiffness matrix defined as

$$\mathbf{k} = \begin{bmatrix} \frac{GA}{h} & 0 & 0 & -\frac{GA}{h} & 0 & 0 & 0 & -GA \\ 0 & kA & 0 & 0 & 0 & 0 & -kA & 0 \\ 0 & 0 & \frac{1}{12}kAb^2 & 0 & 0 & 0 & 0 & -\frac{1}{12}kAb^2 \\ -\frac{GA}{h} & 0 & 0 & \frac{GA}{h} & 0 & 0 & 0 & GA \\ 0 & 0 & 0 & 0 & kA & 0 & -kA & 0 \\ 0 & 0 & 0 & 0 & 0 & \frac{1}{12}kAb^2 & 0 & -\frac{1}{12}kAb^2 \\ 0 & -kA & 0 & 0 & -kA & 0 & 2kA & 0 \\ -GA & 0 & -\frac{1}{12}kAb^2 & GA & 0 & -\frac{1}{12}kAb^2 & 0 & GAh+\frac{1}{6}kAb^2 \end{bmatrix}$$

In closing, the behaviour of the macro-element is described through not only geometrical parameters, but also the following parameters: the stiffnesses G and k related to elastic response in shear and eccentric compression, respectively; the shear strength at zero confining stress f_{v0}; a flexibility coefficient c governing inelastic shearing deformation; the global friction coefficient μ; a factor β associated with toughness R, which allows to account for softening.

Figure 6.13 shows the sensitivity of the normalised force-displacement curve to the parameter β falling in the interval [0,1]. Typically, this parameter is not greater than 0.8.

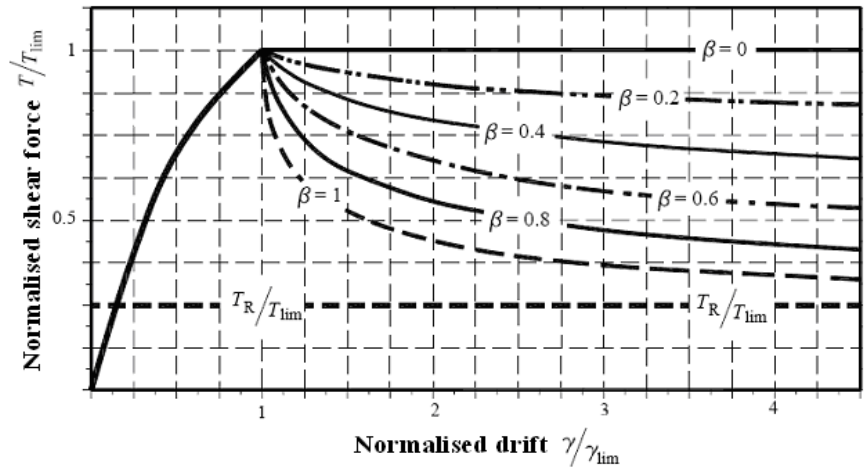

Figure 6.13 Elasto-plastic lateral behaviour of a masonry panel

6.4.3. Modelling and Analysis of the Building

Frame-equivalent modelling of each masonry wall with openings allows to perform matrix structural analysis through modified Newton-Raphson incremental iterative method. In such a procedure, the expected elastic displacements at a given load step are repeatedly updated through non-linear increments due to residual nodal forces. The internal variables (α_k, f_k) of each element k are updated by integrating non-linear constitutive equations within the given load step.

Cattari et al. (2004) validated and calibrated TREMURI through quasi-static lateral loading tests performed on a masonry building model in displacement control. The experimental tests were carried out at the University of Pavia, Italy (Magenes et al., 1995). Numerical analyses were run to make experimental-analytical comparisons, by assuming: G = 300 MPa; E = 2000 MPa; τ_r = 0.15 MPa; c = 1.20; μ = 0.20; and β = 0.50.

It is underlined that yield criterion adopted for sliding shear is the Mohr-Coulomb strength model with friction coefficient of 0.4 in the case of cracked cross-section, and 0.1-0.2 in the case of uncracked cross-section. In the former case the sliding shear strength at zero confining stress is assumed to be equal to the tension cracking shear strength, while in the latter case it is assumed equal to f_{v0}.

In addition, the shear flexibility parameter G_c is to be defined; it allows to include the non-linear behaviour of the masonry panel and is not lower than unity. According to EC8 and IBC, two different drift limits are defined for flexural and shear failure modes. Modelling of the whole building as an assemblage of plane equivalent frames leads to define two types of nodes: a two-dimensional node with three DOFs, belonging to a single plane frame; and a three-dimensional node with five DOFs (three translations and two rotations in two orthogonal planes), belonging to orthogonal frames.

The five displacement components of a three-dimensional node in a local coordinate system are related each other through the following compatibility equations:

$$\begin{aligned} u &= u_x \cos\theta + u_y \sin\theta \\ w &= u_z \\ \varphi &= \varphi_x \sin\theta + \varphi_y \cos\theta \end{aligned} \tag{6.55}$$

which describe the displacement components of a two-dimensional node belonging to a masonry wall forming an angle θ with the global abscisse axis. Similar equations apply to nodal forces. Internal forces in the macro-elements belonging to individual walls, which are transferred to fictitious two-dimensional nodes, are defined in the global coordinate system via the following equations:

$$
\begin{aligned}
F_x &= F_h^1 \cos\theta_1 + F_h^2 \cos\theta_2 \\
F_y &= F_h^1 \sin\theta_1 + F_h^2 \sin\theta_2 \\
F_z &= F_v^1 + F_v^2 \\
M_x &= M^1 \sin\theta_1 + M^2 \sin\theta_2 \\
M_y &= -M^1 \cos\theta_1 - M^2 \cos\theta_2
\end{aligned}
\tag{6.56}
$$

where the superscripts 1 and 2 are respectively related to virtual nodes belonging to the walls 1 and 2 at which belongs the three-dimensional node as well.

In pushover analysis, the evolution in the internal forces acting on the spandrel elements is also taken into account; ultimate bending moment and shear force are defined according to formulas reported into IBC.

Two limit drift ratios are assigned to pier elements; the drift ratio in shear is defined as:

$$\theta_V = \frac{u_i - u_j}{h} + \phi_e \tag{6.57}$$

while that associated with bending deformation is computed as:

$$\theta_M = \frac{\varphi_i + \varphi_j}{2} + \phi_e \tag{6.58}$$

Each drift demand is then compared to the relevant capacity at each analysis step. If the drift ratio of a masonry panel reaches the limit value in shear or flexure, the lateral resistance of the panel is assumed to vanish. In such a condition, the computer program reduces the macro-element to a pendulum with residual axial stiffness and strength against gravity loads.

IBC assumes the following allowable drift ratios for individual masonry panels: $\theta_{V,u} = 0.4\%$; $\theta_{M,u} = 0.6\%$ in the case of existing buildings; and $\theta_{M,u} = 0.8\%$ in the case of new buildings. Regarding the assessment of existing masonry buildings, EC8 (CEN, 2005b) suggests to assume:

- $\theta_{M,u} = 0.008H_0/B$ and $\theta_{V,u} = 0.4\%$ for 'primary' walls, and $\theta_{M,u} = 0.012H_0/B$ and $\theta_{V,u} = 0.6\%$ for 'secondary' walls (where is the distance between the point of zero bending moment and the section in which the failure is reached), at *severe damage limit state*; and
- the above limit drift ratios multiplied by 4/3, at *near collapse limit state*.

Chapter 7 - THE EVOLUTIONARY SPREAD PLASTICITY MACRO-ELEMENT

Visual inspections of masonry buildings damaged by past earthquakes have allowed to identify the main failure modes and to define strategies of simplified geometrical modelling based on the definition of several types of macro-elements (namely, masonry panels). In simplified methods of global seismic analysis, the simulation of non-linear response of masonry buildings requires first the definition of both geometry and mechanical behaviour of each macro-element. As widely discussed in previous chapters, such a behaviour can be defined at different levels of detail by using several mathematical formulations.

In the present chapter, an *evolutionary spread plasticity macro-element* is presented; its strength and displacement capacities changes as cracking and yielding develop under increasing lateral drift demand. Such a model can be applied to both pier and spandrel panels, allowing to carry out pushover analysis by relating 'global' response of a given wall with openings, or the whole masonry building, to the 'local' response of individual macro-elements. Local demand on each masonry panel is controlled during the analysis in the form of (1) axial strain diagrams over the cross-section(s) subjected to the maximum bending moment, and (2) shear stresses over cross-sections likely to fail in shear. This modus operandi allows to assess seismic performance through a unitary approach in which several *EDPs* correlated with different types of damage are controlled, according to PBEE requirements.

As emphasised by Magenes (2010), future research on masonry structures should involve displacement- and deformation-based approaches for their implementation in EC8 and other advanced seismic codes, as done for other types of structures. The formulations developed for the spread plasticity macro-element follow these research needs and were partially implemented in RAN CODE (Augenti et al., 2010a), which is a computer program devoted to both linear and non-linear analysis of masonry walls with openings and entire buildings, subjected to both gravity and seismic loads.

7.1. Non-Linear Behaviour of the Macro-Element

The non-linear behaviour of a masonry panel subjected to lateral actions is described and controlled through a mixed approach. In fact, the flexural contribution to the lateral strength and deformation is simulated through force-displacement curves defined in

deformation control, while the shearing contribution is simulated through force-displacement curve defined in force control. The flexural failure is predicted by means of strength domains derived by a *deformation-based approach*, while the shear failure (diagonal tension cracking, bed-joint sliding shear, or stair-stepped sliding shear) is predicted via strength domains derived by the classical *strength-based approach* discussed in Chapter 6.

The *spread plasticity modelling* used for the macro-element is based on a closed-form integration of strains compatible with the strength of masonry. Through an explicit consideration of the constitutive law, this modelling strategy allows to include also different mechanical behaviour under uniaxial compression along the directions parallel and orthogonal to mortar bed joints, which are the main compression directions in spandrel and pier panels, respectively, under seismic actions. Since different constitutive laws are needed to account for masonry orthotropy in a simplified mode, uniaxial compression tests were carried out on masonry prisms in the framework of ReLUIS-DPC 2005-2008 project, in order to simulate post-elastic behaviour of masonry also at large inelastic deformations (see Appendix A). Figure 7.1 shows a comparison between the stress-strain law defined for uniaxial compression orthogonal to mortar bed joints (red line) and other constitutive laws available in the literature.

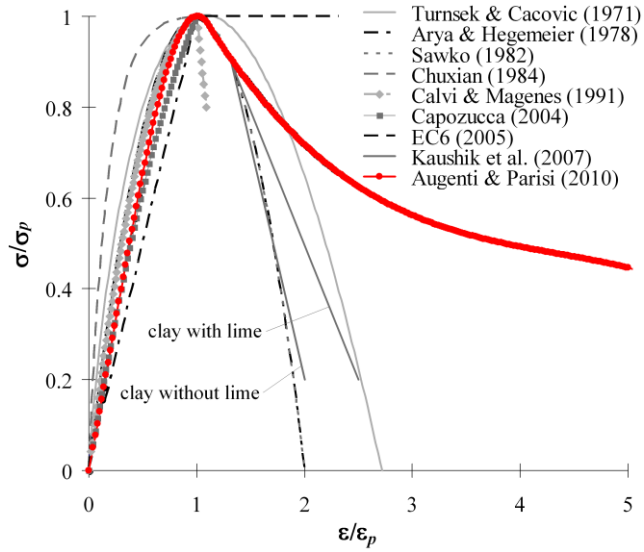

Figure 7.1 Comparison between constitutive laws of masonry under uniaxial compression

The effects of different boundary conditions for masonry panels can be taken into account through a factor related to the ratio between bending moment and shear force. It is emphasised that, in lumped plasticity models, the lateral behaviour of macro-

elements is described through multi-linear force-displacement diagrams which do not explicitly include mechanical behaviour of masonry. Although these diagrams are in compliance with building codes, the influence of masonry texture can be considered only by assuming different values for uniaxial compressive strength and elastic moduli. The macro-element presented in this chapter is affected by the following type of non-linearity: (1) *mechanical non-linearity in the elastic range* due to micro-cracking of masonry, which is described by the rising branch of the stress-strain relationship; (2) *mechanical non-linearity in the plastic range* due to strength degradation of masonry under increasing inelastic strains; and (3) *geometrical non-linearity* due to gradual macro-cracking of the masonry panel under increasing lateral drift. The latter non-linearity consists in the dependence of the effective part of the macro-element (forming an ideal inner strut) on the applied lateral load, and is directly related to low tensile strength of masonry in bending. Tensile strains at small lateral drifts are not compatible with the those allowed by masonry, so the macro-element suffers cracking in a number of cross-sections. As a result, the effective sectional width reduces from the cross-section with maximum bending curvature (namely, the mid cross-section in the case of doubly-fixed panels) to the cross-section with zero bending curvature (namely, the extreme sections in the case of doubly-fixed panels).

The lower is the given axial force on the masonry panel, the heavier is macro-cracking; the latter can influence both elastic and inelastic non-linear behaviour of the panel. Figure 7.2 gives a simplified interpretation of the geometrical evolution experienced by the macro-element in terms of ideal inner strut. In particular, Figure 7.2a shows the elastic behaviour in uncracked conditions, Figure 7.2b illustrates the elastic behaviour in cracked conditions, and Figure 7.2c shows the elasto-plastic behaviour in cracked conditions.

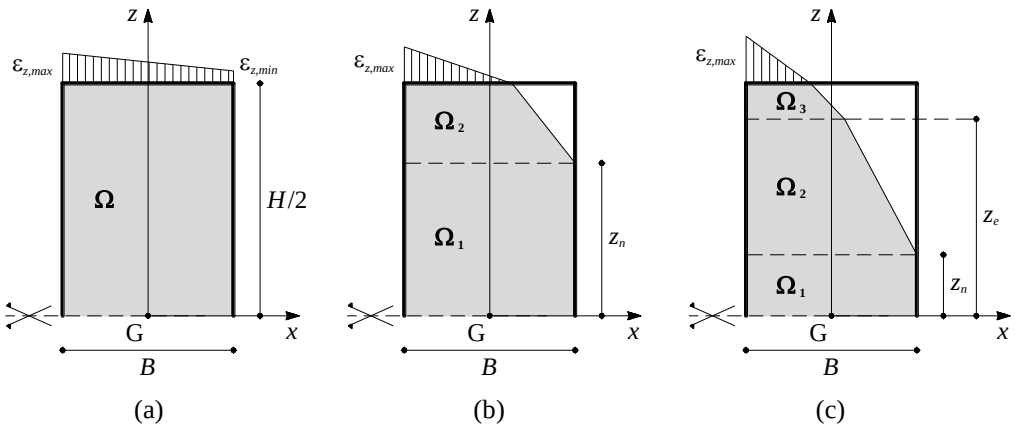

Figure 7.2 Evolution of the macro-element under varying deformation demand

For the sake of simplicity, the evolution of the macro-element is believed to be induced by bending deformation, neglecting shear effects and assuming masonry as NTR homogeneous material.

If the cross-section subjected to the maximum bending moment does not suffer cracking under the lateral drift demand on the panel, the latter is fully resistant and the effective reacting domain $\boldsymbol{\Omega}$ cover the whole nominal rectangular geometry of the panel (Fig. 7.2a). Assuming a doubly-fixed masonry panel, the flexural contribution to displacement capacity can be expressed as the product of the maximum axial strain on the end section by the mid-height of the panel (see Sect. 7.5).

As the drift demand on the macro-element increases, a gradual cracking develops in some cross-sections due to tensile strains larger than those allowed by masonry. Consequently, the effective reacting domain $\boldsymbol{\Omega}$ of the panel changes in a way to be considered as the union of two sub-regions $\boldsymbol{\Omega_1}$ and $\boldsymbol{\Omega_2}$ (Fig. 7.2b): the former has an elastic behaviour with mechanical non-linearity, the latter has an elastic behaviour with both mechanical and geometrical non-linearities (owing to the dependence of effective geometry on the given deformation state). In such conditions, both lateral strength and displacement increase, but the flexural contribution to the lateral displacement is more difficult to be estimated, opposed to the case of unacracked elastic conditions (see Sect. 7.5).

If the cross-section subjected to the maximum bending moment reaches yielding, a further sub-region $\boldsymbol{\Omega_3}$ can be identified within the masonry panel (Fig. 7.2c). This last sub-region corresponds to permanent damage, which causes unreversible modifications in mechanical properties. Therefore, both lateral strength and displacement still increase until the ultimate axial strain of masonry is reached in the cross-section subjected to the maximum bending moment.

For each of the above-mentioned deformation states, displacement capacity of the panel is assumed to be the sum of three contributions. The former is related to flexural deformation and is predicted through a deformation-based approach where theoretical formulas were derived by closed-form double integration of strains over the domains shown in Figure 7.2.

The second contribution to displacement capacity is related to shearing deformation; such a contribution is presently predicted through a force-based approach based on the one-dimensional integration of average shear strains along the height of the panel (see Sect. 6.2.9). In order to apply deformation-based approaches for the estimation of lateral displacement due to shearing deformation, direct shear tests were carried out. The output of such tests was the derivation of τ–γ constitutive laws able to simulate the non-linear behaviour in sliding shear (see Appendix B), but further research is needed to simulate compatibility between shearing and bending deformations.

The last contribution to displacement capacity is related to rocking, namely a rigid-body rotation of the masonry panel around compressed toes. In such conditions, the mechanical approach is based on the removal of the Euler-Bernoulli hypothesis (i.e., plane cross-sections remain plane) and the equilibrium solving in the deformed state. Whilst theoretical analysis is carried out in the range of large displacements, the assumption of small strains can be still applied to masonry. The estimation of rocking-induced lateral displacements for non-linear constitutive laws is presently under investigation and is uncoupled by flexural deformations. A simplified analytical model was proposed by Rai and Goel (2007) asuming masonry as a homogeneous NTR material with EPP behaviour in compression and rigid cantilever panels.

7.2. Strength Domains

Shear strengths corresponding to diagonal tension cracking and sliding can be predicted through classical yield criteria reviewed in Sect. 6.2.8. Vice versa, new formulations for the estimation of flexural strength are presented below and discussed in detail for both pier and spandrel panels.

Flexural strength domains for several limit states of interest were obtained by assuming pre-defined linear diagrams of axial strains over cross-sections subjected to the maximum bending moment and solving equilibrium equations for the relevant diagrams of normal stresses. Sectional analysis was performed through a deformation-based approach, which is believed to be an accurate mechanical approach, especially for non-linear analysis of existing masonry buildings. Nonetheless, classical stress-based approaches could be yet useful for force-based seismic design of masonry buildings and seismic assessment through linear static analysis.

The analytical formulation presented below is based on the following hypotheses:

- plane cross-sections remain plane in bending;
- masonry is a homogeneous NTR material with $\sigma-\varepsilon$ constitutive law in compression having yielding strain ε_k, peak strength σ_k, and ultimate strain ε_u; and
- limit states can be associated with axial strain diagrams over the cross-section(s) subjected to the maximum bending moment.

Depending on several mechanical and geometrical non-linearity sources, flexural strength domains are defined for the following limit states:

- *cracking limit state* (CLS), which corresponds to an axial strain diagram covering the gross cross-section width B, and having the point of zero at an extreme fibre and maximum value ε_k at the compressed extreme fibre (Fig. 7.3a);
- *cracked elastic limit state* (CELS), which corresponds to an axial strain diagram with effective width $b < B$, minimum value equal to zero and maximum value equal

to ε_k (Fig. 7.3b);

- *uncracked elastic limit state* (UELS), which corresponds to an axial strain diagram covering the gross cross-section width *B*, and having minimum value falling in the interval $]0,\varepsilon_k]$ and maximum value equal to ε_k (Fig. 7.3c);
- *cracked ultimate limit state* (CULS), which corresponds to an axial strain diagram with effective width $b < B$, minimum value equal to zero and maximum value equal to ε_k (Fig. 7.3d); and
- *uncracked ultimate limit state* (UULS), which corresponds to an axial strain diagram covering the gross cross-section width *B*, and having minimum value falling in the interval $]0,\varepsilon_u]$ and maximum value equal to ε_u.

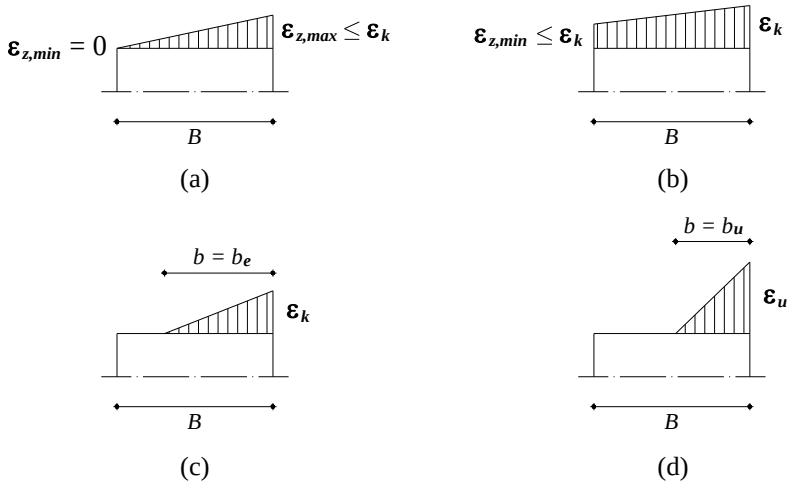

Figure 7.3 Limit states for eccentric compression

It is underlined that CLS is equal to the linear elastic limit state defined in the stress-based approach (see Sect. 6.2.6). Conversely, in the deformation-based formulation presented below no linear branches can be defined within strength domains, because mechanical non-linearity affects masonry behaviour even in the elastic range. If the cross-section yields in cracked conditions, geometrical non-linearity takes place along with mechanical non-linearity.

7.2.1. Pier Panels

Flexural strength of masonry piers was investigated accounting for the direct influence of the constitutive model of masonry in compression (Augenti and Parisi, 2009b). Amongst σ–ε relationships available in the literature, the stress-strain relationships reported in EC6 (CEN, 2005a) and proposed by Turnšek and Čačovič (1971) were

used. In particular, the Turnšek-Čačovič constitutive model is more accurate because it includes also strength degradation of masonry in the plastic range. In fact, it is shown below that the integration of such a stress-strain relationship leads to an equation $V = V(N)$ which is rather equal to that developed by Fusier and Vignoli (1993b) through regression analyses on experimental data.
In addition to the above-mentioned constitutive laws, the stress-strain relationship derived through uniaxial compression tests in the direction orthogonal to mortar bed joints (see Appendix A) was considered in the theoretical analysis. The main scope of this implementation was to assess mechanical behaviour of masonry panels at large inelastic deformations.
It is also underlined that the self-weight of masonry was neglected in the estimation of the lateral strength of masonry panels, so the axial force is constant along the height of the macro-element (Augenti, 2004).

- **Strength domains for Turnšek-Čačovič constitutive model**

The flexural strength domains at ELS and ULS are here defined through equations derived by assuming the following constitutive law proposed by Turnšek and Čačovič (1971) (Fig. 7.4):

$$\bar{f}(\varepsilon) = \frac{\sigma}{\sigma_k} = 6.4\frac{\varepsilon}{\varepsilon_k} - 5.4\left(\frac{\varepsilon}{\varepsilon_k}\right)^{1.17} \tag{7.1}$$

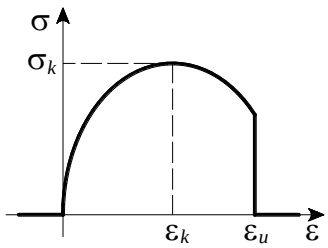

Figure 7.4 Turnšek-Čačovič constitutive law

In current applications, one assume yielding strain of masonry as $\varepsilon_k = 0.002$ and ultimate strain as $\varepsilon_u = 0.0035$. It follows a supply strain ductility $\mu_\varepsilon = 1.75$.
Regarding the *elastic limit state*, one can assume the equilibrium of a cracked cross-section under eccentric compression to be governed by the following unknowns: (1) the effective width b of the axial strain diagram over the end section subjected to the maximum bending moment; and (2) the yielding shear force V_e. The implementation of the stress-strain relationship in the following equation of translational equilibrium:

$$N = \sigma_k \, s \int_{\frac{B}{2}-b}^{B/2} \bar{f}\left(\varepsilon_z\right) dx \tag{7.2}$$

and the following assumption:

$$\varepsilon_z\left(x\right) = \varepsilon_{z,\max}\left(\frac{2b - B + 2x}{2b}\right) \tag{7.3}$$

allows to get:

$$N = \frac{4\sigma_k \, b s\left[8.7\varepsilon_{z,\max} - 6.8\varepsilon_{z,\max}\left(\frac{\varepsilon_{z,\max}}{\varepsilon_k}\right)^{0.17}\right]}{11\varepsilon_k} \tag{7.4}$$

where ε_z is the axial strain along the *z*-axis, which is orthogonal to the cross-section being considered and overlapped to the longitudinal axis of the masonry panel.
If the applied axial force *N* normalised to the maximum axial force N_m corresponding to the peak strength of masonry σ_k is defined as:

$$\bar{N} = \frac{N}{N_m} = \frac{N}{\sigma_k \, B s}$$

Eq. (7.4) can be written as follows:

$$\bar{N} = \frac{4b\left[8.7\varepsilon_{z,\max} - 6.8\varepsilon_{z,\max}\left(\frac{\varepsilon_{z,\max}}{\varepsilon_k}\right)^{0.17}\right]}{11\varepsilon_k \, B} \tag{7.5}$$

Therefore, the effective width of the end section of the panel can be estimated through the following equation:

$$b = \frac{11\varepsilon_k \, N}{4\sigma_k \, s\left[8.7\varepsilon_{z,\max} - 6.8\varepsilon_{z,\max}\left(\frac{\varepsilon_{z,\max}}{\varepsilon_k}\right)^{0.17}\right]} \tag{7.6}$$

which specialises as follows:

$$b = 1.4\frac{N}{\sigma_k \, s} \tag{7.7}$$

if $\varepsilon_{z,max} = \varepsilon_k = 0.002$. The effective width of the cross-section can be normalised to the gross width *B*, resulting in the following equation:

$$\bar{b} = b / B = 1.4\bar{N} \tag{7.8}$$

The maximum normalised axial force corresponding to a cracked cross-section at ELS can be obtained through Eq. (7.8) assuming $b/B = 1$, so it turns out to be $N/N_m = 0.71$. In other terms, if one assume the Turnšek-Čačovič constitutive model, the cross-

section of the panel is cracked for a normalised axial force falling in the interval [0,0.71]. The yielding shear force can be derived from the yielding bending moment of the end section which, in turn, can be computed as:

$$M_e = \sigma_k \, s \int_{\frac{B}{2}-b}^{B/2} \bar{f}(\varepsilon_z) \, x \, dx \tag{7.9}$$

Assuming a factor ς related to the boundary conditions of the panel, one can get the following relationship between bending moment and shear force at the end section:

$$V_e = \frac{M_e}{\varsigma H} \tag{7.10}$$

where ς is between 0.5 (corresponding to doubly-fixed panels) and 1 (corresponding to cantilever panels). The resisting shear force of the uncracked masonry panel can be estimated through the following equation:

$$V = \sigma_k \, b s \frac{\varepsilon_{z,\max}}{2\varsigma H} \frac{0.81(2b-3.2B)\left(\frac{\varepsilon_{z,\max}}{\varepsilon_k}\right)^{0.17} - 1.1(2b-3B)}{\varepsilon_k} \tag{7.11}$$

which specialises as follows:

$$\bar{V} = \frac{B}{2\varsigma H}\left\{\bar{N} - \frac{2.2\cdot 10^3 \varepsilon_k \left(\frac{\varepsilon_{z,\max}}{\varepsilon_k}\right)^{0.17}\left[6.9\varepsilon_k\left(\frac{\varepsilon_{z,\max}}{\varepsilon_k}\right)^{0.83} - 5.1\varepsilon_{z,\max}\right]}{9.5\varepsilon_{z,\max}^2\left[6.8\left(\frac{\varepsilon_{z,\max}}{\varepsilon_k}\right)^{0.17} - 8.7\right]^2}\bar{N}^2\right\} \tag{7.12}$$

considering the relationship between b and N (see Eq. (7.5)). At ELS, one can assume $\varepsilon_{z,max} = \varepsilon_k = 0.002$ so Eq. (7.12) turns out to be:

$$\bar{V}_e = \frac{B}{2\varsigma H}\left(\bar{N} - 1.11\bar{N}^2\right) \tag{7.13}$$

In the case of normalised axial force falling in the interval [0,0.5], it is underlined that Augenti (2004) proposed Eq. (6.3), that is:

$$\bar{V}_e = \frac{B}{2\varsigma H}\left(\bar{N} - \frac{4}{3}\bar{N}^2\right)$$

which for a stress-block coefficient of 0.85 specialises to:

$$\bar{V}_e = \frac{0.6B}{\varsigma H}\left(\bar{N} - 1.6\bar{N}^2\right) \tag{7.14}$$

As the normalised axial force increases in the interval [0,0.5], the ratio between Eqs. (6.3) and (7.14) changes from 0.85 to 1.7 reaching unity at $N/N_m = 0.24$. Thus,

Eq. (7.14) is less conservative for a normalised axial force falling in the interval [0,0.24]. If the normalised axial force exceeds the limit value defined through Eq. (7.5), the end section of the panel is fully resistant at ELS and its equilibrium condition can be defined if the minimum axial strain $\varepsilon_{z,min}$ (or the average strain $\varepsilon_{z,N}$) and the yielding shear force V_e are known. It is also noted that one can get only relationships like V_e–$\varepsilon_{z,min}$, or V_e–$\varepsilon_{z,N}$, rather than a direct relationship V_e–N. In fact, since the axial force is not a monotonic function of the axial strain, inverse functions such as $\varepsilon_{z,min}(N)$, or $\varepsilon_{z,N}(N)$, cannot be defined. As a result, one can define the limit line of the N–V interaction domain only through a numerical procedure.

By defining the axial strains over the cross-section as:

$$\varepsilon_z(x) = \varepsilon_{z,\min} + \frac{\varepsilon_{z,\max} - \varepsilon_{z,\min}}{B}\left(x + \frac{B}{2}\right) \tag{7.15}$$

the following equation of translational equilibrium:

$$N = \sigma_k\, s \int_{-B/2}^{+B/2} \bar{f}(\varepsilon_z)\, dx \tag{7.16}$$

specialises to:

$$\bar{N} = \frac{2.7\varepsilon_{z,\min}^2\left(\frac{\varepsilon_{z,\min}}{\varepsilon_k}\right)^{0.17} - 3.5\varepsilon_{z,\min}^2 + 0.77\varepsilon_k^2}{1.1\left(\varepsilon_k - \varepsilon_{z,\min}\right)\varepsilon_k} \tag{7.17}$$

so the axial force is clearly associated with the minimum axial strain which, in turn, falls within the interval $[0,\varepsilon_k]$. From the following equation of rotational equilibrium:

$$M_e = \sigma_k\, s \int_{-B/2}^{+B/2} \bar{f}(\varepsilon_z)\, x\, dx \tag{7.18}$$

and on the basis of Eq. (7.10), one can get:

$$V_e = \frac{\sigma_k\, s}{\varsigma H} \int_{-B/2}^{+B/2} \bar{f}(\varepsilon_z)\, x\, dx \tag{7.19}$$

The closed-form solution of the integral including Eqs. (7.1) and (7.15) is thus:

$$\bar{V}_e = \frac{B}{2\varsigma H}\left[\begin{array}{l} \dfrac{0.15\varepsilon_k^3 - 0.81\varepsilon_{z,\min}^2\left(3.2\varepsilon_k - 1.2\varepsilon_{z,\min}\right)\left(\frac{\varepsilon_{z,\min}}{\varepsilon_k}\right)^{0.17}}{\varepsilon_k\left(\varepsilon_k - \varepsilon_{z,\min}\right)^2} + \\ -\dfrac{0.13\varepsilon_{z,\min}\left(0.58\varepsilon_k^2 - 2.6\varepsilon_k\,\varepsilon_{z,\min} + 0.87\varepsilon_{z,\min}^2\right)}{\varepsilon_k\left(\varepsilon_k - \varepsilon_{z,\min}\right)^2} \end{array}\right] \tag{7.20}$$

For a normalised axial force falling in the interval [0,0.71], an intermediate limit state of the cross-section can be identified, that is CLS. The strength domain at CLS includes the points (*N*,*V*) corresponding to a fully resistant cross-section. At CLS, the minimum axial strain is zero while the maximum strain does not exceed yielding strain of masonry (which means $\varepsilon_{z,max} \leq \varepsilon_k$). Eq. (7.15) becomes:

$$\varepsilon_z(x) = \frac{\varepsilon_{z,\max}}{B}\left(x + \frac{B}{2}\right) \tag{7.21}$$

and the equilibrium condition is identified once the maximum axial strain and the cracking shear force V_l have been evaluated. The equation of translational equilibrium specialises as follows:

$$\bar{N} = \frac{\varepsilon_{z,\max}\left[3.5 - 2.7\left(\frac{\varepsilon_{z,\max}}{\varepsilon_k}\right)^{0.17}\right]}{1.1\varepsilon_k} \tag{7.22}$$

Under a given axial force, the latter equation can be numerically solved to get the maximum axial strain. The cracking shear force can be predicted through the equation:

$$\bar{V}_l = \frac{B}{2\varsigma H}\frac{\varepsilon_{z,\max}\left[1.1 - 0.95\left(\frac{\varepsilon_{z,\max}}{\varepsilon_k}\right)^{0.17}\right]}{\varepsilon_k} \tag{7.23}$$

Figure 7.5 shows flexural strength domains at CLS and ELS for a doubly-fixed panel.

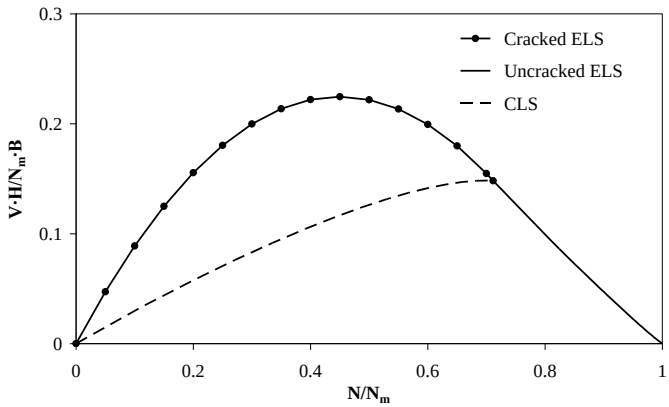

Figure 7.5 Strength domains at CLS and ELS for Turnšek-Čačovič constitutive law

At the *ultimate limit state*, the cracked cross-section has a normalised effective width equal to:

$$\bar{b} = 1.23\bar{N} \tag{7.24}$$

assuming $\varepsilon_k = 0.002$ and $\varepsilon_{z,max} = \varepsilon_u = 0.0035$ into Eq. (7.4).
The maximum normalised axial force corresponding to a cracked cross-section at ULS is $N/N_m = 0.81$; thus, the masonry panel reaches ULS in cracked conditions under a given normalised axial force falling in the interval [0,0.81]. The ultimate bending moment can then be predicted by solving the equation:

$$M_u = \sigma_k \, s \int_{\frac{B}{2}-b}^{B/2} \bar{f}(\varepsilon_z) \, x \, dx \tag{7.25}$$

while the relevant ultimate shear force of the panel can be derived by defining boundary conditions. Eq. (7.21) can be used to predict the ultimate shear force by assuming $\varepsilon_{z,max} = \varepsilon_u$. For $\varepsilon_k = 0.002$ and $\varepsilon_u = 0.0035$, the latter equation specialises to:

$$\bar{V}_u = \frac{B}{2\varsigma H}\left(\bar{N} - 1.08\bar{N}^2\right) \tag{7.26}$$

Such an equation is very similar to that derived by Fusier and Vignoli (1993b) through regression analysis on experimental data. Indeed, for a masonry panel without pre-defined boundary conditions, the equation proposed by Fusier and Vignoli can be expressed as follows:

$$\bar{V}_u = \frac{B}{2\varsigma H}\left(\bar{N} - 1.10\bar{N}^2\right) \tag{7.27}$$

where the coefficient 1.10 appears instead of 1.08. This function vanishes at $N/N_u = 0.92$, so it is defined in the interval [0,0.92]. It is underlined that N_u is the ultimate axial force corresponding to uniform diagram of axial strains equal to $\varepsilon_u = 0.0035$, and is defined as $N_u = 0.81N_m$. It follows that the interaction domain should be truncated by a vertical straight line at N_u, unless a uniform diagram of axial strains equal to $\varepsilon_k = 0.002$ is assumed in concentric compression. IBC (2008) allows to assume a uniform diagram of normal stresses equal to a 15%-reduced compressive strength of masonry. Figure 7.6 shows the comparison between flexural strength domains proposed by Fusier and Vignoli (1993b), Augenti (2004), IBC, and Turnšek and Čačovič (Augenti and Parisi, 2009b), in the case of doubly-fixed panel. It is emphasised that Eqs. (7.26) and (7.27) lead to rather equal predictions of ultimate shear force, especially for a normalised axial force falling in the interval [0,0.5]. For the latter interval, Eq. (6.1) and IBC lead to higher ultimate shear force values[27], while conservative predictions are provided by IBC for N/N_u falling in the interval [0.5,1].

[27] For a normalised axial force falling in the interval [0,0.5], the ultimate shear force predicted by Eq. (6.1) and IBC is up to 9% and 13% higher than that predicted by Eq. (7.26). For a normalised axial force falling in the range [0.5,1], the ultimate shear force predicted by IBC is up to 26% lower than the others.

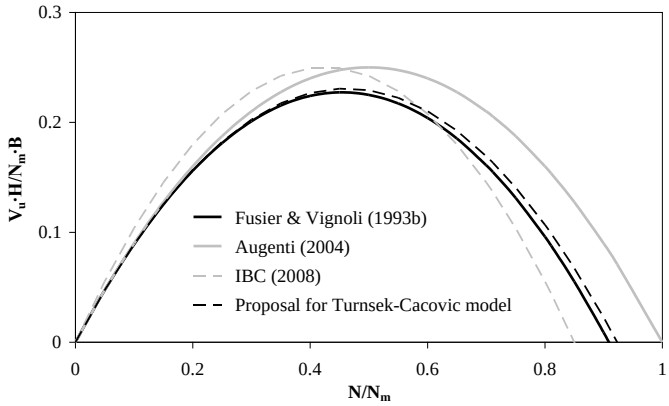

Figure 7.6 Comparison between strength domains at ULS

If the axial force exceeds the limit value defined by Eq. (7.4) assuming specific values for ε_k and ε_u, the cross-section reaches ULS in uncracked conditions and the equation of translational equilibrium specialises as:

$$\bar{N} = \frac{2.7\varepsilon_u^2\left(\frac{\varepsilon_u}{\varepsilon_k}\right)^{0.17} - 2.7\varepsilon_{z,\min}^2\left(\frac{\varepsilon_{z,\min}}{\varepsilon_k}\right)^{0.17} - 3.5\left(\varepsilon_u^2 - \varepsilon_{z,\min}^2\right)}{1.1\left(\varepsilon_{z,\min} - \varepsilon_u\right)\varepsilon_k} \tag{7.28}$$

For $\varepsilon_{z,min} = 0$, $\varepsilon_k = 0.002$, and $\varepsilon_u = 0.0035$, this equation gives $N_u/N_m = 0.81$, so the section is fully resistant for $N/N_m > 0.81$. The ultimate moment can be estimated as:

$$M_u = \sigma_k\, s \int_{-B/2}^{+B/2} \bar{f}\left(\varepsilon_z\right) x\, dx \tag{7.29}$$

so the ultimate shear force can be estimated as follows:

$$V_u = \frac{\sigma_k\, s}{\varsigma H} \int_{-B/2}^{+B/2} \bar{f}\left(\varepsilon_z\right) x\, dx \tag{7.30}$$

By implementating Eqs. (7.1) and (7.15), the normalised ultimate shear force can be expressed as a function of $\varepsilon_{z,min}$, ε_k and ε_u, through the following equation:

$$\bar{V}_u = \frac{B}{2\varsigma H}\left[\frac{0.55\left(\varepsilon_u - \varepsilon_{z,\min}\right)^3 - 0.41\varepsilon_u^2\left(1.2\varepsilon_u - 3.2\varepsilon_{z,\min}\right)\left(\frac{\varepsilon_u}{\varepsilon_k}\right)^{0.17}}{\left(\varepsilon_u - \varepsilon_{z,\min}\right)^2\varepsilon_k} + \right.$$
$$\left. - \frac{0.41\varepsilon_{z,\min}^2\left(3.2\varepsilon_u - 1.2\varepsilon_{z,\min}\right)\left(\frac{\varepsilon_{z,\min}}{\varepsilon_k}\right)^{0.17}}{\left(\varepsilon_u - \varepsilon_{z,\min}\right)^2\varepsilon_k}\right] \tag{7.31}$$

Finally, for $\varepsilon_k = 0.002$ and $\varepsilon_u = 0.0035$, such an equation specialises to:

$$\bar{V}_u = \frac{B}{2\varsigma H}\frac{\kappa_1\left(a\,\varepsilon_{z,\min}^{3.17} + b\,\varepsilon_{z,\min}^{3} + c\,\varepsilon_{z,\min}^{2.17} + d\,\varepsilon_{z,\min}^{2} + e\,\varepsilon_{z,\min} + f\right)}{\left(\kappa_2\,\varepsilon_{z,\min} - 7\right)^2} \tag{7.32}$$

being:

$\kappa_1 = 7.7\cdot10^{-7}$ $\quad \kappa_2 = 2\cdot10^{3}$

$a = 6.9\cdot10^{15}$ $\quad b = -2.8\cdot10^{15}$

$c = -6.5\cdot10^{13}$ $\quad d = 2.9\cdot10^{13}$

$e = -1.5\cdot10^{10}$ $\quad f = 6.3\cdot10^{6}$

Under a given axial force on the masonry panel, one can predict first the minimum axial strain over the cross-section subjected to maximum bending moment, and then the ultimate shear force.

- **Strength domains for EC6 constitutive model**

The flexural strength domains at ELS and ULS are here defined through equations derived by assuming the following constitutive law proposed reported in EC6 (CEN, 2005a) (Fig. 7.7):

$$\begin{aligned} \bar{f}(\varepsilon) &= \frac{\sigma}{\sigma_k} = 2\frac{\varepsilon}{\varepsilon_k} - \left(\frac{\varepsilon}{\varepsilon_k}\right)^2 && \text{for } 0 \le \varepsilon \le \varepsilon_k \\ \bar{f}(\varepsilon) &= \frac{\sigma}{\sigma_k} = 1 && \text{for } \varepsilon_k \le \varepsilon \le \varepsilon_u \end{aligned} \tag{7.33}$$

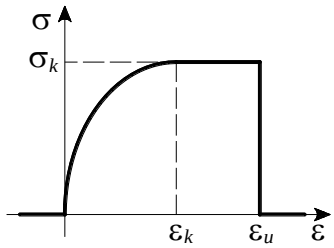

Figure 7.7 EC6 constitutive law

Also in this case, the cross-section can be analysed in cracked and uncracked conditions, separately. In addition, the theoretical analysis is carried out first for ELS and CLS, and then for ULS. To this end, the stress-strain relationship reported in EC6 was replaced by a polynomial approximation in order to simplify integration. The following constitutive equation was then used:

$$\bar{f}(\varepsilon) = \frac{\sigma}{\sigma_k} = \sum_{j=0}^{5} a_j \left(\frac{\varepsilon}{\varepsilon_k} \right)^j \tag{7.34}$$

where:

$a_0 = 0$ $\quad$ $a_1 = 1.88$

$a_2 = -2.4 \cdot 10^{-1}$ $\quad$ $a_3 = -1.48$

$a_4 = 1.05$ $\quad$ $a_5 = -2.12 \cdot 10^{-1}$

This polynomial function is the best fit of the original stress-strain relationship and has a coefficient of determination $R^2 = 0.9998$ (Fig. 7.8).

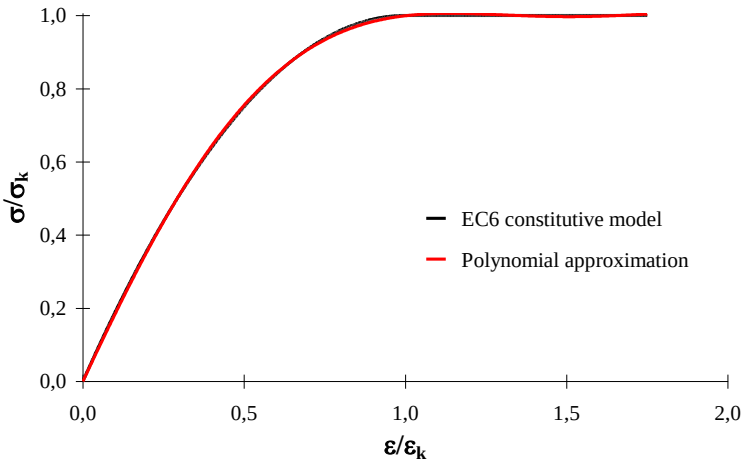

Figure 7.8 Polynomial approximation of EC6 constitutive law

In this case, the maximum resisting axial force is equal to the ultimate axial force (that is, $N_m = N_u$), since the constitutive law does not include strain softening of masonry. For a cracked cross-section at the *elastic limit state*, the equation of translational equilibrium can be expressed as:

$$\bar{N} = \bar{b} \sum_{j=0}^{5} g'_j \, \varepsilon_k^j \tag{7.35}$$

where:

$g'_0 = 0$ $\quad$ $g'_1 = 4.7 \cdot 10^2$

$g'_2 = -2 \cdot 10^4$ $\quad$ $g'_3 = -4.6 \cdot 10^7$

$g'_4 = 1.3 \cdot 10^{10}$ $\quad$ $g'_5 = -1.1 \cdot 10^{12}$

Therefore, the effective width of the axial strain diagram can be estimated by inverting Eq. (7.35). For $\varepsilon_k = 0.002$, it turns out to be:

$$\bar{b} = 1.5\,\bar{N} \tag{7.36}$$

so the cross-section is cracked under a normalised axial force falling in the interval [0,0.67]. The shear force at ELS is then derived by the relevant bending moment and can be predicted through the following equation:

$$\bar{V}_e = \frac{B}{2\varsigma H}\left[\bar{N}^2\,\frac{p_1'(\varepsilon_k)}{\varepsilon_k\,p_2'(\varepsilon_k)^2} - \bar{N}\right] \tag{7.37}$$

including the polynomials:

$$\begin{aligned} p_1'(\varepsilon_k) &= \sum_{j=0}^{4} m_j'\,\varepsilon_k^j \\ p_2'(\varepsilon_k) &= \sum_{j=0}^{4} n_j'\,\varepsilon_k^j \end{aligned} \tag{7.38}$$

where:

$m_0' = -4.9\cdot10^6$ $\quad$ $m_1' = 1.6\cdot10^8$

$m_2' = 2.9\cdot10^{11}$ $\quad$ $m_3' = -6.9\cdot10^{13}$

$m_4' = 4.9\cdot10^{15}$ $\quad$ $n_0' = -5.9\cdot10^4$

$n_1' = 2.5\cdot10^6$ $\quad$ $n_2' = 5.8\cdot10^9$

$n_3' = -1.6\cdot10^{12}$ $\quad$ $n_4' = 1.4\cdot10^{14}$

For ε_k = 0.002, Eq. (7.37) specialises to:

$$\bar{V}_e = \frac{B}{2\varsigma H}\left(\bar{N} - 1.13\,\bar{N}^2\right) \tag{7.39}$$

If the normalised axial force falls within the interval [0.67,1], the masonry panel is fully resistant. As stated in the case of Turnšek-Čačovič constitutive law, for an axial force corresponding to an uncracked cross-section, the limit line of the strength domain at ELS can be defined only numerically, since no direct relationships between the resisting shear force and the given axial force exist. By considering Eqs. (7.34) and (7.15), the equation of translational equilibrium can be written as:

$$\bar{N} = \bar{b}\sum_{j=0}^{5} b_j'\,\varepsilon_k^j \tag{7.40}$$

where:

$b_0' = 6.6\cdot10^{-1}$ $\quad$ $b_1' = 3.3\cdot10^2$

$b_2' = -6.9\cdot10^4$ $\quad$ $b_3' = -2.4\cdot10^7$

$b_4' = 1.1\cdot10^{10}$ $\quad$ $b_5' = -1.1\cdot10^{12}$

if one assume $\varepsilon_{z,max}$ = ε_k = 0.002. It is underlined that the coefficient b'_0 is the

normalised axial force at $\varepsilon_{z,min} = 0$. The normalised yielding shear force can be predicted through the following equation:

$$\bar{V}_e = \frac{B}{2\varsigma H}\sum_{j=0}^{5} d'_j \, \varepsilon_{z,\min}^{j} \tag{7.41}$$

where, assuming $\varepsilon_k = 0.002$, the coefficients are:

$d'_0 = 1.7 \cdot 10^{-1}$ $\quad$ $d'_1 = -1.7 \cdot 10^{2}$

$d'_2 = 2.7 \cdot 10^{4}$ $\quad$ $d'_3 = 2 \cdot 10^{7}$

$d'_4 = -7.8 \cdot 10^{9}$ $\quad$ $d'_5 = 7.9 \cdot 10^{11}$

For yielding strains different from 0.002, the coefficients b'_i and d'_i can be evaluated by means of the following equations:

$$b'_0 = 4.7 \cdot 10^{2}\,\varepsilon_k - 2 \cdot 10^{4}\,\varepsilon_k^2 - 4.6 \cdot 10^{7}\,\varepsilon_k^3 + 1.3 \cdot 10^{10}\,\varepsilon_k^4 - 1.1 \cdot 10^{12}\,\varepsilon_k^5$$

$$b'_1 = 4.7 \cdot 10^{2} - 2 \cdot 10^{4}\,\varepsilon_k - 4.6 \cdot 10^{7}\,\varepsilon_k^2 + 1.3 \cdot 10^{10}\,\varepsilon_k^3 - 1.1 \cdot 10^{12}\,\varepsilon_k^4$$

$$b'_2 = -2 \cdot 10^{4} - 4.6 \cdot 10^{7}\,\varepsilon_k + 1.3 \cdot 10^{10}\,\varepsilon_k^2 - 1.1 \cdot 10^{12}\,\varepsilon_k^3$$

$$b'_3 = -4.6 \cdot 10^{7} + 1.3 \cdot 10^{10}\,\varepsilon_k - 1.1 \cdot 10^{12}\,\varepsilon_k^2$$

$$b'_4 = 1.3 \cdot 10^{10} - 1.1 \cdot 10^{12}\,\varepsilon_k$$

$$b'_5 = -1.1 \cdot 10^{12}$$

$$d'_0 = 1.6 \cdot 10^{2}\,\varepsilon_k - 10^{4}\,\varepsilon_k^2 - 2.8 \cdot 10^{7}\,\varepsilon_k^3 + 8.8 \cdot 10^{9}\,\varepsilon_k^4 - 7.9 \cdot 10^{11}\,\varepsilon_k^5$$

$$d'_1 = -1.6 \cdot 10^{2} - 9.3 \cdot 10^{6}\,\varepsilon_k^2 + 4.4 \cdot 10^{9}\,\varepsilon_k^3 - 4.7 \cdot 10^{12}\,\varepsilon_k^4$$

$$d'_2 = 10^{4} + 9.3 \cdot 10^{6}\,\varepsilon_k - 1.6 \cdot 10^{11}\,\varepsilon_k^3$$

$$d'_3 = 2.8 \cdot 10^{7} - 4.4 \cdot 10^{9}\,\varepsilon_k + 1.6 \cdot 10^{10}\,\varepsilon_k^2$$

$$d'_4 = -8.8 \cdot 10^{9} + 4.7 \cdot 10^{11}\,\varepsilon_k$$

$$d'_5 = 7.9 \cdot 10^{11}$$

For a normalised axial force falling in the interval [0,0.67], the masonry panel reaches first CLS when the minimum axial strain vanishes at the cross-section being monitored, and then ELS when the maximum axial strain reaches yielding strain of masonry. Before CLS is attained, the end section subjected to the maximum bending moment is fully resistant and the maximum axial strain does not exceed the yielding strain of masonry. As a consequence, the axial strain diagram is described by Eq. (7.21) and the translational equilibrium is governed by the following relation:

$$\bar{N} = \sum_{j=0}^{5} f'_j \, \varepsilon_{z,\max}^{j} \tag{7.42}$$

whose coefficients are equal to those of Eq. (7.35). Under a given axial force, Eq. (7.40) allows to numerically evaluate the maximum axial strain. Thus, the cracking

shear force can be predicted via the following equation:

$$\bar{V}_l = \frac{B}{2\varsigma H}\sum_{j=0}^{5} h'_j\,\varepsilon_{z,\max}^{j} \tag{7.43}$$

having coefficients equal to those of the equation that defines b'_0 ($h_0 = 0$). Figure 7.9 shows the strength domains at CLS and ELS, in the case of doubly-fixed panel.

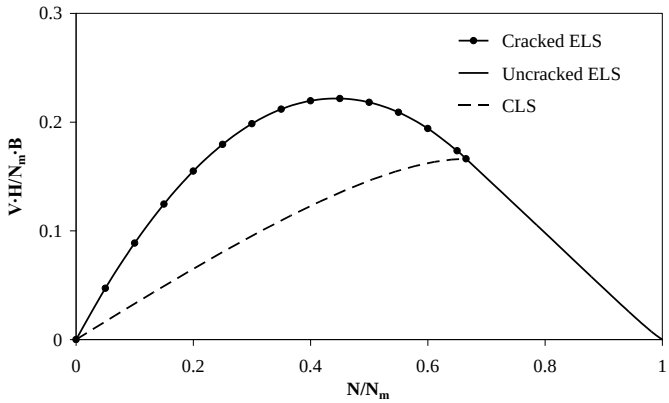

Figure 7.9 Strength domains at CLS and ELS for EC6 constitutive law

For a cracked cross-section at the *ultimate limit state*, the relationship between the given axial force and the ultimate deformation is:

$$\bar{N} = \bar{b}\sum_{j=0}^{5} g'_j\,\varepsilon_u^{j} \tag{7.44}$$

where coefficients are equal to those appearing into Eq. (7.35). The effective width of the axial strain diagram can thus be evaluated by inverting Eq. (7.43). For $\varepsilon_u = 0.0035$, the normalised effective width of the end section can be defined as follows:

$$\bar{b} = 1.24\,\bar{N} \tag{7.45}$$

so the limit condition $b/B = 1$ is reached at $N/N_u = 0.81$. Therefore, if one assume the EC6 constitutive model for masonry, the macro-element reaches ULS in cracked conditions for a normalised axial force falling in the interval [0,0.81]. The ultimate shear force can be predicted by solving Eq. (7.25) and applying Eq. (7.10), so it turns out to be:

$$\bar{V}_u = \frac{B}{2\varsigma H}\left[\bar{N}^2\,p_1(\varepsilon_u) - \bar{N}\,p_2(\varepsilon_u)\right] \tag{7.46}$$

whose polynomials are defined as:

$$p_1(\varepsilon_u) = \sum_{j=0}^{5} m'_j \, \varepsilon_u^j$$
$$p_2(\varepsilon_u) = \sum_{j=0}^{5} n'_j \, \varepsilon_u^j \tag{7.47}$$

where:

$m_0 = 0$ $\quad$ $n_0 = 0$

$m_1 = -4.8 \cdot 10^2$ $\quad$ $n_1 = -5.8 \cdot 10^2$

$m_2 = 1.5 \cdot 10^4$ $\quad$ $n_2 = 2.5 \cdot 10^4$

$m_3 = 2.9 \cdot 10^7$ $\quad$ $n_3 = 5.7 \cdot 10^7$

$m_4 = -6.7 \cdot 10^9$ $\quad$ $n_4 = -1.6 \cdot 10^{10}$

$m_5 = 4.8 \cdot 10^{11}$ $\quad$ $n_5 = 1.4 \cdot 10^{12}$

For $\varepsilon_u = 0.0035$, Eq. (7.46) specialises to:

$$\bar{V}_u = \frac{B}{2\varsigma H}\left(\bar{N} - 1.03\bar{N}^2\right) \tag{7.48}$$

and vanishes at $N/N_u = 0.97$, so it is defined for a normalised axial force falling in the interval [0,0.97]. Figure 7.10 shows a comparison between the strength domain derived for EC6 constitutive model (Augenti and Parisi, 2009b) and those proposed by Fusier and Vignoli (1993b), Augenti (2004), and IBC, in the case of doubly-fixed panel.

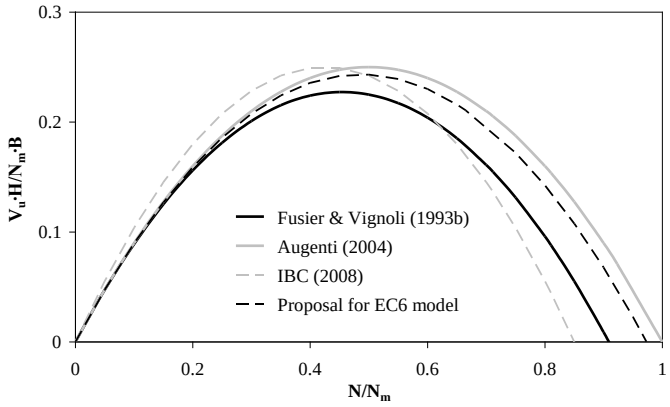

Figure 7.10 Comparison between strength domains at ULS

For a normalised axial force falling in the interval [0.81,1], the end section is fully resistant at ULS. The strength domain can be derived only numerically since no functions $V_u(N)$ can be defined. The normalised axial force is related to the minimum axial strain as follows:

$$\bar{N} = \sum_{j=0}^{5} b_j \, \varepsilon_{z,\min}^{j} \tag{7.49}$$

For $\varepsilon_u = 0.0035$, the coefficients b_j are:

$b_0 = 0.81$ $\quad b_1 = 2.3 \cdot 10^2$

$b_2 = -6.8 \cdot 10^4$ $\quad b_3 = -1.4 \cdot 10^7$

$b_4 = 9.3 \cdot 10^9$ $\quad b_5 = -1.1 \cdot 10^{12}$

where b_0 is the normalised axial force at $\varepsilon_{z,min} = 0$, as shown for ELS. The normalised ultimate shear force can then be predicted via the following equation:

$$\bar{V}_u = \frac{B}{2\varsigma H} \sum_{j=0}^{5} d_j \, \varepsilon_{z,\min}^{j} \tag{7.50}$$

whose coefficients are:

$d_0 = 1.4 \cdot 10^{-1}$ $\quad d_1 = 1.5 \cdot 10^2$

$d_2 = 3.6 \cdot 10^3$ $\quad d_3 = 1.4 \cdot 10^8$

$d_4 = -7.1 \cdot 10^9$ $\quad d_5 = 7.9 \cdot 10^{11}$

for $\varepsilon_u = 0.0035$. If ultimate strain of masonry is assumed to be different from 0.0035 (for instance, in the presence of confinement with fibre-reinforced polymers), the coefficients b_j and d_j are defined by the equations reported above for b'_j and d'_j, respectively, where ε_k is replaced by ε_u.

- **Strength domains for Augenti-Parisi constitutive model related to compression orthogonal to mortar bed joints**

In this sub-section, strength domains at both ELS and ULS are derived for an empirical constitutive law proposed for masonry subjected to uniaxial compression in the direction orthogonal to mortar bed joints (Augenti and Parisi, 2010a; see Appendix A). The constitutive model is defined by the following stress-strain relationships (Fig. 7.11):

$$\bar{f}(\varepsilon) = \frac{\sigma}{\sigma_k} = -0.7144\left(\frac{\varepsilon}{\varepsilon_k}\right)^3 + 0.4549\left(\frac{\varepsilon}{\varepsilon_k}\right)^2 + 1.2595\left(\frac{\varepsilon}{\varepsilon_k}\right) \qquad \text{for } 0 \le \frac{\varepsilon}{\varepsilon_k} \le 1.12$$

$$\bar{f}(\varepsilon) = \frac{\sigma}{\sigma_k} = -0.0107\left(\frac{\varepsilon}{\varepsilon_k}\right)^3 + 0.1388\left(\frac{\varepsilon}{\varepsilon_k}\right)^2 - 0.6487\left(\frac{\varepsilon}{\varepsilon_k}\right) + 1.545 \quad \text{for } 1.12 \le \frac{\varepsilon}{\varepsilon_k} \le 5 \tag{7.51}$$

The yielding axial strain ε_k of masonry can be set to 0.002 and the supply strain ductility in compression can be assumed to be $\mu_\varepsilon = 5$, resulting in an ultimate axial strain $\varepsilon_u = 0.01$.

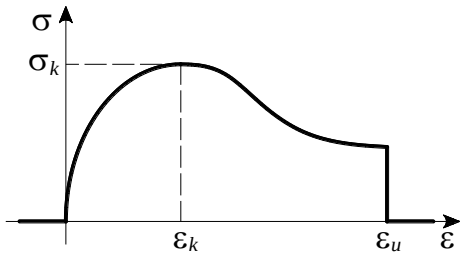

Figure 7.11 Augenti-Parisi constitutive laws (typical form for both directions)

With reference to the *elastic limit state*, the equations of translational and rotational equilibrium of a given cross-section in cracked conditions can be respectively written as follows:

$$\bar{N} = 0.6\bar{b} \tag{7.52}$$

$$\frac{\bar{M}_e}{B} = 0.3\bar{b} - 0.21\bar{b}^2 \tag{7.53}$$

Therefore, the limit line of the flexural strength domain related to a normalised axial force falling in the interval [0,0.6] can be described by means of the following equation:

$$\bar{V}_e = \frac{B}{2\varsigma H}\left(\bar{N} - 1.16\bar{N}^2\right) \tag{7.54}$$

The equilibrium conditions at CLS can be expressed as:

$$\bar{N} = 0.63\frac{\varepsilon_{z,\max}}{\varepsilon_k} + 0.15\left(\frac{\varepsilon_{z,\max}}{\varepsilon_k}\right)^2 - 0.17\left(\frac{\varepsilon_{z,\max}}{\varepsilon_k}\right)^3 \tag{7.55}$$

$$\frac{\bar{M}_l}{B} = 0.11\frac{\varepsilon_{z,\max}}{\varepsilon_k} + 0.04\left(\frac{\varepsilon_{z,\max}}{\varepsilon_k}\right)^2 - 0.05\left(\frac{\varepsilon_{z,\max}}{\varepsilon_k}\right)^3 \tag{7.56}$$

so the cracking shear force can be predicted through the equation:

$$\bar{V}_l = \frac{B}{\varsigma H}\left[0.11\frac{\varepsilon_{z,\max}}{\varepsilon_k} + 0.04\left(\frac{\varepsilon_{z,\max}}{\varepsilon_k}\right)^2 - 0.05\left(\frac{\varepsilon_{z,\max}}{\varepsilon_k}\right)^3\right] \tag{7.57}$$

For $N/N_m > 0.6$, the masonry panel reaches ELS in uncracked conditions and its equilibrium can be assessed through the following equations:

$$\bar{N} = 0.6 + 0.6\left(\frac{\varepsilon_{z,\min}}{\varepsilon_k}\right) - 0.03\left(\frac{\varepsilon_{z,\min}}{\varepsilon_k}\right)^2 - 0.19\left(\frac{\varepsilon_{z,\min}}{\varepsilon_k}\right)^3 \tag{7.58}$$

$$\bar{V}_e = \frac{B}{\varsigma H}\left[0.09 - 0.12\left(\frac{\varepsilon_{z,\min}}{\varepsilon_k}\right) - 0.02\left(\frac{\varepsilon_{z,\min}}{\varepsilon_k}\right)^2 + 0.05\left(\frac{\varepsilon_{z,\min}}{\varepsilon_k}\right)^3\right] \tag{7.59}$$

since no direct relationships between the resisting shear force and the given axial force can be defined. Figure 7.12 shows the strength domains at CLS and ELS, in the case of doubly-fixed panel.

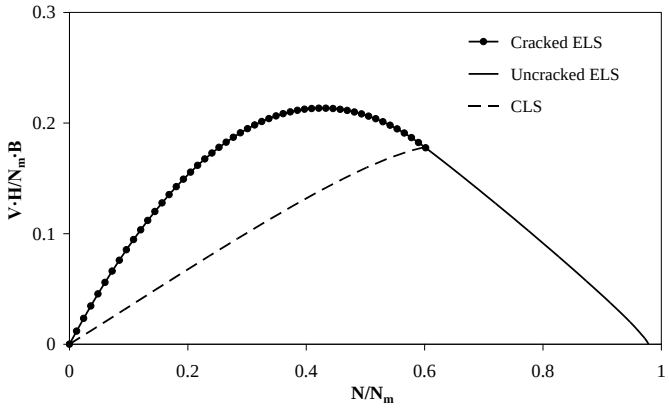

Figure 7.12 Strength domains at CLS and ELS for Augenti-Parisi model (orthog. dir.)

With reference to the *ultimate limit state*, the equations of translational and rotational equilibrium can be respectively expressed as follows:

$$\bar{N} = \bar{b}\left(1.54 - \frac{0.66}{\mu_\varepsilon} - 0.32\mu_\varepsilon + 0.05\mu_\varepsilon^2 - 0.003\mu_\varepsilon^2\right) \tag{7.60}$$

$$\begin{aligned}\frac{\bar{M}_u}{B} = {} & \bar{b}^2\left(-0.77 - \frac{0.2}{\mu_\varepsilon^2} + \frac{0.66}{\mu_\varepsilon} + 0.11\mu_\varepsilon - 0.012\mu_\varepsilon^2 + 0.001\mu_\varepsilon^3\right) + \\ & + \bar{b}\left(0.77 - \frac{0.33}{\mu_\varepsilon} - 0.16\mu_\varepsilon + 0.02\mu_\varepsilon^2 - 0.001\mu_\varepsilon^3\right)\end{aligned} \tag{7.61}$$

so the interaction between the ultimate shear force and the given axial force can be described through the following equation:

$$\bar{V}_u = \frac{B}{\varsigma H}\left[\frac{\bar{N}}{2} - \frac{p_1(\mu_\varepsilon)}{p_2(\mu_\varepsilon)}\bar{N}^2\right] \tag{7.62}$$

where:

$$\begin{aligned} p_1(\mu_\varepsilon) &= 0.2 - 0.66\mu_\varepsilon + 0.77\mu_\varepsilon^2 - 0.11\mu_\varepsilon^3 + 0.012\mu_\varepsilon^4 - 0.001\mu_\varepsilon^5 \\ p_2(\mu_\varepsilon) &= 0.66\mu_\varepsilon - 1.54\mu_\varepsilon^2 + 0.32\mu_\varepsilon^3 - 0.05\mu_\varepsilon^4 - 0.003\mu_\varepsilon^5 \end{aligned} \tag{7.63}$$

Assuming b/B = 1 and μ_ε = 5 into Eq. (7.60), the maximum normalised axial force corresponding to a cracked masonry panel at ULS is N/N_m = 0.61. Thus, Eq. (7.62) applies for a normalised axial force falling in the interval [0,0.61]. For N/N_m > 0.61, the panel reaches ULS in uncracked conditions and the equations of translational and

rotational equilibrium can be respectively written as follows:

$$\bar{N} = 0.63\mu_\varepsilon + 0.15\mu_\varepsilon^2 - 0.18\mu_\varepsilon^3 + \left(0.63 + 0.15\mu_\varepsilon - 0.18\mu_\varepsilon^2\right)\left(\frac{\varepsilon_{z,\min}}{\varepsilon_k}\right) + \left(0.15 - 0.18\mu_\varepsilon\right)\left(\frac{\varepsilon_{z,\min}}{\varepsilon_k}\right)^2 + -0.18\left(\frac{\varepsilon_{z,\min}}{\varepsilon_k}\right)^3 - \frac{\left(0.66 - 1.54\mu_\varepsilon + 0.95\mu_\varepsilon^2 + 0.11\mu_\varepsilon^3 - 0.18\mu_\varepsilon^4\right)\varepsilon_k}{\varepsilon_u - \varepsilon_{z,\min}} \tag{7.64}$$

$$\bar{V}_u = \frac{B}{\varsigma H}\left[\begin{array}{l} 0.11\mu_\varepsilon + 0.04\mu_\varepsilon^2 - 0.05\mu_\varepsilon^3 - \left(0.11 + 0.02\mu_\varepsilon^2\right)\left(\frac{\varepsilon_{z,\min}}{\varepsilon_k}\right) - \left(0.04 - 0.02\mu_\varepsilon\right)\left(\frac{\varepsilon_{z,\min}}{\varepsilon_k}\right)^2 + \\ + 0.05\left(\frac{\varepsilon_{z,\min}}{\varepsilon_k}\right)^3 - \frac{\left(0.33 - 0.77\mu_\varepsilon + 0.48\mu_\varepsilon^2 + 0.05\mu_\varepsilon^3 - 0.09\mu_\varepsilon^4\right)\varepsilon_k}{\varepsilon_u - \varepsilon_{z,\min}} + \\ - \frac{\left(0.2 - 0.66\mu_\varepsilon + 0.77\mu_\varepsilon^2 - 0.32\mu_\varepsilon^3 - 0.03\mu_\varepsilon^4 + 0.04\mu_\varepsilon^5\right)\varepsilon_k^2}{\left(\varepsilon_u - \varepsilon_{z,\min}\right)^2} \end{array}\right] \tag{7.65}$$

Figure 7.13 shows a comparison between the ultimate strength domain corresponding to Augenti-Parisi constitutive model and those related to previous formulations.

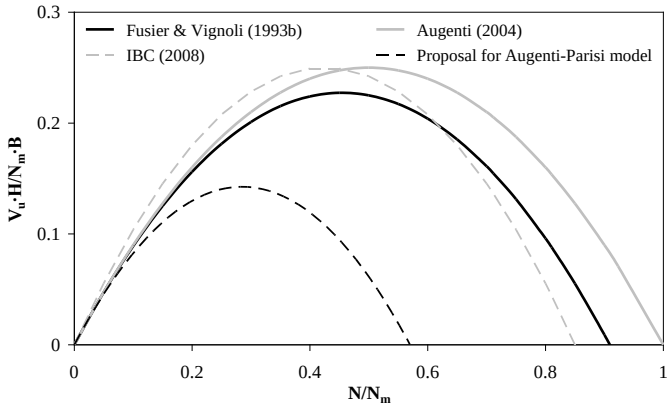

Figure 7.13 Comparison between strength domains at ULS

- **Comparisons between strength domains**

The flexural strength domains derived in previous sub-sections at both CLS and ELS are compared each other in Figure 7.14.

With reference to CLS, the limit line of the strength domain proposed by Augenti (2004) is linear, since mechanical non-linearity in the elastic range is neglected. Conversely, the strength domains derived for Turnšek-Čačovič, EC6, and Augenti-

Parisi constitutive models have non-linear boundaries even at CLS, since the relevant stress-strain relationships are non-linear in the elastic range. Flexural strength domains at CLS have different values of normalised axial force corresponding to the maximum cracking shear force. In fact, the latter is: N_c/N_m = 0.5 in the case of the strength domain proposed by Augenti (2004); N_c/N_m = 0.67 in the case of the strength domain corresponding to Turnšek-Čačovič constitutive model; N_c/N_m = 0.71 in the case of the strength domain corresponding to EC6 constitutive model; and N_c/N_m = 0.6 in the case of the strength domain corresponding to the constitutive law proposed by Augenti and Parisi (2010a) for uniaxial compression orthogonal to mortar bed joints.

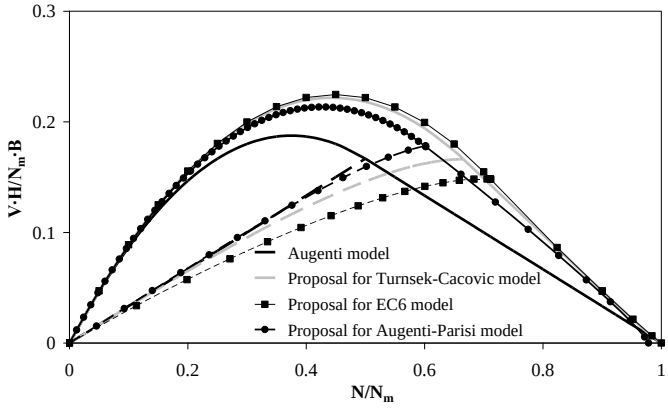

Figure 7.14 Comparison between strength domains at CLS and ELS

The comparison between ultimate strength domains reported in Figure 7.13 has been carried out by assuming a supply strain ductility μ_ε = 5 in Augenti-Parisi constitutive law. As a result, strength degradation of masonry at large inelastic strains has induced a significant contraction in the strength domain, and hence a considerable difference with other domains.

If supply strain ductility of masonry is assumed to be μ_ε = 1.75 (that is, equal to the value considered for Turnšek-Čačovič and EC6 constitutive models), the contraction in the strength domain is less significant and the estimation of the ultimate shear force is more conservative than the others (Fig. 7.15). It is emphasised that this supply ductility value should be adopted for design purposes, while an accurate assessment of masonry structures requires the simulation of mechanical behaviour also at larger inelastic deformations.

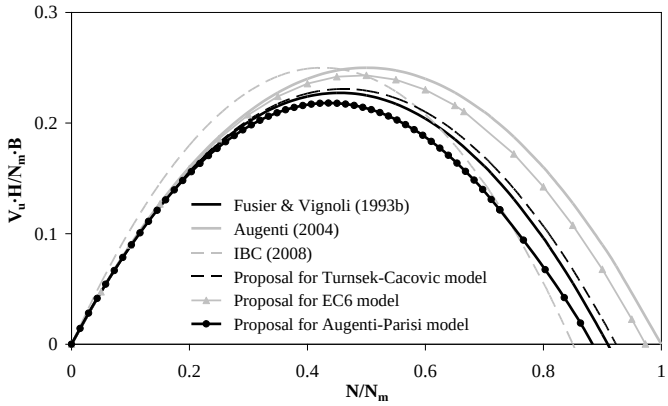

Figure 7.15 Comparison between strength domains at ULS for strain ductility $\mu_\varepsilon = 1.75$

7.2.2. Spandrel Panels

In this sub-section, the flexural strength of spandrel panels is investigated through the development of two-dimensional strength domains corresponding to several $\sigma-\varepsilon$ constitutive laws of masonry. In particular, the discussion deals with strength domains defined at both ELS and ULS (Augenti and Parisi, 2010b). The theoretical analysis was carried out for the following constitutive models: EPP; Turnšek-Čačovič; EC6; and Augenti-Parisi (2010a) related to uniaxial compression parallel to mortar bed joints.

The strength domains presented below are related to a generic cross-section of a masonry panel, but they could be extended to the whole panel through a boundary-dependent factor (see Sect. 7.2.1). Therefore, dimensionless *N–M* interaction domains are presented and discussed by assuming:

$$\bar{N} = \frac{N}{N_m}$$
$$\frac{\bar{M}}{H} = \bar{N}\,\bar{e} = \frac{N}{N_m}\frac{e}{H} \tag{7.66}$$

being: $N_m = \sigma_k\, s\, H$ and H the nominal height of the masonry panel.

The dimensionless representation of interaction domains allows to assess variations in resisting bending moment and other parameters without any dependence on the panel dimensions, nor on the masonry strength. Both the axial force and the bending moment are defined as functions of the neutral axis depth h normalised to the nominal height of the cross-section, as follows:

$$\bar{h} = \frac{h}{H} \tag{7.67}$$

- **Strength domains for EPP constitutive model**

In the case of EPP stress-strain relationship, yielding and ultimate axial strains of masonry were assumed to be ε_k = 0.001 and ε_u = 0.0035, respectively, resulting in a supply compressive strain ductility μ_ε = 3.5. The above-mentioned ultimate strain value is suitable for design purposes, while larger values can be considered in the assessment of existing masonry buildings.

With reference to the *elastic limit state*, the cross-section is cracked if the axial force is applied outside the central core of inertia[28]. Denoting by *e* the axial force eccentricity with respect to the centroid of the cross-section and $\bar{e} = e/H$ its normalised value, the cross-section is cracked for:

$$\frac{1}{6} \le \bar{e} \le \frac{1}{2}$$

The cross-section attains ELS when the maximum axial strain reaches the yielding strain of masonry; this condition corresponds to a normalised axial force falling in the interval [0,0.5]. The equation of translational equilibrium can be written as:

$$\bar{N} = \frac{\bar{h}}{2} \tag{7.68}$$

while the equation of rotational equilibrium specialises to:

$$\frac{\bar{M}_e}{H} = \frac{\bar{h}}{4} - \frac{\bar{h}^2}{6} \tag{7.69}$$

Consequently, for a normalised axial force falling in the interval [0,0.5], the limit line of the interaction domain can be described through the following equation:

$$\frac{\bar{M}_e}{H} = \frac{\bar{N}}{2} - \frac{2}{3}\bar{N}^2 \tag{7.70}$$

On the other hand, the cross-section reaches ELS in uncracked conditions for:

$$0 \le \bar{e} \le \frac{1}{6}$$

namely, if the normalised axial force falls within the interval [0.5,1]. For a balanced cross-section, the given axial force is related to the neutral axis depth as follows:

$$\bar{N} = 1 - \frac{1}{2\bar{h}} \tag{7.71}$$

while rotational equilibrium requires that it is:

$$\frac{\bar{M}_e}{H} = \frac{1}{12\bar{h}} \tag{7.72}$$

As a result, for a normalised axial force falling in the interval [0.5,1], the limit line of

[28] The centre of pressure must fall within the cross-section in order to ensure equilibrium.

the interaction domain can be described through the following equation:

$$\frac{\bar{M}_e}{H} = \frac{1}{6}\left(1-\bar{N}\right) \tag{7.73}$$

With reference to the *ultimate limit state*, for a pre-defined linear diagram of axial strains with a given neutral axis depth, the equation of translational equilibrium can be written as:

$$\bar{N} = \bar{h}\left(1-\frac{1}{2\mu_\varepsilon}\right) \tag{7.74}$$

according to Brencich and De Francesco (2004). Such an equation allows to assess the neutral axis depth under a given axial force, once a supply strain ductility has been assigned to masonry in compression. The rotational equilibrium of the cross-section is governed by the following equation:

$$\frac{\bar{M}_u}{H} = \frac{\bar{h}}{2}\left(1-\frac{1}{2\mu_\varepsilon}\right)-\bar{h}^2\frac{\left(1-3\mu_\varepsilon+3\mu_\varepsilon^2\right)}{6\mu_\varepsilon^2} \tag{7.75}$$

so the limit line of the strength domain can be described as follows:

$$\frac{\bar{M}_u}{H} = \frac{\bar{N}}{2}-\frac{2\left(1-3\mu_\varepsilon+3\mu_\varepsilon^2\right)}{3\left(2\mu_\varepsilon-1\right)^2}\bar{N}^2 \tag{7.76}$$

The crossing condition from cracked to uncracked cross-section is associated with a neutral axis depth equal to the gross height of the cross-section. Assuming μ_ε = 3.5, Eq. (7.74) gives 0.86 so Eq. (7.76) can be applied for a normalised axial force falling in the interval [0,0.86].

Conversely, if N/N_m falls within the interval [0.86,1], the cross-section reaches ULS without cracking and its translational equilibrium is governed by the following equation:

$$\bar{N} = \mu_\varepsilon-\frac{\mu_\varepsilon}{2\bar{h}}-\frac{\bar{h}\left(\mu_\varepsilon-1\right)^2}{2\mu_\varepsilon} \tag{7.77}$$

In such conditions, the equation of rotational equilibrium turns out to be:

$$\frac{\bar{M}_u}{H} = \frac{\bar{h}^2}{6\mu_\varepsilon^2}\left(\mu_\varepsilon-1\right)^3-\frac{\bar{h}}{4\mu_\varepsilon}\left(\mu_\varepsilon-1\right)^2+\frac{\mu_\varepsilon}{12\bar{h}} \tag{7.78}$$

Figure 7.16 shows the strength domains at ELS and ULS in which the parts of limit line corresponding to cracked cross-sections (solid lines) are distinguished from those corresponding to uncracked cross-sections (dashed lines).

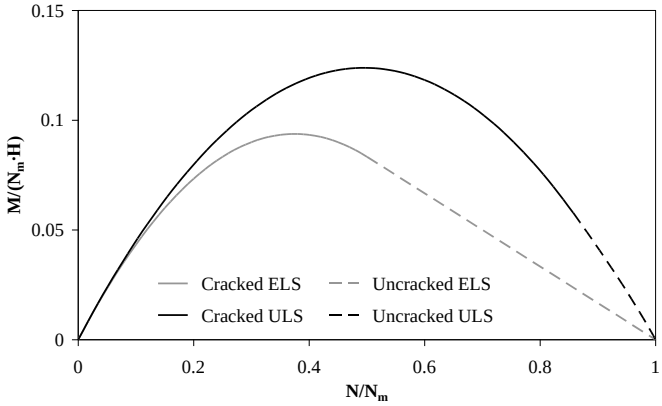

Figure 7.16 Strength domains at ELS and ULS for EPP constitutive law

- **Strength domains for Turnšek-Čačovič constitutive model**

The stress-strain relationship proposed by Turnšek and Čačovič (1971) includes more real characteristics of mechanical behaviour of masonry under uniaxial compression, namely strength degradation due to strain softening. Yielding and ultimate strains of masonry were assumed to be ε_k = 0.002 and ε_u = 0.0035, resulting in a supply strain ductility equal to 1.75 (that is, one-half of that considered for EPP constitutive model).
With reference to the *elastic limit state*, the behaviour of the cracked cross-section is governed by the following equations of translational and rotational equilibrium, respectively:

$$\bar{N} = 0.71\bar{h} \tag{7.79}$$

$$\frac{\bar{M}_e}{H} = 0.36\bar{h} - 0.28\bar{h}^2 \tag{7.80}$$

For a normalised axial force falling in the interval [0,0.71], the limit line of the interaction domain at ELS can be described as follows:

$$\frac{\bar{M}_e}{H} = \frac{\bar{N}}{2} - 0.56\bar{N}^2 \tag{7.81}$$

For a normalised axial force falling in the interval [0.71,1], the cross-section reaches ELS in uncracked conditions and the equations of translational and rotational equilibrium can be respectively written as:

$$\bar{N} = 6.4 - \frac{3.2}{\bar{h}} - 2.49\bar{h}\left(1 - \xi^{2.17}\right) \tag{7.82}$$

$$\frac{\bar{M}_e}{H} = 1.7\xi^{1.17} + \frac{0.53}{\bar{h}} + \bar{h}\left(-1.24 - 3.41\xi^{1.17} + 1.24\xi^{2.17}\right) + \bar{h}^2\left(0.78 + 1.7\xi^{1.17} - 2.49\xi^{2.17}\right) \tag{7.83}$$

being:

$$\xi = \mu_\varepsilon \left(1 - \frac{1}{\bar{h}}\right) \tag{7.84}$$

a current strain-dependent parameter. At ELS, the strain ductility demand is equal to unity, so the latter parameter can be expressed as:

$$\xi_e = 1 - \frac{1}{\bar{h}} \tag{7.85}$$

Eq. (7.83) is not invertible so a direct relationship between the yielding bending moment and the applied axial force cannot be defined.

With reference to the *ultimate limit state*, the equilibrium equations of a cracked cross-section against translation and rotation can be respectively written as follows:

$$\bar{N} = \bar{h}\left(3.2\mu_\varepsilon - 2.49\mu_\varepsilon^{1.17}\right) \tag{7.86}$$

$$\frac{\bar{M}_u}{H} = \bar{h}\left(1.6\mu_\varepsilon - 1.24\mu_\varepsilon^{1.17}\right) + \bar{h}^2\left(-1.07\mu_\varepsilon + 0.78\mu_\varepsilon^{1.17}\right) \tag{7.87}$$

so the limit line of the strength domain can be described through the following equation:

$$\frac{\bar{M}_u}{H} = \frac{\bar{N}}{2} - \frac{0.17\mu_\varepsilon - 0.13\mu_\varepsilon^{1.17}}{\left(\mu_\varepsilon^{1.17} - 1.29\mu_\varepsilon\right)^2}\bar{N}^2 \tag{7.88}$$

which allows to related the ultimate moment to the applied axial force. The latter equation can be applied for a normalised axial force falling in the interval [0,0.81]. Otherwise, the cross-section reaches ULS without cracking, but strength degradation due to strain softening induces an ultimate axial force lower than the maximum axial force. As a consequence, the upper limit of the axial force interval corresponding to an uncracked cross-section at ULS is to be defined.

For a normalised axial force $N/N_m > 0.81$, the equations of translational and rotational equilibrium specialise respectively to:

$$\bar{N} = 6.4\mu_\varepsilon - \frac{3.2\mu_\varepsilon}{\bar{h}} - 2.49\bar{h}\left(\mu_\varepsilon^{1.17} - \frac{\xi^{2.17}}{\mu_\varepsilon}\right) \tag{7.89}$$

$$\begin{aligned}\frac{\bar{M}_u}{H} = {} & \frac{0.53\mu_\varepsilon}{\bar{h}} + 1.7\xi^{1.17} + \bar{h}^2\left(0.78\mu_\varepsilon^{1.17} + 1.7\xi^{1.17} - \frac{2.49\xi^{2.17}}{\mu_\varepsilon}\right) + \\ & + \bar{h}\left(-1.24\mu_\varepsilon^{1.17} - 3.41\xi^{1.17} + \frac{1.24\xi^{2.17}}{\mu_\varepsilon}\right)\end{aligned} \tag{7.90}$$

and the limit line of the interaction domain can be defined just numerically.

Strength domains corresponding to ELS and ULS are reported in Figure 7.17, where the parts of limit line corresponding to cracked cross-sections (solid lines) are distinguished from those corresponding to uncracked cross-sections (dashed lines).

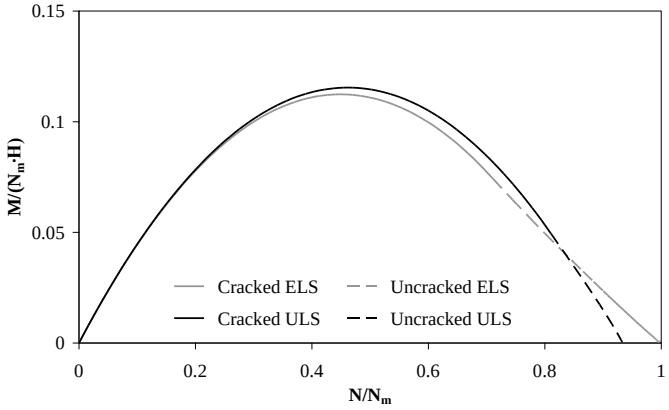

Figure 7.17 Strength domains at ELS and ULS for Turnšek-Čačovič law

- **Strength domains for EC6 constitutive model**

Also in this case, yielding and ultimate strains of masonry were assumed to be $\varepsilon_k = 0.002$ and $\varepsilon_u = 0.0035$, resulting a supply strain ductility $\mu_\varepsilon = 1.75$.

With reference to the *elastic limit state*, if the normalised axial force falls within the interval [0,0.67], the cross-section is cracked and the equations of translational and rotational equilibrium can be respectively written as follows:

$$\bar{N} = \frac{2}{3}\bar{h} \tag{7.91}$$

$$\frac{\bar{M}_e}{H} = \frac{\bar{h}}{3} - \frac{\bar{h}^2}{4} \tag{7.92}$$

so the yielding moment can be predicted as:

$$\frac{\bar{M}_e}{H} = \frac{\bar{N}}{2} - \frac{9}{8}\bar{N}^2 \tag{7.93}$$

If the normalised axial force falls within the interval [0.67,1], the cross-section is fully resistant and its equilibrium against translation and rotation is governed by the following equations:

$$\bar{N} = 1 - \frac{1}{3\bar{h}^2} \tag{7.94}$$

$$\frac{\bar{M}_e}{H} = \frac{1}{12\bar{h}^2} \tag{7.95}$$

so one can get:

$$\frac{\bar{M}_e}{H} = \frac{1}{4}\left(1 - \bar{N}\right) \tag{7.96}$$

With reference to the *ultimate limit state*, the equilibrium equations of a cracked cross-

section against translation and rotation can be respectively written as follows:

$$\bar{N} = \bar{h}\left(1 - \frac{1}{3\mu_\varepsilon}\right) \tag{7.97}$$

$$\frac{\bar{M}_u}{H} = \frac{\bar{h}}{2}\left(1 - \frac{1}{3\mu_\varepsilon}\right) - \frac{\bar{h}^2\left(1 - 4\mu_\varepsilon + 6\mu_\varepsilon^2\right)}{12\mu_\varepsilon^2} \tag{7.98}$$

so the limit line of the strength domain can be described through the following equation:

$$\frac{\bar{M}_u}{H} = \frac{\bar{N}}{2} - \frac{3\left(1 - 4\mu_\varepsilon + 6\mu_\varepsilon^2\right)}{4\left(3\mu_\varepsilon - 1\right)^2}\bar{N}^2 \tag{7.99}$$

Such an equation can be applied if the normalised axial force falls in the interval [0,0.81]. Otherwise, if N/N_m falls in the interval [0.81,1], the cross-section reaches ULS without cracking. Under a given axial force, the neutral axis depth can be evaluated by solving numerically the following equation:

$$\bar{N} = 2\mu_\varepsilon - \mu_\varepsilon^2 + \frac{\mu_\varepsilon^2 - \mu_\varepsilon}{\bar{h}} - \frac{\mu_\varepsilon^2}{3\bar{h}^2} + \frac{\bar{h}\left(\mu_\varepsilon - 1\right)^3}{3\mu_\varepsilon} \tag{7.100}$$

while the equation of rotational equilibrium can be written as:

$$\frac{\bar{M}_u}{H} = -\frac{\bar{h}^2}{12\mu_\varepsilon^2}\left(\mu_\varepsilon - 1\right)^4 + \frac{\bar{h}}{6\mu_\varepsilon}\left(\mu_\varepsilon - 1\right)^3 - \frac{\mu_\varepsilon\left(\mu_\varepsilon - 1\right)}{6\bar{h}} + \frac{\mu_\varepsilon^2}{12\bar{h}^2} \tag{7.101}$$

allowing to predict the ultimate moment.

Strength domains corresponding to ELS and ULS are reported in Figure 7.18, where the parts of limit line corresponding to cracked cross-sections (solid lines) are distinguished from those corresponding to uncracked cross-sections (dashed lines).

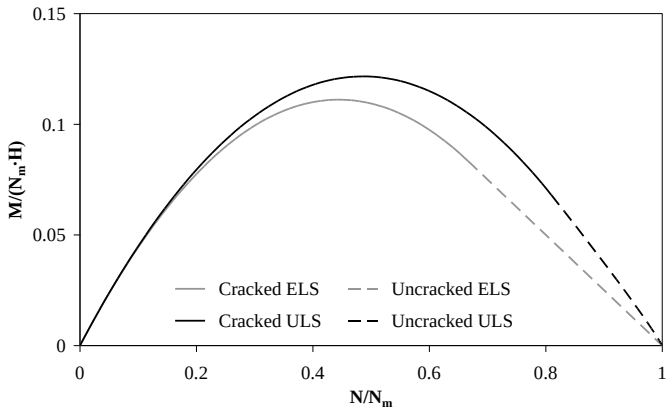

Figure 7.18 Strength domains at ELS and ULS for EC6 constitutive law

- **Strength domains for Augenti-Parisi constitutive model related to compression parallel to mortar bed joints**

The flexural strength domains presented below were derived through the implementation of the empirical stress-strain relationship developed for masonry under uniaxial compression parallel to mortar bed joints (Augenti and Parisi, 2010a). Such a constitutive model is defined by the following equations:

$$\bar{f}(\varepsilon)=\frac{\sigma}{\sigma_k}= -0.3593\left(\frac{\varepsilon}{\varepsilon_k}\right)^3-0.2814\left(\frac{\varepsilon}{\varepsilon_k}\right)^2+1.6407\left(\frac{\varepsilon}{\varepsilon_k}\right) \qquad \text{for } 0\le\frac{\varepsilon}{\varepsilon_k}\le 1$$

$$\bar{f}(\varepsilon)=\frac{\sigma}{\sigma_k}= 0.0008\left(\frac{\varepsilon}{\varepsilon_k}\right)^5-0.0168\left(\frac{\varepsilon}{\varepsilon_k}\right)^4+0.1351\left(\frac{\varepsilon}{\varepsilon_k}\right)^3+ \qquad (7.102)$$

$$-0.4970\left(\frac{\varepsilon}{\varepsilon_k}\right)^2+0.6739\left(\frac{\varepsilon}{\varepsilon_k}\right)+0.702 \qquad \text{for } 1\le\frac{\varepsilon}{\varepsilon_k}\le 6$$

Yielding strain of masonry can be assumed as $\varepsilon_k = 0.002$, while supply strain ductility was set to $\mu_\varepsilon = 6$.

With reference to the *elastic limit state*, if the normalised axial force falls in the interval [0,0.64], the cross-section is cracked and its equilibrium against translation and rotation can be described through the following equations:

$$\bar{N}=0.64\bar{h} \qquad (7.103)$$

$$\frac{\bar{M}_e}{H}= 0.32\bar{h}-0.23\bar{h}^2 \qquad (7.104)$$

In such conditions, the interaction between yielding moment and applied axial force can be expressed as follows:

$$\frac{\bar{M}_e}{H}=\frac{\bar{N}}{2}-0.57\bar{N}^2 \qquad (7.105)$$

Conversely, if the normalised axial force falls in the interval [0.64,1], the cross-section reaches ELS without cracking and its equilibrium against translation and rotation can be described via the following equations:

$$\bar{N}=1-\frac{0.45}{\bar{h}^2}+\frac{0.09}{\bar{h}^3} \qquad (7.106)$$

$$\frac{\bar{M}_e}{H}=\frac{0.11}{\bar{h}^2}-\frac{0.03}{\bar{h}^3} \qquad (7.107)$$

Regarding the *ultimate limit state*, the equations of translational and rotational equilibrium in the case of cracked cross-section can be respectively written as:

$$\bar{N}= \bar{h}\left(0.7-\frac{0.27}{\mu_\varepsilon}+0.34\mu_\varepsilon-0.17\mu_\varepsilon^2+0.03\mu_\varepsilon^3-0.003\mu_\varepsilon^4+0.0001\mu_\varepsilon^5\right) \qquad (7.108)$$

$$\frac{\bar{M}_u}{H}=\bar{h}^2\left(-0.35-\frac{0.07}{\mu_\varepsilon^2}+\frac{0.27}{\mu_\varepsilon}-0.11\mu_\varepsilon+0.04\mu_\varepsilon^2-0.007\mu_\varepsilon^3+0.001\mu_\varepsilon^4\right)+$$
$$+\bar{h}\left(0.35-\frac{0.13}{\mu_\varepsilon}+0.17\mu_\varepsilon-0.08\mu_\varepsilon^2+0.02\mu_\varepsilon^3-0.002\mu_\varepsilon^4\right) \tag{7.109}$$

so the limit line of the strength domain at ELS can be described through the equation:

$$\frac{\bar{M}_u}{H}=\frac{\bar{N}}{2}-\frac{p_1(\mu_\varepsilon)}{p_2(\mu_\varepsilon)}\bar{N}^2 \tag{7.110}$$

where:

$$p_1(\mu_\varepsilon)=0.13-0.35\mu_\varepsilon-0.17\mu_\varepsilon^2+0.08\mu_\varepsilon^3-0.017\mu_\varepsilon^4+0.002\mu_\varepsilon^5$$
$$p_2(\mu_\varepsilon)=0.27-0.7\mu_\varepsilon-0.34\mu_\varepsilon^2+0.17\mu_\varepsilon^3-0.034\mu_\varepsilon^4+0.003\mu_\varepsilon^5-0.001\mu_\varepsilon^6 \tag{7.111}$$

Assuming a supply strain ductility $\mu_\varepsilon = 6$, one can get that Eq. (7.110) can be applied for a normalised axial force falling in the interval [0,0.69]. It follows that the cross-section reaches ULS without cracking if the normalised axial force is $N/N_m > 0.69$. The equations of translational and rotational equilibrium can be respectively expressed as follows:

$$\bar{N}=1.64\mu_\varepsilon-0.28\mu_\varepsilon^2-0.36\mu_\varepsilon^3-\frac{0.82\mu_\varepsilon-0.28\mu_\varepsilon^2-0.54\mu_\varepsilon^3}{\bar{h}}-\frac{0.09\mu_\varepsilon^2+0.36\mu_\varepsilon^3}{\bar{h}^2}+\frac{0.09\mu_\varepsilon^3}{\bar{h}^3}+$$
$$+\bar{h}\left(0.7-\frac{0.27}{\mu_\varepsilon}-0.48\mu_\varepsilon-0.07\mu_\varepsilon^2+0.12\mu_\varepsilon^3-0.003\mu_\varepsilon^4+0.0001\mu_\varepsilon^5\right) \tag{7.112}$$

$$\frac{\bar{M}_u}{H}=\frac{0.14\mu_\varepsilon-0.05\mu_\varepsilon^2-0.09\mu_\varepsilon^3}{\bar{h}}+\frac{0.02\mu_\varepsilon^2+0.09\mu_\varepsilon^3}{\bar{h}^2}-\frac{0.03\mu_\varepsilon^3}{\bar{h}^3}+$$
$$+\bar{h}\left(0.35-\frac{0.13}{\mu_\varepsilon}-0.24\mu_\varepsilon-0.04\mu_\varepsilon^2+0.06\mu_\varepsilon^3-0.002\mu_\varepsilon^4\right)+ \tag{7.113}$$
$$+\bar{h}^2\left(-0.35-\frac{0.07}{\mu_\varepsilon^2}+\frac{0.17}{\mu_\varepsilon}+0.16\mu_\varepsilon+0.02\mu_\varepsilon^2-0.02\mu_\varepsilon^3+0.001\mu_\varepsilon^4\right)$$

Flexural strength domains corresponding to ELS and ULS are illustrated in Figure 7.19, where the parts of limit line corresponding to cracked cross-sections (solid lines) are distinguished from those corresponding to uncracked cross-sections (dashed lines).

It is underlined that the cross-section cannot reach ULS in uncracked conditions at higher levels of strain ductility, namely masonry cracking cannot be avoided. Therefore, the ultimate strength domain shown in Figure 7.19 does not include a dashed line corresponding to the uncracked cross-section.

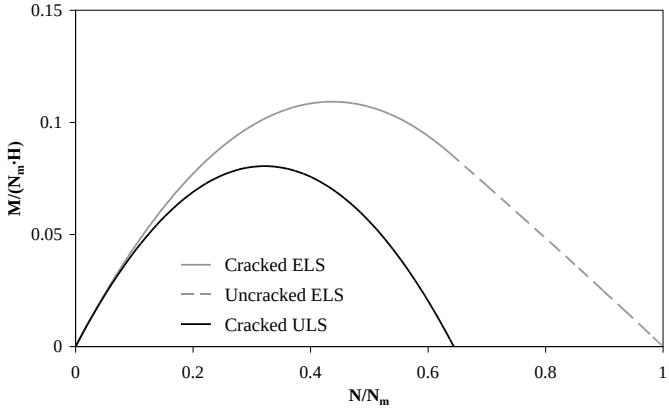

Figure 7.19 Strength domains at ELS and ULS for Augenti-Parisi constitutive law (paral. dir.)

- **Comparisons between strength domains**

Deformation-based sectional analysis have allowed to define flexural strength domains which depend on strain ductility of masonry. The equations presented above could be applied not only in the assessment of existing masonry buildings, but also in deformation-based design methods. When dealing with seismic assessment, flexural strength domains can be considered to change with strain ductility demand. Conversely, in seismic design of masonry buildings, flexural strength can be defined at different limit states, once supply strain ductility has been assigned to masonry. It is underlined that the concept of *evolutionary strength domain* has a meaning only when a strength degrading constitutive model (e.g., the stress-strain relationship proposed by Turnšek and Čačovič, 1971) is assumed for masonry. Figure 7.20 shows a comparison between yielding strength domains related to constitutive laws considered in previous sections. Except for EPP model, yielding moment predictions are about the same.

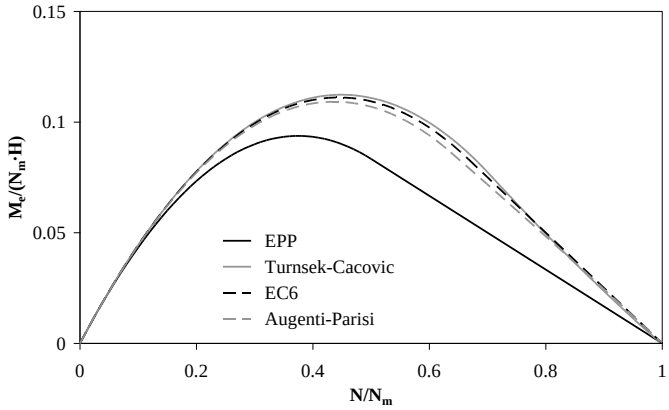

Figure 7.20 Comparison between strength domains at ELS

Figure 7.21 shows the comparison between ultimate strength domains corresponding to the strain ductilities assumed in previous sections. Different ultimate moment predictions are obtained for a normalised axial force falling in the interval [0.3,1], depending on the presence or absence of strength degradation within the constitutive law. Whilst EPP and EC6 models lead to rather equal values of ultimate moment, those proposed by Turnšek and Čačovič (1971) and Augenti and Parisi (2010a) provide significantly different predictions. Low ultimate moments corresponding to Augenti-Parisi constitutive law are clearly due to the high strength degradation of masonry, given that supply strain ductility was supposed to be $\mu_\varepsilon = 6$. Therefore, ultimate strength domains are also compared for $\mu_\varepsilon = 1.75$, including also the domain corresponding to the equation provided by IBC (2008). The latter is plotted for a 15%-reduced compressive strength of masonry.

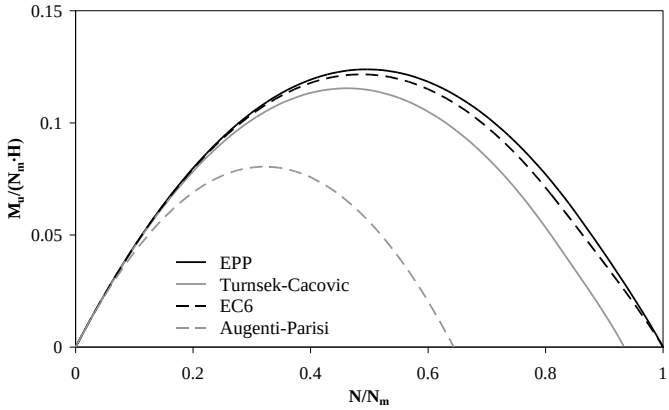

Figure 7.21 Comparison between strength domains at ULS

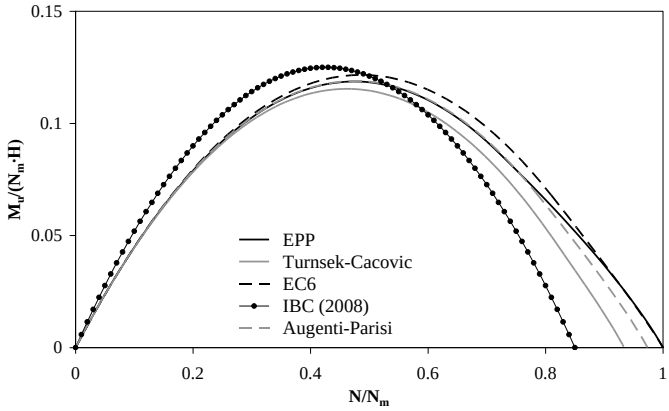

Figure 7.22 Comparison between strength domains at ULS for strain ductility $\mu_\varepsilon = 1.75$

The strain softening effect reduces significantly, so the ultimate strength domain corresponding to Augenti-Parisi constitutive model is much closer to the others. Indeed, the strength domain contraction from that associated with ELS is much smaller. It is also underlined that the interaction formula provided by IBC leads to less conservative predictions of ultimate bending moment for normalised axial forces falling in the interval [0,0.5]. The opposite occurs for higher axial forces.
The implementation of the EC6 constitutive model leads to ultimate moments higher than those corresponding to other models, even though negligible differences are detected for a normalised axial force falling in the interval [0,0.4].
Finally, the influence of simplified constitutive models on ultimate moment was investigated by Brencich et al. (2008), which outlined that: (1) the ultimate strength domain corresponding to elastic-brittle law provides the lower bound of ultimate bending moment; and (2) the assumption of EPP model with limited strain ductility leads to the upper bound of ultimate bending moment. If strain ductility of masonry is limited to $\mu_\varepsilon = 1.75$ in the EPP model, the resulting strength domain is almost entirely superimposed to that corresponding to Augenti-Parisi model.

- **Evolution in ultimate bending moment**

Ultimate bending moment predictions are significantly affected by the value assumed for strain ductility and by the presence or absence of strain softening in the constitutive model. Indeed, the latter can be characterised by a post-peak falling branch which induces a dramatic reduction in the bending moment allowed by the cross-section. On the contrary, if the rising branch of the constitutive law is followed by a plastic plateau, the ultimate bending moment increases. Figure 7.23 shows the evolution in the flexural strength domain corresponding to the *Turnšek-Čačovič constitutive law*, as strain ductility changes from $\mu_\varepsilon = 1$ (ELS) to $\mu_\varepsilon = 1.75$ (ULS).

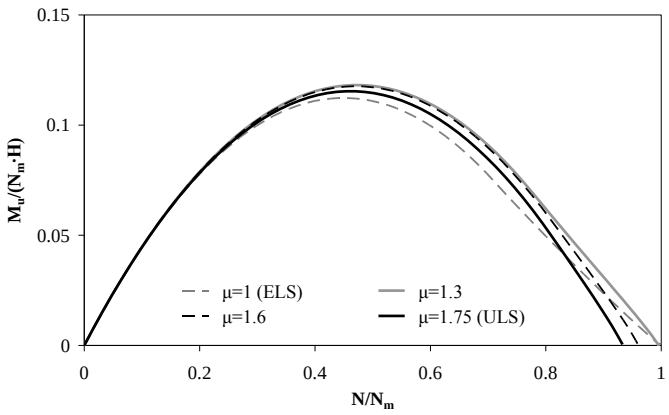

Figure 7.23 Strength domain evolution under increasing strain ductility (Turnšek-Čačovič law)

Whilst a strength domain growth is detected under strain ductility increasing from $\mu_\varepsilon = 1$ (ELS) to $\mu_\varepsilon = 1.3$, a strength domain contraction occurs as yielding develops throughout the cross-section. As a result, the yielding strength domain is intersected by inelastic strength domains corresponding to larger strain ductility values.

For a given axial force, as strain ductility increases in the interval [1,1.75], ultimate moment follows a parabolic law of variation, reaching the maximum value at a strain ductility between 1.4 and 1.45 (Fig. 7.24).

The curvature of the parabola reduces with the normalised axial force and vanishes for normalised axial forces lower than 0.25. Therefore, the variation in ultimate moment with strain ductility demand is more significant under higher values of applied axial force, as shown in Figure 7.23.

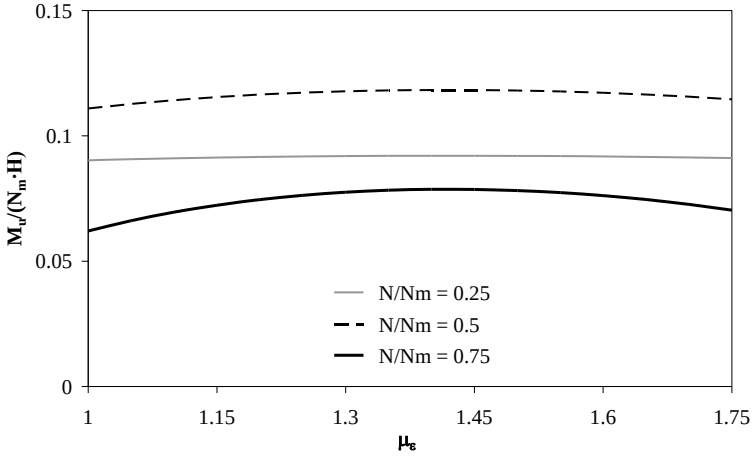

Figure 7.24 Ultimate bending moment versus strain ductility (Turnšek-Čačovič model)

Such an otucome depends on the combination of two opposing effects. In fact, when the cross-section yields, it suffers increasing axial strains resulting in an ultimate moment increase. On the contrary, strength degradation induces a gradual reduction in the ultimate moment. The first effect, which is related to spreading of yielding over the cross-section, prevails on the second effect at small ductility levels, so the flexural strength increases for a strain ductility falling in the interval [1,1.45] in the case of Turnšek-Čačovič constitutive law.

At larger ductility levels the strain softening effect becomes more important, inducing an ultimate moment reduction. The evolution in the flexural strength with strain ductility is clearly evidenced in Figure 7.25, which contains a three-dimensional view of the ductility-dependent interaction domain defined in the space N/N_m–$M/(N_m \cdot H)$–μ_ε.

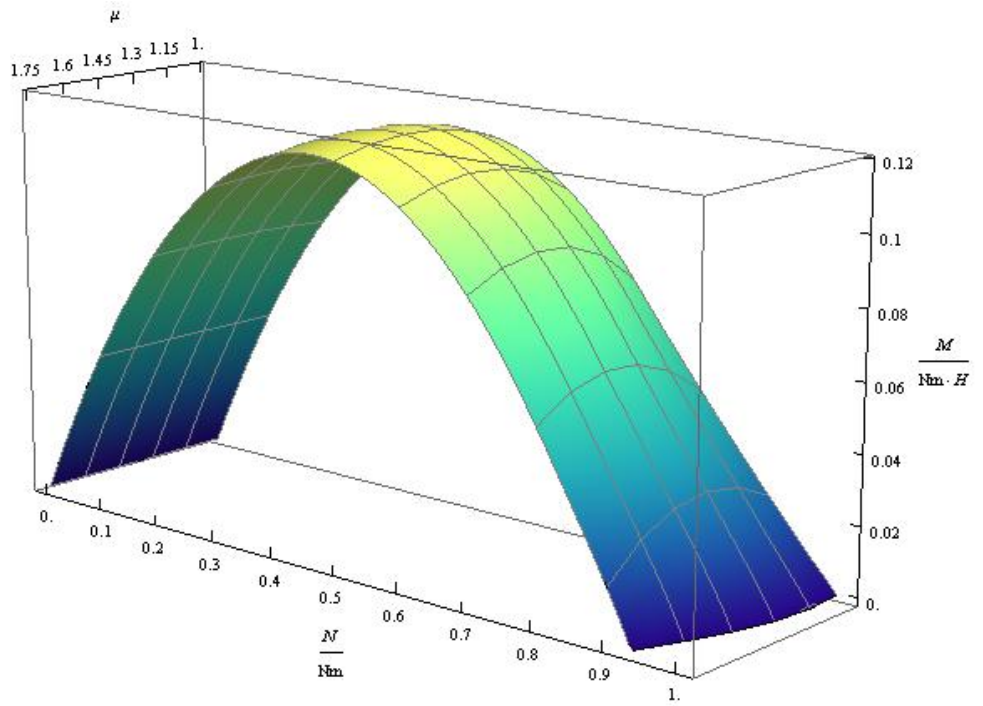

Figure 7.25 N/N_m–$M/(N_m \cdot H)$–μ_ε strength domain for Turnšek-Čačovič model

The intersections between the three-dimensional interaction domain and the planes corresponding to different strain ductility values allow to identify two-dimensional strength domains N/N_m–$M/(N_m \cdot H)$.

Figures 7.26 and 7.27 show some views of the surfaces N/N_m–μ_ε and $M/(N_m \cdot H)$–μ_ε, respectively.

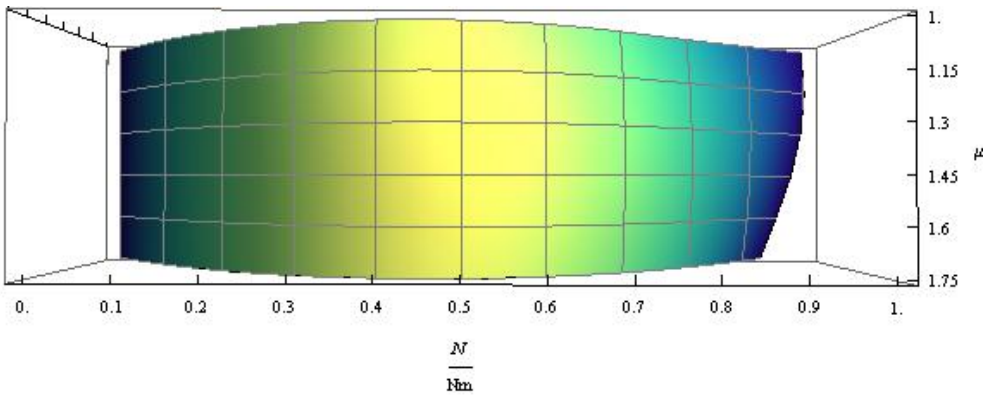

Figure 7.26 N/N_m–μ_ε surface for Turnšek-Čačovič model

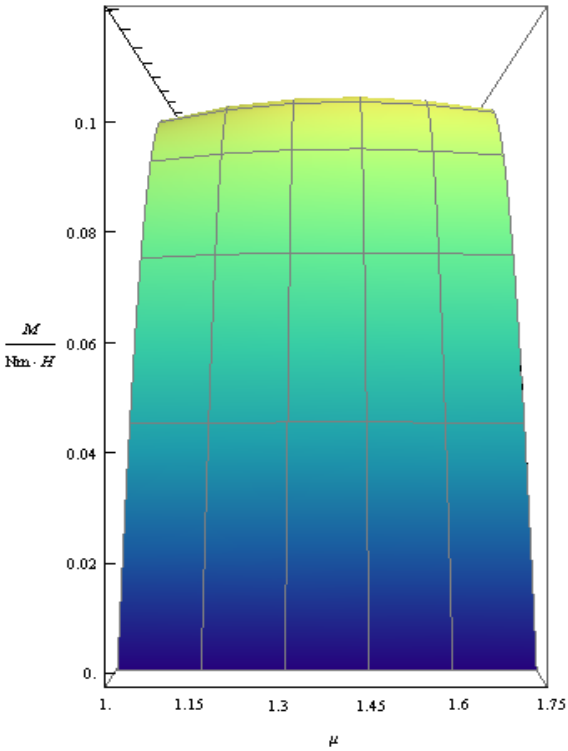

Figure 7.27 $M/(N_m \cdot H)$–μ_ε surface for Turnšek-Čačovič model

Figure 7.28 illustrates the strength domain evolution corresponding to Augenti-Parisi constitutive model, under varying strain ductility. Figure 7.29 shows the ultimate bending moment of the cross-section versus strain ductility, at pre-defined normalised axia forces. The law of variation is not parabolic, but almost consta at a normalised axial force equal to 0.25 (as in the case of Turnšek- Čačovič constitutive model).

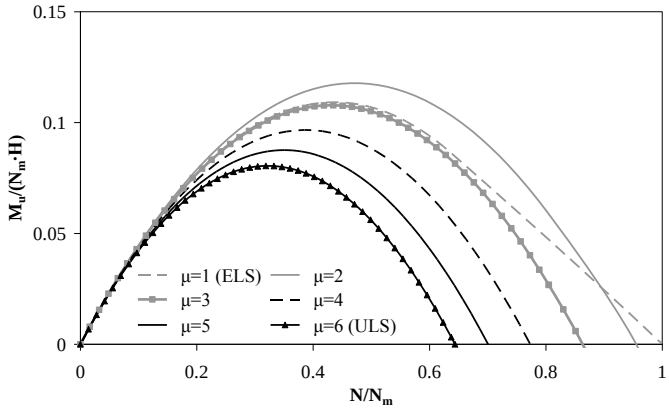

Figure 7.28 Strength domain evolution under varying strain ductility (Augenti-Parisi model)

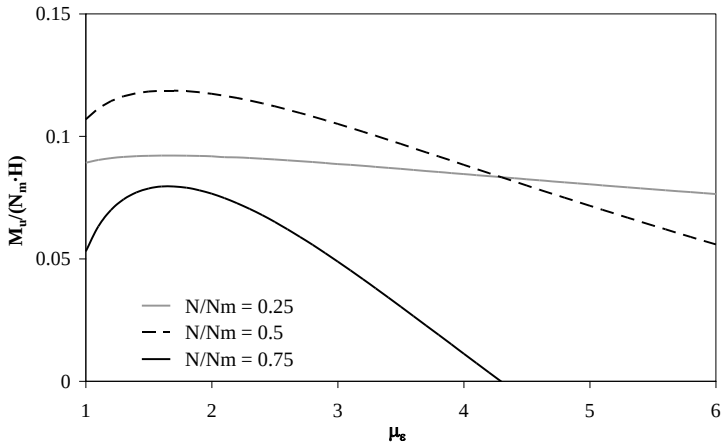

Figure 7.29 Ultimate bending moment versus strain ductility (Augenti-Parisi model)

This indicates that the ultimate moment is most affected by strength degradation of masonry. It is also emphasised that the ultimate moment vanishes at progressively lower values of strain ductility for normalised axial forces greater than 0.5. For N/N_m = 0.75, the ultimate moment vanishes at μ_ε = 4.3 (Fig. 7.29) and the inelastic capacity of masonry can be exploited up to a maximum axial strain ε_i = 0.86%. Also in this case, Figure 7.30 shows a three-dimensional domain in the Cartesian space N/N_m–$M/(N_m \cdot H)$–μ_ε.

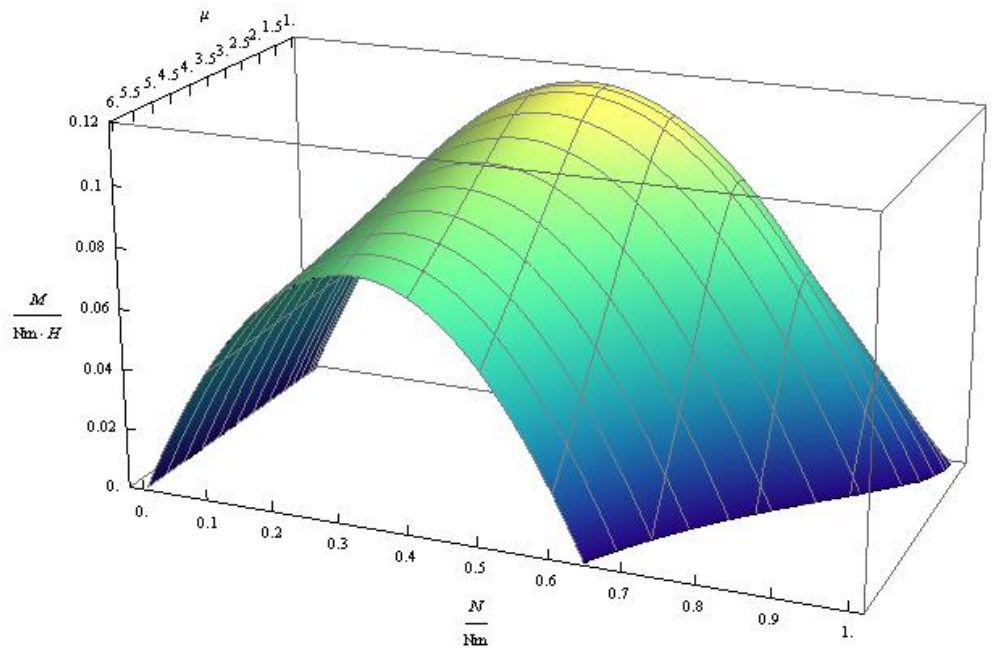

Figure 7.30 N/N_m–$M/(N_m \cdot H)$–μ_ε strength domain for Augenti-Parisi model

This graphic representation confirms the high influence of strain ductility and strength degradation in the Augenti-Parisi constitutive model. Figures 7.31 and 7.32 show some views of the surfaces N/N_m–μ_ε and $M/(N_m \cdot H)$–μ_ε, respectively. The latter is a continuum representation of the ultimate moment's law of variation in Figure 7.29.

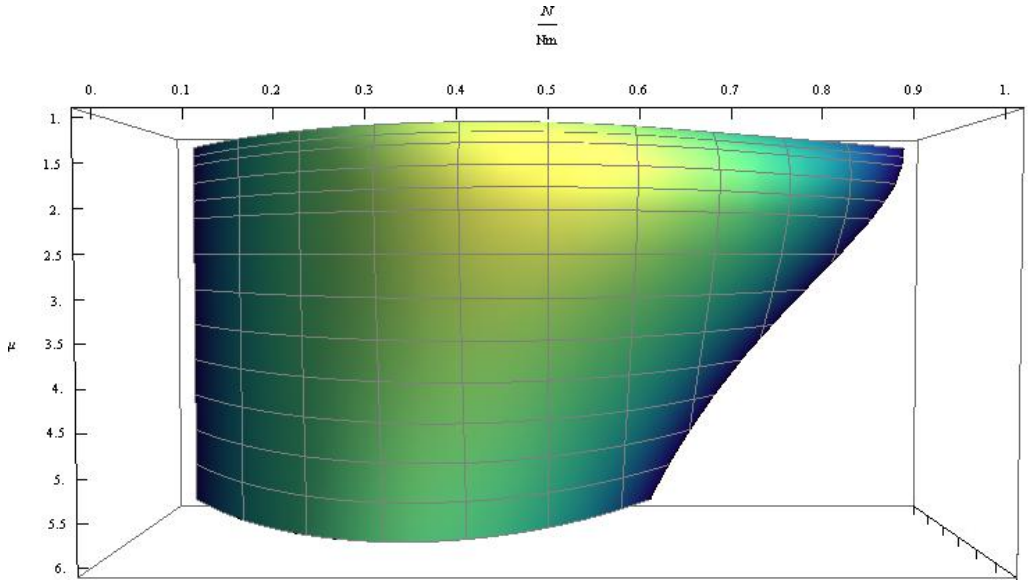

Figure 7.31 N/N_m–μ_ε surface for Augenti-Parisi model

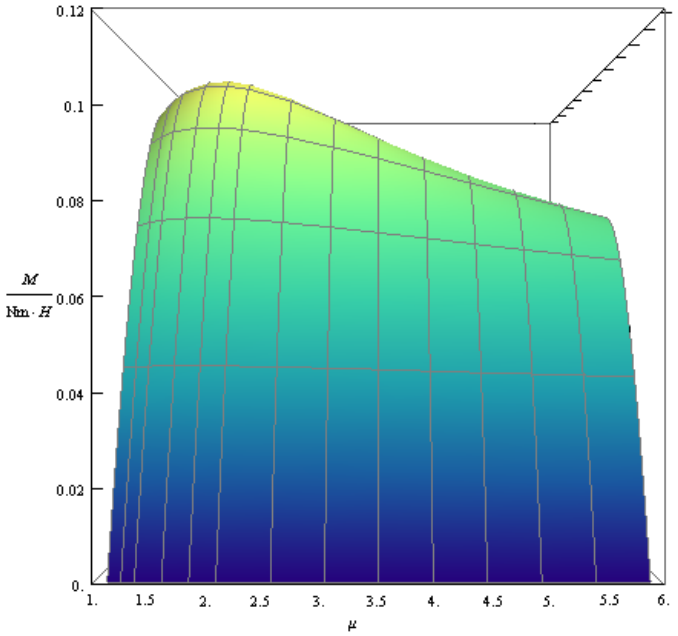

Figure 7.32 $M/(N_m \cdot H)$–μ_ε surface for Augenti-Parisi model

7.3. Three-Dimensional Strength Domains

Three-dimensional strength domains $V/N_m–N/N_m–e/H$ including all actions applied to the panel can be used, as alternative to two-dimensional strength domains $M/(N_m \cdot H)–N/N_m$ presented in previous section. The bending moment is taken into account by means of the axial force eccentricity. This representation was first proposed by Augenti (2007) in order to investigate the flexural strength of spandrel panels at ELS by using an EPP constitutive model for masonry.

In this section, a number of formulations derived for constitutive laws considered in previous sections are presented and discussed with reference to both ELS and ULS. In order to get three-dimensional strength domains, equilibrium is analysed for the entire masonry macro-element, rather than a single cross-section. Therefore, the theoretical analysis was carried out with reference to the simplified scheme shown in Figure 7.33, where the spandrel panel is subjected to combined eccentric compression and shear at both extreme sections, as well as external forces *F*, *P*, and *Q*.

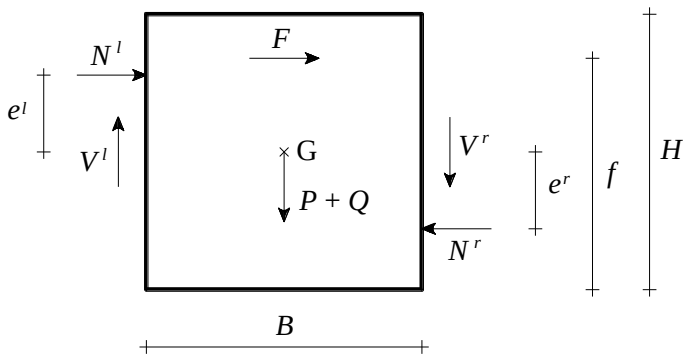

Figure 7.33 Internal and external forces acting on the masonry panel

In particular, the following symbols are used below:

- N^l and N^r, which are the axial forces over the left and right estreme sections, respectively;
- V^s and V^d, which are the shear forces the left and right estreme sections, respectively;
- e^l and e^r, which are the eccentricities of axial forces N^l and N^r, respectively, with respect to the centroid of the panel;
- *Q*, which is the self-weight of the panel;
- *P*, which is the resulting force of both dead and livel loads transmitted by the floor diaphragm to the panel;
- *F*, which is the fraction of seismic force acting on the panel; and
- *f*, which is the distance of the force line from the lower extreme of the panel.

Whilst internal forces and external actions are normalised to the maximum axial force N_m, eccentricities are normalised to the gross height H of the panel. The following sign convention was used in the theoretical analysis:

- $N > 0$ for compressive forces;
- $M > 0$ for clockwise bending moments;
- $V > 0$ for shear forces inducing clockwise bending moments around the centroid of the panel; and
- $e > 0$ for compressive forces inducing clockwise bending moments.

Opposed to two-dimensional strength domains, although dimensionless formulas were derived also for three-dimensional strength domains, the latter can be graphically represented only if the geometry of the panel is defined.

In order to allow comparisons between formulations presented herein to that proposed by Augenti (2007), the same dimensions are assumed for the masonry panel, namely 90×140×60 cm. For each limit state of interest, the peak resisting shear force can be predicted by equations which were derived by imposing rotational equilibrium of the panel with respect to the point where the axial force over the cross-section under verification is applied. The relationship between the shear force V^r over the right section, the axial force N^r and the eccentricities e^l, e^r is:

$$V^r = -\frac{1}{B}\left[N^r \left(e^l + e^r \right) + \left(P + Q \right) \frac{B}{2} + F \left(f - \frac{H}{2} - e^l \right) \right] \tag{7.114}$$

which can be divided by the maximum axial force and gross height of the section, reaching the dimensionless format:

$$\bar{V}^r = -\frac{H}{B}\left[\bar{N}^r \left(\bar{e}^l + \bar{e}^r \right) + \left(\bar{P} + \bar{Q} \right) \frac{B}{2H} + \bar{F} \left(\bar{f} - \frac{1}{2} - \bar{e}^l \right) \right] \tag{7.115}$$

Similarly, for the left section it turns out to be:

$$V^l = -\frac{1}{B}\left[N^l \left(e^l + e^r \right) - \left(P + Q \right) \frac{B}{2} + F \left(f - \frac{H}{2} + e^r \right) \right] \tag{7.116}$$

$$\bar{V}^l = -\frac{H}{B}\left[\bar{N}^l \left(\bar{e}^l + \bar{e}^r \right) - \left(\bar{P} + \bar{Q} \right) \frac{B}{2H} + \bar{F} \left(\bar{f} - \frac{1}{2} + \bar{e}^r \right) \right] \tag{7.117}$$

The implementation of these equilibrium equations of the panel in those related to a single cross-section allowed to get three-dimensional flexural strength domains $V/N_m–N/N_m–e/H$ for several stress-strain relationships of interest. Also in this case, the equations which define the limit surfaces of strength domains are different for cracked and uncracked cross-sections. Nevertheless, key differences between two- and three-dimensional domains are that the latter are not generally the same for the extreme sections of the panel and depend on the sign of the axial force eccentricity.

7.3.1. Strength Domains for EPP Constitutive Model

- **Left section at ELS in cracked conditions**

As shown in Section 7.2.2, if the normalised axial force falls within the interval [0,0.5], the cross-section is cracked at ELS. If the equation of rotational equilibrium is divided by the equation of translational equilibrium of the cross-section, then one can get a function $\bar{N} = \bar{N}(\bar{e})$. The latter can be inverted in order to define the eccentricity as a function of the axial force. Based on algebraic operations, one can define the yielding shear force over the right section (namely, V^r) which induces the attainment of ELS at the left section of the panel. In fact, for the EPP constitutive law one can get the following equations:

$$\bar{V}_e^r = -\frac{H}{B}\left[\bar{N}^r\left(\bar{e}^r + \frac{1}{2}\right) - \frac{2}{3}\left(\bar{N}^r - \bar{F}\right)^2 + \bar{F}\left(\bar{f} - 1\right) + \left(\bar{P} + \bar{Q}\right)\frac{B}{2H}\right] \qquad \text{for } \bar{e}^l > 0 \tag{7.118}$$

$$\bar{V}_e^r = -\frac{H}{B}\left[\bar{N}^r\left(\bar{e}^r - \frac{1}{2}\right) + \frac{2}{3}\left(\bar{N}^r - \bar{F}\right)^2 + \bar{F}\,\bar{f} + \left(\bar{P} + \bar{Q}\right)\frac{3B}{H}\right] \qquad \text{for } \bar{e}^l < 0 \tag{7.119}$$

which define the yielding shear force at the right cross-section as a function of the panel dimensions, the axial force over the same cross-section, and its eccentricity with respect to the centroid of the cross-section.

- **Left section at ELS in uncracked conditions**

If the normalised axial force falls in the interval [0.5,1], the cross-section is fully resistant (i.e., uncracked) at ELS. Based on operations similar to those described above in the case of cracked cross-section, one can get:

$$\bar{V}_e^r = -\frac{H}{B}\left[\frac{1}{6} + \bar{N}^r\left(\bar{e}^r - \frac{1}{6}\right) + \bar{F}\left(\bar{f} - \frac{1}{3}\right) + \left(\bar{P} + \bar{Q}\right)\frac{B}{2H}\right] \qquad \text{for } \bar{e}^l > 0 \tag{7.120}$$

$$\bar{V}_e^r = -\frac{H}{B}\left[-\frac{1}{6} + \bar{N}^r\left(\bar{e}^r + \frac{1}{6}\right) + \bar{F}\left(\bar{f} - \frac{2}{3}\right) + \left(\bar{P} + \bar{Q}\right)\frac{B}{2H}\right] \qquad \text{for } \bar{e}^l < 0 \tag{7.121}$$

The equations related to the right section of the masonry panel are presented below.

- **Right section at ELS in cracked conditions**

$$\bar{V}_e^l = -\frac{H}{B}\left[\bar{N}^l\left(\bar{e}^l + \frac{1}{2}\right) - \frac{2}{3}\left(\bar{N}^l + \bar{F}\right)^2 + \bar{F}\,\bar{f} - \left(\bar{P} + \bar{Q}\right)\frac{B}{2H}\right] \qquad \text{for } \bar{e}^r > 0 \tag{7.122}$$

$$\bar{V}_e^s = -\frac{H}{B}\left[\bar{N}^l\left(\bar{e}^l - \frac{1}{2}\right) + \frac{2}{3}\left(\bar{N}^l + \bar{F}\right)^2 + \bar{F}\left(\bar{f} - 1\right) - \left(\bar{P} + \bar{Q}\right)\frac{B}{2H}\right] \qquad \text{for } \bar{e}^r < 0 \tag{7.123}$$

- **Right section at ELS in uncracked conditions**

$$\bar{V}_e^l = -\frac{H}{B}\left[\frac{1}{6} + \bar{N}^l\left(\bar{e}^l - \frac{1}{6}\right) + \bar{F}\left(\bar{f} - \frac{2}{3}\right) - \left(\bar{P} + \bar{Q}\right)\frac{B}{2H}\right] \qquad \text{for } \bar{e}^r > 0 \tag{7.124}$$

$$\bar{V}_e^l = -\frac{H}{B}\left[-\frac{1}{6} + \bar{N}^l\left(\bar{e}^l + \frac{1}{6}\right) + \bar{F}\left(\bar{f} - \frac{1}{3}\right) - \left(\bar{P} + \bar{Q}\right)\frac{B}{2H}\right] \qquad \text{for } \bar{e}^r < 0 \tag{7.125}$$

- **Left section at ULS in cracked conditions**

If the normalised axial force falls in the interval [0,0.86], the cross-section is cracked at ULS and the limit surface of the flexural strength domain is defined as follows:

$$\bar{V}_u^r = -\frac{H}{B}\left[\bar{N}^r\left(\bar{e}^r + \frac{1}{2}\right) - \frac{2\kappa_\mu}{3}\left(\bar{N}^r - \bar{F}\right)^2 + \bar{F}\left(\bar{f} - 1\right) + \left(\bar{P} + \bar{Q}\right)\frac{3B}{H}\right] \qquad \text{for } \bar{e}^l > 0 \tag{7.126}$$

$$\bar{V}_u^r = -\frac{H}{B}\left[\bar{N}^r\left(\bar{e}^r - \frac{1}{2}\right) + \frac{2\kappa_\mu}{3}\left(\bar{N}^r - \bar{F}\right)^2 + \bar{F}\,\bar{f} + \left(\bar{P} + \bar{Q}\right)\frac{3B}{H}\right] \qquad \text{for } \bar{e}^l < 0 \tag{7.127}$$

where the following strain ductility-dependent parameter is defined as:

$$\kappa_\mu = \frac{1 - 3\mu_\varepsilon + 3\mu_\varepsilon^2}{\left(2\mu_\varepsilon - 1\right)^2}$$

- **Left section at ULS in uncracked conditions**

If the normalised axial force falls in the interval [0.86,1], the cross-section is fully resistant at ULS and the limit surface of the flexural strength domain is defined by the following equations:

$$\bar{V}_u^r = -\frac{H}{B}\left[\bar{N}^r\,\bar{e}^r + \frac{\bar{M}^l}{H}\left(\bar{h}^l\right) + \bar{F}\left(\bar{f} - \frac{1}{2}\right) + \left(\bar{P} + \bar{Q}\right)\frac{B}{2H}\right] \qquad \text{for } \bar{e}^l > 0 \tag{7.128}$$

$$\bar{V}_u^r = -\frac{H}{B}\left[\bar{N}^r\,\bar{e}^r - \frac{\bar{M}^l}{H}\left(\bar{h}^l\right) + \bar{F}\left(\bar{f} - \frac{1}{2}\right) + \left(\bar{P} + \bar{Q}\right)\frac{B}{2H}\right] \qquad \text{for } \bar{e}^l < 0 \tag{7.129}$$

being:

$$\frac{\bar{M}^l}{H}\left(\bar{h}^l\right)=\bar{N}^l\,\bar{e}^l=\frac{\bar{h}^{l2}}{6\mu_\varepsilon^2}\left(\mu_\varepsilon-1\right)^3-\frac{\bar{h}^l}{4\mu_\varepsilon}\left(\mu_\varepsilon-1\right)^2+\frac{\mu_\varepsilon}{12\bar{h}^l}$$

The equations related to the right section of the masonry panel are presented below.

- **Right section at ULS in cracked conditions**

$$\bar{V}_u^l=-\frac{H}{B}\left[\bar{N}^l\left(\bar{e}^l+\frac{1}{2}\right)-\frac{2\kappa_\mu}{3}\left(\bar{N}^l+\bar{F}\right)^2+\bar{F}\,\bar{f}-\left(\bar{P}+\bar{Q}\right)\frac{3B}{H}\right] \qquad \text{for } \bar{e}^r>0 \tag{7.130}$$

$$\bar{V}_u^l=-\frac{H}{B}\left[\bar{N}^l\left(e^l-\frac{1}{2}\right)+\frac{2\kappa_\mu}{3}\left(\bar{N}^l+\bar{F}\right)^2+\bar{F}\,\bar{f}-\left(\bar{P}+\bar{Q}\right)\frac{3B}{H}\right] \qquad \text{for } \bar{e}^r<0 \tag{7.131}$$

- **Right section at ULS in uncracked conditions**

$$\bar{V}_u^l=-\frac{H}{B}\left[\bar{N}^l\,\bar{e}^l+\frac{\bar{M}^r}{H}\left(\bar{h}^r\right)+\bar{F}\left(\bar{f}-\frac{1}{2}\right)-\left(\bar{P}+\bar{Q}\right)\frac{B}{2H}\right] \qquad \text{for } \bar{e}^r>0 \tag{7.132}$$

$$\bar{V}_u^l=-\frac{H}{B}\left[\bar{N}^l\,\bar{e}^l-\frac{\bar{M}^r}{H}\left(\bar{h}^r\right)+\bar{F}\left(\bar{f}-\frac{1}{2}\right)-\left(\bar{P}+\bar{Q}\right)\frac{B}{2H}\right] \qquad \text{for } \bar{e}^r<0 \tag{7.133}$$

being:

$$\frac{\bar{M}^r}{H}\left(\bar{h}^r\right)=\bar{N}^r\,\bar{e}^r=\frac{\bar{h}^{r2}}{6\mu_\varepsilon^2}\left(\mu_\varepsilon-1\right)^3-\frac{\bar{h}^r}{4\mu_\varepsilon}\left(\mu_\varepsilon-1\right)^2+\frac{\mu_\varepsilon}{12\bar{h}^r}$$

- **Graphic representations**

As emphasised by Augenti (2004, 2007), both volume and orientation of flexural strength domains V/N_m–N/N_m–e/H depend on the panel dimensions and the magnitude of the external actions acting on it. For a masonry panel with dimensions 90×140×60 cm and subjected to zero external forces (that is: $F = 0$; $P + Q = 0$), one can plot the strength domains shown in Figures 7.34 and 7.35 for ELS and ULS, respectively. These domains have the same shape, but that related to ULS provides higher shear force values. In such a special case, these domains are the same for both right and left sections of the panel. It is also underlined that three-dimensional domains could be used also for pier panels within masonry walls with openings, by considering boundary conditions which change with damage to spandrels.

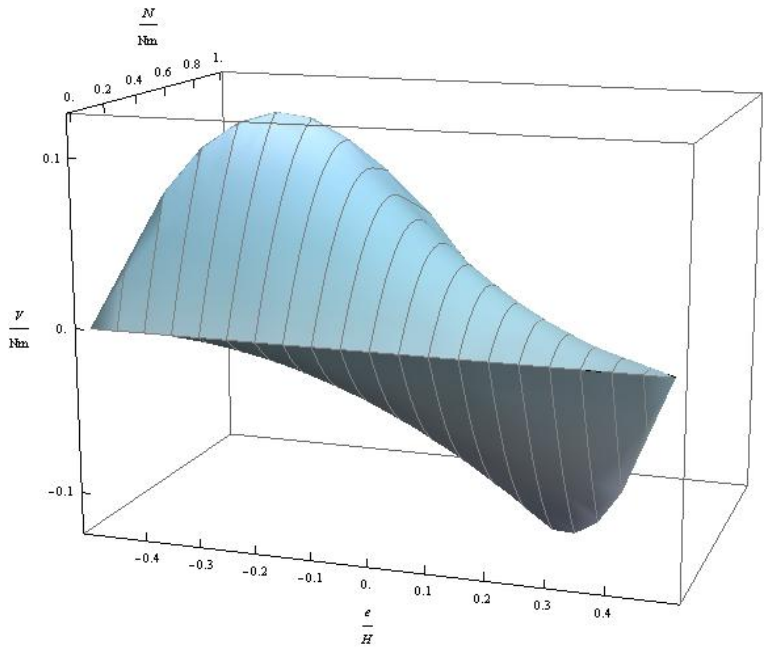

Figure 7.34 Three-dimensional strength domain at ELS for EPP model

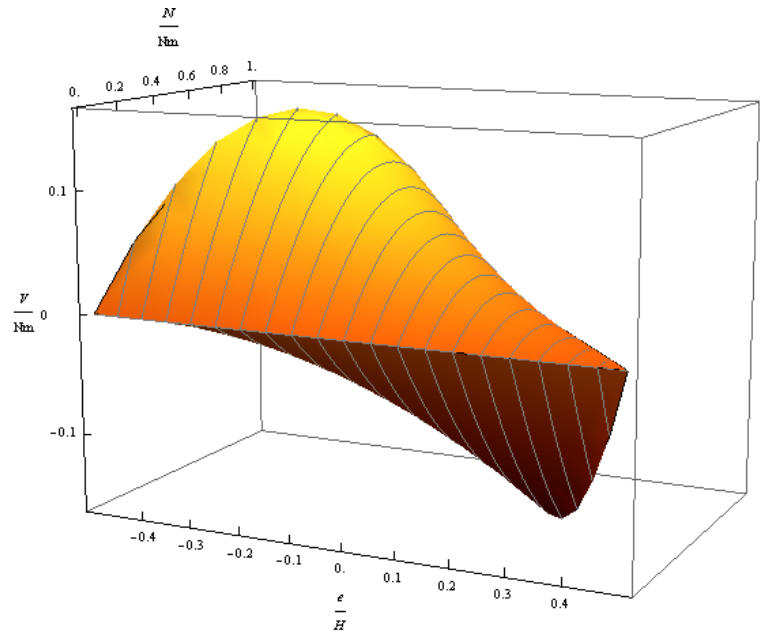

Figure 7.35 Three-dimensional strength domain at ULS for EPP model

In the former graphic representation by Augenti (2007), which is shown in Figure 6.6 (see Sect. 6.2.7), the strength domain V/N_m–N/N_m–e/H was regarded as the union of

planes corresponding to a given normalised eccentricity e/H. In fact, interaction domains V/N_m–N/N_m associated with different values of normalised eccentricity can be derived, as shown in Figures 7.36a and 7.36b.

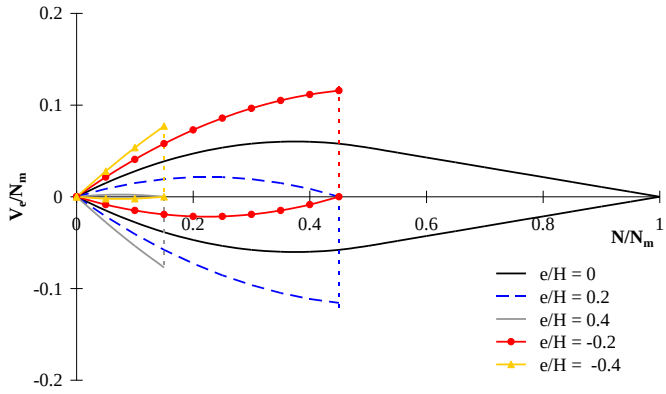

(a)

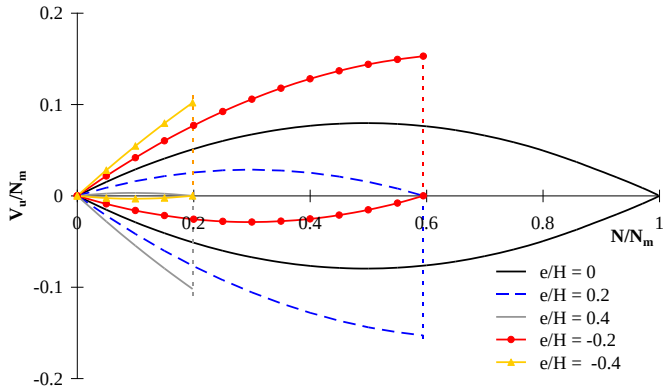

(b)

Figure 7.36 V/N_m–N/N_m strength domains for EPP model: (a) ELS; (b) ULS

Assuming $e/H = 0$, one can define a 'basic domain' which is symmetric with respect to the abscisse axis. As the axial force eccentricity on the cross-section under verification increases, the strength domain experiences increasing rotation around the origin of the coordinate system. It follows that the domain is truncated at decreasing axial force values, since there is a relationship between axial force eccentricity and allowable axial force at ELS [ULS]. As the axial force eccentricity increases, an axial force greater than that allowable at ELS [ULS] leads the cross-section to reach yielding [loss of integrity].

The allowable shear force was derived thorugh sectional equilibrium and can be estimated as follows:

$$\bar{N}_{\max} = \frac{3}{4}\left(1-2\bar{e}\right) \qquad \text{for } \bar{e} > 0 \tag{7.134}$$

$$\bar{N}_{\max} = \frac{3}{4}\left(2\bar{e}+1\right) \qquad \text{for } \bar{e} < 0 \tag{7.135}$$

in the case of cracked cross-section at ELS, and:

$$\bar{N}_{\max} = \frac{1}{1+6\bar{e}} \qquad \text{for } \bar{e} > 0 \tag{7.136}$$

$$\bar{N}_{\max} = \frac{1}{1-6\bar{e}} \qquad \text{for } \bar{e} < 0 \tag{7.137}$$

in the case of uncracked cross-section at ELS. Such equations demonstrate that, under varying normalised eccentricity, the strength domain rotates toward the negative [positive] shear force midspace if the axial force eccentricity is positive [negative]. The allowable axial force at ULS can be estimated through the following equations:

$$\bar{N}_{\max} = \frac{3}{4\kappa_{\mu}}\left(1-2\bar{e}\right) \qquad \text{for } \bar{e} > 0 \tag{7.138}$$

$$\bar{N}_{\max} = \frac{3}{4\kappa_{\mu}}\left(2\bar{e}+1\right) \qquad \text{for } \bar{e} < 0 \tag{7.139}$$

in the case of cracked cross-section. Conversely, no relationships between allowable axial force and eccentricity can be obtained in the case of uncracked cross-sections. The available equations are those related to sectional equilibrium against translation and rotation, and they can be expressed in terms of neutral axis depth normalised to the gross height of the panel, namely $\bar{h} = h/H$. Based on algebraic manipulation of equations, the normalised eccentricity can be defined as a function of *h*/*H*, as follows:

$$\bar{e} = -\frac{\left(-\bar{h}-\mu_{\varepsilon}+\bar{h}\,\mu_{\varepsilon}\right)^2\left(-2\bar{h}+\mu_{\varepsilon}+2\bar{h}\,\mu_{\varepsilon}\right)}{6\mu_{\varepsilon}\left(\bar{h}^2-2\bar{h}^2\mu_{\varepsilon}+\mu_{\varepsilon}^2-2\bar{h}\,\mu_{\varepsilon}^2+\bar{h}^2\mu_{\varepsilon}^2\right)} \qquad \text{for } \bar{e} > 0 \tag{7.140}$$

$$\bar{e} = \frac{\left(-\bar{h}-\mu_{\varepsilon}+\bar{h}\,\mu_{\varepsilon}\right)^2\left(-2\bar{h}+\mu_{\varepsilon}+2\bar{h}\,\mu_{\varepsilon}\right)}{6\mu_{\varepsilon}\left(\bar{h}^2-2\bar{h}^2\mu_{\varepsilon}+\mu_{\varepsilon}^2-2\bar{h}\,\mu_{\varepsilon}^2+\bar{h}^2\mu_{\varepsilon}^2\right)} \qquad \text{for } \bar{e} < 0 \tag{7.141}$$

Therefore, one can first numerically compute the $\bar{h}$ value corresponding to the given axial force eccentricity, and then $\bar{h}$ can be replaced in the following equation:

$$\bar{N}_{\max} = \mu_{\varepsilon} - \frac{\mu_{\varepsilon}}{2\bar{h}} - \frac{\bar{h}\left(\mu_{\varepsilon}-1\right)^2}{2\mu_{\varepsilon}} \tag{7.142}$$

It is underlined the shape of V/N_m–N/N_m strength domains corresponding to a constant *e*/*H* value is different from that corresponding to a constant $M/(N_m \cdot H)$ value. In the

latter case, the normalised eccentricity reduces as the compressive axial force increases. In terms of graph, the two-dimensional strength domain at a given $M/(N_m \cdot H)$ value can be obtained by sectioning the three-dimensional domain through a vertical plan which is not parallel to the set of planes corresponding to constant normalised eccentricities. The angle between the plane at a given $M/(N_m \cdot H)$ value and those at constant normalised eccentricity depends on the normalised bending moment $\bar{M}/H = \bar{N}\,\bar{e}$. Since this angle can be defined as:

$$\alpha = \arctan\left(\frac{\bar{e}}{\bar{N}}\right)$$

the higher is the bending moment, the higher is the slope of the vertical plane at constant moment with respect to the planes at constant eccentricities (Augenti, 2007). Two-dimensional V/N_m–e/H domains can also be derived from the three-dimensional domain, by sectioning the latter at given axial force values (Figs. 7.37a and 7.37b).

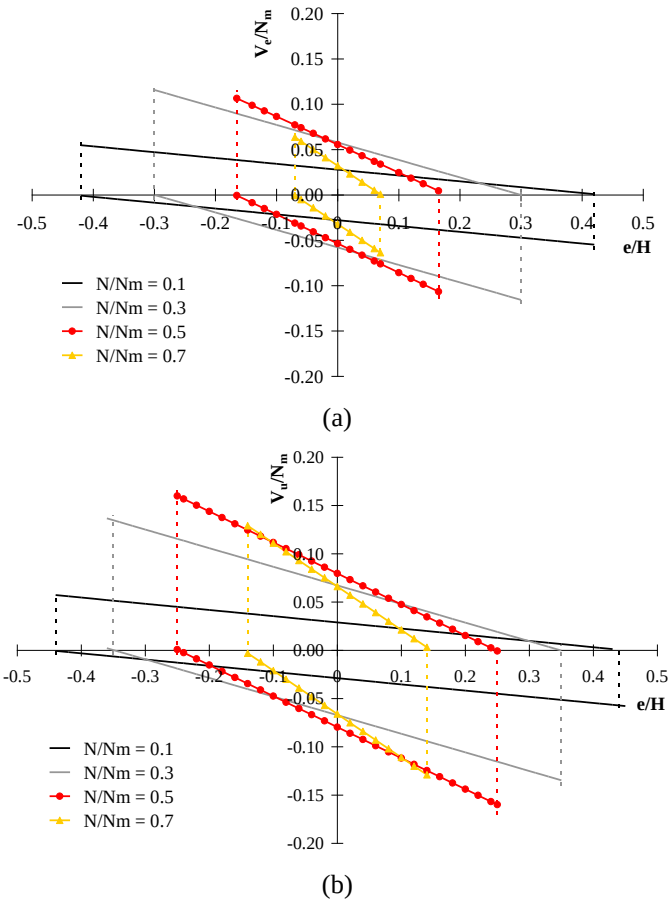

Figure 7.37 V/N_m–e/H strength domains for EPP model: (a) ELS; (b) ULS

As the axial force increases, the strength domain experiences increasing clockwise rotation around the origin of the coordinate system, and reduces up to degenerate in a point when the axial force reaches the allowable axial force associated with zero eccentricity. In fact, as the axial force eccentricity increases, the effective cross-section reduces so the resulting axial force decreases as well.

7.3.2. Strength Domains for Turnšek-Čačovič Constitutive Model

The assumption of the stress-strain relationship proposed by Turnšek and Čačovič (1971) implies that the cross-section reaches ELS in cracked conditions if the normalised axial force N/N_m falls in the interval [0,0.71] and ELS in uncracked conditions for N/N_m falling in the complimentary interval [0.71,1]. At ULS, the cross-section is cracked for N/N_m falling in the interval [0,0.81] and uncracked for N/N_m greater than 0.81. Based on these considerations, the resisting shear forces of the extreme sections of the masonry panel at ELS and ULS (in both cracked and uncracked conditions) can be predicted through the equations presented below.

- **Left section at ELS in cracked conditions**

$$\bar{V}_e^r = -\frac{H}{B}\left[\bar{N}^r\left(\bar{e}^r+\frac{1}{2}\right)-0.56\left(\bar{N}^r-\bar{F}\right)^2+\bar{F}\left(\bar{f}-1\right)+\left(\bar{P}+\bar{Q}\right)\frac{B}{2H}\right] \qquad \text{for } \bar{e}^l>0 \tag{7.143}$$

$$\bar{V}_e^r = -\frac{H}{B}\left[\bar{N}^r\left(\bar{e}^r-\frac{1}{2}\right)+0.56\left(\bar{N}^r-\bar{F}\right)^2+\bar{F}\,\bar{f}+\left(\bar{P}+\bar{Q}\right)\frac{3B}{H}\right] \qquad \text{for } \bar{e}^l<0 \tag{7.144}$$

- **Left section at ELS in uncracked conditions**

$$\bar{V}_e^r = -\frac{H}{B}\left[\bar{N}^r\,\bar{e}^r+\frac{\bar{M}^l}{H}\left(\bar{h}^l\right)+\bar{F}\left(\bar{f}-\frac{1}{2}\right)+\left(\bar{P}+\bar{Q}\right)\frac{B}{2H}\right] \qquad \text{for } \bar{e}^l>0 \tag{7.145}$$

$$\bar{V}_e^r = -\frac{H}{B}\left[\bar{N}^r\,\bar{e}^r-\frac{\bar{M}^l}{H}\left(\bar{h}^l\right)+\bar{F}\left(\bar{f}-\frac{1}{2}\right)+\left(\bar{P}+\bar{Q}\right)\frac{B}{2H}\right] \qquad \text{for } \bar{e}^l<0 \tag{7.146}$$

where:

$$\frac{\bar{M}^l}{H}\left(\bar{h}^l\right)=\bar{N}^l\,\bar{e}^l=1.7\xi_e^{1.17}+\frac{0.53}{\bar{h}^l}+\bar{h}^l\left(-1.24-3.41\xi_e^{1.17}+1.24\xi_e^{2.17}\right)+$$
$$+\bar{h}^{l2}\left(0.78+1.7\xi_e^{1.17}-2.49\xi_e^{2.17}\right)$$

$$\xi_e = 1 - \frac{1}{\bar{h}^l}$$

- **Right section at ELS in cracked conditions**

$$\bar{V}_e^l = -\frac{H}{B}\left[\bar{N}^l\left(\bar{e}^l + \frac{1}{2}\right) - 0.56\left(\bar{N}^l + \bar{F}\right)^2 + \bar{F}\,\bar{f} - \left(\bar{P} + \bar{Q}\right)\frac{B}{2H}\right] \qquad \text{for } \bar{e}^r > 0 \tag{7.147}$$

$$\bar{V}_e^l = -\frac{H}{B}\left[\bar{N}^l\left(\bar{e}^l - \frac{1}{2}\right) + 0.56\left(\bar{N}^l + \bar{F}\right)^2 + \bar{F}\left(\bar{f} - 1\right) - \left(\bar{P} + \bar{Q}\right)\frac{B}{2H}\right] \qquad \text{for } \bar{e}^r < 0 \tag{7.148}$$

- **Right section at ELS in uncracked conditions**

$$\bar{V}_e^l = -\frac{H}{B}\left[\bar{N}^l\,\bar{e}^l + \frac{\bar{M}^r}{H}\left(\bar{h}^r\right) + \bar{F}\left(\bar{f} - \frac{1}{2}\right) - \left(\bar{P} + \bar{Q}\right)\frac{B}{2H}\right] \qquad \text{for } \bar{e}^r > 0 \tag{7.149}$$

$$\bar{V}_e^l = -\frac{H}{B}\left[\bar{N}^l\,\bar{e}^l - \frac{\bar{M}^r}{H}\left(\bar{h}^r\right) + \bar{F}\left(\bar{f} - \frac{1}{2}\right) - \left(\bar{P} + \bar{Q}\right)\frac{B}{2H}\right] \qquad \text{for } \bar{e}^r < 0 \tag{7.150}$$

where the normalised bending moment can be computed as in the case of left section.

- **Left section at ULS in cracked conditions**

$$\bar{V}_u^r = -\frac{H}{B}\left[\bar{N}^r\left(\bar{e}^r + \frac{1}{2}\right) - \kappa_\mu\left(\bar{N}^r - \bar{F}\right)^2 + \bar{F}\left(\bar{f} - 1\right) + \left(\bar{P} + \bar{Q}\right)\frac{3B}{H}\right] \qquad \text{for } \bar{e}^l > 0 \tag{7.151}$$

$$\bar{V}_u^r = -\frac{H}{B}\left[\bar{N}^r\left(\bar{e}^r - \frac{1}{2}\right) + \kappa_\mu\left(\bar{N}^r - \bar{F}\right)^2 + \bar{F}\,\bar{f} + \left(\bar{P} + \bar{Q}\right)\frac{3B}{H}\right] \qquad \text{for } \bar{e}^l < 0 \tag{7.152}$$

being:

$$\kappa_\mu = \frac{0.17\mu_\varepsilon - 0.13\mu_\varepsilon^{1.17}}{\left(\mu_\varepsilon^{1.17} - 1.29\mu_\varepsilon\right)^2}$$

a strain ductility-dependent parameter.

- **Left section at ULS in uncracked conditions**

$$\bar{V}_u^r = -\frac{H}{B}\left[\bar{N}^r\,\bar{e}^r + \frac{\bar{M}^l}{H}\left(\bar{h}^l\right) + \bar{F}\left(\bar{f} - \frac{1}{2}\right) + \left(\bar{P}+\bar{Q}\right)\frac{B}{2H}\right] \qquad \text{for } \bar{e}^l > 0 \tag{7.153}$$

$$\bar{V}_u^r = -\frac{H}{B}\left[\bar{N}^r\,\bar{e}^r - \frac{\bar{M}^l}{H}\left(\bar{h}^l\right) + \bar{F}\left(\bar{f} - \frac{1}{2}\right) + \left(\bar{P}+\bar{Q}\right)\frac{B}{2H}\right] \qquad \text{for } \bar{e}^l < 0 \tag{7.154}$$

being:

$$\frac{\bar{M}^l}{H}\left(\bar{h}^l\right) = \bar{N}^l\,\bar{e}^l = \frac{0.53\mu_\varepsilon}{\bar{h}^l} + 1.7\xi^{1.17} + \bar{h}^{l2}\left(0.78\mu_\varepsilon^{1.17} + 1.7\xi^{1.17} - \frac{2.49\xi^{2.17}}{\mu_\varepsilon}\right) + \\ + \bar{h}^l\left(-1.24\mu_\varepsilon^{1.17} - 3.41\xi^{1.17} + \frac{1.24\xi^{2.17}}{\mu_\varepsilon}\right)$$

$$\xi = \mu_\varepsilon\left(1 - \frac{1}{\bar{h}^l}\right)$$

- **Right section at ULS in cracked conditions**

$$\bar{V}_u^l = -\frac{H}{B}\left[\bar{N}^l\left(\bar{e}^l + \frac{1}{2}\right) - \kappa_\mu\left(\bar{N}^l + \bar{F}\right)^2 + \bar{F}\,\bar{f} - \left(\bar{P}+\bar{Q}\right)\frac{3B}{H}\right] \qquad \text{for } \bar{e}^r > 0 \tag{7.155}$$

$$\bar{V}_u^l = -\frac{H}{B}\left[\bar{N}^l\left(\bar{e}^l - \frac{1}{2}\right) + \kappa_\mu\left(\bar{N}^l + \bar{F}\right)^2 + \bar{F}\,\bar{f} - \left(\bar{P}+\bar{Q}\right)\frac{3B}{H}\right] \qquad \text{for } \bar{e}^r < 0 \tag{7.156}$$

- **Right section at ULS in uncracked conditions**

$$\bar{V}_u^l = -\frac{H}{B}\left[\bar{N}^l\,\bar{e}^l + \frac{\bar{M}^r}{H}\left(\bar{h}^r\right) + \bar{F}\left(\bar{f} - \frac{1}{2}\right) - \left(\bar{P}+\bar{Q}\right)\frac{B}{2H}\right] \qquad \text{for } \bar{e}^r > 0 \tag{7.157}$$

$$\bar{V}_u^l = -\frac{H}{B}\left[\bar{N}^l\,\bar{e}^l - \frac{\bar{M}^r}{H}\left(\bar{h}^r\right) + \bar{F}\left(\bar{f} - \frac{1}{2}\right) - \left(\bar{P}+\bar{Q}\right)\frac{B}{2H}\right] \qquad \text{for } \bar{e}^r < 0 \tag{7.158}$$

- **Graphic representations**

Figures 7.38 and 7.39 show three-dimensional strength domains at ELS and ULS, respectively, while Figures 7.40a and 7.40b show V/N_m–N/N_m two-dimensional domains. The latter are truncated at axial force values defined as follows:

$$\bar{N}_{\max} = 0.9\left(1-2\bar{e}\right) \qquad \text{for } \bar{e} > 0 \tag{7.159}$$

$$\bar{N}_{\max} = 0.9\left(1+2\bar{e}\right) \qquad \text{for } \bar{e} < 0 \tag{7.160}$$

in the case of cracked section at ELS.

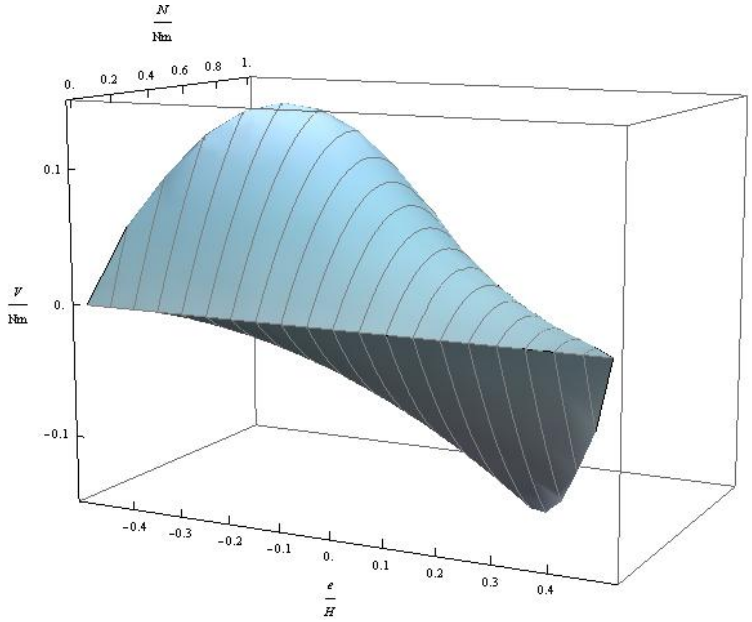

Figure 7.38 Three-dimensional strength domain at ELS for Turnšek-Čačovič model

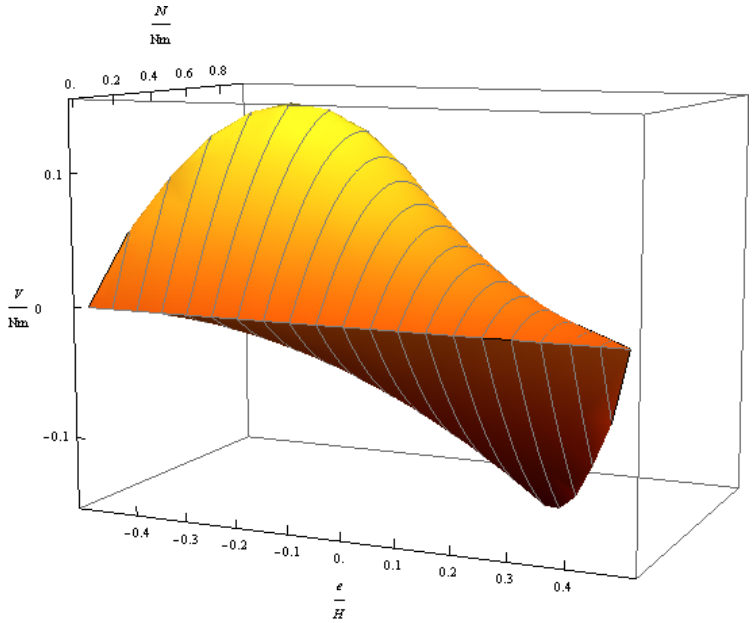

Figure 7.39 Three-dimensional strength domain at ULS for Turnšek-Čačovič model

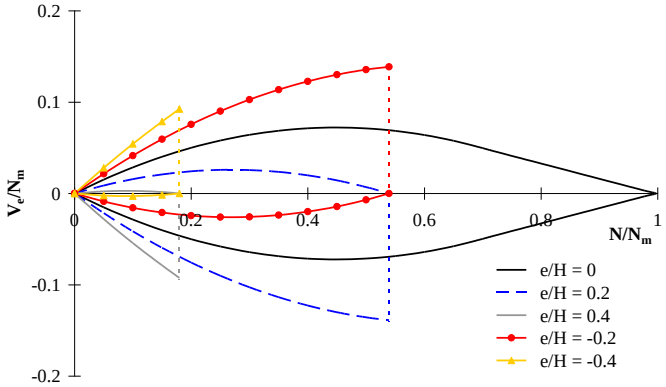

(a)

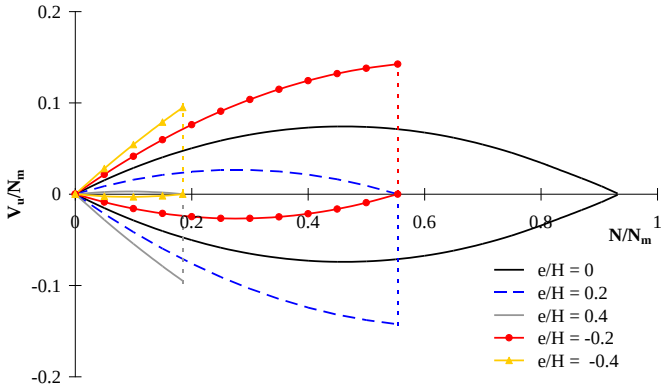

(b)

Figure 7.40 *V*/*N*$_m$–*N*/*N*$_m$ strength domains for Turnšek-Čačovič model: (a) ELS; (b) ULS

In the case of uncracked section, the normalised neutral axis depth (i.e., *h*/*H*) can be first computed by solving numerically the following equations:

$$\bar{e} = \frac{1.7\xi_e^{1.17} + \frac{0.53}{\bar{h}} + \bar{h}\left(-1.24 - 3.41\xi_e^{1.17} + 1.24\xi_e^{2.17}\right) + \bar{h}^2\left(0.78 + 1.7\xi_e^{1.17} - 2.49\xi_e^{2.17}\right)}{6.4 - \frac{3.2}{\bar{h}} - 2.49\bar{h}\left(1 - \xi_e^{2.17}\right)}$$

for $\bar{e} > 0$

(7.161)

$$\bar{e} = -\frac{1.7\xi_e^{1.17} + \frac{0.53}{\bar{h}} + \bar{h}\left(-1.24 - 3.41\xi_e^{1.17} + 1.24\xi_e^{2.17}\right) + \bar{h}^2\left(0.78 + 1.7\xi_e^{1.17} - 2.49\xi_e^{2.17}\right)}{6.4 - \frac{3.2}{\bar{h}} - 2.49\bar{h}\left(1 - \xi_e^{2.17}\right)}$$

for $\bar{e} < 0$

(7.162)

so the allowable axial force can be determined as follows:

$$\bar{N}_{\max} = 6.4 - \frac{3.2}{\bar{h}} - 2.49\bar{h}\left(1 - \xi_e{}^{2.17}\right) \tag{7.163}$$

At ULS, the cracked section is characterised by a V/N_m–N/N_m domain truncated at the allowable axial force defined as:

$$\bar{N}_{\max} = \frac{1}{2\kappa_\mu}\left(1 - 2\bar{e}\right) \qquad \text{for } \bar{e} > 0 \tag{7.164}$$

$$\bar{N}_{\max} = \frac{1}{2\kappa_\mu}\left(1 + 2\bar{e}\right) \qquad \text{for } \bar{e} < 0 \tag{7.165}$$

In the case of uncracked section, the normalised neutral axis depth h/H is first to be computed by solving numerically the following equations:

$$\bar{e} = \frac{\dfrac{0.53\mu_\varepsilon}{\bar{h}} + 1.7\xi^{1.17} + \bar{h}^2\left(0.78\mu_\varepsilon^{1.17} + 1.7\xi^{1.17} - \dfrac{2.49\xi^{2.17}}{\mu_\varepsilon}\right)}{6.4\mu_\varepsilon - \dfrac{3.2\mu_\varepsilon}{\bar{h}^s} - 2.49\bar{h}\left(\mu_\varepsilon^{1.17} - \dfrac{\xi^{2.17}}{\mu_\varepsilon}\right)} + \\ + \frac{\bar{h}\left(-1.24\mu_\varepsilon^{1.17} - 3.41\xi^{1.17} + \dfrac{1.24\xi^{2.17}}{\mu_\varepsilon}\right)}{6.4\mu_\varepsilon - \dfrac{3.2\mu_\varepsilon}{\bar{h}^s} - 2.49\bar{h}\left(\mu_\varepsilon^{1.17} - \dfrac{\xi^{2.17}}{\mu_\varepsilon}\right)} \qquad \text{for } \bar{e} > 0 \tag{7.166}$$

$$\bar{e} = -\frac{\dfrac{0.53\mu_\varepsilon}{\bar{h}} + 1.7\xi^{1.17} + \bar{h}^2\left(0.78\mu_\varepsilon^{1.17} + 1.7\xi^{1.17} - \dfrac{2.49\xi^{2.17}}{\mu_\varepsilon}\right)}{6.4\mu_\varepsilon - \dfrac{3.2\mu_\varepsilon}{\bar{h}} - 2.49\bar{h}\left(\mu_\varepsilon^{1.17} - \dfrac{\xi^{2.17}}{\mu_\varepsilon}\right)} + \\ + \frac{\bar{h}\left(-1.24\mu_\varepsilon^{1.17} - 3.41\xi^{1.17} + \dfrac{1.24\xi^{2.17}}{\mu_\varepsilon}\right)}{6.4\mu_\varepsilon - \dfrac{3.2\mu_\varepsilon}{\bar{h}} - 2.49\bar{h}\left(\mu_\varepsilon^{1.17} - \dfrac{\xi^{2.17}}{\mu_\varepsilon}\right)} \qquad \text{for } \bar{e} < 0 \tag{7.167}$$

so the allowable axial force can be evaluated as follows:

$$\bar{N}_{\max} = 6.4 - \frac{3.2}{\bar{h}} - 2.49\bar{h}\left(1 - \xi_e{}^{2.17}\right) \tag{7.168}$$

Finally, Figures 7.41a and 7.41b show V/N_m–e/H domains for ELS and ULS, respectively.

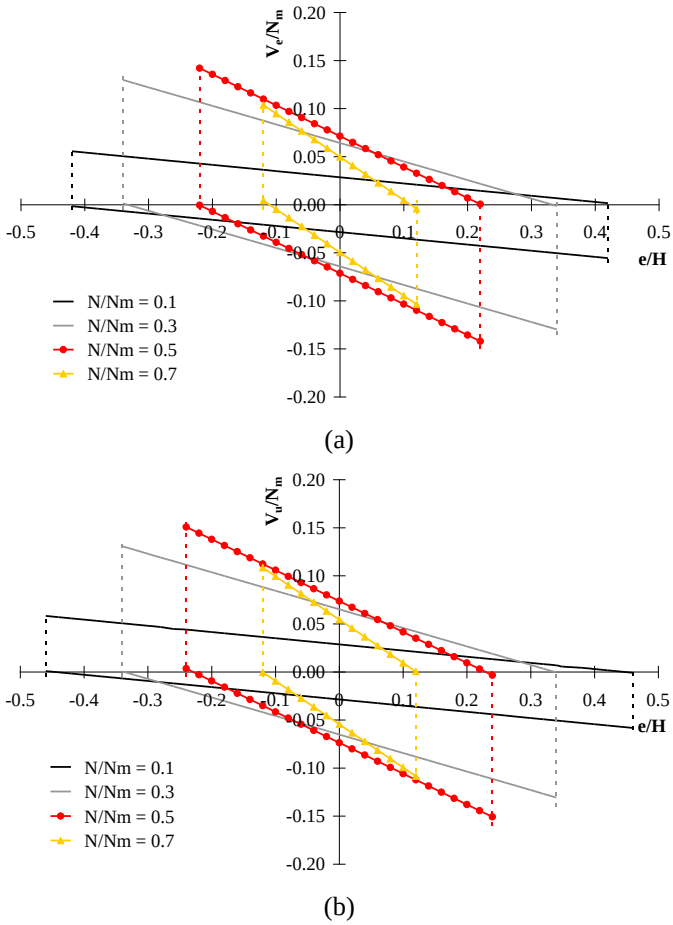

Figure 7.41 V/N_m–e/H strength domains for Turnšek-Čačovič model: (a) ELS; (b) ULS

7.3.3. Strength Domains for EC6 Constitutive Model

The assumption of the stress-strain relationship reported in EC6 (CEN, 2005a) implies that the cross-section reaches ELS in cracked conditions if the normalised axial force N/N_m falls in the interval [0,0.67] and ELS in uncracked conditions for N/N_m falling in the complimentary interval [0.67,1]. At ULS, the cross-section is cracked for N/N_m falling in the interval [0,0.81] and uncracked for N/N_m falling in the interval [0.81,1]. Based on these considerations, the resisting shear forces of the extreme sections of the masonry panel at ELS and ULS (in both cracked and uncracked conditions) can be predicted through the equations presented below.

- **Left section at ELS in cracked conditions**

$$\bar{V}_e^r = -\frac{H}{B}\left[\bar{N}^r\left(\bar{e}^r+\frac{1}{2}\right)-\frac{9}{16}\left(\bar{N}^r-\bar{F}\right)^2+\bar{F}\left(\bar{f}-1\right)+\left(\bar{P}+\bar{Q}\right)\frac{B}{2H}\right] \qquad \text{for } \bar{e}^l>0 \tag{7.169}$$

$$\bar{V}_e^r = -\frac{H}{B}\left[\bar{N}^r\left(\bar{e}^r-\frac{1}{2}\right)+\frac{9}{16}\left(\bar{N}^r-\bar{F}\right)^2+\bar{F}\,\bar{f}+\left(\bar{P}+\bar{Q}\right)\frac{3B}{H}\right] \qquad \text{for } \bar{e}^l<0 \tag{7.170}$$

- **Left section at ELS in uncracked conditions**

$$\bar{V}_e^r = -\frac{H}{B}\left[\frac{1}{4}+\bar{N}^r\left(\bar{e}^r-\frac{1}{4}\right)+\bar{F}\left(\bar{f}-\frac{1}{4}\right)+\left(\bar{P}+\bar{Q}\right)\frac{B}{2H}\right] \qquad \text{for } \bar{e}^l>0 \tag{7.171}$$

$$\bar{V}_e^r = -\frac{H}{B}\left[-\frac{1}{4}+\bar{N}^r\left(\bar{e}^r+\frac{1}{4}\right)+\bar{F}\left(\bar{f}-\frac{3}{4}\right)+\left(\bar{P}+\bar{Q}\right)\frac{B}{2H}\right] \qquad \text{for } \bar{e}^l<0 \tag{7.172}$$

- **Right section at ELS in cracked conditions**

$$\bar{V}_e^l = -\frac{H}{B}\left[\bar{N}^l\left(\bar{e}^l+\frac{1}{2}\right)-\frac{9}{16}\left(\bar{N}^l+\bar{F}\right)^2+\bar{F}\,\bar{f}-\left(\bar{P}+\bar{Q}\right)\frac{B}{2H}\right] \qquad \text{for } \bar{e}^r>0 \tag{7.173}$$

$$\bar{V}_e^l = -\frac{H}{B}\left[\bar{N}^l\left(\bar{e}^l-\frac{1}{2}\right)+\frac{9}{16}\left(\bar{N}^l+\bar{F}\right)^2+\bar{F}\left(\bar{f}-1\right)-\left(\bar{P}+\bar{Q}\right)\frac{B}{2H}\right] \qquad \text{for } \bar{e}^r<0 \tag{7.174}$$

- **Right section at ELS in uncracked conditions**

$$\bar{V}_e^l = -\frac{H}{B}\left[\frac{1}{4}+\bar{N}^l\left(\bar{e}^l-\frac{1}{4}\right)+\bar{F}\left(\bar{f}-\frac{3}{4}\right)-\left(\bar{P}+\bar{Q}\right)\frac{B}{2H}\right] \qquad \text{for } \bar{e}^r>0 \tag{7.175}$$

$$\bar{V}_e^l = -\frac{H}{B}\left[\frac{1}{4}+\bar{N}^l\left(\bar{e}^l-\frac{1}{4}\right)+\bar{F}\left(\bar{f}-\frac{3}{4}\right)-\left(\bar{P}+\bar{Q}\right)\frac{B}{2H}\right] \qquad \text{for } \bar{e}^r<0 \tag{7.176}$$

- **Left section at ULS in cracked conditions**

$$\bar{V}_u^r = -\frac{H}{B}\left[\bar{N}^r\left(\bar{e}^r+\frac{1}{2}\right)-\frac{3\kappa_\mu}{4}\left(\bar{N}^r-\bar{F}\right)^2+\bar{F}\left(\bar{f}-1\right)+\left(\bar{P}+\bar{Q}\right)\frac{3B}{H}\right] \qquad \text{for } \bar{e}^l>0 \tag{7.177}$$

$$\bar{V}_u^r = -\frac{H}{B}\left[\bar{N}^r\left(\bar{e}^r - \frac{1}{2}\right) + \frac{3\kappa_\mu}{4}\left(\bar{N}^r - \bar{F}\right)^2 + \bar{F}\,\bar{f} + \left(\bar{P}+\bar{Q}\right)\frac{3B}{H}\right] \qquad \text{for } \bar{e}^l < 0 \tag{7.178}$$

where:

$$\kappa_\mu = \frac{1 - 4\mu_\varepsilon + 6\mu_\varepsilon^2}{\left(3\mu_\varepsilon - 1\right)^2}$$

- **Left section at ULS in uncracked conditions**

$$\bar{V}_u^r = -\frac{H}{B}\left[\bar{N}^r\,\bar{e}^r + \frac{\bar{M}^l}{H}\left(\bar{h}^l\right) + \bar{F}\left(\bar{f} - \frac{1}{2}\right) + \left(\bar{P}+\bar{Q}\right)\frac{B}{2H}\right] \qquad \text{for } \bar{e}^l > 0 \tag{7.179}$$

$$\bar{V}_u^r = -\frac{H}{B}\left[\bar{N}^r\,\bar{e}^r - \frac{\bar{M}^l}{H}\left(\bar{h}^l\right) + \bar{F}\left(\bar{f} - \frac{1}{2}\right) + \left(\bar{P}+\bar{Q}\right)\frac{B}{2H}\right] \qquad \text{for } \bar{e}^l < 0 \tag{7.180}$$

where:

$$\frac{\bar{M}^l}{H}\left(\bar{h}^l\right) = \bar{N}^l\,\bar{e}^l = -\frac{\bar{h}^{l2}}{12\mu_\varepsilon^2}\left(\mu_\varepsilon - 1\right)^4 + \frac{\bar{h}^l}{6\mu_\varepsilon}\left(\mu_\varepsilon - 1\right)^3 - \frac{\mu_\varepsilon\left(\mu_\varepsilon - 1\right)}{6\bar{h}^l} + \frac{\mu_\varepsilon^2}{12\bar{h}^{l2}}$$

- **Right section at ULS in cracked conditions**

$$\bar{V}_u^l = -\frac{H}{B}\left[\bar{N}^l\left(\bar{e}^l + \frac{1}{2}\right) - \frac{3\kappa_\mu}{4}\left(\bar{N}^l + \bar{F}\right)^2 + \bar{F}\,\bar{f} - \left(\bar{P}+\bar{Q}\right)\frac{3B}{H}\right] \qquad \text{for } \bar{e}^r > 0 \tag{7.181}$$

$$\bar{V}_u^l = -\frac{H}{B}\left[\bar{N}^l\left(\bar{e}^l - \frac{1}{2}\right) + \frac{3\kappa_\mu}{4}\left(\bar{N}^l + \bar{F}\right)^2 + \bar{F}\,\bar{f} - \left(\bar{P}+\bar{Q}\right)\frac{3B}{H}\right] \qquad \text{for } \bar{e}^r < 0 \tag{7.182}$$

- **Right section at ULS in uncracked conditions**

$$\bar{V}_u^l = -\frac{H}{B}\left[\bar{N}^l\,\bar{e}^l + \frac{\bar{M}^r}{H}\left(\bar{h}^r\right) + \bar{F}\left(\bar{f} - \frac{1}{2}\right) - \left(\bar{P}+\bar{Q}\right)\frac{B}{2H}\right] \qquad \text{for } \bar{e}^r > 0 \tag{7.183}$$

$$\bar{V}_u^l = -\frac{H}{B}\left[\bar{N}^l\,\bar{e}^l - \frac{\bar{M}^r}{H}\left(\bar{h}^r\right) + \bar{F}\left(\bar{f} - \frac{1}{2}\right) - \left(\bar{P}+\bar{Q}\right)\frac{B}{2H}\right] \qquad \text{for } \bar{e}^r < 0 \tag{7.184}$$

where:

$$\frac{\bar{M}^r}{H}\left(\bar{h}^r\right)=\bar{N}^r\,\bar{e}^r=-\frac{\bar{h}^{l2}}{12\mu_\varepsilon^2}\left(\mu_\varepsilon-1\right)^4+\frac{\bar{h}^l}{6\mu_\varepsilon}\left(\mu_\varepsilon-1\right)^3-\frac{\mu_\varepsilon\left(\mu_\varepsilon-1\right)}{6\bar{h}^l}+\frac{\mu_\varepsilon^2}{12\bar{h}^{l2}}$$

- **Graphic representations**

The three-dimensional strength domains corresponding to EC6 constitutive model are shown in Figures 7.42 and 7.43 for ELS and ULS, respectively. Figures 7.44a and 7.44b show V/N_m–N/N_m strength domains at the same limit states; they are truncated at axial force values provided by the following equations:

$$\bar{N}_{\max}=\frac{8}{9}\left(1-2\bar{e}\right)\qquad\text{for }\bar{e}>0 \tag{7.185}$$

$$\bar{N}_{\max}=\frac{8}{9}\left(1+2\bar{e}\right)\qquad\text{for }\bar{e}<0 \tag{7.186}$$

in the case of cracked section at ELS, and:

$$\bar{N}_{\max}=\frac{1}{1+4\bar{e}}\qquad\text{for }\bar{e}>0 \tag{7.187}$$

$$\bar{N}_{\max}=\frac{1}{1-4\bar{e}^s}\qquad\text{for }\bar{e}<0 \tag{7.188}$$

in the case of uncracked section at ELS.

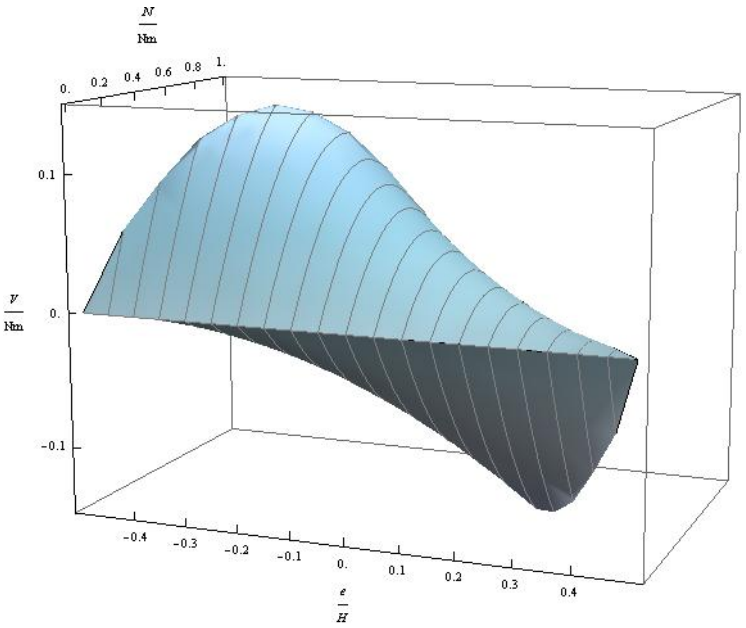

Figure 7.42 Three-dimensional strength domain at ELS for EC6 model

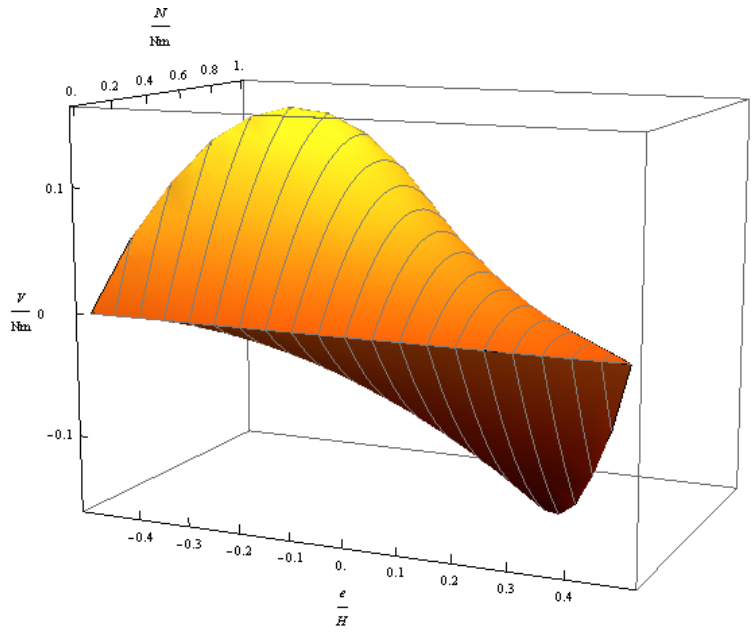

Figure 7.43 Three-dimensional strength domain at ULS for EC6 constitutive model

The allowable axial force for a cracked section at ULS can be predicted as follows:

$$\bar{N}_{\max} = \frac{2}{3\kappa_{\mu}}\left(1-2\bar{e}\right) \qquad \text{for } \bar{e} > 0 \tag{7.189}$$

$$\bar{N}_{\max} = \frac{2}{3\kappa_{\mu}}\left(2\bar{e}+1\right) \qquad \text{for } \bar{e} < 0 \tag{7.190}$$

If the section is uncracked at ULS, the normalised neutral axis depth can be evaluated by solving numerically one of the following equations:

$$\bar{e} = \frac{\left(-\bar{h}-\mu_{\varepsilon}+\bar{h}\,\mu_{\varepsilon}\right)^{3}\left(-\bar{h}+\mu_{\varepsilon}+\bar{h}\,\mu_{\varepsilon}\right)}{4\mu_{\varepsilon}^{4}-12\bar{h}^{2}\left(2\mu_{\varepsilon}^{3}-\mu_{\varepsilon}^{4}\right)-4\bar{h}^{3}\left(-\mu_{\varepsilon}+3\mu_{\varepsilon}^{2}-3\mu_{\varepsilon}^{3}+\mu_{\varepsilon}^{4}\right)-12\bar{h}\left(-\mu_{\varepsilon}^{3}+\mu_{\varepsilon}^{4}\right)} \qquad \text{for } \bar{e} > 0 \tag{7.191}$$

$$\bar{e} = -\frac{\left(-\bar{h}-\mu_{\varepsilon}+\bar{h}\,\mu_{\varepsilon}\right)^{3}\left(-\bar{h}+\mu_{\varepsilon}+\bar{h}\,\mu_{\varepsilon}\right)}{4\mu_{\varepsilon}^{4}-12\bar{h}^{2}\left(2\mu_{\varepsilon}^{3}-\mu_{\varepsilon}^{4}\right)-4\bar{h}^{s3}\left(-\mu_{\varepsilon}+3\mu_{\varepsilon}^{2}-3\mu_{\varepsilon}^{3}+\mu_{\varepsilon}^{4}\right)-12\bar{h}\left(-\mu_{\varepsilon}^{3}+\mu_{\varepsilon}^{4}\right)} \qquad \text{for } \bar{e} < 0 \tag{7.192}$$

so the allowable axial force can be determined as follows:

$$\bar{N}_{\max} = 2\mu_{\varepsilon}-\mu_{\varepsilon}^{2}+\frac{\mu_{\varepsilon}^{2}-\mu_{\varepsilon}}{\bar{h}}-\frac{\mu_{\varepsilon}^{2}}{3\bar{h}^{2}}+\frac{\bar{h}\left(\mu_{\varepsilon}-1\right)^{3}}{3\mu_{\varepsilon}} \tag{7.193}$$

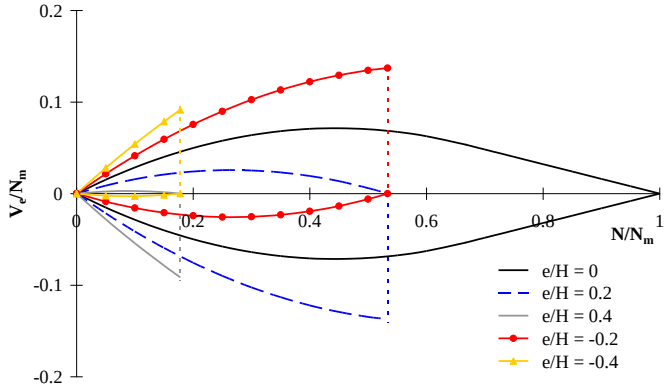

(a)

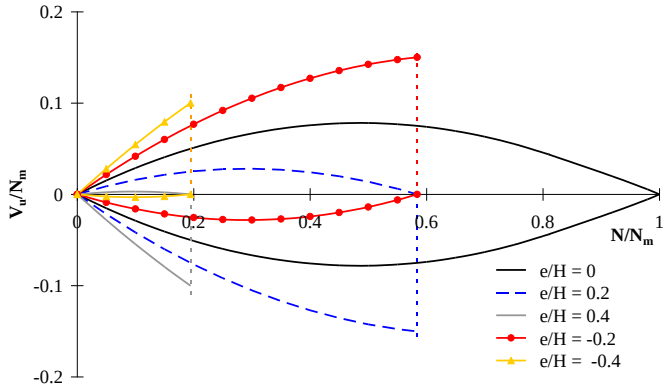

(b)

Figure 7.44 V/N_m–N/N_m strength domains for EC6 model: (a) ELS; (b) ULS

Figures 7.45a and 7.45b show V/N_m–e/H strength domains corresponding to ELS and ULS, respectively.

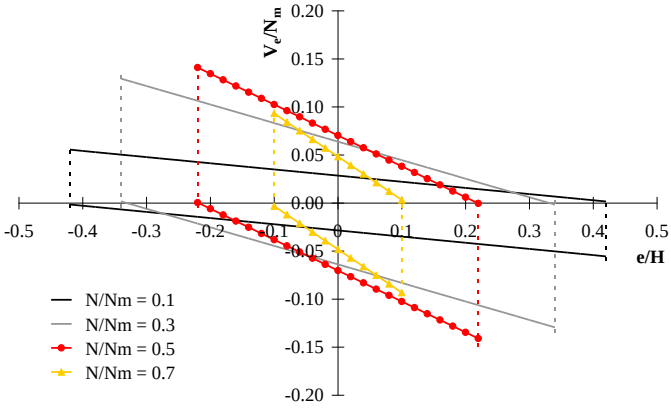

(a)

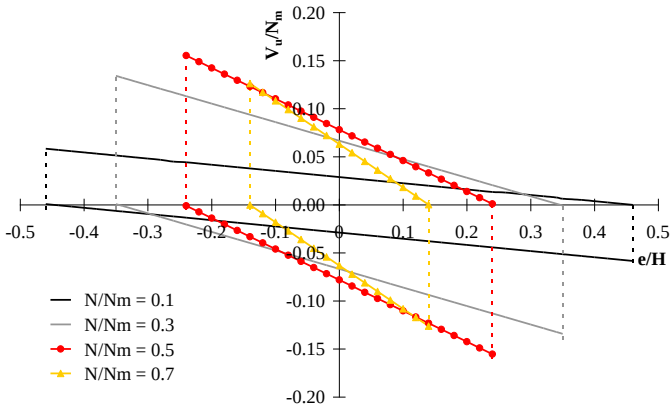

(b)

Figure 7.45 V/N_m–e/H strength domains for EC6 model: (a) ELS; (b) ULS

7.3.4. Strength Domains for Augenti-Parisi Constitutive Model Related to Compression Orthogonal to Mortar Bed Joints

Assuming the stress-strain relationship proposed by Augenti and Parisi (2010a) for compression orthogonal to mortar bed joints (case of pier panels), the cross-section at ELS is cracked if the normalised axial force N/N_m falls in the interval [0,0.6] and uncracked if N/N_m falls in the interval [0.6,1]. At ULS, the cross-section is cracked for N/N_m falling in the interval [0,0.61] and uncracked for N/N_m greater than 0.61. The resisting shear forces of the extreme sections at ELS and ULS (in both cracked and uncracked conditions) can be predicted via the equations presented below.

- **Left section at ELS in cracked conditions**

$$\bar{V}_e^r = -\frac{H}{B}\left[\bar{N}^r\left(\bar{e}^r+\frac{1}{2}\right)-0.58\left(\bar{N}^r-\bar{F}\right)^2+\bar{F}\left(\bar{f}-1\right)+\left(\bar{P}+\bar{Q}\right)\frac{B}{2H}\right] \qquad \text{for } \bar{e}^l>0 \tag{7.194}$$

$$\bar{V}_e^r = -\frac{H}{B}\left[\bar{N}^r\left(\bar{e}^r-\frac{1}{2}\right)+0.58\left(\bar{N}^r-\bar{F}\right)^2+\bar{F}\,\bar{f}+\left(\bar{P}+\bar{Q}\right)\frac{3B}{H}\right] \qquad \text{for } \bar{e}^l<0 \tag{7.195}$$

- **Left section at ELS in uncracked conditions**

$$\bar{V}_e^r = -\frac{H}{B}\left[\bar{N}^r\,\bar{e}^r+\frac{\bar{M}^l}{H}\left(\bar{h}^l\right)+\bar{F}\left(\bar{f}-\frac{1}{2}\right)+\left(\bar{P}+\bar{Q}\right)\frac{B}{2H}\right] \qquad \text{for } \bar{e}^l>0 \tag{7.196}$$

$$\bar{V}_e^r = -\frac{H}{B}\left[\bar{N}^r\,\bar{e}^r - \frac{\bar{M}^l}{H}\left(\bar{h}^l\right) + \bar{F}\left(\bar{f} - \frac{1}{2}\right) + \left(\bar{P}+\bar{Q}\right)\frac{B}{2H}\right] \qquad \text{for } \bar{e}^l < 0 \tag{7.197}$$

where:

$$\frac{\bar{M}^l}{H}\left(\bar{h}^l\right) = \bar{N}^l\,\bar{e}^l = -\frac{0.05}{\bar{h}^{l3}} + \frac{0.14}{\bar{h}^{l2}} + \frac{0.002}{\bar{h}^l}$$

- **Right section at ELS in cracked conditions**

$$\bar{V}_e^l = -\frac{H}{B}\left[\bar{N}^l\left(\bar{e}^l + \frac{1}{2}\right) - 0.58\left(\bar{N}^l + \bar{F}\right)^2 + \bar{F}\,\bar{f} - \left(\bar{P}+\bar{Q}\right)\frac{B}{2H}\right] \qquad \text{for } \bar{e}^r > 0 \tag{7.198}$$

$$\bar{V}_e^l = -\frac{H}{B}\left[\bar{N}^l\left(\bar{e}^l - \frac{1}{2}\right) + 0.58\left(\bar{N}^l + \bar{F}\right)^2 + \bar{F}\left(\bar{f} - 1\right) - \left(\bar{P}+\bar{Q}\right)\frac{B}{2H}\right] \qquad \text{for } \bar{e}^r < 0 \tag{7.199}$$

- **Right section at ELS in uncracked conditions**

$$\bar{V}_e^l = -\frac{H}{B}\left[\bar{N}^l\,\bar{e}^l + \frac{\bar{M}^r}{H}\left(\bar{h}^r\right) + \bar{F}\left(\bar{f} - \frac{1}{2}\right) - \left(\bar{P}+\bar{Q}\right)\frac{B}{2H}\right] \qquad \text{for } \bar{e}^r > 0 \tag{7.200}$$

$$\bar{V}_e^l = -\frac{H}{B}\left[\bar{N}^l\,\bar{e}^l - \frac{\bar{M}^r}{H}\left(\bar{h}^r\right) + \bar{F}\left(\bar{f} - \frac{1}{2}\right) - \left(\bar{P}+\bar{Q}\right)\frac{B}{2H}\right] \qquad \text{for } \bar{e}^r < 0 \tag{7.201}$$

- **Left section at ULS in cracked conditions**

$$\bar{V}_u^r = -\frac{H}{B}\left[\bar{N}^r\left(\bar{e}^r + \frac{1}{2}\right) - \kappa_\mu\left(\bar{N}^r - \bar{F}\right)^2 + \bar{F}\left(\bar{f} - 1\right) + \left(\bar{P}+\bar{Q}\right)\frac{3B}{H}\right] \qquad \text{for } \bar{e}^l > 0 \tag{7.202}$$

$$\bar{V}_u^r = -\frac{H}{B}\left[\bar{N}^r\left(\bar{e}^r - \frac{1}{2}\right) + \kappa_\mu\left(\bar{N}^r - \bar{F}\right)^2 + \bar{F}\,\bar{f} + \left(\bar{P}+\bar{Q}\right)\frac{3B}{H}\right] \qquad \text{for } \bar{e}^l < 0 \tag{7.203}$$

being:

$$\kappa_\mu = \frac{0.2 - 0.66\mu_\varepsilon + 0.77\mu_\varepsilon^2 - 0.11\mu_\varepsilon^3 + 0.01\mu_\varepsilon^4 - 0.001\mu_\varepsilon^5}{0.66\mu_\varepsilon - 1.54\mu_\varepsilon^2 + 0.32\mu_\varepsilon^3 - 0.05\mu_\varepsilon^4 - 0.003\mu_\varepsilon^5}$$

- **Left section at ULS in uncracked conditions**

$$\bar{V}_u^r = -\frac{H}{B}\left[\bar{N}^r\, e^r + \frac{\bar{M}^l}{H}\left(\bar{h}^l\right) + \bar{F}\left(\bar{f} - \frac{1}{2}\right) + \left(\bar{P} + \bar{Q}\right)\frac{B}{2H}\right] \qquad \text{for } \bar{e}^l > 0 \tag{7.204}$$

$$\bar{V}_u^r = -\frac{H}{B}\left[\bar{N}^r\, e^r - \frac{\bar{M}^l}{H}\left(\bar{h}^l\right) + \bar{F}\left(\bar{f} - \frac{1}{2}\right) + \left(\bar{P} + \bar{Q}\right)\frac{B}{2H}\right] \qquad \text{for } \bar{e}^l < 0 \tag{7.205}$$

where:

$$\frac{\bar{M}^l}{H}\left(\bar{h}^l\right) = \bar{N}^l\,\bar{e}^l = -\frac{0.05\,\mu_\varepsilon^3}{\bar{h}^{l3}} - \frac{0.04\,\mu_\varepsilon^2 - 0.18\,\mu_\varepsilon^3}{\bar{h}^{l2}} + \frac{0.11\mu_\varepsilon + 0.08\,\mu_\varepsilon^2 - 0.18\,\mu_\varepsilon^3}{\bar{h}^l} + \\ + \bar{h}^{l2}\left(-0.77 - \frac{0.2}{\mu_\varepsilon^2} + \frac{0.66}{\mu_\varepsilon} + 0.32\,\mu_\varepsilon + 0.03\,\mu_\varepsilon^2 - 0.03\,\mu_\varepsilon^3\right) + \\ + \bar{h}^l\left(0.77 - \frac{0.33}{\mu_\varepsilon} - 0.48\,\mu_\varepsilon - 0.05\,\mu_\varepsilon^2 + 0.09\,\mu_\varepsilon^3\right)$$

- **Right section at ULS in cracked conditions**

$$\bar{V}_u^l = -\frac{H}{B}\left[\bar{N}^l\left(\bar{e}^l + \frac{1}{2}\right) - \kappa_\mu\left(\bar{N}^l + \bar{F}\right)^2 + \bar{F}\,\bar{f} - \left(\bar{P} + \bar{Q}\right)\frac{3B}{H}\right] \qquad \text{for } \bar{e}^r > 0 \tag{7.206}$$

$$\bar{V}_u^l = -\frac{H}{B}\left[\bar{N}^l\left(\bar{e}^l - \frac{1}{2}\right) + \kappa_\mu\left(\bar{N}^l + \bar{F}\right)^2 + \bar{F}\,\bar{f} - \left(\bar{P} + \bar{Q}\right)\frac{3B}{H}\right] \qquad \text{for } \bar{e}^r < 0 \tag{7.207}$$

- **Right section at ULS in uncracked conditions**

$$\bar{V}_u^l = -\frac{H}{B}\left[\bar{N}^l\,\bar{e}^l + \frac{\bar{M}^r}{H}\left(\bar{h}^r\right) + \bar{F}\left(\bar{f} - \frac{1}{2}\right) - \left(\bar{P} + \bar{Q}\right)\frac{B}{2H}\right] \qquad \text{for } \bar{e}^r > 0 \tag{7.208}$$

$$\bar{V}_u^l = -\frac{H}{B}\left[\bar{N}^l\,\bar{e}^l - \frac{\bar{M}^r}{H}\left(\bar{h}^r\right) + \bar{F}\left(\bar{f} - \frac{1}{2}\right) - \left(\bar{P} + \bar{Q}\right)\frac{B}{2H}\right] \qquad \text{for } \bar{e}^r < 0 \tag{7.209}$$

where the bending moment corresponding to the neutral axis depth can be computed as in the case of left section.

- **Graphic representations**

Figures 7.46 and 7.47 show the three-dimensional strength domains corresponding to Augenti-Parisi constitutive model for compression orthogonal to mortar bed joints.

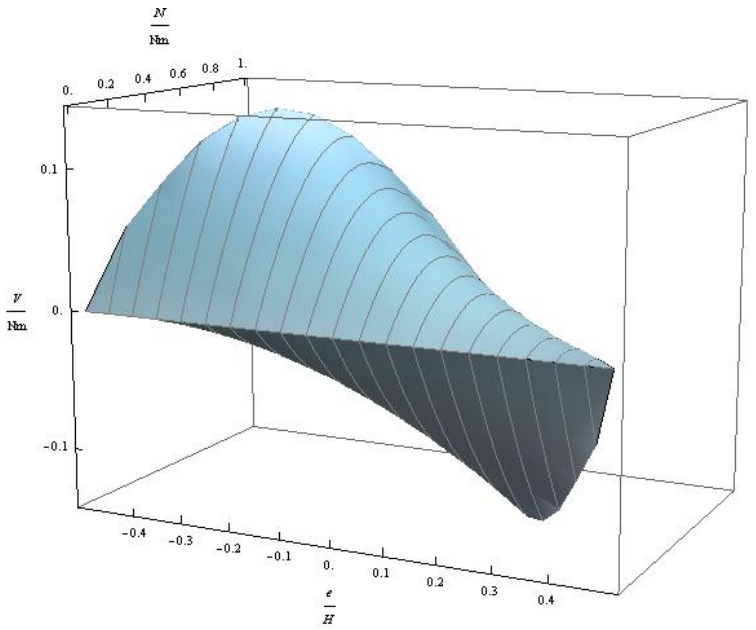

Figure 7.46 Three-dimensional strength domain at ELS for Augenti-Parisi model (orthog. dir.)

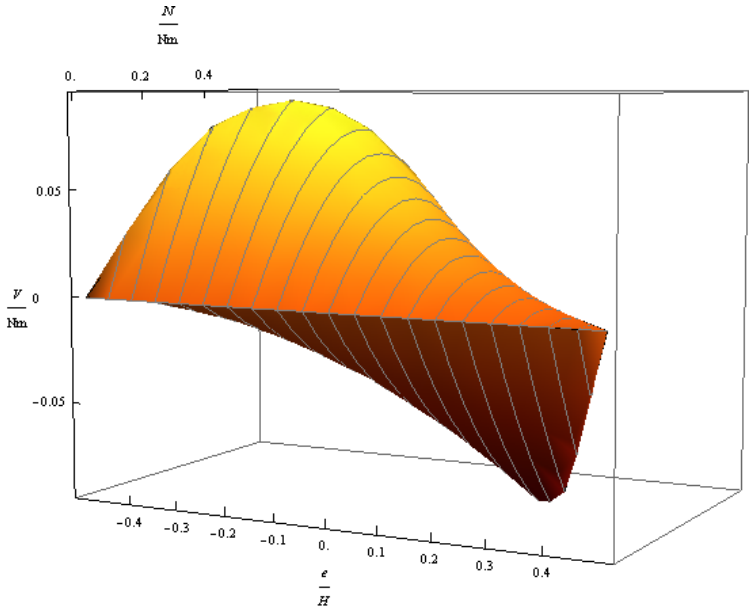

Figure 7.47 Three-dimensional strength domain at ULS for Augenti-Parisi model (orthog. dir.)

Figures 7.48a and 7.48b illustrate V/N_m–N/N_m domains at ELS and ULS, respectively; such domains are truncated at axial force values given by the following equations:

$$\bar{N}_{\max} = 0.86\left(1-2\bar{e}\right) \qquad \text{for } \bar{e} > 0 \tag{7.210}$$

$$\bar{N}_{\max} = 0.86\left(1+2\bar{e}\right) \qquad \text{for } \bar{e} < 0 \tag{7.211}$$

in the case of cracked section at ELS.

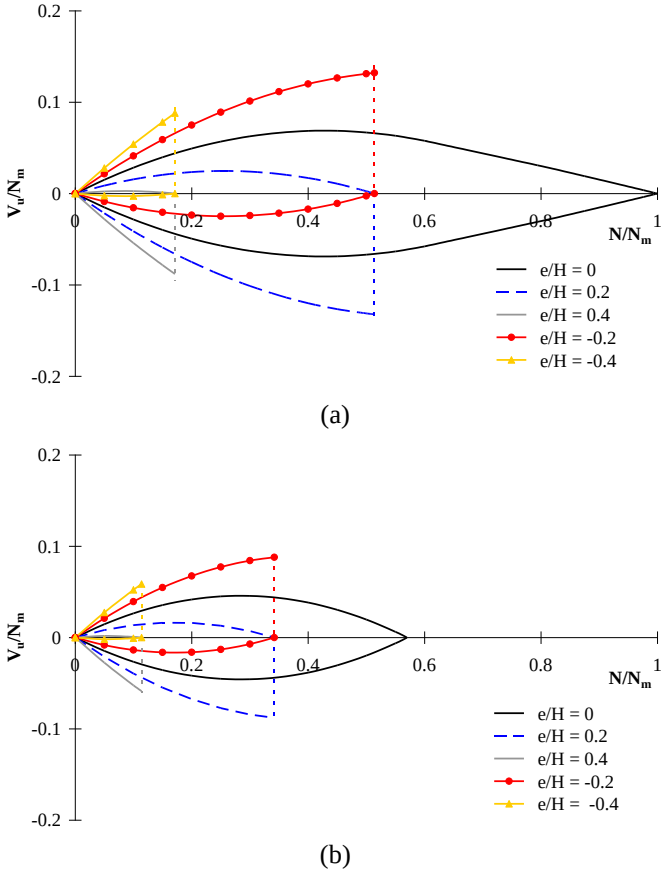

Figure 7.48 V/N_m–N/N_m domains for Augenti-Parisi model (orthog. dir.): (a) ELS; (b) ULS

If the section is fully resistant at ULS, then the normalised neutral axis depth is to be determined first by solving numerically one of the following equations:

$$\bar{e} = \frac{0.002\left(\bar{h}-0.38\right)\left(65.06+\bar{h}\right)}{\left(0.86+\bar{h}\right)\left(0.2-0.88\bar{h}+\bar{h}^2\right)} \qquad \text{for } \bar{e} > 0 \tag{7.212}$$

$$\bar{e} = -\frac{0.002\left(\bar{h}-0.38\right)\left(65.06+\bar{h}\right)}{\left(0.87+\bar{h}\right)\left(0.2-0.88\bar{h}+\bar{h}^2\right)} \qquad \text{for } \bar{e} < 0 \tag{7.213}$$

The allowable axial force can then be determined as:

$$\bar{N}_{\max} = 1 + \frac{0.18}{\bar{h}^3} - \frac{0.56}{\bar{h}^2} - \frac{0.01}{\bar{h}} \tag{7.214}$$

This allowable force is instead provided by the following equation related to cracked section at ULS:

$$\bar{N}_{\max} = \frac{1}{2\kappa_\mu}\left(1 - 2\bar{e}\right) \qquad \text{for } \bar{e} > 0 \tag{7.215}$$

$$\bar{N}_{\max} = \frac{1}{2\kappa_\mu}\left(1 + 2\bar{e}\right) \qquad \text{for } \bar{e} < 0 \tag{7.216}$$

In the case of uncracked section at ULS, the normalised neutral axis depth can be numerically determined through one of the following equations:

$$\bar{e} = \frac{a + b\bar{h} + c\bar{h}^2 + d\bar{h}^4 + f\bar{h}^5}{g + m\bar{h} + n\bar{h}^2 + p\bar{h}^3 + r\bar{h}^4} \qquad \text{for } \bar{e} > 0 \tag{7.217}$$

$$\bar{e} = -\frac{a + b\bar{h} + c\bar{h}^2 + d\bar{h}^4 + f\bar{h}^5}{g + m\bar{h} + n\bar{h}^2 + p\bar{h}^3 + r\bar{h}^4} \qquad \text{for } \bar{e} < 0 \tag{7.218}$$

where:

$a = -0.3\mu_\varepsilon^5$

$b = -0.22\mu_\varepsilon^4 + 1.01\mu_\varepsilon^5$

$c = 0.6\mu_\varepsilon^3 + 0.43\mu_\varepsilon^4 - 1.01\mu_\varepsilon^5$

$d = -1.88\mu_\varepsilon + 4.39\mu_\varepsilon^2 - 2.71\mu_\varepsilon^3 - 0.3\mu_\varepsilon^4 + 0.5\mu_\varepsilon^5$

$f = 1.13 - 3.76\mu_\varepsilon + 4.39\mu_\varepsilon^2 - 1.81\mu_\varepsilon^3 - 0.15\mu_\varepsilon^4 + 0.2\mu_\varepsilon^5$

$g = 1.01\mu_\varepsilon^5$

$m = 0.86\mu_\varepsilon^4 - 4.06\mu_\varepsilon^5$

$n = -3.58\mu_\varepsilon^3 - 2.59\mu_\varepsilon^4 + 6.09\mu_\varepsilon^5$

$p = 7.16\mu_\varepsilon^3 + 2.59\mu_\varepsilon^4 - 4.06\mu_\varepsilon^5$

$r = -3.76 + 8.78\mu_\varepsilon^2 - 5.42\mu_\varepsilon^3 - 0.6\mu_\varepsilon^4 + \mu_\varepsilon^5$

The allowable axial force is then defined as:

$$\bar{N}_{\max} = 1.26\mu_\varepsilon + 0.45\mu_\varepsilon^2 - 0.71\mu_\varepsilon^3 + \frac{0.18\mu_\varepsilon^3}{\bar{h}^3} + \frac{0.15\mu_\varepsilon^2 - 0.71\mu_\varepsilon^3}{\bar{h}^2} + \\ - \frac{0.63\mu_\varepsilon + 0.45\mu_\varepsilon^2 - 1.07\mu_\varepsilon^3}{\bar{h}} + \bar{h}^s\left(1.54 - \frac{0.66}{\mu_\varepsilon} - 0.95\mu_\varepsilon - 0.11\mu_\varepsilon^2 + 0.18\mu_\varepsilon^3\right) \tag{7.219}$$

Figures 7.49a and 7.49b show V/N_m–e/H strength domains related to ELS and ULS, respectively. It is underlined that the assumption of Augenti-Parisi constitutive model

(orthog. dir.) implies that the strength domain cannot be defined also at N/N_m = 0.7. This depends on the fact that supply strain ductility assumed for masonry leads to a maximum normalised axial force N/N_m = 0.57.

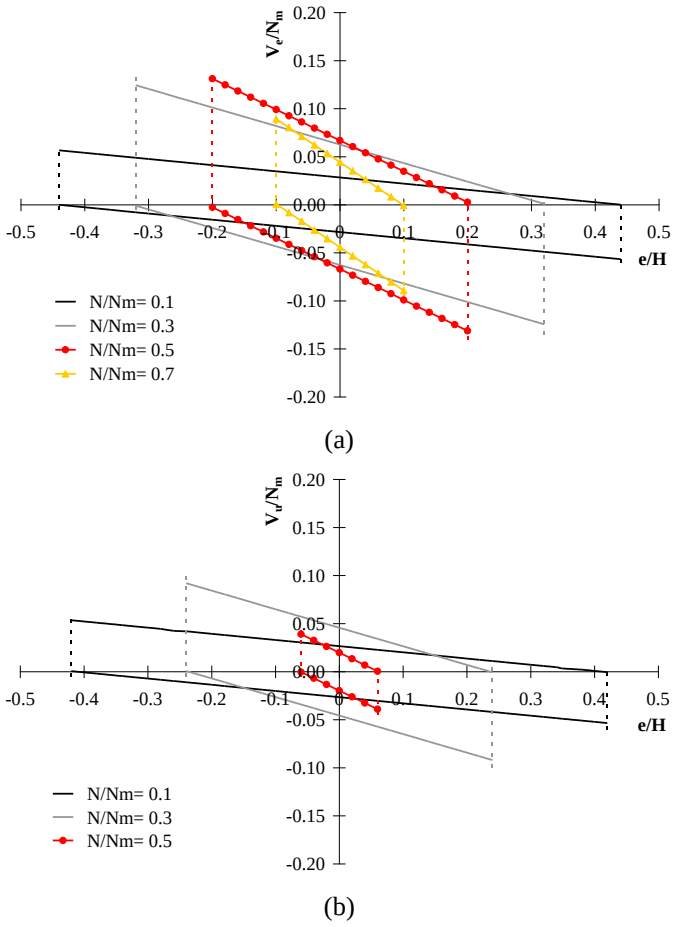

Figure 7.49 V/N_m–e/H domains for Augenti-Parisi model (orthog. dir.): (a) ELS; (b) ULS

7.3.5. Strength Domains for Augenti-Parisi Constitutive Model Related to Compression Parallel to Mortar Bed Joints

Assuming the stress-strain relationship proposed by Augenti and Parisi (2010a) for compression paralle to mortar bed joints (case of spandrel panels), the cross-section reaches ELS in cracked conditions if the normalised axial force N/N_m falls in the interval [0,0.64] and in uncracked conditions for N/N_m falling in the complimentary interval [0.64,1]. At ULS, the cross-section is cracked for N/N_m falling in the interval [0,0.69] and uncracked for N/N_m greater than 0.69. Based on these considerations, the

resisting shear forces of the extreme sections of the masonry panel at ELS and ULS (in both cracked and uncracked conditions) can be predicted through the equations presented below.

- **Left section at ELS in cracked conditions**

$$\bar{V}_e^r = -\frac{H}{B}\left[\bar{N}^r\left(\bar{e}^r+\frac{1}{2}\right)-0.57\left(\bar{N}^r-\bar{F}\right)^2+\bar{F}\left(\bar{f}-1\right)+\left(\bar{P}+\bar{Q}\right)\frac{B}{2H}\right] \qquad \text{for } \bar{e}^l>0 \tag{7.220}$$

$$\bar{V}_e^r = -\frac{H}{B}\left[\bar{N}^r\left(\bar{e}^r-\frac{1}{2}\right)+0.57\left(\bar{N}^r-\bar{F}\right)^2+\bar{F}\,\bar{f}+\left(\bar{P}+\bar{Q}\right)\frac{3B}{H}\right] \qquad \text{for } \bar{e}^l<0 \tag{7.221}$$

- **Left section at ELS in uncracked conditions**

$$\bar{V}_e^r = -\frac{H}{B}\left[\bar{N}^r\,\bar{e}^r+\frac{\bar{M}^l}{H}\left(\bar{h}^l\right)+\bar{F}\left(\bar{f}-\frac{1}{2}\right)+\left(\bar{P}+\bar{Q}\right)\frac{B}{2H}\right] \qquad \text{for } \bar{e}^l>0 \tag{7.222}$$

$$\bar{V}_e^r = -\frac{H}{B}\left[\bar{N}^r\,\bar{e}^r-\frac{\bar{M}^l}{H}\left(\bar{h}^l\right)+\bar{F}\left(\bar{f}-\frac{1}{2}\right)+\left(\bar{P}+\bar{Q}\right)\frac{B}{2H}\right] \qquad \text{for } \bar{e}^l<0 \tag{7.223}$$

where:

$$\frac{\bar{M}^l}{H}\left(\bar{h}^l\right)=\bar{N}^l\,\bar{e}^l=-\frac{0.03}{\bar{h}^{l3}}+\frac{0.11}{\bar{h}^{l2}}$$

- **Right section at ELS in cracked conditions**

$$\bar{V}_e^l = -\frac{H}{B}\left[\bar{N}^l\left(\bar{e}^l+\frac{1}{2}\right)-0.57\left(\bar{N}^l+\bar{F}\right)^2+\bar{F}\,\bar{f}-\left(\bar{P}+\bar{Q}\right)\frac{B}{2H}\right] \qquad \text{for } \bar{e}^r>0 \tag{7.224}$$

$$\bar{V}_e^l = -\frac{H}{B}\left[\bar{N}^l\left(\bar{e}^l-\frac{1}{2}\right)+0.57\left(\bar{N}^l+\bar{F}\right)^2+\bar{F}\left(\bar{f}-1\right)-\left(\bar{P}+\bar{Q}\right)\frac{B}{2H}\right] \qquad \text{for } \bar{e}^r<0 \tag{7.225}$$

- **Right section at ELS in uncracked conditions**

$$\bar{V}_e^l = -\frac{H}{B}\left[\bar{N}^l\,\bar{e}^l+\frac{\bar{M}^r}{H}\left(\bar{h}^r\right)+\bar{F}\left(\bar{f}-\frac{1}{2}\right)-\left(\bar{P}+\bar{Q}\right)\frac{B}{2H}\right] \qquad \text{for } \bar{e}^r>0 \tag{7.226}$$

$$\bar{V}_e^l = -\frac{H}{B}\left[\bar{N}^l\,\bar{e}^l - \frac{\bar{M}^r}{H}\left(\bar{h}^r\right) + \bar{F}\left(\bar{f} - \frac{1}{2}\right) - \left(\bar{P}+\bar{Q}\right)\frac{B}{2H}\right] \qquad \text{for } \bar{e}^r < 0 \tag{7.227}$$

- **Left section at ULS in cracked conditions**

$$\bar{V}_u^r = -\frac{H}{B}\left[\bar{N}^r\left(\bar{e}^r + \frac{1}{2}\right) - \kappa_\mu\left(\bar{N}^r - \bar{F}\right)^2 + \bar{F}\left(\bar{f} - 1\right) + \left(\bar{P}+\bar{Q}\right)\frac{3B}{H}\right] \qquad \text{for } \bar{e}^l > 0 \tag{7.228}$$

$$\bar{V}_u^r = -\frac{H}{B}\left[\bar{N}^r\left(\bar{e}^r - \frac{1}{2}\right) + \kappa_\mu\left(\bar{N}^r - \bar{F}\right)^2 + \bar{F}\,\bar{f} + \left(\bar{P}+\bar{Q}\right)\frac{3B}{H}\right] \qquad \text{for } \bar{e}^l < 0 \tag{7.229}$$

being:

$$\kappa_\mu = \frac{0.13 - 0.35\mu_\varepsilon - 0.17\mu_\varepsilon^2 + 0.08\mu_\varepsilon^3 - 0.02\mu_\varepsilon^4 + 0.002\mu_\varepsilon^5}{0.27 - 0.7\mu_\varepsilon - 0.34\mu_\varepsilon^2 + 0.17\mu_\varepsilon^3 - 0.03\mu_\varepsilon^4 + 0.003\mu_\varepsilon^5 - 0.001\mu_\varepsilon^6}$$

- **Left section at ULS in uncracked conditions**

$$\bar{V}_u^r = -\frac{H}{B}\left[\bar{N}^r\,\bar{e}^r + \frac{\bar{M}^l}{H}\left(\bar{h}^l\right) + \bar{F}\left(\bar{f} - \frac{1}{2}\right) + \left(\bar{P}+\bar{Q}\right)\frac{B}{2H}\right] \qquad \text{for } \bar{e}^l > 0 \tag{7.230}$$

$$\bar{V}_u^r = -\frac{H}{B}\left[\bar{N}^r\,\bar{e}^r - \frac{\bar{M}^l}{H}\left(\bar{h}^l\right) + \bar{F}\left(\bar{f} - \frac{1}{2}\right) + \left(\bar{P}+\bar{Q}\right)\frac{B}{2H}\right] \qquad \text{for } \bar{e}^l < 0 \tag{7.231}$$

where:

$$\frac{\bar{M}^l}{H}\left(\bar{h}^l\right) = \bar{N}^l\,\bar{e}^l = -\frac{0.03\mu_\varepsilon^3}{\bar{h}^{l3}} + \frac{0.02\mu_\varepsilon^2 + 0.09\mu_\varepsilon^3}{\bar{h}^{l2}} + \frac{0.14\mu_\varepsilon - 0.05\mu_\varepsilon^2 - 0.09\mu_\varepsilon^3}{\bar{h}^l} +$$
$$+ \bar{h}^{l2}\left(-0.35 - \frac{0.07}{\mu_\varepsilon^2} + \frac{0.17}{\mu_\varepsilon} + 0.16\mu_\varepsilon + 0.02\mu_\varepsilon^2 - 0.03\mu_\varepsilon^3 + 0.001\mu_\varepsilon^4\right) +$$
$$+ \bar{h}^l\left(0.35 - \frac{0.13}{\mu_\varepsilon} - 0.24\mu_\varepsilon - 0.04\mu_\varepsilon^2 + 0.06\mu_\varepsilon^3 - 0.002\mu_\varepsilon^4\right)$$

- **Right section at ULS in cracked conditions**

$$\bar{V}_u^l = -\frac{H}{B}\left[\bar{N}^l\left(\bar{e}^l + \frac{1}{2}\right) - \kappa_\mu\left(\bar{N}^l + \bar{F}\right)^2 + \bar{F}\,\bar{f} - \left(\bar{P}+\bar{Q}\right)\frac{3B}{H}\right] \qquad \text{for } \bar{e}^r > 0 \tag{7.232}$$

$$\bar{V}_u^l = -\frac{H}{B}\left[\bar{N}^l\left(\bar{e}^l - \frac{1}{2}\right) + \kappa_\mu\left(\bar{N}^l + \bar{F}\right)^2 + \bar{F}\,\bar{f} - \left(\bar{P}+\bar{Q}\right)\frac{3B}{H}\right] \qquad \text{for } \bar{e}^r < 0 \tag{7.233}$$

- **Right section at ULS in uncracked conditions**

$$\bar{V}_u^l = -\frac{H}{B}\left[\bar{N}^l\,\bar{e}^l + \frac{\bar{M}^r}{H}\left(\bar{h}^r\right) + \bar{F}\left(\bar{f} - \frac{1}{2}\right) - \left(\bar{P}+\bar{Q}\right)\frac{B}{2H}\right] \qquad \text{for } \bar{e}^r > 0 \tag{7.234}$$

$$\bar{V}_u^l = -\frac{H}{B}\left[\bar{N}^l\,\bar{e}^l - \frac{\bar{M}^r}{H}\left(\bar{h}^r\right) + \bar{F}\left(\bar{f} - \frac{1}{2}\right) - \left(\bar{P}+\bar{Q}\right)\frac{B}{2H}\right] \qquad \text{for } \bar{e}^r < 0 \tag{7.235}$$

where the normalised bending moment can be computed as a function of the neutral axis depth by using the equation derived for the left section at ULS.

- **Graphic representations**

Different strength domains were obtained also in the case of the constitutive model proposed by Augenti and Parisi (2010a) for compression parallel to mortar bed joints. The three-dimensional strength domains corresponding to ELS and ULS are respectively shown in Figures 7.50 and 7.51.

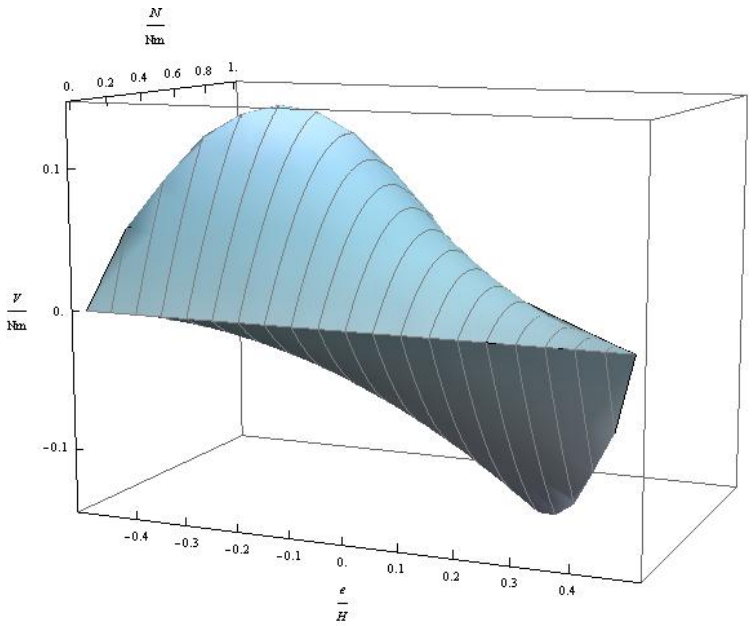

Figure 7.50 Three-dimensional strength domain at ELS for Augenti-Parisi model (paral. dir.)

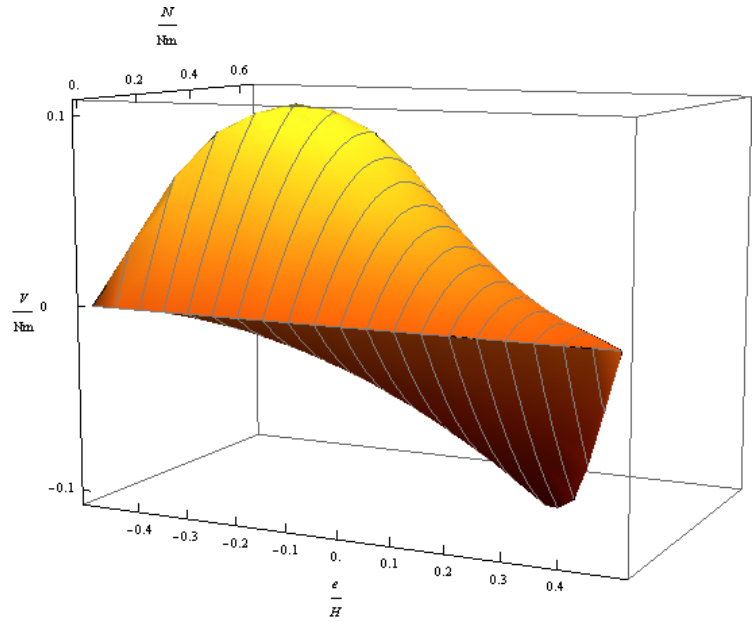

Figure 7.51 Three-dimensional strength domain at ULS for Augenti-Parisi model (paral. dir.)

Figures 7.52a and 7.52b show V/N_m–N/N_m strength domains at ELS and ULS, respectively, which are truncated at axial force values provided by the following equations:

$$\bar{N}_{\max} = 0.87\left(1-2\bar{e}\right) \qquad \text{for } \bar{e} > 0 \tag{7.236}$$

$$\bar{N}_{\max} = 0.87\left(1+2\bar{e}\right) \qquad \text{for } \bar{e} < 0 \tag{7.237}$$

in the case of cracked section at ELS.

Otherwise, for an uncracked section at ULS, the normalised neutral axis depth can be first determined through one of the following equations:

$$\bar{e} = \frac{0.11\left(\bar{h}+0.24\right)}{\left(\bar{h}-0.53\right)\left(\bar{h}-0.22\right)\left(\bar{h}+0.76\right)} \qquad \text{for } \bar{e} > 0 \tag{7.238}$$

$$\bar{e} = -\frac{0.11\left(\bar{h}+0.24\right)}{\left(\bar{h}-0.53\right)\left(\bar{h}-0.22\right)\left(\bar{h}+0.76\right)} \qquad \text{for } \bar{e} < 0 \tag{7.239}$$

so the allowable axial force can be computed as follows:

$$\bar{N}_{\max} = 1+\frac{0.09}{\bar{h}^3}-\frac{0.45}{\bar{h}^2} \tag{7.240}$$

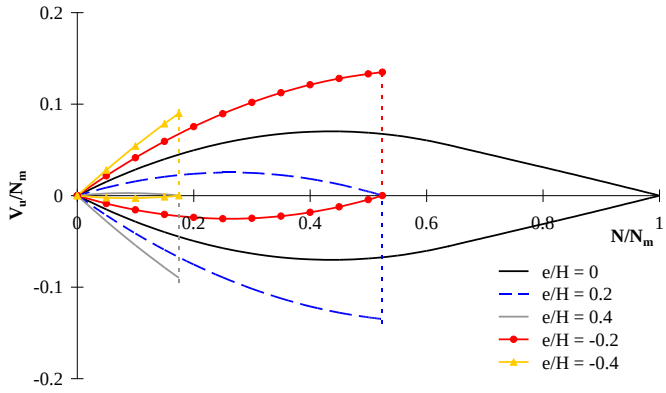

(a)

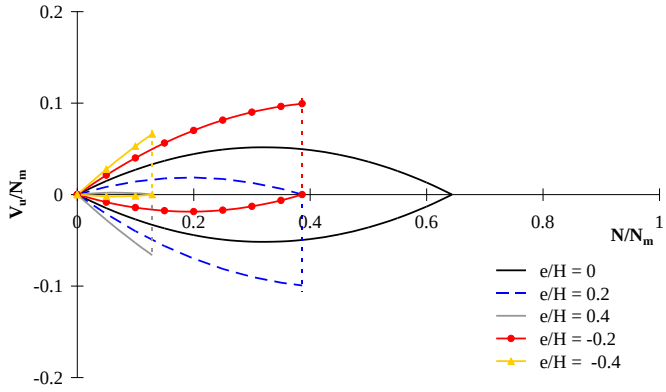

(b)

Figure 7.52 V/N_m–N/N_m domains for Augenti-Parisi model (paral. dir.): (a) ELS; (b) ULS

For a cracked section at ULS the allowable axial force is given by:

$$\bar{N}_{\max} = \frac{1}{2\kappa_\mu}\left(1-2\bar{e}\right) \qquad \text{for}\, \bar{e} > 0 \tag{7.241}$$

$$\bar{N}_{\max} = \frac{1}{2\kappa_\mu}\left(1+2\bar{e}\right) \qquad \text{for}\, \bar{e} < 0 \tag{7.242}$$

while, in the case of uncracked section at ULS, the normalised neutral axis depth can be first computed as:

$$\bar{e} = \frac{a+b\bar{h}+c\bar{h}^2+d\bar{h}^4+f\bar{h}^5}{g+m\bar{h}+n\bar{h}^2+p\bar{h}^3+r\bar{h}^4} \qquad \text{for}\, \bar{e} > 0 \tag{7.243}$$

$$\bar{e} = -\frac{a+b\bar{h}+c\bar{h}^2+d\bar{h}^4+f\bar{h}^5}{g+m\bar{h}+n\bar{h}^2+p\bar{h}^3+r\bar{h}^4} \qquad \text{for}\, \bar{e} < 0 \tag{7.244}$$

where:

$$a = -0.2\mu_\varepsilon^5$$
$$b = 0.18\mu_\varepsilon^4 + 0.67\mu_\varepsilon^5$$
$$c = 1.02\mu_\varepsilon^3 - 0.35\mu_\varepsilon^4 - 0.67\mu_\varepsilon^5$$
$$d = -\mu_\varepsilon + 2.63\mu_\varepsilon^2 - 1.81\mu_\varepsilon^3 - 0.27\mu_\varepsilon^4 + 0.46\mu_\varepsilon^5 - 0.013\mu_\varepsilon^6 + 0.0005\mu_\varepsilon^7$$
$$f = -0.53 + 2\mu_\varepsilon - 2.63\mu_\varepsilon^2 + 1.21\mu_\varepsilon^3 + 0.13\mu_\varepsilon^4 - 0.18\mu_\varepsilon^5 + 0.004\mu_\varepsilon^6 - 0.0001\mu_\varepsilon^7$$
$$g = 0.67\mu_\varepsilon^5$$
$$m = -0.7\mu_\varepsilon^4 - 2.7\mu_\varepsilon^5$$
$$n = -6.15\mu_\varepsilon^3 + 2.11\mu_\varepsilon^4 + 4.04\mu_\varepsilon^5$$
$$p = 12.3\mu_\varepsilon^3 - 2.11\mu_\varepsilon^4 - 2.7\mu_\varepsilon^5$$
$$r = -2\mu_\varepsilon + 5.26\mu_\varepsilon^2 - 3.63\mu_\varepsilon^3 - 0.54\mu_\varepsilon^4 + 0.93\mu_\varepsilon^5 - 0.025\mu_\varepsilon^6 + 0.001\mu_\varepsilon^7$$

Therefore, the allowable axial force can be computed as:

$$\bar{N}_{\max} = 1.64\mu_\varepsilon - 0.28\mu_\varepsilon^2 - 0.36\mu_\varepsilon^3 + \frac{0.09\mu_\varepsilon^3}{\bar{h}^3} - \frac{0.09\mu_\varepsilon^2 + 0.36\mu_\varepsilon^3}{\bar{h}^2} + - \frac{0.82\mu_\varepsilon - 0.28\mu_\varepsilon^2 - 0.54\mu_\varepsilon^3}{\bar{h}} + + \bar{h}\left(0.7 - \frac{0.27}{\mu_\varepsilon} - 0.48\mu_\varepsilon - 0.07\mu_\varepsilon^2 + 0.12\mu_\varepsilon^3 - 0.003\mu_\varepsilon^4 + 0.0001\mu_\varepsilon^5\right) \quad (7.245)$$

Figures 7.53a and 7.53b show V/N_m–e/H strength domains related to ELS and ULS, respectively. Opposed to the case of Augenti-Parisi constitutive model for compression orthogonal to mortar bed joints, a V/N_m–e/H strength domain can be defined also at $N/N_m = 0.7$.

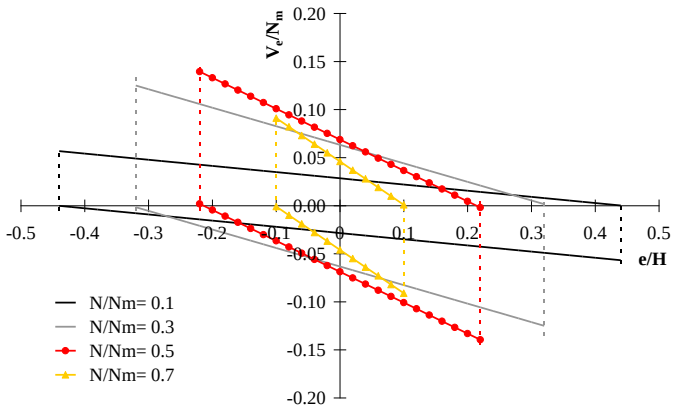

(a)

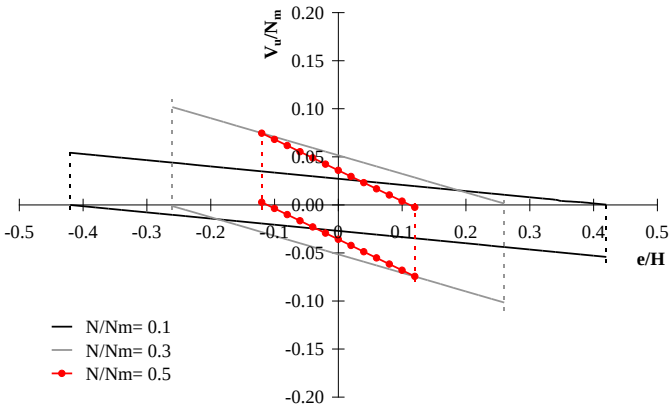

(b)

Figure 7.53 V/N_m–e/H domains for Augenti-Parisi model (paral. dir.): (a) ELS; (b) ULS

7.4. Moment-Curvature Diagrams

The definition of moment-curvature relationships for cross-sections likely to suffer large strains with significant cracking and yielding can play a key role in non-linear analysis of masonry structures. Therefore, proper mechanical parameters should be defined also in lumped plasticity models based on frame-equivalent idealisation of masonry walls with openings. In fact, mechanical modelling of macro-elements includes not only the definition of both flexural and shear strengths through interaction domains, but also their flexibility, ductility, and deformation capacity. To that end, additional information can be provided by moment-curvature diagrams, as well as moment-rotation or force-displacement curves.

In this section, moment-curvature diagrams derived for several constitutive models are presented and discussed (Parisi and Augenti, 2010). Moment-curvature analysis was carried out by assuming:

- a rectangular cross-section with thickness *s* and gross height *H*;
- masonry as a homogeneous material with zero tensile strength in bending; and
- plane cross-sections after bending deformation (Euler-Bernoulli hypothesis).

Since the effective cross-section changes with the applied axial force, moment-curvature diagrams were derived through an incremental iterative procedure based on the application of an increasing maximum axial strain and the computation of the relevant neutral axis depth and resisting bending moment.

Axial force and bending moment were obtained by means of the equations used to define flexural strength domains, but strain ductility was regarded as demand on masonry, rather than a capacity parameter.

For the sake of simplicity, the normalised neutral axis depth (denoted as $\bar{h} = h/H$) was employed for both cracked and uncracked cross-sections. This approach allowed to define both axial force and bending moment as functions of h/H and the *strain ductility demand* $\mu_{\varepsilon,d} = \varepsilon_{max}/\varepsilon_k$ corresponding to the given maximum axial strain (ε_{max}). The average bending curvature of the cross-section was then expressed as $\phi = \varepsilon_{max}/h$. In order to get analytical results independent of both masonry strength and sectional dimensions, bending curvature was multiplied by the gross height H. Therefore, the diagrams presented herein are defined as normalised bending moment $M/(N_m \cdot H)$ versus normalised curvature ϕH.

The cracked and uncracked sectional conditions considered in the moment-curvature analysis are shown in Figures 7.54a and 7.54b. The cross-section is cracked under low compressive forces and large curvature demands, while it is uncracked under high compressive forces and small curvature demands.

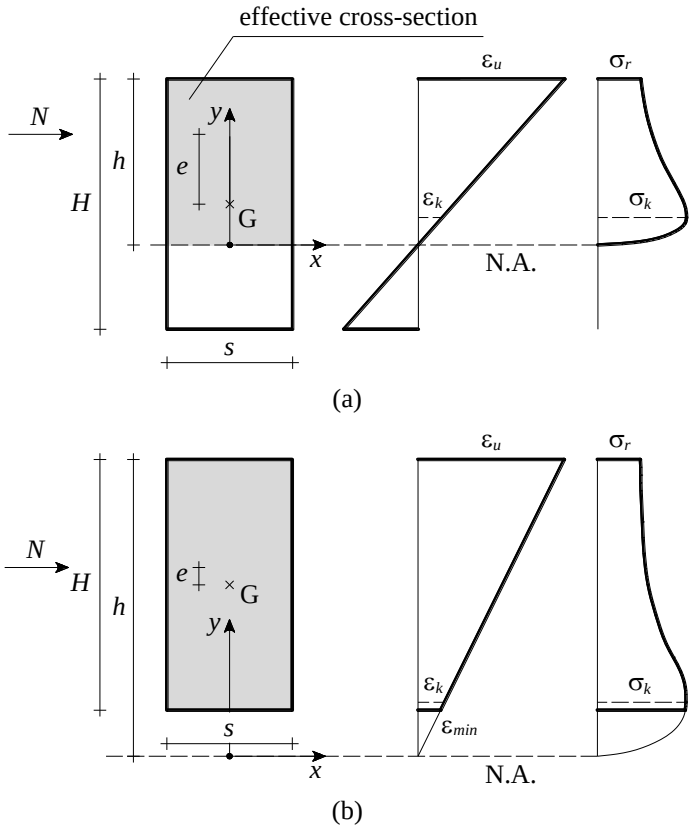

Figure 7.54 Behaviour of URM cross-section under (a) low compression and large curvature and (b) high compression and small curvature

Moment-curvature diagrams were derived for the following axial force levels: N/N_m = 0.1; N/N_m = 0.25; N/N_m = 0.5; and N/N_m = 0.75. The normalised curvature was evaluated at both ELS and ULS, and was denoted as $\phi_e H$ and $\phi_u H$, respectively. In order to ensure a better understanding of the sectional behaviour, the following parameters were assessed at each axial force level:

- the ratio $\alpha_M = M_{max}/M_e$ between the maximum resisting moment and the yielding moment, which allowed to quantify sectional overstrength after yielding of masonry;
- the ratio $\beta_M = M_{max}/M_u$ between the maximum resisting moment and the ultimate moment, which is a capacity index associated with hardening or softening in the plastic range;
- the ratio $\gamma_M = M_u/M_e$, which is associated with the overall sectional behaviour after yielding;
- the curvature ductility $\mu_\phi = \phi_u/\phi_e$;
- the curvature capacity $C_\phi = (\phi_u - \phi_e)/\phi_e = \mu_\phi - 1$; and
- the curvature ratios at ELS and ULS:

$$\rho_{\phi_e}\left(\bar{N}\right) = \frac{\phi_e}{\phi_{e(0.1)}}; \qquad \rho_{\phi_u}\left(\bar{N}\right) = \frac{\phi_u}{\phi_{u(0.1)}}$$

  which describe the curvature variation as the normalised axial force increases from a reference value N/N_m = 0.1. These parameters allow monitoring of sectional deformation capacity under increasing compression level.

Figure 7.55 shows the characteristic points of the moment-curvature diagram, namely those corresponding to yielding (ELS), peak resistance (Peak), and ultimate state (ULS).

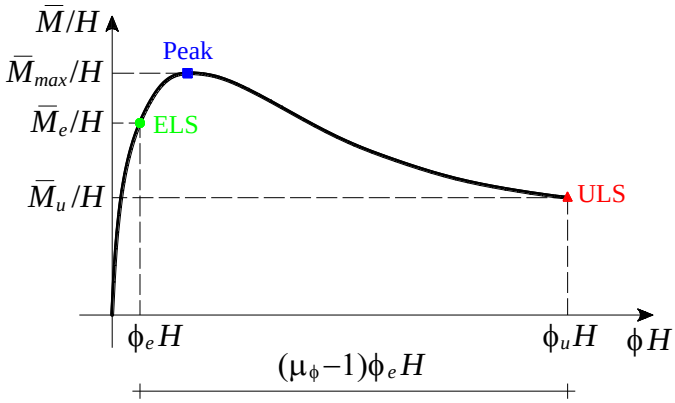

Figure 7.55 Characteristic points of normalised moment-curvature diagram

7.4.1. Moment-Curvature Diagrams for EPP Constitutive Model

If the compressive behaviour of masonry is modelled through the EPP constitutive model, as the normalised axial force increases in the interval [0,0.5], ultimate moment increases while ultimate curvature reduces. As N/N_m increases in the interval [0.5,1], both ultimate moment and ultimate curvature reduce. On the contrary, yielding curvature always increases with the applied axial force. Moment-curvature diagrams corresponding to the axial force levels considered in this study are plotted in Figure 7.56, while Figure 7.57 shows ϕH–N/N_m and ρ_ϕ–N/N_m curves.

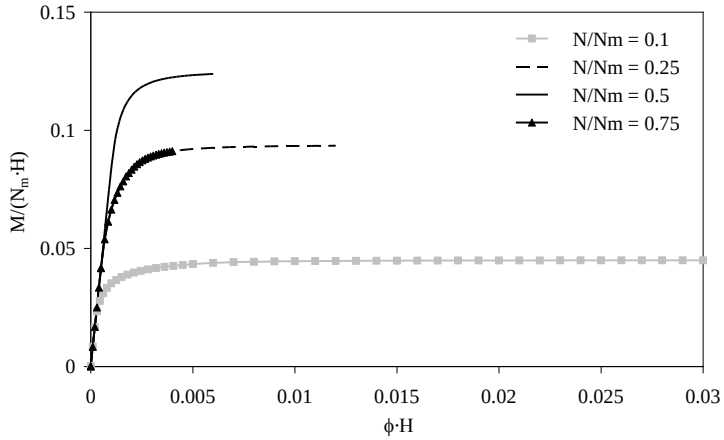

Figure 7.56 Moment-curvature diagrams for EPP model

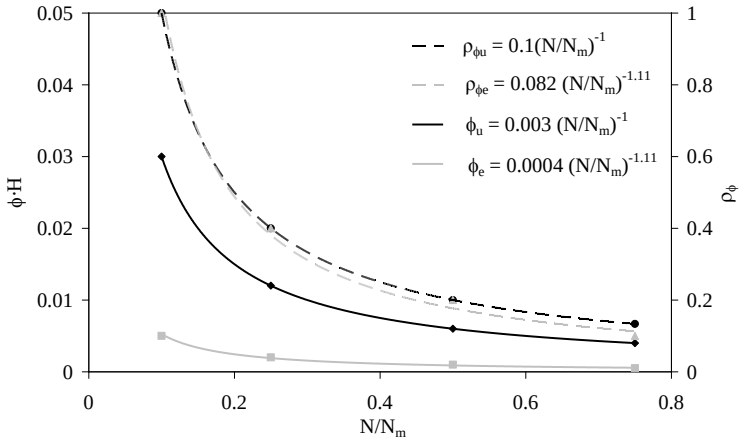

Figure 7.57 Variation in curvatures and curvature ratios for EPP model

The moment-curvature diagram corresponding to N/N_m = 0.75 is partially superimposed to that corresponding to N/N_m = 0.25. Nevertheless, both yielding and

ultimate curvatures at $N/N_m = 0.75$ are lower than the others. The sectional parameters were assessed at each characteristic point of moment-curvature diagrams (Tables 7.1 and 7.2). As the normalised axial force is increased from 0.1 to 0.5, the resisting moments M_e and M_u increases of about 49%; as N/N_m is increased from 0.5 to 0.75, such moments reduce of about 49% and 27%, respectively.

Table 7.1 Resisting moments and other parameters for EPP model

$\bar{N}$	$\bar{M}_e/H$	$\bar{M}_{max}/H$	$\bar{M}_u/H$	α_M	β_M	γ_M
0.10	0.043	0.045	0.045	1.04	1	1.04
0.25	0.083	0.093	0.093	1.12	1	1.12
0.50	0.083	0.124	0.124	1.49	1	1.49
0.75	0.042	0.091	0.091	2.19	1	2.19

Table 7.2 Curvatures and other parameters for EPP model

$\bar{N}$	$\phi_e H$ [%]	$\phi_u H$ [%]	μ_ϕ	C_ϕ	$\rho_{\phi e}(\bar{N})$	$\rho_{\phi u}(\bar{N})$
0.10	0.50	3.00	6.00	5.00	1.00	1.00
0.25	0.20	1.20	6.00	5.00	0.40	0.40
0.50	0.10	0.60	6.00	5.00	0.20	0.20
0.75	0.05	0.40	8.00	7.00	0.10	0.13

Sectional overstrength α_M increases significantly with the given axial force. It is worth noting that EPP model leads to $M_u = M_{max}$ (and hence $\beta_M = 1$) and $\alpha_M = \gamma_M$. Curvature reduces rapidly under increasing normalised axial force. In fact, the curvature at $N/N_m = 0.25$ is about 60% lower than that associated with $N/N_m = 0.1$, reaching 20% of the initial value at $N/N_m = 0.5$. In the case of $N/N_m = 0.75$, both yielding and ultimate curvatures are 10% of those related to $N/N_m = 0.1$.

For a strain ductility $\mu_\varepsilon = 3.75$ for the EPP constitutive model, curvature ductility is $\mu_\phi = 6$ for N/N_m falling in the interval [0,0.5]. For $N/N_m = 0.75$, curvature ductility is equal to 8 since the cross-section is fully resistant at ELS and cracked at ULS.

7.4.2. Moment-Curvature Diagrams for Turnšek-Čačovič Constitutive Model

Moment-curvature diagrams corresponding to the Turnšek-Čačovič constitutive model are plotted in Figure 7.58, while both curves ϕH–N/N_m and ρ_ϕ–N/N_m are plotted in Figure 7.59.

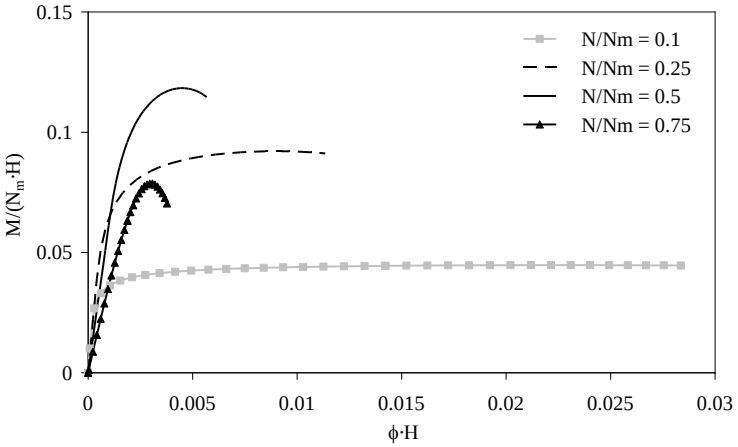

Figure 7.58 Moment-curvature diagrams for Turnšek-Čačovič model

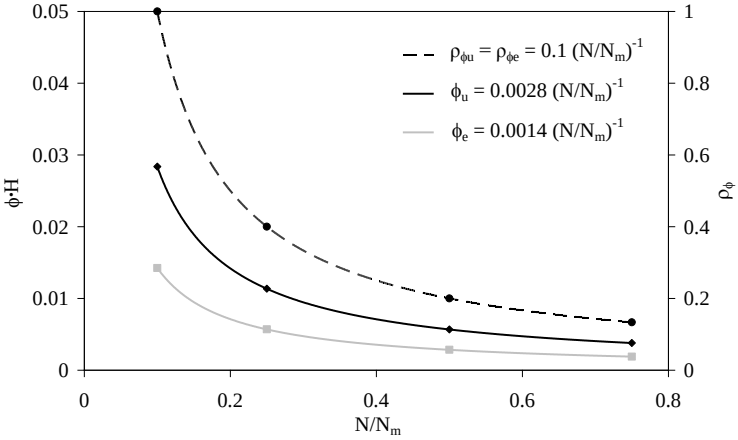

Figure 7.59 Variation in curvatures and curvature ratios for Turnšek-Čačovič model

For the maximum compression level considered in the analysis, the resisting moment increases linearly up to peak as the given curvature increases. A significant strength deterioration occurs under larger curvatures. Strain softening of masonry does not considerably affect the moment-curvature relationship corresponding to $N/N_m = 0.1$.
Non-linear sectional parameters were also assessed and are listed in Tables 7.3 and 7.4. Sectional overstrength α_M is slightly higher than γ_M since the resisting moment increases as yielding develops over the masonry cross-section. On the other hand, γ_M is almost equal to β_M, because strength degradation is rather equal to hardening. Yielding curvature is larger than that corresponding to EPP and EC6 constitutive laws (see Sects. 7.4.1 and 7.4.3). Ultimate curvature reduces as the given axial force increases. Curvature ductility is lower and equal to about 2 at any compression level.

Table 7.3 Resisting moments and other parameters for Turnšek-Čačovič model

$\bar{N}$	$\bar{M}_e/H$	$\bar{M}_{max}/H$	$\bar{M}_u/H$	α_M	β_M	γ_M
0.10	0.044	0.045	0.045	1.01	1.00	1.00
0.25	0.090	0.092	0.091	1.02	1.01	1.01
0.50	0.111	0.118	0.115	1.07	1.03	1.03
0.75	0.063	0.079	0.070	1.24	1.12	1.11

Table 7.4 Curvatures and other parameters for Turnšek-Čačovič model

$\bar{N}$	$\phi_e H$ [%]	$\phi_u H$ [%]	μ_ϕ	C_ϕ	$\rho_{\phi e}\left(\bar{N}\right)$	$\rho_{\phi u}\left(\bar{N}\right)$
0.10	1.42	2.84	1.99	0.99	1.00	1.00
0.25	0.57	1.13	1.99	0.99	0.40	0.40
0.50	0.28	0.57	1.99	0.99	0.20	0.20
0.75	0.19	0.38	2.01	1.01	0.13	0.13

7.4.3. Moment-Curvature Diagrams for EC6 Constitutive Model

The moment-curvature diagrams derived for EC6 constitutive model are plotted in Figure 7.60. The curves ϕH–N/N_m and ρ_ϕ–N/N_m are shown in Figure 7.61. The relationship between the bending moment and the given curvature is rather linear up to ULS in the case of normalised axial force N/N_m = 0.75. The variations in both yielding and ultimate curvatures are not considerably different from those observed in the case of EPP constitutive model.

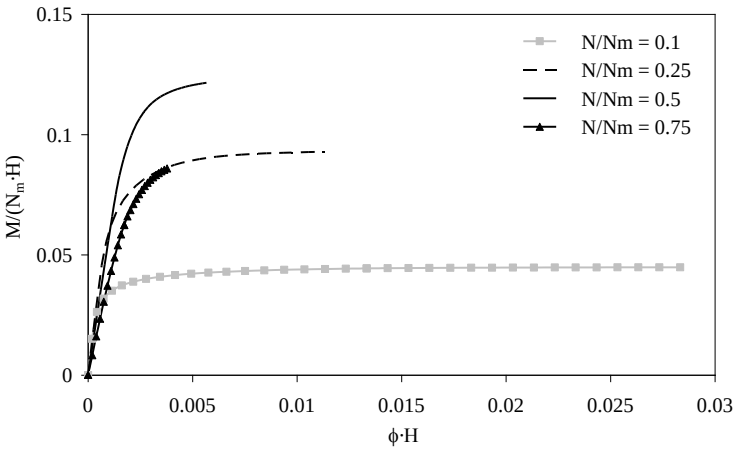

Figure 7.60 Moment-curvature diagrams for EC6 model

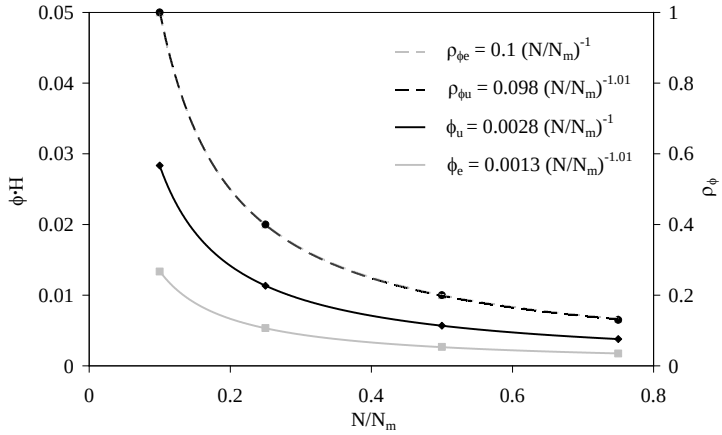

Figure 7.61 Variation in curvatures and curvature ratios for EC6 model

The presence of a plastic plateau in EC6 stress-strain relationship leads to $M_u = M_{max}$ (and hence $\beta_M = 1$) and $\alpha_M = \gamma_M$ (Table 7.5). Such coefficients are lower than those related to the EPP constitutive model, showing a lower resisting moment increase in the post-elastic range. This depends on the fact that the assumption of EC6 model produces a yielding moment higher than that related to the EPP model. Sectional overstrength is about 63% and 75% those evaluated for N/N_m = 0.1–0.5 and N/N_m = 0.75, respectively, in the case of EPP model. Yielding curvature is 2.7 and 3.4 times those corresponding to N/N_m = 0.1–0.5 and N/N_m = 0.75, respectively, in the case of EPP model (Table 7.6). On the contrary, ultimate curvature is about 95% that corresponding to the EPP constitutive model, resulting in lower curvature ductility.

Table 7.5 Resisting moments and other parameters for EC6 model

$\bar{N}$	$\bar{M}_e/H$	$\bar{M}_{max}/H$	$\bar{M}_u/H$	α_M	β_M	γ_M
0.10	0.044	0.045	0.045	1.01	1	1.01
0.25	0.090	0.093	0.093	1.03	1	1.03
0.50	0.109	0.121	0.121	1.11	1	1.11
0.75	0.062	0.086	0.086	1.38	1	1.38

Table 7.6 Curvatures and other parameters for EC6 model

$\bar{N}$	$\phi_e H$ [%]	$\phi_u H$ [%]	μ_ϕ	C_ϕ	$\rho_{\phi e}\left(\bar{N}\right)$	$\rho_{\phi u}\left(\bar{N}\right)$
0.10	1.33	2.83	2.12	1.12	1.00	1.00
0.25	0.53	1.13	2.12	1.12	0.40	0.40
0.50	0.27	0.57	2.12	1.12	0.20	0.20
0.75	0.17	0.38	2.18	1.18	0.13	0.13

7.4.4. Moment-Curvature Diagrams for Augenti-Parisi Constitutive Model Related to Compression Orthogonal to Mortar Bed Joints

The moment-curvature diagrams corresponding to Augenti-Parisi constitutive model for compression orthogonal to mortar bed joints are plotted in Figure 7.62. The curves $\phi H–N/N_m$ and $\rho_\phi–N/N_m$ are plotted in Figure 7.63.

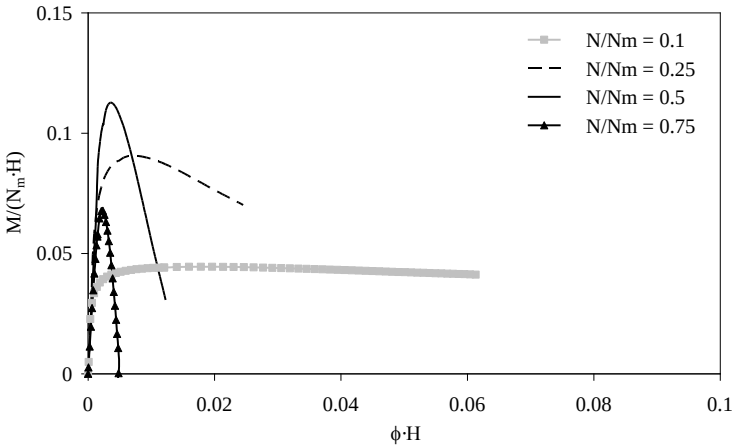

Figure 7.62 Moment-curvature diagrams for Augenti-Parisi model (orthog. dir.)

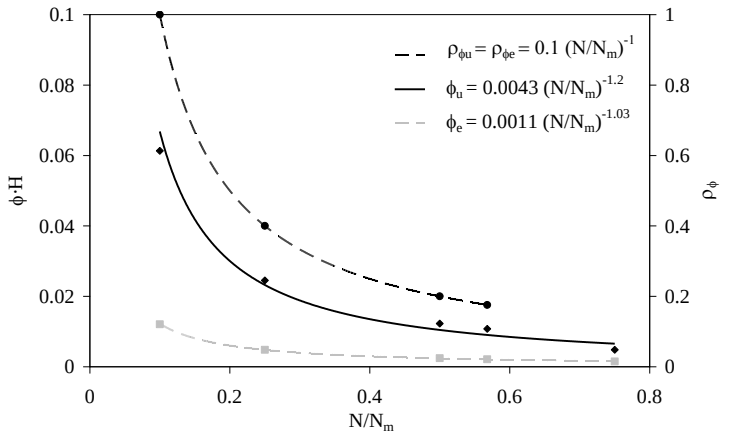

Figure 7.63 Variation in curvatures and curvature ratios for Augenti-Parisi model (orthog. dir.)

The resisting moments are not considerably different from those corresponding to other constitutive laws (Table 7.7), while the moment-curvature relationship is significantly affected by strain softening of masonry, except in the case of $N/N_m = 0.1$. In fact, the parameter β_M is very high in the case of $N/N_m = 0.5$.

For a strain ductility $\mu_\varepsilon = 5$, curvature ductility is $\mu_\phi = 5.09$ for $N/N_m = 0.1–0.5$ and $\mu_\phi = 3.22$ for $N/N_m = 0.75$ (Table 7.8). Amongst the constitutive models considered in the analysis, the stress-strain relation proposed by Augenti and Parisi (2010a) for masonry subjected to compression orthogonal to mortar bed joints is the only one where curvature ductility is lower than strain ductility at $N/N_m = 0.75$. This depends on the fact that a ductility demand equal to 2.6 (i.e., a few higher than one-half of supply ductility) corresponds to ultimate curvature.

Table 7.7 Resisting moments and other parameters for Augenti-Parisi model (orthog. dir.)

$\bar{N}$	$\bar{M}_e/H$	$\bar{M}_{max}/H$	$\bar{M}_u/H$	α_M	β_M	γ_M
0.10	0.044	0.044	0.041	1.01	1.08	0.93
0.25	0.088	0.091	0.070	1.02	1.29	0.79
0.50	0.104	0.113	0.031	1.08	3.67	0.29
0.75	0.058	0.068	0	1.17	∞	0

Table 7.8 Curvatures and other parameters for Augenti-Parisi model (orthog. dir.)

$\bar{N}$	$\phi_e H$ [%]	$\phi_u H$ [%]	μ_ϕ	C_ϕ	$\rho_{\phi e}(\bar{N})$	$\rho_{\phi u}(\bar{N})$
0.10	1.21	6.13	5.09	4.09	1.00	1.00
0.25	0.48	2.45	5.09	4.09	0.40	0.40
0.50	0.24	1.23	5.09	4.09	0.20	0.20
0.75	0.15	0.48	3.22	2.22	0.12	0.08

7.4.5. Moment-Curvature Diagrams for Augenti-Parisi Constitutive Model Related to Compression Parallel to Mortar Bed Joints

The moment-curvature diagrams corresponding to Augenti-Parisi constitutive model for compression orthogonal to mortar bed joints are plotted in Figure 7.64. The curves $\phi H–N/N_m$ and $\rho_\phi–N/N_m$ are plotted in Figure 7.65.

Also in this case, the resisting moments are not considerably different from those corresponding to other constitutive laws (Table 7.9), while the moment-curvature relationship is significantly affected by strain softening of masonry. For a strain ductility $\mu_\varepsilon = 6$, curvature ductility is $\mu_\phi = 6.53$ at any compression level (Table 7.10). Whilst yielding curvature is lower than those corresponding to EC6 and Turnšek-Čačovič constitutive models, ultimate curvature is 2.9 and 3.4 higher for $N/N_m = 0.1–0.5$ and $N/N_m = 0.75$, respectively. Nonetheless, the law of variation of both curvatures versus axial force does not diverge from that corresponding to Turnšek-Čačovič model.

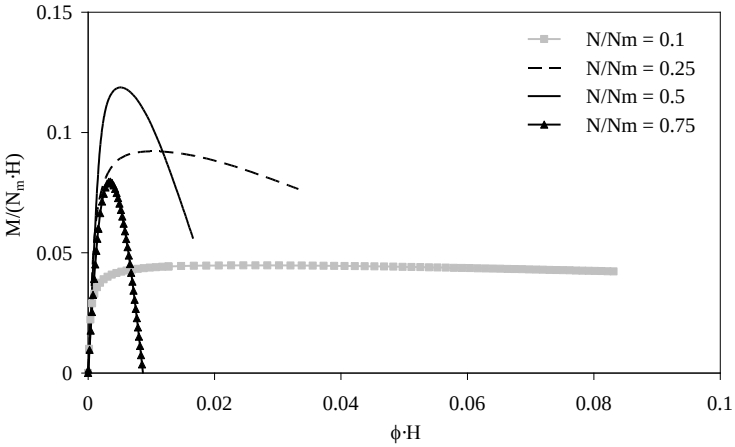

Figure 7.64 Moment-curvature diagrams for Augenti-Parisi model (paral. dir.)

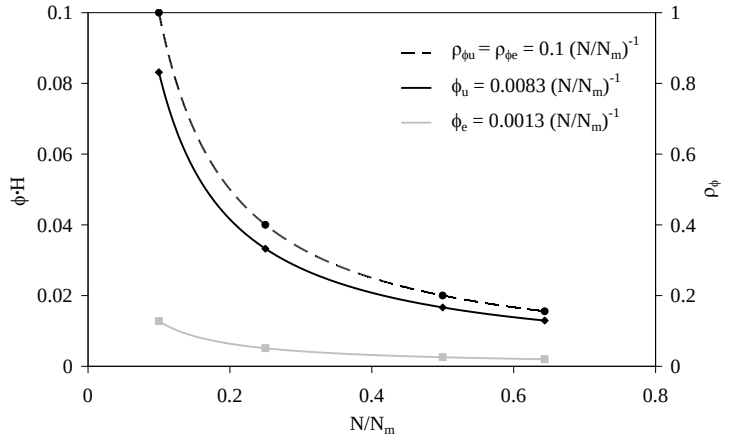

Figure 7.65 Variation in curvatures and curvature ratios for Augenti-Parisi model (paral. dir.)

Table 7.9 Resisting moments and other parameters for Augenti-Parisi model (paral. dir.)

$\bar{N}$	$\bar{M}_e/H$	$\bar{M}_{max}/H$	$\bar{M}_u/H$	α_M	β_M	γ_M
0.10	0.044	0.045	0.042	1.01	1.06	0.95
0.25	0.089	0.092	0.076	1.03	1.21	0.86
0.50	0.107	0.119	0.056	1.11	2.13	0.52
0.75	0.060	0.080	0	1.23	∞	0

Table 7.10 Curvatures and other parameters for Augenti-Parisi model (paral. dir.)

$\bar{N}$	$\phi_e H$ [%]	$\phi_u H$ [%]	μ_ϕ	C_ϕ	$\rho_{\phi e}(\bar{N})$	$\rho_{\phi u}(\bar{N})$
0.10	1.27	8.31	6.53	5.53	1.00	1.00
0.25	0.51	3.33	6.53	5.53	0.40	0.40
0.50	0.25	1.66	6.53	5.53	0.20	0.20
0.75	0.20	1.29	6.53	5.53	0.15	0.15

7.4.6. Remarks

Comparisons between ϕH–N/N_m curves related to the stress-strain relations considered above were made for both yielding and ultimate curvatures (Figs. 7.66 and 7.67).

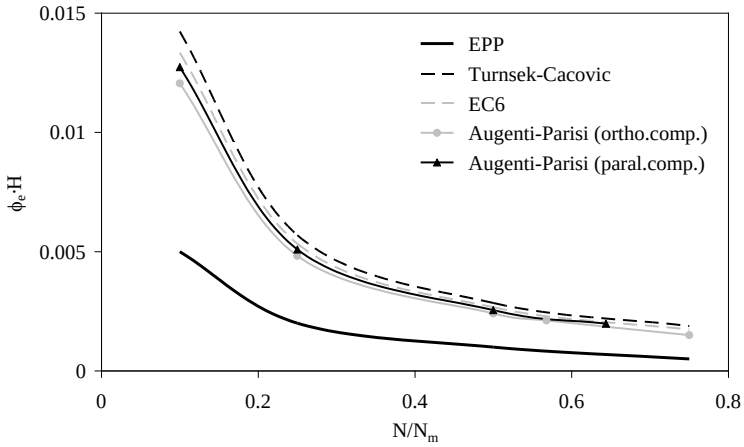

Figure 7.66 Yielding curvature versus axial force

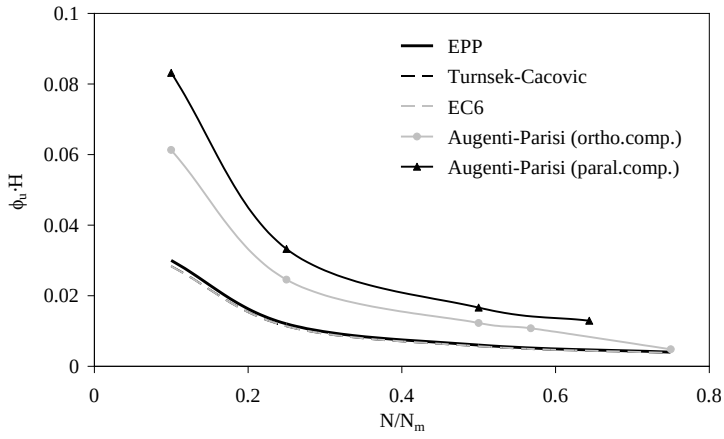

Figure 7.67 Ultimate curvature versus axial force

It is clear that curvatures depend on their relevant strains at yielding and ultimate limit states of masonry. Moment-curvature diagrams corresponding to different constitutive laws for N/N_m = 0.1 are compared themselves in Figure 7.68 (ultimate curvatures are identified by vertical lines). Yielding curvature is almost the same for all constitutive models, except for the EPP model. Ultimate moments are almost equal, while ultimate curvatures are notably different.

Curvature ductility is never less than 2 and always higher than strain ductility of masonry, except for N/N_m = 0.75 in the case of Augenti-Parisi model for compression orthogonal to mortar bed joints (Fig. 7.69). Only for this value of normalised axial force and for μ_ε = 3.5 (EPP model) and μ_ε = 5 (Augenti-Parisi model for compression orthogonal to mortar bed joints) the ratio μ_ϕ/μ_ε depends on the applied axial force. Vice versa, in all other cases, such a ratio is independent of the compression level.

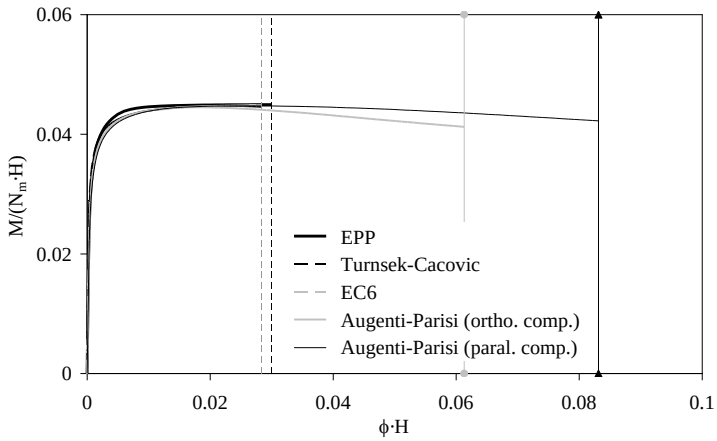

Figure 7.68 Comparison between moment-curvature diagrams for N/N_m = 0.1

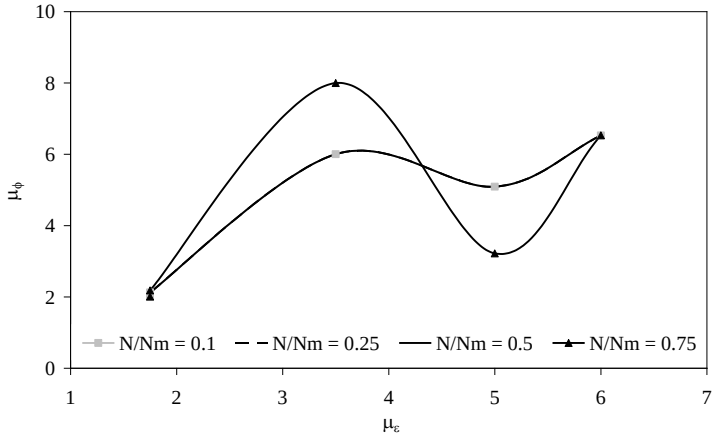

Figure 7.69 Curvature ductility versus strain ductility

7.5. Force-Displacement Diagrams

The definition of force-displacement curves can be carried out not only for individual masonry panels, but also for single storeys of walls with openings.

The force-displacement diagrams related to single panels allow to predict non-linear seismic response of masonry buildings accounting for equilibrium and displacement compatibility among several macro-elements.

The force-displacement diagrams related to wall storeys could be used in the case of building aggregates in historical centres. For these structures, IBC (IMIT, 2008) allows to perform storey-by-storey seismic analysis without considering interaction effects due, for instance, to axial flexibility of piers. It is also underlined that the former version of the RAN method assumes doubly-fixed pier panels due to the presence of rigid spandrels. The latter are assumed to be able to provide coupling up to the collapse of piers. Although these hypotheses could have some limitations in the case of existing buildings without RC ring beams nor lintels above openings, global seismic analysis can be carried out on both entire buildings and single walls by using force-displacement curves independent of boundary conditions on masonry panels. Nonetheless, matrix analysis of frame-equivalent models allows to account for actual constraints between pier and spandrel panels, as a function of their stiffness and strength characteristics associated with the global deformation state of the structure.

7.5.1. Force-Displacement Diagrams of Macro-Elements

The relative lateral displacement between extreme sections of a masonry panel is typically regarded as the sum of two contributions related to *shearing* and *flexural deformations* (see Sect. 6.2.9). Some researchers have proposed also some simplified formulations aimed at capturing *rocking* behaviour of masonry panels without complex integrations on bending curvatures or two-dimensional strain fields (see for instance: Rai and Goel, 2007).

As well known, rocking consists in a rigid-body rotation of a cracked masonry panel around its compressed toes. Assuming that this kind of behaviour is not associated with deformations suffered by the panel, but is just a consequence of crack opening within the non-reacting part, rocking can be separated from contributions due to flexural and shearing deformations. Therefore, one can assume that: (1) the lateral strength of the macro-element is associated with flexural and shearing deformations; and (2) the lateral displacement is a consequence of flexural and shearing deformations, as well as a ‘pure’ rigid-body rotation which is said to be ‘rocking’. Under these hypotheses, the mechanics of the macro-element can be analysed in detail through deformation-based approaches. In this regard, this section focuses on lateral displacements due to flexural deformations (Augenti and Parisi, 2009c). In fact, lateral displacements due to shearing

deformation can be predicted by using the classical force-based approach discussed in Section 6.2.9, while rocking-induced displacements (in strictly speaking) are still under investigation. It is emphasised once again that current analytical models assume rocking as a unique phenomenon where flexural deformations are not analysed in detail.

In the present section, the lateral displacement of a masonry panel is then assumed to be the sum of three contributions, as follows:

$$\delta = \delta_V + \delta_M + \delta_R \tag{7.246}$$

where: δ_V is the lateral displacement induced by shearing deformation; δ_M is the lateral displacement induced by flexural deformation; and δ_R is the lateral displacement induced by crack opening within the non-reacting part of the panel (which could also be called 'pure rocking').

Under a given axial force on the panel, the force-displacement curve can be defined by increasing monotonically the maximum axial strain $\varepsilon_{z,max}$ at the most stressed extreme section in bending (both extreme sections in the case of doubly-fixed panels). As a result, bending curvature increases up to ULS and produces a monotonically-increasing lateral displacement δ_M. At each strain step, one can compute the lateral displacement and the resisting shear force, so the output of the analysis is a force-displacement curve V–δ_M related only to bending deformation. Since current models for the estimation of shearing and rocking contributions are based on force-based procedures, one can estimate δ_V and δ_R under varying shear force related to bending deformation. Hence, the overall force-displacement curve V–δ is obtained by adding shearing and rocking displacements to the flexural displacement, at each given shear force.

The maximum axial strain at the most stressed extreme section in bending is increased until the ultimate strain of masonry (that is, ε_u) is reached. Each point of the V–δ_M curve depends not only on the applied axial force, the macro-element dimensions, and the boundary conditions, but also on the constitutive model assumed for masonry in compression.

Through a strain-controlled procedure, one can get relationships $\delta = \delta(\varepsilon_{z,max})$ and $V = V(\varepsilon_{z,max})$, where z is the longitudinal axis of the macro-element. The latter is based on formulations presented in Section 7.2 for flexural strength domains. In this way, the V–δ diagram can be numerically defined as a series of points (V,δ) associated with a given maximum axial strain $\varepsilon_{z,max}$. In other terms, the force-displacement diagram is a parametric representation rather than the graph of a function $V = V(\delta)$. The strain control, as well as the definition of flexural displacements through double integration of curvatures over an evolutionary reacting domain including the constitutive model of masonry, allow assessing the lateral evolutionary behaviour of the macro-element

under increasing drift demand. The mechanical behaviour of the masonry panel depends on the occurrence and spreading of cracking and yielding within the masonry (see Sect. 7.1). Non-linear elasticity of masonry due to micro-cracking and strain ductility are not considered in classical stress-based approaches (where strength domains are derived through limit stress diagrams) and force-controlled procedures (where force-displacement curves are defined under increasing shear force or as simplified multi-linear diagrams).

Assuming a plane strain field within the masonry panel and small strains, the maximum axial strain at the extreme section subjected to the maximum bending moment can be expressed as follows:

$$\varepsilon_{z,\max} = \varepsilon_z^N + \varepsilon_{z,\max}^M \tag{7.247}$$

where: ε_z^N is the average axial strain corresponding to the applied axial force N; and $\varepsilon_{z,\max}^M$ is the maximum axial strain corresponding to the resisting bending moment M.

The maximum axial strain $\varepsilon_{z,max}$ is assumed to fall within the interval $[0,\varepsilon_u]$, in order to ensure integrity of masonry. The average axial strain due to the given axial force can be copmuted through the equation of translational equilibrium over the extreme section being monitored. The maximum axial strain due to flexure is applied over the monitored section along with the entire strain field within the masonry panel. The plane strain field is defined as the union of one-dimensional strain diagrams along the axes x, z which are respectively assumed to be the transverse and longitudinal axes of the panel with origin in the centroid G (Fig. 7.70).

The effective width b of cross-sections changes along the z-axis, resulting in a convex reacting domain within the masonry panel. Once the geometry of this domain (namely, a function $b(z)$) has been defined, the lateral displacement can be estimated by increasing monotonically the maximum axial strain $\varepsilon_{z,max}$ in the interval $[0,\varepsilon_u]$.

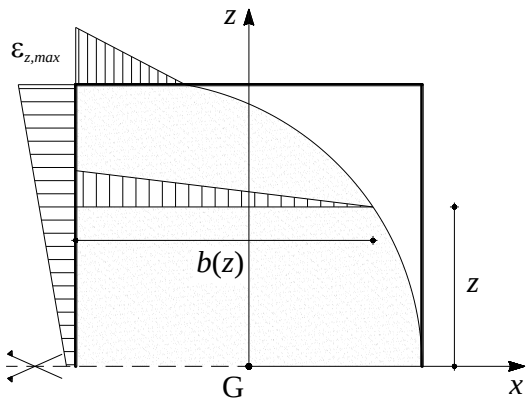

Figure 7.70 Axial strain field throughout the inner resistant domain of the macro-element

The axial strain field can be defined as:

$$\varepsilon_z(x,z) = \frac{2\varepsilon_{z,\max}}{H}\left(1 - \frac{B}{2b(z)} + \frac{x}{b(z)}\right)z \tag{7.248}$$

so the lateral displacement due to flexural deformation can be computed through the following double integration:

$$\delta_M = 2\iint_{A_p}\left[\frac{2\varepsilon_{z,\max}}{H}\left(1 - \frac{B}{2b(z)} + \frac{x}{b(z)}\right)z\frac{1}{x}\right]dx\,dz \tag{7.249}$$

where A_p is the midarea of the reacting domain of the masonry panel. The calculus of such an integral is the key step of the formulation presented herein, in order to define the force-displacement curve of a masonry panel through a deformation-based approach. A closed-form double integration was carried out for several integration domains with increasing level of complexity and accuracy (Augenti and Parisi, 2009c). The analytical solution presented below was obtained for an evolutionary reacting domain inside the panel which changes with the given deformation state, as discussed in Section 7.1. To simplify the double integration of the axial strain field, the Cartesian coordinate system was suitably defined in a way to get a reacting domain normal on R^2 with respect to the longitudinal axis. To that end, a transformation of variables was carried out, so the order of integration was reduced in a way to solve double integrals as series of integrals of one variable.

The collapse criterion considered for the panel in this approach does not consist in assuming that the panel fails when the maximum shear force is attained. In fact, the collapse of the panel is assumed to occur in one of the following cases:

(1) the maximum axial strain over the most stressed extreme section reaches the ultimate strain of masonry; or
(2) the ultimate displacement for shear mechanisms is reached.

The latter capacity parameter can be defined as: the displacement associated with the minimum shear strength (among those related to sliding shear and diagonal tension cracking) times a displacement ductility factor; or the displacement associated with the limit drift provided by seismic codes.

- **Double integration through reduction formulae**

Denoting by V_l, V_e, and V_p the resisting shear forces at CLS, ELS, and ULS for flexure, respectively, it is assumed herein that the masonry panel fails in flexure. In this case, it follows that $V_u = V_p$, where V_u is the lateral strength corresponding to the dominant failure mode (see Sect. 6.1). For the sake of simplicity, the masonry panel can be assumed to be doubly-fixed, but any other boundary condition could be considered. In such hypothesis, one can consider just a half of the panel, since its lateral behaviour is

emisymmetric.

If the shear force falls in the interval $[0,V_l]$, the macro-element is fully resistant so the lateral displacement due to flexure can be computed by double integration over the whole masonry panel (see Fig. 7.2a in Sect. 7.1). It follows that:

$$\delta_M = \frac{\varepsilon_{z,\max} H}{2} \tag{7.250}$$

If the shear force falls in the interval $[V_l,V_e]$, the macro-element behaves elastically but its effective part reduces due to cracking of masonry. In such conditions, the limit line of the reacting domain can be idealised as bilinear, so the reacting domain $\mathbf{\Omega}$ can be assumed to be the union of two sub-regions $\mathbf{\Omega_1}$ and $\mathbf{\Omega_2}$ (see Fig. 7.2b in Sect. 7.1). The sub-region $\mathbf{\Omega_1}$ corresponds to an elastic behaviour affected by mechanical non-linearity of masonry; thus, $\mathbf{\Omega_1}$ is composed by uncracked cross-sections located at heights z falling in the interval $[0,z_n]$. The latter sub-region $\mathbf{\Omega_2}$ is affected by both mechanical and geometrical non-linearities and is composed by cracked cross-sections located at heights z falling in the interval $[z_n,H/2]$. The above trapezoidal domain is normal with respect to the z-axis, so variables were suitably transformed in a way to apply reduction formulae to the double integral in Eq. (7.249). To that end, the effective width at ELS of the most stressed estreme section was denoted as b_e (It is underlined that this width depends also on the constitutive model assumed for masonry in compression.) and the dilogarithm function:

$$\operatorname{dilog} z = \int_1^z \frac{\log t}{1-t}\, dt \tag{7.251}$$

was introduced, where z is a variable for which $|z| < 1$. Such a special function has the following series expansion:

$$\operatorname{dilog} z = \sum_{k=1}^{\infty} \frac{z^k}{k^2} \tag{7.252}$$

which was used to solve Eq. (7.249). Assuming $b_e = \beta B$ and $z_n = \zeta H$, the lateral displacement of a cracked panel in the elastic range was found to be expressed as follows:

$$\delta_M = 2\varepsilon_{z,\max} H \left[\zeta^2 + \frac{(1-2\zeta)\sum_{i=1}^{3} \lambda_i}{96(\beta-1)^2} \right] \tag{7.253}$$

where:

$$\lambda_1 = 24(2\beta\zeta - 1)\operatorname{dilog}(2\beta)$$

$$\lambda_2 = \ln(2\beta-1)^2 \left\{ 6(2\beta\zeta-1)\ln\beta^2 + 12(2\beta\zeta-1)\ln 2 - 3[4\beta^2(2\zeta+1) - 12\beta - 2\zeta + 5] \right\}$$

$$\lambda_3 = 2\left\{6\beta^2(10\zeta+3)+2\beta\left[\zeta\left(\pi^2-42\right)-27\right]+24\zeta-\pi^2+36\right\}$$

The left and right terms in bracketed parentheses into Eq. (7.253) are respectively associated with the sub-regions $\mathbf{\Omega_1}$ and $\mathbf{\Omega_2}$.

If the masonry panel is fully resistant in the plastic range (for instance, the shear force falls in the interval $[V_e,V_p]$), the analytical solution has a form similar to that associated with a shear force falling in the interval $[V_l,V_e]$, provided that z_l and b_e are considered instead of z_n and b_u, respectively. It follows that coefficients β_l and ζ_l should be considered instead of β_n and ζ_n, respectively. It is also emphasised that the heights z_l and z_n can be simply calculated by inverting equilibrium equations written at ELS and ULS.

If the shear force falls in the interval $[V_e,V_p]$, the reacting domain of the panel can be assumed to be composed by three sub-regions: $\mathbf{\Omega_1}$, $\mathbf{\Omega_2}$ and $\mathbf{\Omega_3}$ (see Fig. 7.2c in Sect. 7.1). Such sub-regions are composed by cross-sections located at heights falling in the intervals $[0,z_n]$, $[z_n,z_e]$ and $[z_e,H/2]$, respectively. As stated above, the first two sub-regions correspond to an elastic behaviour of the panel (in both cracked and uncracked conditions); on the other hand, $\mathbf{\Omega_3}$ is associated with a plastic behaviour of masonry. The double integral was regarded as the sum of three integrals related to the aforementioned sub-regions, so the following relation was obtained for the computation of the lateral displacement due to flexure:

$$\delta_M = 2\varepsilon_{z,\max} H\left[\zeta_n^2+\frac{(\zeta_n-\zeta_e)\sum_{i=1}^{4}s_i}{24(B-H\beta_e)}+\frac{(1-2\zeta_e)\sum_{i=5}^{8}s_i}{32(\beta_e-\beta_u)^2}\right] \tag{7.254}$$

where:

$$s_1 = 24B\Phi_1\left[\operatorname{dilog}\left(\frac{2H\beta_e}{B}\right)+\ln^2 B\right]$$

$$s_2 = 3\ln(B-2H\beta_e)^2\left[\Gamma-4B\Phi_1\ln B\right]$$

$$s_3 = -6\ln(B)\Gamma$$

$$s_4 = 2\left\{B^2\left[\zeta_e\left(\pi^2-36\right)-12\zeta_n\right]+BH\beta_e\left[54\zeta_e+\zeta_n\left(42-\pi^2\right)\right]-6H^2\beta_e^2\left(3\zeta_e+5\zeta_n\right)\right\}$$

$$s_5 = 8\Phi_2\left[\operatorname{dilog}(2\beta_e)-\operatorname{dilog}(2\beta_u)\right]$$

$$s_6 = \ln(2\beta_e-1)^2\left[4\Phi_2\ln(2\beta_e)-4\beta_e^2(2\zeta_e+1)+8\beta_e\zeta_e(2\beta_u+1)-8\beta_u\zeta_e-2\zeta_e+1\right]$$

$$s_7 = -\ln(2\beta_u-1)^2\left\{4\Phi_2\ln(2\beta_u)+(1-2\beta_u)\left[4\beta_e-2\beta_u(2\zeta_e+1)-2\zeta_e+1\right]\right\}$$

$$s_8 = 4(\beta_e-\beta_u)\left[\beta_e(6\zeta_e+5)-\beta_u(10\zeta_e+3)-2\zeta_e+1\right]$$

$$\Phi_1 = B\zeta_e - H\beta_e\zeta_n$$
$$\Phi_2 = \beta_e - 2\beta_u\zeta_e$$
$$\Gamma = 4B\Phi_1\ln(2H\beta_e) + B^2(5\zeta_e - \zeta_n) - 12BH\beta_e\zeta_e + 4H^2\beta_e^2(\zeta_e + \zeta_n)$$

- **Incremental iterative procedure**

Under a given axial force applied to the panel, the average axial strain can be evaluated by solving numerically the equation of translational equilibrium along the *z*-axis. For instance, if the Turnšek- Čačovič constitutive model is assumed for masonry and the extreme section is fully resistant (that is, $b = B$), the average axial strain can be computed through the following equation:

$$\overline{N} = \frac{1}{5}\left[32 - 27\left(\frac{\varepsilon_z^N}{\varepsilon_k}\right)^{0.17}\right]\frac{\varepsilon_z^N}{\varepsilon_k} \tag{7.255}$$

Once ε_z^N has been computed, the maximum axial strain due to bending can be increased in the interval $[0,\ \varepsilon_u - \varepsilon_z^N]$. As the axial force increases, the amplitude of this interval reduces so the ultimate curvature and the relevant displacement capacity reduce as well.

The incremental iterative procedure employed to define the relationship V–δ_M can start by assigning an increment $\Delta\varepsilon_z$ to ε_z^N in a way to get the maximum axial strain. At the *k*-th strain step, one has to determine if the extreme section is cracked or uncracked under a given axial force and the imposed maximum axial strain. Therefore, the geometry of the extreme section can be assessed through a series of iterations, in order to compute the lateral displacement and the resisting shear force. If the extreme section is fully resistant, the axial strain diagram can be defined only once the minimum axial strain has been numerically computed through Eq. (7.28), where the current strain $\varepsilon_{z,max}$ is used instead of the ultimate strain of masonry ε_u. If numerical convergence is reached, then the hypothesis of uncracked extreme section is met and the axial strain diagram is actually trapezoidal. The shear force can then be determined by Eq. (7.31), where $\varepsilon_{z,max}$ is used instead of ε_u. Conversely, if the procedure for the evaluation of the minimum axial strain does not converge within the allowable number of iterations, the extreme section of the panel is cracked and its effective width can be derived by means of Eq. (7.6). In such a case, the resisting shear force is provided by Eq. (7.11).

At the *k*-th increment of the maximum axial strain due to flexure, one can get the lateral displacement and the resisting shear force (Fig. 7.71). Each point of the force-displacement diagram is not derived through a functional relationship between shear force and flexural displacement, but is the output of a numerical procedure at a given

maximum axial strain on the extreme section subjected to the maximum bending moment. The shearing deformation of the panel produces a lateral displacement which can be predicted as follows:

$$\delta_V = \chi \frac{V H}{G A} \zeta_V \tag{7.256}$$

under the shear force corresponding to the flexural deformation; the factor ζ_V can be defined according to Augenti (2004).

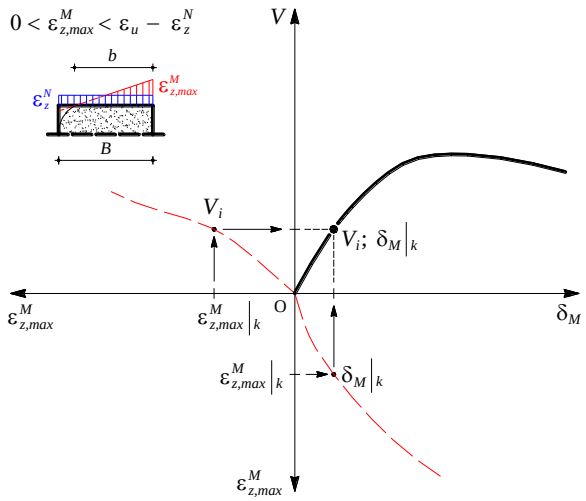

Figure 7.71 Building up V–δ_M curve in strain control

The rocking-induced lateral displacement can also be summed to the lateral displacements due to shearing and flexural deformations, so the force-displacement curve can be derived by the V–δ_M curve.

The numerical procedure described above allows to define the force-displacement curve of a macro-element failing in flexure. If the resisting shear force at a given strain step reaches the lateral strength corresponding to sliding shear or diagonal tension cracking, the procedure is stopped and the failure point on the force-displacement curve is assumed to be followed by a plastic plateau up to the ultimate displacement defined for shear mechanisms.

A series of numerical analyses showed that the procedure presented above can be modified in a way to reduce numerical errors and to increase the rate of convergence. To that end, it was found that the extreme sections can first be assumed to be cracked at a given strain step, searching for the effective width b (Fig. 7.72). If Eq. (7.6) leads to the absurd of $b > B$, then the hypothesis of cracked section is not met and the minimum axial strain is to be determined.

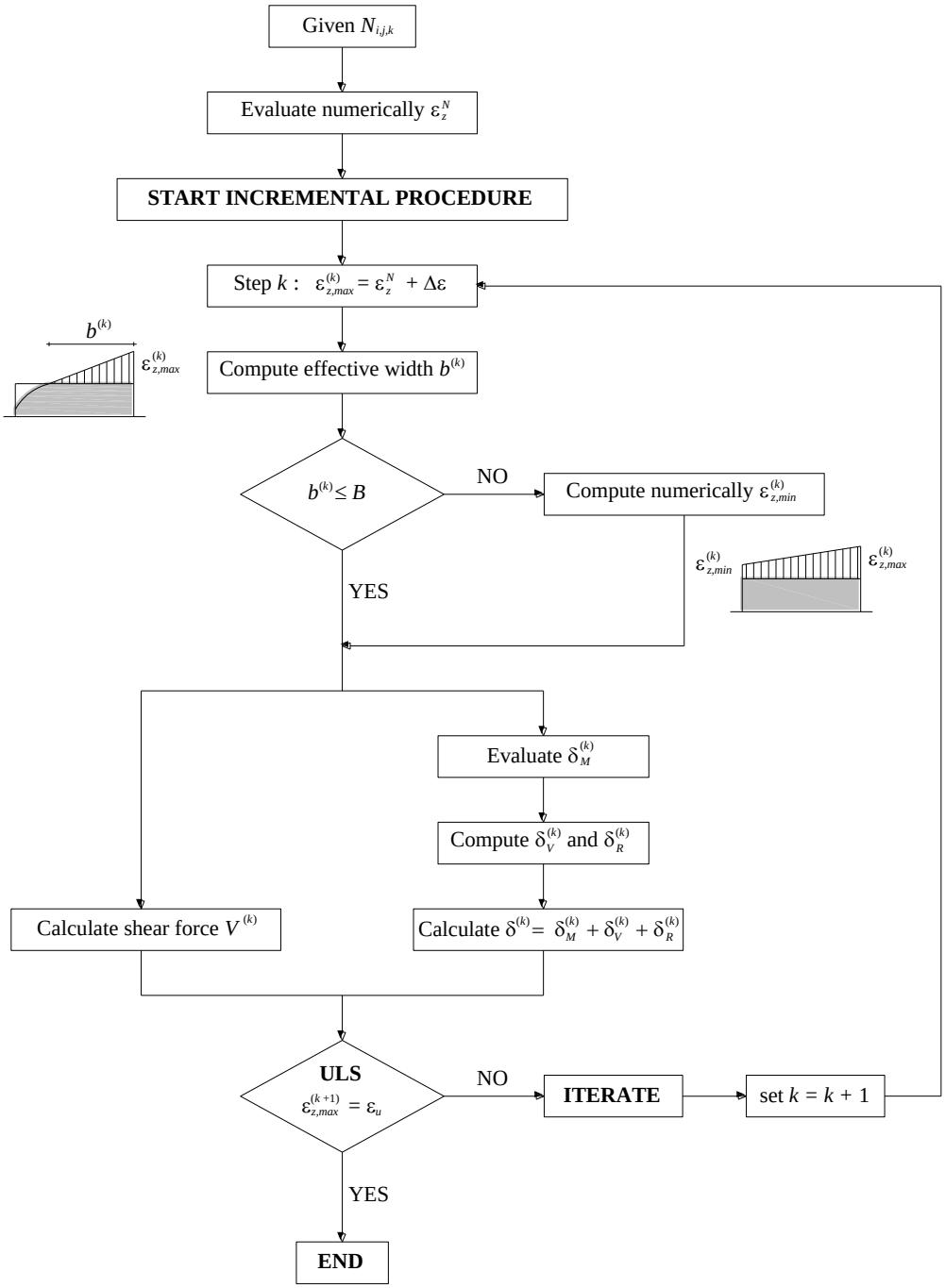

Figure 7.72 Incremental iterative procedure for the force-displacement curve of a panel

Figure 7.73 shows the typical force-displacement curve of a URM panel failing in flexure, due to its length-to-width ratio, the mechanical properties of masonry, and the magnitude of the applied axial force.

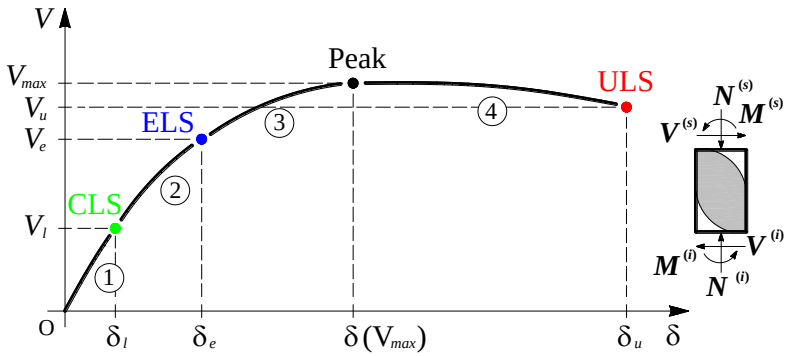

Figure 7.73 Force-displacement curve of a URM panel failing in flexure

The force-displacement curve is formed by four branches. The former is associated with the interval $[0,\delta_l]$ and its non-linearity is due to mechanical non-linearity of masonry in the elastic range. The masonry panel is fully resistant and its lateral behaviour is reversible.

The second branch of the curve simulates the effect of masonry tension cracking on the elastic behaviour of the masonry panel; such a cracking due to a limited tensile strength induces a reduction in the effective width of cross-sections, resulting in a reacting domain of the panel which depends on the lateral drift demand.

The last branches of the curve are affected by yielding of the most stressed cross-sections in bending and by strain softening of masonry. The peak of the force-displacement curve is not typically associated with the attainment of ULS. In fact, especially at higher pre-compression levels, compressive strength degradation of masonry can significantly affect the lateral behaviour of the panel, 'hiding' the hardening effect due to localization of inelastic strains.

Figure 7.74 shows force-displacement diagrams of a doubly-fixed URM panel having the following characteristics: uniaxial compressive strength σ_k = 3.00 MPa; shear strength at zero confining stress τ_0 = 0.30 MPa; height H = 300 cm; length B = 250 cm; and thickness s = 70 cm. It is outlined that:

- For a normalised axial force equal to 0.04, force-controlled and deformation-controlled procedures led to almost equal predictions of lateral stiffness and maximum resisting shear force, while displacement capacity predicted through a flexural deformation control was found to be more than two times higher.
- For a normalised axial force equal to 0.4, the deformation-controlled procedure led

to slightly lower predictions of lateral stiffness and maximum resisting shear force, while displacement capacity was not more than two times higher.

- The effect of strain softening of masonry increased with the magnitude of the axial force applied to the masonry panel.

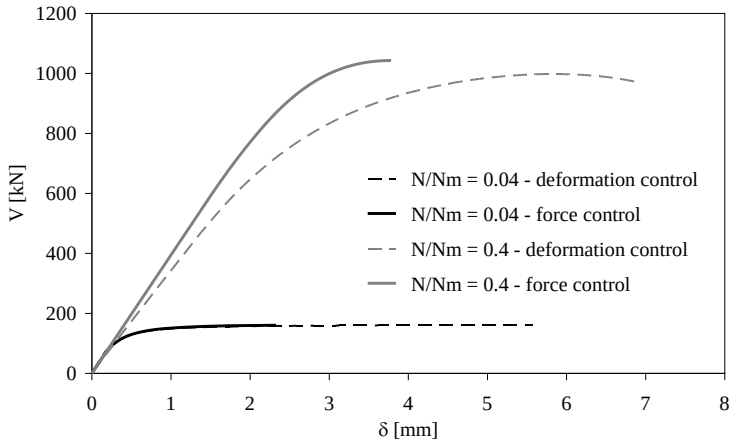

Figure 7.74 Force- versus deformation-controlled force-displacement curves

7.5.2. Force-Displacement Diagrams of Wall Storeys

The force-displacement curve of a wall storey can be defined through a further incremental iterative procedure based on one of the following assumptions: rigid spandrel up to failure of piers; or piers connected by spandrel panels with limited resistance and flexibility. For a given lateral displacement one can compute shear forces on pier panels. The lateral resistance of the wall storey can be considered as the sum of the lateral strengths of individual pier panels.

In order to estimate both strength and displacement capacities, one can remove the assumption that the global collapse occurs when a pier panel reaches its own lateral strength corresponding to shear or flexural failure. As a result, the force-displacement diagram of the wall storey is non-monotonic and fully non-linear. If the lateral strength of a masonry panel is reached, the lateral stiffness of the wall storey reduces; on the contrary, the attainment of the ultimate displacement of a pier panel causes a reduction in the lateral resistance of the wall storey.

The displacement capacity of the wall storey cannot exceed the following value:

$$\delta_{u,\max} = \max\left\{\delta_p\left(\varepsilon_u\right)_{i,j}\right\}_{j=1,\ldots,m} \tag{7.257}$$

where m is the number of pier panels forming the wall storey.

For a given lateral displacement in the interval $[0,\delta_{u,max}]$, the maximum axial strain due to flexure in each pier panel can be numerically computed until the following convergence criterion is met:

$$\left|\frac{\delta^{(k)}-\delta^{*}}{\delta^{*}}\right| \le \mathrm{tol}_{\delta} \tag{7.258}$$

The lateral displacement $\delta^{(k)}$ is estimated through Eq. (7.246) and the numerical tolerance can be set, for instance, to $\mathrm{tol}_{\delta} = 10^{-5}$. The resisting shear force of the wall storey can then be estimated as follows:

$$V_{i,k} = \sum_{j=1}^{m} V_{i,j,k}\left(\varepsilon_{z,\max}^{M}\right) \tag{7.259}$$

The shearing contribution to the lateral displacement of each pier panel can be predicted only if the resisting shear force corresponding to the maximum axial strain has been determined. It follows the need for an iterative procedure aimed at the computation of a lateral displacement equal to δ^{*}. To this end, the latter can be assumed to be caused only by flexural deformations. At the first analysis step each pier panel is fully resistant, so one can first assume that the maximum axial strain due to flexure at the extreme section is equal to:

$$\varepsilon_{z,\max}^{M(1)} = \frac{2\delta^{*}}{H} \tag{7.260}$$

After the computation of the axial force acting on the pier panel, one can determine the resisting shear force $V^{(1)}$ through the formulas of interaction domains presented in previous sections for different constitutive laws of masonry. The lateral displacement due to shearing deformation can thus be evaluated as:

$$\delta_{V}^{(1)} = \chi \frac{V^{(1)} H}{G A} \zeta_{V}^{(1)} \tag{7.261}$$

while the lateral displacement due to flexure can be derived as follows:

$$\delta_{M}^{(1)} = \delta^{*} - \delta_{V}^{(1)} \tag{7.262}$$

If the pier panel is fully resistant, the maximum axial strain can be updated to:

$$\varepsilon_{z,\max}^{M(2)} = \frac{2\delta_{M}^{(1)}}{H} \tag{7.263}$$

Consequently, for each pier panel in uncracked conditions and in the elastic range, the recursive formulas to be applied at the *k*-th analysis step are:

$$\varepsilon_{z,\max}^{M(k)} = \frac{2\delta_{M}^{(k-1)}}{H} \tag{7.264}$$

$$\delta_V^{(k)} = \chi \frac{V^{(k)} H}{G A} \zeta_V^{(k)} \tag{7.265}$$

$$\delta_M^{(k+1)} = \delta^* - \delta_V^{(k)} \tag{7.266}$$

and the iterative procedure can be stopped when the convergence criterion (7.258), or the following:

$$\left| \frac{\delta_M^{(k+1)} - \delta_M^{(k)}}{\delta_M^{(k)}} \right| \leq \mathrm{tol}_\delta \tag{7.267}$$

is met. Conversely, if pier panels are cracked and/or in the plastic range, the equations to be applied for the estimation of the maximum axial strain due to flexure are those presented in previous sections for different constitutive laws of masonry. Boundary conditions different from that of doubly-fixed panel can also be considered, by using proper values of the constraint factor included in the equations of interaction domains (see Sect. 7.2). It is underlined that the integral which defines the displacement capacity associated with flexural deformation of an URM panel is multiplied by a factor equal to 2 (see Eq. (7.249)). It is clear that the displacement capacity of cantilever panels is four times that corresponding to doubly-fixed panels.

In Figure 7.75, the force-displacement curve defined in force control is compared to that defined in deformation control for a wall storey composed by three pier panels. It is clear that displacement capacity is highly underestimated by the force-controlled procedure, even if it is associated with a residual lateral strength which is about one-half of the peak strength.

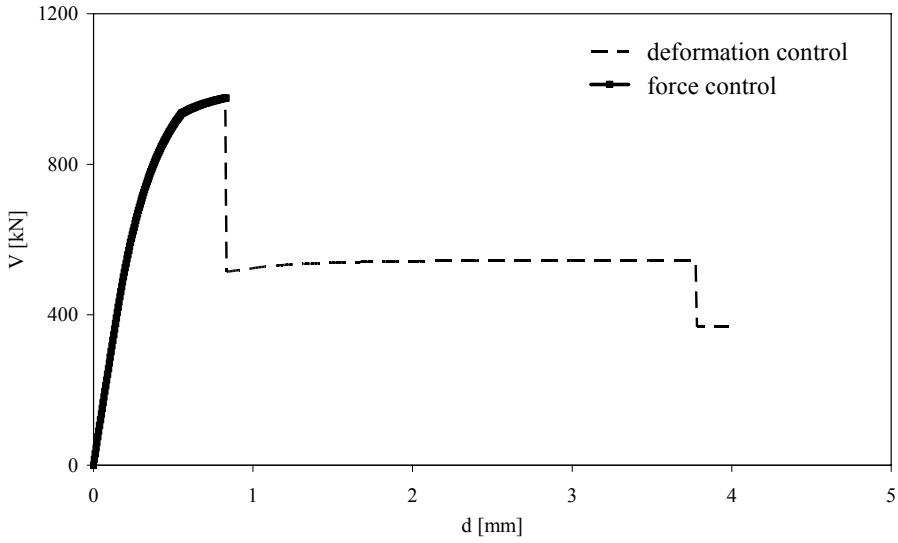

Figure 7.75 Force- versus deformation-controlled force-displacement curves for a wall storey

Chapter 8 - NEW STATIC PUSHOVER PROCEDURES

The use of linear elastic analysis (be it static or dynamic) has significant limitations in the case of masonry buildings, especially because of major difficulties in a reliable definition of strength reduction factors which affect the estimation of seismic demand. On the other hand, there are still key open issues in non-linear dynamic analyses on masonry buildings regarding the definition of seismic input (record selection and, in the case of incremental analysis, scaling), the hysteretic modelling of masonry walls, and the definition of proper collapse criteria. Such problems have led to pay major care in the development of non-linear static procedures. In most cases, pushover analysis allows to get realistic predictions of seismic capacity of masonry buildings, and hence of their seismic performance at different earthquake intensity levels, once the seismic demand has been estimated (see Chap. 5.2).

Based on the N2 method (Fajfar, 2000) for the estimation of seismic performance and on the assessment of pushover methods available in the literature (see Chap. 5), different pushover procedures were separately developed for single masonry walls with openings and entire masonry buildings. To that aim, the RAN method (Augenti, 2004) was extended to the non-linear range through an evolutionary spread plasticity macro-element modelling of walls (see Chap. 7) and force-based pushover procedures in response control (Antoniou, 2002; Antoniou and Pinho, 2004a).

The pushover procedures presented and discussed in this chapter follow a ‘unitary’ approach which allows to control both ‘global’ performance of the whole masonry building and ‘local’ performance of individual constituent macro-elements. In fact, the actual deformed shape of the structure is directly associated with the given increment of the response parameter (namely, the horizontal translation of the control point along the direction under constideration), resulting in the prediction of strength and displacement demands on single macro-elements.

The definition of the flexural behaviour of each macro-element through a ‘deformation-based’ approach allows also to predict deformation demands on masonry (that is, at material level) and strength evolution in the plastic range. Geometrical and mechanical non-linearities are considered in both seismic demand estimation for single components and capacity assessment.

8.1. Pushover Analysis of Masonry Walls with Openings

Existing masonry buildings are often characterised by floor diaphragms with large in-plane flexibility and lack, or ineffectiveness, of diaphragm-to-wall and wall-to-wall connections (that is, no flanges at building corners). In such cases, global assessment of non-linear seismic response of a masonry building may lead to unrealistic predictions, so one should perform pushover analysis on the constituent masonry walls subjected to their relevant gravity loads. On the other hand, global seismic response is significant only if safety verifications against potential out-of-plane mechanisms of walls are met.

In the case of building aggregates, which are typically present in historical centres, global seismic assessment of single building units is purely conventional. Therefore, IBC (IMIT, 2008) allows to use simplified methods and, in the presence of flexible floor diaphragms, to perform seismic analysis of individual walls and coplanar wall systems.

Non-linear analysis of a masonry wall with openings should be carried out for each lateral load pattern (e.g., proportional to inertia masses or to fundamental modal shape) and for each orientation of lateral actions, separately. It is underlined that a specific modelling of pier panels within masonry walls with irregular layout of openings should be based on the orientation of lateral forces (Augenti, 2006).

The following symbols are used in this chapter: the subscripts i and j indicate respectively the horizontal strip (or level) and the vertical strip at which a masonry panel or opening belongs (see also Sect. 6.2.5); and the superscripts j and k in round parentheses to denote an iteration and a displacement step, respectively. Horizontal and vertical strips of the masonry wall are progressively numbered from the top to the base and from the left to the right, respectively, according to the RAN method (Augenti, 2004).

Figure 8.1 shows the flow-chart of the pushover procedure developed for a single masonry wall. The incremental iterative procedure begins with the computation of inertia masses m_i and initial elastic stiffnesses $k_{i,1}$ at each storey of the wall. A lateral force pattern is then defined to be kept constant during pushover analysis under increasing lateral displacement at the control point. According to what discussed in Sect. 5.1.2, a lateral force profile $\mathbf{F}_0 = (1 \ldots \beta_i \ldots \beta_n)^T$ is defined by assuming $\beta_i = m_i \phi_i / m_1$ and $\phi_i = z_i / H$ for 'modal' load pattern, and $\beta_i = m_i / m_1$ for 'uniform' load pattern. The coefficient β_i is referred to as 'force distribution factor at the i-th floor level'. The lateral force vector $\mathbf{F}^{(k)} = (F_1 \ldots F_i \ldots F_n)^T$ at the k-th analysis step is thus defined as follows:

$$\mathbf{F}^{(k)} = \lambda^{(k)} \mathbf{F}_0 \tag{8.1}$$

where $\lambda^{(k)}$ is the load multiplier derived from total updating strategy (see Sect. 5.1.3).

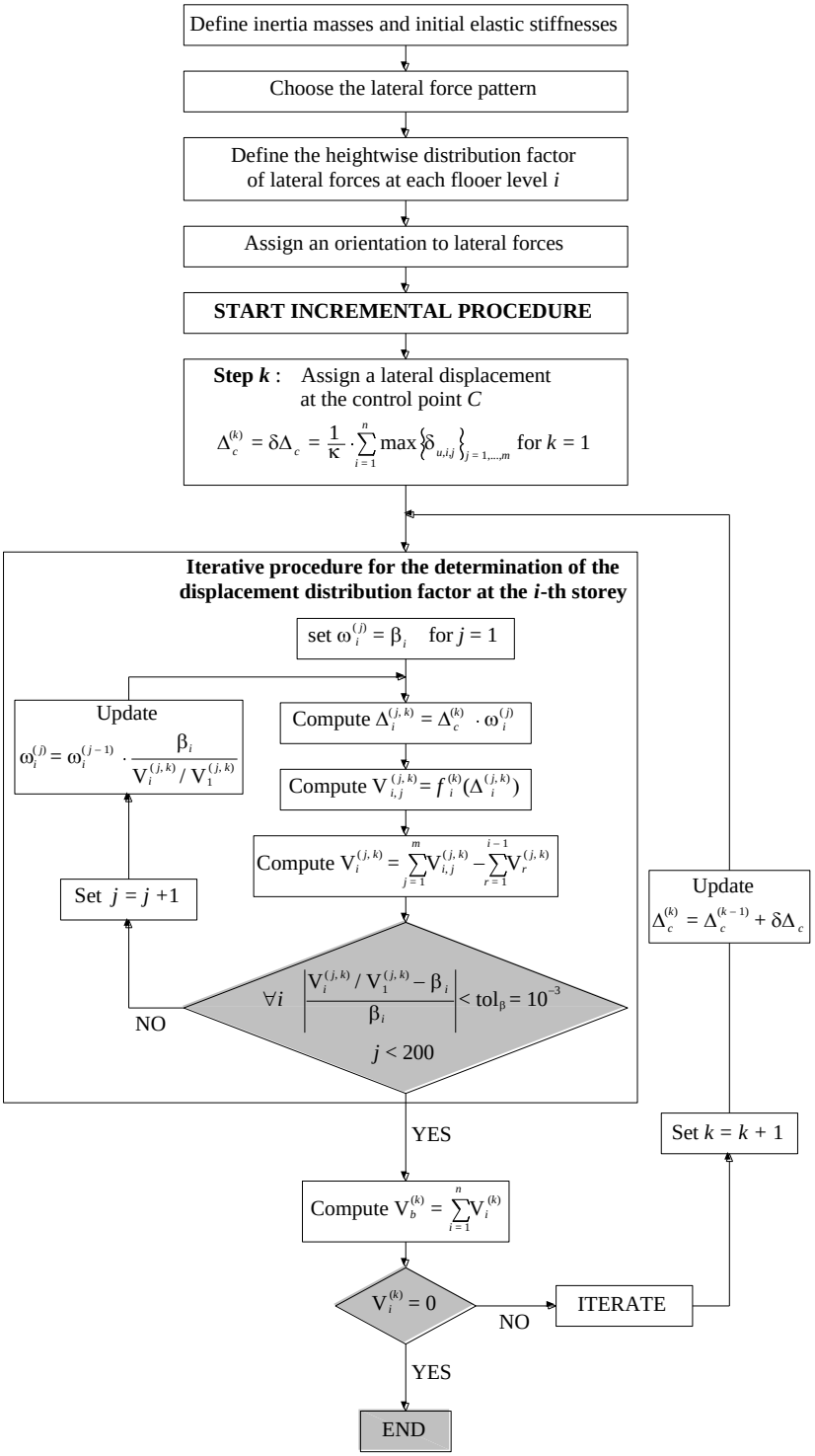

Figure 8.1 Flow-chart of pushover procedure for the masonry wall with openings

Once the orientation of lateral forces has been chosen, the first analysis step (k = 1) consists in the application of a horizontal displacement at the control point of the wall:

$$\Delta_c^{(k)} = \delta\Delta_c = \frac{1}{\kappa}\sum_{i=1}^{n}\max\left\{\delta_{u,i,j}\right\}_{j=1,\ldots,m} \tag{8.2}$$

The factor κ is suitably defined as a function of the target accuracy level. The deformed shape of the masonry wall is not known because it depends on the effective stiffness of storeys at each given lateral drift. Therefore, a numerical procedure is needed to computed lateral displacements at each floor level. At the first iteration (j = 1), the displacement profile (response) can be assumed equal to the force profile (load), namely:

$$\mathbf{\Delta}_0^{(j,k)} = \mathbf{F}_0 \tag{8.3}$$

being $\mathbf{\Delta}_0^{(j,k)} = \left(1...\omega_i^{(j,k)}...\omega_n^{(j,k)}\right)^{\mathrm{T}}$. The lateral displacement vector at the i-th iteration within the k-the analysis step is then computed as:

$$\mathbf{\Delta}^{(j,k)} = \Delta_c^{(k)}\mathbf{\Delta}_0^{(j,k)} \tag{8.4}$$

while the corresponding shear force on a pier panel can be obtained through the force-displacement relationship of the wall storey:

$$V_{i,j}^{(j,k)} = \mathrm{f}_i^{(k)}\left(\Delta_i^{(j,k)}\right) \tag{8.5}$$

The latter equation applies once axial forces due to both gravity loads and seismic actions, as well as the lateral stiffness k_i, have been computed.

At the k-the analysis step, the horizontal force at the i-the floor level of the wall can be evaluated by means of the following equation:

$$F_i^{(j,k)} = \sum_{j=1}^{m} V_{i,j}^{(j,k)} - \sum_{r=1}^{i-1} F_r^{(j,k)} \tag{8.6}$$

namely, as the difference between the storey shears related at the floor levels i and $i - 1$. If the resulting lateral forces meet the assigned lateral force pattern within a pre-defined numerical tollerance (for instance, $\mathrm{tol}_\beta = 10^{-3}$) and the maximum allowable number of iterations (for instance, j_{max} = 200), that is:

$$\forall i \quad \left|\frac{F_i^{(j,k)}/F_1^{(j,k)} - \beta_i}{\beta_i}\right| \le \mathrm{tol}_\beta \tag{8.7}$$

$$j < j_{\max}$$

the base shear of the wall at the k-th analysis step can be computed as follows:

$$V_b^{(k)} = \sum_{i=1}^{n} F_i^{(k)} \tag{8.8}$$

Thus, a point $(V_b^{(k)}, \Delta_c^{(k)})$ of the pushover curve can be plotted.

If the first of inequalities (8.7) is not met, then the assumed displacement profile is wrong and can be corrected through the following equation:

$$\omega_i^{(j,k)} = \omega_i^{(j-1,k)} \frac{\beta_i}{F_i^{(j-1,k)} / F_1^{(j-1,k)}} \tag{8.9}$$

to be applied at each displacement distribution factor. It follows the need for iterating the procedure from Eq. (8.4) to the check on the lateral force pattern. It is underlined that the corrective factor which is multiplied by the distribution factor $\omega_i^{(j-1,k)}$ is assumed to be the ratio between the factor β_i (representing the 'target' load pattern) and $F_i^{(j-1,k)}/F_1^{(j-1,k)}$ (representing the 'resulting' load pattern at the previous iteration $j - 1$). Such an interative procedure is stopped until the convergence criterion described by inequalities (8.7) is met. In this case, a load multiplier $\lambda^{(k)}$ corresponding to the analysis step under consideration can be defined.

At the successive analysis step ($k = k + 1$), a larger horizontal displacement is applied to the control point and is defined as follows:

$$\Delta_c^{(k)} = \Delta_c^{(k-1)} + \delta\Delta_c \tag{8.10}$$

Then, a new deformed shape of the wall can be predicted by checking that the assigned lateral force pattern is met by resulting forces.

The whole static pushover procedure is stopped when the resisting base shear at a wall storey vanishes, that is:

$$V_i^{(k)} = 0 \tag{8.11}$$

This means that the collapse of the wall is assumed to occur when the lateral load-bearing capacity at a storey reaches zero. It is emphasised that the location of the centre of axial stiffnesses is also updated at each displacement step and wall storey, in order to assess axial forces induced by current lateral forces.

8.2. Pushover Analysis of Masonry Buildings

The seismic response of masonry buildings without significant irregularities depends mainly on the fundamental mode of vibration; damage suffered by those structures does not typically induce a modification in spectral acceleration at the fundamental period. Therefore, several researchers recongnise the chance for the assumption of single-mode load profiles in a way to minimise computational work in pushover analysis.

If the building is quite regular in plan, its elastic torsional response is generally more significant than the inelastic response, because the occurrence and propagation of damage throughout the structure induces a uniform redistribution of shear forces. At each floor level, the centre of shear moves from the location of centre of initial elastic

stiffness toward the centre of strength, resulting in the minimum eccentricity with respect to the centre of mass.
Conversely, if the building is irregular in plan, non-linear redistribution of shear forces among walls at each floor level is not uniform, so the centre of shear at ULS can be considerably different from the centre of strength.
Such features of non-linear torsional behaviour of the building are included in pushover procedures presented below, since torsional rotations of storeys are updated at each analysis step accounting for both structural and accidental eccentricities. The evolution in torsional response induces variations in the location of the centre of shear at each floor level, and hence in the distribution of both strength and displacement demands in plan.
A numerical procedure is used to derive the deformed shape corresponding to a pre-defined lateral force pattern, at each displacement increment assigned to the control point of the building. As in the case of a single masonry wall with openings, the magnitude (not the shape) of lateral forces is updated through a load multiplier derived from a total (rather than incremental) updating strategy. This technique allows to avoid any relationship between equilibrium solutions corresponding to successive displacement steps, and hence the propagation of numerical errors during the analysis is minimised.
The spread plasticity modelling of masonry macro-elements, the deformation-based approach used for the definition of both strength and displacement capacities, and the response-controlled pushover procedure are perfectly consistent themselves.
A mechanical approach allows to relate the ‘global’ response of the masonry building to the ‘local’ response of each macro-element. The mechanical behaviour of the macro-element is not pre-defined, nor idealised as bilinear or multi-linear, but it depends on the displacement demand derived from the overall response of the building, according to equilibrium and displacement compatibility conditions. Geometrical and mechanical non-linearities are included in the analysis since they affect significantly performance of masonry structures, at both serviceability and ultimate limit states. In this way, the global seismic assessment (which is based on the comparison between displacement demand and capacity at the limit states of interest) include directly the control of strength and deformation demands on individual macro-elements. It is thus a ‘unitary’ approach for the estimation of seismic building performance.
In the following sub-sections, a non-adaptive pushover procedure based on the application of lateral forces in response control is first presented to be used for masonry buildings. Second, a potential adaptive variant is proposed, but it requires numerical/experimental validation to assess both reliability of response predictions and its computational work.

8.2.1. Non-Adaptive Pushover Analysis

The pushover procedure implemented in RAN CODE (Augenti et al., 2010a) is based on the incremental application of a pre-defined lateral force profile (load) in a way to get monotonically-increasing displacements at a control point (response). Such a point, denoted as *C* below, is generally assumed to be the centre of mass at the roof of the building.

As in the case of single masonry walls with openings, response control was preferred over load control in order to assess post-peak strength degradation of the structure. The analysis proceeds also if some masonry panels reach collapse and is stopped at the global collapse of a wall storey, or loss of numerical stability.

The pushover procedure developed for masonry buildings is summarised in a flow-chart reported in Figure 8.2.

The first stage of the analysis consists in the definition of inertia masses m_i, initial elastic stiffnesses k_i, and location of their relevante centres at each floor level of the building. The initial stiffness of masonry piers can be initially assumed to be associated with doubly-fixed panels. According to IBC and EC8, an accidental eccentricity not lower than 5% is to be assigned at the centres of mass along the height of the building. Pushover analysis is carried out at least along mutually orthogonal directions of the building plan, so the pattern, direction and orientation of lateral forces are to be assigned and are kept constant during the analysis. To this end, a load shape vector $\mathbf{F}_0$ is defined and is said to be 'nominal load vector'. In the case of non-adaptive pushover, this vector is kept constant to a uniform profile.

The non-adaptive procedure begins with the definition of a horizontal displacement at the control point. At the first step of the analysis (k = 1), such a displacement is assumed as follows:

$$\Delta_c^{(k)} = \delta\Delta_c = \frac{1}{\kappa}\max\left\{\sum_{i=1}^{n}\max\left\{\delta_{u,i,j}\right\}_{j=1,\ldots,m}\right\}_{k=1,\ldots,w} \tag{8.12}$$

where κ is a factor greater than unity which is defined as a function of the target accuracy level. The deformed shape of the building at the displacement given at the control point is not known and is estimated through an iterative procedure.

At the first iteration (j = 1), the displacement shape vector can be defined as:

$$\boldsymbol{\Delta}_0^{(j,k)} = \mathbf{F}_0^{\mathrm{T}}\,\bar{\mathbf{k}} \tag{8.13}$$

being: $\bar{\mathbf{k}} = \left(1 \ldots k_1/k_i \ldots k_1/k_n\right)^{\mathrm{T}}$.

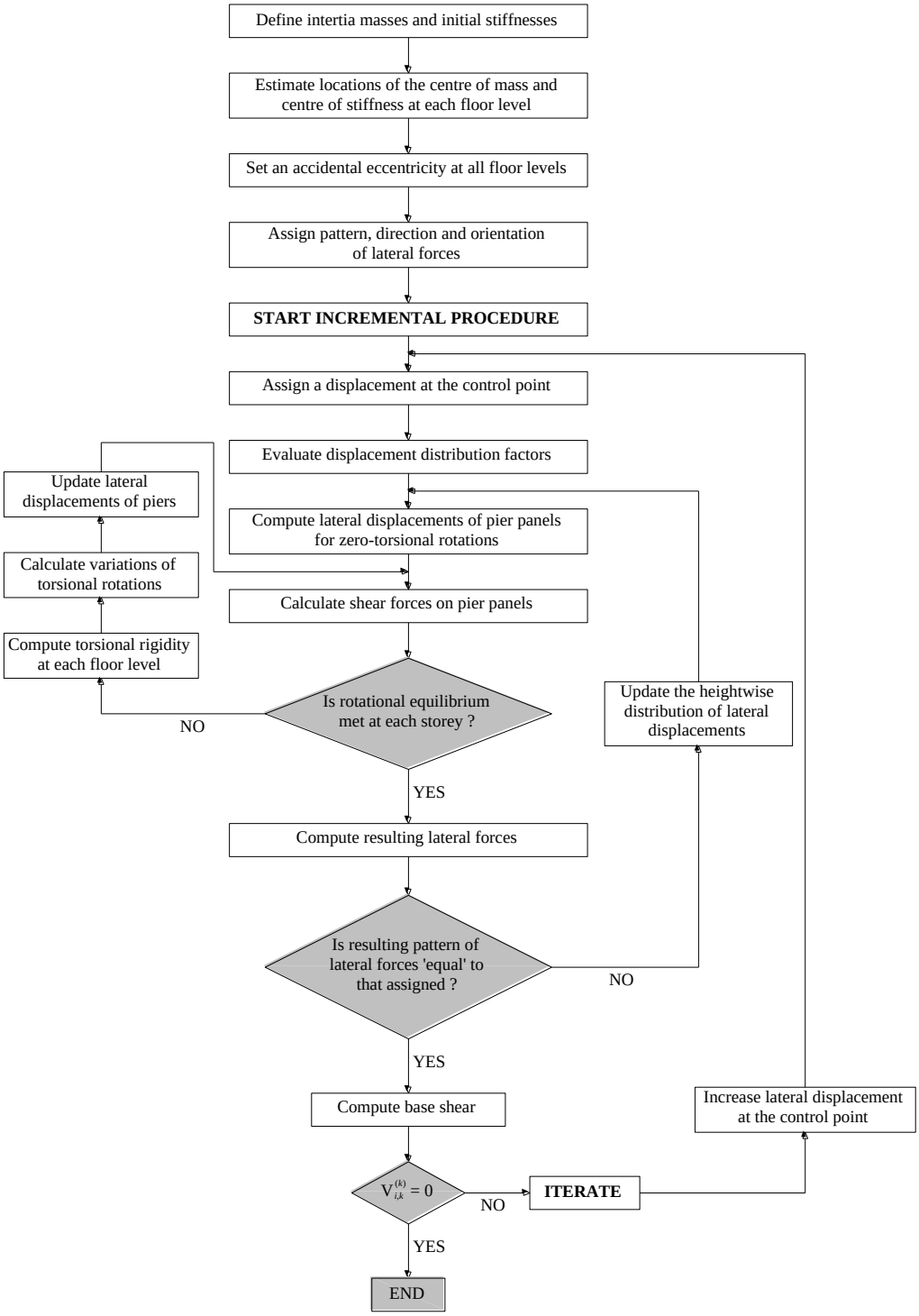

Figure 8.2 Flow-chart of pushover procedure for the masonry building

In other terms, the displacement distribution factor ω_i at the *i*-th floor level is assumed to be the product of the lateral force distribution factor β_i by the ratio between the initial lateral stiffness of the top storey and that of the storey under consideration:

$$\omega_i^{(j,k)} = \beta_i \frac{k_1}{k_i} \tag{8.14}$$

Numerical analyses showed that the assumption $\omega_i = \beta_i$ produces a lower rate of convergence in the case of a whole building.

The displacement vector of the centres of mass at the *i*-th iteration within the *k*-th analysis step is then computed through the following equation:

$$\mathbf{\Delta}_G^{(j,k)} = \Delta_C^{(k)} \mathbf{\Delta}_0^{(j,k)} \tag{8.15}$$

In the case of rigid floor diaphragms, the lateral displacement of a given wall *k* at the *i*-th floor level is computed by considering also the torsional rotation, as follows:

$$\Delta_{i,k}^{(i,j,k)} = \Delta_{G,i}^{(j,k)} + \varphi_i^{(i,j,k)} \left(d_{i,k} - d_{G,i} \right) \tag{8.16}$$

where $d_{i,k}$ and $d_{G,i}$ are the distances of the wall axis and the centre of mass *G*, respectively, from the coordinate axis.

In the case of existing masonry buildings, Eq. (8.16) does not typically apply because the in-plane flexibility of diaphragms affects the horizontal distribution of seismic actions among walls. To that end, some researchers proposed the modelling of floor diaphragms through orthotropic membrane elements (Galasco et al., 2006). This modelling can be rather effective especially in the presence of wooden or mixed steel-tile diaphragms, having they a different behaviour in the directions parallel and orthogonal to the joists.

A further superscript *i* (in round parentheses) appears into Eq. (8.16): it is related to a further iteration cycle which is needed to assess torsional rotations $\varphi_i^{(i,j,k)}$ at each floor level. At the first iteration ($i = 1$), torsional rotations can be assumed to be zero; this hypothesis is not met also in the case of symmetric-plan buildings, due to accidental eccentricities. The storey shear at the *i*-th floor level of the *k*-th wall can be computed through force-displacement diagrams, namely by the following symbolic relation:

$$V_{i,k}^{(i,j,k)} = \mathrm{f}_{i,k}^{(k)} \left(\Delta_{i,k}^{(i,j,k)} \right) \tag{8.17}$$

If spandrel panels are modelled as inextensible elements, shear forces on pier panels belonging to the same wall storey can be computed assuming equal lateral displacements. On the other hand, if a shear-type behaviour cannot be assumed for masonry walls with openings under lateral actions, Eq. (8.17) sould include actual boundary conditions of pier panels which, in turn, depend on their interaction with spandrel panels. In this case, axial flexibility of spandrel panels should be included in the capacity model in order to get a better estimation of lateral displacements of

walls[29].

Once shear forces on pier panels have been determined, the storey shear at the *i*-th floor of the building can be clearly computed as:

$$V_i^{(i,j,k)} = \sum_{k=1}^{w} V_{i,k}^{(i,j,k)} \tag{8.18}$$

A structural analysis of the building allows to estimate the secant lateral stiffness of pier panels, defined as the ratio between the resulting shear force and lateral displacement. The location of the centre of stiffness S_i can then be estimated at each floor, in order to compute storey torques through the following equation:

$$M_{T,i}^{(i,j,k)} = V_{i,k}^{(i,j,k)} \left(d_{i,k} - d_{S,i}^{(i,j,k)} \right) \tag{8.19}$$

If torsional rotations are zero at all floor levels, the torsional rigidity of the *i*-th floor is expressed as follows:

$$I_{S,i}^{(i,j,k)} = \sum_{k=1}^{w} k_{i,k}^{(i,j,k)} \left(d_{i,k} - d_{S,i}^{(i,j,k)} \right)^2 \tag{8.20}$$

where $k_{i,k}^{(i,j,k)}$ is the secant lateral stiffness defined as the sum of stiffnesses $k_{i,j,k}^{(i,j,k)}$ of individual pier panels. In such a case, torsional rotations at different floor levels can be set to the ratios between resulting storey torques and torsional rigidities. By using corrected torsional rotations into Eq. (8.16), the iterative procedure on torsional rotations goes on until one of the following convergence criteria is met:

$$\forall i \quad \frac{\left| M_{T,i}^{(i,j,k)} / V_i^{(i,j,k)} \right| - \left| d_{G,i} - d_{S,i}^{(i,j,k)} \right|}{\left| d_{G,i} - d_{S,i}^{(i,j,k)} \right|} \le \mathrm{tol}_d \tag{8.21}$$

$i < i_{\max}$

or else:

$$\forall i \quad \sum_{k=1}^{w} V_{i,k}^{(i,j,k)} \left(d_{i,k} - d_{S,i}^{(i,j,k)} \right) - \left(\sum_{k=1}^{w} \sum_{r=1}^{i-1} V_{r,k}^{(i,j,k)} \right) \left(d_{G,k} - d_{S,i}^{(i,j,k)} \right) \le \mathrm{tol}_M \tag{8.22}$$

$i < i_{\max}$

If no convergence criterion is met, then torsional rotations at different floors are corrected as follows:

$$\varphi_i^{(i+1,j,k)} = \varphi_i^{(i,j,k)} \frac{V_i^{(i,j,k)}}{M_{T,i}^{(i,j,k)}} \left(d_{G,i} - d_{S,i}^{(i,j,k)} \right) \tag{8.23}$$

and inputted into Eq. (8.16), in order to assess the rotational equilibrium at each floor,

[29] To this end, a preliminary assessment of the contribution of spandrels on non-linear behaviour of URM walls with openings is reported in Appendix C. The role of spandrel panels was estimated in terms of both strength and energy dissipation capacity.

through the convergence criterion (8.21) or (8.22). If numerical convergence is reached, lateral forces associated with horizontal translations and torsional rotations along the height of the building can be computed as follows:

$$F_i^{(i,j,k)} = V_i^{(i,j,k)} - \sum_{r=1}^{i-1} V_r^{(i,j,k)} \tag{8.24}$$

The lateral force pattern derived from non-linear structural analysis under a given displacement at the control point is compared to that assumed at the beginning of pushover analysis. Namely, one has to check the the following convergence criterion:

$$\forall i \quad \left| \frac{F_i^{(i,j,k)} / F_1^{(i,j,k)} - \beta_i}{\beta_i} \right| \leq \mathrm{tol}_\beta \tag{8.25}$$

$$j < j_{\max}$$

If also this convergence criterion regarding lateral forces is met, the base shear can be computed and a point of the pushover curve can be defined. Otherwise, the displacement shape vector $\mathbf{\Delta}_0^{(j,k)}$ is corrected and a further iteration $j = j + 1$ is needed to get resulting lateral forces matching the assigned force pattern. Such an operation is carried out by means of the *Pegasus method* (Dowell and Jarratt, 1972), which combines robustness of the *Regula Falsi method* with the higher rate of convergence of the *Secant method*. Another iteration cycle (on the superscript *i*) is then started in order to estimate torsional rotations, as well as their relevant distribution of horizontal translations and forces along the height of the building.

When both convergence criteria related to rotational equilibrium and lateral force pattern matching are met, the actual load multiplier associated with the magnitude of resulting lateral forces can be computed. Also, the base shear at the *k*-th displacement step can be defined to plot a point of the pushover curve.

Pushover analysis proceeds until all pier panels at the same wall storey reach their ultimate displacement and, consequently, the resisting storey shear vanishes. If this collapse condition is not attained, a further displacement increment is given at the control point of the building by means of Eq. (8.10). Then, a new step ($k = k + 1$) of the incremental analysis begins to get another point of the pushover curve.

8.2.2. Adaptive Pushover Analysis

The single-mode load profile used in pushover analysis can be assumed to be 'adaptive' without inducing significant increase of computational work. In fact, other researchers (see for instance: Galasco et al., 2006) have recognised the chance for a step-by-step updating of the force vector, based on the current deformed shape of the masonry structure. Then, pushover analysis allows to predict the evolutionary non-

linear response without multi-mode dynamic analysis. The updating of the lateral force pattern follows response variations in terms of stiffness, strength, and deformations, as damage develops throughout the masonry walls. In the case of both frame and frame-wall structures, force-based adaptive pushover (FAP) was found to be inable to provide significant improvements in non-linear response prediction (see Antoniou and Pinho, 2004a, for a discussion). Conversely, Galasco et al. (2006) showed that FAP can significantly improve the response prediction in the case of masonry buildings; furthermore, pushover results were found to be rather independent of the lateral force pattern assumed at the beginning of the analysis. Based on these considerations, the RAN method was also extended to an adaptive pushover procedure based on the application of lateral forces and the implementation of some features of procedures proposed by Antoniou and Pinho (2004a) for RC buildings and by Galasco et al. (2006) for masonry buildings.

First of all, the so-called *spectral amplification*, namely the spectral acceleration $S_a(T)$ at a given mode of vibration in force-based procedures (see Sect. 5.1.4), can be left equal to $S_a(T_1)$ during the analysis. Such a simplification is acceptable if the fundamental period of the masonry building falls within the constant-acceleration period interval of the elastic response spectrum and does not significantly change as damage develops within the structure. Otherwise, structural damage can produce a considerable period elongation, and hence a potential modification in spectral acceleration. In this case, spectral amplification should be updated at each significant change in the secant global stiffness of the building.

Second, masonry buildings are typically low-rise structures, so higher mode effects can be neglected within pushover analysis. As stated above, this characteristic allows to avoid multi-mode dynamic analysis, ensuring a limited computational work. The effects of this simplification should be clearly assessed in the case of masonry buildings with large irregularities in plan or elevation.

A single-mode FAP can then be performed to assess seismic capacity of the masonry building, by including also geometrical and mechanical non-linearities through a spread plasticity macro-element modelling of walls.

The adaptive force vector $\mathbf{F}^{(k)}$ at a given analysis step is directly derived from the displacement vector $\boldsymbol{\Delta}^{(k-1)}$ corresponding to the lateral displacement assigned at the control point in the previous step. Using a total updating strategy of the load vector, Eq. (8.1) specialises as follows:

$$\mathbf{F}^{(k)} = \lambda^{(k)} \Gamma_1 \mathbf{M} \bar{\boldsymbol{\Delta}}^{(k-1)} S_a\left(T_1\right) \tag{8.26}$$

where: $\mathbf{M}$ is the mass matrix of the building; and Γ_1 is the participation factor of the fundamental mode. The displacement vector is considered to be able to define a damage-dependent load vector. At the first step of the analysis, a uniform nominal load

vector $\mathbf{F}_0$ (see Sect. 5.1.5) is employed instead of the vector $\bar{\mathbf{\Delta}}^{(k-1)}$. For the sake of clarity, Eq. (8.26) includes also the modal participation factor even though it affects only the magnitude (not the shape) of lateral forces. Spectral amplification can also be computed during the analysis as a function of the current lateral stiffness of the structure. The latter can be defined as the secant stiffness corresponding to the lateral displacement assigned at the previous analysis step.

The load multiplier is computed at each analysis step through a normalisation of the displacement vector corresponding to the previous step, as follows:

$$\bar{\Delta}_i^{(k-1)} = \frac{\Delta_i^{(k-1)}}{\max\left\{\Delta_i^{(k-1)}\right\}_{i=1\ldots n}} \tag{8.27}$$

and assuming the vector $\mathbf{F}_0 = (1\ldots\beta_i\ldots\beta_n)^{\mathrm{T}}$ equal to $\bar{\mathbf{\Delta}}^{(k-1)}$. Since the load vector derived from Eq. (8.26) can produce unrealistic concentrations of shear forces in some walls, Galasco et al. (2006) suggested to 'bind' the current force vector between those corresponding to uniform and modal force patterns. Such a criterion is acceptable for regular buildings, while it should be validated on a large number of irregular buildings.

It is underlined that the iterative procedure still includes a convergence criterion on the resulting force pattern, since lateral forces are computed for each deformed state of the structure. Nevertheless, the computational work could be significantly reduced since the lateral force pattern is adaptive, and hence more consistent with the deformed shape of the structure. The resulting displacement profile should correspond to a lateral force pattern matching that defined by Eq. (8.26).

It is also emphasised that FAP would halve the number of pushover analyses on the building, because it should be not carried out for two pre-defined lateral force patterns. Nonetheless, IBC provides that pushover analysis should be conservatively carried out for two lateral force patterns: one should belong to a *Group 1 - primary patterns* and the other to a *Group 2 - secondary patterns*. *Group 1* includes:

- the inverse triangular pattern (which can be applied only if the uniform pattern is assumed as secondary pattern);
- the modal pattern; and
- a force pattern proportional to storey shears provided by multi-mode dynamic analysis (which can be applied for structures with $T_1 > T_C$).

Group 2 includes:

- the uniform pattern (i.e., a mass-proportional force pattern corresponding to a uniform distribution of horizontal accelerations along the height); and
- an adaptive pattern.

It follows that FAP should be performed along with a primary modal pattern.

Chapter 9 - APPLICATION ON A MASONRY BUILDING

The pushover procedures developed for seismic assessment of single masonry walls with openings and entire buildings were implemented into RAN CODE (Augenti et al., 2010a), a computer program devoted specifically to masonry buildings. RAN CODE allows: (1) to check structural safety under gravity loads at ULS; (2) to perform simplified safety verifications against potential out-of-plane mechanisms due to local seismic actions on individual masonry walls; and (3) to assess global seismic performance of masonry walls and buildings through both linear and non-linear static analyses.

In the present chapter, the main results of pushover analyses on a three-storey URM school building are presented and discussed. The numerical application was aimed at assessing seismic performance of the building under varying incidence angle of seismic input. Damage maps are also discussed and proposed as effective tools for preliminary cost estimations of seismic repair, strengthening, and upgrading interventions on masonry buildings. In fact, damage maps could provide an effective support to decision-makers, since they allow to perform cost-benefit analysis in order to identify the optimal design solution among different technical chances.

9.1. Description of the Structure

The masonry building was supposed to be located in Gesualdo (Italy) [41.00° latitude, 15.07° longitude], which is a town near the fault system that generated the M_w 6.9 Irpinia, Italy, earthquake on 23 November 1980 (with maximum Mercalli-Cancani-Sieberg intensity $I_{MCS,max}$ = 10). The building had a courtyard and the staircases located in the entrance hall (Fig. 9.1).

The structure was designed in compliance with both EC8 and IBC. All walls were assumed to be well connected themselves and to rigid mixed RC-tile floor diaphragms through RC ring beams. The walls had a regular layout of openings at each floor level, except for the wall located on the front side of the building. The irregularity of this masonry wall was caused by the presence of a higher and larger opening. The masonry above the openings was also supported by lintels well anchored to adjoining piers, so spandrel panels were included in the capacity model of the structure.

Figure 9.2 shows a global view of the macro-element structural model of the building. The walls were supposed to be made of yellow tuff masonry having the following

mechanical properties: unit weight γ = 16 kN/m^3; Young's modulus E = 3000 MPa; shear modulus G = 1200 MPa; mean uniaxial compressive strength f_m = 4.3 MPa; shear strength at zero confining stress $\tau_{0,m}$ = 0.14 MPa; yielding strain ε_k = 0.2%; and ultimate strain ε_u = 0.35%.

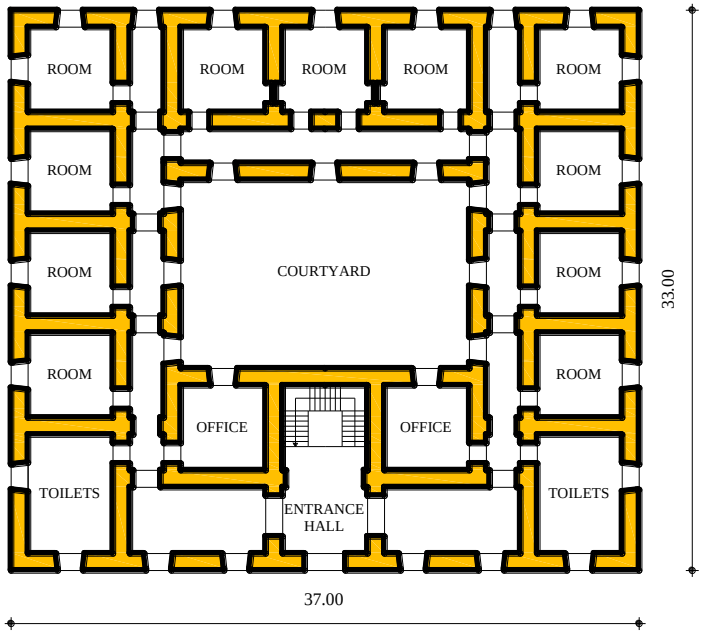

Figure 9.1 Ground floor plan of the building

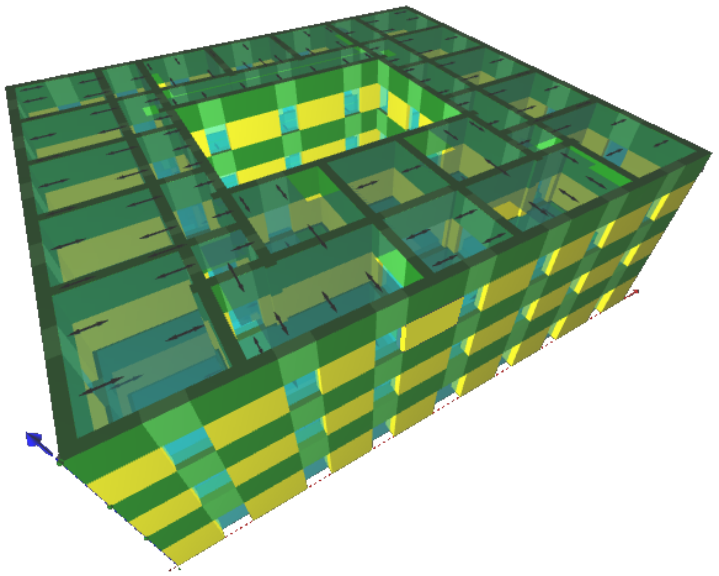

Figure 9.2 Macro-element model of the building

Given that displacement ductility associated with flexural yielding of macro-elements is computed during the analysis, owing to the evolution of the inner effective domain, just displacement ductility for shear mechanisms ($\mu_{d,V}$) was defined before the analysis was run. Based on experimental data selected from *Database Murature UNINA-DIST* [URL: http://www.reluis.it/dbuninadist], such a ductility was set to $\mu_{d,V} = 3$ for yellow tuff masonry panels.

9.2. Seismic Hazard Assessment

9.2.1. Framework and Methodology

The seismic hazard assessment procedure provided by IBC is rather different from those of previous Italian codes. Based on the seismic source zone model ZS9 developed by Meletti et al. (2008) (Fig. 9.3a), the Italian National Institute of Geophysics and Vulcanology (INGV) estimated seismic hazard parameters at each node of a regular grid having 5 km spacing and covering the whole Italian territory with 10751 nodes. If the construction site is not located on a reference node of the grid, one should identify the elementary grid which includes the site. Hazard parameters at the site are estimated as weighed average of those related to reference nodes by the distances of the nodes from the site (see Annex A in: IMIT, 2008). The seismic hazard assessment approach is thus site-dependent, rather than zone-dependent.

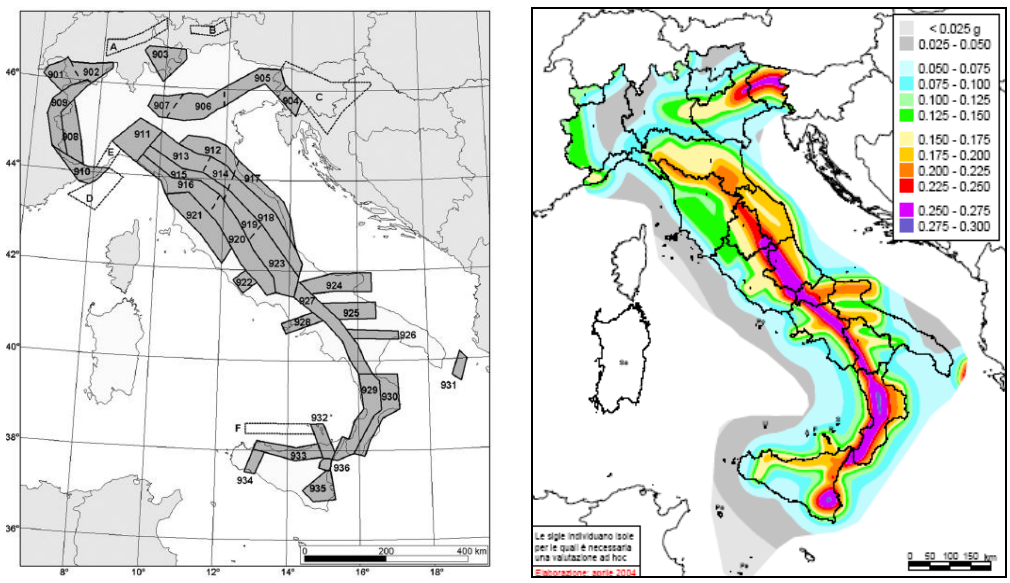

(a) (b)

Figure 9.3 (a) Seismic source model ZS9 and (b) a_g map for probability of exceedance of 10% in 50 years (URL: http://zonesismiche.mi.ingv.it/)

Probabilisitc seismic hazard analysis (PSHA) by INGV allowed to estimate seismic hazard at each site of the reference grid. The computations resulted in hazard curves in terms of peak horizontal acceleration for soil type A (a_g) and spectral acceleration ($S_a(T)$) for ten different periods of vibration from 0.1 to 2 s. Hazard curves were lumped in nine probabilities of exceedance in 50 years (from 2% to 81%), so both static and interactive maps (Fig. 9.3b) were obtained [URL: http://esse1-gis.mi.ingv.it/s1_en.php]. For seismic design practice, the hazard parameters were listed in Annex B of IBC.

The seismic hazard parameters provided by IBC are: the reference peak horizontal acceleration on soil type A (namely, the bedrock for any other soil type), a_g; the maximum amplification factor of the horizontal acceleration response spectrum, F_o; and upper limit of the period of the constant spectral acceleration branch on type A ground, T_C^*. Such parameters are associated with a given return period T_R of the design earthquake which, in turn, is defined as a function of a reference (temporal) period V_R and the probability of exceeding the a_g value in V_R, denoted as P_{V_R}. Whilst V_R is defined as the nominal life V_N times the importance factor C_U assigned to the building, the probability of exceedance changes with the limit state of interest. Therefore, once the return period of the design earthquake is computed for the building, the seismic hazard at a site is known and the peak ground acceleration (*PGA*) can be evaluated accounting for local soil conditions. Similarly to EC8, IBC provide a soil factor S as the product of a stratigraphic amplification factor S_S by a topographic amplification factor S_T. *PGA* is then obtained as Sa_g (see Sect. 3.1).

Finally, the upper limit of the period of the constant spectral acceleration branch (denoted as T_C) is evaluated as a factor related to soil type (denoted as C_C) times the period T_C^*. The lower limit of the period of the constant spectral acceleration branch is then defined as $T_B = T_C/3$, while the lower limit of the period of the constant spectral displacement branch (also called 'corner period') is defined as $T_D = 4a_g/g + 1.6$, being g the gravitational acceleration.

9.2.2. Seismic Hazard at the Site of the Building

Assuming a high occupancy for the school building, an importance coefficient $C_U = 1.5$ (corresponding to a building class III, according to IBC) was considered. Considering a soil type B (corresponding to a shear velocity $V_{s,30}$ within a 30 m-deep soil deposit which is between 360 m/s and 800 m/s) and a topographic class T1 (i.e., a ground surface with average slope between 0 and 15°), the stratigraphic amplification factor S_S was greater than unity and limited to 1.2, while the topographic amplification factor S_T was equal to unity. Also, it followed a period modification factor C_C greater than unity.

The seismic hazard parameters corresponding to the four limit states provided by IBC are reported in Table 9.1; the values of S_S, C_C, the characteristic periods of elastic response spectra, and *PGA* demand (PGA_{dem}) are listed in Table 9.2.

Table 9.1 Seismic hazard parameters for Gesualdo (Italy)

Limit state	T_R [years]	a_g [g]	F_o	T_C^* [s]
Operational	45	0.079	2.337	0.291
Limited damage	75	0.104	2.317	0.320
Life safety	712	0.319	2.285	0.393
Near collapse	1462	0.424	2.326	0.417

Table 9.2 S_S and C_C factors, spectrum characteristic periods and *PGA* demand

Limit state	S_S	C_C [g]	T_B [s]	T_C [s]	T_D [s]	PGA_{dem} [g]
Operational	1.200	1.408	0.137	0.410	1.914	0.095
Limited damage	1.200	1.381	0.147	0.442	2.015	0.125
Life safety	1.109	1.326	0.174	0.521	2.874	0.354
Near collapse	1.005	1.310	0.182	0.547	3.298	0.426

9.3. Non-Linear Analyses

9.3.1. Methodology

The building was analysed through the non-adaptive pushover procedure discussed in Section 8.2.1. According to IBC and EC8, the global seismic performance of the building was assessed through the N2 method by comparing capacity to demand. The latter was computed from an elastic response spectrum by assuming an equivalent viscous damping factor ξ_{eq} = 5% (corresponding to a spectrum modification factor η = 1) for the masonry building.

It is underlined that the total height of the building was H = 14.5 m, so the formula $T_1 = 0.05H^{3/4}$ provided by IBC leads to an approximate fundamental period T_1 = 0.371 s falling in the interval $[T_B,T_C]$ which corresponds to the maximum amplification of horizontal acceleration.

Pushover analyses were carried out by imposing a monotonically-increasing horizontal displacement d_c at the control point of the building, which was assumed to be located at the centre of mass CM of the roof floor. In order to assess both demand and capacity parameters under varying seismic input direction, pushover analysis was performed separately for twelve incidence angles α with respect to the *x*-axis (Fig. 9.4). The

centre of initial stiffness was denoted as CS, while the centre of strength at the ultimate displacement related to life safety limit state was denoted as CR.

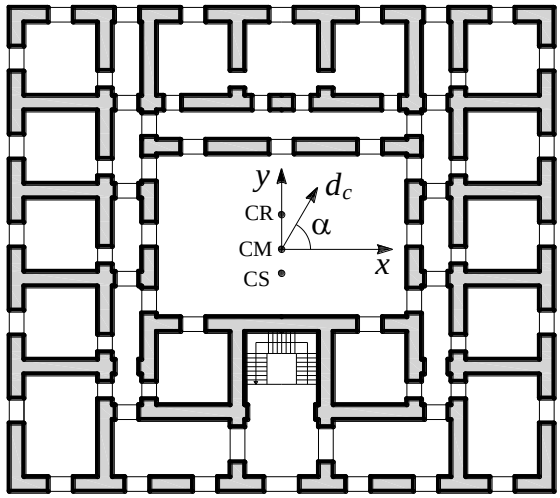

Figure 9.4 Incidence angle of seismic input

For each direction, pushover analysis was carried out for both modal and uniform patterns of lateral forces. A polar representation of seismic capacity allowed to obtain limit domains in terms of lateral strength and displacement, as well as demand domains. The superposition of these domains let to identify both *satisfactory* and *unsatisfactory performance regions*, which correspond to safety and substandard safety levels, respectively. It is underlined that Petti and Marino (2010) proposed a two-dimensional representation of seismic demand through *polar spectra*. Nevertheless, the use of such spectra is presently quite limited because they were derived for single seismic events.

9.3.2. Discussion of Results

Figures 9.5a and 9.5b show the pushover curves corresponding to the modal and uniform patterns of lateral forces, respectively, under varying incidence angle α (expressed in sexagesimal degrees). Half of pushover curves are plotted with solid lines (angles of incidence from 0 to 150°) and the other curves ar plotted with dashed lines (angle of incidence from 180° to 330°), by using the same color for corresponding couples which differ of 180° each other.

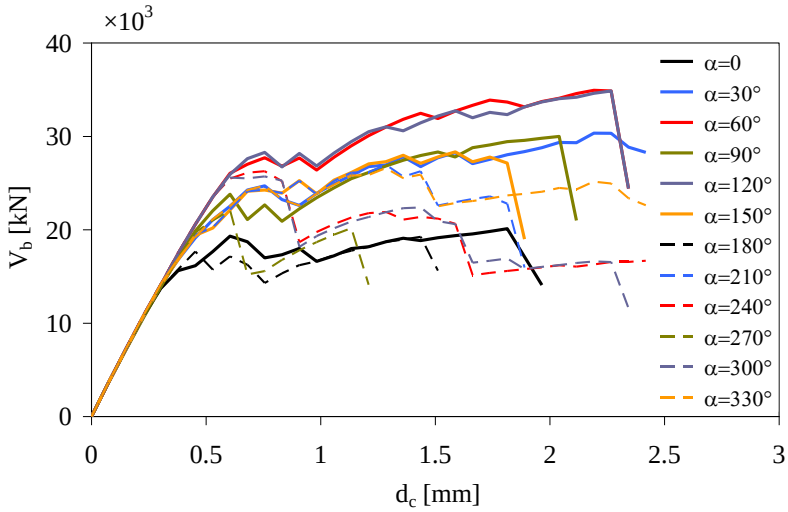

(a)

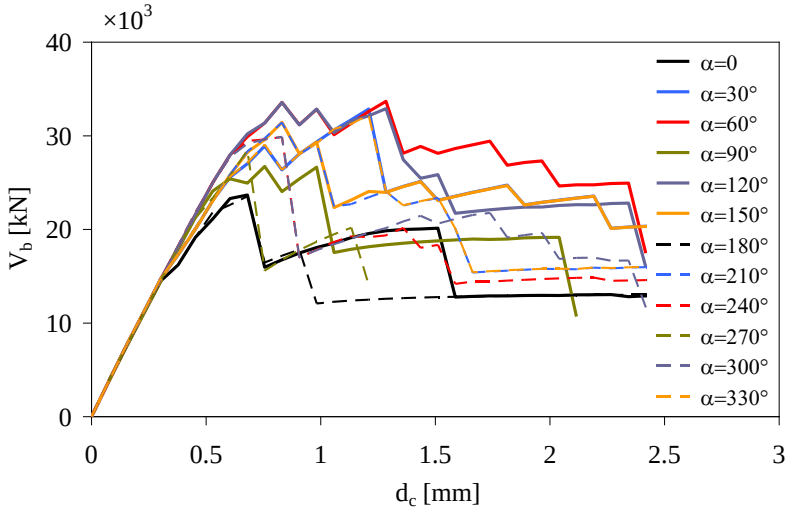

(b)

Figure 9.5 Pushover curves for different incidence angles: (a) modal force pattern; (b) uniform force pattern

It is emphasised that the initial elastic response is not significantly affected by the loading direction, resulting in a rather equal displacement demand. Conversely, peak base shear $V_{b,max}$ is very different from that corresponding to the ultimate displacement of the structure ($V_{b,u}$), due to the variation in the sequence of failure modes with the angle of incidence. Such a variation was mainly due to a non-uniform distribution of gravity loads, especially with reference to the shorter inner walls (only those located from the $-y$ side of the plan were loaded by floor slabs). Figure 9.6a shows the global

displacement demand-to-capacity ratio (denoted as d_{dem}/d_{alw}) versus the incidence angle. The exceedance of unity indicates clearly a substandard safety level of the structure. This occurs for the *x*-direction ($\alpha = 0$) and incidence angles falling in the interval [150°,300°]. The maximum substandard level is associated with a modal force pattern having an incidence angle $\alpha = 270°$.

Figure 9.6b illustrates the variation of *demand ductility index* defined as $I_{DD} = PGA_{dem}/PGA_{max}$, where: PGA_{dem} is the *PGA* demand at life safety limit state; and PGA_{max} is the *PGA* corresponding to the maximum base shear allowed by the building (that is, $V_{b,max}$).

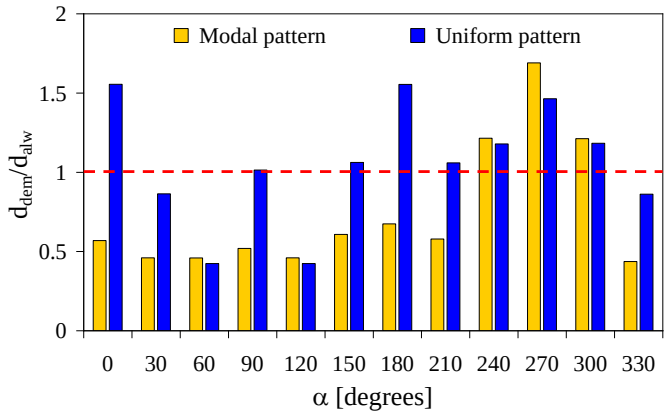

(a)

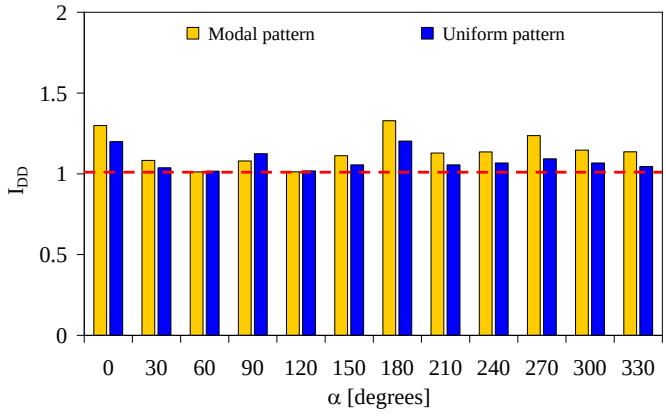

(b)

Figure 9.6 (a) d_{dem}/d_{alw} and (b) I_{DD} versus incidence angle

It is emphasised that, on average, I_{DD} is slightly above unity under varying force pattern and angle of incidence, showing some peaks especially when displacement demand exceeds the relevant capacity. In addition, I_{DD} seems to be more stable than the

demand-to-capacity ratio. The latter is mainly affected by different displacement capacity of the building under varying incidence angle of seismic input and force pattern.

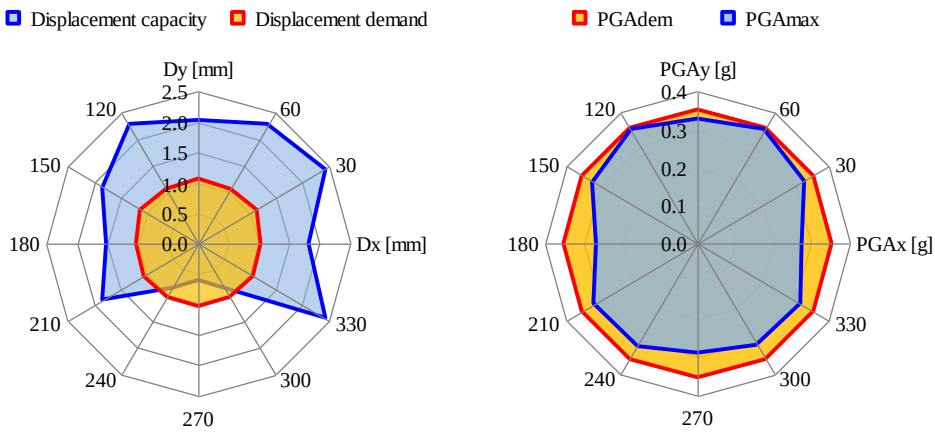

Figure 9.7 Capacity and demand parameters versus incidence angle for modal force pattern

The substandard safety region where the displacement demand exceeds the capacity can then be identified. The law of variation of displacement capacity versus the incidence angle is quite consistent with the geometrical symmetry of the building plan with respect to the *y*-axis, but it seems to be affected by the orientation of seismic actions.

The seismic performance is satisfactory for $\alpha = 90°$ (i.e., seismic action along the *y*-direction) because the displacement demand is about one-half of the displacement capacity. The opposite condition occurs for $\alpha = 270°$ due to the occurrence of different failure modes under non-uniform distribution of gravity loads.

A higher load-bearing capacity of the building for $\alpha = 90°$ with respect to that corresponding to $\alpha = 270°$ is highlighted in Figure 9.7b. Nevertheless, the latter shows lower PGA_{max} sensitivity to the angle of incidence. Figure 9.8a shows a poorer seismic performance of the building for uniform force pattern, while Figure 9.8b does not highlight significant variations compared to Figure 9.7b, showing major earthquake resistance of the building in the *y*-direction.

Variations in both initial and effective stiffnesses were also investigated; the effective stiffness was defined as the secant stiffness at the displacement capacity related to life safety limit state.

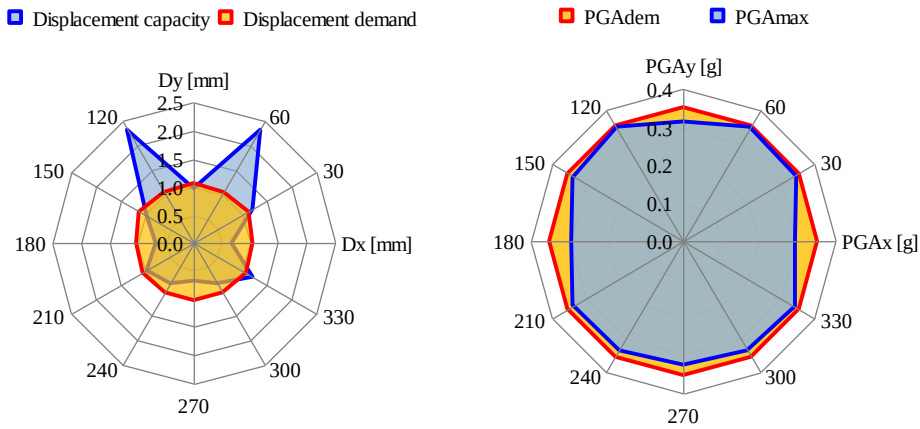

Figure 9.8 Capacity and demand parameters versus incidence angle for uniform force pattern

Figures 9.9a and 9.9b show for modal and uniform force patterns, respectively, that the effective stiffness is lower than one-half of the initial elastic stiffness, emphasising high non-linearity in the structural response. The stiffness reduction is higher in the case of modal force pattern, consistently with the fact that the supply displacement ductility $\mu_{d,max}$ corresponding to this load profile is higher than that associated with the uniform force pattern (Fig. 9.10).

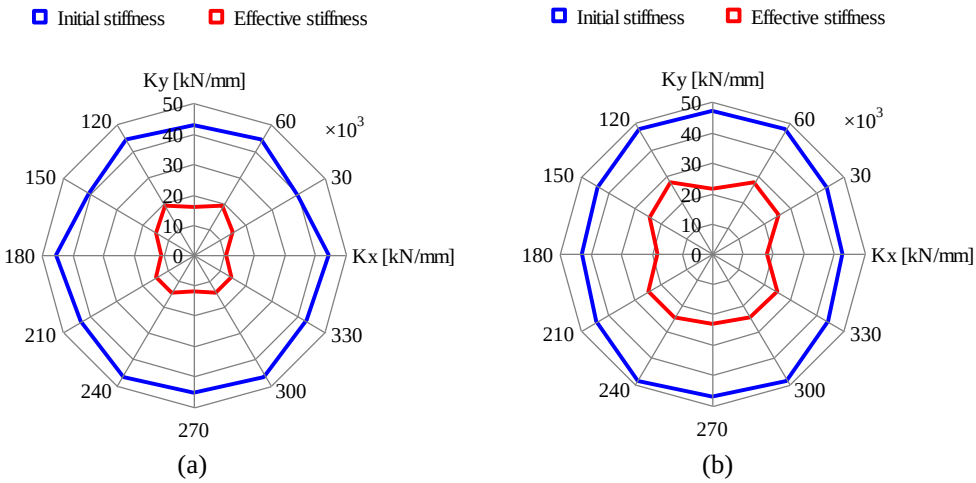

Figure 9.9 Lateral stiffnesses versus incidence angle: (a) modal and (b) uniform patterns

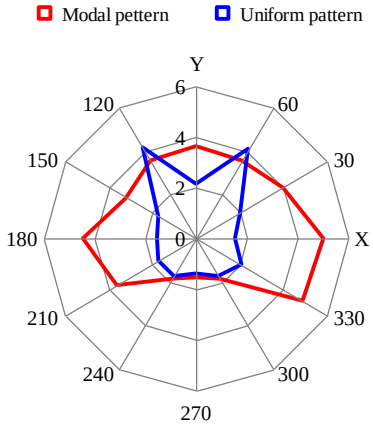

Figure 9.10 Supply displacement ductility versus incidence angle

Figure 9.11a shows the ductility-related strength reduction factor R_μ under varying incidence angle; R_μ was estimated through the following equation (Vidic et al., 1994):

$$R_\mu = 1 + (\mu - 1)\frac{T^*}{T_0} \tag{9.1}$$

which applies to elasto-plastic SDOF systems with period lower than the dominant period of the earthquake, defined as $T_0 = 0.65\mu^{0.3}T_C \leq T_C$ (see Sect. 5.2.3).

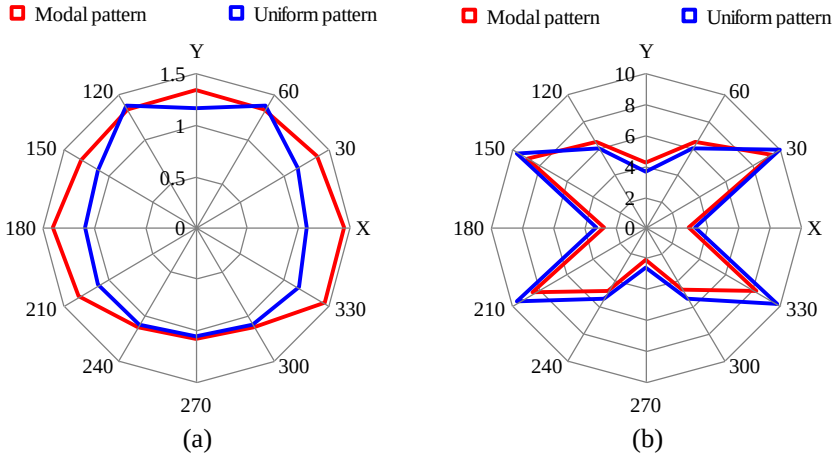

Figure 9.11 (a) R_μ and (b) α_u/α_1 versus incidence angle

Once the overstrength ratio α_u/α_1 was estimated for each loading direction and lateral force pattern (see Sect. 5.2.3 and Fig. 9.11b), the total strength reduction (or behaviour) factor was computed as follows:

$$q = R_{\mu} \frac{\alpha_u}{\alpha_1} \tag{9.2}$$

to be compared with thoseprovided by IBC and EC8 for linear seismic analysis. In such a case, given that the building is irregular in elevation in terms of mass (variations greater than 25%), the behaviour factor for linear seismic analysis should be q_{NTC} = 2.88 (Fig. 9.12) according to IBC, while EC8 provides a behaviour factor q_{EC8} falling in the interval [1.5,2.5] for URM buildings designed for earthquake resistance.

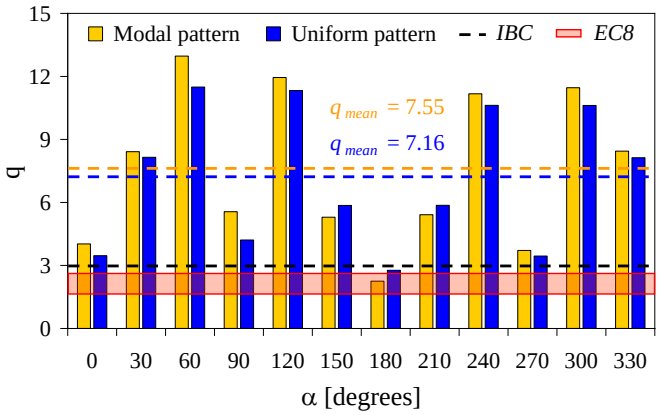

Figure 9.12 Comparison between strength reduction (or behaviour) factors

The average behaviour factors obtained for modal and uniform force patterns are equal to 7.55 and 7.16, respectively, even if they depend significantly on the incidence angle. The minimum behaviour factors are respectively equal to 2.25 and 2.77 for the above-mentioned force patterns and are associated with an incidence angle α = 180°. In any case, it is underlined that behaviour factors provided by IBC and EC8 are conservative and ensure the ductility demand.

9.4. Damage Maps

Results of pushover analyses were processed to assess also the distribution of structural damage in plan. These computations allowed to plot *expected damage maps* at the displacement demand and *collapse maps* at the ultimate displacement, both related to the life safety limit state of the building (Figs. 9.13a–d).

The former type of maps could be used (1) to identify potential damage concentrations due to high ductility demands on some masonry panels, and (2) to preliminary estimate the total repair cost as the damaged area times the average cost per unit area. It is also emphasised the ability to identify the best technical-economical strengthening solution in the case of existing buildings, through cost-benefit analysis.

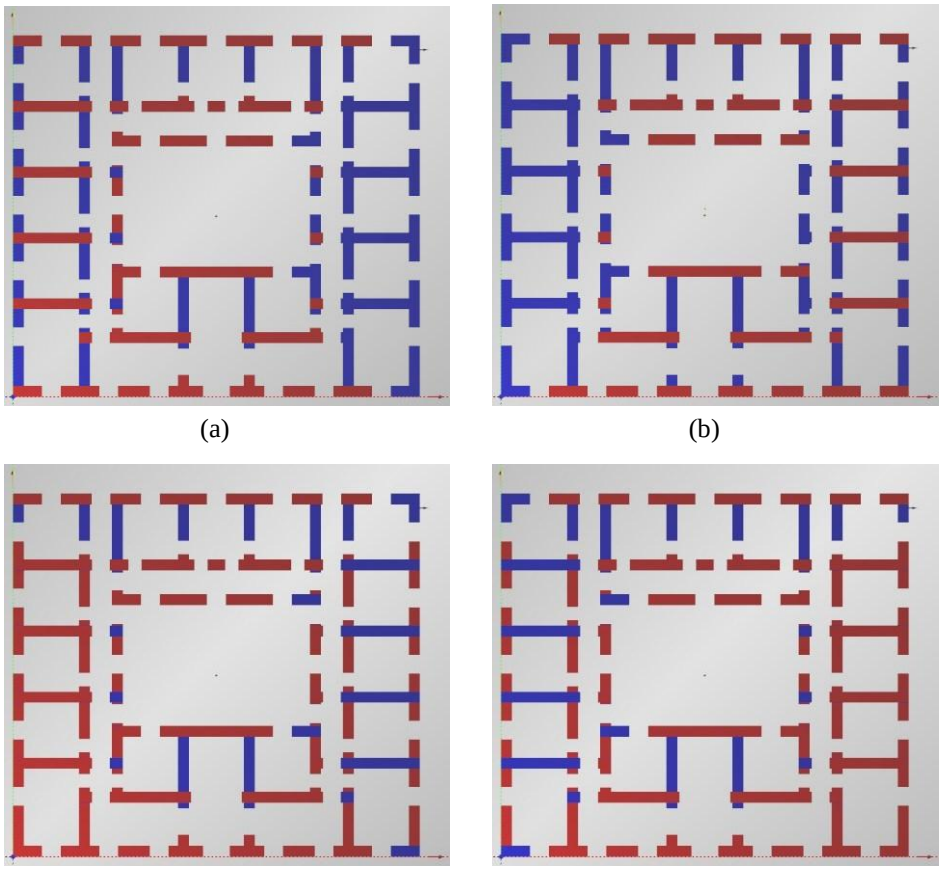

(a) (b)

(c) (d)

Figure 9.13 Expected and collapse damage maps related to ground floor plan: (a,c) $\alpha = 30°$; (b,d) $\alpha = 150°$

The comparison between collapse and expected damage maps allows to identify potential conditions where the inelastic capacity of the structure is poorly exploited. In fact, in the case of the building under study, the percentage of collapsed piers does not increase from the displacement demand to the collapse state, for incidence angles equal to 240°, 270° and 300°. This result indicates clearly that the expected damage distribution is equal to that related to the collapse state for loading directions corresponding to displacement capacity lower than demand. This occurred for the above-mentioned angles, in the case of modal force pattern, and for incidence angles equal to 0, 90°, 150°, 180°, and 210°, in the case of uniform force pattern.

Figures 9.13a and 9.13b show, for instance, the expected damage maps for incidence angles equal to 30° and 150°, respectively, in the case of modal force pattern (in red the collapsed piers and in blu the resisting piers). For these incidence angles, the comparison between the expected damage maps and the collapse maps reported in

Figures 9.13c and 9.13d highlights that the damage at the displacement demand is much lower than that corresponding to the collapse of the building.
Figures 9.14a and 9.14b illustrate the global damage indices defined as the percentage area of collapsed piers at displacement demand and capacity, respectively. Finally, Figure 9.14c shows the variation of the ratio between the global damage indices related to demand and capacity: such a parameter indicates the percentage of masonry piers likely to collapse which would be damaged under the displacement demand.

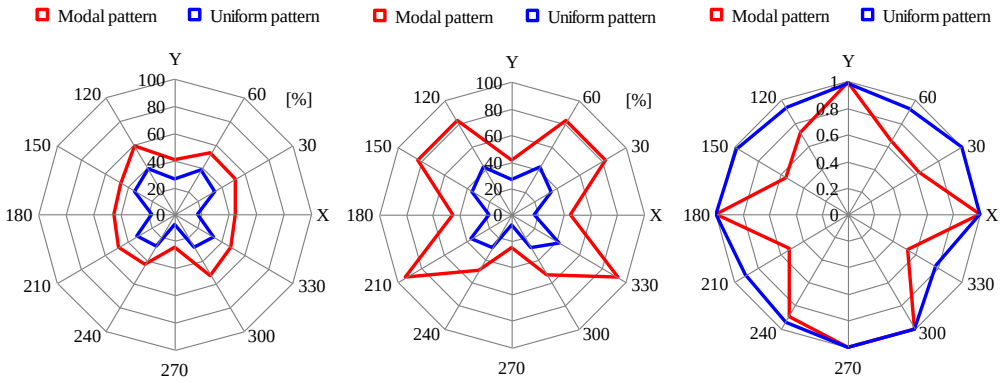

Figure 9.14 Damage indices at (a) displacement demand and (b) collapse; (c) index ratios

9.5. Concluding Remarks

The pushover procedure presented in Chapter 8 was applied on a three-storey URM building designed in compliance with EC8 and IBC. Lateral actions were applied along twelve directions of the building plan in order to assess global performance under different incidence angles of seismic input. Variations in demand and capacity were assessed in terms of peak ground acceleration and lateral roof displacement.
The influence of the loading direction could be deepened by performing pushover analysis on a large number of masonry buildings, especially if irregular in plan. The outcomes of the pushover analyses carried out on the building (which was regular in plan, according to seismic code criteria) have shown that the estimation of seismic vulnerability along two principal directions of the plan would have produced conservative results. In fact, the maximum demand-to-capacity ratio has been detected for one of these directions. Conversely, this statement could be not confirmed in the case of plan-irregular masonry buildings.
In the case of the analysed building, both load-bearing and displacement capacities have been found to depend on the angle of incidence. In fact, the building experienced different non-linear response not only under varying direction of seismic input, but also

at opposite orientations corresponding to the same direction. This outcome depends on a non-uniform distribution of gravity loads, and hence different load-bearing and displacement capacities of walls. Indeed, the walls which supported directly the floor slabs had higher capacity compared to the others.

From a methodological standpoint, it has been also shown that pushover predictions can be processed to obtain *expected damage maps* and *collapse maps*, which allow to assess the damage distribution throughout the structure and to identify potential damage concentrations. The estimation of global damage indices, defined for instance as percentage of damaged area, could lead to rapid preliminary cost estimations of repair, strengthening, and upgrading interventions on masonry buildings. Damage scenarios corresponding to different design solutions can be effective tools for cost-benefit analysis aimed at identifying the optimal solution from both technical and economic viewpoints.

Chapter 10 - CONCLUSIONS AND POTENTIAL FUTURE DEVELOPMENTS

Non-linear seismic response of masonry buildings has been investigated through *macro-element* approaches. Individual masonry walls with openings have been assumed to be systems of two-dimensional elements whose lateral response depends on their loading condition and location within the wall. The following types of macro-elements have been identified in each masonry wall: '*pier panels*', which are the vertical structural elements; '*spandrel panels*', which are the horizontal structural elements; and '*joint panels*', which are the elements that link pier and spandrel panels together. The RAN method, which was proposed by Augenti (2004) for linear static analysis of masonry buildings, was used as starting point for non-linear incremental static (pushover) analysis.

10.1. Research Outcomes

To assess non-linear seismic response of individual masonry walls and buildings, an *evolutionary spread plasticity macro-element* has been formulated. Its lateral response under varying drift demands is affected by both geometrical non-linearity due to sectional cracking and mechanical non-linearity. The latter is explicitly taken into account through specific stress-strain relationships. Non-linear behaviour has been analysed by means of strength domains, moment-curvature diagrams, and force-displacement curves, for each stress-strain relation under consideration.

A three-dimensional assemblage of walls modelled by macro-elements allows to build up the structural model of a whole masonry building and to assess its seismic behaviour. To this aim, the RAN method was extended to *non-linear incremental static (pushover) analysis* separately for single masonry walls with openings and masonry buildings.

10.1.1. Flexural Strength Domains and their Evolution

Flexural strength domains were developed in the following forms: bending moment versus axial force, in the case of spandrel panels; and shear force versus axial force, in the case of pier panels.

Strength domains for spandrel panels refer to cross-sections and could be transformed

in shear force versus axial force domains by assuming a specific boundary factor affecting overall rotational equilibrium of the panel.

Limit lines of strength domains were derived through *deformation-based approaches*, namely by the integration of pre-defined axial strain diagrams on both cracked and uncracked cross-sections. Such domains were defined for cracking, elastic, and ultimate limit states.

Strength domains corresponding to strength *degrading constitutive models* allow to account for more real mechanical properties of masonry. Comparisons among ultimate strength domains have shown that formulas reported in IBC (IMIT, 2008) lead to higher ultimate shear forces and bending moments, if the given axial force is not much greater than one-half of the ultimate axial force (which corresponds to a normalised axial force equal to 0.5). Using a stress-strain relationship derived from uniaxial compression tests on masonry prisms in the direction orthogonal to mortar bed joints, more conservative predictions of ultimate shear force can be obtained. Mechanical non-linearity in the elastic range (namely, that described by the rising branch of the monotonic constitutive law) induces a non-linear relationship between the allowable shear force corresponding to flexural failure and the applied axial force, also at cracking limit state. Such a non-linearity does not appear within classical stress-based approaches, nor if an EPP constitutive model is assumed for masonry under compression in the deformation-based approach used in this work.

The *evolution in strength domains* under varying strain ductility has been also investigated in the case of strength degrading constitutive laws. As strain ductility increases from unity (corresponding to elastic limit state) to the value associated with ultimate strain of masonry (corresponding to ultimate limit state), the flexural strength domain experiences first a growth and then a contraction. It follows that the assumption of different values of strain ductility in seismic design, or alternatively variations in strain ductility demand in non-linear seismic analysis, leads to different ultimate moment predictions at a given axial force. Such variations are less significant at normalised axial forces lower than 0.25.

Three-dimensional strength domains have been proposed in the shear force – axial force – axial force eccentricity format, for left and right extreme sections of spandrel panels separately. Such domains are also affected by loads applied to the panel, being they not affected by pre-defined boundary conditions. Three-dimensional domains have been sectioned with planes corresponding to increasing values of axial force and its eccentricity, resulting in two-dimensional strength domains plotted respectively in the following formats: shear force versus eccentricity and shear force versus axial force.

10.1.2. Moment-Curvature Diagrams, Flexural Strength and Ductility of URM Cross-Sections

Moment-curvature diagrams were developed through a specific incremental iterative procedure, in the case of unreinforced masonry (URM) rectangular cross-sections without reinforcing elements. *Sectional parameters* derived by moment-curvature analysis, such as overstrength, strength degradation, yielding and ultimate curvatures, and curvature ductility, have been discussed. These parameters were evaluated for different constitutive laws; furthermore, the relationship between *curvature ductility* and strain ductility of masonry has been investigated. For any given axial force, yielding curvature has been found to be rather the same for all constitutive laws, except for EPP constitutive model; the latter leads to lower curvatures. Assuming strength degrading constitutive laws derived from experimental testing, ultimate curvature predictions have been found to be higher than those corresponding to other constitutive laws. Rather equal predictions of ultimate bending moment have been obtained at a normalised axial force equal to 0.1; conversely, ultimate curvature predictions have been found to be significantly different each other, including those corresponding to empirical stress-strain relationships derived in the directions parallel and orthogonal to mortar bed joints. At normalised axial forces not greater than 0.5, the ratio between curvature ductility and strain ductility has been found to be greater than unity and independent of the given axial force.

10.1.3. Force-Displacement Diagrams

Force-displacement curves of individual URM panels have been formulated by considering the lateral displacement associated with the axial force as the sum of flexural, shear, and rocking contributions. Both shear and rocking contributions (the latter occurs after masonry cracking) are typically estimated through force-controlled procedures based on the assumption of a pre-defined displacement ductility for shear mechanisms. On the other hand, non-linear flexural behaviour of URM panels has been deeply investigated in the present thesis. To this aim, an incremental iterative procedure has been developed. Given an axial force on the panel, the maximum axial strain over end section(s) subjected to the maximum bending moment is monotonically increased until the ultimate strain of masonry is attained. Both the shear force and the lateral displacement are computed at each axial strain step in order to get the force-displacement curve related only to bending deformation. The overall force-displacement diagram is then obtained by summing both shear- and ‘pure’ rocking-induced lateral displacements to that associated with bending deformation, at each shear force level. If the lateral behaviour of the panel is shear-controlled, the force-

displacement curve is truncated by a plateau with a pre-defined displacement ductility. The latter can be defined before analysis is run on the basis of experimental data available in the literature. To this end, a useful tool for rapid selection of experimental data on mechanical properties of the main masonry types is the electronic archive named *Database Murature UNINA-DIST*, which is available on the website of the Italian Network of University Laboratories for Earthquake Engineering (ReLUIS) [URL: http://www.reluis.it/dbuninadist] and was developed in the framework of ReLUIS-DPC 2005-2008 project.

Comparisons between force-displacement curves plotted in force control and those derived by controlling the maximum axial strain have shown that the former can lead to underestimate the ultimate displacement of masonry panels. It follows that the significant contribution of strain ductility of masonry on displacement capacity of walls is not considered (at least explicitly) in classical approaches. As the given axial force increases, force-controlled procedures can lead to overestimate both lateral stiffness and strength, without considering potential strength degradation at larger displacements.

10.1.4. Pushover Procedures for Masonry Walls and Buildings

In order to assess seismic capacity and demand on masonry buildings, different force-based pushover procedures in response control have been developed to be coupled with inelastic spectra in the framework of the N2 method (according to EC8 and IBC). Pushover procedures have been separately formulated for single masonry walls with openings and entire masonry buildings.

The pushover procedure developed for single masonry walls could be used in the case of both individual buildings and building units within aggregates. Historical buildings are often characterised by the presence of flexible diaphragms, and lack or ineffectiveness of both diaphragm-to-wall and wall-to-wall connections. In such cases, global assessment of non-linear seismic response of a masonry building can lead to unrealistic predictions, so one should perform pushover analysis on the constituent masonry walls subjected to their relevant gravity loads. This modus operandi is specifically allowed by IBC.

The pushover procedure developed for entire masonry buildings includes torsional effects due to both inherent (structural) and accidental eccentricities between centre of mass and centre of stiffness at each floor level. The proposed procedure applies in the case of rigid floor diaphragms and effective diaphragm-to-wall and wall-to-wall connections. Load-bearing walls not parallel to the loading direction participates to the non-linear response of the structure by warping torsion. The use of an evolutionary spread plasticity macro-element, whose lateral behaviour is also affected by

deformation demand, allows to relate the 'local' response of macro-elements to the 'global' response of the building. In this way, seismic assessment is performed through a 'unitary' approach.

Both pushover procedures were implemented in a computer program devoted to structural analysis of masonry buildings and named RAN CODE (Augenti et al., 2010a). In addition, an adaptive force-based pushover procedure was developed to be applied in the seismic assessment of irregular buildings, but it requires numerical/experimental validation.

Among numerical applications on different building models aimed at testing RAN CODE, an example of seismic assessment for a new masonry building designed in compliance with EC8 (CEN, 2004) and IBC has been discussed. Capacity and demand on the building were estimated for different *incidence angles* of seismic input. The occurrence of different failure modes and significant variations in demand-to-capacity ratios under varying incidence angle have been detected. *Expected damage maps* and *collapse maps* corresponding to global demand and capacity, respectively, were developed. They could be attractive tools to assess the damage distribution within a masonry building and to identify potential damage concentrations. The estimation of *global damage indices*, defined for instance as percentage of damaged elements, could easily lead to preliminary estimations of repair costs (if damage scenarios are derived) and strengthening costs (if an existing building does not meet code safety requirements). Therefore, damage scenarios could be obtained for different design solutions and then cost-benefit analysis could be carried out in order to select the optimal solution from both technical and economic viewpoints.

10.1.5. Experimental Outcomes Supporting Non-Linear Analysis

An experimental program was carried out on masonry panels and walls in the framework of ReLUIS-DPC 2005-2008 project. Empirical constitutive models more accurate than those available in the literature were developed and are discussed in Appendices A and B of this thesis. The influence of spandrels on lateral resistance, stiffness, and energy dissipation/absorption capacity of masonry walls with openings, has been preliminary assessed. The main results about in-plane lateral loading tests on a full-scale masonry wall with a opening are presented in Appendix C.

Uniaxial compression tests and direct shear tests were carried out to characterise the mechanical behaviour of masonry. Two series of uniaxial compression tests were performed on masonry panels, separately in the directions parallel and orthogonal to mortar bed joints, in order to define the mechanical behaviour of regular masonry assemblages in the cases of spandrel and pier panels, respectively. Non-linear regression analyses on experimental results allowed to derive constitutive models able

to simulate non-linear behaviour of masonry at both small elastic and large inelastic strains. Such empirical models consist of σ–ε *constitutive equations* and *probabilistic stress-strain data sets* representing characteristics, median, and maximum likelihood constitutive models. Probabilistic constitutive models could be used for seismic analysis of both new and existing buildings, considering explicitly the uncertainty level related to normal stresses conditional on axial strains.

Three series of *direct shear tests* have been carried out on two-layer masonry specimens, in order to characterise not only classical *shear strength parameters* at both peak and residual stress states, but also mode II fracture energy, shearing dilatancy, and τ–γ constitutive laws at different confining stress levels. A multiple non-linear regression analysis allowed to derive a '*shear response surface*' including both constitutive law with softening and failure strength model. Such experimental results could be employed in both linear and non-linear structural models (be they simplified or numerical). In macro-element method of seismic analysis, bed-joint sliding shear could be simulated with higher accuracy.

In-plane lateral loading tests on a full-scale masonry wall with a opening were performed in a quasi-static mode and displacement control in order to assess lateral response at different drift levels and to capture strength degradation. The tests highlighted some interesting features of non-linear behaviour of masonry walls with spandrel panels weaker than pier panels and without RC bond beams (that is the typical case of existing buildings).

In particular, a first monotonic test was carried out to investigate lateral behaviour of the wall up to the first significant damage to the spandrel panel above the opening. A second test was carried out under cyclic displacements to assess residual properties of the pre-damaged masonry wall. Finally, a cyclic lateral loading test was carried out on the same wall after repairing and upgrading by external strengthening of the spandrel panel. The strengthening system was made of inorganic matrix-grid (IMG) composites. The effectiveness of the IMG system has been assessed not only for seismic strengthening/upgrading of masonry structures, but also for rapid remedial works in earthquake emergency scenarios. It has been shown that significant damage to the spandrel panel affected both peak lateral resistance and strength degradation of the wall, while rocking of piers produced large displacement capacity and small residual displacements.

10.2. Potential Future Developments

The research presented and discussed in the present thesis could be used as a basis for future developments in theoretical, numerical, and experimental fields.

Regarding mechanical modelling of masonry, cyclic constitutive laws could be defined

for both uniaxial compression and bed-joint sliding shear, based on experimental data available in the literature or derived by proper laboratory tests. The development of such constitutive laws could lead to simulate evolutionary cyclic behaviour of macro-elements through refined hysteretic force-displacement curves, especially with reference to spandrel panels. Historical masonry types could be also investigated for their constitutive modelling.

The deformation-based approach employed for the analytical simulation of the in-plane flexural behaviour of macro-elements under lateral actions could be used also to investigate the contributions of both shearing deformation, especially to displacement capacity. In order to simulate the non-linear behaviour of spandrel panels, moment-curvature diagrams could be derived in the presence of tensile-resistant elements, at upper and/or lower edges. Capacity models could be obtained in the presence of composite grids or sheets.

Although force-based pushover procedures (either adaptive or not) comply with the most advanced seismic codes, at both national and international levels, displacement-based adaptive procedures could be attractive tools to get better seismic performance predictions of masonry buildings. The direct application of lateral displacement patterns, rather than forces, could be appropriate especially in the case of buildings which are highly irregular in plan or elevation and for which damage affects significantly higher modes of vibration.

Future developments for seismic assessment of existing masonry buildings could include also: (1) modelling and analysis of walls with irregular layout of openings; (2) modelling of flexible diaphragms; and (3) investigation on the effects of flexible diaphragms, and partially effective diaphragm-to-wall and wall-to-wall connections.

Finally, a great contribution to modelling and analysis of masonry walls with openings could be given by further in-plane lateral loading tests on walls with: tensile-resistant elements (e.g., RC bond beams, ties, well-anchored lintels); other relative stiffnesses between spandrel and pier panels; and multi-leaf or chaotic masonries.

REFERENCES

Akkar, S.D. and Metin, A. (2007). Assessment of improved nonlinear static procedures in FEMA 440. *Journal of Structural Engineering*, ASCE, **133(9)**:1237-1246.

Albanesi, T., Nuti, C. and Vanzi, I. (2000). A simplified procedure to assess the seismic response response of nonlinear structures. *Earthquake Spectra*, **16(4)**:715-734.

Amadio, C. and Rajgelj, S. (1991). Shear behavior of brick-mortar joints. *Masonry International*, **5(1)**:19-22.

Antoniou, S. (2002). Advanced inelastic static analysis for seismic assessment of structures. *Ph.D. Thesis*, Imperial College of Science, Technology and Medicine, University of London, London, U.K.

Antoniou, S. and Pinho, R. (2004a). Advantages and limitations of adaptive and non-adaptive force-based pushover procedures. *Journal of Earthquake Engineering*, **8(4)**:497-522.

Antoniou, S. and Pinho, R. (2004b). Development and verification of a displacement-based adaptive pushover procedure. *Journal of Earthquake Engineering*, **8(5)**:643-661.

Arias, A. (1970). A measure of earthquake intensity. In: *Seismic design of nuclear power plants*, The MIT Press, 438-468.

Arya, S.K. and Hegemeier, G.A. (1978). On nonlinear response predictions of concrete masonry assemblies. *Proceedings of the North American Masonry Conference*, Boulder, Colorado, U.S.A.

ASCE, American Society of Civil Engineers (2000). *Prestandard and commentary for the seismic rehabilitation of buildings*, *FEMA 356 Report*. Federal Emergency Management Agency, Washington, D.C., U.S.A.

Aslani, H. e Miranda, E. (2005). *Probabilistic earthquake loss estimation and loss disaggregation in buildings*, Report No. 157. The John A. Blume Earthquake Engineering Center, Stanford University, U.S.A.

ASTM, American Society for Testing and Materials (2004). *Standard tests method for Young's modulus, tangent modulus, and chord modulus, ASTM E 11-04*, West Conshohocken, Pennsylvania, U.S.A.

ATC, Applied Technology Council (1996). *Seismic evaluation and retrofit of concrete buildings*, *ATC 40 Report*. Redwood City, California, 1996.

ATC, Applied Technology Council (1997a). *NEHRP guidelines for the seismic rehabilitation of buildings*, *FEMA 273 Report*. Federal Emergency Management

Agency, Washington, D.C., U.S.A.

ATC, Applied Technology Council (1997b). *NEHRP commentary on the guidelines for the seismic rehabilitation of buildings*, *FEMA 274 Report*. Federal Emergency Management Agency, Washington, D.C., U.S.A.

ATC, Applied Technology Council (2005). *Improvement of nonlinear static seismic analysis procedures*, *FEMA 440 Report*. Redwood City, California, U.S.A.

ATC, Applied Technology Council (2006). *Next-generation performance-based seismic design guidelines program plan for new and existing buildings*, *FEMA 445 Report*. Redwood City, California, U.S.A.

Atkinson, R.H, Amadei B.P., Saeb, S. and Sture S. (1989). Response of masonry bed joints in direct shear. *Journal of Structural Engineering*, ASCE, **115(9)**:2276-2296.

Augenti, N. et al. (1984a). La verifica dei pannelli murari. *Proceedings of the 2nd Italian National Conference ASS.I.R.C.CO.*, Ferrara, Italy (in Italian).

Augenti, N. et al. (1984b). La deformazione dei pannelli murari. *Proceedings of the 2nd Italian National Conference ASS.I.R.C.CO.*, Ferrara, Italy (in Italian).

Augenti, N. et al. (1984c). Il pannello murario pesante. *Proceedings of the 2nd Italian National Conference ASS.I.R.C.CO.*, Ferrara, Italy (in Italian).

Augenti, N. et al. (1984d). Il pannello murario vincolato. *Proceedings of the 2nd Italian National Conference ASS.I.R.C.CO.*, Ferrara, Italy (in Italian).

Augenti, N. et al. (1984e). Il pannello murario armato o contornato. *Proceedings of the 2nd Italian National Conference ASS.I.R.C.CO.*, Ferrara, Italy (in Italian).

Augenti, N. et al. (1984f). Classificazione e tipologia delle pareti murarie. *Proceedings of the 2nd Italian National Conference ASS.I.R.C.CO.*, Ferrara, Italy (in Italian).

Augenti, N. et al. (1984g). Introduzione al calcolo delle pareti murarie. *Proceedings of the 2nd Italian National Conference ASS.I.R.C.CO.*, Ferrara, Italy (in Italian).

Augenti, N. et al. (1987a). Il legame T-Δ nei pannelli murari. *Proceedings of the 3rd Italian National Conference on Earthquake Engineering*, Rome, Italy (in Italian).

Augenti, N. et al. (1987b). La deformazione ultra-elastica nei pannelli murari. *Proceedings of the 3rd Italian National Conference on Earthquake Engineering*, Rome, Italy (in Italian).

Augenti, N. (2004). *Il calcolo sismico degli edifici in muratura*. UTET Libreria, Turin, Italy (in Italian).

Augenti, N. (2006). Seismic behaviour of irregular masonry walls. *Proceedings of the 1st European Conference on Earthquake Engineering and Seismology*, Geneve, Switzerland, Paper No. 86.

Augenti, N. (2007). Resistenza delle "fasce di piano" di edifici in muratura sollecitate da azioni sismiche. *Proceedings of the 12th Italian National Conference on Earthquake Engineering*, Pisa, Italy, Paper No. 7 (in Italian).

Augenti, N. and Parisi, F. (2008a). Preliminary analysis on masonry-RC combined systems: structural assessment. *Proceedings of the 14th International Brick & Block Masonry Conference*, Sydney, Australia, Paper No. 104, pp. 58-67.

Augenti, N. and Parisi, F. (2008b). Soil-foundation-wall interaction in masonry combined systems. *Proceedings of the 14th World Conference on Earthquake Engineering*, Beijing, China, Paper No. 05-04-0009.

Augenti, N. and Parisi, F. (2008c). Three-dimensional seismic analysis of masonry combined systems. *Proceedings of the 14th World Conference on Earthquake Engineering*, Beijing, China, Paper No. 05-04-0010.

Augenti, N. and Parisi, F. (2009a). Numerical analyses of masonry-RC combined systems. *Proceedings of the PROHITECH 2009 Conference*, Rome, Italy, Paper No. 392, **2**:1109-1114.

Augenti, N. and Parisi, F. (2009b). Influence of the constitutive law on the flexural strength of masonry panels. *Proceedings of the 13th Italian National Conference on Earthquake Engineering*, Bologna, Italy, Paper No. S4-03.

Augenti, N. and Parisi, F. (2009c). Force-displacement curves in displacement control. *Proceedings of the 13th Italian National Conference on Earthquake Engineering*, Bologna, Italy, Paper No. S4-02.

Augenti, N. and Parisi, F. (2010a). Constitutive models for tuff masonry under uniaxial compression. *Journal of Materials in Civil Engineering*, ASCE, **22(11)**:1102-1111.

Augenti, N. and Parisi, F. (2010b). Ultimate flexural strength of unreinforced masonry spandrel panels. *Proceedings of the 8th International Masonry Conference*, Dresden, Germany, Paper No. 61, pp. 1653-1662.

Augenti, N. and Parisi, F. (2010c). Constitutive modelling of tuff masonry in direct shear. *Construction and Building Materials*, doi: 10.1016/j.conbuildmat.2010.10.002 (in press).

Augenti, N., Parisi, F. and Acconcia, E. (2010a). New tools for non-linear analysis of masonry buildings. *Proceedings of the 14th European Conference on Earthquake Engineering*, Ohrid, Macedonia, Paper No. 424.

Augenti, N., Parisi, F., Prota, A. and Manfredi, G. (2010b). In-Plane lateral response of a full-scale masonry sub-assemblage with and without an inorganic matrix-grid strengthening system. *Journal of Composites for Construction*, ASCE, doi: 10.1061/(ASCE)CC.1943-5614.0000193 (in press).

Benedetti, D., Carydis, P., and Pezzoli, P. (1998). Shaking table tests on 24 masonry buildings. *Earthquake Engineering and Structural Dynamics*, **27(1)**:67-90.

Benedetti, D., Carydis, P., and Limongelli, M.P. (2001). Evaluation of the seismic response of masonry buildings based on energy functions. *Earthquake Engineering and Structural Dynamics*, **30(7)**:1061-1081.

Benjamin, J.R. (1959). *Statically Indeterminate Structures*. McGraw-Hill, New York, U.S.A.

Binda, L., Fontana, A. and Mirabella, G. (1994). Mechanical behavior and stress distribution in multiple-leaf stone walls. *Proceedings of the 10th International Brick & Block Masonry Conference*, Calgary, Canada, pp. 51-59.

Bracci, J.M., Kunnath, S.K. and Reinhorn, A.M. (1997). Seismic performance and retrofit evaluation of reinforced concrete structures. *Journal of Structural Engineering*, ASCE, **123(1)**:3-10.

Bramerini, F. e Di Pasquale, G. (2008). Aggiornamento delle mappe di rischio sismico in Italia. *Ingegneria Sismica*, **2**:5-23 (in Italian).

Brencich, A. and Lagomarsino, S. (1998). A macro-element dynamic model for masonry shear walls. In: G.N. Pande, J. Middleton, B. Kralj (eds.), *Proceedings of the 4th International Symposium on Computer Methods in Structural Masonry*, E&FN Spon, London, U.K., pp. 67-75.

Brencich, A., Gambarotta, L. and Lagomarsino, S. (1998). A macroelement approach to the three-dimensional seismic analysis of masonry buildings. *Proceedings of the 11th European Conference on Earthquake Engineering*, Paris, France.

Brencich, A. and De Francesco, U. (2004). Assessment of Multispan Masonry Arch Bridges. I: Simplified Approach. *Journal of Bridge Engineering*, ASCE, **9(6)**:582-590.

Brencich, A., Corradi, C. and Gambarotta, L. (2008). Eccentrically loaded brickwork: Theoretical and experimental results. *Engineering Structures*, **30**:3629-3643.

BSSC, Building Seismic Safety Council (1999). *Case studies*: *an assessment of the NEHRP guidelines for the seismic rehabilitation of buildings*, *FEMA 343 Report*. Federal Emergency Management Agency, Washington, D.C., U.S.A.

Calderini, C. and Lagomarsino, S. (2008). Continuum model for in-plane anisotropic inelastic behavior of masonry. *Journal of Structural Engineering*, ASCE, **134(2)**:209-220.

Calvi, G.M. and Magenes, G. (1991). Experimental evaluation of seismic strength of old masonry structures. *Proceedings of the 9th International Brick & Block Masonry Conference*, Berlin, Germany, pp. 490-497.

Calvi, G.M. and Magenes, G. (1994). Experimental results on unreinforced masonry shear walls damaged and repaired. *Proceedings of the 10th International Brick & Block Masonry Conference*, Calgary, U.S.A., pp. 509-518.

Capozucca, R. (2004). Masonry panels with different mortar joints under compression. *Proceedings of the 13th International Brick & Block Masonry Conference*, Amsterdam, The Netherlands, pp. 27-34.

Cattari, S., Galasco, A., Lagomarsino, S. e Penna, A. (2004). Analisi non lineare di

edifici in muratura con il programma TREMURI. *Proceedings of the 11th Italian National Conference on Earthquake Engineering*, Genova, Italy (in Italian).

Cattari, S. e Lagomarsino, S. (2007). Formulazione di elementi non lineari per l'analisi degli edifici esistenti a struttura mista muratura-c.a. *Proceedings of the 12th Italian National Conference on Earthquake Engineering*, Pisa, Italy, Paper No. 107 (in Italian).

Cattari, S. and Lagomarsino, S. (2008). A strength criterion for the flexural behaviour of spandrels in un-reinforced masonry walls. *Proceedings of the 14th World Conference on Earthquake Engineering*, Beijing, China, Paper No. 05-04-0041.

CEN, Comité Européen de Normalisation (1999). *Methods of test for masonry - Part 1*: *Determination of compressive strength*, *EN 1052-1*, Brussels, Belgium.

CEN, Comité Européen de Normalisation (2002). *Methods of test for masonry - Part 3*: *Determination of initial shear strength*, *EN 1052-3*, Brussels, Belgium.

CEN, Comité Européen de Normalisation (2004). *Eurocode 8*: *Design of structures for earthquake resistance - Part 1*: *General rules, seismic actions and rules for buildings*, EN 1998-1, Brussels, Belgium.

CEN, Comité Européen de Normalisation (2005a). *Eurocode 6*: *Design of masonry structures - Part 1-1*: *General rules for reinforced and unreinforced masonry structures*, EN 1996-1-1, Brussels, Belgium.

CEN, Comité Européen de Normalisation (2005b). *Eurocode 8*: *Design of structures for earthquake resistance - Part 3*: *Assessment and retrofitting of buildings*, EN 1998-3, Brussels, Belgium.

Chopra, A.K. and Goel, R.K. (1999). Capacity-demand-diagram methods based on inelastic design spectrum. *Earthquake Spectra*, **15(4)**:637-656.

Chopra, A.K. and Goel, R.K. (2002). A modal pushover analysis procedure for estimating seismic demands for buildings. *Earthquake Engineering and Structural Dynamics*, **31(3)**:561-582.

Chopra, A.K., Goel, R.K. and Chintanapakdee, C. (2004). Evaluation of a modified MPA procedure assuming higher modes as elastic to estimate seismic demands. *Earthquake Spectra*, **20(3)**:757-778.

Chuxian, S. (1984). Analysis of the strength for compressive members of brick masonry under eccentric loads. *Proceedings of the CIB 3rd International Symposium on Wall Structures*, Warsaw, Poland.

Clough, R.W. and Penzien, J. (1994). *Dynamics of Structures*. 2nd Edition, McGraw-Hill, New York, U.S.A.

Cornell, C.A. (1968). Engineering seismic risk analysis. *Bulletin of the Seismological Society of America*, **58**:1583-1606.

Cosenza, E., Manfredi, G. e Ramasco, R. (1989). La caratterizzazione della risposta

sismica dell'oscillatore elasto-plastico. *Ingegneria Sismica*, **6(3)**:19-29 (in Italian).

Cosenza, E. and Manfredi, G. (1992). Seismic analysis of degrading models by means of damage functions concepts. In: P. Fajfar, H. Krawinkler (eds.), *Nonlinear analysis and design of reinforced concrete buildings*, Elsevier Applied Science, London, New York, pp. 77-93.

Cosenza, E. and Manfredi, G. (1997). The improvement of the seismic-resistant design for existing and new structures using damage criteria. In: P. Fajfar, H. Krawinkler (eds.), *Seismic Design Methodologies for the Next Generation of Codes*, Balkema, Rotterdam, The Netherlands, pp. 119-130.

Cosenza, E. e Manfredi, G. (eds.) (2000). *Indici e misure di danno nella progettazione sismica*. CNR-GNDT, Rome, Italy (in Italian).

Cosenza, E., Manfredi, G. and Polese, M. (2010). Simplified method to include cumulative damage in the seismic response of single-degree-of-freedom systems. *Journal of Engineering Mechanics*, ASCE, **135(10)**:1081-1088.

Cundall, P.A. (1988). Formulation of a three-dimensional distinct element model - Part I: A scheme to detect and represent contacts in a system composed of many polyhedral blocks. *International Journal of Rock Mechanics and Mining Sciences & Geomechanics Abstracts*, **25(3)**:107-116.

De la Llera, J.C. and Chopra, A.K. (1995). Understanding the inelastic seismic behaviour of asymmetric-plan buildings. *Earthquake Engineering and Structural Dynamics*, **24(4)**:549-572.

De Stefano, M. and Pintucchi, B. (2008). A review of research on seismic behaviour of irregular building structures since 2002. *Bulletin of Earthquake Engineering*, **6**:285-308.

Dolce, M. (1991). Schematizzazione e modellazione degli edifici in muratura soggetti ad azioni sismiche. *L'Industria delle Costruzioni*, **25**:44-57 (in Italian).

Dowell, M. and Jarratt, P. (1972). The "Pegasus" method for computing the root of an equation. *BIT Numerical Mathematics*, **12(4)**:503-508.

Drysdale, R.G., Vanderkyle, R. and Hamid, A. (1979). Shear strength of brick masonry joints. *Proceedings of the 5th International Brick & Block Masonry Conference*, Washington, D.C., U.S.A., Paper No. II-13, pp. 106-113.

Elnashai, A.S. (2001). Advanced inelastic static (pushover) analysis for earthquake applications. *Structural Engineering and Mechanics*, **12(1)**:51-69.

Erduran, E. and Kunnath, S.K. (2010). Enhanced displacement coefficient method for degrading multi-degree-of-freedom systems. *Earthquake Spectra*, **26(2)**:311-326.

Faccioli, E. e Paolucci, R. (2005). *Elementi di Sismologia applicata all'Ingegneria*. Pitagora Editrice, Bologna, Italy (in Italian).

Faccioli, E., Paolucci, R. and Rey, J. (2004). Displacement spectra for long periods.

Earthquake Spectra, **20(2)**:347-376.

Faella, G. and Kilar, V. (1998). Asymmetric multi-storey R/C frame structures: push-over versus nonlinear dynamic analysis. *Proceedings of the 11th European Conference on Earthquake Engineering*, Paris, France.

Fajfar, P. and Fischinger, M. (1989). N2 – a method for non-linear seismic analysis of regular buildings. *Proceedings of the 9th World Conference on Earthquake Engineering*, Tokyo, Kyoto, Japan, Vol. 5, 111-116, Paper No. 7-3-2.

Fajfar, P. (1992). Equivalent ductility factors taking into account low-cycle fatigue. *Earthquake Engineering and Structural Dynamics*, **21(9)**:837-848.

Fajfar, P. and Gašpersič, P. (1996). The N2 method for the seismic damage analysis of RC buildings. *Earthquake Engineering and Structural Dynamics*, **25(1)**:31-46.

Fajfar, P. (1999). Capacity spectrum method based on inelastic demand spectra. *Earthquake Engineering and Structural Dynamics*, **28(9)**:979-993.

Fajfar, P. (2000). A nonlinear analysis method for performance-based seismic design. *Earthquake Spectra*, **16(3)**:573-592.

Fajfar, P. (2006). The N2 method for asymmetric buildings. *Proceedings of the 1st European Conference on Earthquake Engineering and Seismology*, Geneva, Switzerland, Paper No. 539.

Freeman, S.A., Nicoletti, J.P. and Tyrell, J.V. (1975). Evaluation of existing buildings for seismic risk - A case study of Puget Sound Naval Shipyard Bremerton, Washington. *Proceedings of the U.S. National Conference on Earthquake Engineering*, Berkeley, California, U.S.A., pp. 113-122.

Freeman, S.A. (1998). The Capacity Spectrum Method as a Tool for Seismic Design. *Proceedings of the 11th European Conference on Earthquake Engineering*, Paris, France.

Fusier, F. e Vignoli, A. (1993a). Proposta di un metodo di calcolo per edifici in muratura sottoposti ad azioni orizzontali. *Ingegneria Sismica*, **10(1)**:10-24 (in Italian).

Fusier, F. e Vignoli, A. (1993b). Analisi della capacità portante ultima di pareti murarie pressoinflesse. *Ingegneria Sismica*, **10(2)**:22-31 (in Italian).

Galasco, A., Lagomarsino, S. and Penna, A. (2006). On the use of pushover analysis for existing masonry buildings. *Proceedings of the 1st European Conference on Earthquake Engineering and Seismology*, Geneve, Switzerland, Paper No. 1080.

Gambarotta, L. and Lagomarsino, S. (1997a). Damage models for the seismic response of brick masonry shear walls. Part I: The mortar joint model and its applications. *Earthquake Engineering and Structural Dynamics*, **26(4)**:423-439.

Gambarotta, L. and Lagomarsino, S. (1997b). Damage models for the seismic response of brick masonry shear walls. Part II: The continuum model and its applications.

Earthquake Engineering and Structural Dynamics, **26(4)**:441-462.

Gasparini, P., Manfredi, G. and Zschau, J. (2007). *Earthquake Early Warning Systems*. Springer.

Gattesco, N., Macorini, L., Clemente, I. and Noè, S. (2009). Shear resistance of spandrels in ancient brick-masonry buildings. *Proceedings of the 13th Italian National Conference on Earthquake Engineering*, Bologna, Italy, Paper No. S4-18.

Goel, R.K. and Chopra, A.K. (2005). Role of higher-"mode" pushover analysis in seismic analysis of buildings. *Earthquake Spectra*, **21(4)**:1027-1041.

Gulkan, P. and Sozen, M.A. (1977). Inelastic responses of reinforced concrete structures to earthquake motions. In: *Reinforced Concrete Structures in Seismic Zones*, SP-53, American Concrete Institute (ACI), Detroit, U.S.A., pp. 109-115 (reprinted from *Journal of the American Concrete Institute*, **71(12)**:604-610, 1974).

Gupta, A. and Krawinkler, H. (2000). Estimation of seismic drift demands for frame structures. *Earthquake Engineering and Structural Dynamics*, **29(9)**:1287-1305.

Gupta, B. and Kunnath, S.K. (2000). Adaptive spectra-based pushover procedure for seismic evaluation of structures. *Earthquake Spectra*, **16(2)**:367-391.

Hart, R.D., Cundall, P.A. and Lemos, J. (1988). Formulation of a three-dimensional distinct element model - Part II: Mechanical calculations for motion and interaction of a system composed of many polyhedral blocks. *International Journal of Rock Mechanics and Mining Sciences & Geomechanics Abstracts*, **25(3)**:117-125.

Hegemeier, G.A., Arya, S.K., Krishnamoorthy, G., Nachbar, W. and Furgerson, R. (1978). On the behaviour of joints in concrete masonry. *Proceedings of the North American Masonry Conference*, Boulder, Colorado, U.S.A.

Hernández-Montes, E., Kwon, O-S. and Aschheim, M. (2004). An energy-based formulation for first- and multiple-mode nonlinear static (pushover) analyses. *Journal of Earthquake Engineering*, **8(1)**:69-88.

Homand, F., Belem, T. and Souley, M. (2001). Friction and degradation of rock joint surfaces under shear loads. *International Journal for Numerical and Analytical Methods in Geomechanics*, **25**:973-999.

Kaushik, H.B., Rai, D.C. and Jain, S.K. (2007). Stress-strain characteristics of clay brick masonry under uniaxial compression. *Journal of Materials in Civil Engineering*, ASCE, **19(9)**:728-739.

Kilar, V. and Fajfar, P. (1996). Simplified push-over analysis of building structures. *Proceedings of the 11th World Conference on Earthquake Engineering*, Acapulco, Mexico, Paper No. 1011.

Kilar, V. and Fajfar, P. (1997). Simplified push-over analysis of asymmetric buildings. *Earthquake Engineering and Structural Dynamics*, **26(2)**:233-249.

Kilar, V. and Fajfar, P. (2001). On the applicability of pushover analysis to the seismic performance evaluation of asymmetric buildings. *European Earthquake Engineering*, **15(1)**:20-31.

Kim, S. and D'Amore, E. (1999). Push-over analysis procedure in earthquake engineering. *Earthquake Spectra*, **15(3)**:417-434.

Kramer, S.L. (1996). *Geotechnical Earthquake Engineering*. Prentice-Hall, Upper Saddle River, New Jersey, U.S.A.

Krawinkler, H. and Nassar, A.A. (1992). Seismic design based on ductility and cumulative damage demands and capacities. In: P. Fajfar, H. Krawinkler (eds.), *Nonlinear seismic analysis and design of reinforced concrete buildings*, Elsevier Applied Science, New York, U.S.A.

Krawinkler, H. (1995). New trends in seismic design methodology. *Proceedings of the 10th European Conference on Earthquake Engineering*, Balkema, Rotterdam, The Netherlands, Vol. 2, 821-830.

Krawinkler, H. and Seneviratna, G.D.P.K. (1998). Pros and cons of a pushover analysis of seismic performance evaluation. *Engineering Structures*, **20(4-6)**:452-464.

Kunnath, S.K. and Gupta, B. (2000). Validity of deformation demand estimates using nonlinear static procedures. *Proceedings of the U.S.-Japan Workshop on Performance-Based Engineering for Reinforced Concrete Building Structures*, Sapporo, Hokkaido, Japan.

Kunnath, S.K. (2004). Identification of modal combinations for nonlinear static analysis of building structures. *Computer-Aided Civil and Infrastructure Engineering*, **19**:246-259.

Lanzo, G. e Silvestri, F. (1999). *Risposta sismica locale*. Hevelius Edizioni, Benevento, Italy (in Italian).

Lawson, R.S., Vance, V. e Krawinkler, H. (1994). Nonlinear static push-over analysis - why, when, and how? *Proceedings of the 5th U.S. National Conference on Earthquake Engineering*, Earthquake Engineering Research Institute (EERI), Oakland, California, U.S.A., Vol. 1, pp. 283-292.

Lemos, J.V. (2006). Modeling of historical masonry with discrete elements. *Proceedings of the 3rd European Conference on Computational Mechanics. Solids, Structures and Coupled Problems in Engineering*, Lisbon, Portugal, Paper No. 2591, pp. 23-40.

Lourenço, P.B. (1996). Computational Strategies for Masonry Structures. *Ph.D. Thesis*, University of Delft, Delft, The Netherlands.

Lourenço, P.B. and Rots, J.G. (1997). Multisurface interface model for analysis of masonry structures. *Journal of Engineering Mechanics*, ASCE, **123(7)**:660-668.

Lourenço, P.B. and Ramos, L.F. (2004). Characterization of cyclic behavior of dry

masonry joints. *Journal of Structural Engineering*, ASCE, **130(5)**:779-786.

Lourenço, P.B., Barros, J.O. and Oliveira, J.T. (2004). Shear testing of stack bonded masonry. *Construction and Building Materials*, **18(2)**:125-132.

Luciano, R. and Sacco, E. (1998). A damage model for masonry structures. *European Journal of Mechanics, A/Solids*, **17(2)**: 285-303.

Magenes, G. (1992). Seismic behavior of brick masonry: strength and failure mechanisms. *Ph.D. Thesis*, University of Pavia, Pavia, Italy (in Italian).

Magenes, G., Kingsley, G.R. and Calvi, G.M. (1995). Static testing of a full-scale, two-story masonry building: test procedure and measured experimental response. In: *Experimental and numerical investigation on a brick masonry building prototype*, CNR-GNDT, Report No. 3, Numerical prediction of the experiment, pp. 11-41.

Magenes, G. e Calvi, G.M. (1996). Prospettive per la calibrazione di metodi semplificati per l'analisi sismica di pareti murarie. *Proceedings of the Italian National Conference "La Meccanica delle Murature tra Teoria e Progetto"*, Pitagora, Bologna, Italy (in Italian).

Magenes, G. and Calvi, G.M. (1997). In-plane seismic response of brick masonry walls. *Earthquake Engineering and Structural Dynamics*, **26(11)**:1091-1112.

Magenes, G. and Della Fontana, A. (1998). Simplified non-linear seismic analysis of masonry buildings. *Proceedings of the British Masonry Society*, **8**:190-195.

Magenes, G., Braggio, C. and Bolognini (eds.) (2001). *Metodi semplificati per l'analisi sismica non lineare di edifici in muratura*. CNR-GNDT, Rome, Italy (in Italian).

Magenes, G. (2010). Earthquake resistant design of masonry structures: rules, backgrounds, latest findings. *Proceedings of the 8th International Masonry Conference*, Dresden, Germany, pp. 29-45.

Magliulo, G., Maddaloni, G. and Cosenza, E. (2008). Extension of N2 method to plan irregular buildings considering accidental eccentricity. *Proceedings of the 14th World Conference on Earthquake Engineering*, Beijing, China, Paper No. 08-02-0037.

Manfredi, G., Masi, A., Pinho, R., Verderame, G. e Vona, M. (2007). *Valutazione degli edifici esistenti in Cemento Armato*, IUSS Press, Pavia, Italy (in Italian).

Meireless, H., Pinho, R., Bento, R. and Antoniou, S. (2006). Verification of an adaptive pushover technique for the 3D case. *Proceedings of the 1st European Conference on Earthquake Engineering and Seismology*, Geneve, Switzerland, Paper No. 619.

Meletti, C. e Montaldo, V. (2007). *Stime di pericolosità sismica per diverse probabilità di superamento in 50 anni*: *valori di* a_g. Progetto DPC-INGV S1, Deliverable D2, <http://esse1.mi.ingv.it/d2.html> (in Italian).

Meletti, C., Galadini, F., Valensise, G., Stucchi, M., Basili, R., Barba, S., Vannucci, G.

and Boschi, E. (2008). A seismic source zone model for the seismic hazard assessment of the Italian territory. *Tectonophysics*, **450(1-4)**:85-108.

Mirabella Roberti, G., Binda, L. and Cardani, G. (1997). Numerical modeling of shear bond tests on small brick-masonry assemblages. In: G.N. Pande, J. Middleton, B. Kralj (eds.), *Computer methods in structural masonry - 4*, E & FN Spon, London, U.K., pp. 144-153.

Miranda, E. (1993). Site-dependent strength-reduction factors. *Journal of Structural Engineering*, ASCE, **119(12)**:3503-3519.

Miranda, E. and Bertero, V.V. (1994). Evaluation of strength reduction factors for earthquake-resistant design. *Earthquake Spectra*, **10(2)**:357-379.

Miranda, E. (2000). Inelastic displacement ratios for displacement-based earthquake resistant design. *Proceedings of the 12th World Conference on Earthquake Engineering*, Auckland, New Zealand, Paper No. 1096.

Misra, A. (2002). Effect of the asperity damage on shear behaviour of single fracture. *Engineering Fracture Mechanics*, **69**:1997-2014.

IMIT, Italian Ministry of Infrastructures and Transportation (2008). *D.M. 14.01.2008*: *Norme Tecniche per le Costruzioni*, Roma, Italy (in Italian).

Moghadam, A.S. and Tso, W.K. (1996). Damage assessment of eccentric multi-storey buildings using 3-D pushover analysis. *Proceedings of the 11th World Conference on Earthquake Engineering*, Acapulco, Mexico, Paper No. 997.

Moghadam, A.S. and Tso, W.K. (2000a). 3-D pushover analysis for damage assessment of buildings. *Journal of Seismology and Earthquake Engineering*, **2(3)**:23-31.

Moghadam, A.S. and Tso, W.K. (2000b). Pushover analysis for asymmetric and set-back multi-storey buildings. *Proceedings of the 12th World Conference on Earthquake Engineering*, Auckland, New Zealand, Paper No. 1093.

Mondkar, D.P. and Powell, G.H. (1975). *ANSR-I General Purpose Computer Program for Analysis of Nonlinear Structural Response*. Report EERC 75-37, University of California, Berkeley, California, U.S.A.

Mwafy, A.M. (2001). Seismic performance of code-designed RC buildings. *Ph.D. Thesis*, Department of Civil and Environmental Engineering, Imperial College of Science, Technology and Medicine, London, U.K.

Mwafy, A.M. and Elnashai, S.A. (2001). Static pushover versus dynamic collapse analysis of RC buildings. *Engineering Structures*, **23(5)**:407-424.

Naeim, F. and Lobo, R. (1999). Avoiding common pitfalls in pushover analysis. *Proceedings of the 8th Canadian Conference on Earthquake Engineering*, Vancouver, British Columbia, Canada, pp. 269-274.

Newmark, N.M. and Hall, W.J. (1982). *Earthquake spectra and design*. Earthquake

Engineering Research Institute (EERI), Berkley, California, U.S.A.

NZSEE, New Zealand National Society for Earthquake Engineering (1996). *The assessment and improvement of the structural performance of earthquake risk buildings*. Draft for general release, New Zealand.

OES, California Office of Emergency Services (1995). *Vision 2000*: *Performance Based Seismic Engineering of Buildings*. Structural Engineers Associations of California, Sacramento, U.S.A.

Pampanin, S., Christopoulos, C. and Priestley, M.J.N. (2002). *Residual Deformations in the Performance-Based Seismic Assessment of Frame Structure*. ROSE Research Report No. 2002/02, IUSS Press, Pavia, Italy.

Paret, T.F., Sasaki, K.K., Eilbekc, D.H. and Freeman, S.A. (1996). Approximate inelastic procedures to identify failure mechanisms from higher mode effects. *Proceedings of the 11th World Conference on Earthquake Engineering*, Acapulco, Mexico, Paper No. 966.

Park, R. and Paulay, T. (1975). *Reinforced Concrete Structures*. John Wiley & Sons, New York, U.S.A.

Parisi, F. and Augenti, N. (2010). Curvature ductility of masonry spandrel panels. *Proceedings of the 14th European Conference on Earthquake Engineering*, Ohrid, Macedonia, Paper No. 417.

Penelis, Gr.G. and Kappos, A.J. (2002). 3-D pushover analysis: The issue of torsion. *Proceedings of the 12th European Conference on Earthquake Engineering*, London, U.K., Paper No. 15.

Penna, A. (2002). Una procedura a macro-elementi per l'analisi dinamica non lineare di edifici in muratura. *PhD Thesis*, Polytechnic of Milan, Milan, Italy (in Italian).

Petti, L. and Marino, I. (2010). The polar spectrum: a new spatial representation of seismic demand. *Proceedings of the 14th European Conference on Earthquake Engineering*, Ohrid, Macedonia, Paper No. 926.

Pettinga, J.D., Pampanin, S., Christopoulos, C. and Priestley, M.J.N. (2007). *Developments in the Prediction and Mitigation of Residual Deformations due to Seismic Demand, including Asymmetric Structural Response*. ROSE Research Report No. 2007/01, IUSS Press, Pavia, Italy.

Priestley, M.J.N. and Elder, D.M. (1983). Stress-strain curves for unconfined and confined concrete masonry. *ACI Journal*, **80(3)**:192-201.

Priestley, M.J.N. (2003). *Myths and Fallacies in Earthquake Engineering, Revisited*, IUSS Press, Pavia, Italy.

Priestley, M.J.N., Calvi, G.M. and Kowalsky, M.J. (2007). *Displacement-Based Seismic Design of Structures*. IUSS Press, Pavia, Italy.

Rahnama, M. and Krawinkler, H. (1993). *Effects of soft soil and hysteresis model on*

seismic demands. Report No. 108, The John A. Blume Earthquake Engineering Center, Stanford University, Stanford, California, U.S.A.

Rai, D.C. and Goel, S.C. (2007). Seismic strengthening of rocking-critical masonry piers. *Journal of Structural Engineering*, ASCE, **133(10)**:1445-1452.

Riddell, R. (1995). Inelastic design spectra accounting for soil conditions. *Earthquake Engineering and Structural Dynamics*, **24(11)**:1491-1510.

Rutenberg, A. and De Stefano, M. (1997). On the seismic performance of yielding asymmetric multistorey buildings: Review and case study. In: P. Fajfar, H. Krawinkler (eds.), *Seismic Design Methodologies for the Next Generation of Codes*, Balkema, Rotterdam, The Netherlands, pp. 299-310.

Saiidi, M. and Sozen, M.A. (1981), Simple nonlinear seismic analysis of R/C structures. *Journal of Structural Division*, ASCE, **107(5)**:937-952.

Sasaki, K.K., Freeman, S.A. and Paret, T.F. (1998). Multimode pushover procedure (MMP) - A method to identify the effects of higher modes in a pushover analysis. *Proceedings of the 6th U.S. National Conference on Earthquake Engineering*, Seattle, Washington, U.S.A.

Sawko, F. (1982). Numerical analysis of brick walls under compressive loading. In: H.W.H. West (ed.), *Proceedings of the British Ceramic Society, Load-bearing brickwork*, **7(30)**:213-222.

Sheppard, P., and Lutman, M. (1988). Estimation of expected seismic vulnerability: a simple methodology for medium sized groups of older buildings. In: A. Koridze (ed.), *Seismic risk assessment and design of building structures*, Omega Scientific, Wallingford, U.K., pp. 47-62.

Shibata, A. and Sozen, M.A. (1976). Substitute-structure method for seismic design in R/C. *Journal of the Structural Division*, ASCE, **102(1)**:1-18.

Shing, P.B., Noland, J.L., Klamerus, E., and Spaeh, H. (1989). Inelastic behavior of concrete masonry shear walls. *Journal of Structural Engineering*, ASCE, **115(9)**:2204-2225.

Soong, T.T. (2004). *Fundamentals of Probability and Statistics for Engineers*. John Wiley & Sons, New York, U.S.A.

Stöckl, S. and Hofmann, P. (1986). Tests on the shear-bond behaviour in the bed-joints of masonry. *Masonry International*, **9**:1-15.

Tomaževič, M. and Lutman, M. (1996). Seismic Behavior of Masonry Walls: Modeling of Hysteretic Rules. *Journal of Structural Engineering*, ASCE, **122(9)**:1048-1054.

Tomaževič, M. (2000). Earthquake-resistant design of masonry buildings. In: A.S. Elnashai, P.J. Dowling (eds.), *Series on innovation in structures and construction*, Vol. 1, Imperial College Press, London, U.K.

Turnšek, V. and Čačovič, F. (1971). Some experimental results on the strength of brick masonry walls. *Proceedings of the 2nd International Brick & Block Masonry Conference*, Stoke-on-Trent, U.K., pp. 149-156.

Uang, C. (1991). Establishing R (or Rw) and Cd factors for building seismic provisions. *Journal of Structural Engineering*, ASCE, **117(1)**:19-28.

Valles, R., Reinhorn, A., Kunnath, S., Li, C. and Madan, A. (1996). *IDARC2D version 4.0: a computer program for the inelastic analysis of buildings*. Tech. Rep. No. NCEER-96-0010, National Center for Earthquake Engineering Research, State University of New York at Buffalo, New York, U.S.A.

Vamvatsikos, D. and Cornell, C.A. (2002). Incremental dynamic analysis. *Earthquake Engineering and Structural Dynamics*, **31(3)**:491-514.

van der Pluijm, R. (1993). Shear behaviour of bed joints. In: A.A. Hamid, H.G. Harris (eds.), *Proceedings of the 6th North American Masonry Conference*, The Masonry Society, Philadelphia, U.S.A., pp. 125-36.

van Zijl, G.P.A.G. (2004). Modeling masonry shear-compression: role of dilatancy highlighted. *Journal of Engineering Mechanics*, ASCE, **130(11)**:1289-1296.

Vasconcelos, G. and Lourenço, P. (2009). Experimental characterization of stone masonry in shear and compression. *Construction and Building Materials*, **23**:3337-3345.

Vidic, T., Fajfar, P. and Fischinger, M. (1994). Consistent inelastic design spectra: strength and displacement. *Earthquake Engineering and Structural Dynamics*, **23(5)**:523-537.

Vinale, F. (ed.) (2000). *Indirizzi per studi di microzonazione sismica*. AMRA, Naples, Italy (in Italian).

Whittaker, A., Constantinou, M. and Tsopelas, P. (1998). Displacement estimates for performance-based seismic design. *Journal of Structural Engineering*, ASCE, **124(8)**:905-912.

Appendix A - EXPERIMENTAL TESTING FOR CONSTITUTIVE MODELLING IN COMPRESSION

The definition of the mechanical properties of masonry is a complex engineering problem, since the interaction among the constituents (i.e., masonry units and mortar joints) induces multi-axial stress/strain fields which are difficult to be mathematically described. Besides this, several factors of uncertainty should be considered as a result of the following issues related to the employed construction technique: (1) geometrical layout of masonry units; (2) filling of joints; (3) ratios between joint thickness and masonry unit sizes; (4) workmanship accuracy; and (5) randomness in constituents' dimensions. Furthermore, the definition of masonry properties is often based on experimental data gathered by different types of tests on non-standard specimens. This needs for specific mechanical characterisation of the main masonry types.

In the framework of ReLUIS-DPC 2005-2008 project, the author carried out an experimental program aimed at defining the mechanical behaviour of masonry under compression. The main output of this research was the development of constitutive models able to simulate compressive behaviour of masonry in both pre-peak (elastic) and post-peak (inelastic) ranges, including strength degradation due to strain softening. The effects of loading direction with respect to mortar bed joints in regular masonry assemblages were explicitly investigated, in order to allow different modelling of masonry within pier and spandrel panels of masonry walls with openings (see Chap. 7). To that end, σ–ε constitutive laws and mechanical parameters were characterised through uniaxial compression tests on masonry prisms in the directions orthogonal and parallel to mortar bed joints. The masonry prisms were made of tuff masonry, because a few experimental data are available for this masonry type, opposed to clay brick masonry (Calvi and Magenes, 1991; Capozucca, 2004; Chuxian, 1984; Kaushik et al., 2007; Sawko, 1982; Turnšek and Čačovič, 1971) and concrete masonry (Arya and Hegemeier, 1978; Priestley and Elder, 1983).

In this appendix, the research objectives of this experimental program are first summarised and the mechanical behaviour of masonry in uniaxial compression is briefly described. Second, the main properties of constituent materials of masonry prisms and the experimental program (specimens geometry, test setup, and test procedure) are described. Finally, experimental data and empirical models derived in the form of both equations and probabilistic data are presented and discussed.

A.1. Research Objectives

The constitutive modelling of masonry was carried out by means of: (1) the definition of the most significant strength, flexibility, and strain ductility properties, to be used into linear analyses on FE or macro-element models; (2) the derivation of probabilistic stress-strain data sets, to be implemented in FE models; and (3) the derivation of constitutive equations via nonlinear regression analysis, to be used in any structural model of a masonry construction.

Therefore, the compression tests were aimed not only at evaluating compressive strength and secant moduli of masonry in the elastic range of behaviour, but also at computing significant parameters able to describe the inelastic behaviour.

Secondly, stress-strain probabilistic data sets were obtained for each loading direction, in order to generalise the concept of characteristic and mean values of mechanical parameters, such as compressive strength and ultimate strain. This allows to consider the uncertainty about the behaviour of tuff masonry under uniaxial compression.

Finally, stress-strain relationships were derived for each loading direction separately, in order to simulate the compressive behaviour of masonry in more accurate, but rather simple, mode up to large inelastic strains.

A.2. Non-Linear Behaviour of Masonry in Compression

In this study, masonry is regared a san equivalent homogeneous material from a mechanical point of view. Such an 'ideal' material does not behave linearly under compressive loading even in the range of small deformations, due to the spreading of internal cracking (Fig. A.1). While masonry is quite stable at small stress levels, it becomes unstable close to the *peak strength* σ_k, causing the first macroscopic cracks.

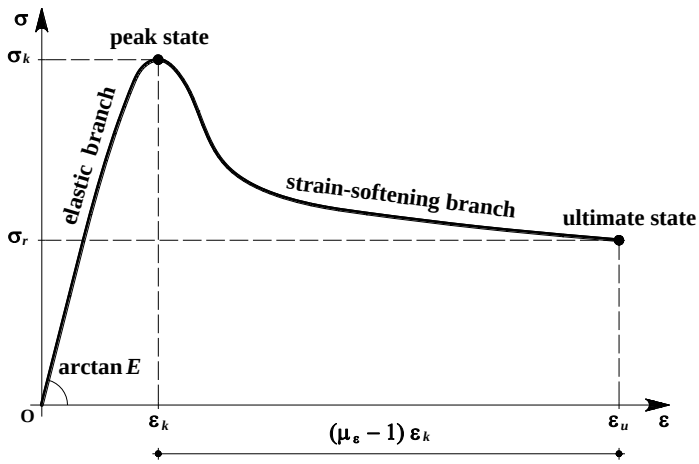

Figure A.1 Typical constitutive law of masonry under uniaxial compression

As the axial strain increases, macro-cracking develops in uncontrolled way due to damage localization, so the crack width increases rapidly. Owing to local equilibrium of the material, compressive strength reduces and *strain softening* affects significantly the post-elastic behaviour of masonry until the ultimate strain ε_u is reached. The latter is associated with the *residual strength* of masonry σ_r, so a *strength degradation ratio* can be defined as $SDR = \sigma_r/\sigma_k$.

Supply strain ductility can be also evaluated as the ratio between the ultimate strain and the one associated with the peak strength (namely, as $\mu_\varepsilon = \varepsilon_u/\varepsilon_k$), which is said to be *peak strain* and denoted by ε_k. This is true if it is assumed that masonry behaves elastically up to the peak point (σ_k,ε_k). Actually, yielding of masonry may occur at $\sigma_e < \sigma_k$, which corresponds to $\varepsilon_e < \varepsilon_k$. In such a case, strain ductility should be defined as $\mu_\varepsilon = \varepsilon_u/\varepsilon_e$. Nonetheless, the laboratory tests described below showed that σ_e is almost equal to σ_k. The presence of a post-peak falling branch in constitutive diagrams has led to define masonry as a 'quasi-brittle' material.

A.3. Materials Used for Experimental Testing

The masonry prisms tested under uniaxial compression were made of yellow tuff stones coming from a pit near Naples (Italy) and a premixed hydraulic mortar with low-medium mechanical characteristics, adhesion, and consistency. This type of mortar was used in order to reproduce actual conditions of masonry within existing buildings. It is also underlined that tuff masonry constructions are a large part of the historical and monumental heritage in Europe, and are located in earthquake-prone regions like as Italy and Turkey.

The masonry units had dimensions equal to 300×150×100 mm and unit weight of 12.50 kN/m^3. The mortar was based on natural sand and a special binder with pozzolana-like reactive aggregates; according to the supplier's instructions, the masons added 4 l of water per 0.25 kN of sand-binder mixture (i.e., a water/sand ratio by weight 1:6.25).

Laboratory tests were first carried out on both mortar and stone specimens, according to European standards, in order to compute the main mechanical properties of the constituent materials in compression and tension, separately. Mean compressive strength of tuff stones was estimated in f_{bm} = 4.13 MPa, while Young's and shear moduli were found to be E_b = 1540 MPa and G_b = 444 MPa, respectively. Mean compressive strength of the pozzolana-based mortar, which is a typical kind of mortar used in the Campania Region (Southern Italy), was estimated as f_{mm} = 2.5 MPa. Detailed information about materials can be found in the work by Augenti and Parisi (2010a).

A.4. Experimental Program and Main Results

The experimental program consisted of eight monotonic uniaxial compression tests along the direction orthogonal to the bed joints, and seven monotonic uniaxial compression tests along the direction parallel to the bed joints. Two series of six-layer tuff masonry prisms with 10 mm-thick mortar joints were manufactured by professional masons and tested.

A.4.1. Experimental Setup and Test Protocol

A universal testing machine was used for the experimental investigation; its actuator allows to perform displacement-controlled tests (with a total ram stroke of 150 mm) and load-controlled tests (with a maximum capacity of 3000 kN in compression and 2400 kN in tension). Two inductive linear variable differential transformers (LVDTs) were placed on each side of the masonry specimens: one orthogonal to the loading direction, with a stroke of 20 mm; the other parallel to the loading direction, with a stroke of 50 mm.

Each compression test consisted of three stages: (1) two initial cycles aimed at reaching contrast between the load machine and the specimen; (2) application of compression in load control in a way to produce the rising branch of the constitutive law up to one-half of the expected peak strength; and (3) application of compression in displacement control, in order to capture non-linear elastic behaviour up to the peak load, as well as strength degradation due to strain softening along the post-peak falling branch up to about one-fourth of the peak strength. The load was increased linearly with time during the second stage at a rate of 0.3 kN/s, while a constant displacement rate (i.e., actuator stroke rate) equal to 0.01 mm/s was imposed in the third stage, in order to monitor the development of macro-cracking and the occurrence of transverse splitting within the specimen. Details on instrumentation and test procedures are reported in the work by Augenti and Parisi (2010a).

The main experimental results provided by the tests were: stress-strain data sets; secant Young's modulus E; secant Poisson's ratio ν; secant shear modulus G; peak strength σ_k; yielding strain ε_k; residual strength σ_r; ultimate strain ε_u; and strain ductility μ_ε.

A.4.2. Compression Tests in the Direction Orthogonal to Bed Joints

A first set of uniaxial tests were carried out on single-leaf masonry prisms having dimensions of 610×650×150 mm (Fig. A.2a). The fracture process was well captured by the instruments over the whole test duration (Fig. A.2b). Figure A.3 shows the experimental σ-ε curves derived by the tests. Normal compressive stresses were calculated as ratios between the applied load and the gross area of the cross-section.

(a) (b)

Figure A.2 Specimen (a) before and (b) after compression test in the direction orthogonal to mortar bed joints

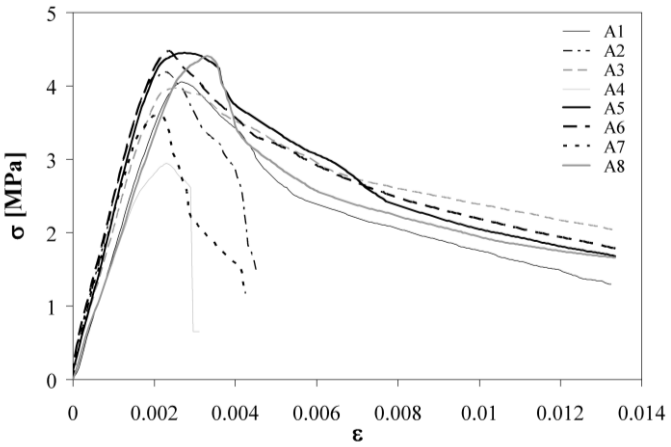

Figure A.3 Experimental stress-strain curves (orthog. dir.)

Axial strains were computed by averaging the LVDT readings corresponding to the same value of applied load and, then, by dividing the average displacements by the gage length. Since stroke measurements are inevitably affected by the take-up of the testing setup and by the machine flexibility, LVDT measurements were expected to produce more reliable estimates of the masonry flexibility parameters than ram stroke records. Experimental data were processed to compute mean values of mechanical parameters, as well as their standard deviation *s* and coefficient of variation *CoV*. In order to get an unbiased estimation of mechanical properties, standard deviation was estimated by applying the Bessel correction as follows:

$$s = \sqrt{\frac{1}{n-1}\sum_{i=1}^{n}\left(x_i - \bar{x}\right)^2} \tag{A.1}$$

where: n is the number of tested specimens; x_i is the realisation of the random variable X from the i-th test; and $\bar{x}$ is the sample mean.

The comparison between experimental results shows that the rising branch of the stress-strain curve is well defined and the scatter in the peak point is very low (Table A.1). Conversely, statistical characterisation of the post-peak behaviour was inevitably affected by potential setup imperfections and randomness in the fracture process, which induces a larger scatter in the (σ,ε) data sets. As a result, a higher uncertainty affects residual strength (defined along the falling branch as the normal stress corresponding to an inelastic strain ε_i = 1.5%), ultimate strain, and strain ductility. Therefore, a reliable value of fracture energy should be quite complex to be defined.

Table A.1 Strength, limit strains and strain ductility (orthog. dir.)

	σ_k [MPa]	σ_r [MPa]	*SDR* [%]	ε_k [%]	ε_u [%]	μ_ε
$\bar{x}$	3.96	1.45	36.4	0.244	1.67	6.57
s	0.50	0.34	5.90	0.022	1.22	4.60
CoV [%]	12.5	23.4	16.2	9.06	73.1	70.0

It is worth noting that the mean residual strength is quite large. Peak strength is associated with an axial strain of 0.24%, which confirms the typical value of 0.2% assumed as yielding strain by masonry standards and building codes.

The European standard EN 1052-1 (CEN, 1999) refers to a secant modulus $E_{1/3}$ corresponding to a normal stress equal to one-third of the peak strength. Instead, ASTM E 11-04 (ASTM, 2004) refers to a secant modulus $E_{1/2}$ corresponding to a normal stress equal to one-half of the peak strength.

Table A.2 shows mean values, standard deviations, and *CoVs* of the following parameters: Young's moduli $E_{1/3}$ and $E_{1/2}$; Poisson's ratios $\nu_{1/3}$ and $\nu_{1/2}$; and their relevant shear moduli, $G_{1/3}$ and $G_{1/2}$.

Table A.2 Secant elastic moduli and Poisson's ratios (orthog. dir.)

	$E_{1/3}$ [MPa]	$E_{1/2}$ [MPa]	$\nu_{1/3}$	$\nu_{1/2}$	$G_{1/3}$ [MPa]	$G_{1/2}$ [MPa]
$\bar{x}$	2222	2159	0.22	0.27	917	854
s	372	335	0.06	0.07	162	137
CoV [%]	16.7	15.5	26.8	27.2	17.7	16.1

The latter were estimated through the Lamé formula $G = E/2(1 + \nu)$. The computation of the secant moduli and Poisson's ratio at one-third of the peak strength may be more appropriate for design purposes, while the analyst should use $E_{1/2}$, $\nu_{1/2}$, and $G_{1/2}$ in the assessment of existing structures. Indeed, the latter parameters give a better estimation of the material compliance given that masonry experiences a nonlinear behaviour even in the elastic strain range.

A.4.3. Compression Tests in the Direction Parallel to Bed Joints

A second set of laboratory tests were performed on masonry prisms having dimensions of 650×610×150 mm, by applying compressive loading along the direction parallel to the mortar bed joints. Figures A.4a shows the masonry specimens before the test, while its fractured condition can be observed in Figure A.4b.

(a) (b)

Figure A.4 Specimen (a) before and (b) after compression test in the direction parallel to mortar bed joints

The behaviour observed during these tests was strongly different from that detected along the other loading direction. Due to low tensile strength of the stone-mortar interface, the prisms suffered extensive cracking even at small deformations. The failure mechanism of the prisms started with vertical transverse splitting shortly before the maximum load was reached (Fig. A.5). This type of cracking was followed by lateral flaking of vertical courses and spalling off of faces, resulting in a wide crushing of the specimen and a rapid load reduction under small increments of ram stroke.

Figure A.6 shows experimental σ-ε curves obtained for the seven tested masonry prisms. Mean values of peak and residual strengths, peak and ultimate strains, and strain ductility are listed in Table A.3, along with their statistical indices.

Figure A.5 Transverse splitting of a specimen

Table A.3 Strength, limit strains and strain ductility (paral. dir.)

	σ_k [MPa]	σ_r [MPa]	*SDR* [%]	ε_k [%]	ε_u [%]	μ_ε
$\bar{x}$	3.85	1.69	44.0	0.240	2.49	10.6
s	0.21	0.41	10.5	0.055	1.10	4.33
CoV [%]	5.56	24.0	23.8	22.7	44.2	40.7

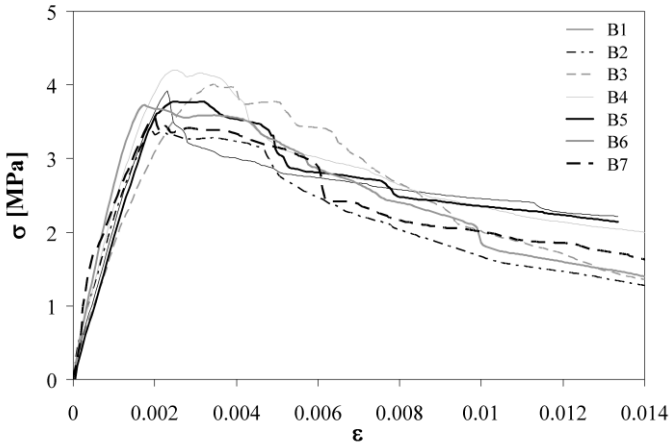

Figure A.6 Experimental stress-strain curves (paral. dir.)

By comparing values in Table A.3 with those listed in Table A.1, it can be noted that the peak strength is a bit less than that evaluated along the direction orthogonal to mortar bed joints, while residual strength is greater. The peak strain is equal to that evaluated along the direction orthogonal to mortar bed joints, even though it is affected by higher uncertainty, while both ultimate strain and strain ductility are larger.
Table A.4 shows secant values of elastic moduli and Poisson's ratios. Whilst elastic moduli are lower than those computed in the direction orthogonal to mortar bed joints, Poisson's ratios are higher.

Table A.4 Secant elastic moduli and Poisson's ratios (paral. dir.)

	$E_{1/3}$ [MPa]	$E_{1/2}$ [MPa]	$\nu_{1/3}$	$\nu_{1/2}$	$G_{1/3}$ [MPa]	$G_{1/2}$ [MPa]
$\bar{x}$	2074	2016	0.24	0.35	857	777
s	258	261	0.20	0.27	186	217
CoV [%]	12.5	12.9	81.9	76.0	21.7	28.0

A.5. Probabilistic Data Sets and Constitutive Equations

Experimental data gathered through compression tests were processed in several modes to get different types of stress-strain data sets and laws. Since normal stresses were associated with different values of axial strain, the experimental data sets were suitably corrected to obtain a *n*-tuple $\{\sigma(\varepsilon)\}$ at each given axial strain. In particular, the range $[0,\varepsilon_u]$ was divided in a number of bins in a way first to approximate the axial strains falling in each bin with its central value, and then to associate each normal stress with the relevant central value of axial strain.

A.5.1. Masonry Subjected to Compression in the Direction Orthogonal to Bed Joints

Data processing allowed first to develop the following probabilistic σ–ε curves: *mean* and *characteristic curves*, namely series of (σ,ε) couples with normal stresses having non-exceeding probabilities of 5% and 50%, respectively, for each axial strain ε^* falling in the interval $[0,\varepsilon_u]$; and *maximum likelihood curves*, namely series of (σ,ε) couples with normal stresses having the maximum probability of occurrence for each axial strain ε^* falling in the interval $[0,\varepsilon_u]$. Such curves are plotted in Figure A.7 along with experimental stress-strain data sets.
The Gaussian probability density function (PDF), with different mean and standard deviation over the strain range under consideration, was assumed for each distribution

of normal stresses associated with a given axial strain. Due to this hypothesis, the mean stress-strain diagram matches the median one. Each set of normal stresses corresponding to a given axial strain was tested in order to assess whether it was well-modelled by a normal PDF or not. This assumption allowed to simplify maximum likelihood estimation (Soong, 2004).

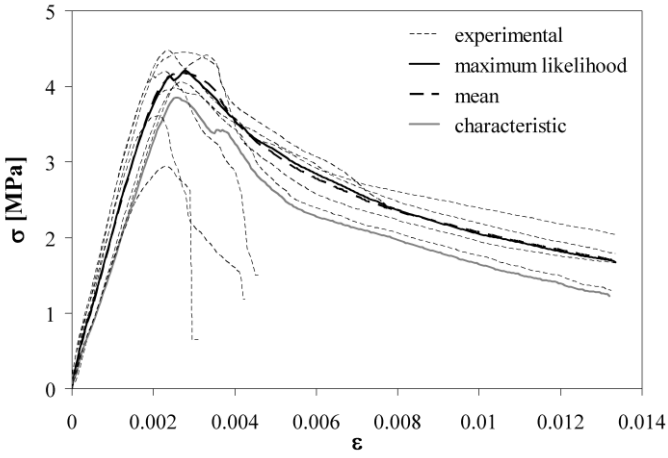

Figure A.7 Probabilistic stress-strain curves (orthog. dir.)

Such stress-strain data sets could be directly implemented in computer programs based on elasto-plastic FE models. In particular, median constitutive data sets could be used for non-linear seismic analysis of existing constructions (according to national and international codes); characteristic constitutive models scaled by a material safety factor could be employed in seismic design of new structures. Mean and characteristic values of mechanical parameters are reported in the work by Augenti and Parisi (2010a).

The ratio between characteristic and mean compressive strengths was computed over the whole strain range considered for defining stress versus strain diagrams. The average ratio is equal to 0.81, while it is $f_k / f_m = 0.91$ at the peak state, being $f_k \equiv \sigma_{kk}$ and $f_m \equiv \sigma_{km}$ the characteristic and mean values of peak strength, respectively. Furthermore, mean Young's modulus at one-third of the peak strength can be related to the characteristic strength by the equation $E_m = 580\ f_k$, while both EC6 (CEN, 2005a) and IBC (IMIT, 2008) suggest to assume $E_m = 1000\ f_k$ for design purposes. Vice versa, the ratio G/E is almost equal to 0.4, which is the value provided by EC6 and IBC.

Non-linear regression analysis on experimental data sets was then carried out to develop empirical stress-strain relationships for non-linear seismic analysis of masonry constructions. In particular, such a regression analysis was performed on stress and

strains normalised to their relevant values at the peak state, namely σ/σ_k and $\varepsilon/\varepsilon_k$. The constitutive equations are reported in Section 7.2.1 [Eq. (7.51)] and were used to develop interactions domains, moment-curvature diagrams, and force-displacement curves (see Chap. 7). Figure A.8 demonstrates that the proposed constitutive model fits well the experimental behaviour of masonry, showing a coefficient of determination $R^2 = 0.93$. A comparison between the proposed constitutive model (Augenti and Parisi, 2010a) and those available in the literature is also shown in Figure A.9.

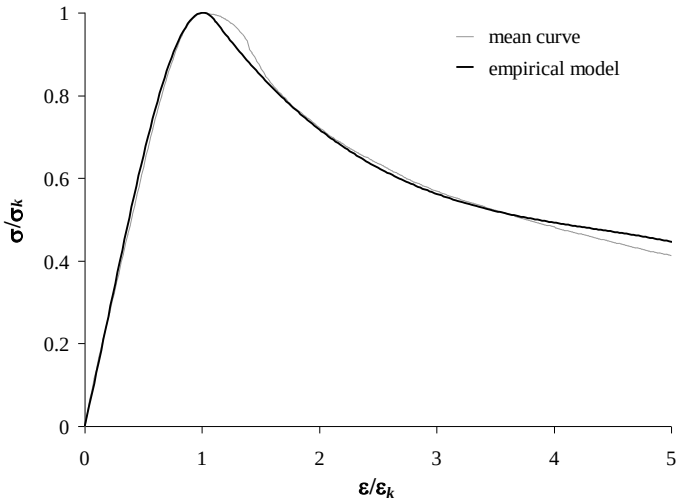

Figure A.8 Comparison between empirical and mean experimental curves (orthog. dir.)

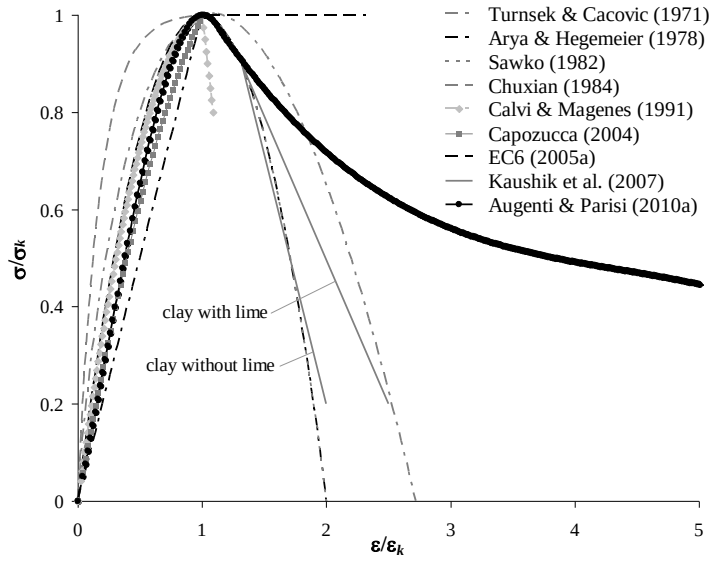

Figure A.9 Comparison between proposed and existing constitutive models

In particular, the constitutive laws selected from the literature are related to clay brick masonry (Calvi and Magenes, 1991; Chuxian, 1984; Kaushik et al., 2007; Sawko, 1982; Turnšek and Čačovič, 1971), clay block masonry (Capozucca, 2004), unconfined concrete masonry (Arya and Hegemeier, 1978), and conventional masonry reported in EC6 (CEN, 2005a). Stress-strain diagrams have similar rising branches, with exception of Chuxian (1984); conversely, falling branches are considerably different depending on the type and shape of masonry units. The constitutive laws proposed by Kaushik et al. (2007) and Calvi and Magenes (1991) include a linear falling branch, but the latter constitutive law has a lower strength degradation. The constitutive law derived from compression tests on tuff masonry prisms (Augenti and Parisi, 2010a) is fully non-linear up to large inelastic strains.

A.5.2. Masonry Subjected to Compression in the Direction Parallel to Bed Joints

Data sets from compression tests in the direction parallel to mortar bed joints were also processed to get maximum likelihood, mean, and characteristic constitutive curves (Fig. A.10), as well as stress-strain relations reported in Section 7.2.2 [Eq. (7.102)] and having $R^2 = 0.99$.

The average ratio between characteristic and mean strengths is 0.75, while it is $f_k/f_m = 0.86$ at the peak state. Mean Young's modulus at one-third of the peak strength can be associated with the characteristic strength through the equation $E_m = 640\ f_k$. Finally, the ratio G/E is still equal to 0.4. Figure A.11 shows a satisfactory agreement between the constitutive model and the mean experimental curve.

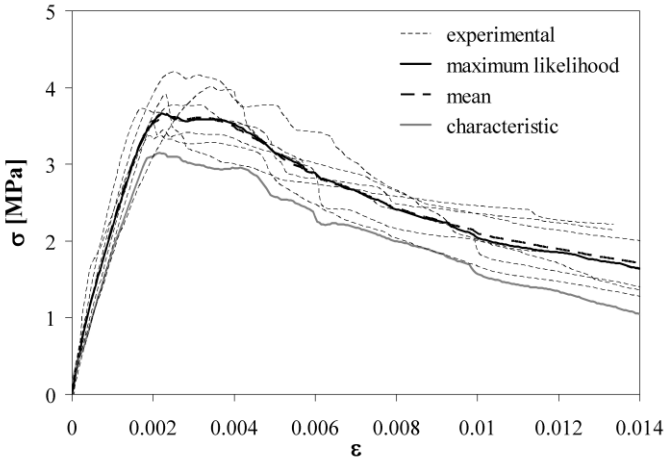

Figure A.10 Probabilistic stress-strain curves (paral. dir.)

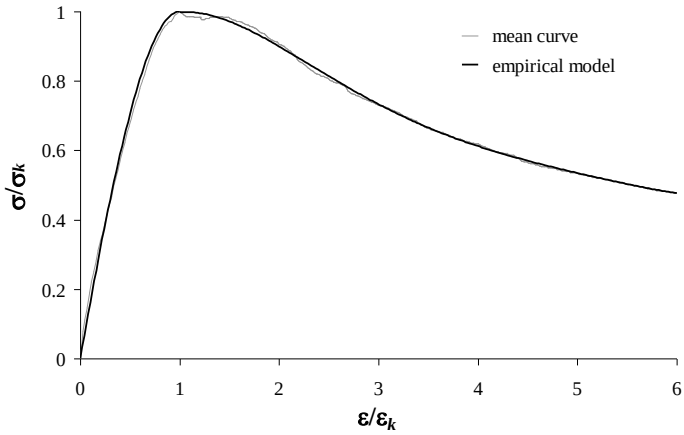

Figure A.11 Comparison between empirical and mean experimental curves (paral. dir.)

Appendix B - EXPERIMENTAL TESTING FOR CONSTITUTIVE MODELLING IN SHEAR

Shear failure of individual URM panels can consists in diagonal cracking or bed-joint sliding and is significantly governed by the unit-mortar interface. As well known, two basic failure modes can be identified for such an interface: tensile failure (mode I) and shear failure (mode II). The former is the separation of the interface normal to the joints, the latter may consist of a shear failure of the mortar joint or sliding mechanism of the masonry units, namely bricks, blocks, or stones (Lourenço, 1996).

Both vertical and horizontal masonry joints act as planes of weakness causing a large variability of mechanical properties with the loading direction. The mechanical behaviour of masonry along these material discontinuities has been deeply investigated for a number of masonry classes by, amongst others, Atkinson et al. (1989), van der Pluijm (1993), Lourenço and Ramos (2004), and Binda et al. (1994). Such researchers have detected the potential for *strain softening*, in both dry and mortar joints with rough surfaces, as well as a dilatational behaviour under shearing deformation. In such conditions, *dilatancy* has been recognised to be an important phenomenon which affects drastically the inelastic response of the unit-mortar interface. Indeed, as the shearing deformation of the masonry joint increases, a transverse expansion develops resulting in a volume growth of mortar, and thus into a *non-isochoric plasticity*, as opposed to metals and plastics (van Zijl, 2004). If such a volume increase is prevented or resisted by confining boundary conditions, the normal uplift results in a pressure buildup. Consequently, shear strength of the unit-mortar interface may significantly increase with the normal compressive stress. Typically, shearing dilatancy is arrested at high pressure levels and at large shear strains, so that shear resistance does not enhance.

Another aspect has to be kept in mind with reference to the effects of these phenomena on non-linear behaviour of laterally-loaded masonry elements. As highlighted by FEMA 356 (ASCE, 2000), shear modulus of masonry reduces substantially as sliding along bed joints develops or as diagonal tension cracks open. Hence, shear stiffness of post-cracked masonry should be taken as a fraction of the initial one and should be evaluated through proper experimental tests. This task along with that related to the basic criteria for defining strength and deformation capacity have never been examined for tuff masonry. In addition, experimental data are still not available for shear flexibility parameters and residual strength.

In order to characterise the non-linear behaviour of unit-mortar interface, shear direct tests were carried out on tuff masonry specimens with proper geometry and subjected to different pre-compression levels in the direction orthogonal to the interface (Augenti and Parisi, 2010c). Such tests were also performed in the framework of ReLUIS-DPC 2005-2008 project.

In this appendix, after the test setup and procedures are briefly described, the main experimental results and empirical models are presented and discussed in order to be implemented in refined methods of seismic analysis where non-linear sliding shear behaviour is explicitly taken into account.

B.1. Research Objectives

The experimental program and the relevant data processing were aimed at (1) the characterisation of classical strength parameters of the Mohr-Coulomb yield criterion, and (2) the definition of deformation and energy parameters proposed in the last decade for masonry structures. The strength parameters are compared to those available in the literature for other masonry assemblages.

Similarly to the characterisation of compressive behaviour (see Appendix A), the experimental research was devoted not only to the estimation of parameters typically employed in linear analysis, but also to the estimation of parameters and the derivation of empirical models to be used in non-linear analysis based on FE, or macro-element, models.

In this case, data processing was first addressed to the evaluation of shear modulus, shear strength at zero confining stress (i.e., cohesion), and friction coefficient in the range of small strains. Fracture energy and dilatancy angle were also estimated to be used in FE analyses.

Second, the Mohr-Coulomb failure model was characterised at both peak and residual states. Such a model could be combined with a cap model in compression (Lourenço and Rots, 1997) and cut-off in tension (Binda et al., 1994).

Finally, several regression analysis techniques were employed (1) to define τ–γ constitutive laws at different pre-compression levels, and (2) to obtain a *shear response surface* $\tau(\sigma,\gamma)$ including both constitutive laws and Mohr-Coulomb failure model.

B.2. Experimental Program

The experimental research for the characterisation of unit-mortar interface in shear consisted of three series of monotonic direct shear tests in displacement control.

This type of tests was preferred over couplet and triplet tests on stones and bricks, even though the latter are the European standard method (CEN, 2002). In fact, triplet tests

are more difficult to be controlled in the post-peak range since two joints are tested all together, while couplet tests are affected by parasite bending effects inducing a non-uniform distribution of stresses at the unit-mortar interface.

B.2.1. Materials and Tested Specimens

The description of the materials employed also for such experimental program, as well as with their main mechanical characteristics, are reported in Section A.3.

As shown in Figure B.1, each specimen consisted of a one-leaf, two-layer tuff masonry assemblage with a mortar bed joint. The gross dimensions of the specimen were 852×210×150 mm, while both head and bed joints had a thickness of 10 mm.

The layers were shifted to each other in order to apply and measure the horizontal forces via simple contact between devices and specimen. The geometry of the latter resulted in a smaller effective shear-resistant portion, whose dimensions were 678×210×150 mm.

Two linear variable differential transformers (LVDTs) were placed on each side of the specimen for measuring the relative horizontal and vertical displacements induced by the shearing deformation and dilatancy. The vertical and horizontal LVDTs had a stroke of 20 mm and 50 mm, respectively. The latter were fixed to both masonry layers.

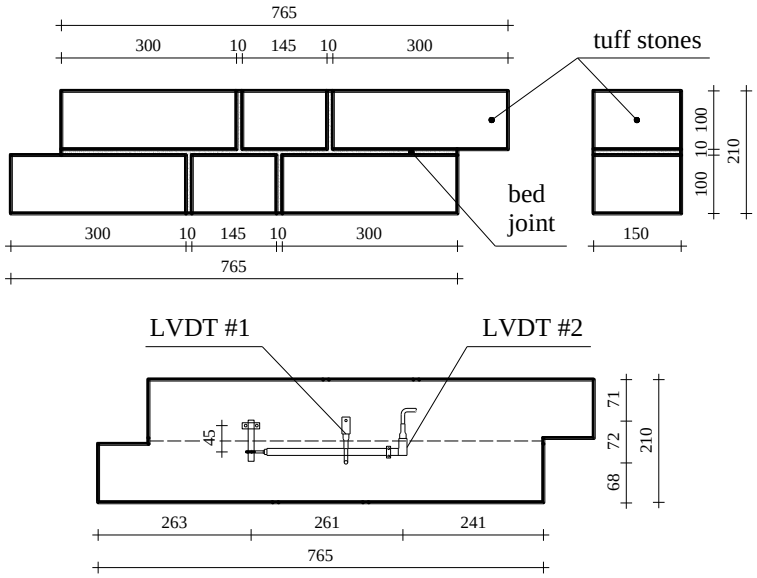

Figure B.1 Specimen geometry (dimensions in mm) and arrangement of LVDTs

B.2.2. Experimental Setup and Test Protocol

The experimental program consisted of three series of deformation-controlled tests performed at different pre-compression load levels. Each experimental test was performed by subjecting the masonry specimen to increasing shear deformation along the mortar bed joint. The test setup was slightly different from that used by Atkinson et al. (1989) for clay brick masonry, even if the ability to induce a rather uniform distribution of shear and normal stresses along the bed joint was preserved (Figs. B.2 and B.3).

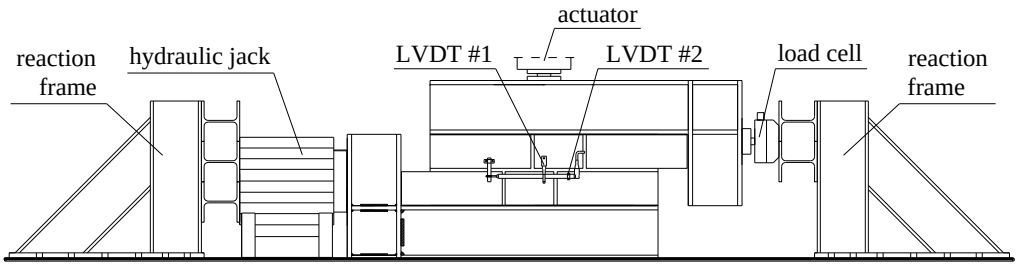

Figure B.2 Experimental setup for direct shear tests

Figure B.3 Front view of a specimen

The masonry specimen was placed onto a L-shaped steel I-beam which was enabled to slip over the rigid base of a universal testing machine by means of two Teflon layers and two lateral unequal angles (Fig. B.4). A double-effect hydraulic jack with a maximum load capacity of 500 kN was positioned against the beam and a reaction frame. A further L-shaped I-beam was put on the specimen and was forced against a

load cell anchored to another reaction frame. The nominal load cell capacity was equal to 100 kN. Once two further Teflon layers were placed over the upper metallic beam, the hydraulic actuator of the universal testing machine, with a load capacity of 3000 kN in compression, was pushed against the specimen. The loading plate of the universal machine was pinned to minimise any undesirable bending effect in the specimen.

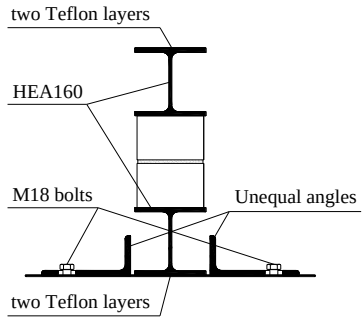

Figure B.4 Cross-section of the experimental setup

Three sets of direct shear tests were carried out at different pre-compression loads corresponding to about 5%, 10% and 15% of the ultimate axial force resisted by the effective (horizontal) cross-section of the specimen. Namely, three direct shear tests were carried out under a pre-compression load of 25 kN corresponding to a vertical confining stress σ = 0.25 MPa (specimens C1 to C3). A second group of four tests were performed under a pre-compression load of 50 kN corresponding to σ = 0.50 MPa (specimens C4 to C7). A third set of two tests were conducted under a pre-compression load of 75 kN corresponding to σ = 0.75 MPa (specimens C8 and C9).

The loading protocol of each direct shear test consisted of two phases. In the former, the vertical confining pressure was imposed to the specimen by means of the hydraulic actuator and was kept constant during the complete test duration. At this stage, the upper beam allowed to get a rather uniform distribution of the vertical pressure over the specimen.

In the second stage of the test, a horizontal load was applied to the lower masonry layer and its magnitude was calibrated by a computer program in such a way to get a target increasing stroke of the hydraulic jack, namely an increasing shearing deformation of the bed joint, under a given normal pressure level. The shear load was applied at a displacement rate of 10 μm/s, so that non-linear response of the bed joint was fully measured during the test until a target displacement (corresponding to a shear strain of about 10%) was reached. The horizontal force applied to the specimen was transmitted

to the lower masonry layer resulting in a relative movement with respect to the upper layer. The load cell at the opposite side with respect to the hydraulic jack enabled the estimation of the actual shear force resisted by the bed joint.
The testing system was able to avoid uncontrolled actions potentially due to unbalanced forces; furthermore, no in-plane and out-of-plane rotations were detected.

B.3. Processing of Experimental Data

B.3.1. Experimental Constitutive Curves

Force and displacement readings were carefully processed accounting for the effective shear force transferred by the unit-mortar interface, as well as the actual gage length of the bridged horizontal LVDT. The effective shear force resisted by the bed joint was not equal to that applied by the hydraulic jack, nor that measured by the load cell located on the reaction frame. Indeed, a rate of the applied shear force (measured by a further load cell placed between the hydraulic jack and the lower beam) was dissipated through the interface between the lower layer and the base of the universal machine and was absorbed as axial deformation of stone units and head joints. Conversely, the force measured by the opposite load cell was lower than the effective shear force resisted by the bed joint, since the former was affected by frictional dissipation along the upper beam-actuator interface. Therefore, the effective shear force V_{eff} was computed as the sum of the load cell reading (right side in Fig. B.2) and the frictional force dissipated along the beam-actuator interface. This force was assumed as proportional to the ratio between the contact area of the actuator plate and the area of the lower masonry layer. The following relation was used:

$$V_{eff} = V_{cell} + V_f \tag{B.1}$$

assuming:

$$V_f = \Delta V \frac{A_{plate}}{A_{layer}} \tag{B.2}$$

and:

$$\Delta V = V_{cell} - V_{jack} \tag{B.3}$$

Such equations include: the force measured at the load cell, V_{cell}; the frictional force, V_f; the force applied at the jack, V_{jack}; the contact area of the actuator plate, A_{plate}; and the area of the lower masonry layer, A_{layer}. The friction coefficient of Teflon was assumed to be constant under varying applied normal stress. Actually, the latter had different values at the plate-upper beam interface and the interface between the lower beam and the base of the testing machine.
To get the experimental shear stress-strain diagrams, the computed shear forces V_{eff}

were divided by the effective bed-joint area and the relative horizontal displacement readings were divided by the LVDTs' gage length. These computations were limited to the strain range [0,0.1], which was divided into a number of bins in order to associate shear stresses falling in a given bin with its central shear strain. This manipulation of data was carried out similarly to the characterisation of compressive behaviour (see Appendix A).

Figures B.5, B.6 and B.7 show the experimental and mean stress-strain curves derived for the three confining stress levels. A large shear strain ductility μ_γ was identified for all tests due to high frictional dissipation capacity of the bed joint. According to what has been reported in the literature (see for instance: Homand et al., 2001; Misra, 2002), rough fracture surfaces induced strength degradation under increasing inelastic displacement. As the shear strain increases, the joint roughness reduces ranging from the mobilization of the asperities in the pre-peak region to their gradual smoothening in the post-peak region. Conversely, no softening was recorded for masonry assemblages with dry joints (Vasconcelos and Lourenço, 2009).

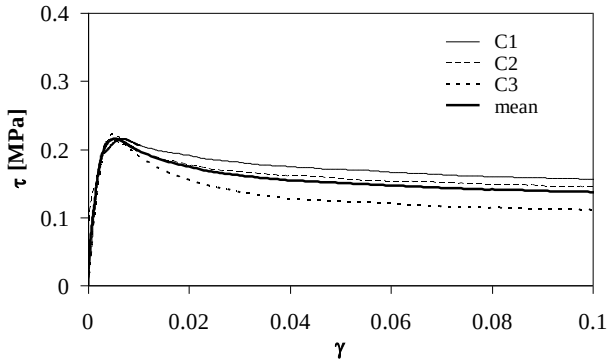

Figure B.5 Experimental and mean stress-strain curves for (a) σ = 0.25 MPa

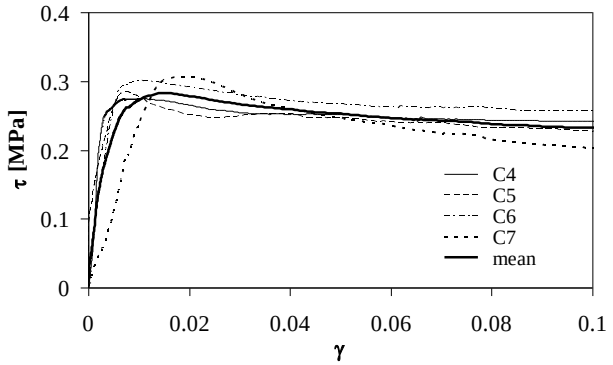

Figure B.6 Experimental and mean stress-strain curves for σ = 0.50 MPa

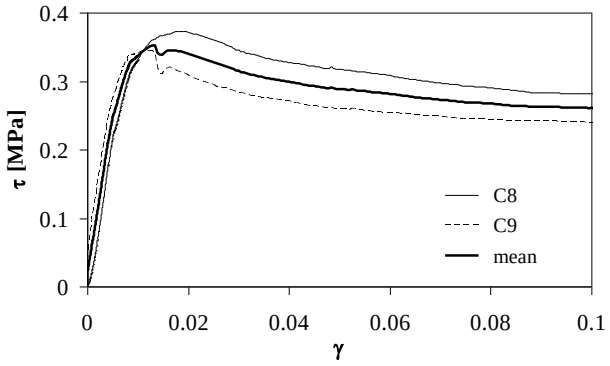

Figure B.7 Experimental and mean stress-strain curves for σ = 0.75 MPa

B.3.2. Strength and Deformation Parameters

The mean values of peak shear strength τ_p, residual shear strength τ_r, strength degradation ratio $SDR = \tau_r/\tau_p$, and peak shear strain γ_p, are listed in Table B.1. The peak and residual strengths, as well as peak strain, increase with the confining stress.

Table B.1 Mean strength and strain parameters

Test series	σ [MPa]	τ_p [MPa]	τ_r [MPa]	*SDR*	γ_p [%]
1	0.25	0.22	0.14	0.63	0.52
2	0.50	0.29	0.23	0.80	1.1
3	0.75	0.36	0.26	0.72	1.5

It is worth noting that the scatter in the peak shear strength is very limited, being the coefficient of variation (*CoV*) equal to 2.11%, 4.95% and 5.72% for a pre-compression level of 0.25 MPa, 0.50 MPa and 0.75 MPa, respectively. The uncertainty in the residual strength estimation is higher, with a *CoV* ranging between 9.96% and 16.97%. Shear softening plays a relevant role, since *SDR* ranges from 20% (for σ = 0.5 MPa) to 37% (for σ = 0.25 MPa). For triplets made of solid mud bricks and hydraulic lime mortar with joint thickness of 10 mm, Mirabella Roberti et al. (1997) found a *SDR* between 0.51 and 0.69 for confining stress ranging between 0.12 and 1.25 MPa. The shear strain at the peak stress increases with the confining normal stress.

B.3.3. Shear Modulus, Fracture Energy and Dilatancy

The variation of the mean secant shear modulus *G* versus shear strain γ was investigated and plotted for the pre-compression levels imposed during the direct shear

tests (Fig. B.8). The secant shear modulus at one-third of the peak shear stress was found to be 93, 72 and 63 MPa for a pre-compression level of 0.25, 0.50 and 0.75 MPa, respectively. The uncertainty in shear modulus is quite limited, since *CoV* is not larger than 15%.

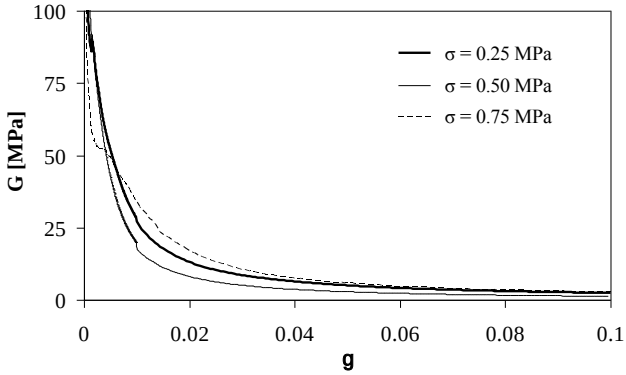

Figure B.8 Secant shear modulus versus shear strain for different pre-compression levels

To simulate the shear response of masonry in the plastic range, strain softening has to be characterised for representing the progressive internal crack growth, due to the presence of micro-cracks and material heterogeneity. In the case of tuff masonry, softening behaviour is believed to be increased by the presence of some pumice inclusions within the stone units, which result in higher concentrations of cracking and acceleration of crack formation over non-porous masonry units (e.g., clay bricks).
Shear softening of the unit-mortar interface may be conveniently described via the mode II fracture energy, defined as the integral of the shear stress versus relative horizontal displacement diagram. Figure B.9 shows that the fracture energy increment ΔG_f^{II} reduces considerably as shear strain increases.

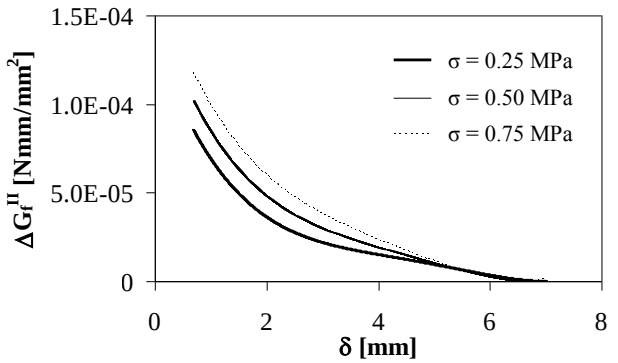

Figure B.9 Fracture energy increment versus horizontal relative displacement

This is consistent with stress-strain diagrams of a large number of masonry assemblages, as extensively discussed by Lourenço (1996). The mean mode II fracture energy G_f^{II} was numerically computed for each set of direct shear tests (Fig. B.10) and was found to be 0.12, 0.13 and 0.16 Nmm/mm^2 for a pre-compression level of 0.25, 0.50 and 0.75 MPa, respectively.

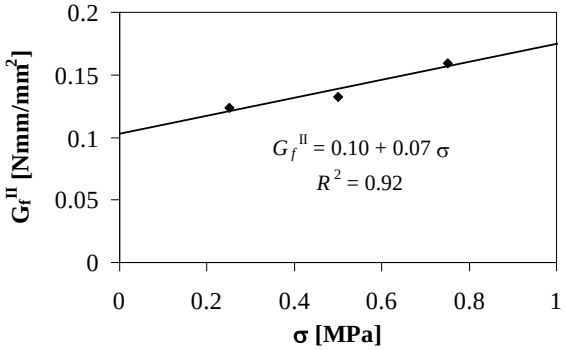

Figure B.10 Fracture energy versus confining stress

A linear regression analysis allowed to estimate fracture energy at zero confining stress as 0.1 Nmm/mm^2, showing a high dissipation capacity of the tuff stone-mortar joint interface under shear loading. This value is in agreement with that obtained by van der Pluijm (1993) for masonry specimens with solid clay or calcium-silicate units, for which shearing fracture energy was between 0.01 and 0.25 Nmm/mm^2. Moreover, also van Zijl (2004) found that fracture energy increases linearly with normal stress.

Dilatancy of tuff masonry was also investigated by means of normal versus shear displacement curves (i.e., δ_v–δ_h diagrams). In the context of the Mohr-Coulomb failure criterion, one can assume that the effective friction angle of the bed joint is the sum of an *inherent angle* due to adhesion and a *dilatancy angle* defined as $\psi = \arctan(\delta_v/\delta_h)$. In Figures B.11a, B.11b and B.11c, the relative vertical displacement is plotted versus the relative horizontal displacement for different pre-compression levels. The dilatational behaviour under shearing deformation is in agreement with that observed by other researchers (e.g., Misra, 2002) and consists typically of three different trends. In the former, the normal displacements are negative (i.e., the masonry layers tend to approach). Afterwards, vertical displacements become positive and increase with the shear displacements. Finally, as the shearing deformation increases, the vertical displacements tend to a constant steady-state value. Figure B.12 shows that dilatancy coefficient depends considerably on the confining stress, since the uplift movement reduces as the confining pressure increases. However, a large scatter was detected in such a parameter, as demonstrated by the coefficient of determination $R^2 = 0.29$.

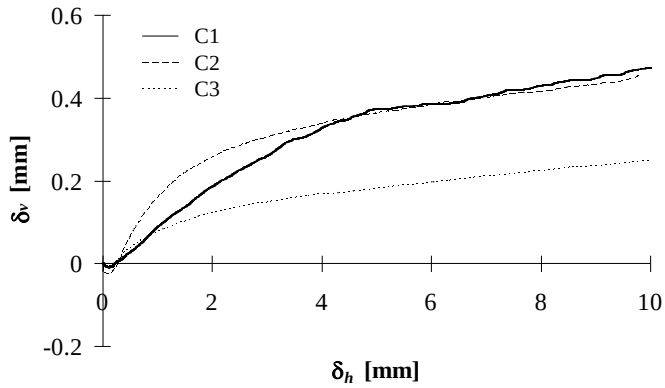

(a)

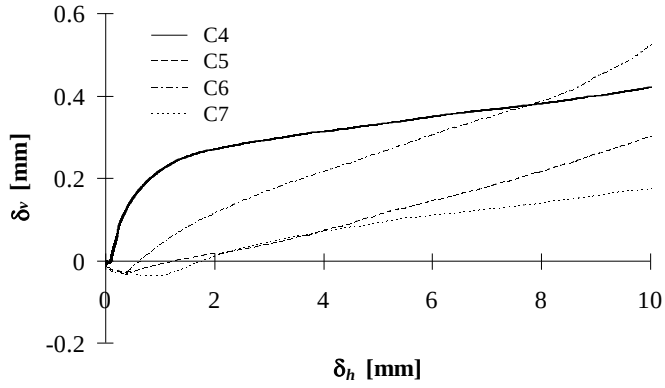

(b)

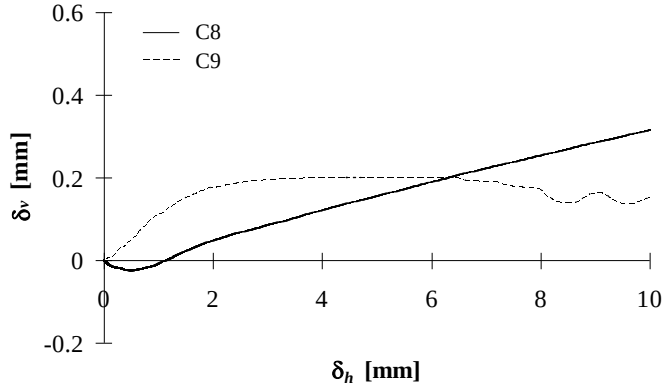

(c)

Figure B.11 Dilatancy curves for (a) σ = 0.25 MPa, (b) σ = 0.50 MPa, and (c) σ = 0.75 MPa

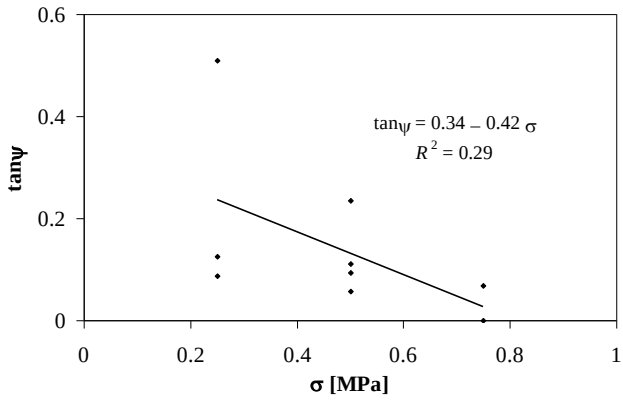

Figure B.12 Dilatancy coefficient versus confining stress

B.4. Characterisation of Mohr-Coulomb Strength Model

The shear strength of the unit-mortar interface was characterised through linear regression analysis, assuming the Mohr-Coulomb failure criterion for predicting both peak and residual shear strengths. This strength criterion establishes a linear relationship between the shear stress τ and the normal stress σ as follows:

$$\tau = c + \mu\sigma \tag{B.4}$$

where c and μ are respectively the cohesion and the friction coefficient (i.e., the tangent of the friction angle ϕ) of the contact surface, assumed to be strength parameters at peak and residual strength levels. It is noted that this strength criterion has a 'local' meaning being related only to shear sliding mechanisms of masonry panels (see Sect. 6.2.8). Therefore, such parameters could be used to define lateral strength of URM panels corresponding to bed-joint sliding shear in macro-element methods of seismic analysis (see Eq. (6.6)).

Figure B.13a shows the shear bond strength models derived for the peak and residual stress states, at which corresponds a friction angle of 16° and 15°, respectively. The proposed empirical model provides good predictions of peak shear strength, being the coefficient of determination R^2 = 0.96, while it has a lower predictive power at the residual stress state (R^2 = 0.77).

Assuming the residual strength as an exponential function of the confining stress, one can get $\tau = 0.34\sigma^{0.63}$ and R^2 = 0.82, but this model would not be easy-to-use if coupled with a linear model at the peak stress state.

It is also worth noting that the residual cohesion of the bed joint was not set to zero within regression analysis, because it is believed to be associated with a non-zero frictional resistance of the slip surface. This evidence was observed by van der Pluijm

(1993), while no residual cohesion was detected for dry masonry joints by Lourenço and Ramos (2004) through cyclic couplet tests.

The cohesive bond strength and the friction coefficient reduced of 47% and 10%, respectively, from the peak to the residual state, whilst results of linear regression analysis by Binda et al. (1994) showed that cohesion and friction coefficient reduce, respectively, of 61% and 12% for sandstone masonry triplets, and of 43% and 26% for calcareous stone masonry.

In Figure B.13b, the tangent of the friction angle of the unit-mortar interface is plotted versus confining stress, along with non-linear models derived for peak and residual states. Once more, the predictive power is lower at the residual state.

In Table 1, peak cohesion and friction coefficient estimated by the authors for tuff masonry are compared to those derived for other masonry assemblages.

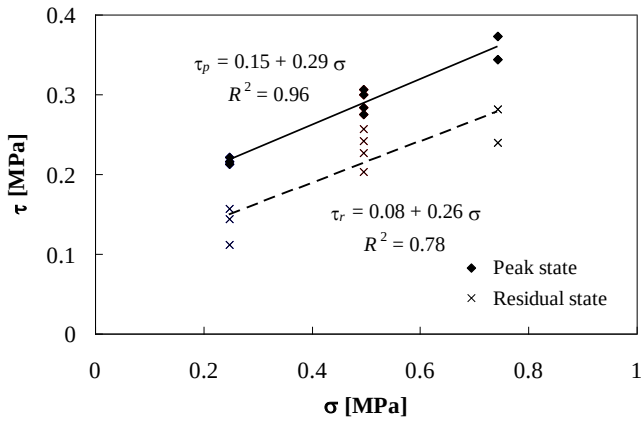

(a)

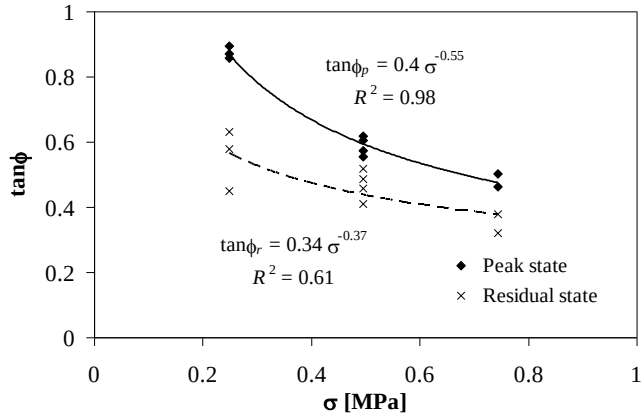

(b)

Figure B.13 (a) Characterisation of Mohr-Coulomb strength model and (b) friction angle versus confining stress

Table B.2 Peak cohesion and friction angle for different masonry types

Reference	Unit	Mortar*	*c* [MPa]	tanϕ
Amadio and Rajgelj (1991)	Solid brick	Cement mortar	0.65	0.723
		Lime-cement mortar		
Atkinson et al. (1989)	Old clay brick	1:2:9 (13 mm)	0.127	0.695
	Old clay brick	1:2:9 (7 mm)	0.213	0.640
	New clay brick	1:1.5:4.5 (7 mm)	0.811	0.745
Binda et al. (1994)	Sandstone	Hydraulic lime mortar	0.33	0.74
	Calcareous stone	Hydraulic lime mortar	0.58	0.58
Drysdale et al. (1979)	Clay brick	1:0.5:4	0.57	0.90
Hegemeier et al. (1978)	Concrete block	Type S	0.25	0.89
Lourenço et al. (2004)	Hollow brick	Micro-concrete	1.39	1.03
Magenes (1992)	Solid brick	Hydraulic lime mortar	0.206	0.813
		Lime mortar	0.081	0.652
Mirabella Roberti et al. (1997)	Solid mud brick	Hydraulic lime mortar	0.23	0.57
Stöckl and Hofmann (1986)	Clay brick	1:0.68:15	0.95	0.7
		1:0:9.7	1.45	0.56
Vasconcelos and Lourenço (2009)	Granitic brick	Lime mortar	0.359	0.630
This study	Tuff stone	Pozzolana-based	0.146	0.287

* Mortar composition as cement:lime:sand ratio by volume and joint thickness in round parentheses.

B.5. Development of a Shear Response Surface

Based on the experimental data gathered from the laboratory tests, a non-linear stress-strain model was first fitted to the experimental data associated with each pre-compression level (Fig. B.14a) and then it was suitably regularised for further processing (Fig. B.14b). The aim of these computations was to obtain a dimensionless *shear response surface* of the unit-mortar interface by merging the constitutive laws and the Mohr-Coulomb failure criterion together. This response surface is to be distinguished from the classical failure surface (which does not include the constitutive law) and was defined to get a unique function $\overline{\tau}(\overline{\sigma},\overline{\gamma})$ describing the shear stress under

varying shear strain and confining stress. The symbol $\bar{\tau}$ denotes the shear stress τ normalised to the peak strength τ_p, $\bar{\sigma}$ represents the given confining stress σ normalised to a reference normal stress σ_{ref}, and $\bar{\gamma}$ stands for the given shear strain γ normalised to the shear strain γ_p corresponding to the peak strength. It is underlined that this strain was identified for each experimental stress-strain curve and that the symbol γ_p does not represents the maximum shear strain reached during the tests. It was employed just to emphasise the relationship between the shear strain and the peak strength.

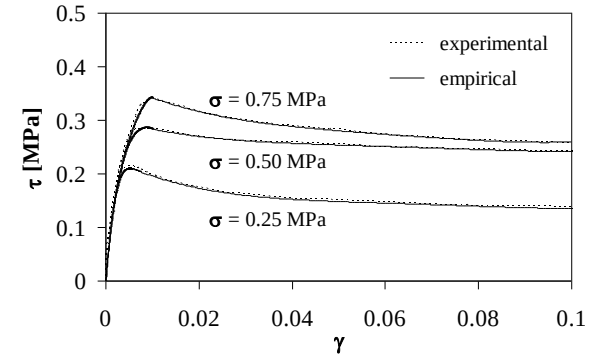

(a)

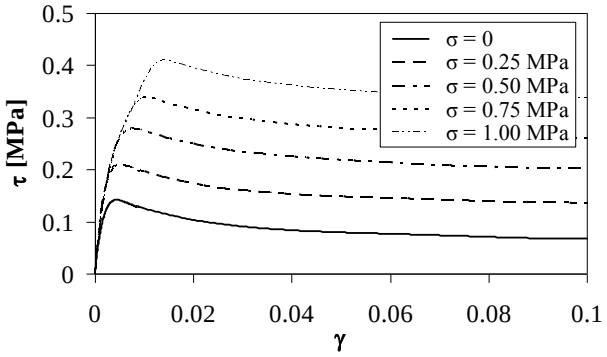

(b)

Figure B.14 (a) Empirical and mean experimental stress-strain curves; (b) regularised curves

Non-linear regression analysis on stress-strain data was carried out for two strain ranges, separately, in order to simulate the softening behaviour. Therefore, for each given confining stress level, the authors identified a 'crossing' shear strain $\bar{\gamma}_c$ corresponding to the counterflexure point of the constitutive model, so as to get the best fit on experimental data and to attain the continuity of the constitutive function

and its first derivative. The stress-strain diagrams at σ = 0 and σ = 1.00 MPa were derived by extrapolating those directly associated with experimental data. Both cohesive and frictional terms were assumed to be dependent on the shear strain, in order to define the shear stress at the interface as a linear function of the confining stress, as follows:

$$\bar{\tau}\left(\bar{\sigma},\bar{\gamma}\right)=c\left(\bar{\gamma}\right)+\mu\left(\bar{\gamma}\right)\bar{\sigma} \tag{B.5}$$

where $\bar{\sigma}$ represents the confining stress σ normalised to a reference normal stress σ_{ref} assumed to be 0.18 times the uniaxial compressive strength of masonry. The adoption of a linear relationship between the shear stress and the normal stress allowed to split the multiple regression analysis in two simple non-linear regression analyses carried out on the shear strain. To describe the variation of the crossing shear strain versus the normal stress, the authors derived the following equation:

$$\bar{\gamma}_c=1+0.275\bar{\sigma} \tag{B.6}$$

As shown in Figure B.15, was obtained to divide the $(\bar{\sigma},\bar{\gamma})$ plane in two different regions (denoted by $\mathbf{\Omega}_1$ and $\mathbf{\Omega}_2$) and, thus, to split the response surface for simulating shear softening. Given a normal stress $\bar{\sigma}_i$, one can estimate the shear strain $\bar{\gamma}_{c,i}$ at which corresponds the counterflexure point of the stress-strain diagram.

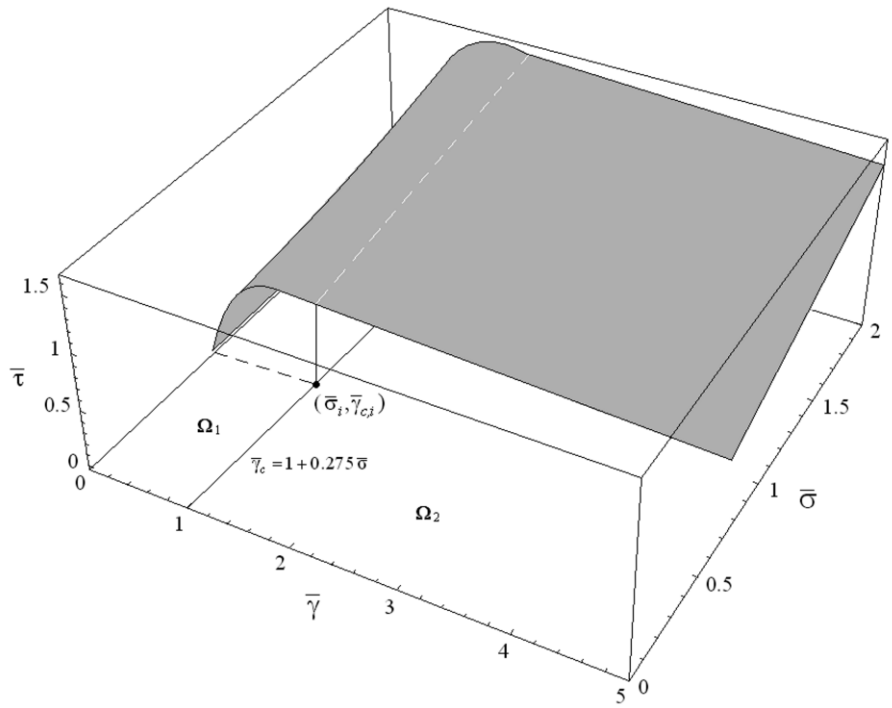

Figure B.15 Partition of $(\bar{\sigma},\bar{\gamma})$ plane and construction of shear response surface

Figure B.16 shows the shear response surface for the unit-mortar interface (R^2 = 0.96), where the cohesive and frictional contributions are response functions defined as:

$$c(\overline{\gamma}) = 2.719\,\overline{\gamma} - 4.644\,\overline{\gamma}^2 + 2.289\,\overline{\gamma}^3 - 0.6\,\overline{\gamma}^4 \tag{B.7}$$

$$\mu(\overline{\gamma}) = 0.082\,\overline{\gamma} - 1.695\,\overline{\gamma}^2 - 1.54\,\overline{\gamma}^3 + 0.371\,\overline{\gamma}^4 \tag{B.8}$$

for $\overline{\gamma} \in [0,(1+0.275\,\overline{\sigma})]$ and:

$$c(\overline{\gamma}) = 0.464 + 0.146\,\overline{\gamma} + 0.034\,\overline{\gamma}^2 - 3.8\cdot10^{-3}\,\overline{\gamma}^3 + 1.5\cdot10^{-4}\,\overline{\gamma}^4 \tag{B.9}$$

$$\mu(\overline{\gamma}) = 0.64 + 0.002\,\overline{\gamma} - 0.001\,\overline{\gamma}^2 + 1.5\cdot10^{-4}\,\overline{\gamma}^3 - 4.474\cdot10^{-5}\,\overline{\gamma}^4 \tag{B.10}$$

for $\overline{\gamma} \in [(1+0.275\,\overline{\sigma}),5]$.

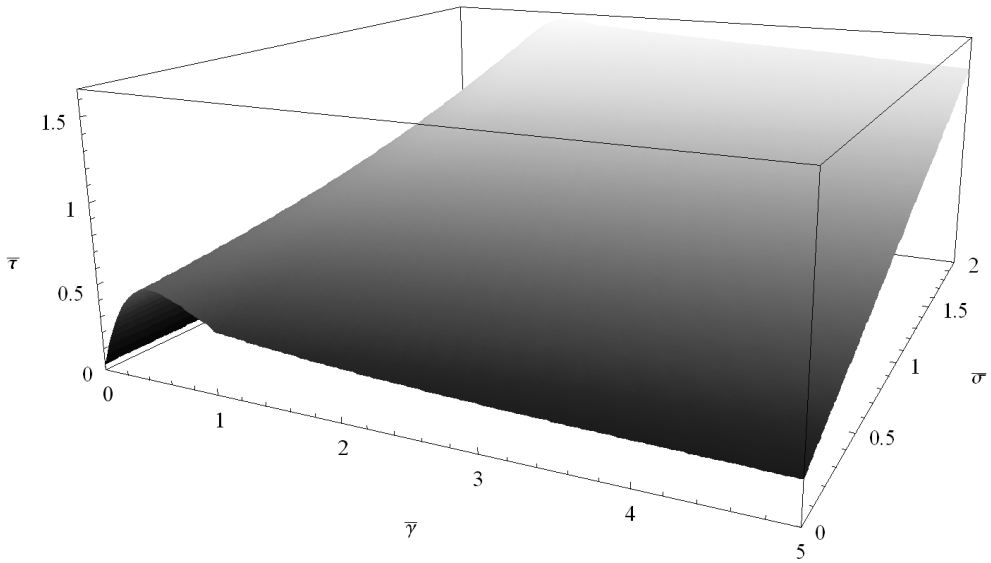

Figure B.16 Shear response surface

It is underlined that the shear response surface defines the shearing behaviour of the unit-mortar interface from the elastic range to the inelastic range, including strength degradation due to strain softening. The response parameters $c(\overline{\gamma})$ and $\mu(\overline{\gamma})$ should not be confused with the classical strength parameters of the Mohr-Coulomb failure criterion (denoted *c* as and μ in this study), because they depend on the shear strain and are used to characterise the shear response over the whole range of allowable shear strains. Therefore, cohesion *c* and friction coefficient μ could be used in linear equivalent models, while the shear response surface could be employed within non-linear models. Finally, it is also emphasised that the empirical model represented by the shear response surface allows to define the τ–γ constitutive law at any confining stress level compatible with strength of masonry.

Appendix C - EXPERIMENTAL TESTING FOR NON-LINEAR SEISMIC ANALYSIS

On site inspections after severe earthquakes have shown that URM buildings suffer frequently most part of damage within spandrel panels; the latter play a key role in the absorption and dissipation of seismic input energy. Although non-linear behaviour of masonry walls with openings is significantly affected by such structural elements, knowledge about their modelling within macro-element methods is still lacking and current seismic codes do not provide specific rules for design and assessment. On the other hand, preliminary theoretical investigations (e.g., Cattari and Lagomarsino, 2008) have shown that masonry interlocking at the interface between spandrel panel and adjoining pier provide a significant contribution to flexural strength of spandrel panels, even in the absence of tensile-resistant elements (typical case of existing buildings). The non-linear behaviour is also affected by spandrel-pier interaction, which depends on their own length-to-width ratios, flexural and shear strength/stiffness, and the magnitude of gravity loads. Such an interaction can change in the presence of retrofit systems on spandrels and/or piers, resulting in potential modifications in failure modes.

A negative effect of retrofit was observed, for instance, by Benedetti et al. (1998, 2001) after shaking-table tests on brick masonry building models before and after strengthening of spandrels with RC bands. The absorbed and dissipated energy was high in the case of as-built specimens and low in the case of repaired specimens. As-built specimens suffered significant damage to spandrels, while repaired specimens experienced a premature collapse due to damage localization in piers. Based on those results, Benedetti et al. (2001) suggested to design devices able to absorb and dissipate energy through heavy damage, while controlling it. In this context, the use of composite materials can be very promising for seismic retrofit of URM structures. Namely, the application of mortar-based matrices allows to overcome the well-known limitations of fibre-reinforced polymers, especially in terms of bond to highly-porous existing masonry substrates, such as tuff masonry.

In order to investigate non-linear response of masonry walls with openings, a series of quasi-static lateral loading tests were carried out on a full-scale URM wall with a opening (Augenti et al., 2010b). The specimen had a lintel with limited anchorage length and no tensile-resistant elements (e.g., RC bond beams, steel ties), to simulate actual conditions of a large part of existing masonry buildings in seismic regions.

C.1. Research Objectives

The tested wall was supposed to be taken out from a typical multi-storey wall with vertically-aligned openings. The geometry of the specimen and the vertical forces applied on piers to simulate the effects of gravity loads were designed in a way to avoid any pre-defined boundary condition for the spandrel panel and to develop most part of damage within it.

The first lateral loading test was carried out on the as-built wall in order to investigate non-linear response up to the attainment of first significant (i.e., permanent) damage to the spandrel panel.

The second tests was performed on the pre-damaged wall in order to preliminary assess residual properties of URM buildings subjected to earthquake sequences.

The third and last test was conducted on the repaired and upgraded wall up to a near-collapse state. Repair involved both piers and the spandrel panel, while upgrade consisted in the application of an inorganic matrix-grid (IMG) composite system on the spandrel. The main scope of this test was to assess the effectiveness of the IMG system for retrofit and upgrading of URM structures, as well as rapid remedial works in seismic emergency scenarios. The effectiveness of the IMG system was intended as the ability to provide energy dissipation capacity to spandrels, according to suggestions by Benedetti et al. (2001). At the same time, the IMG system was selected to meet principles of minimum intervention and reversibility, which are mandatory for historical constructions.

C.2. Experimental Program

Mechanical properties of constituent materials of tuff masonry and the IMG system were characterised through specific laboratory tests (see also Appendix A for tuff masonry materials). Afterwards, an URM masonry wall was built up and three quasi-static lateral loading tests were carried out in displacement control in order to capture non-linear degrading response. The first test was monotonic, the others were cyclic.

C.2.1. Design of the Tested Wall

The tested wall and the test setup were designed through the pushover procedure presented in Section 8.1. The design was based on a trial-and-error procedure aimed at predicting most part of damage in the spandrel panel, ensuring the absence of sliding shear mechanisms at the bases of piers.

The analytical prediction was then based on a macro-element idealisation of the wall, by assuming different compressive strengths and elastic moduli for the masonry of the spandrel panel and the piers (see Table C.1 in Sect. C.2.2). Joint panels were assumed

to be rigid and infinitely resistant up to wall collapse. The unit weight of tuff masonry was assumed to be 16 kN/m^3, while the following limit values of shear strength at zero confining stress were considered: $\tau_{0,min}$ = 0.05 MPa and $\tau_{0,max}$ = 0.10 MPa. Such an assumption was motivated by the absence of characterisation tests about diagonal tensile shear strength. Pushover analysis provided a lateral resistance of the wall equal to 185.45 kN for the minimum shear strength value and 189.97 kN for the maximum shear strength value.

C.2.2. Geometry of the As-Built Wall and Material Properties

The wall subjected to the first and second tests was made of single-leaf tuff masonry and consisted of two piers connected by a spandrel panel with a wooden lintel. The latter had an anchorage length equal to 15 cm at both sides (Fig. C.1).

The gross dimensions of the wall (with and without IMG system) were: length equal to 510 cm; height equal to 362 cm; and thickness equal to 31 cm. In order to apply vertical forces ensuring structural continuity with an ideal upper storey, three masonry layers were realised above the piers. The length of both piers and spandrel panel was 170 cm, while the height of the spandrel panel was 100 cm. Vertical joints were alternated and had a thickness equal to 10 mm. Therefore, in the context of a macro-element modelling of the masonry wall, the pier and spandrel panels had an aspect length-to-width ratio equal to 1.35 and 1.70, respectively. The joint panels defined as intersections between spandrel and piers had dimensions 170×100×31 cm.

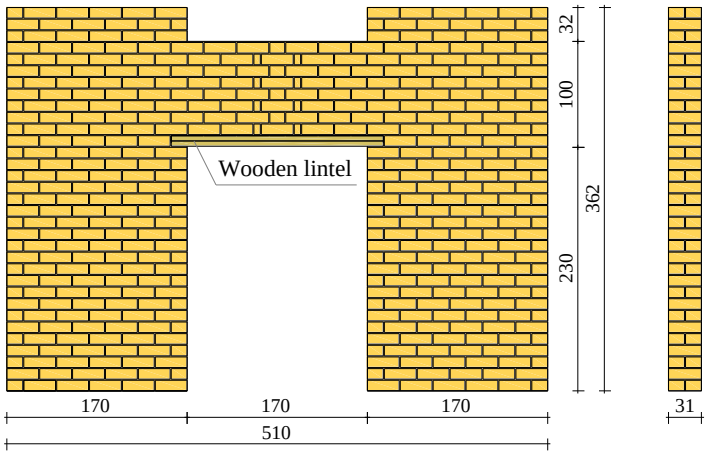

Figure C.1 Geometry of as-built specimen (dimensions in cm)

Composition and characteristics of tuff masonry are described in Appendix A, while mechanical properties of both masonry and its constituent materials are listed in

Table C.1. The latter includes the following properties: tensile strength f_t; compressive strength f_c; Young's modulus E; and shear modulus G. Tuff stones were characterised by means of uniaxial compression tests on specimens with edge 70 mm, while mortar was characterised through similar tests on specimens with dimensions 40×40×160 mm. Mechanical parameters of masonry are distinguished for directions parallel and orthogonal to mortar bed joints to allow different modelling of spandrel and piers, respectively. It is underlined that the employed mortar is classified as M2.5 by IBC (IMIT, 2008), while compressive strength of tuff masonry exceeded the referential interval [1.4 MPa, 2.4 MPa] suggested by IBC for existing masonry buildings in the absence of specific experimental characterisation.

Table C.1 Mechanical properties of constituent materials

	f_t [MPa]	f_c [MPa]	E [GPa]	G [GPa]
Tuff stones	0.23	4.13	1.54	0.44
Pozzolana-like mortar	1.43	2.50	1.52	0.66
Tuff masonry (compression ∥ to bed joints)	-	3.85	2.07	0.86
Tuff masonry (compression ⊥ to bed joints)	-	3.96	2.22	0.92
IMG system matrix	6.00	16.0	8.00	-
IMG system grid	1276	-	72.0	-

C.2.3. Geometry of the Repaired Wall and Material Properties

The fibre-reinforced composite material used for external reinforcement of the masonry wall was composed by a special two-component matrix and a glass fibre grid. The matrix was made of hydraulic lime and sand (ratio by weight 1:3) added with glass fibers (ratio by total weight 1:10) and mixed with latex and water (ratio by weight 2:1). The glass fibre-reinforced matrix ensured higher ductility and tensile strength, resulting in a high-performance composite. The grid was a bidirectional alkali-resistant glass coated net with texture 25×25 mm, unit weight of 225 g/m^2, and ultimate strain lower than 2%. Also mechanical properties of the IMG composite are listed in Table C.1.

The IMG system was applied on both sides of the spandrel (Fig. C.2). Cracks induced by the previous tests within the spandrel panel were filled with mortar (Figs. C.3a and C.3b). The masonry was suitably prewetted and the mortar was troweled onto both sides of the specimen with a 5 mm-thick layer. The fabric sheet was firmly hand-pressed into the wet binder with the fibers aligned to the mortar bed joints of the wall (Fig. C.3c). The overlapping length of grids was 100 mm. Finally, a second layer of

pozzolana-like mortar was applied to the specimen by troweling a further 5 mm-thick layer (Fig. C.3d). The nominal thickness of the IMG system was then equal to about 10 mm. The strengthening system involved the first stone layer below the spandrel to ensure anchorage.

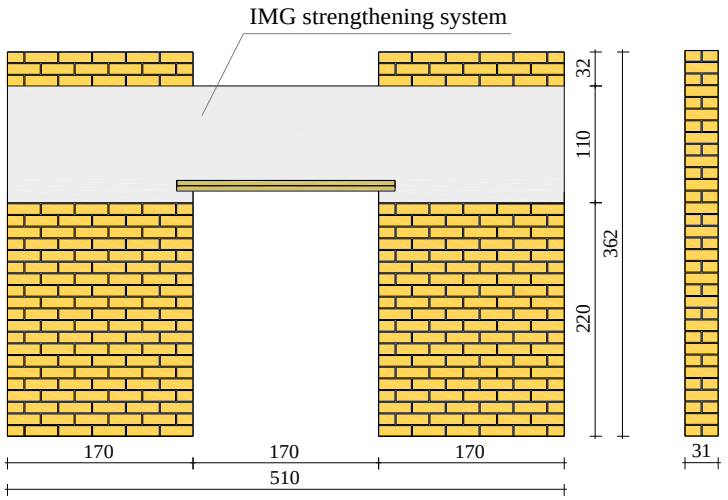

Figure C.2 Geometry of IMG-repaired specimen (dimensions in cm)

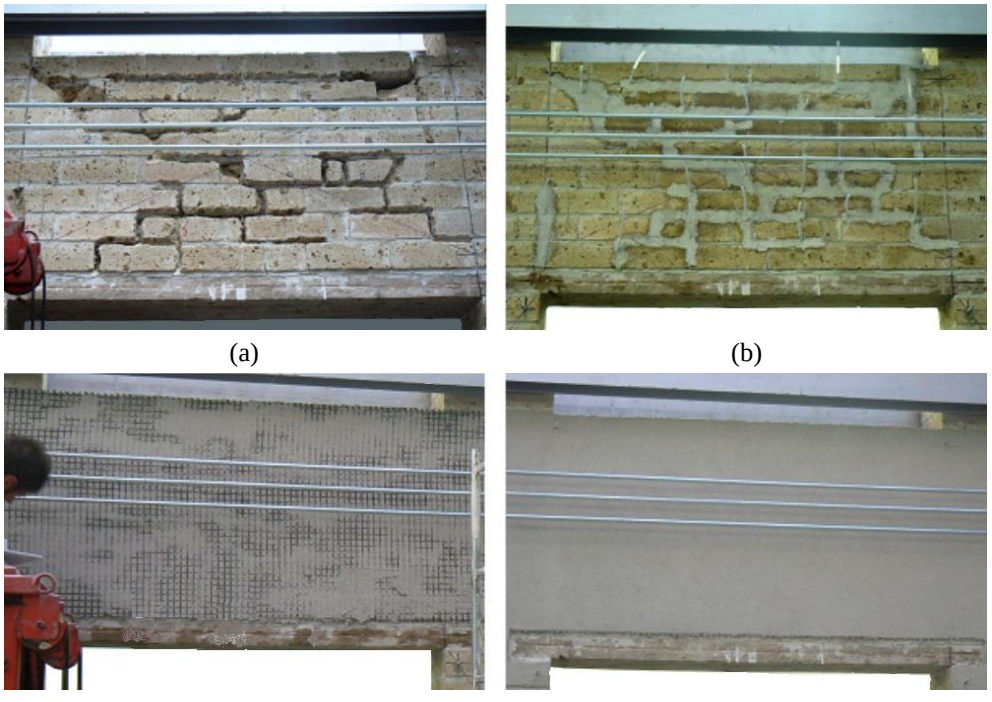

Figure C.3 (a,b) Filling of cracks with mortar injections; (c,d) application of IMG system

C.2.4. Experimental Setup and Instrumentation

Figure C.4a and C.4b show the experimental setup for lateral loading tests. Horizontal steel bars were placed at both sides of the wall during cyclic tests, in order to ensure the application of load reversals.

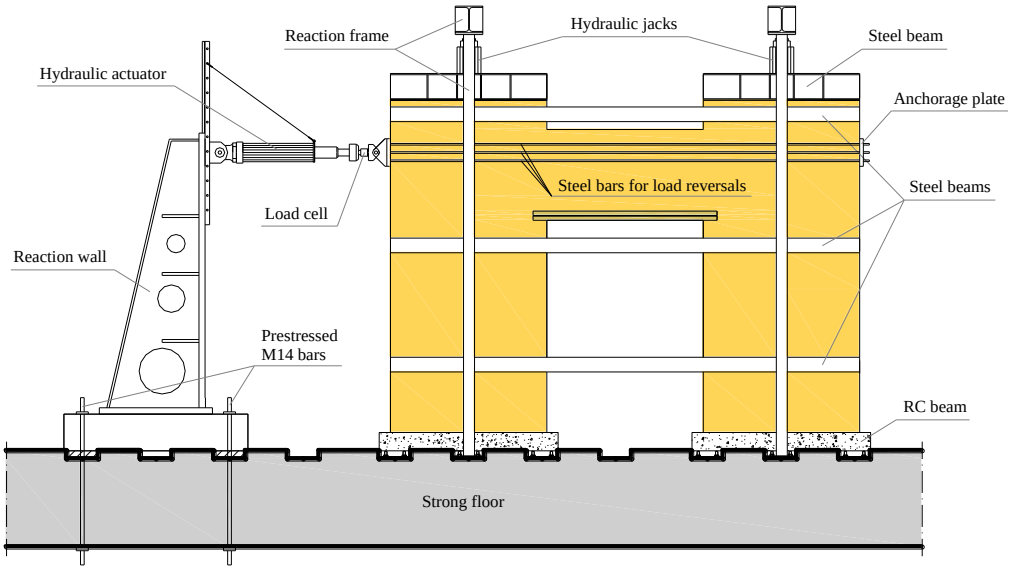

(a)

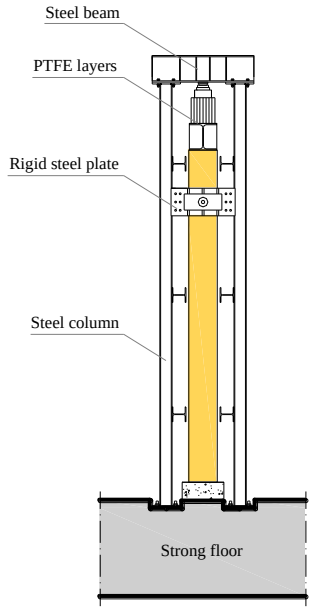

(b)

Figure C.4 Experimental setup: (a) front view and (b) lateral view

To rigidly connect the specimen with the laboratory strong floor, RC beams with dimensions 1700×310×200 mm were realised below the piers and were cast to Ω-shaped steel plates. The latter were in turn bolted to squared holes of the laboratory floor slab. Two different reaction systems were installed to apply vertical and horizontal loads to the masonry wall. The former consisted of two transverse steel frames located at the centerlines of the masonry piers and allowed to apply vertical forces simulating gravity loads on the specimen. Bidirectional hydraulic jacks with maximum capacity of 500 kN were placed over rigid steel beams and were put in contrast with the cap beams of the transverse frames. The rigid steel beams placed over the piers of the specimen were employed to get rather uniform distribution of normal stresses throughout cross-sections of the piers. Two Teflon layers were placed between the jacks and the rigid steel beams in order to avoid any frictional resisting force at their interface.

The lateral loading was applied through a horizontal servo-controlled hydraulic actuator (maximum capacity of 500 kN and stroke of ±250 mm) bolted to a non-prismatic reaction wall having a lateral load-carrying capacity of 250 kN and a corresponding horizontal displacement equal to 0.77 mm. A suspension system was installed to provide further support to the actuator. The reaction wall had a rigid base fixed to the laboratory slab through four steel bars, each pretensioned at 400 kN. The other end of the horizontal actuator was pinned at a perforated steel plate which in turn, for cyclic tests only, allowed to employ six steel bars (18 mm in diameter) aimed at applying force at the opposite end of the specimen. These bars ran along the wall spandrel at both sides of the wall. Finally, three steel beams were bolted to the columns of the transverse frames at both sides of the masonry wall to prevent potential out-of-plane failure modes. Such mechanisms were not detected during the tests due to zero eccentricity of the lateral load at the actuator plate. Since the columns were loaded in tension owing to the pushing forces at the jacks, the transverse reaction system was in a stable condition.

A load cell with capacity of 200 kN was positioned between the central part of the horizontal actuator and its rigid end plate. This cell was employed to get real-time measurements of the actual horizontal force applied to the specimen. Linear variable differential transformers (LVDTs) and string potentiometers were installed. LVDTs were placed at the end sections of the spandrel and pier panels to obtain information about flexural deformations. Potentiometers were mounted along the diagonals of the pier and spandrel panels to capture shearing deformations. The joint panels were not instrumented as their behaviour was expected to be rigid owing to the wall geometry. This assumption was confirmed by the tests.

Figures C.5a and C.5b show the arrangement of the displacement transducers on the front and back side of the specimen, respectively. Lateral displacements were measured at the opposite side of the wall through a potentiometer transducer tagged as PT#1. The displacement readings at this horizontal potentiometer were associated with the lateral force readings at the load cell, to plot the force-displacement curve for each test. Indeed, the aforementioned readings were considered to be more accurate than load and stroke readings at the horizontal actuator.

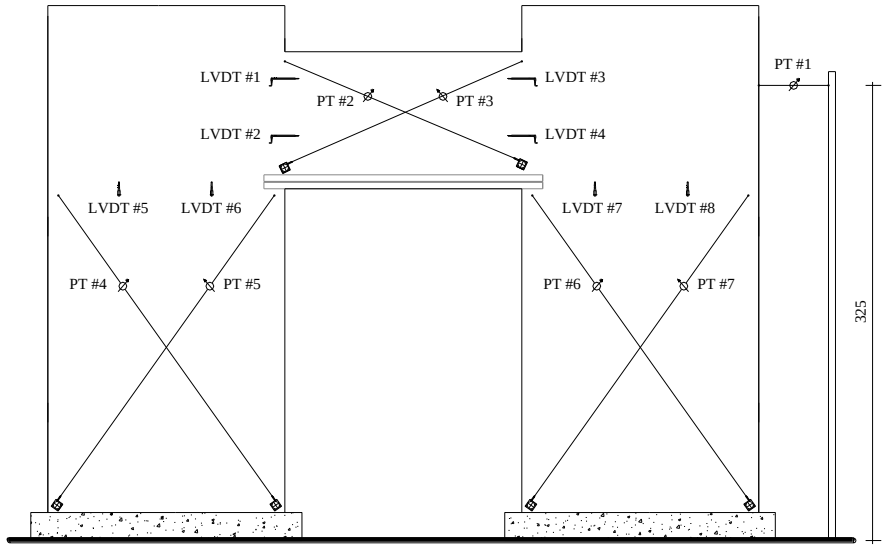

(a)

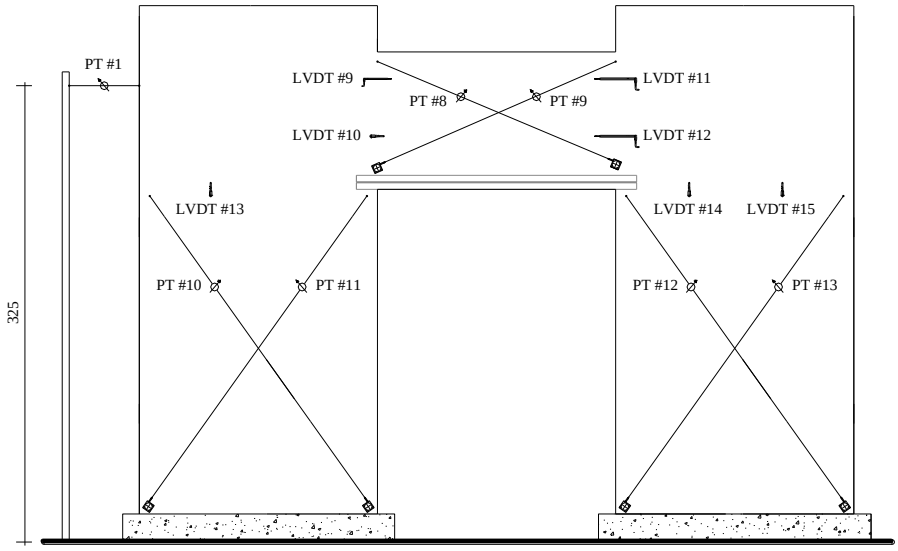

(b)

Figure C.5 Arrangement of displacement transducers on the wall: (a) front; (b) back

C.2.5. Loading Protocols

The quasi-static tests on the masonry wall consisted of two stages: in the former, vertical forces of 200 kN were applied to the piers by the hydraulic jacks to simulate gravity loads; in the latter, the wall was subjected to in-plane lateral loading through the horizontal actuator, while the vertical forces on the piers were kept constant. The tests were performed in displacement control to capture strength degradation and cumulative damage in the post-peak softening range. The lateral force was modulated by the computer program of the data acquisition system in a way to obtain the target displacement time-history. All measurements were recorded at a sampling rate of 5 Hz.

The first lateral loading test was carried out on the plain masonry wall under monotonically-increasing displacements. Two initial displacement cycles between 0.15 and 0.25 mm were applied on the specimen to reach good contrast between it and the actuator. The lateral force at the actuator was then applied so as to increase displacements at a constant rate of 10 μm/s up to a displacement reading at the actuator of 28 mm (corresponding to an interstorey drift ratio θ of about 1%).

The second test was performed under cyclic displacements up to a moderate damage level, which was defined as cracking involving not only the spandrel panel, but also a limited part of the piers. The horizontal actuator was driven at a displacement rate of 35 μm/s in a way to attain increasing amplitudes in seven different blocks and repeated three times at each amplitude peak. The increment was set to 5.6 mm, so the target maximum displacement was 39.2 mm (corresponding to θ equal to about 1.2%).

Finally, the specimen repaired with the IMG system was tested under fifteen cyclic displacement blocks up to a lateral displacement of 84 mm (corresponding to θ equal to about 2.8%). The displacement rate was set to 35 μm/s in the first seven blocks and to 70 μm/s in the last eight blocks. In Figure C.6, the time-histories programmed in the computer (input) are compared to those measured (response).

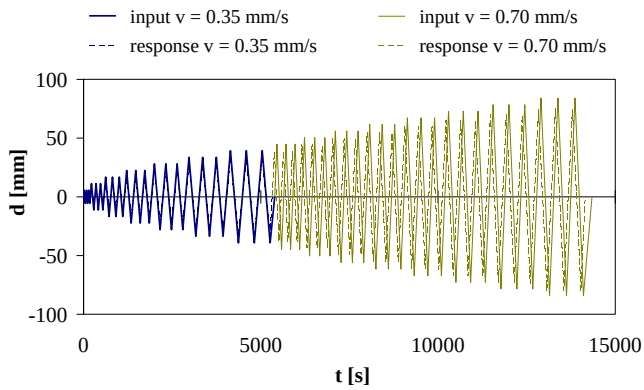

Figure C.6 Input versus response time-histories

C.3. Damage Patterns

Lateral loading on the wall caused mainly damage to the spandrel panel without involving joint panels. Figure C.7a shows the damage pattern observed after the monotonic test on the as-built wall. Vertical cracks due to flexure at the extreme sections of the spandrel panel and diagonal cracking of such a panel due to shear were first observed. Macroscopic cracking was then detected at the bases of the piers; this cracking induced rocking behaviour of larger displacements.

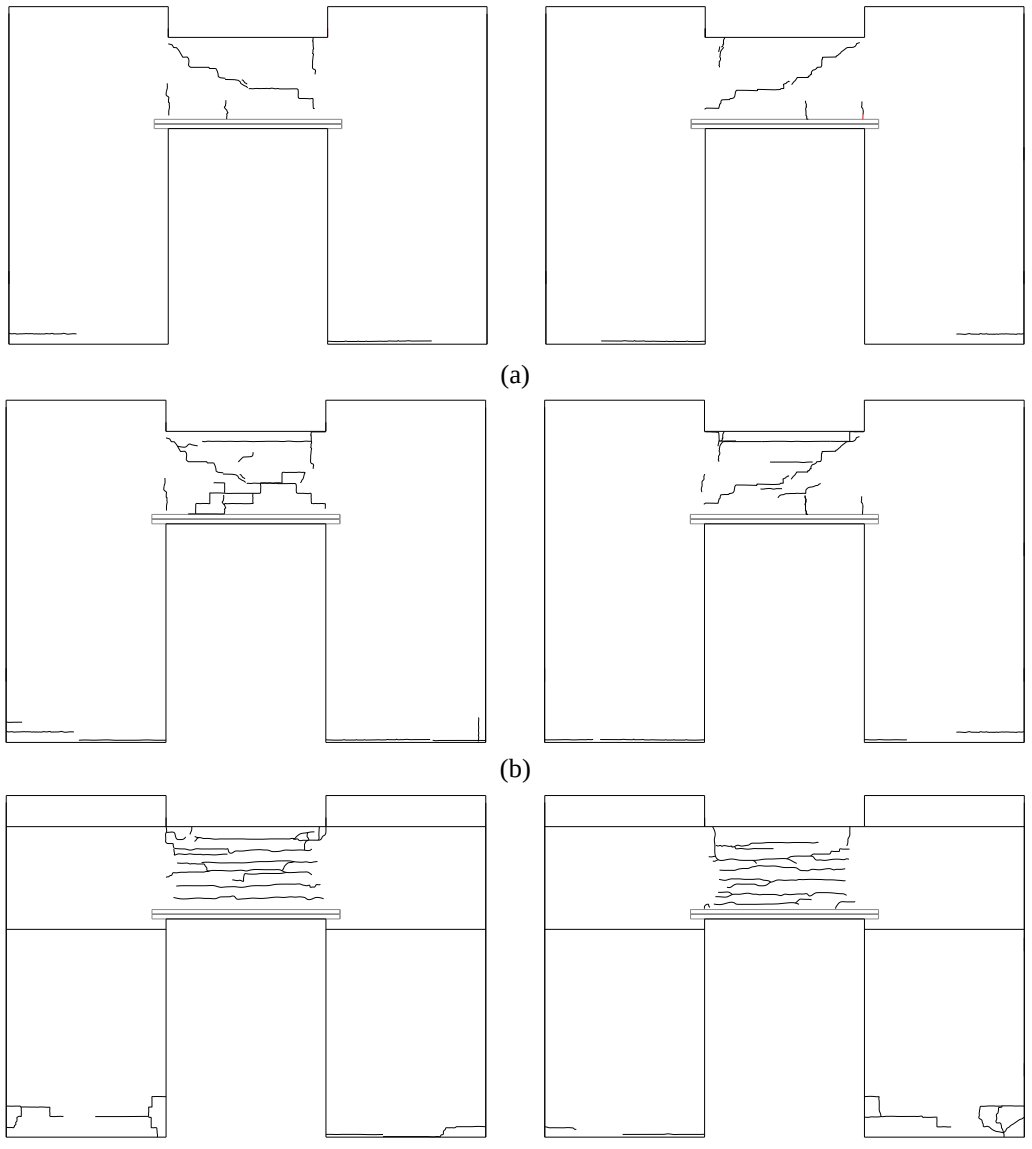

Figure C.7 Damage patterns: (a) as-built wall; (b) pre-damaged wall; (c) repaired wall

Figure C.7b demonstrates that load reversals induced horizontal cracks at the base of the piers due to rocking response, as well as extensive tensile shear failure along the other diagonal of the spandrel panel. The latter suffered shear sliding failure along the first mortar bed joint. Slight masonry crushing occurred at the compressed toes of the piers at larger displacements. The cyclic lateral loading test on the repaired wall demonstrated the effectiveness of the external reinforcement with IMG composites on both sides of weak spandrels. While rocking failure of the piers was still detected also at small displacement levels, fracture propagation in the spandrel panel diverged from the pattern observed during the previous tests resulting in spread horizontal cracking (Fig. C.7c). Extensive horizontal cracking and masonry crushing due to rocking of the piers were identified when the wall was subjected to larger displacements. At the near-collapse state, transverse splitting of the masonry was also detected in the spandrel panel. Such a failure mode consisted of vertical cracking and involved the masonry from the top to the second layer above the wooden lintel.

In all tests, the wooden lintel played a key role because it supported the masonry above and constrained the spandrel panel in transmitting the applied load between the piers. This resulted in damage accumulation in the spandrel panel also at large displacements. Damage to the spandrel panel after each test is shown in Figures C.8a, C.8b and C.8c.

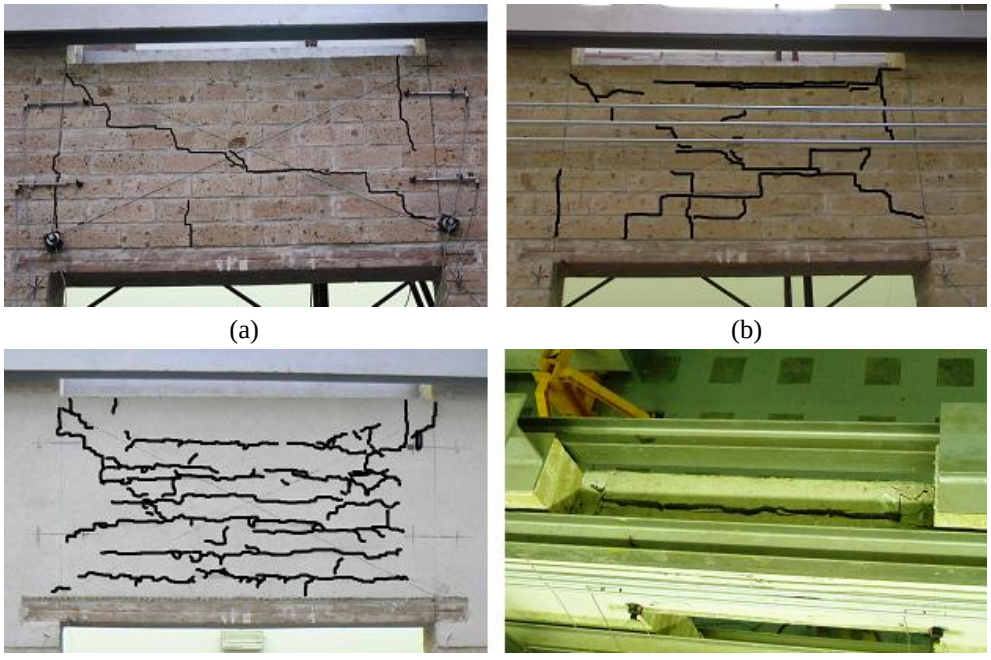

(a) (b)

(c) (d)

Figure C.8 Damage to the spandrel panel: (a) as-built wall; (b) pre-damaged wall; (c,d) repaired wall

Figure C.8d illustrates a detail of the transverse splitting which occurred at the near-collapse state of the wall. This failure mechanism has never been observed in the past for wall with openings and is currently under study.

Increasing damage to piers from the monotonic test to the second cyclic test is shown in Figures C.9a–d. Figure C.9a demonstrates a small horizontal crack at the base of the right pier (front side of the wall) due to its rocking response. Figure C.9b shows early crushing after cyclic test on the pre-damaged wall, while Figures C.9c and C.9d give a good explanation of large rocking-induced cracking with early splitting and extensive masonry crushing in the left pier (front side of the wall), respectively. Crack width at the pier base exceeded 25 mm.

An interesting view of the repaired wall at the near-collapse state is illustrated in Figure C.10a, where piers' rocking and the corresponding drift demands on the spandrel panel are particularly evident. Finally, Figure C.10b gives a better idea of the heavy damage suffered by the spandrel panel and its deformed shape at the maximum drift attained in the test.

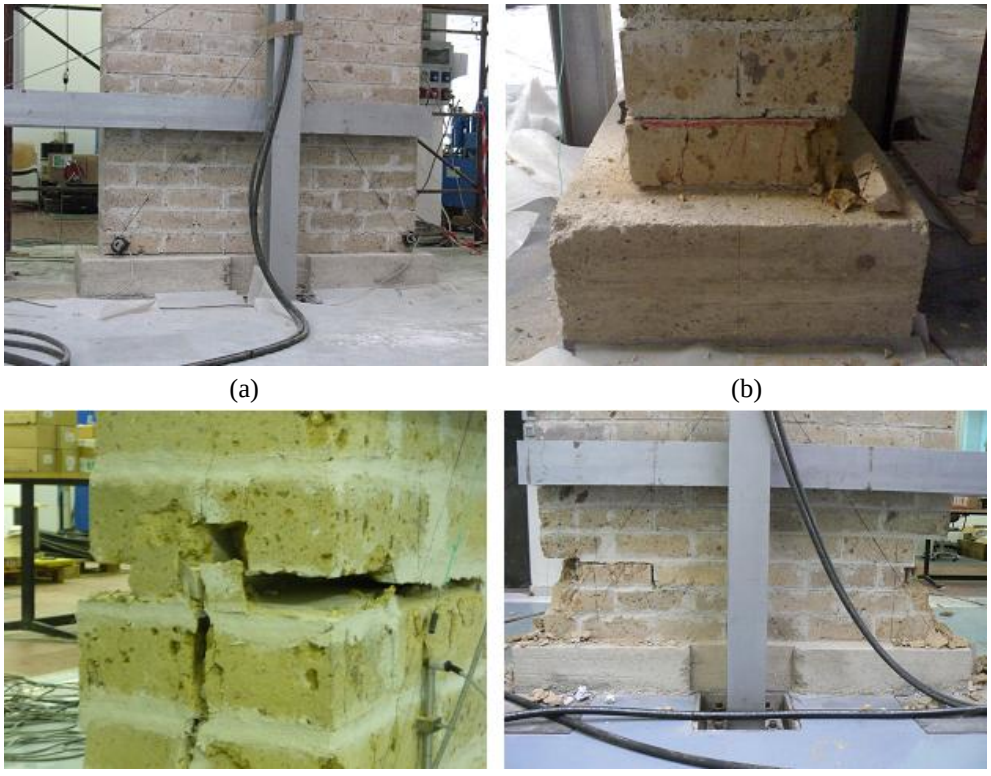

(a) (b)

(c) (d)

Figure C.9 Damage to the pier panels: (a) as-built wall; (b) pre-damaged wall; (c,d) repaired wall

(a) (b)

Figure C.10 (a) Near-collapse state of the repaired wall; (b) damage to the spandrel panel

C.4. Analysis of Experimental Force-Displacement Curves

Quasi-static testing allowed to obtain global response parameters of the masonry wall in as-built, pre-damaged, and IMG-repaired conditions. In all tests, the relationship between the resisting force and the given lateral displacement was rather linear before the occurrence of flexural cracking in the piers and the spandrel panel. As the drift demand increased, the resisting force changed in different modes depending on specimen characteristics. The cracking point in the experimental force-displacement diagrams (the envelopes for cyclic tests) was defined at a lateral stiffness reduction of 10%. The latter was captured by monitoring the ratio between the secant stiffness *K* (i.e., the ratio between the measured resisting force *H* and the given displacement *d*) and the simple moving average at each force step (Fig. C.11)[30].

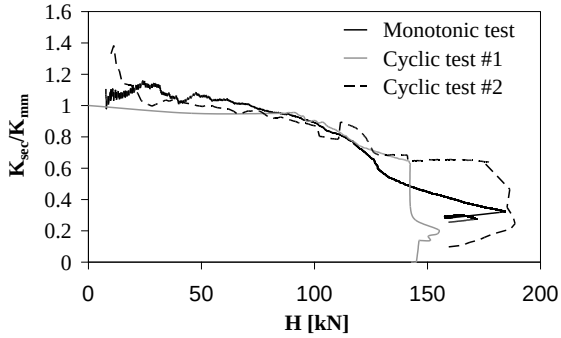

Figure C.11 Monitoring of lateral stiffness under increasing resisting force

[30] This running average (denoted as *SMA*) is typically employed in *time series analysis* and is defined as the unweighted average of data associated with a given subset of the entire data set. Other moving averages (e.g., *cumulative moving average*, *weighted moving average*, *exponential moving average*) should be employed to assign different weights to data.

In this way, significant variations in stiffness were identified and the secant lateral stiffness at cracking was defined as the ratio between the estimated cracking force H_{cr} and the relevant displacement d_{cr}.

Figure C.12 shows the experimental force-displacement diagram for the monotonic test. The lateral stiffness of the as-built wall changed significantly when flexural cracks formed at the base of the piers. This rocking-type damage could be approximately associated with the cracking force and interstorey drift ratio listed in Table C.2, whose relevant elastic stiffness is 50.76 kN/mm. As the lateral displacement increased, the stiffness of the as-built wall was rather constant up to the attainment of the maximum resisting force H_{max} = 184 kN at a displacement of 19.74 mm (i.e., θ_{Hmax} equal to 0.65%). The experimental lateral resistance confirmed the value predicted through a simplified macro-element analysis of the as-built wall (namely about 185 kN) for the minimum shear strength of masonry. At this performance state of the wall, the occurrence of diagonal cracking in the spandrel panel induced an instantaneous resistance drop of about 15%.

Table C.2 Experimental response parameters of the specimens

Specimen	H_{cr} [kN]	θ_{cr} [%]	H_{max} [kN]	θ_{Hmax} [%]	$H_{\theta max}$ [kN]	θ_{max} [%]
As-built	98.91 ($0.5H_{max}$)	0.06	184.31	0.65	171.56	0.89
Pre-damaged	97.44 ($0.6H_{max}$)	0.07	154.95	0.57	146.53	1.10
Repaired	90.55 ($0.5H_{max}$)	0.07	188.72	1.11	159.42	2.46

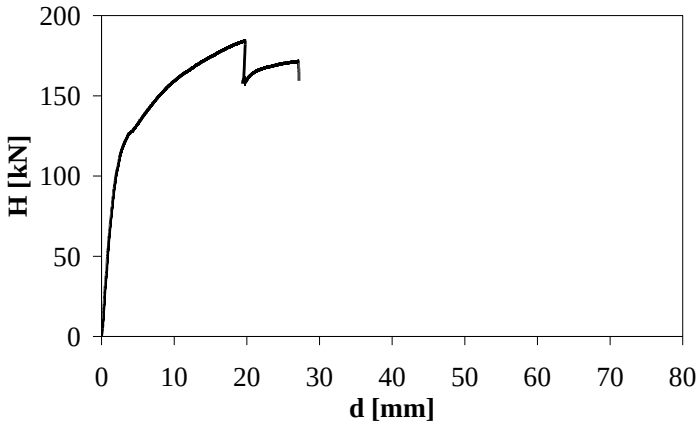

Figure C.12 Experimental force-displacement curve for monotonic test on as-built wall

At larger displacements, lateral resistance began to rise again up to a resisting force $H_{\theta max}$ = 172 kN at a displacement of 27.18 mm (i.e., θ_{max} equal to 0.89%). Strength degradation factor *SDR*, defined as the ratio between $H_{\theta max}$ and H_{max} according to Tomaževič (2000), was found to be about 0.93. It is noted that actual drifts in the post-elastic range were lower than those associated with the horizontal displacements imposed at the actuator, due to some deformability sources in the test setup (Fig. C.6).
Hysteretic force-displacement diagrams in Figures C.13 and C.14 demonstrate that global in-plane response of the wall was essentially governed by rocking motion of the piers. While this type of mechanical behaviour allowed large displacements, low residual displacements and wall re-centring, diagonal shear failure in the spandrel panel affected the maximum resistance of the wall. Indeed, no considerable differences in the global response were detected up to cracking of piers (Table C.2).

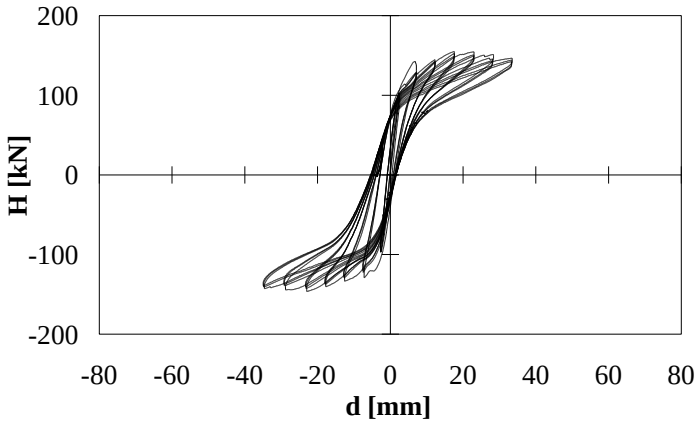

Figure C.13 Experimental force-displacement curve for cyclic test on pre-damaged wall

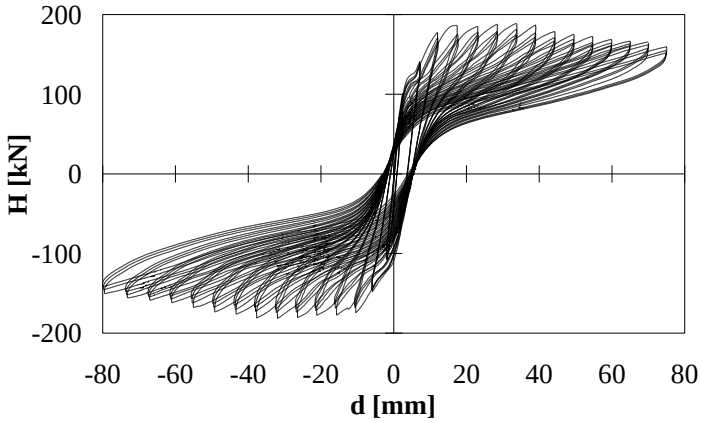

Figure C.14 Experimental force-displacement curve for cyclic test on repaired wall

The elastic stiffness was estimated in 47.89 and 44.36 kN/mm for the pre-damaged and repaired wall systems, respectively. Conversely, the maximum resistance of the pre-damaged wall was rather different from those of the as-built and repaired specimens. This outcome is clearly shown in Figure C.15, where the experimental force-displacement curve for monotonic test is compared to the envelopes of the cyclic tests.

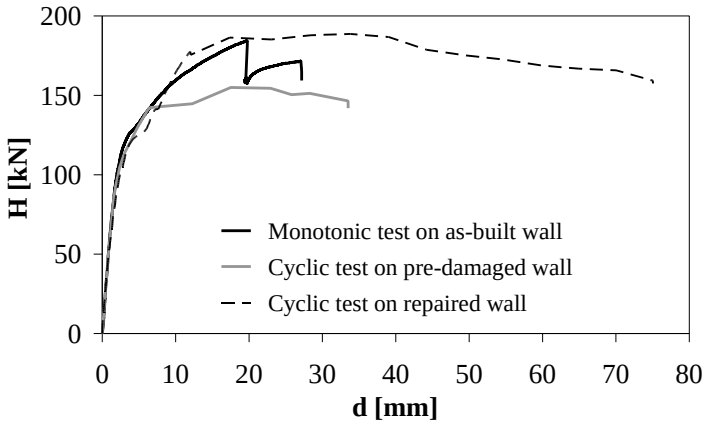

Figure C.15 Envelopes of experimental force-displacement curves

It is noteworthy that the maximum resisting force computed for the pre-damaged wall was rather equal to that computed for the as-built wall at the occurrence of diagonal cracking in the spandrel panel (that is, 157 kN). As displacement increased during the cyclic test on the pre-damaged wall, the resisting force reduced to 146 kN at a maximum displacement of 33.51 mm (i.e., θ_{max} equal to 1.10%). For the pre-damaged wall, *SDR* was then found to be 0.95 and strength degradation was caused by cyclic damage accumulation. In fact, load reversals induced diagonal shear cracking also along the other diagonal of the spandrel panel resulting in a significant loss of integrity to withstand deformations in the opposite loading orientation.

Data processing for the cyclic test on the repaired wall demonstrated that the external reinforcement with IMG composites at both sides of the spandrel allowed not only to restore the load-bearing capacity of the as-built wall, but also to shift strength degradation at larger displacement levels. Actually, *SDR* was estimated in 0.85 but it was associated with a maximum displacement of 75.06 mm (corresponding to θ_{max} of 2.46%), that is, more than two times the maximum drift imposed to the pre-damaged wall. In all tests, *SDR* was higher than the typical coded value of 0.8, which is assumed to define displacement capacity and to compute displacement demand of building structures at the life safety limit state (CEN, 2004; IMIT, 2008). The dramatic improvement in the lateral response of the pre-damaged wall can be preliminary

explained as follows: (1) the IMG system was able to bridge existing cracks of the pre-damaged wall and to ensure the lack of debonding failure at the matrix-substrate interface; (2) the failure mode of the spandrel panel changed from brittle diagonal shear cracking to ductile horizontal uniform cracking; (3) the cyclic behaviour of the composite system was quite stable; and (4) the IMG system did not induced any modification in the stiffness of the spandrel panel, and hence in the spandrel-piers interaction, so the rocking response of the piers led to large displacement capacity, allowing re-centring behaviour of the wall.

C.5. Idealisation of Experimental Force-Displacement Curves

The experimental force-displacement curves were idealised as bilinear to characterise the response of an equivalent SDOF system. The bilinear idealisation has been used by several researchers as a simplified method to assess seismic response of masonry walls in their own plane, especially under cyclic loading (Shing et al., 1989; Magenes and Calvi, 1997; Vasconcelos and Lourenço, 2009). In this study, two linearisation procedures were used to estimate ultimate force H_u, yielding interstorey drift θ_e (corresponding to d_e), elastic stiffness K_e, displacement ductility μ, overstrength ratio Ω, ductility-related strength reduction factor R_μ, and total strength reduction factor R (Table C.3).

Table C.3 Parameters of idealised SDOF system, overstrength and strength reduction factor

Specimen	H_u [kN]	θ_e [%]	K_e [kN/mm]	μ	Ω	R
As-built	162.15	0.10	50.76	8.51	1.64	6.56
	($0.88H_{max}$)					[R_μ = 4.00]
	170.86	0.19	29.45	4.68	1.73	5.00
	($0.93H_{max}$)					[R_μ = 2.89]
Pre-damaged	146.73	0.10	47.89	10.94	1.51	6.88
	($0.95H_{max}$)					[R_μ = 4.57]
	147.99	0.12	41.04	9.29	1.52	6.37
	($0.96H_{max}$)					[R_μ = 4.19]
Repaired	176.89	0.13	44.36	10.99	1.95	8.95
	($0.94H_{max}$)					[R_μ = 4.58]
	188.37	0.30	20.74	4.82	2.08	6.12
	(H_{max})					[R_μ = 2.94]

Note: For each specimen, the first and second lines refer to linearisation procedures by Tomaževič (2000) and by EC8 (CEN, 2004) and IBC (IMIT, 2008).

To compute displacement ductility as $\mu = d_u/d_e$, the ultimate displacement d_u was defined as the experimental value corresponding to the minimum strength degradation observed during the tests and hence to a resisting force reduction of 5%. This assumption derived from the fact that strength degradation was lower than that typically considered in seismic codes (that is, 20%) and different values of *SDR* were computed for the tested specimens. It is also underlined that the bilinear idealisation for the as-built and pre-damaged walls was aimed at reaching some hints on displacement ductility and strength reduction factors, being they related to moderate damage levels. The computation of these seismic capacity parameters was useful especially to compare the global performances of the tested models and to discuss current coded values.

The first linearisation procedure was based on the assumption of elastic stiffness equal to the experimental secant stiffness at cracking. The latter was equal to $0.5H_{max}$ for the as-built and repaired walls, and $0.6H_{max}$ for the pre-damaged wall. Yielding displacement was computed by imposing equal areas below the actual and idealised curves (Tomaževič, 2000). The ultimate force of the idealised system was derived as the product of the assumed elastic stiffness for the computed yielding displacement. In this way, the ultimate resistance of the idealised envelope was evaluated by assuming equal energy dissipation capacity of the actual and idealised wall systems.

The second bilinear idealisation procedure used in this study is reported in IBC (IMIT, 2008) and EC8 (CEN, 2004). These building codes suggest to assume cracking at $0.7H_{max}$. The elastic stiffness is then computed as the ratio between the idealised cracking force and the corresponding displacement identified on the actual force-displacement curve. The yielding displacement is derived by assuming equal areas below the actual and idealised force-displacement diagrams. The idealised force-displacement diagrams derived for the tested specimens are shown in Figures C.16, C.17, and C.18.

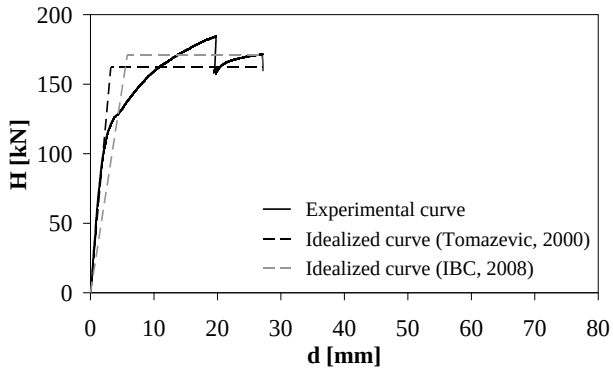

Figure C.16 Bilinear idealisation of experimental curves for monotonic test on as-built wall

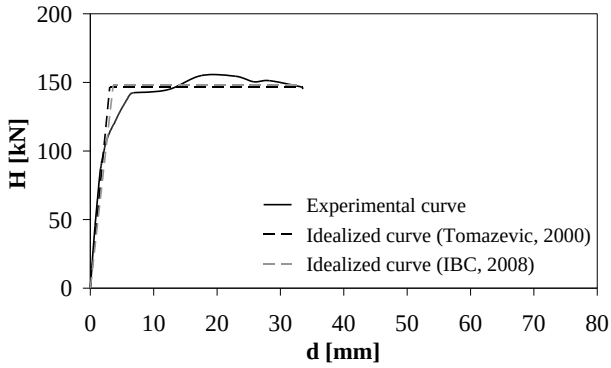

Figure C.17 Bilinear idealisation of experimental curves for cyclic test on pre-damaged wall

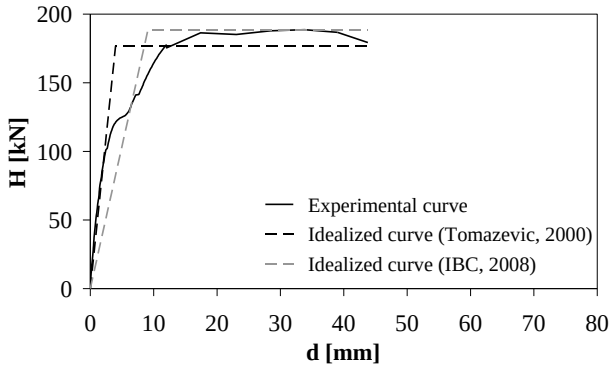

Figure C.18 Bilinear idealisation of experimental curves for cyclic test on repaired wall

The ratio between the ultimate and maximum resisting forces (values in round parentheses in Table C.3) was found to be 0.88-0.93 for the as-built wall, 0.95-0.96 for the pre-damaged wall, and 0.94-1.00 for the repaired wall.

The first interval related to the as-built wall is consistent with past experimental results on URM walls by, among others, Sheppard and Lutman (1988), which found a mean value equal to 0.9. Different predictions of ultimate force, interstorey drift ratio at yielding, and displacement ductility were obtained for the as-built and repaired walls through the bilinear idealisation procedures (Table C.3). Conversely, their values were quite similar for the pre-damaged wall. For the as-built and repaired walls, secant stiffness at $0.7H_{max}$ was about one-half of its counterpart used in the first bilinear idealisation procedure (i.e., the estimate of the experimental stiffness at cracking). This was not the case of the pre-damaged wall, since the elastic stiffnesses used in the two bilinear idealisation procedures were very similar due to the presence of a post-cracking branch with high stiffness. As a result, the elastic stiffness predicted through IBC for the pre-damaged wall was found to be apparently higher than the relevant

values computed for the other specimens. The latter were characterised by lower post-cracking stiffness. The clear presence of a post-cracking branch led to different, even if rather high, values of displacement ductility for the as-built and repaired walls. It is emphasised that Tomaževič (2000) proposed a trilinear idealisation of experimental force-displacement curves to improve consistency between the SDOF system representation and the actual structure response.

The overstrength factor of the wall system, denoted as Ω in Table C.3, was defined as the ratio between the ultimate and cracking forces. Its average values were 1.7, 1.5, and 2.0 for the as-built, pre-damaged, and repaired walls, respectively. It is noted that IBC provides a value of 1.4 for single-storey URM buildings and 1.3 for single-storey RM buildings.

Strength reduction factor was computed for each tested specimen. According to IBC and Uang (1991), the total strength reduction factor R to be used in linear seismic analysis was defined as ductility-related strength reduction factor R_μ (bracketed values in Table C.3) multiplied by Ω. The former factor was evaluated as:

$$R_\mu = \sqrt{2\mu - 1} \tag{C.1}$$

according to the 'equal energy rule' typically assumed for low-period structures like masonry buildings (Uang, 1991). Although the as-built and pre-damaged walls were subjected to medium displacement demands, their ductility-related strength reduction factors were quite high. It is worth noting that the average values of R_μ for the as-built and damaged walls were 3.4 and 4.4 respectively, while an average value equal to 3.8 was found for the repaired wall. Conversely, IBC provides R_μ-values of 2.0 for URM buildings and 2.5-3.0 for RM buildings. Instead, EC8 provides a strength reduction factor equal to 1.5-2.5 for earthquake-resistant URM buildings, 1.5 for URM buildings not designed for seismic actions, and 2.5-3.0 for RM buildings. In this context, it is emphasised that the bilinear idealisation procedure by Tomaževič (2000) was found to be more appropriate to capture the main features of the global nonlinear response of the walls, especially for the pre-damaged wall.

Although both displacement ductility and strength reduction factor estimated for the as-built and pre-damaged walls are not to be considered as actual 'supply' parameters, all linearisation procedures used in this study led to strength reduction factors higher than those provided by EC8 and IBC. Regardless of the particular linearisation method used in this study, the benefits of the IMG strengthening system were clear not only in terms of high supply displacement ductility, but also in terms of providing high strength reduction factors. The estimation of these capacity parameters was affected by the truncation of the experimental force-displacement curve at a lateral displacement significantly lower than the maximum displacement attained during the test. The

effectiveness of the IMG system can be fully expressed by considering the entire post-peak degrading branch (i.e., a force reduction of about 15%). In this case, the linearisation procedure by Tomaževič (2000) led to $\mu = 19.16$, $R_\mu = 6.11$, $\Omega = 1.92$, and $R = 11.73$, while the procedure provided by EC8 and IBC led to $\mu = 8.67$, $R_\mu = 4.04$, $\Omega = 1.98$, and $R = 8.02$. These values are significantly higher than those presented in Table C.3 for the same force reduction percentage (i.e., 5%).